SJKFU

المجلة العلمية لجامعة الملك فيصل

The Scientific Journal of King Faisal University

2021, 22, 2

العلوم الأساسية والتطبيقية

Basic and Applied Sciences

ISSN: 1658-0311 Online ISSN: 1658-8371

في هذا العدد:

In this issue:

وصف المجلة

تصدر جامعة الملك فيصل مجلتين علميتين محكمتين نصف سنوية وذات "الوصول المفتوح". الأولى هي "المجلة العلمية لجامعة الملك فيصل: العلوم الإنسانية والإدارية" (ردمد مطبوع: 1319-6944، ردمد إلكتروني: ×838-1658)، والتي تصدر في مارس وسبتمبر وهي مسجلة في قاعدة بيانات معامل التصنيف العربي. الثانية هي "المجلة العلمية لجامعة الملك فيصل: العلوم الأساسية والتطبيقية" (ردمد مطبوع: 0311-1658، ردمد إلكتروني: 8371-1658)، والتي تصدر في يونيو وديسمبر وهي مفهرسة في سكوبس. بدأ إصدار المجلتين في عام 1420هـ (2000م)، تحت إشراف المجلس العلمي للجامعة. أول رئيس لهيئة التحرير أ.د. خالد سعد آل عبدالسلام (12/4/1419هـ)، تلاه أ.د. عادل إبراهيم العفالق (12/6/1421هـ)، عقبه د. محمد سعد الوصالي (17/7/1432هـ)، وجاء بعده أ.د. غازي فيصل بسيوني (11/1/1433هـ)، وحالياً أ.د. عبدالرحمن عيسى الليلي (5/5/1441هـ).

رئيس الجامعة

محمد عبدالعزيز العوهلي، جامعة الملك فيصل، السعودية

وكيل الجامعة للدراسات العليا والبحث العلمي

ماجد عادي الشمري، جامعة الملك فيصل، السعودية

رئيس هيئة التحرير

عبدالرحمن عيسى الليلي، جامعة الملك فيصل، السعودية

المحررون الاستشاريون

شار سعد الشهري، جامعة الملك فيصل، السعودية
ديفيد إل ستولوف، جامعة ولاية كونيتيكت الشرقية، الولايات المتحدة الأمريكية
دوناتيلا بيرسيكو، المجلس الوطني للبحوث، إيطاليا
هوانسو لي، جامعة دانكوك، كوريا الجنوبية
أنطونيلا ناجي، جامعة فاسيلي غولديس الغربية بأراد، رومانيا
كريستين باول، جامعة كاليفورنيا اللوثرية، الولايات المتحدة الأمريكية
محمد سانتالي، جامعة موريشيوس، موريشيوس
مايك جوي، جامعة وارويك، المملكة المتحدة
سي جون ميكر، جامعة أريزونا، الولايات المتحدة الأمريكية
بشيرة طعمة، جامعة روان، فرنسا
سام محمد، مدرسة إدارة الأعمال الدولية، هنغاريا
خالد عبدالله الهديب، جامعة الملك فيصل، السعودية
شاهر ربحي سعيد عليان، جامعة صحار، سلطنة عمان
فيصل قريشي، المركز الجامعي بآفلو الأغواط، الجزائر
ماريا كريستينا لوبيز دي لا مدريد، جامعة غوادالاخارا، المكسيك
نفيسة أفولاكي أديدوكون شيتو، جامعة فاونتن أوسوجبو، نيجيريا
أوبانغا سامبو، جامعة منغوليا الوطنية، منغوليا
كارولين مونتاجو، متقاعدة، المملكة المتحدة
راديم بادوسيك، جامعة أوستارفا، جمهورية التشيك
عبدالرؤوف عبدالوهاب العتيبي، جامعة الملك فيصل، السعودية
هيلين سارة فارلي ، جامعة جنوب كوينزلاند ، أستراليا
إيزابيلا إم فينتر ، جامعة وسترن كيب ، جنوب إفريقيا
وصفي محمد الخزاعله، جامعة اليرموك، الأردن
كارولين مونتاجو، متقاعدة، المملكة المتحدة
راديم بادوسيك، جامعة أوستارفا، جمهورية التشيك
سو جريجوري ، جامعة نيو إنجلاند ، أستراليا
جمال أحمد عباس، جامعه الكوفه، العراق
وائل محمد أبو المكارم الديب، جامعة الملك فيصل، السعودية
مصطفى محمد علي الحارونى، جامعة حلوان، مصر
ابراهيم محمد الفكي احمد، جامعة وادي النيل، السودان
الحبيب كشيدة الدرويش، جامعة الملك فيصل، السعودية
بسام حسن زاهر، جامعة تشرين، سوريا
هاني أمين الصاوي مصطفى، جامعة الملك فيصل، السعودية
معن علي احمد الخطيب، جامعة فلسطين التقنية، فلسطين
مجذوب رحمة الله عامر، جامعة الملك فيصل، السعودية
يوسف يعقوب هلال، جامعة الموصل، العراق
أحمد محمد الشريف، جامعة الملك فيصل، السعودية

مديرو التحرير

عادل مصطفى أبو سلامة، جامعة الملك فيصل، السعودية
علي خليفة عبداللطيف، جامعة الملك فيصل، السعودية
عبدالرحيم فتحي إسماعيل، جامعة الملك فيصل، السعودية

مساعدو التحرير

فاضل محمد العامر، جامعة الملك فيصل، السعودية
عبد رب الأمير سلمان البوعلي، جامعة الملك فيصل، السعودية
حسين معتوق الهدلق، جامعة الملك فيصل، السعودية
إبراهيم جواد العبدالله، جامعة الملك فيصل، السعودية
صلاح عبدالعزيز المحيميد، جامعة الملك فيصل، السعودية
سلطان أحمد الدحيحي، جامعة الملك فيصل، السعودية

المراسلات العامة

رئيس هيئة التحرير، المجلة العلمية لجامعة الملك فيصل
ص. ب 400 الاحساء 31982، المملكة العربية السعودية
00966135895238، 00966135895237
scijkfu@kfu.edu.sa

Description

King Faisal University has two open-access refereed journals published bi-annually. The first is 'The Scientific Journal of King Faisal University: Humanities and Management Sciences' (ISSN: 1319-6944, E-ISSN: 1658-838x), issued in March and September and named in the Arab Impact Factor. The second is 'The Scientific Journal of King Faisal University: Basic and Applied Sciences' (ISSN: 1658-0311, E-ISSN: 1658-8371), which is published in June and December and indexed in Scopus. The two journals were founded in 2000 under the guidance of the Scientific Council of the University. Editors-in-chief are as follows: Prof. Khalid S. Al Abdulsalam (2000-2), Prof. Adel I. Al Afaleq (2002-14), Dr Muhammed S. Al Wasli (2014-15), Prof. Ghazi F. Basiouni (2015-2020) and Prof. Abdulrahman E. Al Lily (2020-present).

President

Mohammad Al Ohali, King Faisal University, Saudi Arabia

Vice-Rector for Higher Studies and Scientific Research

Majed Alshamari, King Faisal University, Saudi Arabia

Editor-in-Chief

Abdulrahman Al Lily, King Faisal University, Saudi Arabia

Consulting Editors

Shar Saad Al-Shihry, King Faisal University, Saudi Arabia
David L. Stoloff, Eastern Connecticut State University, USA
Donatella Persico, National Research Council, Italy
Hwansoo Lee, Dankook University, South Korea
Antoanela Naaji, Vasile Goldis Western University of Arad, Romania
Christine Powell, California Lutheran University, USA
Mohammad Santally, University of Mauritius, Mauritius
Mike Joy, University of Warwick, UK
C. June Maker, University of Arizona, USA
Bachira Tomeh, Université de Rouen, France
Sam Mohamad, International Business School (IBS), Hungary
Khalid A. Alhudaib, King Faisal University, Saudi Arabia
Shaher Rebhi Said Elayyan, Sohar University, Oman
Korrichi Fayçal, University Center of Aflou Laghouat, Algeria
María Cristina López de la Madrid, University of Guadalajara, Mexico
Nafisat Afolake Adedokun-Shittu, Fountain University Osogbo, Nigeria
Uyanga Sambuu, National University of Mongolia, Mongolia
Caroline Montagu, Retired, UK
Radim Badosek, University of Ostrava, Czech Republic
A. Raouf A. Wahab Alotaibi, King Faisal University, Saudi Arabia
Helen Sara Farley, University of Southern Queensland, Australia
Isabella M. Venter, University of the Western Cape, South Africa
Wasfi Mohammad Alkhazaleh, Yarmouk University, Jordan
Caroline Montagu, Retired, UK
Radim Badosek, University of Ostrava, Czech Republic
Sue Gregory, University of New England, Australia
Jamal Ahmed Abbass, University of Kufa, Iraq
Wael Mohamed Abou Elmakarem El-Deeb, King Faisal University, Saudi Arabia
Mostafa M Ali Elharony, Helwn University, Egypt
Ibrahim Mohamed Alfaki Ahmed, Nile Valley University, Sudan
Habib Kechida Derouiche, King Faisal University, Saudi Arabia
Bassam Hassan Zaher, Tishreen University, Syria
Hany Amin Elsawy Mostafa, King Faisal University, Saudi Arabia
Maan Ali Ahmad Alkhateeb, Palestine technical University, Palestine
Majzoub Alamir, King Faisal University, Saudi Arabia
Yousif Yakoub Hilal, Mousul University, Iraq
Ahmed Ech-Cherif, King Faisal University, Saudi Arabia

Managing Editors

Adel Mostafa Abousalama, King Faisal University, Saudi Arabia
Ali Khaleifa Abdullatif, King Faisal University, Saudi Arabia
Abdelrahim Fathy Ismail, King Faisal University, Saudi Arabia

Editorial Assistants

Fadel Mohammad Al-Amer, King Faisal University, Saudi Arabia
Abd Rab Alameer S. Al-Boali, King Faisal University, Saudi Arabia
Husain Matouq Al-Hadlag, King Faisal University, Saudi Arabia
Ibrahim Jawad Al-Abdullah, King Faisal University, Saudi Arabia
Salah Abdulaziz Al-Mohameed, King Faisal University, Saudi Arabia
Sultan Ahmad Aldohihi, King Faisal University, Saudi Arabia

Correspondence

Editor-in-Chief, Scientific Journal of King Faisal University
P.O. Box 400 Al Ahsa, 31982, Saudi Arabia
00966135895238, 00966135895237
scijkfu@kfu.edu.sa

Table of Contents

جدول المحتويات

المجلة العلمية لجامعة الملك فيصل
The Scientific Journal of King Faisal University

العلوم الأساسية والتطبيقية
Basic and Applied Sciences

Generalized Groups

Khaled Ahmed Ali Aldwoah
Mathematics Department, Faculty of Science, Islamic University of Madinah, Saudi Arabia

الزمر المعممة

خالد أحمد علي الدوه
قسم الرياضيات، كلية العلوم، الجامعة الإسلامية، المدينة المنورة، المملكة العربية السعودية

LINK الرابط	RECEIVED الاستقبال	ACCEPTED القبول	PUBLISHED ONLINE النشر الإلكتروني	ASSIGNED TO AN ISSUE الإحالة لعدد
https://doi.org/10.37575/b/sci/0071	29/12/2020	05/03/2021	05/03/2021	01/12/2021

NO. OF WORDS عدد الكلمات	NO. OF PAGES عدد الصفحات	YEAR سنة العدد	VOLUME رقم المجلد	ISSUE رقم العدد
2695	4	2021	22	2

ABSTRACT

The aim of this paper is to generalize the concept of a group where the triple (G, E, ⋆) represents a generalized group if G is a nonempty set, E represents an equivalence relation defined on G and the operation ⋆ is a function of G×G satisfying some conditions. The paper also reveals some concepts and provides some examples related to generalized groups.

الملخص

يهدف البحث إلى تعميم مفهوم الزمرة، حيث يمثل الثلاثي (G,E,⋆) زمرة معممة إذا كانت G مجموعة غير خالية و E تمثل علاقة تكافؤ معرفة على G والعملية ⋆ دالة على G×G تحقق بعض الشروط. كما يكشف البحث عن بعض المفاهيم ويقدم بعض الأمثلة المرتبطة بالزمر المعممة.

KEYWORDS
الكلمات المفتاحية
Generalized subgroup, generalized semigroup, equivalence relation
الزمرة الجزئية المعممة، شبه الزمرة المعممة، علاقة التكافؤ

CITATION
الإحالة
Aldwoah, K.A.A. (2021). Generalized groups. *The Scientific Journal of King Faisal University: Basic and Applied Sciences*, **22**(2), 1–4.
DOI: 10.37575/b/sci/0071

1. Introduction

A generalized group has a deep physical background in the unified gauge theory, see (Molaei, 2000). The concept of equivalence relations will be used to generalize the concept of a group which has wide applications in our life. The aim of this work is to introduce the concepts of generalized groups, generalized subgroups, and generalized group homomorphisms.

This work will open a new area for scientific research. Indeed, the concept that had been generalized in this work will be the beginning of a lot of scientific research based on this generalized concept.

Historically, there have been several attempts to generalize the concept of group. Clifford characterized the semigroups that admit relative inverse (Clifford, 1941). A semigroup $(S,\star)$ is called a *semigroup admit relative inverses* if for any $x \in S$ there exist $e, y \in S$ such that $e \star x = x \star e = x$ and $x \star y = y \star x = e$. Later, these semigroups were called Clifford semigroups.

Molaei introduced generalized groups, as a class of algebras of interest in physics (Molaei, 1999). A semigroup $(S,\star)$ is called a *generalized group* if for any $x \in S$ there exist unique elements $e(x), x^{-1} \in S$ such that $e(x) \star x = x \star e(x) = x$ and $x \star x^{-1} = x^{-1} \star x = e(x)$. We call these semigroups Molaei generalized groups.

It is known that Molaei generalized groups are tools for constructions in unified geometric theory and electroweak theory. Araújo and Konieczny showed that Molaei generalized groups are the completely simple semigroups (Araújo and Konieczny, 2004; see also Akinmoyewa, 2009).

In this work, we generalize the concept of group using different meanings from Vagner (Vagner, 1952) generalized groups (Santilli, 1979), Clifford semigroups (Clifford, 1941; Clifford and Preston, 1961) and Molaei generalized groups (Molaei 1999 and 2000). Molaei generalized group will be a special case of generalized group which has been introduced in this work.

This paper is organized as follows:

- **In Section 2:** We begin by generalize the concept of a group as follows. Roughly speaking, a triple $(G, E, \star)$ is called a generalized group if G is a nonempty set, E is an equivalence relation on G, and $\star$ is a function on $G \times G$ that satisfies some conditions. New concepts are introduced as well as new examples of generalized groups. In addition, we investigate if some results that are true in classical group theory are also true in generalized groups.
- **In Section 3:** We continue our discussion of the basic properties of generalized groups with special attention to generalized subgroups.
- **In Section 4:** We consider one of the most important fundamental ideas of algebra, homomorphisms of generalized groups.

2. Generalized Groups

In this section, we generalize the classical definition of a group. Throughout this work, we consider a triple of the form $(G, E, \star)$, where G is an arbitrary nonempty set, E is an equivalence relation on G, and $\star$ is a function defined from $G \times G$ to a set X containing G.

The following definition widens the scope of groups and preserves the classical ones as special cases.

2.1. Definition:

A triple $(G, E, \star)$ is a *generalized group* if it satisfies the following conditions:

i. Closure: $x \star y \in G$ for any $x, y \in G$.
ii. Associativity: $x \star (y \star z) = (x \star y) \star z$ for any $x, y, z \in G$.
iii. Identity: for any $t \in G$, there is $e(t) \in [t]$ such that $e(t) \star x = x \star e(t) = x$ for any $x \in [t]$.
iv. Inverses: for any $t \in G$ and $x \in [t]$ there is $x^{-1} \in [t]$ such that $x \star x^{-1} = e(t)$.

Where $[t]$ denotes the equivalence class that contains $t \in G$.

A generalized group $(G, E, \star)$ with E begin the universal equivalence relation on G; *i.e.* $E = G \times G$, is a group. Throughout this work, one can see that all concepts (generalized subgroups, generalized normal subgroups, generalized homomorphisms, etc.) with respect to a generalized group $(G, E, \star)$ where E is the universal equivalence relation on G, coincide with the corresponding ones with respect to the classical concepts.

Often, if there is no confusion concerning E and $\star$, we denote

Corresponding Author: Khaled Ahmed Ali Aldwoah aldwoah@iu.edu.sa ,00966551976509 المؤلف المراسل: خالد أحمد علي الدوه

$(G, E, \star)$ simply by stating G.

The following proposition says that from a collection of pairwise disjoint groups we can construct a generalized group. But, in the main, a generalized group is not just a union of a collection of pairwise disjoint groups, see 2.5. Example.

2.2. Proposition:

Assume that $\{(G_i, \star_i)\}_{i\in\Lambda}$ is a collection of pairwise disjoint groups (resp. semigroups), i.e. $G_i \cap G_j = \emptyset$ for any $i, j \in \Lambda$ with $i \neq j$ and E is an equivalence relation on $\cup_{i\in\Lambda} G$ defined by xEy iff $x, y \in G_i$ for some $i \in \Lambda$. If we define $\star$ on $\cup_{i\in\Lambda} G \times \cup_{i\in\Lambda} G$ by $x \star y := x \star_i y$ if $x, y \in G_i$ for some $i \in \Lambda$, and $x \star y := x$ if $x \in G_i, y \in G_j, i \neq j$ for some $i, j \in \Lambda$. Then, the triple $(\cup_{i\in\Lambda} G, E, \star)$ is a generalized group.

The following proposition shows that Molaei's generalization is a special case of the generalization detailed in this article.

2.3. Proposition:

Assume that $(G, \star)$ is a Molaei generalized group. Let E be an equivalence relation defined on G by xEy iff $e(x) = e(y)$ for any $x, y \in G$. Then, $(G, E, \star)$ is a generalized group.

In Adeniran *et al.* (2009), they show that an abelian Molaei generalized group is a group. This is not true in the generalization detailed in this article as shown in 2.8 Example.

2.4. Proposition:

For a generalized group G and $x \in G$, we have the following:

i. $[x] = [x^{-1}] = [e(x)]$.
ii. The identity element $e(x)$ of $[x]$ is unique.
iii. The inverse x^{-1} is unique.
iv. For any $x, y \in G$, $e(x) = e(y)$ iff $[x] = [y]$.
v. $e(e(x)) = e(x^{-1}) = e(x)$.

Proof. (i) It is clear, since $e(x), x^{-1} \in [x]$.

(ii) Suppose that $e_1(x)$ and $e_2(x)$ are both identities elements of x. Then, for $t \in [x]$, $t = te_1(x) = e_1(x)t$ and $t = te_2(x) = e_2(x)t$. Since, $e_1(x), e_2(x) \in [x]$ and $e_1(x), e_2(x)$ are identities of $[x]$, $e_1(x) = e_1(x)e_2(x) = e_2(x)e_1(x)$ and $e_2(x) = e_2(x)e_1(x)$ which implies that $e_1(x) = e_2(x)$.

(iii) Suppose x has two inverses $y, z \in [x]$. Then, $y = ye(y) = ye(x) = yxz = e(x)z = e(z)z = z$.

(iv) Let $e(x) = e(y)$. Since $e(x) \in [x]$ and $e(y) \in [y]$, $e(x) = e(y) \in [x] \cap [y]$ and hence $[x] = [y]$. Conversely, if $[x] = [y]$, then by uniqueness of the identity $e(x) = e(y)$.

(v) The proof is directly obtained from part (iv), since $e(x), x^{-1} \in [x]$.

In the following, we introduce some examples of generalized groups which are not groups.

2.5. Example:

Consider the set $\mathbb{Z}_{12} := \{0,1,2,\cdots,11\}$. Define the equivalence relation E on $\mathbb{Z}_{12}$ by rEs iff there exists $k \in \mathbb{Z}$ such that $r = s +_{12} 3k$ for any $r, s \in \mathbb{Z}_{12}$. The equivalence classes of this relation are $[0] = \{0,3,6,9\}, [1] = \{1,4,7,10\}, [2] = \{2,5,8,11\}$. Let $\overline{t} := \min[t]$ for $t \in \mathbb{Z}_{12}$ and $k_t := \frac{t-\overline{t}}{3}$ for any $t \in \mathbb{Z}_{12}$. Then, $\overline{0} = 0$, $\overline{1} = 1, \overline{2} = 2, \overline{3} = 0, \overline{4} = 1, \overline{5} = 2, \overline{6} = 0, \overline{7} = 1, \overline{8} = 2, \overline{9} = 0$, $\overline{10} = 1$, $\overline{11} = 2$ and $k_0 = 0, k_1 = 0, k_2 = 0, k_3 = 1, k_4 = 1, k_5 = 1, k_5 = 1, k_6 = 2, k_7 = 2, k_8 = 2, k_9 = 3, k_{10} = 3, k_{11} = 3$. Assume that the binary operation $\star$ on $\mathbb{Z}_{12}$ is defined by

$$r \star s = \overline{r} +_{12} 3(k_r + k_s) \; for \; r, s \in \mathbb{Z}_{12}.$$

From Table 1, the triple $(\mathbb{Z}_{12}, E, \star)$ is a generalized group with $\overline{t}$ the identity element of $[t]$ and $0^{-1} = 0, 1^{-1} = 1, 2^{-1} = 2, 3^{-1} = 9, 4^{-1} = 10, 5^{-1} = 11, 6^{-1} = 6, 7^{-1} = 7, 8^{-1} = 8, 9^{-1} = 3, 10^{-1} = 4, 11^{-1} = 5$. One can check easily that $(\mathbb{Z}_{12}, \star)$ is not a group.

Table 1: The binary operation $\star$ on $\mathbb{Z}_{12}$.

★	0	1	2	3	4	5	6	7	8	9	10	11
0	0	0	0	3	3	6	6	6	6	9	9	9
1	1	1	1	4	4	7	7	7	7	10	10	10
2	2	2	2	5	5	8	8	8	8	11	11	11
3	3	3	3	6	6	9	9	9	9	0	0	0
4	4	4	4	7	7	10	10	10	10	1	1	1
5	5	5	5	8	8	11	11	11	11	2	2	2
6	6	6	6	9	9	0	0	0	0	3	3	3
7	7	7	7	10	10	1	1	1	1	4	4	4
8	8	8	8	11	11	2	2	2	2	5	5	5
9	9	9	9	0	0	3	3	3	3	6	6	6
10	10	10	10	1	1	4	4	4	4	7	7	7
11	11	11	11	2	2	5	5	5	5	8	8	8

2.6. Example:

Let $\mathbb{R}$ be the set of all real numbers and fix $q \in \mathbb{R}$, $0 < q < 1$. Define E on $\mathbb{R}$ by xEy iff there is a $k \in \mathbb{Z}$ such that $x = q^k y$ for any $x, y \in \mathbb{R}$. One can easily show that E is an equivalence relation. Now, define $\star_q$ by

$$x \star_q y = q^{k_x + k_y}\overline{x} \; for \; x, y \in \mathbb{R},$$

where $\overline{x} := \max([x] \cap [0,1))$ and $k_x := \log_q(x/\overline{x})$ for any $x \in \mathbb{R}$. Clearly, the operation $\star_q$ is well defined. For any $x, y \in [t]$ and $t \in \mathbb{R}$, we can check that $\overline{(\overline{x})} = \overline{x} = t$, $\overline{q^{k_y}\overline{x}} = \overline{x}$, $\overline{q^{-k_y}\overline{x}} = \overline{x}$, $k_{\overline{x}} = 0$, $k_{q^{k_y}\overline{x}} = k_y$, and $k_{q^{-k_y}\overline{x}} = -k_y$. Also, we can show that for $[t] \subseteq \mathbb{R}$ and $x, y, z \in [t]$:

• $x \star_q y = q^{k_x + k_y}\overline{t} \in [t]$,

• $x \star_q (y \star_q z) = x \star_q \left(q^{k_y + k_z}\overline{y}\right) = q^{\left\{k_x + k_{\overline{q^{k_y+k_z}\overline{y}}}\right\}}\overline{x} = q^{k_x+k_y+k_z}\overline{x}$, and similarly $(x \star_q y) \star_q z = q^{k_x+k_y+k_z}\overline{x}$,

• $\overline{t} \star_q x = q^{\{k_{\overline{t}}+k_x\}}\overline{(\overline{t})} = q^{k_x}(\overline{t}) = x$, and similarly $x \star_q \overline{t} = x$.

Hence, the triple $(\mathbb{R}, E, \star_q)$ is a generalized group.

2.7. Example:

Fix $\omega \in \mathbb{R}, \omega > 0$. Assume the triple $(\mathbb{R}, E, \star_\omega)$ where E is defined by xEy iff there is $k \in \mathbb{Z}$ such that $x = y + k\omega$. Easily, one can show that E is an equivalence relation. The binary operation $\star_\omega$ is defined by $x \star_\omega y = \overline{x} + (k_x + k_y)\omega \; for \; x, y \in \mathbb{R}$,

where $\overline{t} := \min([t] \cap [0, \infty))$ and $k_t := \frac{t-\overline{t}}{\omega}$ for any $t \in \mathbb{R}$. The operation $\star_\omega$ is well defined. One can check for any $x, y \in [t]$ and $t \in \mathbb{R}$ that $\overline{(\overline{x})} = \overline{x} = t$, $\overline{\overline{x} + k_y\omega} = \overline{x}$, $\overline{\overline{x} - k_y\omega} = \overline{x}$, $k_{\overline{x}} = 0$, $k_{\overline{x}+k_y\omega} = k_y$, and $k_{\overline{x}-k_y\omega} = -k_y$. Now, for $[t] \subseteq \mathbb{R}$, we have the following:

• For any $x, y \in [t]$, $x \star_\omega y = \overline{t} + (k_x + k_y)\omega \in [t]$.

• For any $x, y, z \in [t]$, we have $x \star_\omega (y \star_\omega z) = x \star_\omega \left(\overline{y} + (k_y + k_z)\omega\right) = \overline{x} + \left(k_{(\overline{y}+(k_y+k_z)\omega)} + k_x\right)\omega = \overline{x} + (k_y + k_z + k_x)\omega$

and similarly $(x \star_\omega y) \star_\omega z = \overline{x} + (k_x + k_y + k_z)\omega$ which show that $\star_\omega$ is associative on $[t]$.

• For $x \in [t]$, $\overline{t} \star_\omega x = \overline{(\overline{t})} + (k_{\overline{t}} + k_x)\omega = \overline{t} + (0 + k_x)\omega = \overline{x} + k_x\omega = x$ and $x \star_\omega \overline{t} = \overline{x} + (k_x + k_{\overline{t}})\omega = \overline{x} + k_x\omega = x$. Therefore $\overline{t}$ is the identity element of $[t]$.

Hence, the triple $(\mathbb{R}, E, \star_\omega)$ is a generalized group.

2.8. Example:

Consider the set $\mathbb{Z}_6 := \{0,1,2,3,4,5\}$. Define the equivalence relation E on $\mathbb{Z}_6$ by rEs iff there exists $k \in \mathbb{Z}$ such that $r = s +_6 2k$ or $s = r +_6 2k$. Then clearly, the equivalence classes are $[0] = \{0,2,4\}$ and $[1] = \{1,3,5\}$. The binary operation $\star$ on $\mathbb{Z}_6$ is defined by Table 2. This triple $(\mathbb{Z}_6, E, \star)$ is an abeilan generalized group and $(\mathbb{Z}_6, \star)$ is not a group.

Table 2: The binary operation $\star$ on $\mathbb{Z}_6$.

★	0	1	2	3	4	5
0	0	0	2	0	4	0

1 2 3 4 5	0 2 0 4 0	1 0 3 0 5	0 4 0 0 0	3 0 5 0 1	0 0 0 2 0	5 0 1 0 3

3. Generalized Subgroups

In this section, we introduce and study the concept of a generalized subgroup.

3.1. Definition:

A nonempty subset H of a generalized group $(G, E, \star)$ is said to be a generalized subgroup if $(H, E, \star)$ is a generalized group.

The following proposition gives an easier criterion to decide whether a subset of a generalized group G is actually a generalized subgroup.

3.2. Proposition:

Assume that G is a generalized group and $\emptyset \neq H \subseteq G$. Then, H is a generalized subgroup if it satisfies the following conditions:

I. $x \star y \in H$ for any $x, y \in H$,
II. $e(x) \in H$ for any $x \in H$,
III. $x^{-1} \in H$.

3.3. Theorem:

Assume that G is a generalized group and $\emptyset \neq H \subseteq G$. Then, H is a generalized subgroup iff $x \star y^{-1} \in H$ for each $x, y \in H$.

Proof. For the ``only if'' part: Let $H$ be a generalized subgroup and $x, y \in H$. Since $H$ is a generalized subgroup, $y^{-1} \in H$. Then, $x, y^{-1} \in H$ which implies that $x \star y^{-1} \in H$. For the ``if'' part: Let us assume that $x \star y^{-1} \in H$ for each $x, y \in H$. Since $H \neq \phi, \exists t \in H$ and by assumption, we have $e(t) = t \star t^{-1} \in H$. If $y \in H$, then $e(y) \in H$ which implies that $y^{-1} = e(y) \star y^{-1} \in H$. Finally, for $x, y \in H$, $x, y^{-1} \in H$ and then $x \star y = x \star (y^{-1})^{-1} \in H$. In section 3.2. Proposition, H is a generalized subgroup.

3.4. Remark:

Let G be a generalized group. Then, the following statements hold:

i. G and $\{e(t)\}$ for each $t \in G$ are generalized subgroups of G. They are called trivial generalized subgroups of G.
ii. If $[t]$ is a generalized subgroup of G for each $t \in G$, then G is a union of pairwise disjoint generalized subgroups.
iii. If G is a group, then every generalized subgroup of G is a subgroup of G.
iv. The intersection of a family of generalized subgroups is necessarily a generalized subgroup.

3.5. Example:

Consider the generalized group $(\mathbb{R}, E, \star_q)$ which is defined in Example 2.6. Define the subsets H_1, H_2 as, $H_1 := \{x \in \mathbb{R}: k_x \in 2\mathbb{Z}\}$ and $H_2 := \{x \in \mathbb{R}: k_x \in 2\mathbb{Z} + 1\}$. We use Theorem 3.3 to show that H_1 is a generalized subgroup, but H_2 is not a generalized subgroup. Let $x, y \in H_1$ with $[x] = [y]$. Then, $\overline{x} = \overline{y}$ and $k_x, k_y \in 2\mathbb{Z}$. Note that $-k_y \in 2\mathbb{Z}$, and $k_x - k_y \in 2\mathbb{Z}$. Now, $x \star y^{-1} = q^{k_x - k_y}\overline{x} \in H_1$. Hence, H_1 is a generalized subgroup. However, H_2 is not a generalized subgroup, because $q^3 x, q^5 x \in H_2$ and $q^3 x \star (q^5 x)^{-1} = q^3 x \star q^{-5} x = q^2 x \notin H_2$.

4. Homomorphism of Generalized Groups

In this section, we give a definition of a homomorphism of generalized groups with some results.

4.1. Definition:

Assume that G and G' are generalized groups. A map $f: G \longrightarrow G'$ is called a *homomorphism* if for any $a, b \in G$, we have $f(ab) = f(a)f(b)$, and $[f(a)] = [f(b)]$ if $[a] = [b]$. The set $Ker_a(f) := \{x \in G: f(x) = e(a)\}$ is called the kernel of f with respect to $a \in G$.

The following theorem shows some of the basic results of the generalized groups homomorphisms.

4.2. Theorem:

Let G and G' be generalized groups and $f: G \longrightarrow G'$ be a homomorphism. Then:

i. $f(e(a)) = e(f(a))$.
ii. $f(a^{-1}) = (f(a))^{-1}$.
iii. $f(H)$ is a generalized subgroup of G' for any generalized subgroup H of G.
iv. $Ker_a(f)$ is a generalized subgroup of G for $a \in G$.
v. f is injective iff $Ker_a(f) = \{e(a)\}$ for all $a \in G$.

Proof. (i) Let $b = f(e(a))$ for $a \in G$. Then, $b = f(e(a)) = f(e(a)e(a)) = f(e(a))f(e(a)) = bb$ which implies that $e(b) = b$. That is, $e(f(a)) = f(e(a))$.

(ii) Let $b = a^{-1}$. Then, $e(f(a)) = f(e(a)) = f(aa^{-1}) = f(ab) = f(a)f(b)$ and $e(f(a)) = f(e(a)) = f(a^{-1}a) = f(a^{-1})f(a) = f(b)f(a)$ which show that $f(b)$ is the inverse of $f(a)$, completing the proof of (ii).

(iii) Let $K = f(H)$. It suffices to check that K is nonempty and $ab^{-1} \in K$ for any $a, b \in K$. Since $H \neq \phi$, there is $a \in H$ which implies that $f(a) \in K$; and so $K \neq \phi$. If $a, b \in K$, then $f^{-1}(a), f^{-1}(b) \in H$ and then $f^{-1}(a)(f^{-1}(b))^{-1} \in H$. Now, $f(f^{-1}(a)(f^{-1}(b))^{-1}) \in f(H) \Longrightarrow$
$f(f^{-1}(a))f((f^{-1}(b))^{-1}) \in K \Longrightarrow$
$f(f^{-1}(a))(f(f^{-1}(b)))^{-1} \in K \Longrightarrow ab^{-1} \in K$.

(iv) Let $a \in G$. Since $e(a) \in Ker_a(f)$, $Ker_a(f) \neq \phi$. Now, if $x, y \in Ker_a(f)$, then $f(x) = f(y) = f(e(a))$. We have

$$f(xy^{-1}) = f(x)f(y^{-1}) = f(e(a))(f(y))^{-1}$$
$$= f(e(a))(f(e(a)))^{-1}$$
$$= f(e(a))f(e(a)) = f(e(a)).$$

This implies that $xy^{-1} \in K$. Hence, K is a generalized subgroup.

(iv) Assume that f is injective. Then, for $a \in G$ there is at most one element that can be sent to the identity $e(f(a))$. Since $f(e(x)) = e(f(x))$, $Ker_a(f) = \{e(a)\}$. Conversely, let $Ker_a(f) = \{e(a)\}$ for all $a \in G$ and $f(x) = f(y)$ for some $x, y \in G$. Then, $f(x^{-1}y) = f(x^{-1})f(y) = f(x^{-1})f(x) = f(x^{-1}x) = f(e(x)) = e(f(x))$. This implies that $x^{-1}y \in Ker_x(f)$, and then $x^{-1}y = e(x)$. Thus, $x^{-1} = y^{-1}$, but the inverse is unique and so $x = y$. Therefore, f is injective.

Biography

Khaled Ahmed Ali Aldwoah

Mathematics Department, Faculty of Science, Islamic University of Madinah, Madinah, Saudi Arabia, aldwoah@iu.edu.sa, aldwoah@yahoo.com, 00966551976509

Dr. Aldwoah has been an assistant professor since 2009, of Yemeni nationality, and holder of a PhD from Cairo University, Egypt in 2009. He is interested in generalizing some mathematical concepts, time scales calculus, and dynamic equations. He worked as an assistant professor in some Yemeni and Saudi universities and is currently working at the Islamic University of Madinah. The author has attended five international conferences, and he has published many scientific papers in specialized scientific journals (ISI, Scopus).

References

Adeniran, J., Akimnoyewa, J., Solarin, A. and Jaiyeola, T. (2009). On some algebraic properties of generalized groups. *Octogon Mathematics Magazine*, **17**(1), 125–134.

Akinmoyewa, J. (2009). A study of some properties of generalized groups. *Octogon Mathematics Magazine*, **17**(2), 599–626.

Araújo, J. and Konieczny, J. (2004). Molaei's generalized groups are completely simple semigroups. *Buletinul Institului Polithnic Din Iasi*, **52**(n/a), 1–5.

Clifford, A. (1941). Semigroups admitting relative inverses. *Annals of Mathematics*, **42**(4), 1037–49.

Clifford, A. and Preston, G. (1961). The algebraic theory of semigroups. *American Mathematical Society*, **52**(n/a), 1–5.

Molaei, M. (1999). Generalized groups. *Buletinul Institului Polithnic Din Iasi Tomul*, **XLV**(XLIX), 21–24.

Molaei, M. (2000). Topological generalized groups. *International Journal of Pure and Applied Mathematics*, **2**(9), 1055–60.

Santilli, R.M. (1979). Isotopic breaking of Gauge theories. *Physical Review D*, **20**(n/a), 555–70.

Vagner, V. (1952). Generalized groups. *Doklady Akademi Nauk SSSR (Russian)*, **84**(n/a), 1119–22.

The Scientific Journal of King Faisal University

Basic and Applied Sciences

An IoT Based Model for a Trucking Transport System Using Predictive Analytics

Renuka Mahajan [1], Preetam Suman [2] and Richa Misra [1]

[1] Jaipuria Institute of Management, Noida, India

[2] Jaipuria Institute of Management, Lucknow, India

LINK	ACCEPTED	PUBLISHED ONLINE	ASSIGNED TO AN ISSUE
https://doi.org/10.37575/b/cmp/2255	11/09/2020	11/09/2020	01/12/2021

NO. OF WORDS	NO. OF PAGES	YEAR	VOLUME	ISSUE
5342	6	2021	22	2

ABSTRACT

The Internet of Things (IoT) has enormous potential to revolutionize the transport industry. IoT can be used to optimize mobility of goods and people, add transparency, update information, and provide convenience at lesser cost. Speed of transportation drives requirements of the trucking industry with sustainability, safety without stress. After reviewing current challenges of supply chain networks, this paper proposes a new solution for booking freight, integrating data from multiple sources using smart cloud-based solutions. This paper provides a solution using two modules. The first module is development of a mobile application for order updates and live monitoring of vehicles. The second module is an IoT device that works as an intelligent device by using sensors and microcontrollers. This results in organizations' transparency on live monitoring of the status of their entire supply chain network, anticipating problems in advance, and providing immediate response to the problem. This paper has implications for organizations driven by enhanced customer expectations pertaining to lead time delivery services, product availability and reliability.

KEYWORDS

Intelligence transportation system, Internet of Things (IoT), trucking, logistics sector, smart city, smart transportation

CITATION

Mahajan, R., Suman, P. and Misra, R. (2021). An IoT based model for a trucking transport system using predictive analytics. *The Scientific Journal of King Faisal University: Basic and Applied Sciences*, **22**(2), 5–10. DOI: 10.37575/b/cmp/2255

1. Introduction

Smart technology implies the integration of software, hardware, cloud and sensor-based technologies. The objective is to utilize live data collected from numerous touchpoints, and applying statistical and analytical operations so that the user is able to make informed decisions about their routine and other tasks (Sharma and Tiwari, 2016). Smart cities would soon be using such smart technologies to provide innovative solutions for problems in urban development, ensuring high standards of sustainability and profitability. Smart Cities form an integral part of any developing country; they bring new reforms and inspire new aspirations in city residents (Ianuale et al., 2015). Smart cities enable residents with information and technology-based infrastructure that is smart, connected and viable (Myeong et al., 2018). Benefits of smart city implementation include efficient infrastructure, e-Governance, power management and traffic management, among several others. Such cities will open up for new job opportunities for all residents, leading to economic growth, which forms the backbone of any country. Smart technology is a self-service application that needs minimal or no human involvement. As an evolving technology, the Internet of Things (IoT) enables innovative solutions to transform industrial systems such as transportation systems and manufacturing systems. IoT is widely used to build intelligent transportation systems. The latest innovative services have started using the Internet of Things (IoT) for smarter traffic management. It enables commuters to be better informed, better coordinated and provides more safety (Prabhu et al., 2017). Such technological progress on IoT can change methods of different business operations (Atzori et al., 2010). Smart transportation is essential for smart cities. Transportation industry is dependent on IT transformation to provide customer satisfaction (Zanella, 2014). Involvement of smart transportation with smart cities will lead to Intelligent Traffic Management, Integrated Multi-Modal Transport, and the Internet of Things to improve overall mobility. All of this can be implemented by encouraging new technology such as IoT, Big data, dashboards and predictive analytics, complemented by a different mode of communication network, global positioning system, camera system, artificial vision, and in-vehicle systems (Ahmed et al., 2014). Tiny sensors embedded in each finished product, generate new patterns that provides new insights. Smart Transportation system has three major components: Smart Infrastructure or Station Subsystem (such as electronic toll collection, automated traffic signals, fare collection and multimodal transport), Data Integration (data monitoring center pertaining to weather, traffic and emergency services) and Smart Services (smart parking vehicle monitoring system). Internet of Things (IoT) includes connecting physical devices to the network. Government of India has ambitious plans to proliferate the IoT industry, touching USD 15 billion by 2020. The objective is to attain reliability, efficacy and security of the transport infrastructure. Moreover, connected vehicles are gaining popularity because they make driving more reliable, enjoyable and efficient.

Automotive sector is a major contributor to Indian GDP. Its growth rate is predicted to be 6.7% to 12% in the future (Huawei Technologies Co. Ltd). Global market size of vehicle tracking devices surpassed 18,984 thousand units in 2018, with an industry value of over USD 600 million. It is forecasted to develop at a CAGR of over 20% from 2019 to 2025 (Bhutani and Wadhwani, 2019). Many telecom operators are focusing on commercialization of next-generation 5G technology. Thus, smart transportation solution is the need of the hour, as citizens have major requirements for transporting goods to other places and cities. According to Business Wire (2017), transportation industry is the second largest segment investing in the Internet of Things (IoT), spending approximately USD 78 billion since 2016. Due to recent advancements in connectivity, this has particularly impacted the trucking industry. This would immensely benefit business the world over, in the sectors of transportation and logistics (Qu et al., 2016), which have been known

Corresponding Author: Renuka Mahajan renuka.mahajan@jaipuria.ac.in, 009873605079

for shying away from innovation and adaptation for a long time. Consumers can expect increased convenience, safety, and commitment to service, by businesses within the industry.

Government of India has the agenda to build 100 smart cities by 2024, and smart transportation system is the key component in transforming smart cities. India has the second-largest road network, fourth-largest rail network (Grant Thornton, 2016), as per the International Journal of Multidisciplinary Research and Development, but India has been ranked as low as 46 among 155 countries in the World Bank International Logistics Performance Index.

This paper aims to develop an intelligent transportation system using a hybrid of technologies such as mobile applications, cloud computing and IoT. The proposed system can plug data gaps such as supplier and customer location, customer forecasts, transportation costs, and realized raw and adjusted service levels, among other key inputs. It will give the organization access to reliable data reporting and the capability to perform the required analytics.

Some problems faced in the absence of Smart Transportation are listed below:

- Retailers and dealers dealing in all sorts of goods and products use heavy vehicles such as trucks and mini trucks to transfer their goods. Usually, while returning, the trucks are empty, which leads to huge loss for the users.
- Usually, while returning, the trucks come back empty, which leads to huge money loss for them.
- It also results in wastage of manpower resources for the dealers, often leading to time delays, corruption in fare negotiations etc.
- There is additional expenditure to maintain the heavy vehicles.
- Different variants of trucks play on roads, leading to complexity of matching available load to available capacity.
- Renting involves brokers' involvement. Confirmations and cost negotiations incur delays, which leads to extra expenditure.
- Proof of delivery of goods arrives late, and hence there are delays in final payment.
- Loss of revenue is common due to breakdown of vehicles on the road.
- Due to delays in transport, or weather conditions and breakdowns, there is loss of goods that are specified as perishable items.
- Tracking position and speed of vehicles on the road in real-time is a challenge.

According to the American Trucking Association, "The revenue of the global Freight Trucking market was estimated at USD 3,844.76 billion in 2016, and it is expected to reach USD 6,252.81 billion by 2025." With the Uber ride-sharing system and similar companies like Lyft, there was a revolution in urban traffic management. This is because now independent drivers can easily connect with commuters, benefiting more than 8 million people who now use app-based ride-sharing services.

Valuation of Uber has risen to over USD 60 billion, and they intend to extend the ride-share model to the shipping freight industry. According to Morgan Stanley analyst Ravi Shanker, Uber Freight, and other similar services, have the potential to act as a true disruptive influence in this sector.

2. Literature Review

In order to address the challenges described in the previous Section, supply chain managers need interconnection of equipment and devices. Hence, organizations started experimenting and involving in detailed literature review of several parameters. Fernando et al., (2020) studied the measurement of attributes of moving vehicles and on how sensors can be used for data retrieval in tracking devices. Qiu et al., (2018) assessed how various data are used in transferring methods for transmission, networks and protocols utilized for communication. Chaniotakis (2020) analyzed different data sources, algorithms, and apps that can be utilized for capture and analysis of raw data.

An in-depth literature review of researches conducted in the last decade, on different architectures related to Smart Transportation/IoT in different settings, is presented in Table 1.

Table 1: Literature Review of papers on Smart Transportation Solutions

Author(s)	Major Direction of Study
Kyriazis et al. (2013)	The paper has devised two IoT based smart city applications. The first application was meant for power management using electricity meter for commercial and residential categories. The second application was meant for the public transport system, utilizing different resources for optimizing travel time (such as environmental and traffic sensing).
Qureshi and Abdullah (2013)	It presents a wide-ranging area of intelligent transportation systems as well as its applications and a range of technologies.
Gayathri (2017)	This study developed a system for intelligent health monitoring of the car using sensor monitors on vehicles to check health of the vehicle.
Hemalatha (2015)	Researcher developed IoT and cloud-based applications to deal with transportation issues in metro cities. This would help in handling heavy traffic, ensuring vehicle security and reducing congestion on busy roads.
Javed et al. (2019)	They proposed the Cooperative Intelligent Transport System (C-ITS), a futuristic application for traffic management. Data analytics has a critical role in C-ITS application.

Redesigning strategies of the company with Transport Management System (TMS) increases upper end of the Return of Investment (ROI) since TMS facilitates end-to-end supply chain visibility (Goshare, 2020). Currently, increasing number of devices are being furnished with bar codes, RFID tags or sensors. With increased density and usage of mobile devices and services, TMS solutions integrate smartphone applications that can be used to create location of specific trucks at any given time. IoT and TMS are definitely set to play a promising role in the transportation industry.

However, for the industry that is modernized by new trucking models, both drivers and freight companies have to deal with issues related to cost and time-saving (Al-Sakran, 2015); (Bandyopadhyay and Sen, 2011). According to Bansal (2015), the transport system in India, particularly involving large trucks, is complicated and unorganized with respect to its functioning model and multiple stakeholders. In India, road transport represents around sixty-five percent of total freight transport, railway comprises thirty-two percent, while water and air present seven and one percent respectively. Globally, India has the second-largest road linkage involving freight of around seven million transport vehicles (Bansal, 2015).

Previous researches done so far have disadvantages such as technology trust (Mengru, 2018), huge cost of the system (Pham, 2015), difficulty in payment (Gandhi et al., 2016), system does not provide guidance (Lotlikar et al., 2016), drivers cannot make reservation for parking (Tsaramirsis et al., 2016) etc. There is no single solution that meets all the needs required for cooperation between devices, infrastructure, and cloud (Van Den Abeele et al., 2015).

3. The Proposed System

Review of literature demonstrated that: (i) IoT based sensors embedded on the location tracking devices in cloud data centres can be used remotely by retrieving real-time data; (ii) The GPS sensors based on the RFID technology can be utilized; (iii) Wi-Fi networks are the most popular networks; (iv) The most used storage method was observed to be cloud for smart vehicle tracking systems.

We propose that the IoT can further make this trucking system more effective by incorporating some additional features. IoT in the warehouse has given clear visibility to the supply chain, right from ordering of materials till the shipment reaches the end customer. This

can reduce inefficiencies in logistics and improve overall efficiency, while reducing costs. By including weather forecast data, data related to government services, road closure advisories, and emergency services, operations can run more smoothly. It could also inform stakeholders about the status of operations in real-time using predictive analytics and feedback mechanism, leading to instant gratification.

By merging IoT with the latest innovations, we can add more value to the business in a systematic manner (Qureshi and Abdullah, 2013). This will help in monitoring supply chain operations right from the stage of new order booking to final delivery of the shipment to the end-user or the customer.

The proposed system consists of two modules.

- The first module is an online order booking system.
- The second module is real-time vehicle monitoring.

3.1. Module 1:

The first module is shown in Figure 1 and consists of storage, application and infrastructure. These components are implemented on cloud infrastructure.

- Storage: It stores all online orders given by customers, and all tracking records of vehicles.
- Application: It is a mobile app that provides an interface to customers for online orders. It also provides an interface to the vehicle driver to get order details.
- Infrastructure: It is a cloud-based service to integrate all the components needed for the mobile app.

Figure 1: Module 1: **Online Order Booking System**

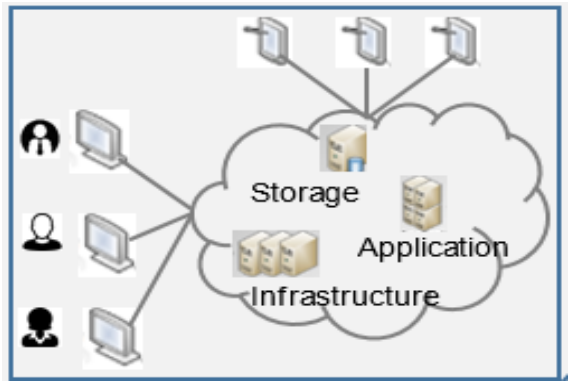

Figure 2: Flow chart of Order Booking Process

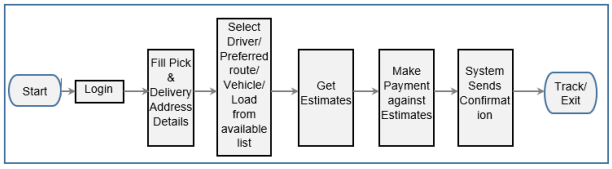

Figure 2 shows an online order booking system. The user can interact with the booking system through the mobile app. Apache Cordova is used to develop the mobile application so that the same source runs on both Android and iOS platforms. Amazon Elastic Compute cloud can be used to connect the application for real-time communication between the mobile app and cloud.

3.2. Module 2:

The second module is real-time truck/ vehicle monitoring. It consists of a device that can be mounted on a vehicle. Figure 3 shows a device that is mounted on a truck, near the steering. There are wireless sensors which can be used to monitor health of the vehicle. In Figure 3, a wireless sensor is plotted, which can measure air pressure and temperature of tires. These sensors will be connected to the device through Bluetooth.

Figure 3: Mounting device on the truck

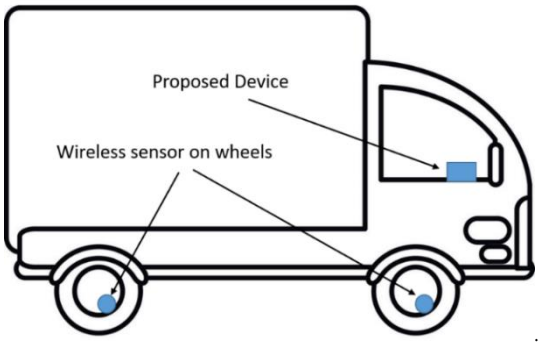

Figure 4: Elements of the proposed device

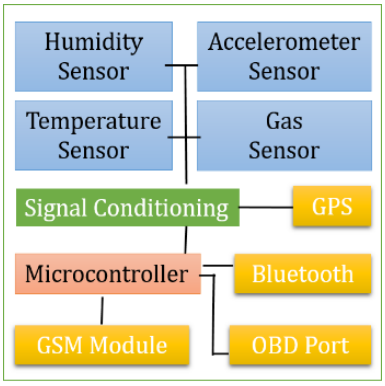

Figure 4 shows components of the proposed device. The components are as follows:

- Humidity sensor: This sensor will collect information about humidity in the air,
- Temperature sensor: This sensor will collect information on temperature from the environment. There will be one more setup of the temperature sensor to measure temperature of the engine.
- Accelerometer: This will record data of movement by the vehicle. In the case of crashes, the microcontroller can predict accidents and report to the owner.
- Gas Sensor: It is also for safety of the vehicle. Gas sensors can sense the presence of methane gas.
- Microcontroller: It collects all data from the sensor and stores all information to cloud storage. In this device, 8-bit ATmega328P has been used.
- GPS: It provides the GPS location to the microcontroller:
- GSM Module: This module will be used to provide connectivity to cloud storage and send messages in emergency situations. It also provides internet connectivity to the app.
- OBD port: It is used to provide connectivity to devices from the vehicle. It includes power supply and other input values from the vehicle.
- Bluetooth: This module will be used to connect the sensor to the device through Bluetooth.

This system has the facility of booking various truck types through different means such as mobile internet, email, or field agents. The user can book by giving the pickup and delivery address, preferences for the type of carrier (emergency vehicles, light commercial vehicles, passenger vehicles etc.), cargo type (perishable items/pharmaceutical products, etc.), preferred driver, favorite route etc. User's preferences

are saved on the cloud so that the same history can be used to understand preferences for the next booking and notification. This information will be matched with professional truck drivers registered with the app, who are vetted by the app and are willing to carry shipment. This way, the dispatcher 'does not have to deal with the challenge of finding, negotiating and booking. Also, truck drivers do not have to negotiate the fare as the price is predetermined in this booking system. One can see the available route and how much will be charged. Pricing also depends upon a number of factors such as the cargo type, location, with distance being the most prominent one. Directly connecting them eliminates price surprises, negotiation delays, and corruption practices. Bookings can be made several weeks in advance or on the same day. This mobile app will be hosted on the cloud to optimize infrastructure cost and on-the-fly scalability as per requirement. This will eliminate data loss because of networked backups and load balancing. Cloud computing will save the shipper/dispatcher the cost of data storage and maintenance.

This module also has the provision of field agents or brokers who can take requests from dispatchers using landline/mobile/web/email. Role of Administrator is crucial in cases where field agents take manual orders and book them on behalf of the dispatchers, they have the provision to handle queries faced by end-users, or generate ad-hoc reports required by them. This results in better customer satisfaction.

Once the load is dispatched, there could be other bottlenecks such as traffic jams, that cause frustration and delay. GPS can be effectively used to address such pain points in transportation. GPS enables smarter route mapping to avoid congestion. Re-routing decisions can be made in case of congestions. The data can be integrated using IoT from multiple sources such as weather forecast, traffic advisory, government services, policies (related to driver hours of service).

Vehicle Health Monitoring- All modern vehicles have a microchip installed which controls working and performance of the engine. This generates much real-time information on vehicle performance that can be used to help manufacturers and mechanics determine a vehicle's health. Drivers have access to this information now through devices such as automatic adapters which plug into a port to monitor engine health, along with an abundance of other capabilities (like tracking the vehicle to its parking spot). This information can be made available directly over the mobile through freely available apps. This makes vehicle maintenance easy and can save both time and costs of vehicle maintenance. The data on vehicle health can be shared with the garage and any issue can be documented, creating a predictive and efficient vehicle maintenance model. Thus, based on these details on vehicle's health, one can predict possible failures. One can use this to book the scheduled maintenance slot at the nearest in-route workshop. Failure codes give a reason and remedy for immediate repairing, and no matter where they are, drivers can catch the issues before they occur. In case of a major breakdown, driver can send details regarding breakdown of the truck, and consequently, a nearest truck can be identified and consignment can be shifted. This facility helps drivers greatly in tackling on-road hassles and vehicle breakdown/maintenance issues.

Invoice generation process – Generally, in the manufacturing industry, an invoice is generated as soon as a customer starts using the goods. However, there is no real-time system available to find the exact time of usage of goods. A physical visit is often carried out by field agents, which is usually done weekly or fortnightly, to check usage of goods and raise invoices accordingly. Looking at the volume involved, there is huge revenue loss to the manufacturer. In such a scenario, containers can be fixed with IoT sensors to send signals as soon as the container is opened and invoice can be raised accordingly. This can significantly help manufacturers in reducing losses. This will also help manufacturers specifically in short shelf life items, to keep track of the batches available in the warehouse and deliver them according to their date of expiry. This is a million-dollar idea, especially for FMCG companies, particularly in the food industry dealing with perishable items (with short shelf lives) or environmentally sensitive products since it minimizes loss by reducing downtime, generating huge value for the business (Verdouw et al., 2016; Verdouw et al., 2014; Ramundo et al., 2016).

Shippers can have real-time information about whereabouts of the truck and how far it has traveled, since the trucks are GPS enabled. This real-time tracking and predictability analytics can be used to find date of delivery, distance covered status, real-time traffic information such as traffic condition on each road, number of vehicles, and average speed, weather forecast, route diversion, over-speeding, stoppage etc. (Sijs et al., 2008).

Thus, this proposed mechanism will provide instant rates, insights into shipment delivery including available real-time tracking, lowering downtime time through the use of IoT. The admin, dispatcher, or end-user can track and access latest information, predict anticipated date of delivery, and other details on-the-go, anywhere, anytime. This will eliminate several bottlenecks while providing real-time location information, live monitoring of goods for shipment to customer's place, resulting in lower cost of investment. The IoT technology can provide benefits in improving visibility, reducing cost and travel, providing convenience, eliminating dependencies on middlemen, identifying and predicting future vehicle breakdown, and providing tactical information all throughout the process. Major advantage of this architecture is reduction in downtime, which is one of the biggest causes of cost and concern for transport organizations. Thus, upcoming freight marketplaces can train their machine learning models to match the right load with the right truck variant and routes.

4. Conclusion

In this paper, a novel IoT based app for smart transportation is proposed, using a hybrid of technologies (cloud computing, IoT and mobile application), to make the online transportation process easy for the modern end-user. This offers numerous advantages and conveniences such as handling traffic congestion, real-time tracking, vehicle health monitoring, emergency resolution and quick payment turnaround time, thus saving cost and time. Truckers can use the app to browse and book available trucks in preferred locations. These truck aggregators are leveraging technology to focus on the entire network consisting of demand-supply scheduling, GPS tracking, safety and maintenance of the vehicle, as well as mobile/web app support and cloud-based documentation. Transporters can gain intelligence on real-time traffic patterns, weather conditions, fuel efficiency while predicting maintenance and repair needs, leading to better speed management, sustainability and elimination of stress.

As per previous studies (Hashem, 2016; Bandyopadhyay and Sen, 2011), smart logistics have played a pivotal role in facilitating communication between customers and organizations, and also assisted them in handling real-time queries, leading to customer satisfaction by providing efficient and quality services. There are many sub-steps to the execution as well as pitfalls to avoid as a company goes through the implementation of a new supply chain network e.g., dependence of internet for vehicle tracking, inaccurate GPS tracking, and privacy and security issues. Appropriate planning is crucial for the success of implementation of a technology-based solution; for that, it is essential to involve all stakeholders in designing a smart transportation system. Working in silos may lead to poor

implementation. Every company has its own problems and complexities; the challenge lies in finding the best fit to appropriately address core objectives of smart transportation in a simple, environment-friendly, secure and connected solution.

5. Future Scope

Further research can focus on the dispatch and unload modules that can be redefined by including IoT sensors in each product. While unloading, alerts will notify both truckers and management when the shipment is opened, for fast invoice payment. This is also important in avoiding damages because conditions of some sensitive products can go awry during shipment,

Bios

Renuka Mahajan

Jaipuria Institute of Management, Noida, India, renuka.mahajan@jaipuria.ac.in, 009873605079

Prof Dr. Renuka Mahajan is working with Jaipuria, Noida in Information Technology (IT). She has completed her Doctorate in Computer Science and Engineering from Amity University. She has published research papers in various Scopus indexed International journals like Springer Education and Information Technologies, Journal of Information and Organizational Sciences, International Journal of Product Development, International Journal of Innovation and Learning, International Journal of Data Analysis Techniques and Strategies, International Journal of Logistics Economics and Globalisation, International Journal of Asian Business and Information Management, e-service Journal and several conference proceedings.

Preetam Suman

Jaipuria Institute of Management, Lucknow, India, preetam.suman@jaipuria.ac.in, 00987376333523

Prof Dr Preetam Suman completed his doctorate from the Indian Institute of Information Technology, Allahabad. His core areas of expertise include medical imaging, real-life applications of artificial, intelligence, and embedded systems. He is involved in a project related to implementing sensor networks in forests to save wildlife. He is nominated by various forums and associations in their committees. He has published more than thirty papers in international journals and conferences and various seminars organized by professional bodies and industry associations worldwide. Dr. Preetam holds professional associations with the IEEE Technical Committee, IEEE Young Professionals, Association of Knowledge Workers of Lucknow.

Richa Misra

Jaipuria Institute of Management, Noida, India, richa.misra@jaipuria.ac.in, 009868357892

Prof Dr. Richa Misra is working at Jaipuria Institute of Management, Noida. She has done her Doctorate in Management from Amity University. Her research papers and cases have been published in reputed journals like International Journal of Management Education, Elsevier, On the horizon Emerald, International Journal of Logistics and Economics, Journal of Information and Organizational Sciences, ECCH, Abhigyaan, BHU, IBS Business Review, Smart Journal of Management, Fortune Business Review and International Islamic University Malaysia. She has imparted training in various organizations in the areas of IT Security, Qualitative and Quantitative research methods, Data analysis etc.

References

Ahmed, K.B., Bouhorma, M. and Ahmed, M.B. (2014). Age of big data and smart cities: privacy trade-off. *International Journal of Engineering Trends and Technology (IJETT),* **16**(6), 298–304.

Al-Sakran, H.O. (2015). Intelligent traffic information system based on integration of internet of things and agent technology. *International Journal of Advanced Computer Science and Applications (IJACSA),* **6**(2), 37–43.

Atzori, L., Iera, A. and Morabito, G. (2010). The internet of things: A survey. *Computer networks*, **54**(15), 2787–805.

Bandyopadhyay, D. and Sen, J. (2011). Internet of things: Applications and challenges in technology and standardization. *Wireless personal communications*, **58**(1), 49–69.

Bansal S. (2015). *The Uber Freight Impact on the Trucking Industry in India*. Available at: http://www.iamwire.com/2017/06/uber-freight-impact-truck-logistics-industry-india/154547 (accessed on 03/03/2020)

Bhutani A., Wadhwani P. (2019). *Global Market Insights*. Available at: https://www.gminsights.com/industry-analysis/vehicle-tracking-market (accessed on 03/03/2020)

BusinessWire (2017). *Internet of Things Spending Forecast to Grow 17.9% in 2016 Led by Manufacturing, Transportation, and Utilities Investments, According to New IDC Spending Guide*. Available at: https://www.businesswire.com/news/home/20170104005270/en/Internet-Things-Spending-Forecast-Grow-17.9-2016 (accessed on 03/03/2020)

Chaniotakis, E., Efthymiou, D. and Antoniou, C. (2020). 'Data aspects of the evaluation of demand for emerging transportation systems'. *In*: E. Chaniotakis, D. Efthymiou and C. Antoniou (eds.) *Demand for Emerging Transportation Systems* (pp. 77–99). Amsterdam, Netherlands: Elsevier.

Kyriazis, D., Varvarigou, T., White, D., Rossi, A. and Cooper, J. (2013), Sustainable smart city IoT applications: Heat and electricity management & Eco-conscious cruise control for public transportation. In: *2013 IEEE 14th International Symposium on "A World of Wireless, Mobile and Multimedia Networks" (WoWMoM)*, Madrid, Spain, pp. 1–5.

Fernando, W.U.K., Samarakkody, R. M. and Halgamuge, M.N. (2020). Smart Transportation Tracking Systems Based on the Internet of Things Vision. In: Z. Mahmood (eds) *Connected Vehicles in the Internet of Things* (pp. 143–66). New York, NY: Springer.

Gandhi, B.K. and Rao, M.K. (2016). A prototype for IoT based car parking management system for smart cities. *Indian Journal of Science and Technology*, **9**(17), 1–6.

Gayathri, T. (2017). A Survey on Vehicle Health Monitoring and Prediction System. *International Journal of Computer Science Trends and Technology (IJCST)*, **5**(3), 191–3.

Goshare (2020). *The On-Demand Truck App Being Called Uber for Trucks*. Available at: https://www.goshare.co/uber-for-moving/ (accessed on 03/03/2020)

Grant Thornton (2016), *Smart Transportation - Transforming Indian Cities*. Available at: https://www.grantthornton.in/globalassets/1.-member-firms/india/assets/pdfs/smart-transportation-report.pdf (accessed on 03/03/2020)

Hashem, I.A.T., Chang, V., Anuar, N. B., Adewole, K., Yaqoob, I., Gani, A., ... and Chiroma, H. (2016). The role of big data in smart city. *International Journal of Information Management*, **36**(5), 748–58.

Hemalatha, M. (2015, March). Intelligent parking system using vehicular data cloud services. In: *2015 International Conference on Innovations in Information, Embedded and Communication Systems (ICIIECS)* (pp. 1-5), IEEE., Coimbatore,19–20/03/2015.

Hsu, C.Y., Yang, C.S., Yu, L.C., Lin, C.F., Yao, H.H., Chen, D.Y., ... and Chang, P.C. (2015). Development of a cloud-based service framework for energy conservation in a sustainable intelligent transportation

system. *International Journal of Production Economics*, **164**(n/a), 454–61.

Ianuale, N., Schiavon, D. and Capobianco, E. (2015). Smart cities and urban networks: are smart networks what we need. *Journal of Management Analytics*, **2**(4), 285–94.

Javed, M.A., Zeadally, S. and Hamida, E.B. (2019). Data analytics for cooperative intelligent transport systems. *Vehicular communications*, **15**(n/a), 63–72.

Lotlikar, T., Chandrahasan, M., Mahadik, A., Oke, M. and Yeole, A. (2016). Smart parking application. *International Journal of Computer Applications*, **149**(9), 32–37.

Mengru, T (2018). An exploratory study of Internet of Things (IoT) adoption intention in logistics and supply chain management: A mixed research approach. *The International Journal of Logistics Management*. **29**(1), n/a. DOI: 10.1108/IJLM-11-2016-0274.

Myeong, S., Jung, Y. and Lee, E. (2018). A study on determinant factors in smart city development: an analytic hierarchy process analysis. *Sustainability*, **10**(8), 2606. DOI:10.3390/su10082606

Pham, T.N., Tsai, M.F., Nguyen, D.B., Dow, C.R. and Deng, D-J. (2015). A Cloud-Based Smart-Parking System Based on Internet-of-Things Technologies. *IEEE Access*, **3**(n/a), 1581–91. DOI: 10.1109/ACCESS.2015.2477299

Prabhu, B., Balakumar, N. and Antony, J. (2017). A Research on Smart Transportation Using Sensors and Embedded Systems. *International Journal of Innovative Research in Computer Science & Technology*. **5**(1), n/a. 198-202. DOI: 0.21276/ijircst.2017.5.1.5.

Qiu, T., Chen, N., Li, K., Atiquzzaman, M. and Zhao, W. (2018). How can heterogeneous Internet of Things build our future: A survey? *IEEE Communications Surveys & Tutorials*, **20**(3), 2011–27.10.1109/COMST.2018.2803740

Qureshi, K.N. and Abdullah, A.H. (2013). A survey on intelligent transportation systems. *Middle-East Journal of Scientific Research*, **15**(5), 629–42.

Ramundo, L., Taisch, M. and Terzi, S. (2016). State of the art of technology in the food sector value chain towards the IoT. In:*2016 IEEE 2nd International Forum on Research and Technologies for Society and Industry Leveraging a better tomorrow (RTSI)*, p. 1-6. Chicago, 07–09/09/2016.

Sharma, V. and Tiwari, R. (2016). A review paper on "IOT" & It's Smart Applications. *International Journal of Science, Engineering and Technology Research (IJSETR),* **5**(2), 472–76.

Sijs, J., Papp, Z. and van den Bosch, P.P.J. (2008, June). Vehicle motion-state-estimation using distributed sensing. In: *2008 IEEE Intelligent Vehicles Symposium* (pp. 458-463). IEEE., Eindhoven, the Netherlands, 04-06/06/2008.

Tsaramirsis, G., Karamitsos, I. and Apostolopoulos, C. (2016, March). Smart parking: An IoT application for smart city. In: *2016 3rd International Conference on Computing for Sustainable Global Development (INDIACom)* (pp. 1412-1416). IEEE., New Delhi,16-18/03/2016.

Verdouw, C.N., Vucic, N., Sundmaeker, H. and Beulens, A. (2013). Future internet as a driver for virtualization, connectivity and intelligence of agri-food supply chain networks. *International Journal on Food System Dynamics,* **4**(4), 261–72.

Verdouw, C.N., Wolfert, J., Beulens, A.J. M. and Rialland, A. (2016). Virtualization of food supply chains with the internet of things. *Journal of Food Engineering,* **176**(n/a), 128–36.

Wang, X. and Li, Z. (2016). Traffic and Transportation Smart with Cloud Computing on Big Data. *International Journal of Computer Science and Applications,* **13**(1), 1–16.

Wang, Y., Tan, G., Wang, Y. and Yin, Y. (2012). Perceptual control architecture for cyber–physical systems in traffic incident management. *Journal of Systems Architecture,* **58**(10), 398–411.

Zanella, A., Bui, N., Castellani, A., Vangelista, L. and Zorzi, M. (2014). Internet of things for smart cities. *IEEE Internet of Things journal,* **1**(1), 22–32.

Zhu, L., Yu, F.R., Wang, Y., Ning, B. and Tang, T. (2018). Big data analytics in intelligent transportation systems: A survey. *IEEE Transactions on Intelligent Transportation Systems,* **20**(1), 383–98.

المجلة العلمية لجامعة الملك فيصل
The Scientific Journal of King Faisal University
العلوم الأساسية والتطبيقية
Basic and Applied Sciences

Study of the Electric Quadrupole Transitions in $^{50-51}Mn$ Isotopes by Using *F742pn* and *F7cdpn* Interactions

دراسة الانتقالات رباعية القطب الكهربائي في نظائر $^{50-51}Mn$ باستعمال تفاعلات *F742pn* و *F7cdpn*

Ali Khalaf Hasan, Fatema Hameed Obeed and Azahr Nadham Rahim
Department of Physics, Faculty of Education for Girls, University of Kufa, Najaf, Iraq

علي خلف حسن، فاطمة حميد عبيد، ازهار ناظم رحيم
قسم الفيزياء، كلية التربية للبنات، جامعة الكوفة، النجف، العراق

LINK الرابط	RECEIVED الاستقبال	ACCEPTED القبول	PUBLISHED ONLINE النشر الإلكتروني	ASSIGNED TO AN ISSUE الإحالة لعدد
https://doi.org/10.37575/b/sci/0070	27/12/2020	14/03/2021	14/03/2021	01/12/2021

NO. OF WORDS عدد الكلمات	NO. OF PAGES عدد الصفحات	YEAR سنة العدد	VOLUME رقم المجلد	ISSUE رقم العدد
4267	5	2021	22	2

ABSTRACT

The nuclear shell-model has been used to compute excitation levels of ground band and electric quadrupole transitions for $^{50-51}Mn$ isotopes in f-shell. In the present study, *f742pn* and *f7cdpn* effective interactions have been carried out in full f-shell by using Oxbash Code. The radial wave functions of the single-particle matrix elements have been calculated in terms of the harmonic oscillator (*Ho*) and Skyrme20 potentials. The predicted theoretical results have been compared with the available experimental data; it has been seen that the predicted results are in agreement with the experimental data. From the current results of the calculations, many predictions of angular momentum and parities of experimental states have been made, and the energy spectra predictions of the ground band and $B(E2;\downarrow)$ electric quadrupole transitions in $^{50-51}Mn$ isotopes of the experimental data are not known yet. In the nuclear shell-model calculations framework, energy levels have been determined for $^{50-51}Mn$ isotopes; new values of electric quadrupole transitions have been predicted in the studied results. This investigation increases the theoretical knowledge of all isotopes with respect to the energy levels and reduced transition probabilities.

الملخص

استعملنا أنموذج القشرة النووي لحساب مستويات الأثارة للحزمة الأرضية والانتقالات رباعية القطب الكهربائية لنظائر $^{50-51}Mn$ في القشرة –f. ، في الدراسة الحالية التفاعلات المؤثرة *f742pn* و *f7cdpn* نفذوا في القشرة الكاملة f- باستعمال كود الاوكسباش. تم حساب الدوال الموجية القطرية لعناصر المصفوفة للجسيم المنفرد في حدود جهود المذبذب التوافقي (*Ho*) وسكايرم 20. وتمت مقارنة النتائج النظرية المتوقعة مع البيانات التجريبية المتوافرة، وقد لوحظ أن النتائج المتوقعة تتفق بشكل جيد مع البيانات التجريبية. من النتائج الحالية للحسابات: هناك عدة تنبؤات للزخم الزاوي والتماثلات في الحالات التجريبية، فضلا عن توقعات أطياف الطاقة للحزمة الأرضية واحتمالات الانتقالات رباعية القطب الكهربائي $B(E2;\downarrow)$ في نظائر $^{50-51}Mn$ للبيانات التجريبية غير المعروفة حتى الآن. في نطاق حسابات أنموذج القشرة النووي، تم تحديد مستويات الطاقة لنظائر $^{50-51}Mn$ ، كما تم توقع قيم جديدة للانتقالات رباعية القطب الكهربائي في النتائج المدروسة. هذا الاقتراح يزيد المعرفة النظرية لجميع النظائر فيما يتعلق بمستويات الطاقة و احتمالات الانتقال المختزلة.

KEYWORDS
الكلمات المفتاحية
Effective charges, excitation levels, Oxbash Code, shell-model, ground band, angular momentum, and parity
الشحنات المؤثرة، مستويات التهيج , كود الاوكسباش، أنموذج القشرة، الحزمة الأرضية ،الزخم الزاوي والتماثل

CITATION
الإحالة
Hasan, A.K., Obeed, F.H. and Rahim, A.N. (2021). Study of the electric quadrupole transitions in $^{50-51}Mn$ isotopes by using *F742pn* and *F7cdpn* Interactions. *The Scientific Journal of King Faisal University: Basic and Applied Sciences*, **22**(2), 11–5. DOI: 10.37575/ b/sci/0070

1. Introduction

The nuclear structure of neutron-rich nuclei above ^{40}Ca magic nucleus has been the recent experimental focus. The mechanism can cause changes in nuclear structure as neutron numbers increase in any nuclear system mechanism (it is an open question)!!(Srivastava and Mehrotra 2010). Neutron-rich f-shell isotopes are of private interest, too. In astrophysics, like the electron capture rate in supernovae explosion, experimental and theoretical explanations can be achieved as a satisfactory description for these isotopes (Kaneko et al., 2008). Previously, several neutron-rich nuclei in $f_{7/2}$-shell studies have been carried out and investigated by many researchers, including the three-body force manifestations in spectra, binding energies, seniority mixing, particle-hole symmetry, electromagnetic and particle transition rate (Volya, 2009). The energy states and electric quadrupole transitions for the $0f_{7/2}$ proton-shell nuclei (^{50}Ti, ^{51}V, ^{52}Cr, ^{53}Mn, ^{54}Fe, and ^{55}Co) have been calculated within the spherical shell-model framework, assuming a ^{48}Ca as a closed core (Saaymant and Irvine, 1976), as well as $f_{7/2}$ shell-model study ($^{43-46}$Ca and $^{43-45}$Sc) in pure $f^n_{7/2}$ configuration (Muto et al.,1978). Hundreds of years ago, many models and theories were built to describe and illustrate the experimental observations of the nuclear structure and reaction properties for various nuclei (Bacca, 2016). One of those nuclear models is the nuclear shell-model, which has successfully explained the nuclear structure for several nuclei in different areas of the periodic table, such as Ca, Ti, Cr, and Fe (Gambhir et al .,1982). The nuclear shell-model is considered the primary theoretical tool for understanding the nuclei properties. It can be used for preparing qualitative understanding due to its simple single-particle form, which is essentially based on the effective interaction use, actually because of its well-known form. Within the shell-model approach, just the particles outside the close core can make up the filled shells (valence nucleons), which are considered active nucleons, and calculations are achieved in truncated Hilbert space called the model space (Gargano et al., 2014). Nuclear shell-model calculations are carried out within a model space in which the valence nucleons are limited to distribute over a few orbits that are incapable of reproducing the measured static moments or transition strengths and other nuclear properties (Radhi and Bouchebak, 2003). Multipole transition probability, binding energies, separation energies, beta decay, quadrupole moments, and magnetic moments have been calculated based on nuclear shell-model codes such as OXBASH (Brown et al., 2005), NSHELL(Brown and Rae, 2007), ANTOINE (Caurier and Nowacki, 1999), NATHAN (Caurier et al., 1999) and NuShellX@MSU (Brown and Rae, 2004). These had been vastly utilized besides the single-particle wave function, the two-body matrix element (TBME) of variety shell-model spaces, and different effective interactions had been suggested depending on two-body interaction strength. TBME has been

Corresponding Author: Fatema Hameed Obeed fatimahh.alfatlawi@uokufa.edu.iq, 0096407817322815 المؤلف المراسل: فاطمة حميد عبيد

represented as an important action in calculating the nuclear properties (Brown and Rae, 2004). However, in the current calculations, the Oxbash Code has been performed to find some nuclear properties for nuclear structure. This is a set of codes for carrying out shell-model calculations with dimensions up to 50,000 in the *J-T* scheme and about 2,000,000 in the M-scheme. Oxbash comes with a library of model spaces and interactions (Hasan and Obeed, 2017). The current study aims to compute the energy levels and electric quadrupole transitions for $^{50-57}Mn$ isotopes by using effective interactions f742pn and f7cdpn in f-shell then make a comparison of the current results with the available experimental values.

2. Theory

In this work, nucleons of $^{50-51}$Mn isotopes have been distributed to the nucleons in $f_{7/2}$-shell, and these isotopes have proton and neutron numbers lying above the magic numbers Z=20 and N=20. Although the number of active valence nucleons is low enough in these nuclei to allow for a full shell-model description, these nuclei forms can be an interesting island in the nuclide chart. An essential objective of nuclear structure theory has carried out shell-model studies with single-particle (SP) energies and residual two-body interactions that are both derived from a realistic nucleon-nucleon interaction (Coraggio et al., 2007). Generally, a quantum mechanics solution to the Schrödinger equation have been necessary steps to a specified appropriate Hamiltonian, so that a standard shell-model of effective Hamiltonian can be written as:

$$H = \sum_a \varepsilon_a n_a + \sum_{a\le b,c\le d} \sum_{JT} V_{JT}(ab;cd) \sum_{MT_Z} A^{+}_{JMTT_Z}(ab) A_{JMTT_Z}(cd)] \quad (1)$$

Where n_a: describes the number operator of an orbit (a) of quantum numbers (n_a, l_a, j_a) but the symbol ($A_{JMTT_Z}(cd)$) denotes the creation operator of nucleon-pairs in orbits (a and b) with spin quantum numbers (JM) and isospin quantum numbers (T, T_Z), but the last terms in equ. (1) can be written as the following (Honma et al., 2002:135c):

$$\sum_{k<l} V_{kl} = [\sum_{a\le b,c\le d} \sum_{JT} V_{JT}(ab;cd) \sum_{MT_Z} A^{+}_{JMTT_Z}(ab) A_{JMTT_Z}(cd)] \quad (2)$$

Where $\sum_{k<l} V_{k\ell}$ is expressed on residual two-body interactions and can be re-written as:

$$\sum_{k<l} V_{k\ell} = \langle j_1 j_2 | V_{12} | j_3 j_4 \rangle \quad (3)$$

From the equ. (1, 2, and 3) it can get on the following :

$$H = \sum_a \varepsilon_a n_a + \langle j_1 j_2 | V_{12} | j_3 j_4 \rangle = \sum_{k=\ell}^{A} H_0 + \langle j_1 j_2 | V_{12} | j_3 j_4 \rangle \quad (4)$$

By separating the summations into core and valence contributions in eq. (4), the eq. (4) can be re-written:

$$H = H_{core} + H_1 + H_2 + \langle j_1 j_2 | V_{12} | j_3 j_4 \rangle \quad (5)$$

Here, H_{core} implies on all of the interactions of nucleons making up the close core, while H_1 and H_2 refer to the single-particle contributions from particles (1 and 2) and $\langle j_1 j_2 | V_{12} | j_3 j_4 \rangle$ are the residual interactions describing all interactions between particles (1 and 2) as well as any interaction with core nucleons. Inserting this form of the Hamiltonian into the Schrödinger equation yields an analogous expression for the energy (Lawson, 1980:43):

$$E = E_{core} + E_1 + E_2 + \langle j_1 j_2 | V_{12} | j_3 j_4 \rangle \quad (6)$$

The terms of (equ. 6) can be interpreted as follows. E_{core} is the binding energy of the core nucleus, E_1 and E_2 are defined as the single-particle energies of orbitals outside the core, and $\langle j_1 j_2 | V_{12} | j_3 j_4 \rangle$ is the residual interaction. Equation (6) is necessary to calculate the energy levels for pure configurations only. The excitation energy levels, wave functions, effective charges, and core polarization effects are necessary inputs to calculate the reduced electric quadrupole transition probabilities, $B(E2\downarrow)$. Reduced electric quadrupole transition probabilities are considered the observable necessity, and quadrupole moment ratios within the low-lying state bands can provide more information about the nuclear structure (Hasan, 2018:191). The present theoretical results of the reduced quadrupole transition probability $B(E2\downarrow)$ can be carried out from the recent calculations study of the reduced electric matrix element and from the initial and final nuclear states that are given in the following equation (Ali, 2018:1):

$$T(EJ) = \langle J_f \| \sum_k e(k) \hat{Q}_J(\vec{r})_k \| J_i \rangle_{MS} \quad (7)$$

e(k): represents the electric charge for the k-th nucleon and e(k) = 0 for the neutron.

While the electric matrix element can be represented in terms of the model space matrix elements only by assigning effective charges (e_{eff} (t_z)) to the neutrons and protons (Pandya and Singh, 1974:66)

$$T(EJ) = \sum_{t_z} e_{eff}(t_z) \langle J_f || \hat{Q}_2(\vec{r}, t_z z) || J_i \rangle_{MS} \quad (8)$$

It can be the expression for the effective charges to include the neutron excess explicitly (Brown, 2001:575):

$$e_{eff}(t) = e(t) + e\delta e(t), \delta e(t) = \frac{Z}{A} - \frac{0.32(N-Z)}{A} - 2t_z [0.32 - \frac{0.3(N-Z)}{A}] \quad (9)$$

Where $\delta e(t_Z)$ is expressed from the polarization charge for nucleon.

The reduced quadrupole transition probability can be according to the relation:

$$B(E2; I_i \to I_f \downarrow) = \frac{\langle I_f \| T^{E2} \| I_i \rangle^2}{2I_i + 1} \quad (10)$$

The chi-square between the computed and the experimental values for each energy level can be calculated according to the following equation (Walker, 1995:62):

$$\chi^2 = \sum \frac{(E_{exp.} - E_{theor.})^2}{E_{theor.}} \quad (11)$$

But chi-square conditions are not applied for reduced electric quadrupole transition probability.

3. Results and Discussion

In this paper, some properties of nuclear structure for ground bands of $^{50-57}Mn$ isotopes have been calculated using Oxbash Code. Valence nucleons of these isotopes are distributed in f-shell. In these calculations, *f7pn* model space, *f742pn,* and *f7cdpn* interactions have been utilized to estimate the energy levels and the reduced quadrupole transition probability for the isotopes mentioned above. The reduced quadrupole transition probabilities have been carried out using harmonic oscillator (*Ho*) and Skyrme20 potentials at the isotopes' Oxbash Code under this study. So the $^{50,51}Mn$ isotopes can be discussed as follows.

3.1. Energy Levels:

Table.1 illustrates the comparison between the predicted theoretical results of positive parity states in ^{50}Mn nucleus for *f742pn* and *f7cdpn* interactions and the recent experimental data. This nucleus consists of (25 proton) and (25 neutron) outside ^{40}Ca magic core, which have filled out the ($(1f_{7/2})$shell). In table 1, theoretical values of $\{1_1^+$ and $2_1^+\}$ states of f742pn and f7cdpn interactions have agreed very well with experimental energies {0.651 and 0.800} *MeV* respectively (Chen and Singh, 2019: n/a). The experimental energies

{0.659 and 1.765MeV} appeared in good agreement with expected theoretical values at both *f742pn* and *f7cdpn* interactions in order to confirm the states {3_1^+ and 4_1^+} of the above experimental energies. The theoretical states {7_1^+, 9_1^+, and 11_1^+} have confirmed the experimental values {1.030, 2.534, and 4.585} and *MeV* respectively . In current studied results, the states {8_1^+} are determined at the experimental energies {3.177} *MeV*, which are unknown at spins and parities experimentally. New values at energies and states in both *f742pn* and *f7cdpn* interactions have been predicted in the studied present results as the states {6_1^+, 10_1, and 12_1^+} have not been known at the energy and state values experimentally.

Table 1: Comparison between theoretical and experimental excitation energies (*MeV*) (Chen and Singh, 2019:n/a) for ^{50}Mn nucleus by using *F742pn* and *F7cdpn* Interactions

$J^+_{theor.}$	$E_{(x)theor.}$ *F742pn.* Interaction	$E_{(x)theor.}$ *F7cdpn.* Interaction	$J^+_{Exp.}$	$E_{(x)}$ Exp.	χ^2 *F742pn.* Interaction	χ^2 *F7cdpn.* Interaction	Status
0_1^+	0.000	0.000	0^+	0.000	0.0848	0.1120	acceptance
5_1^+	0.355	0.464	5^+	0.225			
1_1^+	0.523	0.637	1^+	0.651			
3_1^+	0.611	0.718	(6^+)	0.659	0.0309	0.0492	determination
6_1^+	0.903	1.001	------	------			
7_1^+	1.139	1.203	(7^+)	1.030			
2_1^+	1.148	1.190	2^+	0.800	0.0025	0.0007	confirmation
4_1^+	1.878	1.979	$(3^+,7^+)$	1.765			
9_1^+	2.809	2.863	(9^+)	2.534			
8_1^+	3.026	3.099	------	3.177	0.1182	0.1619	total
11_1^+	4.658	4.682	(11^+)	4.585			
10_1^+	5.348	5.375	------	------			
12_1^+	7.958	7.936	------	------			

While ^{51}Mn isotope has 25 protons and 26 neutrons, which have occupied the $1f_{7/2}$ shell above ^{40}Ca magic core. The compression between the theoretical and experimental results (Jimin. and Xiaolong, 2017:n/a) are shown in table.2. From these comparisons, there has been a good agreement for theoretical energy values at states {$11/2_1^-$, $15/2_1^-$, $17/2_1^-$, $19/2_1^-$, and $23/2_1^-$} with experimental data. In this study, calculations of the state {$1/2_1^-$} have been affirmed for experimental energy {3.423} *MeV* and have not been affirmed at states experimentally. The theoretical states like {$25/2_1^-$} have been determined as new states of available experimental data {8.498 MeV}. In this nucleus, new levels of energies and states have appeared in this study at both *f742pn* and *f7cdpn* states interactions like states {$3/2_1^-$, $13/2_1^-$, and $21/2_1^-$} and disappeared in the experimental levels scheme.

Table 2.Comparison between theoretical and experimental excitation energies (*MeV*) (Jimin. and Xiaolong, 2017:n/a) for ^{51}Mn nucleus by using F742pn and F7cdpn Interactions

$J^-_{theor.}$	$E_{x,theor.}$ *F742pn.* Interaction	$E_{x,theor.}$ *F7cdpn.* Interaction	$J^-_{Exp.}$	$E_{x,Exp.}$	χ^2 *F742pn.* Interaction	χ^2 *F7cdpn.* Interaction	Status
$5/2_1^-$	0.000	0.000	$5/2^-$	0.000	0.0136	0.0072	acceptance
$7/2_1^-$	0.093	0.054	$7/2^-$	0.237			
$3/2_1^-$	1.526	1.506	------	------			
$9/2_1^-$	1.529	1.508	$9/2^-$	1.139	0.0022	0.0022	determination
$11/2_1^-$	1.571	1.523	$11/2^-$	1.488			
$15/2_1^-$	3.236	3.177	$15/2^-$	3.250			
$1/2_1^-$	3.290	3.291	$(1/2^-,7/2^-)$	3.423	0.0003	0.0047	confirmation
$13/2_1^-$	3.490	3.455	------	------			
$17/2_1^-$	3.720	3.718	$17/2^-$	3.680			
$19/2_1^-$	4.222	4.170	$19/2^-$	4.139	0.0161	0.0141	total
$21/2_1^-$	6.338	6.281	------	------			
$23/2_1^-$	6.522	6.445	$23/2^-$	6.471			
$25/2_1^-$	8.453	8.305	------	8.498			

3.2. Reduced Electric Quadrupole Transition Probability:

The radial wave functions for the single-particle matrix elements have been calculated using the *(Ho)*, default *SK20* potentials, and the effective nucleon charges. Oxbash Code has been used to calculate the reduced electric quadrupole transition for estimating a better fitting with the experimental values. The (*Ho*) and *SK20* parameters are size parameter values of ($^{50-51}Mn$ isotopes) and are *b= 1.928 fm of ^{50}Mn nucleus and b= 1.9235 fm of ^{51}Mn nucleus* and Skyrme parameters *are* t_0, t_2, t_3, w_0, *a*, x_0, x_1, x_2, x_3 of values {1445.322,246.867,-131.786, 12103.863,148.637, 0.5,0.340, 0.580, 0.127, 0.030} respectively. There has been excellent acceptance between the theoretical values of the transition strength *B(E2↓)* of $^{50-51}Mn$ isotopes at both *f742pn* and *f7cdpn* interactions and the experimental data. Tables 3–6 display the comparison between theoretical values of the electric quadrupole transition probability and the experimental data. For ^{50}Mn nucleus, tables 3 and 4 show that the experimental values of B(E2↓) from{$2_1^+ \rightarrow 0_1^+$ } and {$(9_1^+)\longrightarrow(7_1^+)$} have agreed with the predicted theoretical values of *f742pn* and *f7cdpn* interactions. While tables 5 and 6 show the comparison between the predicted theoretical values of the electric quadrupole transition probability and experimental data of ^{51}Mn nucleus. From this comparison, an excellent agreement of theoretical values of the experimental data has appeared, such as {$7\backslash2_1^-\longrightarrow5\backslash2_1^-$,$9\backslash2_1^-\longrightarrow7\backslash2_1^-$,$11\backslash2_1^-\longrightarrow7\backslash2_1^-$,$3\backslash2_1^-\longrightarrow7\backslash2_1^-$ and $1\backslash2_1^-\longrightarrow5\backslash2_1^-$}. New values of the quadrupole electric transitional probability of $^{50-51}Mn$ nuclei have been expected in this studied results like *B(E2↓)* from {$6_1^+\longrightarrow4_1^+$,$(8_1^+)\longrightarrow(6_1^+)$,$10_1^+\longrightarrow 8_1^+$and $12_1^+\longrightarrow10_1^+$} of ^{50}Mn nucleus but of ^{51}Mn nucleus the values have been {$15\backslash2_2^-\longrightarrow11\backslash2_1^-$,$19\backslash2_2^-\longrightarrow15\backslash2_1^-$,$21\backslash2_1^-\longrightarrow17\backslash2_1^-$,$23\backslash2_2^-\longrightarrow19\backslash2_1^-$ and $25\backslash2_1^-\longrightarrow21\backslash2_1^-$}; these values have not been known in the experimental data.

Table 3.Comparison between theoretical and experimental values(Chen and Singh, 2019:n/a) of electric quadrupole transition for ^{50}Mn nucleus by using *F742pn* interaction

$J_i\rightarrow J_f$	$B(E2\downarrow)_{theor.}$ $B(E2\downarrow)$ e^2fm^4 *Ho* e_p=1.523e e_n=0.536e	$B(E2\downarrow)$ W.u *Ho* e_p=1.523e e_n=0.536e	$B(E2\downarrow)$ e^2fm^4 *SK20* e_p=1.523e e_n=0.536e	$B(E2\downarrow)$ W.u *SK20* e_p=1.523e e_n=0.536e	$B(E2\downarrow)_{Exp.}$ W.u
$2_1^+\rightarrow0_1^+$	153.1	13.992	150.9	13.791	13.9^{+24}_{-22}
$4_1^+\rightarrow2_1^+$	0.3272	0.0299	0.3316	0.0303	>15
$6_1^+\rightarrow4_1^+$	37.20	3.399	36.65	3.349	------
$8_1^+\rightarrow6_1^+$	79.64	7.278	78.48	7.172	------
$10_1^+\rightarrow8_1^+$	0.003658	0.000334	0.003604	0.000329	------
$12_1^+\rightarrow10_1^+$	11.76	1.074	11.58	1.058	------
$3_1+\rightarrow1_1^+$	149.9	13.700	147.7	13.498	64^{+30}_{-21}
$9_1^+\rightarrow7_1^+$	163.5	14.943	161.1	14.723	12.9^{+24}_{-17}

Table 4: Comparison between theoretical and experimental values(Chen and Singh, 2019:n/a) of electric quadrupole transition for ^{50}Mn nucleus by using F7cdpn interaction

$J_i\rightarrow J_f$	$B(E2\downarrow)_{theor.}$ $B(E2\downarrow)$ e^2fm^4 *Ho* e_p=1.523e e_n=0.536e	$B(E2\downarrow)$ W.u *Ho* e_p=1.523e e_n=0.536e	$B(E2)$ e^2fm^4 *Sk20* e_p=1.523e e_n=0.536e	$B(E2)$ W.u *Sk20* e_p=1.523e e_n=0.536e	$B(E2\downarrow)_{Exp.}$ W.u
$2_1^+\rightarrow0_1^+$	153.1	13.992	150.9	13.791	13.9^{+24}_{-22}
$4_1^+\rightarrow2_1^+$	1.039	0.0949	1.040	0.0951	>15
$6_1^+\rightarrow4_1^+$	36.99	3.381	36.45	3.331	------
$8_1^+\rightarrow6_1^+$	78.73	7.1954	78.25	7.1516	------
$10_1^+\rightarrow8_1^+$	0.2357	0.0215	0.2309	0.0211	------
$12_1^+\rightarrow10_1^+$	0.2002	0.0182	0.2042	0.0186	------
$3_1^+\rightarrow1_1^+$	148.5	13.572	146.3	13.371	64^{+30}_{-21}
$9_1^+\rightarrow7_1^+$	163.4	14.933	161.0	14.714	12.9^{+24}_{-17}

Table 5: Comparison between theoretical and experimental values (Jimin. and Xiaolong, 2017:n/a) of electric quadrupole transition for ^{51}Mn nucleus by using *F742pn* interaction

$J_i\rightarrow J_f$	$B(E2\downarrow)_{theor.}$ $B(E2\downarrow)$ e^2fm^4 *Ho* e_p=2.168e e_n=1.275e	$B(E2\downarrow)$ W.u *Ho* e_p=2.168e e_n=1.275e	$B(E2)$ e^2fm^4 *SK20* e_p=2.191e e_n=1.311e	$B(E2)$ W.u *SK20* e_p=2.191e e_n=1.311e	$B(E2\downarrow)_{Exp.}$ W.u
$7\backslash2_1^-\rightarrow5\backslash2_1^-$	528.6	46.973	527.6	46.884	47± 13
$9\backslash2_1^-\rightarrow7\backslash2_1^-$	221.5	19.683	220.0	19.549	27 ± 10
$9\backslash2_1^-\rightarrow5\backslash2_1^-$	122.8	10.912	122.0	10.841	156
$11\backslash2_1^-\rightarrow7\backslash2_1^-$	315.5	28.036	313.6	27.867	21± 6
$3\backslash2_1^-\rightarrow7\backslash2_1^-$	110.0	9.774	109.2	9.703	12 ± 10
$1\backslash2_1^-\rightarrow5\backslash2_1^-$	42.78	3.801	43.58	3.872	4.6 ± 15
$17\backslash2_1^-\rightarrow13\backslash2_1^-$	16.75	1.488	16.66	1.480	0.092 ± 4
$15\backslash2_1^-\rightarrow11\backslash2_1^-$	342.3	30.417	340.1	30.222	------

$19\backslash 2_1^- \rightarrow 15\backslash 2_1^-$	136.6	12.138	135.8	12.067	------
$21\backslash 2_1^- \rightarrow 17\backslash 2_1^-$	103.2	9.170	102.8	9.135	------
$23\backslash 2_1^- \rightarrow 19\backslash 2_1^-$	228.1	20.269	227.0	20.171	------
$25\backslash 2_1^- \rightarrow 21\backslash 2_1^-$	139.9	12.431	139.3	12.378	------

Table 6: Comparison between theoretical and experimental values (Jimin. and Xiaolong, 2017:n/a) of electric quadrupole transition for ^{51}Mn nucleus by using *F7cdpn* interaction

$J_i \rightarrow J_f$	$B(E2\downarrow)_{theor.}$				$B(E2\downarrow)_{Exp.}$ W.u
	$B(E2\downarrow)$ $e^2 fm^4$	$B(E2\downarrow)$ W.u	$B(E2)$ $e^2 fm^4$	$B(E2)$ W.u	
	Ho e_p=2.193e e_n=1.315	**Ho** e_p=2.193e e_n=1.315e	**Sk20** e_p=2.193e e_n=1.315e	**Sk20** e_p=2.193e e_n=1.315e	
$7\backslash 2_1^- \rightarrow 5\backslash 2_1^-$	526.7	46.804	523.6	46.528	47 ± 13
$9\backslash 2_1^- \rightarrow 7\backslash 2_1^-$	219.5	19.505	218.1	19.381	27± 10
$9\backslash 2_1^- \rightarrow 5\backslash 2_1^-$	122.6	10.894	121.8	10.823	156
$11\backslash 2_2^- \rightarrow 7\backslash 2_1^-$	317.4	28.205	315.5	28.036	21± 6
$3\backslash 2_1^- \rightarrow 7\backslash 2_1^-$	229.2	20.367	227.8	20.243	<0.14
$3\backslash 2_1^- \rightarrow 7\backslash 2_2^-$	108.3	9.623	107.5	9.552	12 ± 10
$1\backslash 2_2^- \rightarrow 5\backslash 2_1^-$	42.69	3.793	43.44	3.860	4.6± 15
$3\backslash 2_2^- \rightarrow 7\backslash 2_1^-$	0.1509	0.0134	0.1566	0.0139	2.6± 15
$17\backslash 2_1^- \rightarrow 13\backslash 2_1^-$	19.99	1.776	19.87	1.765	0.092± 4
$15\backslash 2_2^- \rightarrow 11\backslash 2_1^-$	343.8	30.551	341.6	30.355	------
$19\backslash 2_2^- \rightarrow 15\backslash 2_1^-$	134.1	11.916	133.2	11.836	------
$21\backslash 2_1^- \rightarrow 17\backslash 2_1^-$	106.1	9.428	105.6	9.383	------
$23\backslash 2_2^- \rightarrow 19\backslash 2_1^-$	227.9	20.251	226.7	20.145	------
$25\backslash 2_1^- \rightarrow 21\backslash 2_1^-$	141.7	12.591	133.7	11.881	------

4. Conclusions

The calculations for the positive and negative parity levels of $^{50\text{-}51}Mn$ isotopes have indicated that the nuclear shell-model and *f742pn* and *f7cdpn* interactions have been very successful in explaining the nuclear structure of these nuclei due to the less complex interactions of valence nucleons. There has been an acceptance agreement of the studied theoretical results and experimental data of all properties that have been calculated in the present results. Also, some spins and parities of these isotopes have been confirmed and determined. This showed in chi-square values that appeared very small when the observed data lies close to the expected data from through agreement values of them as well as determination, confirmation, and total. Furthermore, new values of energy levels and the quadrupole electric transitional probability, which have been predicted in this study's results, have not been known in the experimental data. These values can add more information for theoretical knowledge for all isotopes in this work. All calculations have been compared with the available experimental data; furthermore, they are very functional for compiling nuclear data tables. It has been concluded that the present calculations have consolidated two forms of effective interactions and two types of residual interactions for (f-shell) to calculate the energy levels and the electric quadrupole transition probability whose set has been appropriated for providing theoretical predictions of the nuclear structure for each isotope and can achieve a high degree of conformity with the available results, also succeeded in describing the available transition data.

Biographies

Ali Khalaf Hasan

Department of Physics, Faculty of Education for Girls, University of Kufa, Najaf, Iraq, 0096407802461719, alikh.alsinayyid@uokufa.edu.iq

Dr. Hasan is an Iraqi professor; he obtained his Ph.D. in nuclear physics from the University of Basra-Iraq in 2009. His main research interests are quantum, theoretical, nuclear, and radiation physics. He participated in many local scientific conferences in Iraq. He published around 50 papers in scientific journals in Iraq and international journals within Scopus containers, such as the *International Journal of Physical Sciences, Ukrainian Journal of Physics International Journal of Current Research*, and *AIP Conference Proceedings*. ORCID: 0000-0002-8126-5179

Fatema Hameed Obeed

Department of Physics, Faculty of Education for Girls, University of Kufa, Najaf, Iraq, fatimahh.alfatlawi@uokufa.edu.iq, 0096407817322815

Mrs. Obeed is an Iraqi assistant professor. She obtained a master's in nuclear physics from Kufa University-Iraq in 2010. Her main research interests are theoretical study in nuclear physics of nuclear structure using Fortran and MATLAB programming codes. She obtained training in teaching methods and computer education. Obeed participated in many local and international scientific conferences. She published six research papers in local scientific journals in Iraq and international journals within Scopus containers. ORCID: 0000-0003-2076-0376.

Azhar Nadham Rahim

Physics Department, College of Education for Pure Sciences, University of Karbala, Karbala, Iraq, azhar.n@uokerbala.edu.iq, 0097407728781526

Mrs. Rahim is an Iraqi assistant teacher. She obtained a master's in nuclear physics from the University of Kufa-Iraq in 2018. Her research interests are nuclear structure study of nuclei using Fortran programming codes in addition to theoretical and radiation physics. She obtained training for teaching methods and computer education. Rahim has published research papers in international journals within Scopus containers. The central theme of this research was to calculate and describe the properties of the nuclei. ORCID: 0000-0001-9326-669X

References

Ali, A.H. (2018). Shell-model for study quadrupole transition rates in B2 in some neon isotopes in sd-shell with using different interactions. *Journal of Astrophysics and Aerospace Technology,* **6**(1), 1–6. DOI: 10.4172/2329-6542.1000160.

Bacca, S. (2016). Structure models: From shell-model to ab initio methods. *The European Physical Journal Plus*, **131**(107), 1–27. DOI: 10.1140/epjp/i2016-16107-6.

Brown, B.A. (2001). The nuclear shell-model towards the drip lines. *Progress in Particle and Nuclear Physics*, **47**(2), 517–99. DOI: 10.1016/S0146-6410(01)00159-4.

Brown, B.A. and Rae, W.D.M. (2014). The shell-model code NuShellX@ MSU. *Nuclear Data Sheets*, **120**(n/a), 115–8. DOI: 10.1016/j.nds.2014.07.022.

Brown, B.A. and Rae, W.D.M. (2007). NUSHELL@MSU. *MSU NSCL Report*, **542**(n/a), 1–29.

Brown, B.A, Etchegoyen, A., Godwin, N.S., Rae, W.D.M., Richter, W.A., Ormand, W.E., Warburton, Winfield, E.K., Zhao, L.S. and Zimmerman, C.H. (2005). Oxbash for Windows. *MSU-NSCL Report*, **1289**(n/a), 1–32.

Caurier, E. and Nowacki, F. (1999). Present status of shell-model techniques. *Acta Physica Polonica B*, **30**(3), 705–14.

Caurier, E., Langanke, K., Martfnez-Pinedo, G., Nowacki, E., Poves, A., Retamosa, J. and Zuker, A.P. (1999). Full $0\hbar w$ shell-model calculation of the binding energies of the 1f7/2 nuclei. *Physical Review C*, **59**(4), 2033. DOI: 10.1103/PhysRev C.59.2033.

Chen, J. and Singh, B. (2019). Adopted levels, gammas for 51Mn. *Nuclear Data Sheets*, **157**(1), n/a.

Coraggio. L., Covello, A., Gargano, A., Itaco, N., Entem, D.R., Kuo, T.T.S. and Machleidt, R. (2007). Low-momentum nucleon-nucleon interactions and shell-model Calculations. *Physical Review C*, **75**(24311), 1–8. DOI: 10.1103/PhysRevC.75.024311.

Gambhir, Y.K., Haq, S.,and. Suri, J.K. (1982). Number conserving shell-model for even Ca, Ti, Cr, and Fe isotopes. *Physical ReviewC*, **25**(1), 630–49. DOI: 10.1103/ Phys Rev C.25.630.

Gargano, A., Coraggio, L., Covello, A. and Itaco, N. (2014). Realistic shell-model calculations and exotic nuclei. In: *Journal of Physics Conference on Theoretical Nuclear Physics in Italy*, Cortona, Italy, 29-31/10/2103.

Hasan, A.K. (2018). Shell-model calculations for 18,19,20O isotopes by using usda and usdb interactions. *Ukrainian Journal of Physics*, **63**(3), 189–95. DOI: 10.15407 /ujpe63.3.189.

Hasan, A.K. and Obeed, F.H. (2017). Energy levels and reduced transition probabilities of 18-20F isotopes using USDA and W Hamiltonians. *International Journal of Physical Sciences*, **12**(10), 118 –29. DOI: 10.5897/IJPS2017.4630.

Honma, M., Brown, B.A., Mizusaki, T. and Otsuka, T. (2002). Full pf –shell calculations with a new effective. *Nuclear Physics A*, **704**(n/a),

134c–43c. DOI: 10.1016/S0375-9474(02)00774-1.

Jimin, W. and Xiaolong, H. (2017). Adopted Levels, gammas for 51Mn. *Nuclear Data Sheets*, **144**(1), n/a.

Kaneko, K., Sun, Y., Hasegawa, M. and Mizusaki, T. (2008). Shell-model study of single-particle and collective structure in neutron-rich Cr-isotopes. *Physical Review C*, **78**(064312), 1–9. DOI: 10.1103/PhysRevC.78.064312.

Lawson, R.D. (1980). *Theory of the Nuclear Shell Model*. United States: Oxford University Press.

Muto, K., Oda, T. and, H. (1978). Shell-model study of f7//2 shell nuclei in pure f n7//2 Configuration. *Progress of Theoretical Physics*, **60**(5), 1350–65. DOI: 10.1143 / ptp .60. 1350.

Pandya, S.P. and Singh, B.P. (1974). Effective interactions and charges in58Ni. *Pramana Journal of Physics*, **3**(2), 61–74. DOI: 10.1007/BF02847115.

Radhi, R.A. and Bouchebak, A. (2003). Microscopic calculations of C2 and C4 form factors in sd-shell nuclei. *Nuclear Physics A*, **716**(n/a), 87–99. DOI:10.1016 /S037 5- 9474 (02)01335-0.

Saaymant, R. and Irvine, J. M. (1976). Shell-model calculations for the 0 f7/2 proton-shell nuclei. *Journal of Physics G: Nuclear Physics*, **2**(5), 309–20. DOI: 10.1088 /0305-4616 /2 /5/007.

Srivastava, P.C. and Mehrotra, I. (2010). Large-scale shell-model calculations for odd-odd 58–62Mn Isotopes. *The European Physical Journal A*, **45**(n/a), 185–92. DOI: 10.1140/ epja /i2010-10995 -9.

Volya, A. (2009). Manifestation of three-body forces in f7/2-shell nuclei. *Europhysics Letters*, **86**(5), 1–6. DOI: 10.1209/0295-5075/86/52001.

Walker, B.F. (1995). The chi-square test: An introduction. *Comsig Review*, **4**(3), 61–4.

المجلة العلمية لجامعة الملك فيصل
The Scientific Journal of King Faisal University
العلوم الأساسية والتطبيقية
Basic and Applied Sciences

تعيين بعض الظروف المثلى لإنتاج ثنائي الأستيل من قبل بكتيريا Lactococcus Lactis

سميرة القطامي [1] و صياح أبو غرة [2] و صباح يازجي [2]
[1] قسم العلوم الأساسية، كلية الزراعة، جامعة دمشق، سوريا
[2] قسم علوم الأغذية، كلية الزراعة، جامعة دمشق، سوريا

Determining Optimal Conditions of Diacetyl Production Produced by Lactococcus Lactis Bacteria

Samira Al-Kotami [1], Sayah Abou Ghorra [2] and Sabah Yuzaji [2]
[1] Department of Basic Science, Faculty of Agriculture, Damascus University, Syria
[2] Department of Food Sciences, Faculty of Agriculture, Damascus University, Syria

LINK الرابط	ACCEPTED القبول	PUBLISHED ONLINE النشر الإلكتروني	ASSIGNED TO AN ISSUE الإحالة لعدد
https://doi.org/10.37575/b/agr/2159	09/04/2020	01/12/2020	01/12/2021

NO. OF WORDS عدد الكلمات	NO. OF PAGES عدد الصفحات	YEAR سنة العدد	VOLUME رقم المجلد	ISSUE رقم العدد
4122	4	2021	22	2

الملخص

يعد ثنائي الأستيل من أهم مركبات النكهات في منتجات الألبان المتخمرة نظراً لتأثيراته الحيوية المختلفة، لذلك هدف هذا البحث والذي أجري في مخابر التقانات الحيوية بجامعة دمشق خلال عام 2019، إلى رفع إنتاجية مركب النكهة ثنائي الأستيل المنتج من قبل بكتيريا حمض اللبن Lactococcus lactis، وذلك من خلال تعيين بعض الظروف المثلى لإنتاجه باستخدام البرنامج الإحصائي (RSM). حيث أظهرت النتائج أنّ إنتاجية ثنائي الأستيل بلغت عند تطبيق الظروف المثلى (65.39 ملغ/ل)، مما يعني أنّ الإنتاج ازداد بنحو 180٪ مقارنةً بذلك قبل تطبيق هذه الظروف المثلى، حيث بلغت كمية ثنائي الأستيل المنتجة من قبل بكتيريا حمض اللبن L. lactis (36.21 ملغ/ ل). كما بيّنت النتائج أنّ كمية ثنائي الأستيل المنتجة كانت في حدها الأقصى بقيمة (65.39 ملغ/ ل) عند درجة حرارة 37°م ودرجة الحموضة pH)) 5.5 وتركيز السترات 6 غ/ ل وتركيز سكر الغلوكوز 15 غ/ ل. أظهر التحليل الإحصائي وجود ارتباط معنوي لكلّ من درجة الحرارة ودرجة الحموضة وتركيز السترات وسكر الغلوكوز بمستوى ثقة 5 %، لذلك يوصى بضرورة الاستمرار بالعمل على بكتيريا L. lactis للحصول على سلالات ذات إنتاجية أعلى من ثنائي الأستيل.

ABSTRACT

Diacetyl is considered one of the most important flavor compounds in dairy products due to its vital effects. The main objective of this study is to increase the productivity of diacetyl, which is produced by the lactic acid bacterium, Lactococcus lactis. This is done by determining the optimal conditions for its production, which can be shown using a statistics-based program called Response Surface Methodology (RSM), which was demonstrated at the Biotechnology Library 'National Commission' during 2019. Results reveal that the productivity of diacetyl improves by approximately 180% when the optimum conditions are applied to amounts of 65.39 mg /L. In comparison, diacetyl productivity before applying these optimal conditions only obtains a value of 36.21 mg/L. The results also reveal that the maximum quantity of produced diacetyl is 65.39 mg/L at a temperature of 37 C°, an acidity level (PH) of 5.5, a citrate concentration at 6 g/L, and a glucose concentration of 15 g/L. The statistical analysis has shown an incorporeal relationship between temperature, acidity, citrate concentration and glucose, with a confidence level of 5%. Therefore, it is recommended that work on L. lactis bacteria should be continued to increase the productivity of diacetyl.

KEYWORDS
الكلمات المفتاحية
Flavor compounds, increase productivity, lactic acid bacteria
بكتيريا حمض اللبن، رفع الإنتاجية، مركبات النكهة

CITATION
الإحالة
Al-Kotami, S., Abou Ghorra, S. and Yuzaji, S. (2021). Taeyin bed alzuruf almuthalaa li'iintaj thunayiyin al'astil min qibal bikatiryaa Lactococcus Lactis 'Determining optimal conditions of diacetyl production produced by lactococcus lactis bacteria'. *The Scientific Journal of King Faisal University: Basic and Applied Sciences*, **22**(2), 16–9. DOI: 10.37575/b/agr/2159 [in Arabic]
القطامي، سميرة، أبو غرة، صياح و يازجي، صباح. (2021). تعيين بعض الظروف المثلى لإنتاج ثنائي الأستيل من قبل بكتيريا Lactococcus Lactis. *المجلة العلمية لجامعة الملك فيصل: العلوم الأساسية والتطبيقية*، **22**(2)، 16-19.

1. المقدمة

تعد مركبات النكهة من أكثر المنتجات المستخدمة على نطاق واسع في الصناعات الغذائية، حيث يمكن الحصول عليها إما عن طريق الاصطناع الكيميائي، وبالتالي تسمّى النكهات الاصطناعية. أو عن طريق التخمير عندئذ تسمّى النكهات الطبيعية، التي تعد مرغوبة بشكل أكبر من قبل المُستهلِك، وبالتالي زيادة الطلب في الحصول عليها. احدى هذه المنتجات هو ثنائي الأستيل، الذي يشكل عنصرا هاماً في نكهة الزبدة، وإن كان بعضها الآخر، مثل أسيتوين، الأسيتل الدهيد و2-3 البيوتانديول أيضاً تلعب دوراً في النكهة، رغم وجودها في كميات ضئيلة. وبالتالي فإنّ خليط من كلّ هذه المركبات التي تنتج أثناء التخمر اللبني بنسب مناسبة هو ما يعطي الزبدة نكهته المميزة. تعد بكتيريا حمض اللبن المنتجة للنكهة هي المسؤولة عن تخمر السترات إلى ثنائي الأستيل، الذي يعطي طعم مميز ونكهة لمنتجات الألبان المتخمرة حتى عند تواجده بتراكيز منخفضة جداً (1-2 ملغ/ ل) (Bakirci *et al.*, 2002).

ارتبطت علاقة بكتيريا حمض اللبن بإنتاج ثنائي الأستيل منذ زمن بعيد. حيث خلص Hammer (1980) إلى أنّ الكائنات الحية الدقيقة في مزارع الزبدة كانت مسؤولة عن الحموضة، الرائحة ونكهة منتج الألبان المتخمر.

هناك القليل من أنواع بكتيريا حمض اللبن قادرة على إنتاج ثنائي الأستيل (Hugenholtz, 1993). من هذه الأنواع *Lactococcus lactis* و *Leuconostoc mesenteroides* التي تستقلب السترات بوجود السكر المتخمر، حيث يؤدي استخدام السترات إلى تجمعات داخل الخلايا من البيروفات، وفيما بعد مجموعة متنوعة من نواتج الاستقلاب. تستخدم سلالات *Lactococcus* على نطاق واسع في الصناعات الغذائية لقدرتها على تحويل السترات إلى مركبات نكهة وثاني أكسيد الكربون، مما يساهم في تعزيز الخصائص الحسية للمنتجات المتخمرة. تنقسم سلالات *Lactococcus* إلى تحت نوعين *L. lactis* subsp. *Lactis* و *L. lactis* subsp. *cremoris* الذي يعرف بـ *L. lactis* subsp. *diacetylactis* نظرا لقدرته على تحويل السترات إلى ثنائي الأستيل (Bandell *et al.*, 1998).

ينتج ثنائي الأستيل بشكل طبيعي بفعل بكتيريا حمض اللبن، خصوصاً *L. lactis subsp. lactis bv. diacetylactis* ، عن طريق استخدام السترات بحضور اللاكتوز، فيما بعد أصبحت كفاءة إنتاجه من اللاكتوز بدلا من السترات الهدف لعدة دراسات. *L. lactis* يوّلد أيضاً حمض اللبن وبالتالي لديه القدرة على التغلب على الانخفاض الحمضي المفروض ذاتياً. تستخدم سلالات *L. lactis subsp. lactis bv. diacetylactis* كبادئات منتجة للنكهة في منتجات الألبان المتخمرة. هذه الأنواع البكتيرية هي أحياء دقيقة متجانسة التخمر

Corresponding Author: Samira Al-Kotami samira.alkotami@gmail.com ,00963994273768 المؤلف المراسل: سميرة القطامي

تستقلب الجلوكوز والسترات لإنتاج مركبات النكهة من خلال المسار الحيوي ثنائي الأستيل/أسيتوين (Davidson *et al.*, 1995).

وفقاً لدراسات عديدة، يعتمد إنتاج ثنائي الاستيل بواسطة بكتيريا حمض اللبن على عدة عوامل مثل السلالة، تركيز السترات أو البيروفات، تركيز السكر الأولي، إضافة أيونات المعادن، تركيز الأكسجين الأولي في وسط الزرع، درجة pH ودرجة الحرارة. كما تتوقف إنتاجية بكتيريا حمض اللبن من هذا المركب على معدل وكفاءة استقلاب حمض الستريك، لذلك من الضروري لزيادة معدل الإنتاج توفير كميات كافية من حمض الستريك في وسط الزرع المستخدم عن طريق إضافة حمض الستريك أو حمض البيروفيك كطلائع لإنتاج ثنائي الأستيل (Kaneko *et al.*, 2011). حيث تعتمد الاختلافات بين البكتيريا بخصوص استخدام السترات على وجود أو غياب إنزيم أكزالوأسيتات ديكربوكسيلاز، في حال تواجد هذا الإنزيم يقود تمثيل السترات إلى زيادة مجمع البيروفات الذي يؤدي بدوره إلى إنتاج ثنائي الأستيل و الأسيتوئين. وفي حال غياب هذا الإنزيم يكون الطريق البديل هو مسار إنتاج حمض السكسنيك (Wessels *et al.*, 2004).

تعد القدرة على استقلاب السترات إلى CO2، اسيتات، أسيتوين، ثنائي الأستيل وأحياناً 2.3- بيوتانيديول هي سمة شائعة للعديد من بكتيريا حمض اللبن، بشكل خاص *Lactococcus* و *Leuconostoc spp.* التي تتواجد في بعض مزارع البادئ، بينما لم يتم توثيق استقلاب حامض الستريك بواسطة *Lactobacillus spp.* بشكل جيد، على الرغم من أن الجوانب المختلفة منه قد تم تناولها في العديد من الدراسات الحديثة (Hugenholtz, 2014).

تعد الطريقة التقليدية المستخدمة في أمثلة ظروف التجربة عن طريق تثبيت كافة المتغيرات عند مستوى واحد وتغيير متغير واحد فقط في كلّ مرّة، من الأمور الصعبة والطويلة وعادةً ما تقود إلى استنتاجات غير دقيقة. لذلك هدف هذا البحث إلى تعيين الظروف المثلى لإنتاج ثنائي الأستيل من قبل بكتيريا حمض اللبن *Lactococcus lactis* باستخدام البرنامج الإحصائي RSM، الذي صمم ليس لتقليل عدد التجارب المستخدمة في عملية الأمثلة فحسب وانما لإعطاء نتائج أكثر منطقية ووضوح من الطريقة التقليدية عن طريق دراسة تأثير كلّ عامل على حده وتأثير العوامل المتفاعلة مع بعضها البعض (Pardeep and Satyanarayana, 2006).

2. المواد وطرق العمل

2.1. الكائن الحي الدقيق المستخدم:

استخدمت بكتيريا حمض اللبن *L. lactis* المعزولة من الحليب البقري، حيث عُزلت مسبقاً في مخابر كلية الزراعة/ قسم علوم الأغذية خلال عامي 2011-2012، وصنفت اعتماداً على تقنية *API 20 Strep* للتمييز بين أنواع المكورات اللبنية المعزولة من بيئة M17، و *API 50 CHL* للتمييز بين أنواع العصيات اللبنية المعزولة من بيئة Rogosa. كما حُفظت في مخابر الهيئة العامة للتقانة الحيوية في المجمدة عند درجة حرارة -80°م (Al-kotami *et al.*, 2015).

2.2. إنتاج ثنائي الأستيل وفقاً لتعيين الظروف المثلى:

نُميّت بكتيريا حمض اللبن *L. lactis* حسب (Macciola *et al.*, 2008)، من خلال التخمير هوائياً في دوارق مخروطية سعة 250 مل تحتوي على 50 مل من وسط حليب منزوع الدسم المعقم و 1 % (حجم/ حجم) لقاح بكتيري نشيط بعمر 16-18 ساعة (ما يعادل 10^8 CFU/مل حيث تصل بعض اللقاحات إلى هذا التعداد خلال 16 ساعة و بعضها خلال 18 ساعة). ضبطت درجات حرارة التحضين والحموضة (pH) وتركيز السترات والغلوكوز حسب التصميم الإحصائي المعتمد في الجدول (1).

2.3. تقدير ثنائي الأستيل:

قيست كمية ثنائي الأستيل المنتجة من قبل بكتيريا حمض اللبن *L. lactis* باستخدام جهاز المطياف الضوئي على طول موجة 535 نانومتر (Nadal *et al.*, 2009). حيث مُزج 5 مل من الطافي الناتج عن عملية التثفيل 9000 دورة / دقيقة لمدة 30 دقيقة عند درجة حرارة 4 °م، في أنبوب اختبار مع 1 مل من محلول 0.5% أرجينين، تتبع بإضافة 1 مل من 5% α- نفتول محلول ضمن 2.5 NaOH نظامي محضر آنياً ثم تركت العينة لمدة 10 دقائق عند درجة حرارة الغرفة 22°م، حيث تتحد مجموعة غوانيدينو من الأرجينين خلال هذه الفترة الزمنية مع ثنائي الأستيل في وجود الكاشف و يعطي لون أحمر أرجواني. حسبت كمية ثنائي الأستيل الكلية حسب طريقة Westerfeld (1945)، والتي تعتمد على المعادلة الآتية:

$$(y= 0.0213_X + 0.0902 , (R^2 =0.999))$$

حيث X كمية ثنائي الأستيل الكلية (ملغ/ ل) = $(Y- 0.0902)/0.0213$

حيث 0.0902 ثابت، Y قيمة الامتصاصية الضوئية على طول موجة 535 نانومتر.

2.4. دراسة الظروف المثلى لإنتاج ثنائي الأستيل باستخدام التصميم الاحصائي RSM:

درست الظروف المثلى لإنتاج ثنائي الأستيل (درجة الحرارة، درجة الحموضة، تركيز السترات وتركيز الغلوكوز) باستخدام برنامج Minitab والتصميم الإحصائي RSM. حيث درس تأثير كلّ متغير عند ثلاثة مستويات - (1+, 0 , 1) لكلّ من درجات الحرارة (37 ,34 ,31)°م، ودرجات الحموضة (pH) (6 ,5.5 ,5)، وتركيز السترات (8 ,6 ,4) غ/ ل وتركيز سكر الغلوكوز (15 ,10 ,5) غ/ ل. وبعدد 30 معاملة لكافة التصميم. قيم المتغيرات المدروسة ومستوياتها موضحة في الجدول (1). كما يبين الجدول (2) طريقة التصميم المعتمدة في هذه الدراسة.

الجدول (1): المتغيرات المدروسة ومستوياتها

مستويات المتغيرات بصورة رمز	المتغيرات			
	درجة الحرارة (°م)	درجة الحموضة	تركيز السترات(غ/ل)	تركيز سكر الغلوكوز(غ/ل)
-1	31	5	4	5
0	34	5.5	6	10
+1	37	6	8	15

الجدول (2): التصميم الإحصائي للتجربة

العدد	المتغيرات			
	تركيز سكر الغلوكوز(غ/ل)	تركيز السترات(غ/ل)	درجة الحموضة	درجة الحرارة (°م)
1	-1	-1	-1	1
2	-1	-1	1	-1
3	-1	1	-1	-1
4	-1	1	1	1
5	1	-1	-1	-1
6	1	-1	1	1
7	1	1	-1	1
8	1	1	1	-1
9	0	0	0	0
10	0	0	0	0
11	-1	-1	-1	-1
12	-1	-1	1	1
13	-1	1	-1	1
14	-1	1	1	-1
15	1	-1	-1	1
16	1	-1	1	-1
17	1	1	-1	-1
18	1	1	1	1
19	0	0	0	0
20	0	0	0	0
21	0	0	0	-1
22	0	0	0	1
23	0	-1	0	0
24	0	1	0	0
25	0	0	-1	0
26	0	0	1	0
27	-1	0	0	0
28	1	0	0	0
29	0	0	0	0
30	0	0	0	0

3. النتائج والمناقشة

3.1. كمية ثنائي الأستيل المنتجة من قبل بكتيريا حمض اللبن *L. lactis*:

من خلال دراستنا تمكنا من تحديد بعض الظروف المثلى التي أدى تطبيقها على البكتيريا المختبرة *L. lactis* إلى الحصول على أعلى إنتاجية لثنائي الأستيل بلغت (65.39 ملغ/ ل)، عند استخدام البرنامج الإحصائي Minitab والتصميم الإحصائي Response Surface Methodology (RSM). حيث يبين الجدول (3) نتائج كمية ثنائي الأستيل المنتجة من بكتيريا حمض اللبن *L. lactis* حسب التصميم الإحصائي المعتمد في الجدول (2) من حيث تركيز السترات، تركيز سكر الغلوكوز، درجة حموضة الوسط (pH) ودرجة

الحرارة المئوية.

الجدول (3): كمية ثنائي الأستيل المنتجة من *L. lactis* بعد تعريضها لعدة متغيرات

رقم التجربة	درجة الحرارة (°م)	درجة الحموضة	تركيز السترات (غ/ل)	تركيز سكر الغلوكوز (غ/ل)	ثنائي الأستيل (ملغ/ل)
1	37	5	4	5	20.57
1	31	6	4	5	29.39
1	31	5	8	5	29.32
1	37	6	8	5	16.09
1	31	5	4	15	30.79
1	37	6	4	15	33.86
1	37	5	8	15	20.22
1	31	6	8	15	42.66
1	34	5.5	6	10	30.38
1	34	5.5	6	10	30.52
2	31	6	4	5	10.85
2	37	6	4	5	14.48
2	37	5	8	5	20.44
2	31	6	8	5	35.38
2	37	5	4	15	43.6
2	31	6	4	15	28.28
2	31	5	8	15	21.16
2	37	5.5	8	15	65.39
2	34	5.5	6	10	31.24
2	34	5.5	6	10	30.6
3	31	5.5	6	10	28.88
3	37	5.5	6	10	57.91
3	34	5	6	10	34.87
3	34	6	6	10	20.6
3	34	5.5	4	10	31.88
3	34	5.5	8	10	24.26
3	34	5.5	6	5	30.56
3	34	5.5	6	15	33.62
3	34	5.5	6	10	31.4
3	34	5.5	6	10	41.73

يلاحظ تفاوت وتباين في كمية ثنائي الأستيل المنتجة في كافة المعاملات بلغت في الحد الأقصى بالمعاملة رقم 18 وبكمية إنتاج بلغت (65.39 ملغ/ ل) عندما كان تركيز سكر الغلوكوز وتركيز السترات ودرجة الحموضة ودرجة الحرارة المئوية 15غ/ ل، 8 غ/ ل، 5.5 و 37°م على التوالي، بينما كانت في حدها الأدنى بالمعاملة رقم 11 وبكمية إنتاج بلغت (10.85 ملغ/ ل) عندما كان تركيز سكر الغلوكوز وتركيز السترات ودرجة الحموضة ودرجة الحرارة المئوية 5غ/ ل، 4 غ/ ل، 6 و 31°م على التوالي. ويعود الانخفاض الشديد في المعاملة السابقة إلى انخفاض تركيز السترات إلى 4 غ/ ل وبالتالي انخفاض كمية ثنائي الأستيل المنتجة وهذا يتوافق مع Kaneko و زملائه (2011).

توافقت نتائجنا مع ما توصل إليه Medina وزملائه (2001)، في دراسة تأثير درجة الحرارة على إنتاج مركبات النكهة من السترات بواسطة *Lb. rhamnosus*، فتبيّن أنّ الإنتاج الحيوي للأستيل ازداد بشكل متزامن مع النمو عند 30°م و 37°م، بينما كان الإنتاج منخفضاً عندما كانت درجة الحرارة 45°م. في درجات الحرارة الأخرى كانت القيم أعلى ولكن لم تظهر أي فروق ذات دلالة إحصائية بين بعضها البعض. ومع ذلك، تمّ الحصول على أعلى كفاءة لتحويل السترات إلى ثنائي الأستيل عند 37°م يفسر ذلك: إلى أنّه عند درجة الحرارة هذه لوحظ الحد الأقصى لنشاط أنزيم citrate lyase الذي يساهم في انتقال السترات إلى داخل الخلايا واتحاده مع أكزالوأسيتات وبالتالي تشكل البيروفات التي تعد الركيزة الأساسية في إنتاج ثنائي الأستيل والأسيتوين (Wang *et al.*, 2017). كما توصل Habil وزملائه (1982)، إلى أنّه عندما ارتفعت درجة حرارة التحضين من 23 إلى 30°م، تمّ الحصول على حوالي 30 ٪ زيادة في إنتاج ثنائي الأستيل، حيث يكون نشاط diacetyl reductase بحده الأدنى عند درجة الحرارة هذه مما يقلل من مستوى تحول ثنائي الأستيل المنتج إلى الأسيتوين.

تماثلت نتائجنا أيضاً مع ما توصل إليه Palles وزملائه (1998) في دراسة تأثير درجات pH مختلفة تراوحت بين 4 و 6 على إنتاج ثنائي الأستيل من قبل بكتيريا *Lb. casei* و *Lb. plantarum*، فكانت 5.5 هي درجة الـ pH المثالية للنمو وإنتاج أعلى كمية من ثنائي الأستيل يفسر ذلك: إلى أنّ الاستهلاك الأمثل للسترات ومصادر الكربون من قبل بكتيريا حمض اللبن وبالتالي تراكم ثنائي الأستيل في الوسط لا يتم إلاّ عند قيم الـ pH المنخفضة والتي تتراوح من 4-5.5 (Rea and Cogan, 2003).

كما بلغ إنتاج ثنائي الأستيل أقصاه عند استخدام الغلوكوز بتركيز 15 غ/ ل، وذلك يعود إلى أنّ الكربوهيدرات وبشكل خاص سكر الجلوكوز ذات أهمية بالغة بالنسبة للتركيب الحيوي لكلّ من حمض اللبن ومركبات النكهة ثنائي الأستيل والأسيتوين (Ines and Falco, 2018). حيث يؤدي الاستقلاب المشترك للجلوكوز والسترات في الوسط إلى تحفيز معدل نمو سلالات *L. lactis* subsp. *lactis* وبالتالي إنتاجية أفضل لثنائي الأستيل مقارنة بالجلوكوز وحده في الوسط وهذا يتوافق مع Schmitt و Divies (1992). كما أشار Goupry وزملائه (2000)، إلى أنّ وجود الكربوهيدرات ساهم بنسبة 65 ٪ من مصدر الكربون لتشكيل مركبات منتجة للنكهات.

3.2. تعيين الظروف المثلى لإنتاج ثنائي الأستيل بوساطة البرنامج الإحصائي RSM:

يبين الشكل (1) الظروف المثلى لإنتاج ثنائي الأستيل من بكتيريا حمض اللبن *L. lactis* بوساطة البرنامج الإحصائي RSM، حيث يلاحظ بأنّ إنتاج ثنائي الأستيل كان في حده الأقصى عند درجة حرارة 37°م ودرجة الحموضة (pH) 5.5 وتركيز السترات 6 غ/ ل و تركيز سكر الغلوكوز 15 غ/ ل، ويبيّن التحليل الإحصائي وجود ارتباط معنوي لكلّ من درجة الحرارة ودرجة الحموضة وتركيز السترات وسكر الغلوكوز بمستوى ثقة 5 % جدول (4).

الشكل (1): الظروف المثلى لإنتاج ثنائي الأستيل من *L. lactis* بوساطة البرنامج الإحصائي RSM

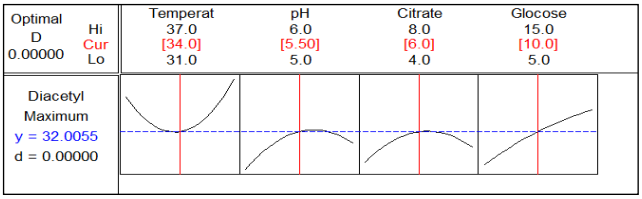

3.3. نتائج تحليل وتفسير البرنامج الإحصائي RSM في إنتاج ثنائي الأستيل:

يبين الجدول (4) تأثير العوامل المدروسة (كلّ عامل على حدا, ومربع العوامل, والعلاقة بين العوامل) في إنتاج ثنائي الأستيل، نلاحظ من الجدول أن قيمة *P* لكلّ المتغيرات الأربعة أقل من 5 % (*P*<0.05) وبالتالي هناك تأثير خطي معنوي لكلّ من هذه المتغيرات في كمية ثنائي الأستيل المنتجة كعوامل منفردة، و كانت قيمة *P* لتأثير مربع العوامل A*A ، B*B ، C*C و D*D أقل من 5 % وهذا يعني أن هناك تأثير معنوي لهذه العوامل المربعة الأربعة في إنتاج ثنائي الأستيل, و العلاقة بين العوامل المربعة الأربعة وكمية ثنائي الأستيل الناتجة على شكل منحني (قطع مكافئ). أما في تأثير العوامل المترابطة (المتداخلة) في إنتاج ثنائي الأستيل فيلاحظ من الجدول(4) أنّ علاقة درجة الحرارة كانت معنوية مع درجة الحموضة pH، وعلاقة درجة الحموضة pH معنوية مع تركيز السترات (*P* <0.05)، بينما كانت العلاقات الأخرى غير معنوية. معامل التحديد R^2 = 88.95 % وهذا يدل على أنّ معادلة الانحدار للعوامل المتغيرة تؤثر بنسبة 88.95 % على مقدار التغير في كمية ثنائي الأستيل المنتجة.

واعتماداً على الجدول (4) يمكن كتابة معادلة إنتاج ثنائي الأستيل كتالي:

$$Y= 32.006 + 1.992X_1 + 3.017X_2 + 1.734X_3 + 6.250\ X_4 + 10.028\ X_1^2 - 5.632\ X_2^2 - 5.297X_3^2 - 1.277X_4^2 - 1.163X_1X_2 - 1.224X_1X_3 + 4.596X_1X_4 + 4.261X_2X_3 + 2.516X_2X_4 - 0.815.4X_3X_4$$

الجدول (4): تأثير العوامل المدروسة على إنتاج ثنائي الأستيل من L. lactis

Term	Coef	T	P
Constant	32.006	7.608	0.000
A	1.992	0.758	0.022
B	3.017	1.148	0.015
C	1.734	0.660	0.001
D	6.250	2.379	0.033
A*A	10.028	1.433	0.005
B*B	-5.632	-0.805	0.012
Term	Coef	T	P
A*B	-1.163	-0.417	0.023
C*C	-5.297	-0.757	0.002
D*D	-1.277	-0.183	0.048
A*C	-1.224	-0.439	0.668
A*D	4.596	1.649	0.123
B*C	4.261	1.529	0.050
B*D	2.516	0.903	0.383
C*D	-0.815	-0.292	0.775

*A درجة الحرارة, B درجة الحموضة, C تركيز السترات, D تركيز الغلوكوز, (T) الخطأ المعياري للمعامل, الاحتمالية (P)

من النتائج المتحصل عليها من البحث تبين أنّ:

- هناك تأثيراً معنوياً لكلّ من درجة الحرارة، درجة الحموضة، تركيز السترات وتركيز سكر الغلوكوز في كمية إنتاج ثنائي الأستيل.

- علاقة درجة الحرارة كانت معنوية مع درجة الحموضة pH، وعلاقة درجة الحموضة pH معنوية مع تركيز السترات ($P < 0.05$) بينما كانت العلاقات الأخرى غير معنوية.
- الظروف المثلى للإنتاج هي درجة حرارة 37°م ودرجة الحموضة (pH) 5.5 وتركيز السترات 6 غ/ ل و تركيز سكر الغلوكوز 15 غ/ ل.
- أمكن التوصل الى تحديد بعض الظروف المثلى للحصول على أعلى إنتاجية لثنائي الأستيل من قبل بكتيريا L. lactis بلغت (65.39 ملغ/ ل) عند استخدام البرنامج الإحصائي Minitab والتصميم الإحصائي (RSM) Response Surface Methodology.
- ضرورة الاستمرار بالعمل على بكتيريا L. lactis للحصول على سلالات ذات إنتاجية أعلى من ثنائي الأستيل، وبالتالي زيادة الكمية المنتجة من ثنائي الأستيل الذي يعد من أهم مركبات النكهة في منتجات الألبان المتخمرة. وكذلك إمكانية استخدامه على نطاق واسع في العديد من الصناعات الغذائية بشكل خاص تعزيز النكهة الطبيعية للزبدة.

نبذة عن المؤلفين

سميرة القطامي

قسم العلوم الأساسية، كلية الزراعة، جامعة دمشق، دمشق، سوريا، 00963994273768+
samira.alkotami@gmail.com

م. القطامي، سورية، بكالوريوس في الهندسة الزراعية (جامعة دمشق 2008) وماجستير قسم علوم الأغذية / كلية الزراعة 2012. حاليا طالبة دكتوراه قسم علوم الأغذية. موظفة لدى جامعة دمشق / كلية الزراعة في قسم العلوم الأساسية من تاريخ 2012 حتى الآن، في الإشراف على الجوانب التطبيقية في الكيمياء العامة والتحليلية والكيمياء العضوية والإشراف على الجوانب التطبيقية في الرياضيات والفيزياء/ لطلاب كلية الزراعة سنة أولى. ساهمت في بعض المؤتمرات العلمية. عملت لدى الهيئة العامة للتقانة الحيوية خلال تنفيذ الاختبارات العملية للأبحاث.

صياح أبو غرة

قسم علوم الأغذية، كلية الزراعة، جامعة دمشق، دمشق، سوريا، 00963934197581+
s.aboughorrah@yahoo.com

أ.د. أبو غرة دكتوراه (جامعة نانسي الأولى)، سوري، إجازة عامة في العلوم الزراعية، جامعة دمشق، دبلوم دراسات معمقة، كلية العلوم، جامعة نانسي الأولى، فرنسا، الدرجة العلمية: أستاذ منذ عام 2007 في قسم علوم الأغذية، كلية الزراعة، جامعة دمشق. الاختصاص الدقيق: كيمياء وتحليل الألبان، له عدة مؤلفات أهمها كتاب كيمياء الألبان وتحليلها الجزء النظري. كتاب كيمياء وتحليل الألبان الجزء العملي، كتاب تكنولوجيا الألبان (مشتقات الحليب الدهنية). منشورات جامعة دمشق 1995، نشر في العديد من المجلات داخل الجمهورية العربية السورية وخارجها.

صباح يازجي

قسم علوم الأغذية، كلية الزراعة، جامعة دمشق، دمشق، سوريا، 00963944048523+
ryaziy@hotmail.com

أ.د. يازجي دكتوراه (جامعة برلين الحرة)، سورية، إجازة عامة في العلوم الزراعية، جامعة حلب، سوريا، دبلوم في مجال مكروبيولوجيا الأغذية جامعة برلين الحرة، ألمانيا، الدرجة العلمية: أستاذ منذ عام 2011، في قسم علوم الأغذية، كلية الزراعة، جامعة دمشق، سوريا. الاختصاص الدقيق: مكروبيولوجيا الأغذية، نشرت أبحاث عديدة في مكروبيولوجيا وتقانة التخمرات وهندسة الأنزيمات الميكروبية نشرت في مجلات علمية عديدة داخل الجمهورية العربية السورية وخارجها. لها عدة مؤلفات. ساهمت في العديد من المؤتمرات العلمية والندوات.

المراجع

القطامي، سميرة سليم، أبو غرة، صياح محمد، ويازجي، صباح رضا. (2019). إنتاج ثنائي الأستيل ميكروبياً. *مجلة جامعة دمشق للعلوم الزراعية*، **بدون رقم مجلد**(بدون رقم عدد)، بدون أرقام صفحات.

Al-Kotami, S.S., Abou-Ghorrah, S.M. and Yazaji, S.R. (2015). Detection and isolation of lactic acid bacteria and its use as local starters in Syrian akawi cheese processing. *International Food Research Journal*, **22**(4), 1699–704.

Al-kotami, S.S., Abou-Ghorrah, S.M. and Yazaji, S.R. (2019). Microbial diacetyl production. *Damascus University Journal for the Agricultural Sciences*, **n/a**(n/a), n/a. [in Arabic]

Bakirci, I., Celik, S. and Ozdemir, C. (2002). The effects of commercial starter culture and storage temperature on the oxidative stability and diacetyl production in butter. *International Journal of Dairy Technology*, **55**(4), 177–81.

Bandell, M., Lhotte, M.E., Marty, C., Veyrat, A. and Prevost, H. (1998). Mechanism of the citrate transporters in carbohydrate and citrate cometabolism in *Lactococcus* and *Leuconostoc* species. *Applied and Environmental Microbiology*, **64**(5), 1594–600.

Davidson, B.E., Llanos, R.M., Cancilla, M.R., Redman, N.C. and Hillier, A.J. (1995). Current research on the genetics of lactic acid production in lactic acid bacteria. *International Dairy Journal*, **5**(8), 763–84.

Goupry, S., Croguennec, T., Gentil, E. and Robins, R.J. (2000). Metabolic flux in glucose/citrate co-fermentation by lactic acid bacteria as measured by isotopic ratio analysis. *FEMS Microbiology Letters*, **182**(2), 207–11.

Habil, H., Oberman, A., Piątkiewicz, K. and Z. Libudzisz. (1982). Production of diacetyl and acetoin by lactic acid bacteria. *World Journal of Microbiology and Biotechnology*, **26**(7,8), 615–23.

Hammer, B.W. (1920). Volatile acid production of *Streptococcus lacticus* and the organisms associated with it in starters. *Agricultural Experiment Station, Iowa State College of Agriculture and Mechanic Arts*, **5**(63), 61-79.

Hugenholtz, J. (1993). Citrate metabolism in lactic acid bacteria. *FEMS Microbiology Reviews*, **12**(1,2), 165–78.

Hugenholtz, J. (1993). Diacetyl production by different strains of *Lactococcus lactis subsp. lactis biovar. diacetylactis* and *Leuconostoc* sp. *Applied Microbiology and Biotechnology*, **38**(n/a), 17–22.

Ines, A. and Falco, V. (2018). *Lactic Acid Bacteria Contribution to Wine Quality and Safety. In Generation of Aromas and Flavours.* Available at: https://doi.org/10.5772/intechopen.81168 (accessed on 05/11/2018)

Kaneko, T., Takahashi, M. and Suzuki, H. (1990). Acetoin fermentation by citrate-positive *Lactococcus lactis* subsp. *lac* 262. *Microbiological Research*, **56**(9), 2644–9.

Macciola, V., Candela, G. and Leonardis, A.D. (2008). Rapid gas-chromatographic method for the determination of diacetyl in milk, fermented milk and butter. *Food Control*, **19**(9), 873–8.

Medina, R., Oliver, G. and Benito, L. (2001). Influence of temperature on flavor compound production from citrate by *Lactobacillus rhamnosus* ATCC 7469. *Microbiological Research*, **155**(4), 257–62.

Nadal, I., Rico, J., Pérez-Martínez, G., Yebra, M.J. and Monedero, V. (2009). Diacetyl and acetoin production from whey permeate using engineered *Lactobacillus casei*. *Journal of Industrial Microbiology and Biotechnology*, **36**(9), 1233–7.

Palles, T., Beresford, T., Condon, S. and Cogan, T.M. (1998). Citrate metabolism in *Lactobacillus casei* and *Lactobacillus plantarum*. *Journal of Applied Microbiology*, **85**(1), 147–54.

Pardeep, K. and Satyanarayana, T. (2006). Optimization of culture variables for improving glucoamylase production by alginate-entrapped *Thermomucor indicae-seudaticae* using statistical methods. *Bioresource Technology Journal*, **98**(6), 1252–9.

Rea, M.C. and T.M. Cogan. (2003). Glucose prevents citrate metabolism by Enterococci. *International Journal Food Microbiology*, **88**(2,3), 201–6.

Schmitt, P. and Divies, C. (1992). Effect of varying citrate levels on C4 compound formation and on enzyme levels in *Leuconostoc mesenteroides* subsp. *cremoris* grown in continuous culture. *Applied Microbiology and Biotechnology Journal*, **37**(4), 426–30.

Wang, J.Y., Wang, X.J., Hui, X., Hua, S.H., Li, H. and Gao, W.Y. (2017). determination of diacetyl in beer by a precolumn derivatization-HPLC-UV method using 4-(2,3-Dimethyl-6-quinoxalinyl)-1,2-benzenediamine as a derivatizing reagent. *Journal of Agricultural and Food Chemistry*, **65**(12), 2635–41.

Wessels, S., Axelsson, L., Hansen. E.B., De Vuyst, L., Laulund, S., Lähteenmäki, L., Lindgren, S., Mollet, B., Salminen, S. and Wright, A.V. (2004). The lactic acid bacteria, the food chain, and their regulation. *Trends in Food Science and Technology*, **15**(10), 498–505.

Westerfeld, W.W. (1945). A colorimetric determination of blood acetoin. *Journal of Biological Chemistry*, **161**(n/a), 495–502.

المجلة العلمية لجامعة الملك فيصل
The Scientific Journal of King Faisal University
العلوم الأساسية والتطبيقية
Basic and Applied Sciences

Land Use/Land Cover Change Detection in the Baer and Al-Bassit Region, Latakia, Syria, 1972–2018

O. A. Merhej [1], M. K. Ali [1], A. S. Thabeet [2] and Y. Idriss [3]
[1] Department of Forestry and Ecology, Agriculture Faculty, Tishreen University, Latakia, Syria
[2] Department of Natural Resources, Agriculture Faculty, Aleppo University, Aleppo, Syria
[3] General Organization of Remote Sensing, Damascus, Syria

كشف تغير استعمالات الأراضي/الغطاء الأرضي في منطقة البابر والبسيط، اللاذقية، سورية خلال الفترة 1972 - 2018

علا مرهج [1]، محمود علي [1]، علي ثابت [2]، يونس ادريس [3]
[1] قسم الحراج والبيئة، كلية الزراعة، جامعة تشرين، اللاذقية، سوريا
[2] قسم الموارد الطبيعية، كلية الزراعة، جامعة حلب، حلب، سوريا
[3] الهيئة العامة للاستشعار عن بعد، دمشق، سوريا

LINK الرابط	ACCEPTED القبول	PUBLISHED ONLINE النشر الإلكتروني	ASSIGNED TO AN ISSUE الإحالة لعدد
https://doi.org/10.37575/b/sci/2070	10/12/2019	25/03/2020	01/12/2021

NO. OF WORDS عدد الكلمات	NO. OF PAGES عدد الصفحات	YEAR سنة العدد	VOLUME رقم المجلد	ISSUE رقم العدد
6042	6	2021	22	2

ABSTRACT

Monitoring land use/ land cover (LULC) changes is important for assessing the dynamics between land cover types and understanding the anthropogenic impact on these changes. Remote sensing techniques also represent important tools to achieve this goal. This paper aimed at mapping and analysing LULC changes in the Baer and Al-Bassit region of the Latakia Governorate in Syria. For this goal, 15 multi-temporal Landsat images from the period of 1972–2018 were used, and each image was classified using maximum likelihood algorithm-supervised classification into four categories of land use: forests, agricultural land, water and urban areas. Accuracy assessment of all images was performed; the average value of the overall accuracy of the classification was 89%, and the average value of the Kappa index was 0.85. The area of each land use category was calculated in each LULC map, and each category's trends over the study period were analysed using linear regression analysis. The forest category was the only group that decreased (by 21.8% between 1972 and 2018), compared to an increase in all other categories over the same period (0.6%, 4.3% and 16.8% for water, urban areas and agricultural land, respectively). This indicates a conversion of forests into agricultural land and urban areas. The results of this study can be used as an efficient tool to manage and improve the Baer and Al-Bassit forests in terms of physiographical and human characteristics; they could also facilitate the creation of a database for LULC changes in this region.

الملخص

تعد مراقبة تغيرات الغطاء الأرضي / استخدام الأرض أمراً مهماً لتقييم الديناميات بين أنواع الغطاء الأرضي وفهم التأثير البشري المنشأ على هذه التغييرات، وتمثل تقنيات الاستشعار عن بعد أدوات هامة لتحقيق هذا الهدف. تهدف هذه الورقة إلى رسم خرائط وتحليل تغير استعمالات الأراضي/ الغطاء الأرضي في منطقة البابر والبسيط، محافظة اللاذقية، سورية. استخدمت 15 صورة لاندسات متعددة الأزمنة للفترة 1972- 2018 وتم تصنيف كل صورة باستخدام خوارزمية الاحتمالية القصوى للتصنيف المراقب إلى أربع فئات من استعمالات الأراضي هي: الغابات، الأراضي الزراعية، المياه والمناطق الحضرية. تم تقييم دقة التصنيف لجميع الصور وبلغ متوسط قيم الدقة الإجمالية للتصنيف (89%) ومتوسط قيمة مؤشر كابا (0.85). حُسبت مساحة كل فئة من فئات استعمالات الأراضي في كل صورة وتم تحليل اتجاه التغيير لهذه الفئات خلال فترة الدراسة باستخدام علاقات الانحدار الخطي. كانت الغابات هي الفئة الوحيدة التي تعرضت للانخفاض بين عامي 1972 و2018 بنسبة (21.8%) في مقابل زيادة لجميع الفئات الأخرى (0.6، 4.3، 16.8 % للمياه، المناطق الحضرية وللزراعة، على الترتيب)، مما يشير إلى كسر أراضي الغابة لصالح الأراضي الزراعية والمناطق الحضرية. يمكن استخدام نتائج هذه الدراسة كأداة فعالة لإدارة وتحسين غابات البابر والبسيط فيما يتعلق بالخصائص الفيزيائية والبشرية ويمكن أن تسهل إنشاء قاعدة بيانات لتغيرات LULC في هذه المنطقة.

KEYWORDS
الكلمات المفتاحية
Landsat, linear regression, LULC dynamic, remote sensing, satellite Images, supervised classification
الاستشعار عن بعد، الانحدار الخطي، التصنيف المراقب، تغير استعمالات الأراضي، صور الأقمار الاصطناعية، لاندسات

CITATION
الإحالة
Merhej, O.A., Ali, M.K., Thabeet, A.S. and Idriss, Y. (2021). Land use/land cover change detection in the baer and al-bassit region, Latakia, Syria, 1972–2018. *The Scientific Journal of King Faisal University: Basic and Applied Sciences*, **22**(2), 20–5. DOI: 10.37575/b/sci/2070

1. Introduction

Land cover refers to the physical attributes of the earth's surface, including those made by human activities (e.g., settlements). Land use refers to the manner in which land has been used by people, usually with an emphasis on its functional role for economic activities (Ramachandra and Kumar, 2004). The land use/land cover (LULC) patterns of a region are a result of natural and socio-economic factors and their utilisation by humans in time and space (Rawat and Kumar, 2015).

It is increasingly acknowledged that LULC changes have become a key subject that urgently needs to be addressed in the study of global environmental changes (Hu et al., 2019). This is particularly true in light of major current environmental issues such as desertification, biodiversity loss and climate change, which in turn cause the loss of related environmental services to such a degree that more than half of the world's forest cover has been lost (FAO, 2010).

Many actions of local populations and government organisations (e.g., urban extension, expansion of agricultural land, forest fires) have resulted in the loss of extensive amounts of forest cover and other land use. LULC change analysis is a vital step in managing natural resources, monitoring environmental changes and protecting and planning for the future of Earth's resources (Torahi and Rai, 2011).

Geographic information systems (GIS) and remote sensing techniques are widely used to analyse the distribution, patterns and trends of the LULC processes. These tools have proven to be very valuable for obtaining exact, coherent information according to spatial reality (Monjardín et al., 2017). Another important tool that planners use to control the trends of forest cover changes is regression relations. Because environmental science deals with different phenomena, multiple regression is very important in dealing with ecological issues (Jahanifar et al., 2018).

In the last few decades, many specialists (Batar et al., 2017; Ramachandran and Reddy, 2017; Teka et al., 2018) have studied LULC changes explicitly, using LULC maps with the application of GIS and remote sensing data. In Syria, Ibrahim et al. (2014) used a time series of Landsat images of the Tartous Governorate to study the relationship between the applied agricultural policy and land use changes in this region. The study showed an expansion in the cultivation of citrus and greenhouses as a result of the agricultural plan implemented in the

Corresponding Author: O. A. Merhej olamerhej@gmail.com, 00963932044199 المؤلف المراسل: علا مرهج

same time period. It also confirmed the possibility of determining the spatial relationship between LULC changes and agricultural policies through remote sensing applications. Al-Fares (2013) also relied on Landsat-MSS, TM and ETM+ images and Terra: Aster for mapping LULC and irrigated agricultural projects for the years 1975, 1987, 2005 and 2007 in the Euphrates River Basin in Syria. The results showed that the area of irrigated agricultural projects in the Euphrates basin increased by 148% between 1975 and 2007.

Although the Baer and Al-Bassit region is among the most important forested areas of Syria, it suffers from different human encroachments. Therefore, detecting forest land cover changes can provide enough knowledge to design a forest management strategy. This study attempts to identify the spatio-temporal patterns of land cover changes in the last five decades using multi-temporal Landsat images. The main objectives of this research are (a) to accurately map the extent of the different LULC classes from 1972 to 2018 and (b) to detect the deforestation rate and the changes that have taken place during the study period.

2. Materials and Methods

The Baer and Al-Bassit region extends between longitudes (350 47' 49.2", 360 15' 57.44" E) and latitudes (350 57' 0.6", 350 35' 42.7" N) and encompasses an area of 73,000 hectares. It lies in the north-western part of the coastal mountains in the north and north-west of Latakia, Syria (Figure 1). The study area is characterised by brown Mediterranean soils and a Mediterranean climate type with a rainy winter and a long dry summer. The altitude above sea level is between 300 and 1,400 meters, and the average rainfall ranges between 800 and 1,200 mm/year.

The area is characterised by forest cover over more than 70% of its surface and has the most important forests in terms of area and diversity in Syria, consisting mainly of conifers and oak. Villages are located in the western and southern parts of the study area, and the majority of people living there depend on agriculture for their livelihoods, so agricultural land is mostly concentrated around the villages.

Figure 1. Location of the Study Area, the Baer and Al- Bassit Region, Latakia Governorate, Syria

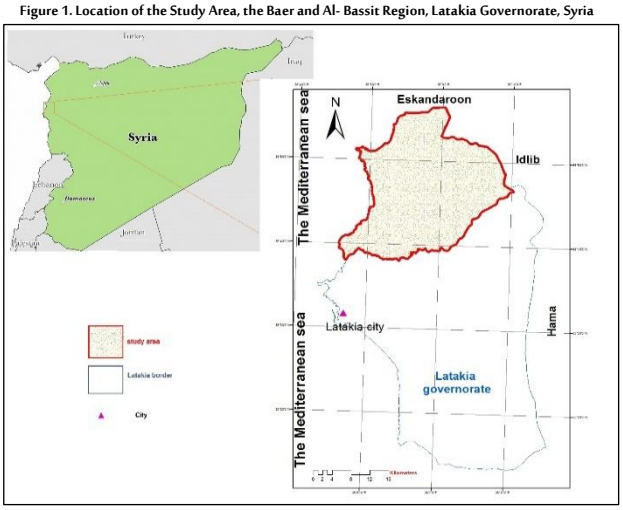

The Landsat data are available freely on NASA's website (USGS, 2018), and we directly downloaded 15 images for the period of 1972–2018 from the website. Because the changes that have occurred in this region are so frequent, we have chosen one image for every 2 or 3 years. The selected time period was in the summer (June to October) to avoid changes due to different seasons and to obtain cloud-free images as much as possible. Table 1 shows the resolution and other specifications of these images.

Image pre-processing is very important for LULC analysis because different sensors were used, so geometric and radiometric corrections were applied (e.g., in Ali *et al.* [2018]), and because of the differences in spatial resolution between MSS and other images, the resampling process was applied using Erdas Imagine 2015 software.

Google Earth images for different years, a set of topographic maps of northern Latakia at 1:25000 and a 1969 image from the Corona KH-4A satellite with a 9-foot resolution, black-and-white spatial resolution were used to assess the accuracy of the Landsat images classification.

The overall goal of image classification procedures is to automatically classify all pixels in an image into categories or features of land cover, and, typically, multi-spectral data are used to make a classification. In fact, the spectral pattern within the data for each pixel is used as a numerical basis for classification (Lillesand *et al.*, 2008).

Table 1. Characteristics of Landsat Scenes Used in the Classification

SENSOR_ID	Date Acquired	Spatial Resolution (m)	Spectral Resolution	Used Bands
L1 MSS	22/10/1972	80	4	4 to 7
L5 TM	04/07/1984	30	8	1 to 5 + 7
L5 TM	15/09/1987	30	8	1 to 5 + 7
L5 TM	20/09/1989	30	8	1 to 5 + 7
L5 TM	12/09/1992	30	8	1 to 5 + 7
L5 TM	15/10/1998	30	8	1 to 5 + 7
L5 TM	04/10/2000	30	8	1 to 5 + 7
L5 TM	20/06/2002	30	8	1 to 5 + 7
L5 TM	16/09/2005	30	8	1 to 5 + 7
L5 TM	21/08/2007	30	8	1 to 5 + 7
L5 TM	11/11/2008	30	8	1 to 5 + 7
L5 TM	31/07/2011	30	8	1 to 5 + 7
OLI_TIRS	08/10/2013	30	11	2 to 7
OLI_TIRS	12/09/2015	30	11	2 to 7
OLI_TIRS	19/10/2017	30	11	2 to 7
OLI_TIRS	06/10/2018	30	11	2 to 7

To determine the classification of LULC, the supervised classification method was applied in the Erdas Imagine 2015 software using the reflective bands in each image (Table 1). Supervised classification is based primarily on pre-determination of training areas and samples; Figure 2 summarises the three basic steps involved in a typical supervised classification procedure (Lillesand *et al.*, 2008).

Figure 2. Basic Steps in Supervised Classification (Lillesand *et al.*, 2008)

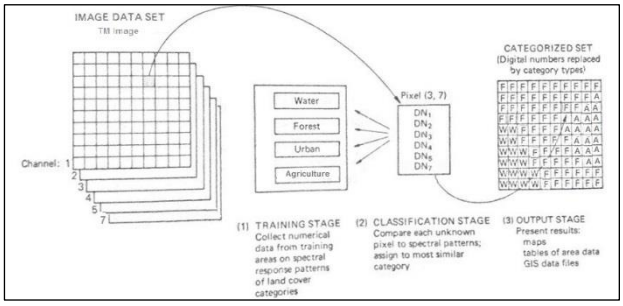

The training samples were taken from each image individually, and a spectral signature file of each image was created using a signature editor tool which sampled each of the studied areas according to Congalton (1991) for the number of samples.

Four categories of land use for all images were identified and mapped: agricultural areas, urban areas, water and forests. The maximum likelihood classification (MLC) method, as the most widely used in the scientific literature, is fast and easy to apply and enables a clear interpretation of the results (Bolstad and Lillesand, 1991). This algorithm can obtain a spectral image of each land use class through variance and covariance statistics of the set of training sites identified in the image and calculates the probability of belonging to each class according to the spectral signature; this method has been proven in works such as those of Hassan et al. (2016) and López and Plata (2009), with satisfactory results.

The classification is not fully considered until its accuracy is assessed (Lillesand et al., 2008). Therefore, to verify the validity of the results obtained, we assessed the accuracy using the accuracy assessment tool in Erdas Imagine by distributing random points representing all classes of land use in the image and then comparing the classification of these

points with the facts provided by a Corona image and topographic maps for 1972, the 1980s and the 1990s, respectively. For the remaining images, we used Google Earth imagery with no field survey because the study area has not been accessible since 2011 (it is out of government control).

The Kappa index shows the level of similarity between a set of control fields and the classified image. It is utilised as a standard part of precision evaluation to measure the accuracy between the remote sensing-derived classification map and the reference data, referred to as row and column totals (Jensen, 2003).

The value of Kappa is between 0 and 1. If the value is equal to 0, then there is no agreement between the map and the reference. If Kappa is equal to 1, it shows that there is a strong agreement between the map and the reference.

The general overall accuracy indicates the percentage of pixels that are properly classified. The percentage of producer's accuracy signifies the percentage of a particular land use change that is correctly classified in the image. The percentage of user's accuracy provides the percentage of a land use class in the image that matches with the class that corresponds to the land (Congalton et al., 1983).

The simple linear regression is a technique used to analyse the relationships between two quantitative variables. In linear regression, we assume that there is a linear relationship between dependent and independent variables (Salman-Mahini and Kamyab, 2012). It is used in this study to determine the general trend of the land use change and its significance during the period of 1972–2018, where the dependent variable was time, the independent variable was LULC class area and the calculation was done by SPSS V25 software.

3. Results and Discussion

3.1. Land Use/Land Cover Maps:

LULC maps were prepared and presented for all the images in Figure 3. The maps show that there is an increase and a decrease in different land use categories. We noted a decline in the extent of forest area during this period of 1972 to 2018.

Figure 3. LULC Maps for the Study Area (Baer and Al-Bassit) Between 1972 and 2018

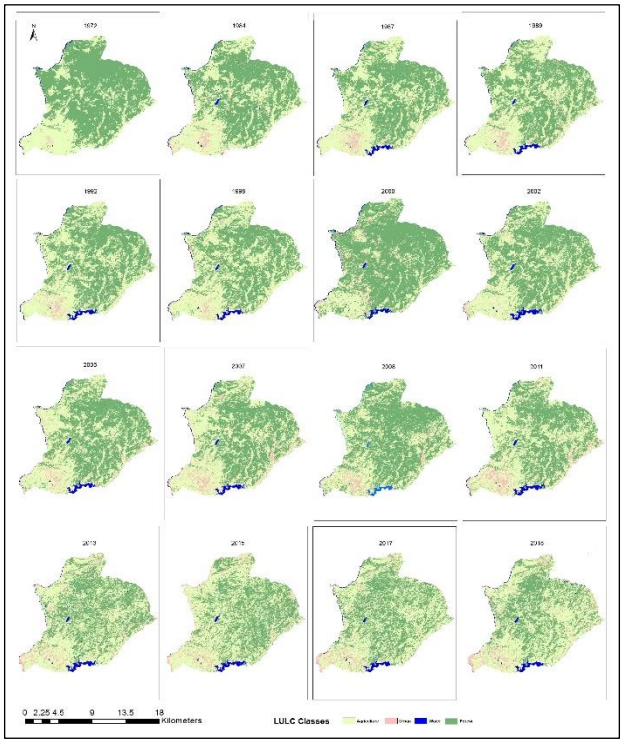

Table 2 clarifies the area and percentage of each land cover category derived from the LULC maps.

The total area of the Baer and Al-Bassit region is 72,300 hectares (Ha), divided into the four LULC categories. In 1972, the largest percentage of the study area fell into the forest category, which accounted for 55.23% of the total area, followed by agricultural land (39.43%).

Table 2. Area (Ha) and Percentage of the Land Use Classes

Land Cover Class		Water	Forest	Urban	Agriculture	Total
1972	Area	820.0	39,959.6	3,045.6	28,529.01	72,354.15
	%	1.13	55.23	4.21	39.43	100
1984	Area	818.46	35,794.62	3,406.77	32,334.3	72,354.15
	%	1.1	49.5	4.7	44.7	100
1987	Area	1,066.5	32,325.39	7,545.33	31,365.81	72,303.03
	%	1.5	44.7	10.4	43.4	100
1989	Area	1,115.73	29,648.52	7,079.04	34,396.20	72,239.49
	%	1.5	41.0	9.8	47.6	100
1992	Area	1,209.15	32,372.28	6,196.86	32,575.86	72,354.15
	%	1.671155	44.741428	8.564623	45.022794	100
1998	Area	1,174.59	34,729.56	5,191.74	31,268.25	72,364.14
	%	1.623166	47.992777	7.174465	43.209592	100
2000	Area	1,164.42	48,763.8	4,084.29	18,218.34	72,230.85
	%	1.612081	67.511043	5.654495	25.222381	100
2002	Area	1,276.38	37,067.67	3,397.59	30,612.51	72,354.15
	%	1.764073	51.230883	4.695778	42.309266	100
2005	Area	1,154.97	34,180.74	4,111.2	32,867.37	72,314.28
	%	1.597153	47.26693	5.685184	45.450733	100
2007	Area	1,151.82	31,157.73	6,302.7	33,690.78	72,303.03
	%	1.593045	43.093256	8.717062	46.596636	100
2008	Area	1,029.06	36,508.95	2,980.08	31,802.76	72,320.85
	%	1.422909	50.481915	4.120637	43.974538	100
2011	Area	1,266.39	35,630.1	1,989.9	33,416.64	72,303.03
	%	1.751503	49.278848	2.752167	46.217482	100
2013	Area	1,235.34	26,915.58	5,450.58	38,730.87	72,332.37
	%	1.707866	37.210975	7.535464	53.545695	100
2015	Area	926.37	27,661.32	5,213.43	38,519.73	72,320.85
	%	1.280917	38.248057	7.208751	53.262275	100
2017	Area	1,136.79	27,809.82	4,952.52	38,455.02	72,354.15
	%	1.571147	38.435694	6.844832	53.148327	100
2018	Area	1,247.94	24,205.14	6,154.11	40,713.66	72,320.85
	%	1.72556	33.469103	8.509455	56.295881	100

Water bodies accounted for 1.1 % of the study area in 1972, which is the lowest among land use categories, but this does not make the study area water-poor. The water area changed only slightly from year to year, except for the period of 1984–1987, when the water area increased by 0.4% (from 818.46 to 1,066 hectares). This increase was due to the construction of the 16 October Dam on Kabeer Shemali River. The dam was built at the expense of agricultural land and surrounding forests. In contrast, the decline in water area (from 1,235.34 to 926.37 hectares) between 2013 and 2015 was due to the drought recorded during those two years.

Forested areas rotated with the agriculture class by occupying the largest proportion of land use categories during the study period (Table 2). The forest area decreased in favour of agricultural land from 1972 to 1992 (from 39,959.6 hectares to 32,372.28 hectares), while the other categories increased. In the 1990s, the proposed afforestation projects began to show results, with an increase of about 7% in forest area in 1992, 1998 and 2000; after the 2004 Bassit fire, forest area decreased again (from 51.23% of the study area in 2002 to 43.1% in 2007).

Maps of 2005 and 2007 show the effects of the Bassit fire: the affected area has been turned into agricultural land, due to the decline of vegetation biomass in the region. This land returned to forest class in 2008 after the increase of this biomass thanks to regeneration of pine forests and reforestation with several forest species (Kassas, 2008).

The sharp decline in forest area in the years after 2011 is due to war and large forest fires in northern Latakia. In the crisis years (since 2011), the forest area has declined in different parts of the study area, especially in the Hafah region, where armed operations took place, in addition to fires and over-cutting for heating and cooking (Figure 3). The forest area decreased from 35,630.1 hectares in 2011 to 26,915.58 hectares in 2013 and continued to decline to its lowest value in 2018, with an area of 24,205 hectares (equivalent to 33.47% of the study area). This corresponds to the study of the borders and areas of fire in northern Latakia between 2002 and 2017, whereas the normalised burn ratio values were low in Bassit in 2005 and 2006, and in Hafah in 2014 and 2015 (Merhej *et al.*, 2019).

The largest proportion of forest area (22%[1]) lost between 1972 and 2000 has been turned into low forms of vegetation (maquis), while some parts have also been lost for agricultural use.

In the Tartous Governorate, which is climatically similar to the Baer and Al-Bassit region and has a variety of vegetation types and human activities, forest area decreased by 262.4 km^2 during the period of 1987–2017 (651.84 km^2 in 1987, 389.44 km^2 in 2017). The majority of the decline (72.5%) occurred during the period of 2002–2017 due to excessive logging for fuel by the local communities, especially during the war, and it was accompanied by a significant increase in the area of agricultural land (Hammad *et al.*, 2018).

After the water class, urban areas accounted for the lowest percentage among the land use categories, with a percentage of 4.21% in 1972. The values of the urban category fluctuated widely, but we can say that it increased from 3,045.6 hectares in 1972 to 6,154.11 hectares in 2018. The largest increase was between 1984 and 1987 (from 3,406.77 to 7,545.33 hectares). In contrast, there was a decline in the area of urban sites in the period of 2007–2011 of about 6% (from 6,302.7 hectares to 1,989.9 hectares), and then in 2018 they increased to 8.5% of the study area (6,154.11 hectares). This is again due to the spectral confusion (Yang, 2002). This finding is consistent with the results of Aragrande and Argenti's (2001) study, which concluded that urban expansion causes a loss of agricultural land due to high competition for other uses (e.g., housing, industry).

The difference in the proportion of the urban class may be due to the lower accuracy of the classification of this category, which represents a lower producer's accuracy in most classified images. This can be attributed to the similarity between the spectral reflection of urban and agricultural land, leading to low accuracy of the maps (Seto *et al.*, 2002), especially since most of the urban areas in the study area are agricultural villages comprising both houses and cultivated land. Natural and agricultural ecosystems are rapidly being converted into urban/built-up areas to meet the residential and economic needs of the ever-increasing urban populace (Yang and Liu, 2005).

It is evident from Table 2 that agricultural land occupied 39.43% of the study area in 1972, and that number increased by about 17% between 1972 and 2018 (from 28,529.01 hectares in 1972 to 40,713.66 hectares in 2018). The increase in agricultural land can be linked to the war and the rapidly resulting poverty in the last several years, which caused increases in forest cutting to convert land for agriculture use and to sell fuel woods.

3.2. Accuracy Assessment of Supervised Classification:

The accuracy of the classification images was evaluated; Table 3 shows the accuracy assessment details for all the images used in the study in terms of overall accuracy and Kappa index, respectively. The results show that the Kappa index gave very good values for the applicable classification, ranging from 0.8 in 2015 to 0.91 in 2005. The overall accuracy ranged from 87.36% in 1972 to 92.94% in 2005.

Deriving signatures from multiple images can make the signatures more robust in the sense that they result in reasonably good classifications across years, but on the other hand, it does not necessarily produce the best classification in any single year (Laborte *et al.*, 2010). The different values of the Kappa index and overall accuracy may be due to the fact that each image is classified according to its spectral profile. The absence of field surveys and dependence on Google Earth images to evaluate accuracy may be the reasons for the consistent accuracy of the OLI images with the images from the 1970s and 1980s that used an aerial Corona image and a set of topographic maps.

Table 3. Overall Accuracy and Kappa Values for the Images Used in the Study Period

Year	1972	1984	1987	1989	1992	1998	2000	2002	2005	2007	2008	2011	2013	2015	2017	2018
Overall Accuracy %	87.36	88.46	89.23	90.85	92.31	88.59	92.5	92.07	92.94	89.38	91.08	91.95	88.28	88.16	89.78	88.13
Kappa (K^)	0.84	0.84	0.85	0.88	0.89	0.84	0.86	0.89	0.91	0.86	0.85	0.89	0.84	0.8	0.85	0.84

The producer's accuracy values were lowest for the urban and agricultural land classes compared to higher values for the water category; the producer's accuracy of the urban category was 61.54% and 66.67% in 2015 and 2017, respectively. This is due to the spectral confusion, where farms at the beginning of the agricultural seasons show a spectral reflection similar to that of urban areas (Yang, 2002).

3.3. LULC Change Analyses Between 1972 and 2018:

The coefficient of determination R^2 describes the relationship between the LULC area and time and determines how much variable variation (the LULC area) is dependent on the independent variable (the year; Bihamta and Zare, 2011; Zar, 1984). Figures 4, 5 and 6 illustrate the LULC change trends and the linear regression analysis for 1972–2018.

The regression analysis showed a significant trend towards an increase in water surface area during the study period (ANOVA, $F = 5.85$, $P < 0.05$; Figure 4).

Figure 4. General Trend for Water Surface Area During the Period of 1972—2018

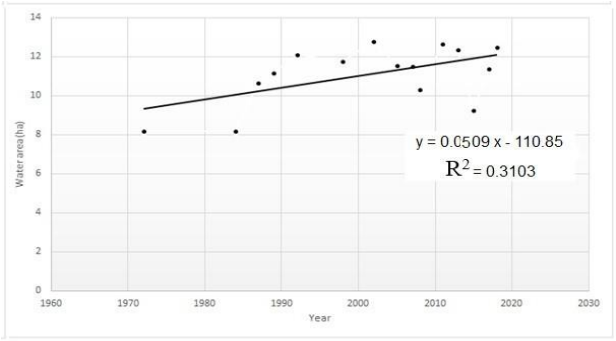

Figure 5 presents forest area changes between 1972 and 2018, during which period the overall forest area decreased. The regression analysis also showed a significant general trend towards decreasing forest area (ANOVA, $F = 8.068$, $P < 0.05$). According to the value of the determination coefficient (0.38), we can say that 38% of the decreases in forest land cover were made by the independent variable (time).

The regression analysis for urban areas, however, showed no significant general trend during the study period (ANOVA, $F = 0.001$, $P > 0.05$).

Figure 5. General Trend for Forest Surface Area During the Period of 1972—2018

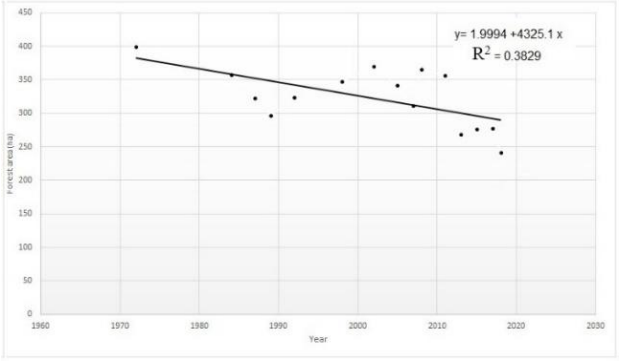

[1] **(24200- 39960/72354)*100**

Figure 6 presents the changes in agriculture land area that occurred between 1972 and 2018. The value of R^2 was the highest, indicating that the trend of increases in the area of agricultural land was consistent throughout the study period; 57% of increases in agriculture were made by time.

The regression analysis shows a significant general trend towards an increase in agricultural land area during the study period (ANOVA, F = 17.378, P <0.05).

These changes are not systematic for most types of land use in the study area, where the greater the area of the land type and its importance, the greater the magnitude of the calculated changes. Currently, the main factor in reducing forest cover in the region is human activity. Residents of residential districts in the area are busy removing and cutting down the forests to cover their fuel consumption and the expansion of their agricultural lands.

Figure 6. General Trend for Agricultural Areas During the Period of 1972—2018

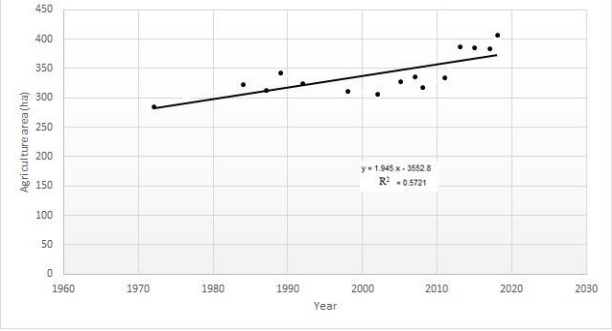

Table 4 shows the analysis of changes between 1972 and 2018. Figure 7 provides a chart for a better understanding of this change.

Table 4. LULC Changes in the Baer and Al-Bassit Region Between 1972—2018

Land Cover Class	Area in Ha (1972)	% of Total Area (1972)	Area in Ha (2018)	% of Total Area (2018)	Change in Ha
Water	820.0	1.13	1,247.94	1.7	427.95
Forest	39,959.6	55.23	24,205.14	33.5	-15,754.4
Urban	3,045.6	4.21	6,154.11	8.5	3,108.51
Agriculture	28,529.01	39.43	40,713.66	56.3	12,184.65
Total	72,354.15	100	72,320.85	100	

The results show that the forest category is the only category that decreased during the study period, while agriculture was the category that increased the most significantly. Statistical analysis shows a 21.8% decline in forest area between 1972 and 2018 (about 15,755 hectares). Agricultural land, on the other hand, increased by 16.87% (about 12,185 hectares). Therefore, we concluded that the rapid increase in agriculture is primarily due to the conversion of forest cover to agricultural land.

Figure 7. Percentage Change in LULC Categories Between 1972—2018

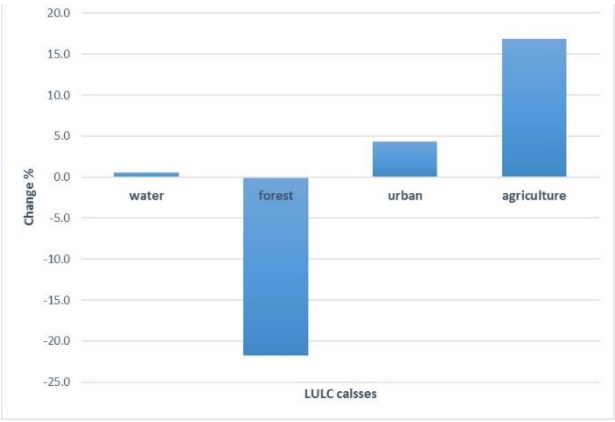

4. Conclusion

In situations of rapid land use changes, satellite remote sensing provides detailed information that aids in understanding a region's LULC. This study used images from the same season each year to produce a series of land use classification maps.

The accuracy coefficients obtained in this study indicate that the classification methods used were a good reflection of the real LULC changes that took place during the study period. Nevertheless, when possible, the classification procedure should still be enriched with field verification.

The LULC changes that occurred in the Baer and Al-Bassit region between 1972 and 2018 were quantified using multi-temporal Landsat data. It became clear that the change is threatening the forests, of which more than 150 km^2 were affected by deforestation between 1972 and 2018; this value has an impact on future environment and urban management. The agricultural lands were found to have increased by 16.8% between 1972 and 2018. The majority of this change, however, occurred after 2011 with the beginning of the war, when the increase in agricultural areas happened at the expense of the forests.

Our results suggest that large-scale agricultural activities should be restricted in the Baer and Al-Bassit region. In addition, while the success of forest restoration programs and conservation measures depends on the availability of quality assistive data, these are important steps that should be initiated and implemented in the study area.

Biographies

O.A. Merhej

Forestry and Ecology Department, Agriculture Faculty, Tishreen University; Researcher, General Organization of Remote Sensing, Latakia, Syria, olamerhej@gmail.com, 00963932044199

PhD from Tishreen University, Syrian, researcher at the General Organization of Remote Sensing, lecturer at the Agriculture Faculty at Tishreen University, supervisor for many masters and doctoral theses in the agriculture faculties of Aleppo and Tishreen Universities, supervisor for many projects at the General Organization of Remote Sensing, digital image processing trainer, author of scientific papers in Arabic and English in many journals. ORCID: 0000-0003-1657-5047.

M.K. Ali

Forestry and Ecology Department, Agriculture Faculty, Tishreen University, Latakia, Syria, mali.atiaf@gmail.com, 00963933547737

PhD from Texas A&M, USA; Syrian; professor in the Forestry and Ecology Department at Tishreen University; post director of Arab Organization for Agricultural Development; post director of Arab Technical Institute for Agriculture and Fisheries; supervisor of many masters and doctoral theses at agriculture faculties in Syria; lecturer at agriculture faculties in Damascus and Tishreen Universities; author of scientific papers in local and international journals in Arabic and English.

A.S. Thabeet

Natural Resources Department, Agriculture Faculty, Aleppo University, Aleppo, Syria, thabeet@alepuniv.edu.sy, 00963999775045

PhD from Paul Cezanne University (X-Marseille 3) in France, Syrian, assistant professor of forest measurements at Aleppo University, lecturer at the Arab Forest Institute, associate in preparing national policy for the agricultural sector in Syria, supervisor of many masters and doctoral theses in agriculture faculties, consultant on projects to improve livelihoods at the United Nations Development Program, author of many scientific papers in local and international journals. ORCID: 0000-0003-2597-201X.

Y. Idriss

General Organization of Remote Sensing, Damascus, Syria, younes.idriss@gmail.com, 00963948395124

PhD from Moscow University; Syrian; research manager at the General Organization of Remote Sensing; director of the Research and Applications Department of the Remote Sensing Center; a founder of the Syrian Scientific Olympiad; author of many papers in Arabic, English, and Russian; programmer in several programming languages; supervisor of dozens of diploma, master and doctoral theses; instructor of geographic information systems, remote sensing, development planning and land use planning at Damascus University.

References

Aragrande, M. and Argenti, O. (2001). *Studying Food Supply and Distribution Systems to Cities in Developing Countries and Countries in Transition*. Available at: http://www.fao.org/DOCREP/003/X6996E/x6996e07.htm#TopOfPage (accessed on 28/01/2018).

Al-Fares, W. (2013). *Historical Land Use/Land Cover Classification and Its Change Detection Mapping Using Different Remotely Sensed Data from Landsat (MSS, TM And ETM+) and Terra (ASTER) Sensors: A Case Study of The Euphrates River Basin in Syria with Focus on Agricultural Irrigation Projects*. Germany: Springer International Publishing.

Ali, M., Thabeet, A., Idriss, Y. and Merhej, O. (2018). Almoalja almosbaka lisowar landsat almostakhdama fi rasm kharaet ndvi fi ghabat shamal alladekia 'preprocessing of landsat imageries used to mapping ndvi in north latakia forests'. *Tishreen University Journal for Research and Scientific Studies - Biological Sciences Series*, **4**(5), 92–108. [in Arabic]

Batar, A.K., Watanabe, T. and Kumar, A. (2017). Assessment of land-use/land-cover change and forest fragmentation in the Garhwal Himalayan Region of India. *Environments*, **4**(2), 34–7.

Bihamta, M. and Zare-Chahouki, M. (2011). *Principles of Statistics for the Natural Resources Science*. Iran: University of Tehran Press.

Bolstad, P. and Lillesand, T.M. (1991). Rapid maximum likelihood classification. *Photogrammetry Engineering Remote Sensing*, **57**(1), 67–74.

Congalton, R.G. (1991). A Review of assessing the accuracy of classifications of remotely sensed data. *Remote Sensing Environment*, **37**(1), 35–46.

Congalton, R.G., Oderwald, R.G. and Mead, R.A. (1983). Assessing Landsat classification accuracy using discrete multivariate statistical techniques. *Photogrammetry Engineering and Remote Sensing*, **49**(12), 1671–8.

FAO. (2010). Global Forest Resources Assessment: Mexico National Report; FAO: Roma, Italy. Available at: http://www.fao.org/docrep/013/al567S/al567S.pdf (Accessed on 31/05/2018)

Jahanifar, K., Amirnejad, H., Mojaverian, M. and Azadi, H. (2018). Land change detection and effective factors on forestland use changes: Application of land change modeler and multiple linear regression. *Journal of Applied Science and Environment Management*, **22**(8), 1269–75.

Kassas, H. (2008). *Deraset Alttajadod Ba'd Alhareek Le Assanoubar Albroty Ba'd Hareek Ras Albassit Fi 2004 Wa Aba'adeh Alejtimae'ya-Alektisadeya* 'Studying Post Fire Regeneration of Pinus Brutia Ten. after the 2004 Fire in Ras – Al- Bassit and Its Socio- Economic Dimensions'. Master's Dissertation, Tishreen University, Latakia, Syria. [in Arabic]

Hammad, M., László M. and Boudewijn L. (2018). Land cover change investigation in the southern syrian coastal basins during the past 30-years using landsat remote sensing data. *Journal of Environmental Geography*, **11**(1-2), 45–51.

Hassan, Z., Shabbir, R., Ahmad, S.S., Malik, A.H., Aziz, N., Butt, A. and Erum, S. (2016). Dynamics of land use and land cover change (LULCC) using geospatial techniques: A case study of Islamabad Pakistan. *Springer Plus*, **5**(1), 1–11.

Hu, Y., Batunacun, Zhen, L. and Zhuang, D. (2019). *Assessment of Land-Use and Land-Cover Change in Guangxi, China*. Available at: doi.org/10.1038/s41598-019-38487-w. (accessed on 22/05/2018)

Ibrahim, W.Y., Sam, B. and Paul, M. (2014). Agricultural policy effects on land cover and land use over 30 years in tattoos, Syria, as seen in Landsat imagery. *Journal of Applied Remote Sensing*, **8**(1), n/a.

Jensen, J.R. (2003). *Introductory to Digital Image Processing, A Remote Sensing Perspective*. 3rd edition. US: Prentice Hall.

Laborte, A.G., Maunahan, A.A. and Hijmans, R.J. (2010). Spectral Signature Generalization and Expansion Can Improve the Accuracy of Satellite Image Classification. *PLoS One*, **5**(5), e10516. Available at: doi:10.1371/journal.pone.0010516. (accessed on 17/11/2018)

Lillesand, T.M., Kiefer, R.W. and Chipman, J.W. (2008). *Remote Sensing and Image Interpretation*. 6th edition. India: John Wiley and Sons. Inc.

López, V.V.H. and Plata, R.W. (2009). Análisis de los cambios de cobertura de suelo derivados de la expansión urbana de la Zona Metropolitana de la Ciudad de México 1990- 2000 'Analysis of land cover changes derived from the urban expansion of the Metropolitan Area of Mexico City 1990-2000'. *Investigating Geography*, **68**(n/a), 85–101. [in Spanish]

Merhej, O.A., Ali, M., Thabeet, A. and Idriss, Y. (2019). Takyeem khatar wa adrar haryek alghabat fi shamal alladekia khelal sanawat alazma be estekhdam almoa'sher alkeyasi lelmanatek almahroka 'Evaluation of forest fire damage and risk in northern Latakia during the crisis years using the Normalized Burn Ratio'. *Syrian Remote Sensing Journal*, **14**(2), 12–21. [in Arabic]

Monjardín, A.S.A., Pacheco, A.C.E., Plata, R.W. and Corrales, B.G. (2017). La deforestación y sus factores causales en el estado de Sinaloa, México 'Deforestation and its causal factors in the state of Sinaloa, Mexico'. *Madera y Bosques*, **23**(1), 7–22. [in Spanish]

Ramachandran, R.M. and Reddy, C.S. (2017). Monitoring of deforestation and land use changes (1925–2012) in Idukki district, Kerala, India using remote sensing and GIS. *Journal of the Indian Society of Remote Sensing*, **45**(1), 163–70.

Ramachandra, T.V. and Kumar, U. (2004). GRDSS for land use land cover dynamics analysis. In: *FOSS/GRASS Users Conference,* Bangkok, Thailand, 12-14/09/2004.

Rawat, J.S. and Kumar, M. (2015). Monitoring land use/cover change using remote sensing and GIS techniques: A case study of Hawalbagh block, district Almora, Uttarakhand, India. *The Egyptian Journal of Remote Sensing and Space Sciences*, **18**(1), 77– 84.

Salman-Mahini, A. and Kamyab, H. (2012). *Applied Remote Sensing and GIS with Idrisi*. 2nd edition. Tehran, Iran: Publication of Mehrmahdis.

Seto, K.C., Woodcock, C.E., Song, C., Huang, X., Lu, J. and Kaufmann, R.K. (2002). Monitoring land use change in the Pearl River delta using Landsat TM. *International Journal of Remote Sensing*, **23**(10), 1985–2004.

Teka, H., Madakadze, C.I., Botai, J.O., Hassen, A., Angassa, A. and Mesfin, Y. (2018). Evaluation of land use land cover changes using remote sensing Landsat images and pastoralists' perceptions on range cover changes in Borana rangelands, Southern Ethiopia. *International Journal of Biodiversity and Conservation*, **10**(1), 1–11.

Torahi, A. and Rai, S.C. (2011). Land cover classification and forest change analysis, using satellite imagery-a case study in Dehdez area of Zagros Mountain in Iran. *Journal of Geographic Information System*, **3**(1), 1–11.

USGS. (2018). *U.S. Geological Survey*. Available at: https://earthexplorer.usgs.gov/. (Accessed on 15/02/2018)

Yang, X. (2002). Satellite monitoring of urban spatial growth in the Atlanta metropolitan area. *Photogrammetric Engineering and Remote Sensing*, **68**(7), 725–34.

Yang, X. and Liu, Z. (2005). Using satellite imagery and GIS for land use and land cover change mapping in an estuarine watershed. *International Journal of Remote Sensing*, **26**(23), 5275–96.

Zar, J.H. (1984). *Biostatistical Analysis*. 2nd edition. US: Prentice Hall.

The Scientific Journal of King Faisal University

Basic and Applied Sciences

Investigation of Phytochemical and Evaluation of Antioxidant and Antibacterial Activities from *Abies* Extract

Djamila Benouchenne [1], Ines Bellil [1], Salah Akkal [2] and Douadi Khelifi [1 3]

[1] Laboratory of Genetics Biochemistry and Plant Biotechnologies, Faculty of Natural and Life Sciences, University of Frères Mentouri Constantine 1, Constantine, Algeria
[2] Laboratory of Phytochemistry and Physicochemical and Biological Analyses, University of Frères Mentouri Constantine 1, Constantine, Algeria
[3] High National School of Biotechnology, Constantine, Algeria

LINK	RECEIVED	ACCEPTED	PUBLISHED ONLINE	ASSIGNED TO AN ISSUE
https://doi.org/10.37575/b/sci/210009	05/03/2021	23/05/2021	23/05/2021	01/12/2021

NO. OF WORDS	NO. OF PAGES	YEAR	VOLUME	ISSUE
6176	7	2021	22	2

ABSTRACT

Algerian fir (*Abies numidica* de Lannoy) is an endemic evergreen tree belonging to the Pinaceae family. Little is known about this plant, and few papers have been reported, despite its traditional uses. The objectives of this study were to investigate the chemical composition of n-butanol extract from *A. numidica* leaves as well as to evaluate its biological activities (antibacterial and antioxidant). The total phenolics and total flavonoids were found in high amounts (381.15±22.70µg GAE/ml; 49.79±2.81 µg QE /ml, respectively). The data of the antibacterial effect showed a potential inhibitory zone, especially against *Proteus vulgaris* (17.5±0.70 mm). The antioxidant activity findings disclosed that this fraction has a moderate radical scavenging power and metal chelating ability, compared with the standards used. The liquid chromatography–mass spectrometry (LC–MS/MS) analysis results showed that the major compounds presented in this extract were hyperoside (399.91µg/g), astragalin (147.22 µg/g) and rutin (102.62 µg/g). Thus, *A. numidica* leaves were suggested as being useful to prevent free radicals and bacterial infections diseases.

KEYWORDS

Abies numidica leaves, antibacterial activity, antioxidant assays, LC–MS/MS analysis

CITATION

Benouchenne, D., Bellil, I., Akkal, S. and Khelifi, D. (2021). Investigation of phytochemical and evaluation of antioxidant and antibacterial activities from *Abies* extract. *The Scientific Journal of King Faisal University: Basic and Applied Sciences*, **22**(2), 26–32. DOI: 10.37575/b/sci/210009

1. Introduction

Free radicals are molecules involved in normal organisms physiology (Hazeena Begum and Muthukumaran, 2014); the accumulation of these reactive oxygen species leads to oxidative stress and cellular dysfunction by either DNA oxidation or lipids peroxidation (Medini et al., 2014), resulting in chronic and degenerative diseases, such as cancer and diabetes (Pallab et al., 2011). The human body has several means to fight and neutralise these free radicals by producing enzymes, but when the oxidative stress is high, the internal mechanisms become insufficient, so the administration of antioxidants is needed.

Another problem faced by human health, aside from free radicals, is the resistance to many synthetic antibiotics by bacterial strains that cause bacterial infections (Blonk and Cock, 2019) and food spoilage. These concerns supported and accommodated the researchers to seek beneficial substitutes from plants.

Abies is a genus belonging to the Pinaceae family. It includes 50 species distributed around the world (Yang et al., 2008) in temperate and boreal regions of the northern hemisphere. It has been reported that *Abies* species possess medicinal properties; they are used in folk medicine to treat colds, indigestion and respiratory problems (Seo et al., 2016). Gupta et al. (2011) disclosed that *A. pindraw* leaves acetone extract was highly rich in phenolic and flavonoids compounds. Vasincu et al. (2013)reported their results showed that *A. alba* Mill. ethylacetate fraction from bark was abundant in polyphenols and flavonoids. It has been reported that *A. silicica* and *A. koreana* essential oils have potential antifungal and antibacterial effects (Bağci and Diğrak, 1996: Noreikaitė et al., 2017). While investigating the chemical constituents of plant extracts (Koch, 2019), our interest was directed to *A. numidica* de Lannoy.

A. numidica de Lannoy is an endemic evergreen tree that originally occupied a restricted region, found only in the Babor Range, north of Sétif, Algeria, until it was introduced in Constantine, Annaba and Tizi Ouzou through plantation. Its essence was used in traditional medicine to make healing wounds, to treat respiratory pathologies and inflammations (Bennadja et al., 2012). The gum from this fir is one of the essential remedies in folk treatment; it is used as an anti-scorbutic, and as an antiseptic in wounds and injuries. Different arrangements were made from this gum, such as turpentine oil. However, little is known about this tree, and few studies have been reported on the phytochemical composition of this species. The cones of this plant were used to treat stomach aches, wounds, colds, inflammations and respiratory problems (Tlili-Ait Kaki et al., 2013). There are no previous data about polyphenol and flavonoid contents in *A. numidica* leaves extracts. Essential oil extracted from *A. numidica* needles was found to have a potential antibacterial effect (Bağci and Diğrak, 1996; Ramdani et al., 2014). Ghadbane et al. (2016)reported that fractions extracted from *A. numidica* leaves (collected from Babor, Sétif) showed a potential 1,1-Diphenyl-2-picrylhydrazyl (DPPH) free radicals scavenging ability, and that it presented a strong antibacterial effect. Benouchenne et al. (2020) disclosed that ethylacetate fraction extracted from *A. numidica* needles has powerful antioxidant activity in all assays, and that it exhibited a potent inhibitory effect against bacterial strains. The selection of this plant was guided by its traditional uses, and as there has neither been any chemical composition determination nor biological investigations done on its extracts.

In this study, the objectives were to determine the chemical composition of n-butanol extract from *A. numidica* leaves as well as to evaluate the antibacterial and the antioxidant activities using several in vitro biochemical assays.

2. Material and Methods

2.1. Chemicals and Reagents:

Folin–Ciocâlteu reagent (FCR), aluminium trichloride, 1,1'diphenyl-2-picrylhydrazyl (DPPH), butylatedhydroxyanisole (BHA),

Corresponding Author: Ines Bellil 00213666510247, bines07@yahoo.fr

butylatedhydroxytoluene (BHT), α-Tocopherol, ascorbic acid, neocuproine, 2,2'-azino-bis (3-ethylbenzothiazoline-6-sulfonicacid) diammonium salt (ABTS), dimethylsulfoxide (DMSO), sodium carbonate, copper(II) chloride and potassium persulfate were obtained from BiochemChemopharma. All other chemicals and solvents were of analytical grade. Bacterial strains were obtained from the Pasteur Institute, Algiers.

2.2. Collection of Plant Material:

Algerian fir needles were collected from Constantine in September 2018; they were dried for 15 days in the dark at room temperature. The sample was powdered and kept in a dry, dark place until it was used.

2.3. Extraction of Secondary Metabolites:

The extraction procedure was carried out according to the method described by Boudjada et al. (2017) with minor modifications. The extraction was realised by cold maceration via taking the powdered needles (50g) and soaking it in 400ml of methanol as solvent (80% v/v); it was shaken for 24hours at room temperature. After filtration, the solvent was then removed under reduced pressure by rotary evaporator apparatus Buchi R-215 type at 40°C. The methanolic extract was dissolved in distilled water (400 ml) to obtain the aqueous phase that undergoes the fractionating step via different organic solvents with increased polarities starting with dichloromethane then ethylacetate and n-butanol (100ml x 3times).The n-butanol fraction was taken to evaluate its biological activities.

2.4. Phytochemical Screening:

The n-butanol fraction was subjected to the phytochemical screening, which was performed according to the method described by Cavé (1993).

2.4.1. Test for Flavonoids

A volume of n-butanol extract (2 ml) was mixed with 0.5 ml of concentrated hydrochloric acid and 0.5g of metal magnesium. A pink/red colouration developed after 3 minutes indicated the presence of flavonoids.

2.4.2. Test for Tannins

To 1ml of n-butanol extract, a few drops of 1% ferric chloride were added. The appearance of blue/dark colour revealed the presence of gallic tannins; however, the green/blue developed colour-proved the existence of catechin tannins.

2.4.3. Test for Anthocyanins

To 2ml of n-butanol extract, 5ml of concentrated sulphuric acid and 5ml of ammonium hydroxide were added. The appearance of pink/red colouration or blue colouration revealed the presence of anthocyanins.

2.4.4. Test for Alkaloids

To 5ml of the extract, 1ml of diluted sulphuric acid was added (50%). After that, two tubes were prepared. One contained 2ml of the acidified extract and 1ml of Mayer's reagent. The second tube contained 2ml of the extract and 1ml of Dragendorff-Wagner's reagent. The appearance of turbidity/precipitation indicated the presence of alkaloids.

2.4.5. Test for Coumarins

In a test tube, a few drops of distilled water were added to 1ml of n-butanol extract. The tube was covered with sodium hydroxide (10%) soaked paper, after that the tube was heated till ebullition. The yellowish fluorescence under UV lamp indicated the presence of coumarins.

2.4.6. Test for Saponins

To 1ml of extract placed in a test tube, 9ml of distilled water was added and shaken vigorously for 15 seconds, and then the extract was left to stand for 10 minutes. Formation of stable foam (1cm) indicated the presence of saponins.

2.4.7. Test for Triterpenes, Sterols and Steroids

A volume of 5 ml of the extract were evaporated. The dried extract was dissolved in a mixture of acetic anhydride: chloroform (5:5) (v/v). After that, a few drops of concentrated sulphuric acid were added. The appearance of green colouration indicated the presence of steroids, while the appearance of purple colouration revealed the triterpenes.

2.4.8. Test for Reducing Sugars

To 1ml of n-butanol extract, 1ml distilled water was added in a test tube. The mixture was heated till ebullition, after that twenty drops of Fehling's solution was added. The observed brick red precipitate disclosed the presence of reducing sugars.

2.5.Determination of Total Phenolic Content:

The amount of total phenolic content (TPC) in n-butanol fraction extracted from Algerian fir leaves was determined by using Singleton and Rossi's (1985) method with FCR. A volume of 20µl plant extract was mixed with 100 µl of FCR (diluted 1:10 with deionised water) and 75µl of sodium carbonate (7.5% w/v). The reaction mixture was incubated in obscurity for 2 hours. The absorbance of the resulting colour was measured at 765 nm using a microplate reader. The TPC was determined from the linear equation of a standard curve prepared with gallic acid (Y= 0.0034X+ 0.1044; R2 = 0.9972) and was expressed in mg per gram of dry extract (Gulcin, 2020).

2.6. Determination of Total Flavonoids Content:

Total flavonoids content (TFC) in n-butanol extract was determined by the aluminium chloride colorimetric assay adopted from Topçu et al. (2007) with slight modifications. The mixture reaction contained 50µl of n-butanol extract, 130µl methanol, 10µl potassium acetate (CH_3COOK; 9.8% w/v) and 10µl of aluminium chloride ($AlCl_3$; 10% w/v), after that it was incubated for 40minutes. The absorbance was measured at 415nm. The blank was prepared by replacing the extract by solvent of extraction (methanol). The total flavonoids content was obtained using the calibration curve with quercetin (Y=0.0048X; R2 =0.997) and was expressed as mg of quercetin equivalence per gram of dry extract (Gulcin, 2020).

2.7. Antibacterial Activity:

The antibacterial assay was carried out according to a modified method from Bensari et al. (2020), using disc diffusion against six human pathogenic bacteria strains, including Gram-positive: *Bacillus subtilis* (ATCC 6633) and *Staphylococcus aureus* (ATCC 43300);and Gram-negative: *Escherichia coli* (ATCC 25922), *Pseudomonas aeruginosa* (ATCC 27853), *Morganella morganii* (ATCC 25830)and *Proteus vulgaris* (ATCC 29905); these were obtained from the Pasteur Institute in Algiers, Algeria. Bacterial suspensions were spread on the surface of Mueller-Hinton agar plates. The sterile discs (6mm in diameter) were immersed with n-butanol extract (10µl). The plates were incubated at 37°C for 24hours. Tests were carried out in triplicate. The antibacterial activity was determined by measuring the inhibition zone surrounding the discs.

2.8. Antioxidant Activities:

2.8.1. Free Radical Scavenging Activity by DPPH Assay

The DPPH· free radical scavenging assay was performed according to the methods in Tel et al. (2012) with some modifications. The different dilutions of the n-butanol sample were prepared in methanol. 40µl of various sample concentrations were added to 160µl of methanolic DPPH solution (6% w/v) in 96-well microplate. Solvent with DPPH reagent mixture was served as control. After 30 minutes of incubation in the dark at room temperature, the absorbance of each solution was determined at 517 nm using a microplate reader. BHT and BHA were used as standards. Reduction of DPPH· radical in percent (R%) was calculated in the following way:

% Inhibition= $[A_{blank} - A_{sample}/A_{blank}] \times 100$

A_{blank}: absorbance of control reaction; **A_{sample}**: absorbance of test sample.

Tests were carried out in triplicates. The inhibition concentration (IC_{50}) is half of the free radicals (50%) calculated from the graph of DPPH radical scavenging effect percent against extract concentration.

2.8.2. $ABTS^{\bullet+}$Radical Cation Decolourisation Assay

This anti-radical activity was measured using a radical cation decolourisation assay as described by Re et al.(1999). $ABTS^{\bullet+}$ solution was prepared by mixing an $ABTS^{\bullet+}$ solution (7 mM; 1.92mg/ml) with potassium persulfate solution (2.45 mM; 0.33mg/ml). The mixture was left in the dark at room temperature for 16 hours before use. This solution was diluted and was adjusted to obtain an absorbance of 0.70±0.02 at 734 nm. 160µl of $ABTS^{\bullet+}$ was added to 40µl of n-butanol sample at different concentrations. The mixture was incubated in the dark for 10minutes at room temperature. The blank solution was methanol; $ABTS^{\bullet+}$ solution was used as control. The antioxidant standards were BHT and BHA. The experiment was performed in triplicate. The inhibition percentage was calculated the same as described in $DPPH^{\bullet}$radical assay.

2.8.3. Reducing Power Antioxidant Assay

The reducing power ability of the extract was performed using Oyaizu's (1986)method with minor modifications. The reaction mixture contained 10µl of the n-butanol extract at different concentrations, 40µl phosphate buffer (pH 6.6) and 50µl potassium ferricyanide [$K_3Fe(CN)_6$] (1% w/v). The mixture was incubated at 50°C for 20minutes before 50µl of trichloroacetic acid (TCA; 10% w/v) was added. The absorbance was measured at 700nm using a microplate reader. The reducing power ability of the sample was determined by an increased in absorbance of the sample. Ascorbic acid, tannic acid and α-tocopherol were used as standards for comparison.

2.8.4. Cupric Reducing Antioxidant Capacity (CUPRAC)

Cupric ion reducing capacity was measured in accordance to the method in Apak et al. (2007). 60µl of ammonium acetate buffer (pH 7), 50µl of neocuproine (0.156% w/v) and 50 µl of cupric chloride (0.17% w/v) solutions were added to 40 µl of n-butanol fraction at different concentrations. This mixture was incubated for 1hour at room temperature and measured against blank at 450 nm. BHA and BHT were used as standards. The test was repeated in triplicate for each concentration in order to get the mean value.

2.8.5. Sun Protection Factor Activity (SPF)

SPF was determined according to the method in Mansur et al. (1986). 2g of the extract were dissolved in 1ml of methanol. The absorbances were measured at different wavelengths starting at 290 nm to 320 nm, each 5nm increments, and the SPF was calculated by applying the mathematic equation below:

$$SPF_{spectrophotometric} = CF * \sum_{290}^{320} EE(\lambda) * I(\lambda) * Abs(\lambda)$$

EE: erythemal effect spectrum; **I**: solar intensity spectrum; **Abs**: absorbance of sunscreen product; **CF**: correction factor (= 10);**EE* I**: is a constant determined by Sayre et al. (1979).

2.9. Identification and Quantification of Polyphenols by Liquid Chromatography Coupled with Mass Spectrometry–Mass Spectrometry (LC–MS/MS) Analysis:

The chemical profile by LC–MS/MS analysis was obtained according to Akdeniz's (2018) method. The LC–MS/MS system used for the quantitative and qualitative analyses of 15 phytochemicals consists of Shimadzu Nexera model UHPLC coupled to Shimadzu LCMS 8040 model triple quadrupole mass spectrometer. The liquid chromatograph composed of LC-30AD model gradient pump, DGU-20A3R model degasser, CTO-10ASvp model column oven and SIL-30AC model autosampler. The chromatographic separation was performed on an Agilent Poroshell 120 model (EC-C18 2.7 µm, 4.6 mm×150 mm) column. The column temperature was kept at 40ºC during the analysis. The mobile phase consisted of water (A; 5 mM ammonium formate, 0.15% formic acid) and methanol (B; ammonium formate, 0.15% formic acid). The applied gradient profile was optimised at 20-100% B (0-25 min), 100% B (25-35 min), 20% B (35-45 min). The flow rate of the mobile phase was 0.5 mL/min and the injection volume was 3 µL. The optimum ESI parameters for the mass spectrometer were determined as: 350ºC interface temperature, 250ºC DL temperature, 400ºC heat block temperature, 3 L/min and 15 L/min were nebuliser and drying gas (N2) flow rates, respectively.

2.10. Statistical Analysis:

The results are presented as the mean of three replications. Regression analysis was carried out by best-fit method and IC_{50} values were calculated using regression equations. The significance of results was checked at $p < 0.05$ using ANOVA test.

3. Results

3.1. Phytochemical Screening, Total Phenolic and Flavonoid Contents:

The qualitative determination of phytochemicals present in n-butanol fraction extracted from *A. numidica* leaves is presented in Table 1. Results showed that this fraction was rich in flavonoids and saponins; it contained trace amounts of sterols and reducing sugars; however, tannins, anthocyanins, coumarins and triterpenes were absent. The total phenolics and flavonoids contents revealed that n-butanol extract contained a high number of phenols and flavonoids [381.15±22.70 µg gallic acid equivalence/ml and 49.79±2.81 µg quercetin equivalence /ml, respectively].

Table 1: The qualitative determination of phytochemicals in n-butanol extract of *A. numidica* leaves.

Phyto-constituents	Methods/ reagents	Modifications/results	n-BuOH extract
Tannins	$FeCl_3$	Blue/dark or blue/green	–
Flavonoids	Magnesium	Pink/red	+++
Anthocyanins	Sulphuric acid + ammonium hydroxide	Purplishblue	–
Coumarins	Sodium hydroxide	Yellow fluorescence	–
Alkaloids	Mayer/Dragendoff-Wagner	Turbidity	–
Sterols and steroids	Sulphuric acid	Green	+
Triterpenes	Sulphuric acid	Purplish green	–
Saponosides	Foaming formation	Persistent Foaming>1cm	+++
Reducing sugars	Fehling	Precipitated brick red	+

+ = Present, – = Absent

3.2. Antibacterial Activity:

Results are obtained from the antibacterial assay presented in Table 2 at the concentration of 100 mg/ml, the n-butanol extract of *A.*

numidica leaves exhibited varying degrees of antibacterial activity against all bacterial strains tested. For several different bacterial strains, n-butanol fraction exhibited a higher inhibition zones for *P. vulgaris* (17.5±0.70 mm) and *E. coli* (16.5±0.70mm), followed by *P. aeruginosa, M. morganii* (16±00 mm). It showed a moderate activity towards other strains: *S. aureus* and *B. subtilis* (14.33±0.57 mm; 14. 33 ± 1.15 mm), respectively.

Table 2: Antibacterial activity of n-butanol fraction extracted from *A. numidica* leaves.

Extracts	Inhibition zone (mm)					
	Gram-positive bacteria		Gram-negative bacteria			
	B. subtilis	*S. aureus*	*E.coli*	*P. aeruginosa*	*M. morganii*	*P. vulgaris*
n-BuOH (100 mg/ml)	14.33±1.15	14.33±0.57	16.5±0.70	16±0.00	16±0.00	17.5±0.70
OX (1µg/ml)	Nt	NA	Nt	Nt	Nt	Nt
CD (2µg/ml)	NA	Nt	Nt	Nt	Nt	Nt
CIP (5µg/ml)	28±0.75	Nt	Nt	30±0.0	Nt	Nt
E (15µg/ml)	NA	22±1.25	Nt	Nt	Nt	Nt
Pi (20µg/ml)	Nt	Nt	18±0.0	Nt	NA	NA
C (30µg/ml)	Nt	28±0.80	Nt	Nt	Nt	25±0.0
AK (30µg/ml)	Nt	Nt	28±1	24±0.0	27±0.81	Nt
PRL (100µg/ml)	Nt	Nt	NA	NA	NA	NA
FEP (30µg/ml)	15.33±0.57	Nt	20±0.0	19±0.0	18.33±1.15	16.33±0.57

Ox: oxacillin, Pi: pipemedic acid, E: erythromycin, PRL: piperacillin, C: chloramphenicol, CD: clindamycin, AK: amikacin, CIP: ciprofloxacin, NA: Not active. Nt: Not tested.

3.3. Antioxidant Activities:

The DPPH· free radical scavenging activity of n-butanol extract was investigated (Table 3). The n-butanol fraction extracted from *A. numidica* leaves showed a moderate capacity to scavenge DPPH$^{\bullet}$ free radical with an IC_{50} value of 5.28±0.26 (µg/ml), which is lower than BHT (6.55±0.59 µg/ml) and BHA (15.74 ±0.47 µg/ml) (Figure 1).

In ABTS$^{\bullet+}$ assay, the outcome in Table 3 revealed that n-butanol fraction has an IC_{50}= 3.48±0.02 µg/ml, which is higher than IC_{50} of BHT standard (1.55±0.26 µg/ml); however, it is much lower than BHA standard with IC_{50}= 7.54±0.67 µg/ml (Figure 1).

Figure 1: Inhibition percentage in ABTS$^{\bullet+}$ (A) and DPPH$^{\bullet}$ (B) antioxidant assays of n-butanol fraction (p<0.05)

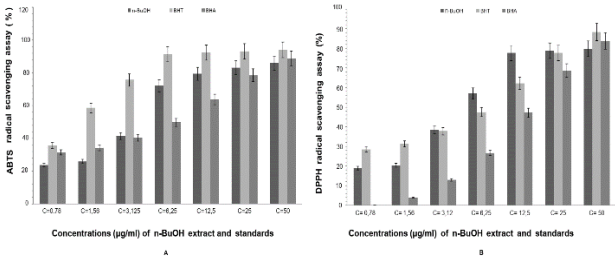

ABTS: 2,2′-azino-bis(3-ethylbenzothiazoline-6-sulfonic acid; DPPH:2,2-diphenyl-picrylhydrazyl; n-BuOH: n-butanol extract; BHT: Butylatedhydroxytoluene; BHA: Butylatedhydroxylanisole; C: Concentrations

The results in Table 3disclosed that this fraction has a weak reducing power antioxidant activity with IC_{50}= 32.30±1.84 µg/ml, compared with ascorbic acid (IC_{50}= 6.77±1.15 µg/ml) and tannic acid (IC_{50}= 5.39±0.91 µg/ml); however, it presented a significant reducing power activity compared with α-tocopherol (IC_{50}=34.93±2.38 µg/ml) (Figure 2).

In CUPRAC assay, the data in Table 3 showed that this fraction presented a mild antioxidant activity compared with standards used, where n-butanol fraction has $A_{0.5}$=5.79±0.33 µg/ml, BHT ($A_{0.5}$= 3.44±0.04 µg/ml) and BHA ($A_{0.5}$= 1.34±0.11 µg/ml), respectively (Figure 2).

Figure 2: Inhibition percentage in CUPRAC (A), reducing power (B) antioxidant assays of n -butanol fraction (p<0.05).

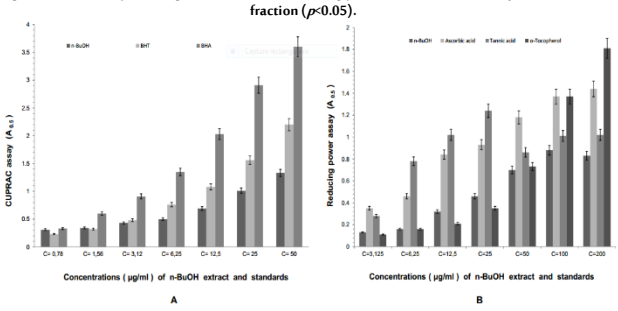

CUPRAC: Cupric reducing antioxidant capacity; n-BuOH: n-butanol extract; BHT: Butylatedhydroxytoluene; BHA: Butylatedhydroxylanisole; C: Concentrations of n-butanol extract and standards used; $A_{0.5}$: Absorbances at 0.5 which correspond to the concentration providing 0.5 absorbance.

For the SPF assay, the results in Table 3 showed that this fraction has an SPF = 45.68±0.26. According to The Comission of the European Communities (2006), this fraction presented a high protection factor.

Table 3: Antioxidant activities results of n-butanol fraction extracted from *A. numidica* leaves.

Extract and standards (0.25µg/ml)	Antioxidant activities				
	DPPH assay IC_{50} µg/mL	ABTS assay IC_{50} µg/mL	Reducing power assay $A_{0.5}$ µg/mL	CUPRAC assay $A_{0.5}$ µg/mL	SPF
n-BuOH	5.28±0.26	3.48±0.02	32.30±1. 84	5.79±0.33	45.68±0.26
BHT	6.55±0.59	1.55±0.26	-	3.44±0.04	-
BHA	15.74±0.47	7.54±0.67	-	1.34±0.11	-
Ascorbic acid	-	-	6.77±1.15	-	-
Tannic acid	-	-	5.39±0.91	-	-
α-tocopherol	-	-	34.93±2.38	-	-

IC_{50}values expressed are means ± SD of three parallel measurements.

3.4. LC–MS/MS Analysis:

The quantitative results summarised in Table 4 showed a total of 8 chemical flavonoids revealed among 15 phytochemical standards used as shown in Figure 3. The compounds were identified by the accurate mass information and retention times. According to LC–MS/MS analysis results, the major components were hyperoside, astragalin and rutin, which acted as reducing agents.

Table 4: Analytical parameters of LC–MS /MS of 15 phytochemical standards used and n-butanol extract.

No	Analytes	RT[a]	$^cR^2$	Linearity (µg/L)	LOD/LOQ (µg/L)[e]	(% RSD[d]) Intraday	Interdays	Recovery (%) Intraday	Interdays	U[f]	n-BuOH (µg/g)
1	Protocatechuicacid	7.00	0.9909	100-3200	4.26/5.32	0.0060	0.0060	1.0096	0.9988	0.0215	N.D
2	Chlorogenicacid	8.03	0.9910	75-2400	2.44/3.36	0.0074	0.0055	0.9941	0.9999	0.0299	9.66
3	Luteolin-7-glucoside	13.20	0.9939	75-2400	2.30/3.02	0.0052	0.0037	1.0014	1.0072	0.0086	14.6
4	Rutin	13.67	0.9902	100-3200	1.283/1.90	0.0063	0.0070	1.0049	1.0037	0.0136	102.62
5	Hesperidin	13.68	0.9942	50-1600	0.96/1.44	0.0081	0.0073	1.0053	0.9994	0.0162	42.02
6	Hyperoside	13.69	0.9905	100-3200	5.48/6.50	0.0074	0.0056	1.0039	1.0015	0.0126	399.91
7	Apigetrin	14.54	0.9902	50-1600	1.23/1.75	0.0047	0.0067	1.0060	1.0047	0.0132	23.19
8	Quercitrin	14.98	0.9918	100-3200	10.51/11.65	0.0079	0.0063	0.9999	1.0002	0.0133	20.44
9	Astragalin	15.13	0.9900	100-3200	5.52/6.77	0.0086	0.0077	1.0002	1.0017	0.0153	147.22
10	Quercetin	17.10	0.9962	50-1600	1.25/1.81	0.0177	0.0227	1.0010	1.0012	0.0573	N.D
11	Luteolin	17.78	0.9901	50-1600	0.61/0.87	0.0119	0.0079	0.9961	1.0007	0.0188	N.D
12	Apigenin	19.20	0.9910	50-1600	0.32/0.52	0.0087	0.0090	0.9985	1.0022	0.0181	N.D
13	Pseudohypericin	26.34	0.9908	50-1600	2.15/2.55	0.0061	0.0089	1.0033	1.0034	0.0172	N.D
14	Hyperforin	28.97	0.9901	10-320	0.32/0.51	0.0218	0.0164	1.0076	1.0061	0.0418	N.D
15	Hypericin	30.18	0.9925	50-1600	1.27/1.88	0.0093	0.0095	1.0104	1.0034	0.0189	N.D

[a]RT: Retention time, [c]R^2:Correlation coefficient, [d]RSD: Relative standard deviation, [e]LOD/LOQ (µg/L): Limit of determination/Limit of quantification, [f]U (%): Percent relative uncertainty at 95% confidence level (k=2), ND: NOT detected.

Figure 3: LC–MS/MS chromatograms of phytochemical standards (A) and n-butanol extract (B).

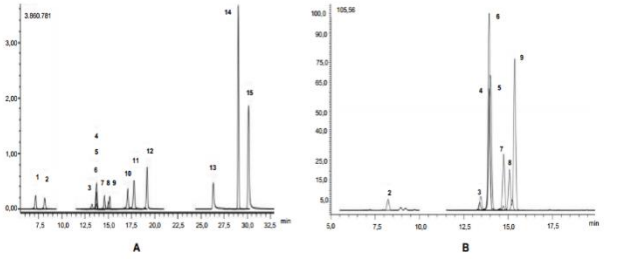

4. Discussion

The qualitative analysis revealed that then-butanol fraction was

abundant in secondary metabolites, which was confirmed by quantitative analyses by the determination of total phenolic and flavonoids contents. The results of the current study were in agreement with the findings in Gupta et al. (2011), which reported that *A. pindraw* leaves acetone extract was highly rich in phenolic and flavonoids compounds. Also, Vasincu et al. (2013) results disclosed that *A. alba* Mill. ethylacetate fraction from its bark was high in polyphenols and flavonoids.

Secondary metabolites (phenols, flavonoids, tannins and alkaloids) are considered as main phytochemical constituents produced by plants; they play a crucial role for both plants and human health. From the results of the antibacterial assay, Gram-negative bacterial strains were found to be the most sensitive. Our findings are in line with those reported by Ghadbane et al. (2016), that this effect is due to the presence of bioactive molecules (Su et al., 2015), as flavonoids and saponins. Many studies have reported that saponins have a potential antibacterial effect (Ravi et al., 2016). Other studies also have stated that flavonoids have a significant antibacterial effect because of their chemical structure, and the presence of aromatic ring substituted with hydroxyl groups. These compounds act on the cell membrane of the sensitive bacterial strains; these active substances can also inhibit enzymes leading to the death of bacterial strains.

The antioxidant activity of extracts has been partly ascribed to phenolic compounds (Russo, 2018). It has been reported that hyperoside showed a strong *P. aeruginosa* biofilm inhibitory activity, by influencing the gene expression (Sun and Miao, 2020). Additionally, astragalin is a flavonoid glycoside which has different pharmacological properties, such as anti-inflammatory and antibacterial substance (Riaz et al., 2018). Additionally, Frutos et al. (2018) results also demonstrated the potent antimicrobial effect of rutin.

Most of the antioxidant potential of plants is due to the redox properties of phenolic compounds, which act as reducing agents, hydrogen donors and singlet oxygen scavengers. Flavonoids are responsible for the antioxidant activity. They have the ability to donate hydrogen attached to the aromatic ring structures. Thus, it can reduce Fe^{+3} to Fe^{+2} which serves as a significant antioxidant indicator (Gulcin, 2020). This activity is referred to as phenolic compounds electron donating power. Several studies agreed that polyphenols and flavonoids are responsible for the reducing power activity since they act as metallic ions quenchers by donating an electron, due to the presence of aromatic ring structure. Sun UV-B causes the formation of free radicals, which is considered how a lot of degenerative diseases are spread, especially skin diseases (Cavinato and Jansen-dürr, 2017). Flavonoids have been found to have a strong ability to scavenge these kinds of reactive oxygen species(Palma-Tenango et al., 2017). We suggest it might be due to the presence of flavonoids and saponins in this fraction.

The results obtained from LC–MS/MS analysis enhance the antioxidant and antibacterial effect of this fraction. Hyperoside is a flavonoid-type flavone glycoside that has been reported to possess a wide range of pharmacological properties, such as an antioxidant agent (Park et al., 2016), anti-Alzheimer, anti-inflammatory and anti-cancer (Li et al., 2014).This is the same as astragalin, which presented several positive effects as antioxidant and anti-cancer (Riaz et al., 2018). Finally, rutin, which is a flavonoid, has anti-inflammatory (Mostafa, 2018), anti-carcinogenic, and antioxidant activities (Farha et al., 2020).

5. Conclusion

Medicinal plants have offered a rich source of compounds that are found in the fields of medicine, pharmacy and biology. The potential effects of the antioxidant and antibacterial properties of n-butanol fraction extracted from *A. numidica* leaves were reported. These biological activities of the extract might be attributed to different phytochemical constituents (flavonoids, saponins). LC–MS/MS analysis showed that the major flavonoids were hyperoside, astragalin and rutin. To use this endemic plant in different domains, several biological studies are needed as purification and isolation of molecules in high amounts from n-butanol extract, and determination of their chemical structures using NMR analysis. Furthermore, molecular docking is very important to understand the mechanism of action (MOA), and to know which parts are responsible for the biological effect. Other investigations are also necessary as the evaluation of in vitro and in vivo anti-cancer possibilities.

Biographies

Djamila Benouchenne

National Centre of Pharmaceutical Research, Department of Biochemistry, Molecular and Cellular Biology, Faculty of Natural and Life Sciences, University of Frères Mentouri Constantine 1, Constantine, Algeria, dbenouchenne1992@gmail.com, 00213667503792

Mrs. Benouchenne is a PhD student. She is an Algerian researcher in the field of biochemistry and nutrition. She had an MSc from the Department of Biochemistry and Molecular and Cellular Biology, Faculty of Natural and Life Sciences, University of Frères Mentouri Constantine 1. She has published three papers in global journals. She participated in several national and international seminars and conferences. She participated at summer school at Hiroshima University, Japan. Currently she is an engineer at the National Centre of Pharmaceutical Research Constantine, Algeria. ORCID: 0000-0002-9432-2742

Ines Bellil

Laboratory of Genetics Biochemistry and Plant Biotechnologies, Department of Applied Biology, Faculty of Natural and Life Sciences, University of Frères Mentouri Constantine 1, Constantine, Algeria, bines07@yahoo.fr, ies.bellil@umc.edu.dz, 00213666510247

Dr. Bellil is an associate professor and an Algerian senior researcher. She holds a PhD in biochemistry and biotechnology from the Department of Biochemistry and Microbiology, Faculty of Natural and Life Sciences, University of Frères Mentouri Constantine 1. She is a member of several national and international research projects. She is head of the Applied Biology Department in charge of pedagogy. She is a member of the scientific council of the Faculty of Natural and Life Sciences at the same university. She participates in several doctoral schools and has published in various fields of science. ORCID: 0000-0003-2718-3102

Salah Akkal

Unit for the Valorisation of Natural Resources, Bioactive Molecules and Physico-Chemical and Biological Analyzes, Faculty of Exact Sciences, Department of Chemistry, University of Frères Mentouri Constantine 1, Constantine, Algeria, algeria.salah4dz@yahoo.fr, 00213558896785

Prof. Dr. Akkal is an Algerian researcher with a PhD in organic chemistry from the Department of Chemistry, Faculty of Exact Sciences, University of Frères Mentouri Constantine 1. He is president of several national and international research projects. He is head of the Laboratory of Phytochemistry and Physico-chemical and Biological Analyzes at University of Frères Mentouri Constantine 1. He is editor in chief and has published in various fields of science and chemistry. His research interests are

biomolecules and phytochemistry. ORCID: 0000-0002-4999-5673

Douadi Khelifi

High National School of Biotechnology, Constantine, Algeria. dkhelifi@yahoo.fr, 00213773181269

Prof. Dr. Khelifi is an Algerian researcher with a PhD in Genetics and Biochemistry from the Department of Biology, Faculty of Sciences, University of Frères Mentouri Constantine 1. He is president of several national and international research projects. He is the director of the High National School of Biotechnology, Constantine, Algeria and the head of the Laboratory of Genetics Biochemistry and Plant Biotechnologies at Frères Mentouri Constantine 1 University. He has published in various fields of science. ORCID: 0000-0001-8139-5064

Acknowledgements

The authors gratefully thank the Algerian Ministry of Higher Education and Scientific Research, the General Directorate of Scientific Research and Technological Development, Algeria and the Biotechnology Research Centre (CRBt) of Constantine, Algeria.

References

Akdeniz, M. (2018). *Screening of Chemical Content Specific to Hypericum species Growing in Different Parts of Turkey by LC-MS/MS and Method Validation; Investigation of Their Biological Activities and Chemometric Evaluation*. PhD Thesis, Department of Chemistry, Dicle University Institute of Science, Diyarbakır, Turkey.

Apak, R., Guclu, K., Ozyurek, M. and Karademir, S.E. (2007). Mechanism of antioxidant capacity assays and the CUPRAC (cupric ion reducing antioxidant capacity) assay. *Microchimia Acta*, **160**(4), 413–9.

Bağci, E. and Diğrak, M. (1996). Antimicrobial activity of essential oils of some Abies (fir) species from Turkey. *Flavour and Fragrance Journal*, **11**(4), 251–6.

Bennadja, S. and Tlili Ait-Kaki Kaki, A.I.T. (2012). The fir of numidia: Athreatened kind. *Kastamonu Üniversitesi Orman Faküftesi Dergisi*, **12**(3), 283–6. DOI: 10.17475/kuofd.75019.

Benouchenne, D., Bellil, I., Akkal, S., Bensouici, C. and Khelifi, D. (2020). LC – MS / MS analysis , antioxidant and antibacterial activities of Algerian fir (Abies numidica de LANNOY ex CARRIÈRE) ethylacetate fraction extracted from needles. *Journal of King Saud University - Science*, **32**(8), 3321–7. DOI: 10.1016/j.jksus.

Bensari, S., Ouelbani, R., Yilmaz, M.A., Bensouici, C., Gokalp, E. and Khelifi, D. (2020). Phytochemical profiles of Iris unguicularis Poir. with antioxidant, antibacterial, and anti-Alzheimer activities. *Acta Scientifica Naturalis*, **7**(2), 74–87. DOI: 10.2478/asn-2020-0021.

Blonk, B. and Cock, I.E. (2019). Interactive antimicrobial and toxicity profiles of Pittosporum angustifolium Lodd. Extracts with conventional antimicrobials. *Journal of Integrative Medicine*, **17**(4), 261–72. DOI: 10.1016/j.joim.2019.03.006

Boudjada, A., Touil, A., Bendif, H., Bensouici, C.H. and Rhouati, S. (2017). Phytochemical constituents, phenolic contents, and antioxidant activity of Crataegus azarolus extracts. *Asian J Pharm Clin Res.*, **11**(4), 133–7.

Cavé, A. (1993). *Pharmacognosy, Phytochemistery, Medicinal Plants*. Paris: Lavoisier.

Cavinato, M. and Jansen-dürr, P. (2017). Molecular mechanisms of UVB-induced senescence of dermal fi broblasts and its relevance for photoaging of the human skin. *Experimental Gerontology*, **94**(n/a), 78–82. DOI: 10.1016/j.exger.2017.01.009

Farha, A.K., Gan, R., Li, H., Wu, D., Atanasov, G., Gul, K., Zhang, J., Yang, Q. and Corke, H. (2020). The anticancer potential of the dietary polyphenol rutin: Current status, challenges, and perspectives. *Critical Reviews in Food Science and Nutrition*, **n/a**(n/a), 1–28. DOI: 10.1080/10408398.2020.1829541.

Flora Mediterranea, **23**(n/a), 123–9. DOI: 10.7320/FlMedit23.123. [In French].

Frutos, M.J., Rincón-Frutos, L. and Valero-Cases, E. (2018). *Rutin. In María José Frutos,Laura Rincón-Frutos, and Estefanía Valero-Cases, Nonvitamin and Nonmineral Nutritional Supplements*. USA: Elsevier. DOI: 10.1016/B978-0-12-812491-8.00015-1.

Ghadbane, M., Bounar, R., Khellaf, R., Medjekal, S., Belhadj, H., Benderradji, L., Smaili, T. and Harzallah, D. (2016). Antioxidant and antimicrobial activities of endemictree abies numidica growing in babor mountains from algeria. *Global Journal of Research on Medicinal Plants & Indigenous Medicine*, **5**(1), 19–28.

Gulcin, İ. (2020). Antioxidants and antioxidant methods: An updated overview. Archives of Toxicology, **94**(3), 651–715. DOI: 10.1007/s00204-020-02689-3.

Gupta, D., Bhardwaj, R. and Gupta, R.K. (2011). In vitro antioxidant activity of extracts from the leaves of Abies pindrow Royle. *African Journal of Traditional, Complementary and Alternative Medicines*, **8**(4), 391–7. DOI: 10.4314/ajtcam.v8i4.8.

Hazeena Begum, V. and Muthukumaran, P. (2014). Phytochemical and free radical scavenging activity of Poorna chandrodayam chendooram (metallic herbal based drug). *The Journal of Phytopharmacology*, **3**(6), 418–22.

Koch, W. (2019). Dietary polyphenols - important non-nutrients in the prevention of chronic noncommunicable diseases. A systematic review. *Nutrients*, **11**(5), 1–35. DOI:10.3390/nu11051039.

Li, W., Liu, M., Xu, Y.F., Feng, Y., Che, J.P., Wang, G.C. and Zheng, J.H. (2014). Combination of quercetin and hyperoside has anticancer effects on renal cancer cells through inhibition of oncogenic microRNA-27a. *Oncology Reports*, **31**(1), 117–24. DOI: 10.3892/or.2013.2811.

Mansur, J.S., Breder, M.N.R., Mansur, M.C.A. and Azulay, R.D. (1986). Determination of the factor of solar protection by spectrophotometry. *An Bras Dermatol Rio de Janeiro*, **61**(n/a), 121–4.

Medini, F., Fellah, H., Ksouri, R. and Abdelly, C. (2014). Total phenolic, flavonoid and tannin contents and antioxidant and antimicrobial activities of organic extracts of shoots of the plant Limonium delicatulum. *Journal of Taibah University for Science*, **8**(3), 216–24. DOI: 10.1016/j.jtusci.2014.01.003

Mostafa, N. M. (2018). Rutin: A potential therapeutic agent for alzheimer disease pharmaceutica. *Pharmaceutica Analytica Acta*, **10**(4), 1–2. DOI: 10.35248/2153-2435.19.10.615

Noreikaitė, A., Ayupova, R., Satbayeva, E., Seitaliyeva, A., Amirkulova, M., Pichkhadze, G., Datkhayev, U. and Stankevičius, E. (2017). General toxicity and antifungal activity of a new dental gel with essential oil from Abies Sibirica L. *Medical Science Monitor*, **23**(n/a), 521–7. DOI: 10.12659/MSM.898630.

Oyaizu, M. (1986). Studies on products of browning reaction. Antioxidative activities of products of browning reaction prepared from glucosamine. *The Japanese Journal of Nutrition and Dietetics*, **44**(6), 307–15. DOI: 10.5264/eiyogakuzashi.44.307

Pallab, K., Tapan K.B., Tapas K.P. and Ramen, K. (2011). Research article estimation of total flavonoids content (Tfc) and anti oxidant activities of methanolic whole plant extract of Biophytum sensitivum Linn. *Journal of Drug Delivery and Therapeutics*, **10**(1), 33–37. DOI: 10.22270/jddt.v3i4.546

Palma-Tenango, M., Soto-Hernández, M. and Aguirre-Hernández, E. (2017). Flavonoids in agriculture. In: G.C. Justino (ed.) *Flavonoids Flavonoids - From Biosynthesis to Human Health* (pp.189- 201). London, UK: IntechOpen. DOI: 10.5772/intechopen.68626.

Park, J.Y., Han, X., Piao, M.J., Oh, M.C., Madushan, P. and Jayatissa, D. (2016). Hyperoside induces endogenous antioxidant system to alleviate oxidative stress. *Journal ListJ Cancer Prev*, **21**(1), 41–7.

Ramdani, M., Lograda, T., Chalard, P. and Figueredo, G. (2014). Chemical and antimicrobial properties of essential. *Int. J. Phytopharm*, **5**(6), 432–40.

Ravi, L., Manasvi, V. and Praveena Lakshmi, B. (2016). Antibacterial and antioxidant activity of saponin from Abutilon indicum leaves. *Asian Journal of Pharmaceutical and Clinical Research*, **9**(1), 344–7. DOI: 10.22159/ajpcr.2016.v9s3.15064

Re, R., Pellegrini, N., Proteggente, A., Pannala, A., Yang, M. and Rice-Evans, C. (1999). Antioxidant activity applying an improved ABTS radical cation decolorization assay. *Free. Radic. Biol. Med.*, **26**(n/a), 1231–7.

Riaz, A., Rasul, A., Hussain, G., Zahoor, M.K., Jabeen, F., Subhani, Z., Younis, T., Ali, M., Sarfraz, I. and Selamoglu, Z. (2018). Astragalin: A bioactive phytochemical with potential therapeutic activities. *Advances in Pharmacological Sciences*, **n/a**(32), 1–15. DOI: 10.1155/2018/9794625.

Russo, D. (2018). Flavonoids and the structure-antioxidant activity relationship. *Journal of Pharmacognosy and Natural Products*, **4**(1), 30–1. DOI: 10.4172/2472-0992.1000e109.

Sayre, R.M., Agin, P.P., Levee, G.J. and Marlowe, E.A. (1979). Comparison of in vivo and in vitro testing of sun screening formulas. *J. Photochem. Photobiol*, **29**(3), 559–66.

Seo, M., Sowndhararajan, K. and Kim, S. (2016). Influence of binasal and uninasal inhalations of essential oil of Abies Koreana Twigs on electroencephalographic activity of human. *Behavioural Neurology*, **2016**(n/a) 11. DOI: 10.1155/2016/9250935

Singleton, V.L. and Rossi, J.A.J. (1985). Colorimetry to total phenolics with phosphomolybdic acid reagents. American Journal of Enology and Viniculture, **16**(n/a), 144–58.

Su, P.W., Yang, C.H., Yang, J.F., Su, P.Y. and Chuang, L.Y. (2015). Antibacterial activities and antibacterial mechanism of polygonum cuspidatum extracts against nosocomial drug-resistant pathogens. *Molecules*, **20**(6), 11119–30. DOI: 10.3390/molecules200611119

Sun, L. and Miao, M. (2020). Dietary polyphenols modulate starch digestion and glycaemic level: A review. *Critical Reviews in Food Science and Nutrition*, **60**(4), 541–55. DOI: 10.1080/10408398.2018.1544883

Tel, G., Apaydın, M., Duru, M.E. and Öztürk, M. (2012). Antioxidant and cholinesterase inhibition activities of three tricholoma species with total phenolic and flavonoid contents: The edible mushrooms from Anatolia. *Food Analytical Methods*, **5**(3), 495–504. DOI: 10.1007/s12161-011-9275-4.

The Comission of the European Communities. (2006). Comission recommendations of 22 September 2006 on the efficacy of sunscreen products and the claims made relating thereto. *Official Journal of the European Union*, **49**(n/a), 39–43.

Tlili-Ait Kaki, Y., Bennadja, S. and Chefrour, A. (2013). Revalorisation d'une essence endémique: Le sapin de Numidie (Abies numidica).'Revaluation of an endemic species: Numidian fir (Abies numidica)'. Topcu, G., Ay, M., Bilici, A., Sarıkurkcu, C. and Ozturk, M. (2007). A new flavone from antioxidant extracts of Pistacia terebinthus. *Food Chemistry*, **103**(3), 816–22. DOI: 10.1016/j.foodchem.2006.09.028.

Vasincu, A., Creţu, E., Geangalău, I., Amalinei, R.L.M. and Miron, A. (2013). Polyphenolic content and antioxidant activity of an extractive fraction from Abies alba bark. *Revista Medico-Chirurgicală a Societăţii de Medici Şi Naturalişti Din Iaşi*, **117**(2), 545–50.

Yang, X.W., Li, S.M., Shen, Y.H. and Zhang, W.D. (2008). Phytochemical and biological studies of Abies species. *Chemistry and Biodiversity*, **5**(1), 56–81. DOI: 10.1002/cbdv.200890015

المجلة العلمية لجامعة الملك فيصل
The Scientific Journal of King Faisal University
العلوم الأساسية والتطبيقية
Basic and Applied Sciences

Effect of *Citrus Limon* Essential Oil on Lipid Profile and Obesity in Wistar Rats

Souhaila Dalichaouche-Benchaoui [1,2], Meriem Gueracheha [2] and Asma Boutebsou [2]

[1] Department of Dental Medicine, Faculty of Medicine, Salah Boubnider Constantine 3 University, Constantine, Algeria
[2] Department of Toxicology, Faculty of Biology, University Mentouri Brothers Constantine 1, Constantine, Algeria

تأثير الزيت الأساسي لليمون على الدهون والسمنة في فئران ويستار

سهيلة دالي شاوش بن شاوي [1,2]، مريم كراشح [2]، أسماء بو طبسو [2]

[1] قسم طب الاسنان، كلية الطب، جامعة صالح بوبنيدر قسنطينة 3، قسنطينة، الجزائر
[2] قسم السمية، كلية العلوم الحيوية، جامعة الاخوة منتوري قسنطينة 1، قسنطينة، الجزائر

LINK الرابط	RECEIVED الاستقبال	ACCEPTED القبول	PUBLISHED ONLINE النشر الإلكتروني	ASSIGNED TO AN ISSUE الإحالة لعدد
https://doi.org/10.37575/b/med/210014	13/03/2021	23/05/2021	23/05/2021	01/12/2021

NO. OF WORDS عدد الكلمات	NO. OF PAGES عدد الصفحات	YEAR سنة العدد	VOLUME رقم المجلد	ISSUE رقم العدد
4048	5	2021	22	2

ABSTRACT

Obesity causes many pathologies; no therapeutic axis has provided an effective solution to this problem. The use of herbal medicine with healthy food and physical activity is recommended, and essential oils are the best known of these natural substances. The objective of this study is to evaluate the effect of *Citrus limon* essential oil on body weight and lipid profile. The plant material is the lemon; the extraction method is hydrodistillation. The experiment lasted 20 days and involved 15 female rats (2 to 3 months old) weighing between 160g and 230g. The rats were divided into 3 groups: the first receiving a standard diet, the second receiving a high-fat diet, and the third receiving a high-fat diet and treated with essential oil. The extraction yield is 1.69%. The physicochemical characteristics comply with AFNOR. This study shows that a high-lipid diet induces obesity characterized by hyperlipidemia. Intraperitoneal administration of the essential oil caused a decrease in body weight, abdominal circumference, plasma total cholesterol, and triglycerides and an increase in HDL-cholesterol. Considering this study, we found that lemon essential oil has beneficial effects on metabolic alterations. Its inclusion in the diet may help improve the metabolic profile and reduce the incidence of obesity and its long-term complications.

الملخص

سبب السمنة المفرطة العديد من الأمراض، ولم يقدم أي محور علاجي دراسي علاجا فعالا ودائمًا لهذه المشكلة. لقد تبين أن الزيوت الأساسية المستخرجة من النباتات الطبيعية ذات فعالية معتبرة لهذه الحالة. هدفنا من هذه الدراسة هو تقييم أثر زيت قشرة ثمرة الليمون على وزن الجسم ودهونه المعتبرة. يتم استخراج الزيوت الأساسية النباتية من قشرة الليمون بطريقة التقطير المائي. استمرت التجربة 20 يومًا على 15 أنثى من فئران التجارب البيضاء، أعمارهن بين شهرين وثلاثة أشهر. أوزانها بين 160 إلى 230 جرام. قسمت الفئران إلى ثلاثة مجموعات: المجموعة الأولى غير معاملة تتلقى نظامًا غذائيًا كاملا. المجموعة الثانية غير معاملة تخضع لنظام غذائي عالي الدهون. أما المجموعة الثالثة فخضعت لنظام غذائي عالي الدهون وبمعالجة بزيت الليمون الأساسي (30 ميكروجرام/كحجم/ يوم). أعطى المستخلص عائدا علاجيا بمقدار 1.60%. تتوافق الخصائص الفيزيائية والكيميائية مع معايير AFNOR. تسبب النظام الغذائي الغني بالدهون بالسمنة لدى الفئران التي تميزت بقرط السمنة وتشحمات الدم. إن إعطاء الزيت الأساسي داخل الصفاق تسبب في انخفاض في وزن جسم الفئران ومحيط البطن، وتركيز الكوليسترول الكلي في البلازما، والدهون الثلاثية الكربون، وزيادة تركيز كوليسترول-HDL. أن الزيت الليمون الأساسي له تأثيرات فعالة على التغيرات الأيضية. قد يؤدي تضمينه في النظام الغذائي إلى تحسين المظهر الأيضي وتقليل حدوث السمنة ومضاعفاتها على المدى الطويل.

KEYWORDS
الكلمات المفتاحية
Abdominal circumference, animal model, body weight, citrus, hyperlipidemia
الحمضيات، فرط شحميات الدم، محيط البطن، نموذج حيواني، وزن الجسم

CITATION
الإحالة
Benchaoui, S.D. (2021). Effect of citrus limon essential oil on lipid profile and obesity in Wistar rats. *The Scientific Journal of King Faisal University: Basic and Applied Sciences,* **22**(2), 33–7. DOI: 10.37575/b/med/210014

1. Introduction

The prevalence of obesity has increased significantly over the past three decades. Algeria is not spared by this modern-day scourge. In 2012, the prevalence of obesity among adults in Constantine was 30.9%, 20.8% of men and 38.3% of women (Dalichaouch, 2015). Obesity is a metabolic disorder characterized by an excessive accumulation of body fat due to a state of dysregulation of energy reserves by external and/or internal factors (Basdevant, 2004). Experimental and epidemiological data suggest a direct correlation between lipid intake and the degree of obesity (Ailhaud, 2008).

Obesity is a risk factor for several diseases and a major public health problem that must be treated. Currently the World Health Organization places its prevention and management as a priority in the field of nutritional pathology. None of the therapeutic approaches have proven to be effective, and all of them reveal an unfavorable benefit–risk balance. The failures of obesity drugs are, above all, linked to their side effects, which are significantly greater than the expected benefits (Favre, 2019). In some traditional societies (China and some African countries), the medical management of so-called chronic pathologies is largely performed using medicinal plants (Ait Ouakrouche, 2015). The search for new herbal treatments with minimal side effects is a current challenge in this field. Essential oils extracted from aromatic plants are beginning to be of great interest as a potential source of natural bioactive molecules with a wide range of applications (Yavari kia, 2014). Lemon (*Citrus limon*) of the *rutaceae* family, the most important citrus fruit after orange and tangerine, is cultivated today in all Mediterranean regions, and its essential oil (EO) is used for several applications (Khan et al., 2010). Lemon peels are rich in nutritional ingredients (water, proteins, sugars, and minerals) and functional ingredients (essential oils, fibers, carotenoids, vitamin C, and phenolic compounds), which give them different properties (Khan et al., 2010). Citrus essential oil contains different types of flavonoids and limonoids, which could have an anti-obesogenic and lipid-lowering effect (Khan et al., 2010). Studies in animals have shown that they lower cholesterol and blood triglycerides (Miceli et al., 2007).

2. Materials and Methods

2.1. Extraction Process of the Essential Oil:

The essential oil of *Citrus Limon* (Eureka) is extracted by hydrodistillation (Clevenger, 1978), and the distillate (essential oil

Corresponding Author: Souhaila Dalichaouche Benchaoui dalisouh@yahoo.fr ,00213557958614 المؤلف المراسل: سهيلة دالي شاوش بن شاوي

plus water) is recovered in a separating funnel for separation of the mixture by density difference. The extraction time is measured from the fall of the first drop of distillate into the separatory funnel. The boiling temperature is lower than the most volatile solvent (water). The oil is recovered then treated with a desiccant – sodium sulfate. The essential oil yield (EOR) is defined as the ratio between the mass of essential oil obtained after extraction (M1) and the mass of plant material used (M0) (Benouli, 2016).

2.2. Experimental Animals:

The experiment lasted 21 days and involved 15 white female rats (*Rattus norvegicus*) aged 2 to 3 months and weighing between 160g and 230g. These rats were subjected to a period of adaptation to the conditions of the animal house: a temperature of 25±2°C and a humidity of 50–55%. The rats were placed in plastic cages, which were lined with a litter made of wood shavings. The cages were cleaned, and the litters were changed every day until the end of the experiment, and the rats had free access to water.

The rats were divided into three groups, each composed of 5 animals (n=5).

- Group 1 (negative control RT-): received 75g/day of standard laboratory food
- Group 2 (RT+ positive control): subjected to the hyperlipidic diet (composed of 50% standard diet and 50% palm oil 8ml/day) administered directly into the stomach by intragastric gavage.
- Group 3 (RH: treated with essential oil): subjected to the hyperlipidic diet administered directly into the stomach by intragastric gavage (50% standard diet and 50% palm oil) and received an EO treatment by an intraperitoneal injection at a dose of 30µl/kg per day for each rat.

2.3. Measured Parameters:

2.3.1. Body Weight and Abdominal Circumference

The body weights were taken with a scale in grams (g). The growth rate of the rats is expressed in percentages (%). Abdominal circumference was measured by placing the tape measure around the waist (between the last rib and the top).

2.3.2. Blood Parameters

Blood sampling was performed by capillary tubes through the retroorbital sinus at eye level. The rats were anesthetized with chloroform for 2–3 minutes. Whole blood, collected in dry tubes, was centrifuged at 3000 rpm for 15 minutes; the tubes containing serum were immediately transported in a cooler to the laboratory for analysis of biochemical parameters (total cholesterol, triglycerides, and HDL cholesterol).

2.3.3. Statistical Analysis

Statistical calculations are often useful for the determination of normal values (or more precisely, reference values) as well as for the evaluation of precision and accuracy of analysis. The statistical analysis of the results was performed using Microsoft Office Excel, 2010. The results are represented as a mean more or less than the standard deviation (Mean±ET). The statistical evaluation is performed by the student T-test. This test compares two averages (Table 1).

Table1: Difference between two averages

p-value	<0.05(*) Insignificant	<0.01 (**) Significant	<0.001(***) Very significant	<0.0001 (****) Highly significant

3. Results and Discussion

3.1 Organoleptic Characteristics and EO Yield:

The essential oil has a yellow to transparent color with a fresh smell and a fluid and mobile appearance. The yield is of the order of 1.69±0.03%. The pH plays a determining role during chemical and biochemical reactions and can influence the stabilizing properties of an essential oil. Our essential oil is acidic (pH6, 2) These results showed that our essential oil is in conformity with the standard of the French Standardization Association (AFNOR, 2000).

3.2 Effects of EO on Body Weight and Abdominal Circumference:

The administration of the hyperlipidic diet induced a very highly significant increase in the body weight of the animals. Indeed, the weight increased from 171.7±4.16g to 250.2±12.53g in group 2 (RT+) rats compared to the weight of group 1 (RT-) which increased from 170.89±4.16g to 184.6±4.16g ($p<0.0001$) (Figure 1). The treatment of obese rats with intraperitoneal administration of EO induced a significant decrease in body weight gain ($p<0.05$) and a decrease in food intake in group 3 (RH) compared to group 2 (RT+) (Figure 1).

Figure 1: Effect of essential oil on body weight

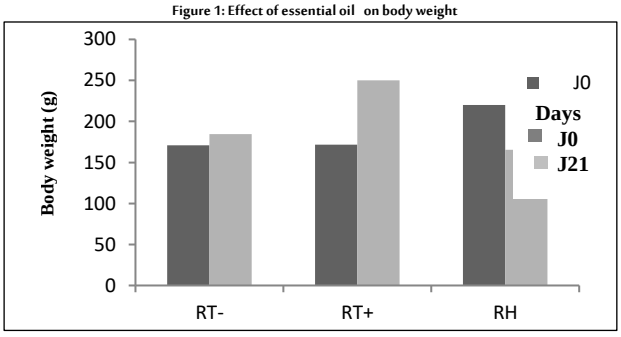

The results show that the hyperlipidic diet induced an increase in the abdominal circumference of the animals (Figure 2). This increased from 13.0±0.4cm to 13.75±0.64cm in RT- (negative control rats) and from 14.12±0.31cm to 15.02±0.31cm in RT+ (positive control rats). Intraperitoneal administration of lemon EO significantly reduced the abdominal circumference of the rats to normal ($p<0.05$). Indeed, the difference between the final and initial values is approximately 14.12±0.31 to 15.02±0.31 in group 2 (RT+) and 14.62±0.31 to 13.48±0.31 in group 3 (RH) respectively (Figure 2).

Figure 2: Effect of essential oil on abdominal circumference

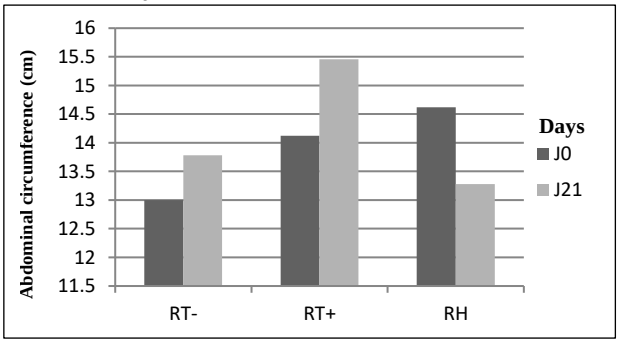

The hyperlipidic diet induced an increase in body weight and abdominal circumference. These results agree with Laissouf's study (Laissouf et al., 2014), which showed that a high-fat diet induces obesity in Wistar rats. Dietary fat has little effect on satiety, and periodic exposure to a high-fat diet, especially when there is a strong feeling of hunger, may be sufficient to cause rats to consume more calories in the form of fat (Laissouf et al., 2014). Most natural anti-obesity products (e.g., algae and medicinal plants) regulate the expression of thermogenin, a key protein of thermogenesis in brown adipose tissue, which converts energy from food into heat.

3.3 Effects of Essential Oil on Lipid Parameters:

Plasma concentrations of the blood lipid parameters, total cholesterol (TC) and triglycerides (TG), increased significantly

($p<0.001$) in group 2 (RT+) compared to the negative control (RT).

Total cholesterol increased from 0.47±0.63g/L (RT-) and 0.58±0.18g/L (RT+) to 0.51±0.34g/L (RT-) and 0.88±0.27g/L (RT+) respectively (Figure 3).

Triglycerides increased from 0.67±0.55g/L (RT-) and 0.68±0.2g/L (RT+) to 0.91±0.97g/L (RT-) and 1.38±0.91g/L (RT+) respectively (Figure 4).

The administration of lemon essential oil in group 3 (RH) resulted in a significant decrease ($p<0.05$) of these parameters. Total cholesterol decreased from 0.64±0.20g/L to 0.34±1.42g/L (Figure 3) and triglycerides decreased from 0.78±0.09g/L to 0.41±0.13g/L (Figure 4).

Figure 3: Plasma concentration of total cholesterol

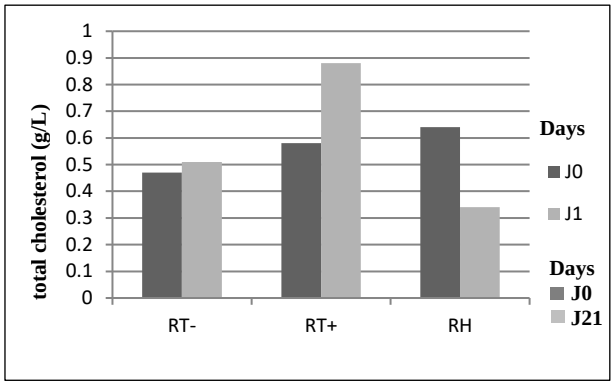

Figure 4: Plasma concentration of triglycerides

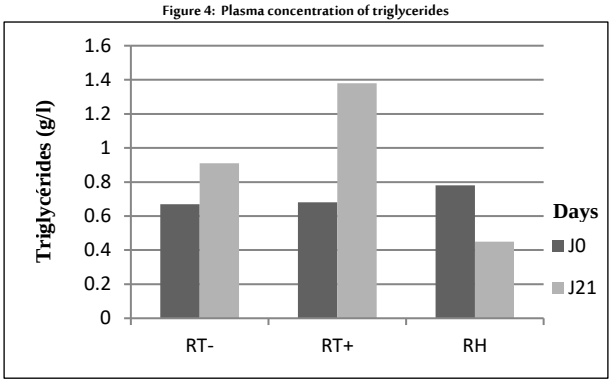

HDL cholesterol increased nonsignificantly ($p>0.05$) in RT- (0.33g/L to 0.34g/L) and RT+ (0.34g/L to 0.35g/L). Administration of lemon essential oil significantly ($p<0.05$) increased HDL-C in Group 3 (HR) from 0.32g/L to 0.55g/L (Figure 5).

Figure 5: Plasma concentration of HDL cholesterol

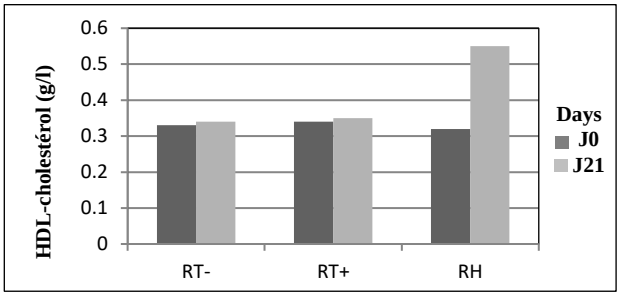

In the present study, obesity induced by a hyperlipidic diet led to an increase in plasma total cholesterol and triglycerides but no significant change in plasma HDL cholesterol in RT+ rats compared to RT- rats.

These results are in concordance with those of several authors who have shown that triglyceride and cholesterol levels in obese rats are higher than in negative control rats receiving a standard diet (Mbundu et al., 2018). The hyperlipidemia observed in RT+ rats can be explained by the high lipid content in the diet. Several authors have found that an increase in the lipid content of the diet causes an increase in plasma cholesterol concentration and changes the composition of plasma lipoproteins, including an increase in the portion of cholesterol esters in VLDL and LDL (Abbas, 2015). Arafa (2005) has reported that hyperlipidemia, particularly hypercholesterolemia, can be induced in animals with a cholesterol-enriched diet. Several studies have shown the effect of dietary cholesterol on cholesterolemia. Dietary supplementation with 0.5% cholesterol and 0.5% cholic acid or with two doses of cholesterol (0.5% and 4%) with or without cholic acid (Assini et al., 2013) has shown an increase in serum total cholesterol (TC). Other studies have shown an increase in serum and hepatic TC with 1% cholesterol and 0.5% cholic acid (Assini et al., 2013).

Several studies have highlighted the effect of dietary cholesterol on triglycerides. In rats, dietary cholesterol induces hypertriglyceridemia (Assini et al., 2013). The increase in serum TG may be due to a decrease in low-density lipoprotein (LDL) receptor activity when the diet is supplemented with cholesterol (Assini et al., 2013).

The decrease observed in the lipid profile (cholesterol and triglycerides) of rats supplemented with lemon essential oil is in accordance with the work of Arafa (2005). The constituents of lemon EO can explain this decrease. Assini et al. (2013) showed that submitting mice to a diet supplemented with citroflavonoids could prevent and treat dyslipidemia and hepatic steatosis by inhibiting hepatic fatty acid synthesis and increasing fatty acid oxidation. In addition, *Citrus limon* might be effective against hyperlipidemia because it is rich in vitamin C and contains different types of flavonoids (Khan et al., 2010). Indeed, the antioxidant effects of limonene, which is 60 to 70% of Citrus limon's composition, contribute to the reduction in the cholesterol level (Assini et al., 2013). Moreover, the presence of hesperidin and eriocitrine, the most abundant flavonoids in lemon, would explain this effect and would contribute to improvements in coronary vasodilatation, decrease blood platelet aggregation, and prevent LDL oxidation (Costa et al., 2014; Manish and Mahesh, 2013).

Previous studies have shown that lemon flavonoids and limonites lower blood cholesterol in rats receiving a cholesterol-enriched diet (Boshtam et al., 2010; Wang et al., 2011). These flavonoids are strong inhibitors of the activity of hydroxymethyl-glutaryl-coenzyme A reductase (HMG-COA reductase) and acylated coenzyme A: cholesterol acyltransferase (ACAT) in vivo and in vitro (Choi et al., 2004). HMG-COA reductase is involved in cholesterol synthesis and VLDL cholesterol secretion, and ACAT is involved in intestinal absorption and esterification of cholesterol (Choi et al., 2004).

In addition, Cirico (2006) noted that citrus juice and EO correct the increase in LDL-C in humans by activating LDL receptors, which induce the uptake and degradation of these lipoproteins. Bochtam (2010) confirmed these results in male rabbits consuming a diet enriched in cholesterol (1%) and supplemented with 1g of the aqueous extract of *Citrus limon* bark. Similarly, some authors have shown that lemon flavonoides decrease LDL-C, increase plasma HDL-C, decrease VLDL and LDL cholesterol, and increase HDL cholesterol, thus correcting dyslipidemia (Akiyama et al., 2010; Miceli et al., 2007).

One study showed that the decrease in LDL was associated with overexpression of the LDL receptor gene and a decrease in the expression and activity of the microsomal triglyceride transfer protein (MTP) in vitro, which plays a role in the assembly of

lipoproteins, mainly triglycerides and VLDL (Wilcox et al., 2001). It is important to note that the consumption of *Citrus limon* could be responsible, in part, for the decrease in plasma TG levels. Indeed, studies have reported that supplementation with hesperitin and maringinine in rats consuming a cholesterol-enriched diet led to a decrease in plasma triglycerides and an amelioration in hypertriglyceridemia (Akiyama et al., 2010). The hypotriglyceridemic effect may be due to the repression of the sterol regulatory element binding protein-1C (SREBP-1C) pathway in adipose tissue and liver and, consequently, to the decrease in triglyceride synthesis. In addition, this hypotriglyceridemia is concomitant with the reduction of TG-VLDL. Indeed, the mass of VLDL is decreased, reflecting the reduction of their various surface (apo and CL) and center (TG) constituents. This result is in accordance with those of other studies (Green et al., 2013; Wilcox et al., 2001).

4. Conclusion

Traditional medicine is widespread and plays a major role in the treatment of various metabolic diseases. The number of research studies for new molecules capable of preventing or delaying the apparition of these diseases is very limited. This work has been performed to evaluate the influence of phytotherapy based on the essential oil of lemon peel (*Citrus limon*) against obesity and its complications in rats made obese by a hyperlipid diet. From our study, we can conclude that the hyperlipidic diet leads to the installation of obesity, associated with metabolic abnormalities such as hyperlipidemia. Our results showed that lemon essential oil reduced body weight gain. Moreover, we observed from our study that lemon EO has a hypolipidemic effect at the plasma level. These results indicate the influence and efficacity of EO on the cellular mechanisms that control lipid metabolism can reduce cardiovascular risk and protect against several diseases.

Biographies

Souhaila Dalichaouch-Benchaoui

Department of Dental Medicine, Faculty of Medicine, Salah Boubnider Constantine 3 University, Constantine, Algeria, dalisouh@yahoo.fr, 00213557958614

Dr. Dalichaouch-Benchaoui is Algerian. She obtained a doctoral degree in cellular and molecular biology from Constantine University, Algeria, in 2013. She has been the first dental year educational committee's chairperson since 2016. She has supervised master's students in molecular and cellular biology, biochemistry, and toxicology. She has attended several research and educational workshops and congresses. She has several articles in national and international scientific journals in the field of obesity and its associated factors. Currently, she is interested in the treatment of obesity and associated diseases using phytotherapy. She speaks and writes Arabic, French, and English.

Meriem Gueracheha

Department of Toxicology, Faculty of Biology, University Mentouri Brothers Constantine 1, Constantine, Algeria. racim20002000@gmail.com, 00213540208013

Miss Gueracheha is Algerian. She obtained her master 1 and master 2 from University Mentouri Brothers of Constantine 1 in life sciences with a toxicology specialty in 2019. She is a very active and motivated team member in project work in addition to being a research assistant in the department of toxicology, faculty of life sciences. She has worked in many fields, notably in medical analysis laboratories. She has participated in several national congresses. She speaks and writes three languages (Arabic, French, and English).

Asma Boutebsou

Department of Toxicology, Faculty of Biology, University Mentouri Brothers Constantine 1, Constantine, Algeria, clepatrasma@gmail.com, 00213557400908

Miss Boutebsou is Algerian. She obtained her master 1 and master 2 from University Mentouri Brothers of Constantine 1 in life sciences with a toxicology specialty in 2019. She is a motivated team member in project work in addition to working as a research assistant in the department of toxicology, faculty of life sciences. She is also a teacher in natural sciences. She has participated in several national congresses. She fluently speaks and writes three languages (Arabic, French, and English).

References

Abbas, K. (2015). *Etude de l'Effet de l'Extrait Aqueux de Portulaca Oleracea sur l'Obésité Chez les Rats Wister. Thèse de Doctorat en Biochimie Appliquée* 'Study of the Effect of Aqueous Extract of Portulaca Oleracea on Obesity in Wister Rats'. PhD Thesis, Department of Biochemistry, Faculty of Biology, University of El Oued, El Oued, Algeria. [in French].

AFNOR. (2000). *Normes Française: Huile Essentielle* 'French Standards: Essential Oil'. Paris: French Association for Standardization. [in French].

Ailhaud, C. (2008). Apports lipidiques et prise de poids 'Lipid intake and weight gain'. *Aspects Qualitatif*, **15**(1), 37–40. DOI: 10.1684/ocl.2008.0157. [in French]

Ait Ouakrouch, I. (2015). *Enquête Ethnobotanique à Propos des Plantes Médicinales Utilisées dans le Traitement Traditionnel du Diabète de Type II à Marrakech. Thèse Doctorat en Médecine Interne* 'Ethnobotanical Survey about Medicinal Plants Used in the Traditional Treatment of Type II Diabetes in Marrakech'. PhD Thesis, Department of Internal Medicine, Centre Hospitalier Universitaire Mohamed VI of Marrakech, Marrakech, Morocco. [in French].

Akiyama, S., Katsumata, S., Suzuki, K. and Ishimi, Y. (2010). Dietary hesperedin exerts hypoglycemic and hypolipidemic effects in streptozotocin-induced margimaltype 1 diabetic rats. *J Clin Biochem Nutr*, **46**(1), 87–92. DOI: 10.3164/jcbn.09-82.

Arafa, H.M. (2005). *Cuminum attenuates* diet-induced hypercholesterolémia in rats. *Med Sci Monit*, **11**(7), 228–34.

Assini, J.M., Mulvihill, E.E. and Huff, M.W. (2013). Citrus flavonoids and lipid metabolism. *Curr Opin Lipidol*, **24**(1), 34–40. DOI: 10.1097/MOL.

Basdevant, Guy-Grand B. (2004). *Traité de Médecine de l'Obésité* 'Treatise on Obesity Medicine'. Paris: Flammarion Médecine Sciences. [in French].

Benayad, N. (2008). *Les Huiles Essentielles Extraites des Plantes Médicinales Marocaines. Moyen Efficace de Lutte Contre les Ravageurs des Denrées Alimentaires Stockées. Département de Chimie. Faculté des Sciences de Rabat Marroc* 'Essential Oils Extracted from Moroccan Medicinal Plants. Effective Means of Controlling Pests of Stored Foodstuffs'. Rabat, Morocco: Department of Chemistry, Faculty of Sciences of Rabat, Rabat. [in French].

Benouli, D. (2016). *Mémoire pour Master en Control de qualité. Extraction et Identification des Huiles Essentielles. Département de Chimie, Physiques Université d'Oran Algérie* 'Extraction and Identification of Essential Oils'. Master's Dissertation, Department of Physical Chemistry, University of Oran, Oran, Algeria. [in French].

Boshtam, M., Moshataghian, J. and Nederi, G. (2010). Citrus limon burn f. can change affinity of LDL and OX-LDL to their receptors in rabbits with atherogenic diet. *Atheroscier Suppl.*, **11**(2), 145–55.

Choi, G.S., Lee, S., Jeong T S. and Lee, M K. (2004) Evaluation of hesperidin 7-O-lauryl ether as lipid-lowring agent in high-cholesterol-fed rats. *Bioorg. Med. Chem.*, **12**(13), 3599–605. DOI: 10.1016/j.bmc.2004.04.020.

Cirico, T.L. and Omaye, S.T. (2006). Additive of synergetic effects of phenolic compounds on human low-density lipoprotein oxidation. *Food Chem Toxicol*, **44**(4), 510–6.

Costa, R., Russo, M., Degrasia S. and Grasso, E. (2014). Thorough investigation of the oxygen heterocyclic fraction of lime (*Citrus aurantifolia* (Chrism) Swingle) juice. *J. Sep. Sci.*, **37**(7), 792–7. DOI: 10.1002/jssc.201300986.

Dalichaouch Benchaoui, S. and Abadi, N. (2015). Obesity and eating habits among adult population in Constantine. *Int. J. Pharm. Sci.Rev.Res*,

32(2), 9–13.

Favre, L. and Golay, A. (2019). L'évolution nécessaire du traitement de l'obésité 'The necessary evolution of obesity treatment'. *Rev Med Suisse*, **15**(1), 615–16. [in French].

Green, C.O., Wheatley, A.O. and Mcgrowder, D.A. (2013). Citrus peel poly methoxylated flavones extract modulates liver and heart induced function parameters in diet induced hypercholesterolemie rats. *Food Chem Toxical*, **51**(1), 306–9. DOI: 10.1016/j.fct.2012.10.005

Khan, Y., Khan, R.A., Afroz, S. and Sidding, A. (2010). Evaluation of hypolipidemic effect of Citrus limon. *J Bas Appl Sci*, **6**(1), 39–43.

Laissouf, A., Mokhtari Soulimane, N.A. and Merzouk, H. (2014). L'éffet therapeutique de l'huile de lim «*linum usitatissimum*» et l'ypercholesterolémie chez des rats obèses âgés 'The therapeutic effect of linen oil '*linum usitatissimum*' and hypercholesterolemia in obese elderly rats'. *Afrique Science*, **10**(2), 409–18. [in French].

Manish, K. and Mahesh, A. (2013). Evolution of antitubercular activity of methanolic extract of *Citrus Sinensis*. *IJPRR*, **2**(8), 18–22.

Mbundu, M.I., Helbling, C., Favre, L. and Collet, T. (2018). Prise en charge de la dyslipidémie liée à l'obésité: Une approche centrée sur l'alimentation 'Management of obesity-related dyslipidemia: A diet-centered approach'. *Rev Med Suisse*, **14**(599), 627–32. [in French].

Miceli, N., Mondello, M.R. and Monforte, M.T. (2007). Hypolipidemic effects of citrus bergamia Risso and poiteau juice in rats fed a hypercholesterolemic diet. *J. Agric Food Chem*, **55**(26), 10671–7. doi: 10.1021/jf071772i.

Wang, X., Hasegawa, J. and Kitamura, Y. (2011). Effects of heperidin on the progression of hypercholesterolemuia and fatty liver induced by high-cholesterol diet in rats. *J Pharmacol Sci*, **117**(3), 129–38. DOI: 10.1254/jphs.11097fp.

Wilcox, L.J., Borradaile, N.M. and Dreu, L.E. (2001). Secretion of hepatocyte apo B inhibited by the flavonoids naringenin and hesperetin, via reduced activity and expression of ACAT2 and MTP. *J Lipid Res*, **43**(9), 1544–54.

المجلة العلمية لجامعة الملك فيصل
The Scientific Journal of King Faisal University
العلوم الأساسية والتطبيقية
Basic and Applied Sciences

رصد الغطاء النباتي في بيئة السبخات السعودية باستخدام التقنيات الجيومكانية

أماني حسين محمد حسن
قسم الجغرافيا، كلية الآداب، جامعة أسيوط، أسيوط، مصر
قسم الدراسات الاجتماعية، كلية الآداب، جامعة الملك فيصل، الأحساء، السعودية

Vegetation Monitoring in the Saudi Marsh Environment Using Geospatial Technologies

Amani Hussein Mohamed Hassan
Department of Geography, Faculty of Arts, Assiut University, Assiut, Egypt
Department of Social Studies, Faculty of Arts, King Faisal University, Al Ahsa, Saudi Arabia

LINK الرابط	RECEIVED الاستقبال	ACCEPTED القبول	PUBLISHED ONLINE النشر الإلكتروني	ASSIGNED TO AN ISSUE الإحالة لعدد
https://doi.org/10.37575/b/agr/210021	29/03/2021	10/06/2021	10/06/2021	01/12/2021

NO. OF WORDS عدد الكلمات	NO. OF PAGES عدد الصفحات	YEAR سنة العدد	VOLUME رقم المجلد	ISSUE رقم العدد
8093	9	2021	22	2

الملخص

يختلف الغطاء النباتي في بيئة السبخات الملحية عن غيره في البيئات الأخرى من حيث الأنواع، والكثافة، والتردد، وفي هذا البحث تم رصد المجتمعات النباتية في بعض السبخات الساحلية والداخلية بالمنطقة الشرقية بالمملكة العربية السعودية، من خلال نهج تحليلي كمي باستخدام التقنيات الجيومكانية ببرنامجي ArcGIS 10.5 وErdas Imagine، والتحقق الميداني برصد المجتمع النباتي في كل سبخة، بالرؤية، والتصوير من حيث الخصائص الكمية والنوعية، وجمع العينات في أبريل 2019. ومعالجة المرئيات الفضائية واستخراج نموذج الارتفاع الرقمي SRTM DEM بدقة مكانية 30م، والتحليل المعملي ميكانيكيًا وكيميائيًا واستخلاص حيود الأشعة السينية X-Ray لعدد 16 عينة. والتحليل الكارتوجرافي للوحة الطبوغرافية NG39.SW، واللوحة الجيولوجية MG-A108 ببرنامج ArcGIS10.5. وتحليل بيانات الأرصاد الجوية لمحطات القيصومة والدمام والأحساء للفترة 1985- 2018م باستخدام برنامج SPSS، وأظهرت النتائج أن 14 نوعًا من النباتات تتواجد في ستة مجتمعات نباتية بالسبخات الساحلية والداخلية، موزعة في شكل نطاقات محددة حيث تسهم ملوحة التربة بدور بارز في توزيعها، وتتمثل المجتمعات في الهَرْم Zygophyllum Qatarens، والسُّواد Saueda Fruticosa، والخُرَّيز Halopeplis Perfoliata، والعِكْرِش Aeluropus Lagopoides، والخُرَّيْط Salsola Imbricate، والشَّنَان Seidlitzia Rosmarinus، وتوصي الدراسة بضرورة تنظيم عملية الرعي، وزراعة الأنواع المتدهورة، ونشر الوعي البيئي.

ABSTRACT

Vegetation in a salt marsh environment differs from that in other environments in terms of species, density, and frequency. In this research, plant communities in some coastal and inland marshes of the Eastern Province of Saudi Arabia were monitored through a quantitative analytical approach using geospatial techniques, namely ArcGIS 10.5 and Erdas Imagine software. Field verification monitored the plant community in each marsh by vision and imaging with regard to the quantitative and qualitative characteristics. Samples were collected in April 2019 and processed by space visuals, extraction of Shuttle Radar Topography Mission (SRTM) Digital Elevation Model (DEM) with 30m spatial accuracy, analysis of the mechanical and chemical laboratory, and extraction of X-ray beams for 16 samples. The cartographic analysis of the NG39.SW topographic plate and the MG-A108 geological plate and the analysis of meteorological data for Al-Qaysumah, Al-Dammam, and Al-Ahsa stations for the period 1985–2018 was conducted using SPSS. The results showed that 14 plant species were found in six coastal and inland marsh plant communities. They were distributed in the form of specific areas in which soil salinity plays a prominent role in their distribution. These communities were Zygophyllum Qatarens, Saueda Fruticosa, Halopeplis Perfoliata, Aeluropus Lagopoides, Salsola Imbricate, and Seidlitzia Rosmarinus. The study recommends that grazing, the cultivation of degraded species, and environmental awareness should be regulated.

KEYWORDS
الكلمات المفتاحية
Dhabia, plant communities, qualitative characteristics, quantitative characteristics, umm haisha
أم حيشة، الخصائص الكمية، الخصائص النوعية، الضبية، المجتمعات النباتية

CITATION
الإحالة
Hassan, A.H.M. (2021). Rasd alghita' alnabatiu fi bayyat alsabakhat alsewdyt biastikhdam altaqniat aljiumkania 'Vegetation monitoring in the Saudi marsh environment using geospatial technologies'. *The Scientific Journal of King Faisal University: Basic and Applied Sciences*, **22**(2), 38–46. DOI: 10.37575/b/agr/210021 [in Arabic]
حسن، أماني حسين محمد. (2021). رصد الغطاء النباتي في بيئة السبخات السعودية باستخدام التقنيات الجيومكانية. *المجلة العلمية لجامعة الملك فيصل: العلوم الأساسية والتطبيقية*، **22**(2)، 38-46.

1. المقدمة

هناك عديد من العوامل البيئية التي تساعد في انتشار التنوع النباتي، منها درجات الحرارة الملائمة للإنبات والنمو، كما يعد الماء عاملًا مهمًا محددًا من حيث كميته أو كمية الرطوبة الموجودة بالتربة، وتوزيعها على مراحل النمو المختلفة لتلك البيئات (Belskey, 1998; Loreau, 2010)، ويعد الضوء عاملًا بيئيًا مهمًا من حيث شدته وقوته التي تؤثر في عملية البناء الضوئي وبالتالي في الحياة النباتية (Askaril *et al.*, 2006). وتعد الملوحة والإجهاد الملحي من أخطر المشكلات البيئية التي تؤثر في نمو النباتات في البيئات المختلفة (Lopez *et al.*, 2002; Munns and Tester, 2008)، وتتسم النباتات التي تعيش تحت تلك الظروف بصفات خاصة تلائم تلك الظروف (Yang *et al.*, 2012).

تناولت عديد من الدراسات بالمناقشة النبات الطبيعي والضوابط البيئية التي تؤثر فيه، ومنها دراسات Henriques and Hay (1988)، النافع (1999)، القاضي (2003)، العرقوبي (2005)، Jose *et al.* (2011) والقاضي (2012)، ولا سيما دراستي القاضي (2003)، والعرقوبي (2005)، التي صنفت المجتمعات النباتية في المنطقة الشرقية ووادي المياه، وتندرج منطقة الدراسة ضمن النطاق الصحراوي المداري لذا تتصف المنطقة إجمالًا بانخفاض الكثافة النباتية، حيث يبلغ مجموع النباتات الصحراوية في المنطقة الشرقية بنحو 392 نوعًا نباتيًا صحراويًا أكدها Mandaville (1990)، ويزيد العدد إلى نحو 570 نوعًا إذا أخذنا في الاعتبار الأنواع النباتية التي تنمو في الأراضي المهجورة، وتلك التي تم تغيير بيئتها الطبيعية.

2. أهمية البحث

تنحصر الأهمية الأكاديمية للبحث في أنه يتناول مجالًا من المجالات غير المغطاة ضمن البناء النظري، حيث تنمو في بيئة سبخات المنطقة الشرقية مجموعة متميزة من الأنواع النباتية، ولعل من الأهمية العملية والمفيد جدًا أن يتم دراسة الغطاء النباتي ودوره في إحداث التوازن البيئي، ومدى الاستفادة منه في الرعي حيث يعطي ذلك قيمة وأهمية على المستوى القومي.

3. أهداف البحث

الهدف الأساسي من البحث حصر الأنواع والمجتمعات النباتية في سبخات المنطقة الشرقية، وذلك من حيث توزيعها وكثافتها، ويندرج تحته

Corresponding Author: Amani Hussein Mohamed Hassan 00966569343198, dr.amani73@hotmail.com المؤلف المراسل: أماني حسين محمد حسن

الأهداف التالية:

- دراسة الخصائص الكمية للمجتمعات النباتية في سبخات المنطقة الشرقية.
- تحديد الخصائص النوعية للمجتمعات النباتية في سبخات المنطقة الشرقية.
- إبراز أهمية الغطاء النباتي في الجانب النفعي، بخاصة الرعوي في السبخات.

4. منطقة البحث

تقع منطقة الدراسة في الجانب الشرقي من المملكة العربية السعودية، وتمتد فلكيًا بين دائرتي عرض 26° 29' 25" و50° 24' 27" شمالًا، وخطي طول 8" 22' 48° و23° 15' 50° شرقًا، ويحدها من الشمال مدينة الخفجي والأطراف الشمالية لمدينة الجبيل، ومن الشرق الخليج العربي، ومن الجنوب قرية الغويبة، أما في الغرب فتحدها قرية العُليا ومنطقة الرياض (شكل 1)، وتبلغ مساحتها 56166.5كم^2، وتشغل السبخات 404.9165كم^2 منها.

شكل (1): التوزيع المكاني للسبخات المدروسة بالمنطقة الشرقية

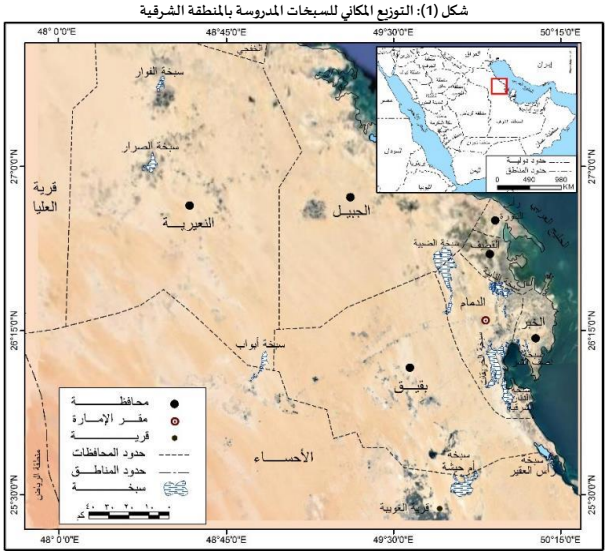

المصدر: وزارة البترول والثروة المعدنية، خرائط طبوغرافية مقياس1: 50000، 1981 باستخدام برنامج ArcGIS 10.5

5. منهجية الدراسة

تعتمد الدراسة على عدة مناهج علمية تتناسب مع طبيعة الدراسة ومراحلها المختلفة، فالمنهج الاستقرائي أُستخدم في العمل الميداني لجمع الجزئيات بغية الوصول إلى الكليات والعموميات، وأُعتمد على المنهج الإقليمي في دراسة كل سبخة بوصفه نمطًا يختلف عما يجاوره بخصائص معينة (التركماني، 2019)، وطبق المنهج الأصولي في دراسة الضوابط الطبيعية المؤثرة في الغطاء النباتي وطبيعته، كما أتبع الأسلوب الوصفي في وصف النباتات، وخصائصها، ومدى ارتباطها، وتأثرها بظروف البيئة المحيطة ومناقشة أثر الأنشطة البشرية في نموها وتوزيعها الجغرافي، وذلك عن طريق التحقق الميداني ورصد المجتمع النباتي في كل سبخة- رؤية وتصوير- من حيث الخصائص الكمية والنوعية، باستخدام أسلوب القياس بعمل مربعات، وتقسيم المربع إلى مربعات ثانوية، مساحة كل مربع 4x4 مترًا (16م^2)، بغاية حساب كثافة النبات، والتغطية، والتردد، والغزارة وفق الطريقة التي اتبعها Assegid and Tesfaye (2011) والنافع (1999)، ثم حُللت البيانات التي تم تجميعها إحصائيًا وبيانات الأرصاد الجوية لمحطات القيصومة والدمام والأحساء للفترة 1985- 2018م باستخدام برنامج SPSS. كما تم اتباع الأسلوب المعملي بتجميع (16) عينة من تربة السبخات وتحليلها ميكانيكيًا وكيميائيًا، واستخلاص حيود الأشعة السينية (X-Ray)، للتعرف على التركيب المعدني، وكذلك معالجة المرئيات الفضائية ببرنامجي ArcGIS 10.5 وErdas Imagine لإنتاج مؤشر اخضرار النبات وتحديد المجتمعات النباتية ومساحتها، واستخراج نموذج الارتفاع الرقمي SRTM DEM بدقة مكانية 30م وأُستخدم أسلوب التحليل الكارتوجرافي للوحة الطبوغرافية NG39.SW، واللوحة الجيولوجية MG-A108 مقياس 1: 50000 ببرنامج ArcGIS 10.5 .

6. المناقشة والتحليل

6.1. الخصائص الطبيعية لبيئة السبخات:

6.1.1. الخصائص الجيولوجية والتضاريس:

تقع منطقة الدراسة ضمن الرصيف العربي في الجزء الشرقي من السعودية، ويتكون من الصخور الرسوبية التي تميل طبقاتها نحو الاتجاه الشمالي الشرقي، وتتدرج في نشأتها من دهر الحياة القديمة غربًا وحتى دهر الحياة الحديثة شرقًا (النافع، 2004)، وقد تكونت صخور المنطقة عبر العصور الجيولوجية المختلفة، حيث يرجع تكوين صخور أم الرؤوس والدمام إلى العصر الأيوسيني، في حين تكونت صخور الهيدروك، واللدام، والهفوف في عصري الميوسين والبليوسين، أما في عصر الزمن الرباعي فتكونت الرمال الريحية، ورواسب السبخات، والرواسب البحرية، بالإضافة إلى الطمي، والرمل، والحصى.

وتنحدر المنطقة الشرقية بصفة عامة من الغرب إلى الشرق (شكل 2)، وتتعدد فيها أشكال السطح، ومنها: سهل الأحساء، وتغطيه الرمال، والكثبان الرملية، وتنتشر فيه السبخات والعيون المائية (النشوان، 2012)، والسهل الساحلي الغربي الذي تنتشر فيه كومات مبعثرة من الرمال تصيدتها الحشائش القصيرة (الوليعي، 2008)، وقد نتج عن ضحالة مياه الخليج العربي انتشار السبخات والمستنقعات والرؤوس الشاطئية مثل رأس العقير (الشريف، 2006)، كما توجد هضبة شدقم وتقع جنوب غرب بقيق وشمال غرب الهفوف (الوليعي، 2008)، أما صحراء الجافورة فتبدو على هيئة حزام ضيق من الرمال والفرشات الرملية وتتخللها السبخات (النافع، 2004)، وتتصف السبخات بالانخفاض والسطح المستوي المغطى بطبقة من الأملاح، والتي تغمر بالمياه في فصل المطر، أما في فصل الجفاف فتغطيها قشرة ملحية (التركماني، 2015)، ومنها: السبخات الساحلية مثل الدنان الشرقية، والعقير في خليج نصف القمر، والسبخات الداخلية مثل الضبية، والنابية، وأم حيشة (الوليعي، 2008).

شكل (2): نموذج الارتفاع الرقمي لسطح منطقة الدراسة

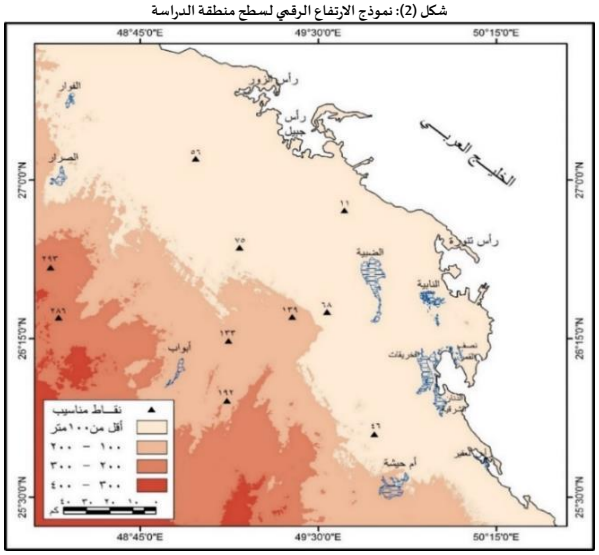

المصدر: وزارة البترول والثروة المعدنية، خريطة طبوغرافية لوحة NG39.SW مقياس 1: 500000، وهيئة المساحة الجيولوجية الأمريكية USGS نموذج الارتفاع الرقمي SRTM، باستخدام برنامج ArcGIS10.5

6.1.2. الخصائص المناخية:

تعد الخصائص المناخية من أهم الضوابط الطبيعية المؤثرة بشكل مباشر في الغطاء النباتي، وأنواعه، وأماكن وجوده، وإمكانية تكاثره، ومن دراسة المعدلات الشهرية والفصلية لدرجات حرارة الهواء بمنطقة الدراسة وتحليلها تبين أن الشتاء يميل إلى البرودة نسبيًا، حيث يتراوح المعدل بين 13.1مْ و16.6مْ، ويتصف الفصل بالمدى الحراري الكبير إذ يبلغ 13.8مْ في الأحساء و11.1مْ في الدمام، أما الصيف فيعد أشد الفصول حرارة وبخاصة نهارًا، حيث يتراوح المعدل بين 35.1مْ و37.1مْ، وتتصف أيضًا بالمدى الحراري الكبير إذ يتراوح بين 14.4مْ و18.0مْ، وتسبب ذلك في زيادة التبخر

من التربة؛ مما يقلل من فاعلية الرطوبة للنبات، بينما يتصف فصلا الربيع والخريف بالتذبذب الحراري، ففي بعض الأيام ترتفع درجات الحرارة بشكل واضح، ولكنها لا تلبث أن تنخفض بشكل سريع نتيجة توزيعات الضغط الجوي التي تؤثر في المنطقة.

وتبين من تحليل اتجاهات الرياح ومعدلات سرعة هبوبها أن الاتجاه السائد للرياح الاتجاه الشمالي بمعدل سرعة 6.9 عقدة في الأحساء، و8.3 عقدة في الدمام، و9.5 عقدة في القيصومة، بينما يسود الاتجاه شمال الشمال الغربي شتاءً بمعدل سرعة 8.2 عقدة في الأحساء، والاتجاه غرب الشمال الغربي في الدمام بنفس معدل السرعة، والاتجاه الشمالي بمعدل سرعة 8.4 عقدة في القيصومة، أما في الربيع فيسود الاتجاه الشمالي بمعدل سرعة 7.3 عقدة في الأحساء، و9.1 عقدة في الدمام، و10.8 عقدة في القيصومة، في حين يسود الاتجاه الشمالي، وشمال الشمال الغربي، وغرب الشمال الغربي خلال فصلي الصيف والخريف بمعدل سرعة تبلغ 7.9 و5.9 عقدة في الأحساء، و8.8 عقدة و7.4عقدة في الدمام، و11.1 و7.7 عقدة في القيصومة على التوالي، ويعزى ذلك إلى سيادة أنظمة الضغط الجوي المرتفع شتاءً، وسيطرة أنظمة الضغط الجوي المنخفض صيفًا، بخاصة منخفض الهند الموسمي، ويترتب على ذلك نقل الرمال وردم السبخات نتيجة زيادة مساحات الفراشات والكثبان الرملية، وينعكس بطبيعة الحال على تناقص مساحة النبات الطبيعي، وتدهوره.

ومن تحليل التبخر تبين ارتفاع معدلات التبخر صيفًا، حيث تبلغ 14 و16 و19مم في الأحساء والدمام والقيصومة على التوالي، ويعزى ذلك إلى جفاف الهواء وارتفاع درجة الحرارة، إلى جانب خلو السطح من النبات الطبيعي، وتنخفض معدلات التبخر لتبلغ أدناها شتاءً إذ تبلغ 9.5مم في الأحساء و9.8مم في الدمام و9مم في القيصومة، ومع حلول الربيع يقل التبخر ويزيد المخزون المائي في التربة، ويسهم ذلك في توافر الاحتياجات المائية للنباتات، ويؤثر التبخر في كمية الرطوبة الجوية حيث يبلغ المعدل السنوي للرطوبة النسبية 37.4% في الأحساء، و52.1% في الدمام، و38.6% في القيصومة، وتتباين المعدلات الفصلية حيث تبلغ 52.7%، و66.7%، و50.7% شتاءً على التوالي، و34.7%، و46.3%، و38% في الربيع على التوالي، وتقل أدناها صيفًا إذ تبلغ 23.3%، و38%، و20% على التوالي، بينما تبلغ في الخريف 39%، و57.7%، و38.6% على التوالي.

ويتصف نظام المطر في منطقة الدراسة بالقلة، والتذبذب الشديد، والتساقط الغزير، وتتباين المتوسطات السنوية والفصلية لكمية المطر، ففي الأحساء تبلغ 87 ملم، بينما يبلغ في الشتاء 43.1 ملم، وفي الربيع 31.1 ملم، وفي الصيف 0.7 ملم، وفي الخريف 12.1 ملم، بينما في الدمام فيبلغ المتوسط السنوي لكمية المطر 103.2 ملم، بينما يبلغ في الشتاء 54.3 ملم، وفي الربيع 25.8 ملم، ويتصف الصيف بانعدام المطر، وفي الخريف 23.1 ملم، أما في القيصومة فيبلغ المتوسط السنوي لكمية المطر 74.9 ملم، بينما يبلغ في الشتاء 37.1 ملم، في الربيع 27.7 ملم، وفي الصيف 0.3ملم، وفي الخريف 10.3 ملم، ويلاحظ أن غالبية المطر في الشتاء والربيع؛ مما يسهم في نمو النبات الحولي، على خلاف انعدامه وجفافه في فترة نقص أو انعدام المطر ، بخاصة صيفًا.

6.1.3. موارد المياه:

تحتوي منطقة الدراسة على نوعين من المياه الجوفية، الأول: المياه الجوفية السطحية، وتتجمع إما عن طريق الجريان السطحي للسيول، أو عن طريق سقوط الأمطار، ويتراوح عمق هذه الطبقات من بضعة أمتار إلى عشرات الأمتار (الطاهر، 1999)، ويستدل على وجودها في المنطقة بانتشار السبخات، وذلك في كل من: واحة الأحساء، والقطيف، وبرين، وبقيق، ووادي المياه، وصحراء الربع الخالي (Twitchell, 1944)، والثاني: المياه الجوفية العميقة، وهي مياه قديمة مختلفة العمق تحملها الطبقات الجيولوجية تحت السطحية مرتبة من الأقدم في الغرب إلى الأحدث في الشرق حسب العمر، وهي تكوينات الوسيع، وأم رضمة، والدمام، والنيوجين (شكل 3)، وتستفيد من مياهها الأحساء ووادي المياه بالمنطقة الشرقية، ومدن الخبر، والدمام، والقطيف (البراك، 1993).

شكل (3): الطبقات الجيولوجية الحاملة للمياه ومو اقع السبخات في منطقة الدراسة

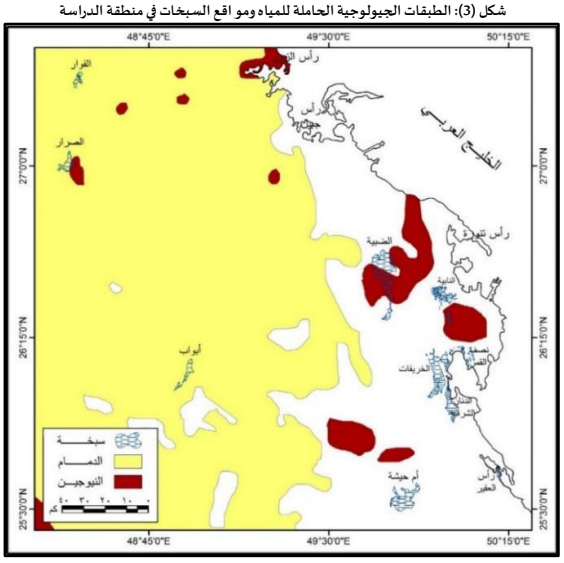

المصدر: وزارة الشئون البلدية والقروية، **2010** باستخدام برنامج **ArcGIS 10.5** بتصرف

6.2. خصائص تربة السبخات:

ترتبط تربة السبخات غالبًا بمواضع منخفضة، وتتلقى مياهًا ورواسب من مواضع أعلى منسوبًا، وترتفع ملوحتها نتيجة ارتفاع منسوب الماء الأرضي حيث تتبخر المياه تاركة الأملاح على السطح في هيئة قشور أو بقع ملحية (التركماني وعطية، 2011)، وفيما يلي عرض لنوعية تربة السبخات وخصائصها الميكانيكية، والكيميائية في منطقة الدراسة:

6.2.1. نوعية التربة:

تبدو مناطق السبخات الداخلية في شكل منخفضات يطوقها خطي كنتور 68 و139 مترًا فوق متوسط منسوب سطح البحر، كما هو الحال في سبخة الفوار والضبية على الترتيب، وتوجد بركة موسمية تشغل أكثر من 40% من مساحة المنخفض (الفوار)، وفي قلبه سبخة في أخفض موضع ويطلق عليه قاع الملح (شكل 4)، أما السبخات الساحلية فغالبًا ما تتصف بتسرب المياه البحرية حيث ينخفض مستوى السهل الساحلي كما في سبخات العقير، والدنان الشرقية، وخليج نصف القمر، والتي لا يزيد ارتفاعها عن 60سم من مستوى منسوب مياه الخليج العربي، وتتصف بانخفاض منسوب القاع ما بين 10- 70سم فوق متوسط منسوب سطح البحر، وبالتالي تتركز الأملاح بشكل واسع في منطقة السبخة.

شكل (4): نموذجا (قاع سبخي الضبية والفوار) لتكوين تربة السبخات الداخلية

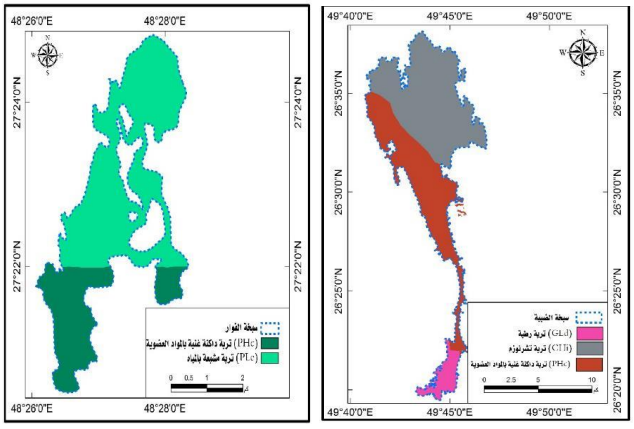

المصدر: اعتمادًا على التحقق الميداني، ولوحات الجبيل والقطيف و أبار الجرثومة والنعيرية مقياس **1: 50000**، باستخدام برنامج**ArcGIS 10.5**

وبناء على دراسة FAO (2012) يتضح أن نسيج رواسب السبخات متشابه، ويتكون من الطمي الرملي، وقد يكون سلتي طمي أو سلتي لومي، كما أن تربة السبخات من نوعية التربة ضعيفة النمو سواء السبخات الداخلية أم

الساحلية، ويصل القطاع العميق منها إلى 100سم حيث مستوى السطح المنخفض.

6.2.2. الخصائص الميكانيكية والكيميائية لتربة السبخات:

من نتائج التحليل المعملي لست عشرة عينة ميكانيكيًا وكيميائيًا تبين أن متوسط نسبة الرمل والسلت والطين تبلغ 83.97%، و7.71%، و8.31% على التوالي، ويدل ذلك على نشاط التعرية الريحية، ولاسيما الترسيب فوق قاع السبخة، وبناء على هذه القيم فإن قوام تربة السبخة يعد قوامًا رمليًا لوميًا أو رمليًا، وأن قيمة pH تتراوح بين 6.6-8.4، أي إنها قلوية وليست حمضية، أما قيمة نسبة كربونات الكالسيوم فإنها تتراوح بين 5.9% و64.8%، بينما تتراوح قيمة المادة العضوية في مكون التربة بين 0.1% و13.0%، والتي تستمد من بقايا النبات الطبيعي والكائنات الأحيائية الدقيقة، كذلك تختلف قيمة العناصر ذات الشحنة الموجبة والعناصر ذات الشحنة السالبة.

ذلك ولوحظ أن قيم عنصر الصوديوم مرتفعة بصفة عامة في السبخات؛ وذلك لتكوين أملاح الصوديوم باتحاده مع عنصر الكلوريد، كما يرجع انخفاض نسبة الماغنسيوم في السبخات الداخلية بمنطقة البحث إلى بُعدها عن البحر، بالإضافة إلى قابلية الماغنسيوم الزائدة للذوبان في الماء، بينما الزيادة في نسبة الكالسيوم تشير إلى أن بيئة الترسيب كانت غنية بالكالسيوم الناتج عن الصخور الجيرية السائدة بالمنطقة، وترجع الزيادة في نسبة البيكربونات إلى قلة ذوبانها في الماء، ويؤدي ذلك إلى تكوين أملاح البيكربونات وتركزها، أما مجموع الأملاح الكلية الذائبة بمياه السبخة فإنها مرتفعة جدًا في العينات التي تم تجميعها، حيث تتراوح بين 10956 و49562 جزء في المليون، وتُعد هذه التركيزات العالية من الأملاح كافية لترسيب الجبس في رواسب السبخات، وذلك نتيجة لقرب منسوب الماء تحت السطح المرتفع الملوحة، والذي يزيد من ملوحته ظهوره على السطح بالخاصة الشعرية، وبخاصة في ظل ظروف التبخر المستمر وتركيز الأملاح، كذلك الحال بالنسبة إلى درجة التوصيل الكهربائي، حيث نجد قيمها عالية للغاية، حيث بلغت أقصى درجاتها إلى 63 ملليموز/سم، وذلك نظرًا للوسط الملحي المناسب للتوصيل الكهربائي.

6.2.3. الخصائص المعدنية لتربة السبخات:

من تحليل سبع عينات من تربة السبخات بواسطة حيود الأشعة السينية (X-Ray)؛ للتعرف على التركيب المعدني، تبين أن المكون الرئيسي لتربات سبخات منطقة الدراسة هو معدن الكوارتزSiO_2، إذ تراوح بين 35.2% و81.3% في العقير والدنان الشرقية على التوالي، وذلك لتعدد مصادر الرمال بها، إذ تقوم الرياح بحمل كميات كبيرة من الرواسب الرملية السافية إلى المواضع الرطبة المنخفضة التي تشغلها السبخة، بالإضافة إلى ذلك تتسبب النباتات الملحية في إعاقة حركة الرياح، وتتسبب في إرساب حمولتها من الرمال، بخاصة أثناء حدوث العواصف الرملية والترابية بالمنطقة الشرقية خصوصًا، كما توجد نسبة قليلة من معدن الجبس $CaSO_4+H_2O$ حيث تراوح بين 3.2% و16.1% في عينتي سبخة الضبية وسبخة خليج نصف القمر على التوالي، حيث يتكون في رواسب السبخة عن طريق ترسيب الأملاح عند التقاء سطح الراسب مع المحلول الملحي؛ نتيجة التبخر الشديد.

وتبين من التحليل وجود نسبة من معدن كلوريد الصوديوم NaCl (الهاليت) في معظم عينات الدراسة، إذ تراوح بين 8.0% و32.13% في خليج نصف القمر وأم حيشة على التوالي، وترجع الزيادة في أم حيشة إلى أن النظام السبخي يتميز بوجود عدة مصادر للمياه، كما تبين وجود معدن كاولينيت (أحد معادن الطين) وتزداد نسبته بزيادة المادة العضوية في الرواسب السبخية والناتجة عن بقايا النبات الطبيعي، حيث بلغت 42.2% في سبخة الفوار، كما تبين وجود معادن أخرى في شكل شوائب بالعينات، ومنها: السلت، والطين، والانهيدريت.

6.3. أنماط الغطاء النباتي في منطقة الدراسة:

أسهمت الظروف البيئية السائدة بالمنطقة الشرقية في ظهور غطاء نباتي ذى ميزات خاصة في هذه السبخات، ويمكن تقسيم النباتات الطبيعية في منطقة الدراسة تبعًا لدورة حياتها إلى ما يلي:

6.3.1. النباتات الحولية:

وتتصف بأنها نباتات سريعة الزوال تنبثق بإرادتها وتتم نموها الخضري سريعًا خلال الموسم المطير الذي تزداد فيه الموارد المائية، وتتناقص فيه معدلات النتح والتبخر نظرًا لانخفاض درجات الحرارة، بالإضافة إلى ارتفاع الرطوبة النسبية، ومن أبرز الأعشاب والحشائش الحولية التي تنمو في منطقة الدراسة: الرَّبْلة، والصَّمْعَاء، والسَعْدان، والثُرْيَة، والقَفْعاء، والنَفَل، غُرْيْراء، ومن أهم خصائصها من الناحية المورفولوجية صغر الحجم، وقلة عمق مجموعها الجذري، حيث تمتص الرطوبة من طبقات لا يزيد عمقها عن 30سم، ذلك على الرغم من انتشارها أفقيًا لتغطي أكبر مساحة من التربة (البتانوني، 1986).

ويعد فصلا الشتاء والربيع الموسمين المفضلين لنمو الحشائش والأعشاب الحولية، إذ يزهر عديد منها خلال الفترة الممتدة بين فبراير- أبريل؛ وذلك بسبب ارتفاع القيمة الفعلية للأمطار خلالهما، لذلك يُلاحظ زيادة في معدل نمو النباتات الطبيعية بشكل عام والحولية على وجه الخصوص مع الوصول المبكر للمنخفضات الجوية، فإذا ما سقطت الأمطار في وقت مبكر (أكتوبر أو نوفمبر أو ديسمبر) فإن ذلك يساعد في نمو النباتات الحولية بغزارة خلال أسابيع معدودة، أما إذا تأخر موسم المطر إلى يناير، فإن الموسم البارد يؤخر نمو النباتات، حتى يحل فصل الربيع الأكثر دفئًا (Mandaville, 1990).

6.3.2. النباتات المعمرة:

يوصف هذا النمط من النباتات بأنها نباتات صحراوية جفافية Xerophytes، حيث تستطيع مواصلة حياتها الخضرية خلال فصلي الأمطار والجفاف، وهذا يعني أنها تتعرض لظروف مناخية قاسية أثناء فصل الجفاف، من نقص في الموارد المائية والغذائية المتاحة، وارتفاع في درجات الحرارة ومعدلات التبخر، والتي تزيد من فقدان الماء خلال عملية النتح؛ لذا تنتهج النباتات المعمرة طرقًا متباينة تختلف باختلاف أنواعها لتظل محافظة على توازنها المائي، وتبقى في حالة تسمح باستمرار حياتها تحت ظروف الجفاف، ومن أهم الحشائش المعمرة المنتشرة في منطقة الدراسة: العَنْدَب، والسَّبْط، والنَصِيّ، والعِكْرِش، والثُمَام، والسَّخْبَر، أما أهم الجُنَيْبَات التي تنمو في المنطقة فتتمثل في العَلْقَى، والقَيْصُوم، والخُرَّيز، والشَّيح، وتشمل النباتات الظاهرة الجَنْبَات مثل: الرَّمْث، والعَرْفَج، والحَاذ، والعَاذِر، كما تضم كذلك الأشجار، ومنها الأرْطَى، والغَضَى، والسَّلَم، والسَّدْر.

6.4. التحليل الكمي للغطاءالنباتي بمنطقة الدراسة:

تبين من المرئيات الفضائية والمسح الميداني لمواقع جمع العينات النباتية، بغية التحقق من نوعها من جهة والتعرف على خصائصها من جهة أخرى، وجود ستة مجتمعات نباتية (شكل 5)، تمثلت في الهَرْم *Zygophyllum qatarens* بنسبة 40.13% من مساحة منطقة الدراسة، والسُّواد *Saueda fruticosa* 22.44%، والخُرَّيز *Halopeplis perfoliata* 17.7%، والعِكْرِش *Aeluropus lagopoides* 8.16%، والخُرَّيْط *Salsola imbricate* 4.86%، أما الشَّنَان *Seidlitzia rosmarinus* فقد بلغت نسبته 0.85%، يرافقهم الرمث، والثمام، ونباتات أخرى بنسبة 5.86% من مساحة منطقة الدراسة، وفيما يلي توضيح الخصائص الكمية لهذه المجتمعات:

6.4.1. مجتمع الهَرْم Zygophyllum qatarensa Community

الهَرْمه عبارة عن جَنْبَة ذات أفرع كثيفة قائمة، وهي تنتمي للفصيلة الرطريطية، ويتراوح ارتفاعها بين 32 و76سم، وقد يصل إلى المتر إذا كانت الظروف البيئية مناسبة لها، وأغصانها عصارية ملساء السطح أسطوانية الشكل يميل لونها إلى الأخضر الداكن، وأحيانًا إلى الأصفر الباهت، أما أوراقها فهي عصارية يميل لونها إلى الأخضر الفاتح (Western, 1989). ويعد هذا المجتمع من أهم المجتمعات النباتية الملحية المنتشرة انتشارًا واسعًا في المنطقة الشرقية، وبخاصة في الأراضي الملحية المسطحة ذات الترب الرملية الناعمة، ومما يميز نبات الهَرْم قدرته الكبيرة على تجميع التربة الرملية الناعمة حوله مكونًا كومات صغيرة، ويتركز نمو هذا المجتمع في منطقة شاطئ العزيزية في منطقة الدمام، والخبر، وحول خليج نصف القمر، ورأس أبو أريقط، وأيضًا حول كل من العقير، والنعيرية، والظهران، ورحيمة،

والهفوف، وبعض المواقع المتفرقة من الأحساء (Mandaville, 1990 ;الدوسري، 1999)، وينمو في هذا المجتمع بعد تساقط الأمطار بعض من الحشائش الحولية أهمها القَرْمَل، والشِرْشِر (العودات وآخرون، 1997).

جدول (1): التحليل الكمي للخصائص النباتية لمجتمع الهَرْم في بعض سبخات المنطقة الشرقية

الانواع	التردد%	الكثافة م^2	التغطية المطلقة %	التغطية النسبية %
الهَرْم	45.81	0.82	31.8	91.64
الرمث	13.7	0.16	2.3	6.63
الرمرام	6.55	0.09	0.6	1.73
المجموع	66.06	1.07	34.7	100

المصدر: المسح الميداني في أبريل 2019، وحساب المعادلات اعتمادًا على النافع (1999)

ومن التحليل الكمي للخصائص النباتية لمجتمع الهَرْم في منطقة الدراسة (جدول 1) تبين أن ارتفاع أفراد النبات يمثل مؤشرًا على ملاءمة الظروف البيئية لنموها، وتكاثرها، وحيويتها، وقوتها، ففي هذه البيئة الملحية بسبخات منطقة الدراسة تعيش النباتات المعمرة في حالة جيدة، حيث يتراوح ارتفاع الهَرْم بين 28 و 69سم، والرمث بين 5 و 36 سم والرمرام بين 4 و 10سم، وكان متوسط ارتفاع أفرادها و47.4 و14.2 و5.7سم على التوالي، ويتوزع نبات الهَرْم في البيئة السبخية بشكل منتظم وثابت، حيث تبلغ نسبة تردده 45.81%، مما يعني تجانس انتشاره في هذا المجتمع، ويرافقه الرمث بنسبة تردد بلغت 13.7%، والرمرام 6.55% من مجموع المربعات المعاينة؛ لأن نموه يتركز في أماكن محددة.

تتصف الكثافة النباتية المطلقة بانخفاضها نسبيًا، حيث بلغت 1.07 نبتة/م^2، ويرجع ذلك لانخفاض خصوبة التربة، ويمثل الهَرْم النوع الأكثر وفرة في منطقة الدراسة، إذ بلغت كثافته 0.82 نبتة/م^2، في حين يُعد الرمث والرمرام نباتات نادرة الوفرة في هذا المجتمع، إذ بلغت كثافتها 0.16 و0.09 نبتة/م^2 على التوالي، ومن تحليل التغطية النباتية المطلقة تبين ارتفاعه، حيث بلغت 34.7%، وذلك بسبب كبر حجم الأنواع وتكتلها، إذ بلغت تغطية الهَرْم 31.8%، في حين أسهم الرمث والرمرام بتغطية ضئيلة تتراوح بين 2.3 و 0.6% على التوالي، ويعزى ذلك إلى قلة كثافتها وترددها مقارنة بالهرم.

شكل (5): المجتمعات النباتية في بيئة السبخات بالمنطقة الشرقية

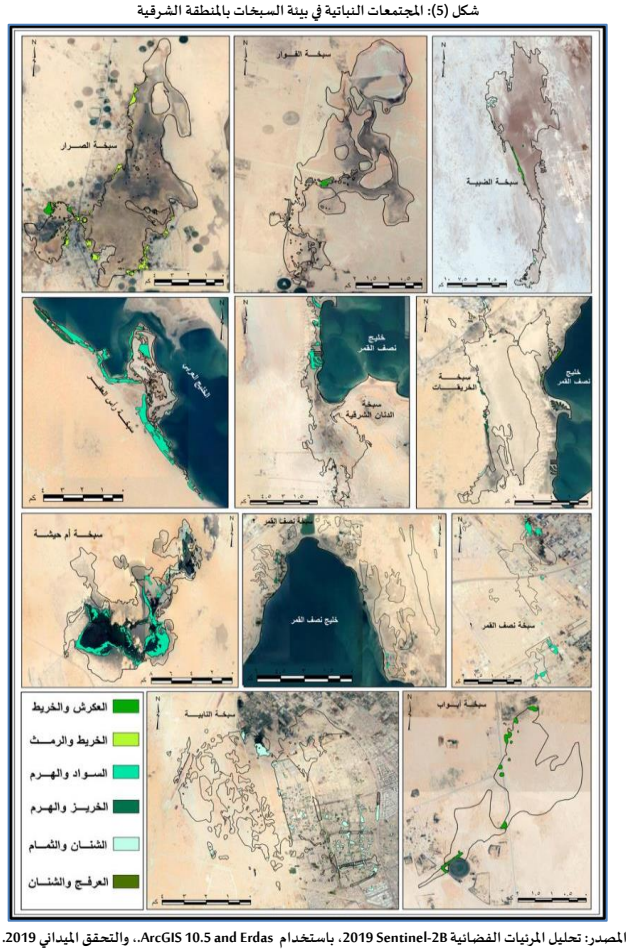

المصدر: تحليل المرئيات الفضائية Sentinel-2B 2019، باستخدام ArcGIS 10.5 and Erdas.، والتحقق الميداني 2019.

6.4.2. مجتمع السُّواد Saueda fruticosa Community

يعد السواد من أنواع الحمض، وهو من الفصيلة السرمقية (Mandaville, 1990)، وتختص نباتات السُّواد بطبيعة تلائم المحتوى الملحي العالي في التربة (شكل 5 و 6)، حيث تتصف بأنها من النباتات العصرية غير الحقيقية، حيث تكتسب صفتها العصيرية من تجمع الأملاح في أنسجتها، وتستطيع التغلب على تركز محلول التربة عن طريق رفع تركيز عصيرها الخلوي، وذلك بزيادة ضغطها الأسموزي بدرجة كبيرة، تكفي للتغلب على مقاومة محلول التربة للامتصاص، حتى ولو كانت درجة التركيز عالية نسبيًا في المستنقعات الملحية والسبخات (الدوسري، 1999).

ومن التحليل الكمي للخصائص النباتية لمجتمع السُّواد في منطقة الدراسة (جدول 2) تبين أن النباتات في بيئة السبخات تتصف بانخفاض معدلات نمو أفرادها، حيث بلغ متوسط ارتفاع أفراد نبات السُّواد بين 23.3 و 51.7 سم، ومن جانب آخر لوحظ عليها بعض مظاهر الذبول والجفاف، نتيجة شدة ملوحة التربة، وانخفاض خصوبتها.

جدول (2): التحليل الكمي للخصائص النباتية لمجتمع السُّواد في بعض سبخات المنطقة الشرقية

الانواع	التردد%	الكثافة م^2	التغطية المطلقة %	التغطية النسبية %
السَّواد	57.22	0.85	52.9	61.51
الشَنان	26.18	0.45	24.2	28.14
الخَرَيْط	12.31	0.11	1.2	1.40
القطف	4.15	0.08	7.7	8.95
المجموع	99.86	1.49	86.0	100

المصدر: المسح الميداني في أبريل 2019، وحساب المعادلات اعتمادًا على النافع (1999)

ويعد نبات السُّواد من أكثر الأنواع انتشارًا في السبخات، حيث وجد في جميع المربعات التي قسمت ميدانيًا بنسبة تردد بلغت 57.22%، ويصاحبه أربعة أنواع أخرى معمرة بنسبب تردد متفاوتة حسب ملاءمة ظروف بيئة السبخات لنموه، إذ تراوحت نسبة ترددها بين 4.15 و 26.18%، حسب قدرتها على تحمل الملوحة المرتفعة.

كما تتصف الكثافة النباتية الكلية في سبخات منطقة الدراسة بالوسطية حيث بلغت 1.49 نبتة/م^2، ويعزى ذلك إلى وقوع هذا المجتمع النباتي في بيئة نائية محمية نسبيًا يصعب الوصول إليها؛ مما جعلها بعيدة عن تأثير التدخلات البشرية، ويعد السُّواد أكثر الأنواع النباتية وفرةً، حيثُ بلغت كثافته 0.85 نبتة/م^2، يليه الشنان بكثافة 0.45 نبتة/م^2، وتتوزع الأفراد داخل هذا المجتمع بشكل عشوائي شبه منتظم، ومن تحليل التغطية النباتية المطلقة تبين ارتفاعها، بسبب شدة ملوحة التربة وارتفاع منسوب المياه الجوفية، حيث بلغت 86.0%، ويلاحظ أن السُّواد هو النوع الأكثر سيادة في هذا المجتمع، إذ بلغت تغطيته المطلقة 52.9%، يليه الشَّنَان 24.2%، بينما كانت التغطية منخفضة لباقي الأنواع، وذلك لقلة ترددها، وانخفاض كثافتها.

6.4.3. مجتمع الخُرَّيْز Halopeplis Perfoliata Community

تعد الخُرَّيْزة جُنَيْبَة من الفصيلة السرمقية *Chenopodiaceae*، وهي شجيرة معمرة صغيرة متفرعة عصارية يبلغ طولها 50 سم، يأخذ الساق شكل الخرز المنظوم، وتنتشر في السبخات القريبة جدًا من ساحل البحر في المنطقة الشرقية، كما في منطقتي الدمام والعقير (الدوسري، 2017)، ويرجع ذلك إلى قرب المياه الجوفية من سطح الأرض؛ مما يجعل تربها الرملية الخشنة رطبة دائمًا، ولكنها غير مشبعة، كما تتصف تربتها باحتوائها على تركيز مرتفع من الأملاح، نظرًا لارتفاع منسوب المياه الجوفية المالحة، وارتفاع معدلات التبخر (العودات وآخرون، 1997)، وعادة ما يصبح الخُرَّيز النبات السائد، نظرًا لقدرته الكبيرة على تحمل الملوحة المرتفعة في التربة (شكل 6)، وقد يرافقه أحيانًا نبات العِكْرِش *Aeluropus lagopoides*.

ومن التحليل الكمي للخصائص النباتية لمجتمع الخُرَّيْز في منطقة الدراسة (جدول 3) تبين أن حالة نمو أفراد الخُرَّيْز جيدة، حيث يتراوح ارتفاعها بين 6 و55سم بمتوسط بلغ 53.03سم لجميع الأفراد، والعكرش بين 8 و53سم، أما النخيل البري فتراوح ارتفاعه بين 120 و320 سم، بينما تراوح ارتفاع العقربان 15و25سم، ويعد نبات الخُرَّيْز من أكثر الأنواع النباتية إذ وجد في جميع المربعات المعاينة (16م^2) بنسبة تردد بلغت 42.86%، ويرافقه أربعة أنواع أخرى معمرة بنسب تردد متفاوتة حسب ملاءمة ظروف بيئة السبخات لنموها، حيث بلغت نسبة ترددها بين 21.34، و28.57%.

جدول (3): التحليل الكمي للخصائص النباتية لمجتمع الخُرَّيز في بعض سبخات المنطقة الشرقية

الانواع	التردد%	الكثافة م^{2}	التغطية المطلقة %	التغطية النسبية %
الخرّيز	42.86	0.67	39.3	86.76
العكرش	28.57	0.30	4.7	10.37
النخيل البري	21.43	0.16	1.0	2.21
العقربان	21.34	0.08	0.3	0.66
المجموع	114.2	1.21	45.3	100

المصدر: المسح الميداني في أبريل 2019، وحساب المعادلات اعتمادًا على النافع (1999)

تمتاز الكثافة النباتية الكلية لمجتمع الخُرَّيز في سبخات منطقة الدراسة بارتفاعها، إذ بلغت 1.21 نبتة/م^{2}، ويتوزع أفراد الخُرَّيز بشكل عشوائي وشبه منتظم، حيث بلغت المسافة بين كل مفردة وأخرى نحو 1-1.5 م، وتأخذ في التباعد كلما اقتربت من الأماكن شديدة الملوحة، ويعد الخريز أكثر الأنواع النباتية وفرة حيث بلغت كثافته 0.67 نبتة/م^{2}، ويليه العكرش بكثافة 0.30 نبتة/م^{2}، أما التغطية النباتية المطلقة Canopy فظهرت بشكل مرتفع، حيث بلغت 45.3% بسبب شدة ملوحة التربة وارتفاع منسوب الماء الأرضي، ويعود ذلك إلى كبر حجم الأنواع نسبيًا وتكتلها، ويلاحظ كذلك أن الخريز هو النوع الأكثر سيادة إذ بلغت تغطيته المطلقة 39.3%، ويليه العكرش 4.7%، بينما كانت التغطية منخفضة لباقي الأنواع نتيجة قلة ترددها، وتناقص كثافتها.

شكل (6): المجتمعات النباتية في سبخات خليج نصف القمر والفوار والصرار وأم حيشة والعقير

مجتمع الخُرَّيز في سبخة خليج نصف القمر

مجتمع الخُرَّيط في سبخة الفوار

مجتمع الشُّنان في سبخة الصرار

مجتمع السُّواد في سبخة أم حيشة

مجتمع العكرش في سبخة الصرار

رعي الابل في سبخة بالعقير

المصدر: تصوير الباحثة خلال الدراسة الميدانية في أبريل 2019

6.4.4. مجتمع العكْرش Aeluropus lagopoides Community

العِكْرِشة من حشائش الفصيلة النجيلية، يبلغ ارتفاعها حوالي 15 سم، ذات فروع كثيفة ومتشابكة، والأوراق متباعدة رمحية الشكل ذات لون أخضر مغبَّر، ومغطاة بشعر قصير ناعم، أما الأزهار فتظهر مجتمعة في نهاية الفروع على هيئة عناقيد زهرية صغيرة بيضاوية إلى مستطيلة الشكل (Migahid, 1996)، وتعد المسطحات الطينية المالحة المنتشرة على طول شواطئ الخليج العربي من أفضل البيئات لنمو وتكاثره، هذا المجتمع (Mandaville, 1990)، بالإضافة إلى المناطق الرطبة حول السبخات شرق الصرار (شكل 5 و6)، ووادي المياه (الدوسري، 2017).

ومن التحليل الكمي للخصائص النباتية لمجتمع السُّواد في منطقة الدراسة (جدول 4) تبين أن النباتات في بيئة السبخات تتصف بحالة نمو جيدة؛ وذلك لانخفاض قيمته الاقتصادية في عملية الرعي، حيث يتراوح ارتفاعه بين 6 و14 سم بمتوسط ارتفاع 15.3 سم، بينما يتراوح ارتفاع الهرم 11 و62 سم بمتوسط ارتفاع 30.56 سم، في حين يتراوح ارتفاع الرطريط بين 13 و18 سم بمتوسط ارتفاع 17 سم، ويلاحظ على بعض الأفراد الاصفرار والذبول والجفاف؛ لانخفاض خصوبة التربة.

جدول (4): التحليل الكمي للخصائص النباتية لمجتمع العكْرش في بعض سبخات المنطقة الشرقية

الانواع	التردد%	الكثافة م^{2}	التغطية المطلقة %	التغطية النسبية %
العكرش	26.32	2.7	17.9	82.87
الهرم	21.05	0.7	2.3	10.65
الرطريط	5.26	0.6	1.4	6.48
المجموع	52.63	4	21.6	100

المصدر: المسح الميداني في أبريل 2019، وحساب المعادلات اعتمادًا على النافع (1999)

يتوزع نبات العِكْرِش في بيئة السبخات بشكل ثابت ومنتظم، حيث بلغت نسبة تردده 26.32% من المربعات المعاينة (16م^{2})، ويرافقه الهرم والرطريط بتردد 21.05% و5.26% على التوالي، وتمتاز الكثافة النباتية الكلية في سبخات منطقة الدراسة بارتفاعها، إذ بلغت 4 نبتة/م^{2}، ويتوزع أفراد العِكْرِش بشكل عشوائي وشبه منتظم، ويعد العِكْرِش أكثر الأنواع النباتية وفرة فيها، حيث بلغت كثافته 2.7 نبتة/م^{2}، يليه الهرم بكثافة 0.7 نبتة/م^{2}. ومن تحليل التغطية النباتية المطلقة تبين ارتفاعه، حيث بلغت نسبته 21.6%، نتيجة شدة ملوحة التربة وارتفاع منسوب المياه الجوفية، ولوحظ أن العِكْرِش النوع الأكثر سيادة في هذا المجتمع إذ بلغت تغطيته المطلقة 17.9%، يليه الهرم 2.3%، بينما كانت التغطية منخفضة للرطريط.

6.4.5. مجتمع الخُرَّيْط Salsola imbricate Community

تنبت الخُرَّيْطة في المناطق السهلية حول السبخات في وادي المياه، وغرب النعيرية، ويبلغ طولها عادة نحو متر واحد (الدوسري، 2017)، وتندرج تبعًا لتصنيف Raunkaier ضمن النباتات الظاهرة، ومن المسح الميداني لوحظ تباين ارتفاع الخُرَّيْطة في المنطقة الشرقية بشكل واضح من مكان إلى آخر، تبعًا للظروف البيئية المناسبة لنموها حيث تتصف بصغر حجمها، إذ يتراوح ارتفاعها بين 10- 40 سم في السبخات والرمال الساحلية الجافة، في حين تصبح أكبر حجمًا فوق الفرشات الرملية، حيث يتجاوز ارتفاعها في الغالب 50 سم (Western, 1989)، والخُرَّيْط من الأنواع النباتية المحبة للملوحة ذات المدى البيئي شبه الواسع المنتشر في منطقة الدراسة؛ لقدرتها على تحمل جميع الظروف الصحراوية القاسية، وتنمو بشكل جيد في السبخات الداخلية ذات مستوى الماء الأرضي المرتفع، وزيادة نسبة الملوحة (شكل 6).

ومن التحليل الكمي للخصائص النباتية لمجتمع الخُرَّيْط في منطقة الدراسة (جدول 5) تبين أن النباتات في بيئة السبخات صغيرة الحجم ومتقزمة، إذ بلغ متوسط ارتفاع أفراد الخريط والثليث 18.8 و11.7سم على التوالي، حيث تراوح ارتفاع الخريط بين 7.9 و41.2سم، وارتفاع الثليث بين 5 و22سم، مما يدل على عدم ملاءمة البيئة الملحية لنمو النباتات الطبيعية وازدهارها، وتتوزع نباتات مجتمع الخُرَّيْط بشكل منتظم وثابت في هذه البيئة الملحية، حيث بلغت نسبة تردد الخريط 52.5%، ونسبة الثليث 30.3% من جميع المربعات المعاينة (16م^{2})، ويرجع ذلك إلى قدرته على تحمل الملوحة والجفاف.

جدول (5) التحليل الكمي للخصائص النباتية لمجتمع الخُرَّيط في بعض سبخات المنطقة الشرقية

الانواع	التردد%	الكثافة م^{2}	التغطية المطلقة %	التغطية النسبية %
الخرّيط	52.2	1.8	17.4	57.05
الثليث	30.3	1.04	9.3	30.49
الشوّع	4.15	0.04	3.8	12.46
المجموع	86.65	2.88	30.5	100

المصدر: المسح الميداني في أبريل 2019، وحساب المعادلات اعتمادًا على النافع (1999)

تمتاز الكثافة النباتية الكلية لمجتمع الخُرَّيْط في سبخات منطقة الدراسة بارتفاعها، إذ بلغت 2.9 نبتة/م^{2}، ويرجع ذلك إلى صغر حجم الأفراد في البيئة الملحية، كما أن بعض الأفراد في طور النمو، ويمثل الخريط أكثر الأنواع النباتية وفرة حيث بلغت كثافته 1.8 نبتة/م^{2}، يليه الثليث بكثافة 1.04 نبتة/م^{2}، وتنخفض التغطية النباتية الكلية لمجتمع الخُرَّيْط في سبخات منطقة الدراسة حيث بلغت 30.5%، ويعزى ذلك إلى شدة الملوحة وانخفاض خصوبة التربة، بالإضافة إلى عمليات إزالة النباتات لأغراض التنمية، ويمثل الخريط النوع الأكثر سيادة في هذا المجتمع، إذ بلغت تغطيته 17.4%، يلية الثليث بنسبة 9.3% من المربعات المعاينة (16م^{2}).

6.4.6. مجتمع الشَّنَان Seidlitzia rosmarinus Community

تعد شجيرة الشَّنَانة من مجتمعات النباتات الملحية المعمرة، حيث تنتشر كثيرًا في منطقة الدراسة بشواطئ الخليج العربي وحول بعض المسطحات الملحية، مثل: سبخة النعيرية، بالإضافة إلى السبخات المنتشرة جنوبي بقيق (Mandaville, 1990)، وسبختي أم حيشة والصرار (شكل 5 و6).

جدول (6): التحليل الكمي للخصائص النباتية لمجتمع الشُّنَان في بعض سبخات المنطقة الشرقية

الانواع	التردد%	الكثافة م^{2}	التغطية المطلقة %	التغطية النسبية %
الشنان	33.3	0.28	31.35	79.91
البرم	26.7	0.14	5.4	13.77
العكرش	13.3	0.15	1.59	4.05
السواد	6.7	0.13	0.89	2.27
المجموع	80	0.7	39.23	100

المصدر: المسح الميداني في أبريل 2019، وحساب المعادلات اعتمادًا على النافع (1999)

ومن التحليل الكمي للخصائص النباتية لمجتمع الشُّنَان في منطقة الدراسة (جدول 6) تبين أن النباتات في بيئة السبخات تتصف بحالة نمو جيدة؛ وذلك لانخفاض قيمته الاقتصادية في عملية الرعي، ويتراوح ارتفاع الشُّنَان بين 16 و57سم بمتوسط 29.04سم، بينما يبلغ ارتفاع البرم 10 و70سم بمتوسط 28.48سم، في حين يتراوح ارتفاع العكرش 12 و68سم بمتوسط ارتفاع 26.5سم، ويُلاحظ على بعض الأفراد الاصفرار والذبول والجفاف نتيجة؛ لانخفاض خصوبة التربة، وتبلغ نسبة تردد نبات الشُّنَان في بيئة السبخات 33.3% من المربعات المعاينة، ويرافقه البرم والعكرش بتردد 26.7% و 13.3% على التوالي، في حين يقل تردد السواد بنسبة 6.7% بوصفها نباتات مصاحبة.

تتصف الكثافة النباتية الكلية في سبخات منطقة الدراسة بالوسطية، إذ بلغت 0.7 نبتة/م^{2}، وتتوزع أفراد الشُّنَان بشكل عشوائي وشبه منتظم، فقد بلغت المسافة بين فرد وآخر من مفردات النبات نحو متر ومتر ونصف، وتأخذ في التباعد كلما اقتربت من الأماكن شديدة الملوحة، ويعد الشنان أكثر الأنواع النباتية وفرة فيها، حيث بلغت كثافته 0.28 نبتة/م^{2}، ويليه العكرش بكثافه 0.15 نبتة/م^{2}، ومن تحليل التغطية النباتية المطلقة تبين ارتفاعها بشكل ملحوظ، حيث تبلغ 39.23%، ويعزى ذلك إلى شدة ملوحة التربة، وارتفاع منسوب المياه الجوفي، وينعكس ذلك على النبتة من خلال كبر حجم الأنواع نسبيًا وتكتلها، كما لوحظ أن الشُّنَان هو النوع الأكثر سيادة في هذا المجتمع، حيث بلغت تغطيته المطلقة 31.35%، يليه البرم 5.4%، بينما كانت التغطية منخفضة لباقي الأنواع؛ لقلة ترددها، وانخفاض كثافتها.

ومن الأهمية بمكان الإشارة إلى أنه تم المراجعة الميدانية لنتائج التحليل القائم على معالجة المرئيات الفضائية من نوع *Sentinel-2B* لعام 2019 مقياس1: 50000، باستخدام برنامجي *ArcGIS 10.5 and Erdas Imagine*، من حيث الخصائص الكمية والنوعية للمجتمعات النباتية، سواء أكانت المساحات أم الأنواع أم الكثافة، أم التردد والتغطية المطلقة والنسبية، وتم التحقق الميداني من النتائج برصد المجتمعات النباتية على مستوى كل سبخة وذلك في أبريل 2019.

6.5. الخصائص النوعية للغطاء النباتي بمنطقة الدراسة:

يمكن تحديد النمط السائد للغطاء النباتي طبقًا لعدة عوامل بيئية مختلفة، أهمها تنوعها الحيوي، ومدى النمو والانتشار لبعض الأنواع النباتية، أو تلك التي يطلق عليها المؤشرات الحيوية أو البيولوجية لظروف المنطقة وطبيعتها (Yang *et al.,* 2011)، وفيما يلي عرض لأهم الخصائص النوعية للمجتمعات النباتية في منطقة الدراسة:

- يتميز مجتمع الخُرَّيْز في منطقة الدراسة ببساطته وقلة تنوعه النباتي، حيث لوحظ خلال المسح الميداني نمو جنيبات الخريز، والعكرش، والعجرم، والنخيل البري، وحشائش العقربان في المناطق المنخفضة من السبخات، بخاصة عند زيادة تركز الأملاح الذائبة في التربة.
- يتصف مجتمع الخُرَّيْط في منطقة الدراسة بالفقر والبساطة، وقلة تنوعه النباتي، حيث لوحظ خلال المسح الميداني نوعين معمرين، هما: الخُرَّيْط والثُّلَيت، بالإضافة إلى الخُرَّيْزة والشُوْع، وكلها من الأنواع العصارية، ذات العصير الخلوي الذي يزداد تركيزه بامتصاص الأملاح من التربة في الأوراق أو الساق أو كليهما معًا خلال المواسم المطيرة؛ لتستهلكه في المواسم الجافة، وذلك بوصفه استراتيجية للتكيف مع ظروف البيئة الملحية القاسية التي تتصف به المنطقة.
- يظهر مجتمع الشُّنَان في شكل بسيط متجانس قليل التنوع، حيث يرافقه أربعة أنواع نباتية معمرة فقط في سبخات منطقة الدراسة، وهي: الهَرْم، والعِكْرِش، والسُّواد، والرَّمْث، والتي تعد من نباتات البيئات الملحية.
- يبرز التكوين النباتي لمجتمع السُّواد ببساطته وقلة أنواعه، حيث تم تسجيل أربعة أنواع ملحية معمرة، هي: جَنْبَات السُّواد، والشَّنَان، والخُرَّيْط، والقَطف، والأخيرة تمثل نباتات مصاحبة، وتنمو نتيجة اختلاف درجة ملوحة التربة على شكل نطاقات متدرجة، فتظهر على أطراف السبخة. وقد تزداد درجة الملوحة نتيجة لتدرج انخفاض سطح الأرض إلى حد لا يستطيع أي من النباتات الزهرية أن تنمو فيه، لذا تبقى هذه التربة خالية من النباتات، وعادة ما تكون في منتصف السبخة الداخلية أو في قلبها، أما في السبخة الساحلية فتكون على أطرافها وهوامشها.
- يختص مجتمع العِكْرِش بالبساطة، حيث إن النباتات المصاحبة له قليلة وغير ممثلة بصورة جيدة، إذ غالبًا ما يكون العِكْرِش النبات السائد في مجتمعه، بالإضافة إلى بعض النباتات المعمرة مثل الهَرْم والرَّطْرِيط (البتانوني، 1986).
- يعد الهَرْم من النباتات العصيرية سريعة النبت بعد سقوط المطر، حتى لو كانت كمية المطر قليلة، وتبقى خضراء مزهرة في الصيف (الدوسري، 1999)، ويتصف تكوينه بالبساطة والتجانس، وهو من النباتات غير المستساغة، الذي لا تقبل عليه الحيوانات، إلا إن الإبل قد تضطر إليه أحيانًا لاسيما خلال الصيف، وينمو في منطقة الدراسة نتيجة قدرته الكبيرة على تحمل مختلف الظروف الصحراوية الجافة والملحية ومقاومتها، وغالبًا ما يصاحبه نباتات الرَمْرام والرمث.

6.6. الأهمية الرعوية للنبات الطبيعي في سبخات منطقة الدراسة:

يمثل الرعي وتربية الماشية أبرز الأنشطة الاقتصادية في منطقة الدراسة، وعليه تمثل المراعي الطبيعية المورد العلفي الطبيعي والمتجدد الذي يعتمد عليه في توفير الاحتياجات الغذائية؛ لتنمية الثروة الحيوانية، وزيادة إنتاجها بتكلفة اقتصادية قليلة جدًا، مقارنة بالأعلاف المنتجة بالزراعة. وإلى جانب ذلك تسهم المراعي الطبيعة في المحافظة على التوازن البيئي، وحماية البيئة من التعرية والانجراف، وزيادة خصوبتها، وحفظ مياه الأمطار، وزيادة المخزون الأرضي منها، والمحافظة على الأصول الوراثية للأنواع النباتية، وحمايتها من الانقراض (محمد ومحل، 2015).

وبناءً على الدراسة الميدانية تبين اختلاف السبخات فيما بينها من حيث العدد، والنوع، والمساحة للنباتات الصالحة للرعي، فبعضها يحتوي على أربعة أنواع صالحة للرعي، كما هو الحال في سبخات الخريقات، والضبية، والعقير بمساحات تغطية تبلغ 0.76 و3.29 و3.7كم^{2} على التوالي، ومن تلك الأنواع الخريط، والشنان، والرمث، والرمرام، الصالحة لرعي الإبل، والغنم (شكل 6).

وتوجد بعض السبخات التي تحتوي على ثلاثة أنواع صالحة للرعي كما هو الحال في سبخات خليج نصف القمر والفوار والنابية وأم حيشة، بمساحة تغطية بلغت 0.45 و0.69 و1.8 و19.44كم^{2} على التوالي، وتمثلت في نباتات العكرش، والثليث، والقطف، وهي تصلح لرعي الغنم ،والإبل، والحمير.

كما توجد سبخات تحتوي على نوعين من الأنواع الصالحة للرعي، وتتوافر في سبخة الصرار والدنان الشرقية، بمساحة 0.83 و0.97كم^{2}، وتتمثل تلك الأنواع في نبات الخريز، والرطريط، وتصلح لرعي الغنم، بينما تواجدت في أغلب السبخات أنواع غير مستساغة للرعي، وهي البرم والسواد.

7. الاستنتاجات والتوصيات

من خلال المناقشة والتحليل القائم على استخدام التقنيات الجيومكانية والتحقق الميداني تبين أن وجود المجتمعات النباتية، وتوزيعها، وتنوعها في سبخات المنطقة الشرقية ما هو إلا انعكاس لتباين الظروف الطبيعية السائدة، وأنماط التفاعل النباتي، التي من أهمها: الخصائص التضاريسية والمناخية، وموارد المياه، والخصائص البيدولوجية لبيئة السبخات، وذلك لما يترتب عليها من وجود بيئات مختلفة للنمو النباتي، كما أن للتدخلات البشرية أيضًا أثرًا في تغير الغطاء النباتي السائد.

تمثلت أهم المجتمعات النباتية في بيئة السبخات في الهَرْم *Zygophyllum qatarens* بنسبة 40.13% من مساحة منطقة الدراسة، والسُّواد *Saueda fruticosa* 22.44%، والخُرَّيز *Halopeplis perfoliata* 17.7%، والعِكْرِش *Aeluropus lagopoides* 8.16%، والخُرَّيْط *Salsola imbricate* 4.86%، أما الشَّنَان *Seidlitzia rosmarinus* فقد بلغت نسبته 0.85%،

يرافقهم الرمث، والثمام، ونباتات أخرى بنسبة 5.86% من مساحة منطقة الدراسة، وكان العكرش أكبر المجتمعات كثافةً حيث بلغ 2.7 نبتة/كم^2، يليه الخريط 1.8 نبتة/كم^2، بينما كان السواد أكثر المجتمعات ترددًا بنسبة بلغت 57.14%، يليه الخريط 52.2%، أما عن التغطية النباتية فكانت نسبتها الأعلى لنبات السواد، وبلغت 52.9%، ويليه الخريز 39.3% من المربعات المعاينة.

يُعد الغطاء النباتي في منطقة الدراسة غطاءًا فقيرًا، يتصف بالتباين في الكثافة من سبخة إلى أخرى حيث تكاد تنعدم في بعض السبخات مثل: سبخة أبواب، بينما توجد بكثرة في السبخات الساحلية مثل: سبخة خليج نصف القمر، كما لوحظ التوزيع غير المنتظم على مستوى السبخة الواحدة، حيث تنتشر النباتات بكثافة متفاوتة كما هو الحال في سبخة أم حيشة، بالإضافة إلى اختلاف المجتمعات النباتية، فأحيانًا تقتصر السيادة على نوع واحد كما في سبخة النابية، أو يوجد أكثر من نوع في السبخة نفسها، كما هو في سبخة الخريقات.

وبصفة عامة تتصف بعض المجتمعات النباتية في منطقة الدراسة بالبساطة والتجانس، والبعض الآخر بالفقر وقلة التنوع، وعليه يتباين الغطاء النباتي في بيئة السبخات من حيث العدد، والنوع، والمساحة الصالحة للرعي، حيث تحتوي كل سبخة على نوعين إلى أربعة أنواع صالحة لرعي الإبل والغنم، بمساحات تتراوح بين 0.45 و19.44كم^2، منها: الخريط، والشنان، والعكرش، والرمث، والرمرام.

وختامًا توصي الدراسة الجهات المعنية بضرورة تقييم الموارد الطبيعية في نطاقات الغطاء النباتي، واتخاذ الإجراءات اللازمة لتطويرها واستغلالها بشكل جيد، ومنها الآتي:

- إعداد خرائط تفصيلية للتربة، وما تحتويه من نباتات طبيعية باستخدام التقنيات الجيومكانية، بهدف التعرف على خصائصها، وتصنيفها، وجدارتها الإنتاجية.
- متابعة تدهور الغطاء النباتي، من خلال مقارنة المرئيات الفضائية في فترات مختلفة بشكل دوري.
- إعادة زراعة النباتات المنقرضة أو المهددة بالانقراض في موطنها الأصلي، مثل: الشنان والرمث.
- وقف الزراعات في مناطق الغطاء النباتي، وتوجيه هذه الزراعات نحو المناطق المخصصة للزراعة، والمناسبة من حيث المناخ والظروف.
- نشر الوعي البيئي وإبراز الأهمية البيئية، والاقتصادية، والطبية للغطاء النباتي، والأضرار المترتبة على تدهوره.

نبذة عن المؤلفين

أماني حسين محمد حسن

قسم الجغرافيا، كلية الآداب، جامعة أسيوط، أسيوط، مصر، dr.amani73@hotmail.com، 00966569343198

د. حسن، مصرية، أستاذ مشارك، دكتوراه من جامعة أسيوط، مصر، وتعمل حاليًا بجامعة الملك فيصل، تتمحور اهتماماتها البحثية في مجال البيئة، والتصحر، والتنمية البيئية، وتقييم الأثر البيئي، نشرت 12 بحثًا في مجلات علمية محكمة، وبعضها في مجلات مصنفة في ISI و Scoups؛ وشاركت في عدد من المشاريع البحثية، والمؤتمرات العلمية داخل مصر وخارجها، وعضو في عديد من الجمعيات العلمية المتخصصة في الجغرافيا بمصر والكويت؛ أشرفت على عديد من رسائل الماجستير والدكتوراه في مصر والسعودية، وقامت بمناقشة عديد من الرسائل العلمية، وعضو وحدة البيئة بوكالة جامعة الملك فيصل للدراسات العليا والبحث العلمي.

أوركيد (ORCID): 0000-0002-0677-9938.

الموقع الشخصي: https://environmentgeography.wordpress.com

المراجع

البتانوني، كمال الدين حسن. (1986). *البيئة وحياة النبات في دولة قطر*. الدوحة، قطر: جامعة الدوحة.

البراك، سعد عبد الله. (1993). *خصائص أراضي الأحساء الزراعية*. الأحساء، السعودية: مطابع الحسيني.

التركماني، جودة فتحي. (2015). *جغرافية الأراضي الجافة والتصحر*. الطبعة السادسة. القاهرة، مصر: دار الثقافة العربية.

التركماني، جودة فتحي. (2019). *أصول البحث الجغرافي: النظرية والتطبيق*. القاهرة، مصر: دار الثقافة العربية.

التركماني، جودة فتحي. وعطية، شربات بشندي. (2019). *جغرافية التربة وتطبيقاتها- دراسة معاصرة*. القاهرة، مصر: دار الثقافة العربية.

الدوسري، حميد مبارك. (1999). *النبات البري في المنطقة الشرقية المملكة العربية السعودية: دراسات ميدانية وبحوث لغوية*. الدمام، السعودية: وزارة الإعلام.

الدوسري، حميد مبارك. (2017). *النبات البري في المنطقة الشرقية المملكة العربية السعودية: دراسات ميدانية وبحوث لغوية*. الطبعة الثالثة. الدمام، السعودية: وزارة الإعلام.

الشريف، عبد الرحمن الصادق. (2006). *جغرافية المملكة العربية السعودية*. الطبعة الثالثة. الرياض، السعودية: دار المريخ.

الطاهر، عبد الله أحمد. (1999). *الأحساء: دراسة جغرافية*. الرياض، السعودية: مكتبة الملك فهد الوطنية.

العودات، محمد عبدو، عبد الله، عبدالسلام محمود والشيخ، عبدالله محمد. (1997). *الجغرافية النباتية*. الطبعة الثانية. الرياض، السعودية: عمادة شؤون المكتبات، جامعة الملك سعود.

القاضي، إيمان عبد الله. (2003). *أثر المناخ في الغطاء النباتي الطبيعي بالمنطقة الشرقية من المملكة العربية السعودية (دراسة في المناخ التطبيقي)*. رسالة ماجستير، جامعة الدمام، الدمام، السعودية.

القاضي، إيمان عبد الله. (2012). أثر المناشط البشرية في الغطاء النباتي الطبيعي وسبل المحافظة عليه بالبيئة الساحلية في شرقي المملكة العربية السعودية-دراسة في حماية البيئة. *رسائل جغرافية*، **بدون رقم مجلد**(376)، 1-112.

محمد، سهام كامل ومحل، محمد عبد الرحمن. (2015). *المراعي الطبيعية وأهميتها الاقتصادية*. عمان، الأردن: دار أمنة.

النافع، عبد اللطيف حمود. (1995). *النبات الطبيعي والجغرافيا الحيوية للبحار الرملية في وسط وشمال المملكة العربية السعودية*. الرياض، السعودية: مكتبة الملك فهد الوطنية.

النافع، عبد اللطيف حمود. (1999). طرق المسح الحقلي للمجتمعات النباتية في المناطق الصحراوية الجافة. في: *الندوة الجغرافية الثانية*، جامعة دمشق، دمشق، سوريا، 27–1999/04/29.

النافع، عبد اللطيف حمود. (2004). *الجغرافيا النباتية للمملكة العربية السعودية*. الرياض، السعودية: مطابع نجوم المعارف.

النشوان، عبد الرحمن عبد العزيز. (2012). *جغرافية المملكة العربية السعودية*. الرياض، السعودية: مكتبة الملك فهد الوطنية.

الهيئة العامة للأرصاد وحماية البيئة. (1985-2018). *بيانات مناخية*. متوفرة بموقع: https://www.pme.gov.sa/ (تاريخ الاسترجاع: 2020/02/14).

هيئة المساحة الجيولوجية الأمريكية USGS. (2020). *نموذج الارتفاع الرقمي SRTM والمرئيات الفضائية Sentinel-2B 2019*، متوفر بموقع: https://www.usgs.gov/ (تاريخ الاسترجاع: 2020/05/18).

وزارة الاقتصاد والتخطيط. (2010). *نتائج التعداد الأولية للتعداد العام للسكان والمساكن لأعوام 1974، 1993، 2004، و2010*. الرياض، السعودية: مصلحة الإحصاءات العامة.

وزارة البترول والثروة المعدنية. (1981). *خرائط طبوغرافية 1: 50000، اللوحات: عريعرة 5-39 NG والجبيل 6-39 NG وآبار صفيان11-4925 وأم حيشة 12-4925 وآبار الجرمانية 13-4926 وغرب الدمام 21-4926 وبئر غونان22-4926 والعزيزية 33-5026 والدمام 34-5026 ورأس العقير 43-5025 ورأس قرية 44-4550*. الرياض، السعودية: إدارة المساحة الجوية.

وزارة البترول والثروة المعدنية. (1984). *خريطة طبوغرافية لوحة NG39.SW مقياس1: 500000*. الرياض، السعودية: إدارة المساحة الجوية.

وزارة الشؤون البلدية والقروية. (2010). *الأوضاع الراهنة لحاضرة الأحساء*. التقرير الثاني، الجزء العاشر، الدمام، السعودية: أمانة المنطقة الشرقية.

الوليعي، عبد الله بن ناصر. (2008). *جيومورفولوجية المملكة العربية السعودية*. الطبعة السادسة. الرياض، السعودية: مكتبة الملك فهد الوطنية.

Al Awdat, M.A., Abdullah, A.M. and Elsheikh, A.M. (1997). *Aljughrafiat Alnibatiatu* 'Plant Geography'. 3rd edition. Riyadh, Saudi Arabia: Library Affairs Deanship, King Saud University. [in Arabic]

Al Barrak, S.A. (1993*). Khasayis Aradi Al-Ahsa Alziraeia* 'Characteristics of Al-Ahsa Agricultural Lands'. Riyadh, Saudi Arabia: Al-Husseini Press. [in Arabic]

Al Batanouni, K.H. (1986). *Albiya and Haya Alnabaatya fi Dawlat Qatar* 'Environment and Plant Life in the State of Qatar'. Doha, Qatar: Doha University. [in Arabic]

Al Dossary, H.M. (1999). *Alnbat Albariyi fi Almintaqat Alsharqiat Almamlakat Alearabiat Alsewdyt: Dirasat Maydaniat and Bihawth lighawiati* 'Wild Plant in Eastern Saudi Arabia: Survey Studies and Language Research'. Damam, Saudi Arabia: Ministry of Information. [in Arabic]

Al Dossary, H.M. (2017). *Alnbat Albariyi fi Almintaqat Alsharqiat Almamlakat Alearabiat Alsewdyt: Dirasat Maydaniat and Bihawth lighawiati* 'Wild Plant in Eastern Saudi Arabia: Survey Studies and Language Research'. 3rd edition. Damam, Saudi Arabia: Ministry of Information. [in Arabic]

Al Nafeh, A.H. (1995). *Alnabat Altabieiu and Aljughrafia Alhayawiat Lilbihar*

Lawhat NG39.SW 1: 500000 'Topographic Map of NG39.SW 1: 500000'. Riyadh, Saudi Arabia: Air Area Management. [in Arabic]

Muhammad, S.K. and Mahal, M.A. (2015). *Almaraei Altabieiat and Ahamiyatuha Alaiqtisadiat* Natural Pastures and their Economic Importance'. Amman, Jordan: Safe House. [in Arabic]

Munns, R. and Tester, M. (2008). Mechanisms of salinity tolerance. *Annul. Rev. Plant Biol.,* **59**(n/a), 651–81.

Twitchell, K.S. (1944). Water resources of Saudi Arabia. *Geographical Review*, **34**(3), 365–86.

US Geological Survey. (2020). *Namudhaj Alairtifae Alraqamiu SRTM and Almaryiyaat Alfadayiyat Sentinel-2B 2019* Digital Height Model SRTM And the Sentinel-2B 2019'. Available at: https://www.usgs.gov/(accessed on 18/05/2020) [in Arabic]

Western, A.R. (1989). *The Flora of the United Arab Emirates: An Introduction*. United Arab Emirates: United Arab Emirates University.

Yang, G., Zhou, R., Tang, T., Chen, X., Ouyang, J., He, L., Li, W., Chen, S., Guo, M., Li, X., Zhong, C. and Shi, S. (2011). Gene expression profiles in response to salt Stress in Hibiscus Tiliaceus. *Plant Mol. Bio. Rep,* **29**(3), 609–17.

Zhang, H.J., Dong, H.Z., Li, W.J. and Zhang, D.M. (2012). Effect of soil salinity and plant density on yield and leaf senescence of field-grown cotton. *Journal of Agronomy and Crop Science,* **198**(1), 27–37.

Alramliat fi Wasat and Shamal Almamlakat Alearabiat Alsaeudiati 'Natural Vegetation and the Biogeography of Sandy Seas in Central and Northern Saudi Arabia'. Riyadh, Saudi Arabia: King Fahd National Library. [in Arabic]

Al Nafeh, A.H. (1999). Turuq almasahu alhaqliu lilmujtamaeat alnabatiat fi almanatiq alsahrawiat aljafa 'Field survey methods for plant communities in dry desert areas'. In: *Second Geographical Symposium*, University of Damascus, Damascus, Syria, 27–29/04/1999. [in Arabic]

Al Nafeh, A.H. (2004). *Aljughrafia Alnabatiat Lilmamlakat Alearabiat Alsaeudiati* 'The Plant Geography of Saudi Arabia'. Riyadh, Saudi Arabia: Knowledge Star Prints. [in Arabic]

Al Nushwan, A.A. (2012). *Jughrafiat Almamlakat Alearabiat Alsaeudiatu* 'Geography of Saudi Arabia'. Riyadh, Saudi Arabia: King Fahd National Library. [in Arabic]

Al Qadi, E.A. (2003). *Athar Almunakh fi Alghita Alnabatii Altabieii bi Almintaqat Alsharqiat min Almamlakat Alearabiat Alsaeudia (Drrasat fi Almunakh Alttbyqy)* Impact of Climate on Natural Vegetation in Eastern Saudi Arabia, Applied Climate Study'. MSc. Thesis, Al Damam University, Dammam, Saudi Arabia. [in Arabic]

Al Qadi, E.A. (2012). Athar almanashit albashariat fi alghita alnabatii altabieii and subul almuhafazat ealayh bi albayyat alssahiliat fi aharqii almamlakat alearabiat alsaeudiati-dirasat fi himayat albayyati 'Impact of human activities on natural vegetation cover and ways of conserving it on the coastal environment in the Eastern Province of Saudi Arabia -Study on environmental protection'. *Geographical Messages*, **n/a**(376), 1–112. [in Arabic]

Al Sharif, A. A. (2006). *Jughrafiat Almamlakat Alearabiat Alsaeudiat* 'Geography of Saudi Arabia'. 3rd Edition. Riyadh, Saudi Arabia: Mars House. [in Arabic]

Al Taahir, A.A. (1999). *Al-Ahsa - Dirasat Jughrafi* 'Al-Ahsa- Geographical Study'. Riyadh, Saudi Arabia: King Fahd National Library. [in Arabic]

Al Turkomani, J.F. (2015). *Jughrafiat Al-Aradi Aljafa and Altashur* 'Geography of Drylands and Desertification'. 6th edition. Cairo, Egypt: Arab Culture House. [in Arabic]

Al Turkomani, J.F. (2019). *Asul Albahth Aljghrafy: Alnazariat and Altatbiq* 'Geographic Search Assets: Theory and Practice'. Cairo, Egypt: Arab Culture House. [in Arabic]

Al Turkomani, J.F. and Attia, S.B. (2019). *Jughrafiat Alturbat and Tatbiqatiha-Dirasat Mueasirat* 'Soil Geography and Application- A Contemporary Study'. Cairo, Egypt: Arab Culture House. [in Arabic]

Al Walei, A.N. (2008). *Jiumurfulujiat Almamlakat Alearabiat Alsaeudiata* 'Geomorphology of the Kingdom of Saudi Arabia'. 6th edition. Riyadh, Saudi Arabia: King Fahd National Library. [in Arabic]

Askaril, H., Edqvist, J., Hajheidari, M., Kafi, M. and Salekdeh, G.H. (2006). Effects of salinity levels on proteome of *Suaeda aegyptiaca* leaves. *Proteomics,* **6**(8), 2542–54.

Assegid, A. and Tesfaye, A. (2010). Wild edible trees and shrubs in the semi-arid lowlands of Southern Ethiopia. *Journal of Science and Development,* **1**(1), 5–19.

Belskey, A.S. (1998). *The Management of Ziziphus Spina Christi as a Component of Integrated Farming System in Wadi Hadhramaut-Yemen.* MSc. Thesis, University of Khartoum, Khartoum, Sudan.

FAO. (2012). *Harmonized World Soil Database* (version 1.2). Rome: FAO.

Lopez, C.M., Takahashi, H. and Yamazaki, S. (2002). Plant-water relations of kidney bean plants treated with NaCl and foliarly applied glycinebetaine. *Journal of Agronomy and Crop Science,* **188**(2), 73–80.

Loreau, M. (2010). Linking biodiversity and ecosystems: Towards a unifying ecological theory. *Phil. Trans. Res. Soc. Bull.*, **365**(1537), 49–60.

Mandaville, J.P. (1990). *Flora of Eastern Saudi Arabia.* London: Kegan Paul Int., Jointly with the National Commission for Wildlife Conservation and Development: Riyadh, Saudi Arabia.

Migahid, A.M. (1996). *Flora of Saudi Arabia.* 4th Edition. Riyadh, Saudi Arabia: Ministry of Agricultural and Water of Saudi Arabia.

Ministry of Economy and Planning. (2010). *Natayij Altaedad Al-Awaliat Liltaedad Aleami Lilsakan and Almasakin Liaewam 1974, 1993, 2004 and 2010.* Results of the Preliminary Census of the General Population and Housing Census for the Years 1974, 1993, 2004 and 2010'. Riyadh, Saudi Arabia: Department of Public Statistics. [in Arabic]

Ministry of Municipal Affairs. (2010). *Al-Awdae Alrrahinat Lihadirat Al-Ahsa* 'The Current Conditions of the Metropolis of Al-Ahsa'. Second Report, Ten Part. Dammam, Saudi Arabia: Eastern Province Municipality. [in Arabic]

Ministry of Petroleum and Mineral Resources. (1984). *Kharitat Tabughirafiat*

The Scientific Journal of King Faisal University

Basic and Applied Sciences

Synthesis and Characterisation of Structural and Electrical Properties of CuMn2O4 Spinel Compound

Rasha Yousef [1], Alaa Nassif [2], Abla Al-Zoubi [1] and Nasser Saad Al-Din [1]

[1] Department of Physics, Faculty of Science, Al-Baath University, Homs, Syria
[2] Faculty of Engineering, Al-Wataniya Private University, Hama, Syria

LINK	RECEIVED	ACCEPTED	PUBLISHED ONLINE	ASSIGNED TO AN ISSUE
https://doi.org/10.37575/b/sci/210028	14/04/2021	08/07/2021	08/07/2021	01/12/2021

NO. OF WORDS	NO. OF PAGES	YEAR	VOLUME	ISSUE
2931	4	2021	22	2

ABSTRACT

CuMn2O4 was synthesized by the solid-state method. MnO2 and CuO were used as precursors. The optimum temperature of synthesis was 850°C. XRD results showed that the prepared compound had a cubic structure with Fd3 m space group. The lattice constant and unit cell volume were a=8.359Å and V=584.14A°3 respectively. The grain size was calculated by the Debye-Scherrer method and was 33.49 nm for CuMn2O4 annealed at 850°C. The experimental density was calculated and compared to the theoretical density. The results were ρt= 5.399 gr/cm^3 and ρE = 5.24 gr/cm^3. The electrical properties of the compound showed that it behaves like a semiconductor, and the activation energy of the compound was 0.1535 eV.

KEYWORDS

Activation energy, copper manganite (CuMO), mixed oxide, solid-state reaction, spinel

CITATION

Yousef, R., Nassif, A., Al-Zoubi, A. and Al-Din, N.S. (2021). Synthesis and characterization of structural and electrical properties of CuMn2o4 spinel compound. *The Scientific Journal of King Faisal University: Basic and Applied Sciences*, **22**(2), 47–50. DOI: 10.37575/b/sci/210028

1. Introduction

Spinels are a member of a large group of materials. They are mixed oxides with the general formula AB_2X_4, where X = O, A and B are cations with oxidation states 2 and 3, respectively. The parent spinel is $MgAl_2O_4$. Oxide ions form a ccp structure. Mg^{+2} and Al^{+3} cations are located in tetrahedral and octahedral sites, respectively. Many oxides and sulphides have the spinel structure that gives its name to the family of compounds that share the same structural arrangement. Consequently, we will use the word spinel to refer to any material of general formula AB_2X_4, which crystallizes in a cubic crystal system with space group $Fd\bar{3}m$. In this structure, shown in Figure 1(a) the X anions (oxide anions) are arranged in a cubic close packed structure, whereas the cations A and B occupy tetrahedral (1/8, 1/8, 1/8) and octahedral (1/2, 1/2, 1/2) sites, respectively.

Figure 1: (a) Schematic view of the spinel structure with octahedral (blue) and tetrahedral units (yellow). (b) The unit cell of spinel structure of $CuMn_2O_4$ (West, 2014)

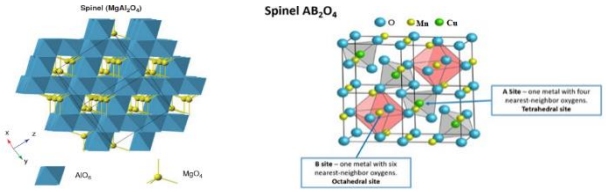

The unit cell of $CuMn_2O_4$ spinel is shown in Figure 1(b). It is a transition metal manganite with the formula MMn_2O_4 (M=Cu, Ni, Zn, Ca or others), and can be described as a cubic close packed structure (Errandonea *et al.*, 2010). The unit cell contains 32 anions forming 64 tetrahedral sites and 32 octahedral sites. Eight tetrahedral and 16 octahedral sites are occupied by cations.

These materials have attracted much attention due to their wide uses in many applications. The spinel $CuMn_2O_4$ has been studied since it has unique electrical, magnetic, thermoelectric and catalyst properties. $CuMn_2O_4$ compound can be applied as an oxidation catalyst for removing air pollutants, such as monoxide and nitrous oxide from exhaust gas, and for destroying volatile organic compounds (VOCs) (Deraz and Abd-Elkader, 2013; Trapp *et al.*, 2017; Sobhani-Nasab *et al.*, 2020).

The spinel materials can be prepared by many methods, such as solid-state method (Waskowska *et al.*, 2001), co-precipitation (George and Sugunan, 2008), citrate-nitrate gel combustion (Barros *et al.*, 2001), sol-gel (Habibi and Fakhri, 2016; Enhessari *et al.*, 2016; Zhang *et al.*, 2020) and hydrothermal processes (Durrani *et al.*, 2012). Out of these methods, the solid-state method was selected because it is the simplest and most common way of preparing solids. High temperatures are generally required, typically between 500 and 2000°C, and thermally unstable MnO_2 returns to Mn_2O_3 at temperatures above 500°C. As a result, this method was selected. During heating above 500°C, the oxidation number of manganese turned from +4 to +3 and MnO_2 to Mn_2O_3 (Berbenni *et al.*, 2006; Shaheen and Selim, 1998).

In this study, $CuMn_2O_4$ was synthesized by the solid-state method. The structural properties were studied using X-ray diffraction and the electrical properties were also studied.

2. Materials and Methods

2.1. Starting Chemicals and Sample Preparation

The $CuMn_2O_4$ high purity (99.99%) powder was prepared by the solid-state method. The two oxides, CuO (99.99%, M/s Sigma Aldrich. Ltd) and MnO_2 (99.99%, M/s Avonchem UK), were used as a precursor. Suitable amounts of these powders in the cation ratio Cu:Mn=1:1 were weighed, then mixed and ground in a pestle mortar. After this, Acetone was added for 15 minutes to form a homogeneous mixture. The grinding process was repeated three times for each sample. The resulting mixture was then dried by heating it to 100°C for a period of time to remove moisture. The powder was then pressed (5000 Kg/cm^2) into pellets 1cm in diameter and 2mm in thickness, to bring the interacting particles closer together and to increase the possibility of interaction between the particles (West, 2014). The weights of the starting materials that were used to form the $CuMn_2O_4$ system were calculated by the following equation:

$$CuO + Mn_2O_3 \xrightarrow{>500°C} CuMn_2O_4 \qquad (1)$$

Corresponding Author: Alaa Nassif 00963988460098, alaa.nassif@wpu.edu.sy

Then, the pellets were placed in a porcelain crucible and heated at 850 ℃ for 6 hours in air. Table 1 shows the weights of the raw materials used and calculated in accordance with the previous equation. Weights required were calculated on the basis that the desired amount equal to 10gr.

Table 1: Weights, supplier's names, and the purity of raw materials used to synthesize $CuMn_2O_4$

Cu:Mn	1:1	
name oxide	MnO_2	CuO
oxide mass (gr)	5.276421	4.848849
supplier's name	M/s Avonchem UK	M/s Sigma Aldrich. Ltd.
purity	99.99%	99.99%

2.2. Experimental Techniques

- X-ray Diffraction (XRD): The crystal structure of the final products were characterised using X-ray powder diffraction (XRD, Philips-PW-1840 with Cu-Kα radiation source λ=1.5406A°). X-ray diffraction (XRD) is one of the primary techniques used to characterise materials (Smart and Moore, 2006). XRD can provide some information about crystalline structure in a sample even when the crystallite size is too small for single crystal X-ray diffraction, including the purity of the substance, phase transitions, lattice constants and presence of foreign atoms in crystal lattice.
- Electrical Resistance Circuit: The samples were heated in the air at a temperature range of 295–667 °K to study their electrical behaviour, using the electrical circuit shown in figure 2. The sample was prepared for electrical measurements by pressing it into pellets 1cm in diameter and 2mm in thickness. Then Ag metal electrodes were deposited on its surface.

Figure 2: Electrical resistance circuit as a function of temperature

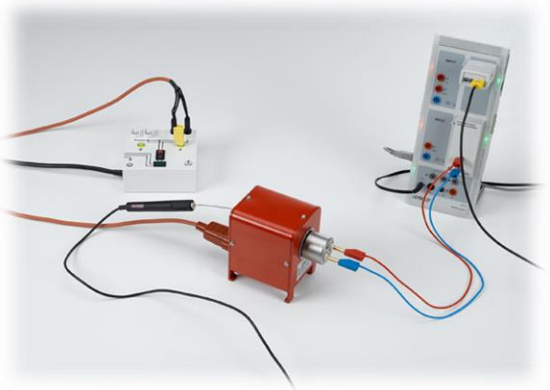

3. Results and Discussion

3.1. Compositional and Structural Characterisations

XRD patterns of the sample at different annealing temperatures were carried out. Figure 3 shows the XRD patterns of $CuMn_2O_4$, which were annealed at 750°C, 850°C, and 950°C for 6 hours.

Figure 3: X-ray diffraction patterns of the samples annealed at different temperatures

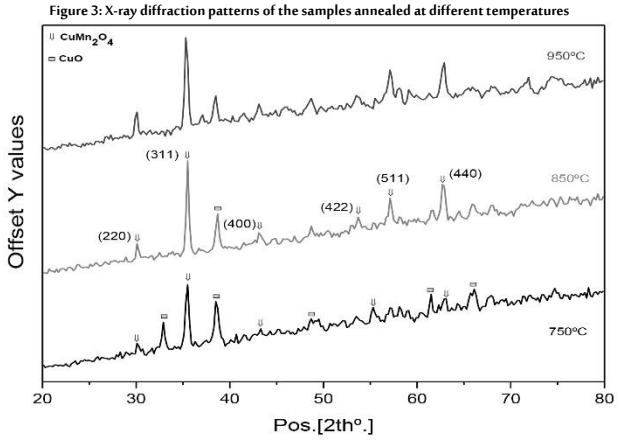

All the diffraction peaks are indexed and are compared with the standard JCPDS data (JCPDS No.34-1400 card).

It was found from Figure 3, for the sample annealed at 850°C, that all the diffraction peaks were attributed to the $CuMn_2O_4$ compound, and one peak was related to copper oxide. This indicates that the optimum temperature synthesis of $CuMn_2O_4$ compound is 850°C. The $CuMn_2O_4$ compound is polycrystalline with a cubic structure.

For the cubic system, the d-spacing is related to the lattice parameters by the following equation:

$$\frac{1}{d^2} = \frac{h^2 + k^2 + l^2}{a^2} \qquad (2)$$

Table 2 shows diffraction angles, inter planar distances and Miller indexes that were calculated from XRD pattern.

Table 2: Diffraction angles, inter planar distances and Muller indexes

$2\theta°$	$\theta°$	I%	$d_{exp}(A°)$	$d_{card}(A°)$	hk
220	2.944	2.963	19.6	15.07	30.140
311	2.510	2.526	100	17.755	35.510
400	2.084	2.088	7.7	21.65	43.300
422	1.700	1.702	7.2	26.9075	53.815
511	1.603	1.608	17.3	28.625	57.250
440	1.473	1.477	24	31.44	62.880
a=8.359 $A°$					

The basic unit cell volume was calculated using the relation: V = a^3. The flask density method (picknometer) was used to measure the experimental density ρ_t of the prepared material (Agnew *et al.*, 2003). Depending on the material's density, the number of formulae in a single crystalline cell Z was calculated by the following equation:

$$\rho = \frac{MZ}{N_a V} \qquad (3)$$

where M is the molecular weight of the material, N the avogadro number and V the basic unit cell volume $(cm)^3$. Thus it was found that:

$$Z = \frac{N_a.V.\rho}{M} = 8.008$$

By using rounding, it was found that Z = 8 (Waskowska *et al.*, 2001), and therefore the general formula for the content of the basic unit cell can be written as follows: $Cu_8Mn_{16}O_{32}$. The obtained results were presented in Table 3.

Table 3: Lattice constant, basic cell size, Z and density.

a (A) lattice constant	V $(A°)^3$ basic cell size	ρ_t (gr/cm^3) exp. density	Z	ρ_E (gr/cm^3) Th. density
8.359	584.14	5.399	8	5.24

The grain size was calculated using Scherrer's equation (Speakman, 2014; Smart and Moore, 2006):

$$D = \frac{0.9\lambda}{\beta.\cos\theta} \qquad (4)$$

where D is the grain size, λ is the wavelength of X-ray, θ is the Bragg's diffraction angle and β is the full width at half maximum of the peak in radians.

The obtained grain sizes are shown in Table 4.

Table 4: Grain sizes of the samples annealed at different temperatures

T(℃)	grain size (L)(nm)
700	44.56
850	33.49
950	30.94

It is necessary to point out that the heating of the manganite compound to 950°C leads to the appearance of some peaks that are related to raw materials, such as $2\theta = 48.7, 71.9$ (Afriani *et al.*, 2018). As a result, we can say that the optimum temperature of $CuMn_2O_4$ synthesis is 850°C.

3.2. Electrical Properties

The electrical resistance variations of the prepared compound were studied as a function of temperature within the range of 295–667

^{o}K . The electrical resistance values decreased with increasing temperature, indicating semiconducting behaviour. Figure 4 shows the exponentially decreasing of $CuMn_2O_4$ resistance.

Figure 4: Plot of $CuMn_2O_4$ resistance as a function of temperature

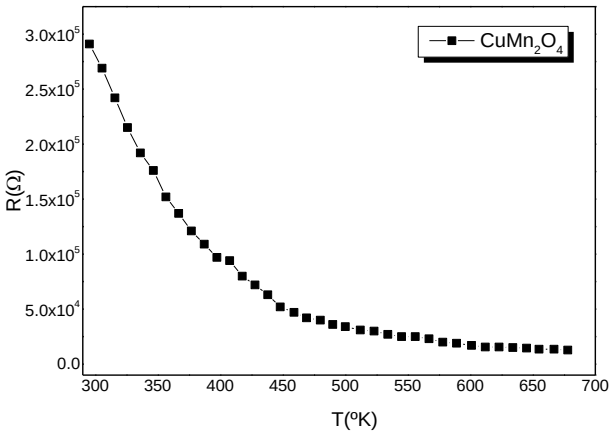

To extract the activation energy, the data were analyzed by using the relation (Das *et al.*, 2017; Ubale *et al.*, 2014; Deshpande *et al.*, 2018):

$$\mathrm{R} = R_0 \exp\left(\frac{E_a}{k_B T}\right) \qquad (5)$$

where E_a is the activation energy, T is the absolute temperature and k_B is the Boltzmann constant. Figure 5 shows variation of $\ln(R)$ as a function of $1/T$ for $CuMn_2O_4$ compound.

Figure 5: Plot of $\ln(R)$ vs. $1/T$ of $CuMn_2O_4$ annealed at 850°C

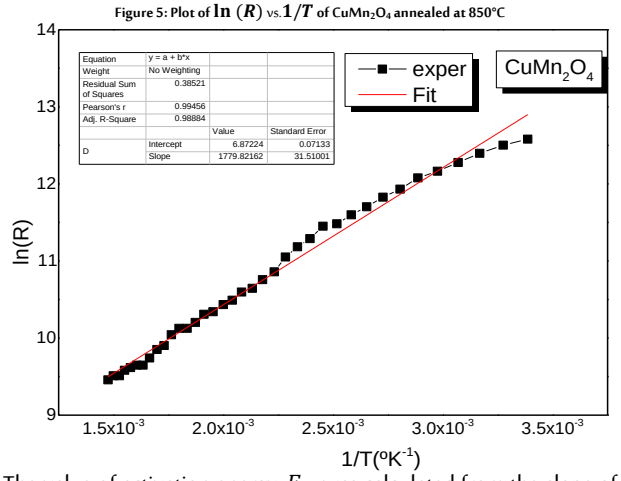

The value of activation energy, E_a, was calculated from the slope of $\ln(R)$ versus $1/T$ plot. The calculated value of activation energy was:

$$\boldsymbol{E_a} = 0.1535 \text{ eV} \qquad (6)$$

The activation energy value is in agreement with that identified by (Chen and Hsu, 2018).

4. Conclusions

Spinel $CuMn_2O_4$ was synthesized successfully by the solid-state method. The structural characterisation of $CuMn_2O_4$ revealed that the optimum temperature of $CuMn_2O_4$ synthesis was 850°C. It had a cubic structure. The crystalline size of $CuMn_2O_4$ annealed at 850°C was about 33nm. The electrical properties of the compound showed that it behaves like a semiconductor, so $CuMn_2O_4$ can be used as a semiconductor in thermoelectric devices. The activation energy of $CuMn_2O_4$ was calculated.

Biographies

Rasha Yousef

Department of Physics, Faculty of Science, Al-Baath University, Homs, Syria
ryousef@albaath-univ.edu.sy, 00963937830961

Ms Yousef is a Syrian doctoral student. She obtained an MSc in condensed matter physics from the Department of Physics, Faculty of Science, Al-Baath University, Syria. She is a lecturer at the Electrical and Mechanical Engineering College. Her research interests are in the fields of crystallography, X-rays software, materials synthesis and superconductors. She was previously a lecturer in I, II solid-state physics laboratories, and I, II general physics laboratories. She has published several articles in the journal of Al-Baath. She participated in scientific research days at Al-Baath University for two years, and Works on Mach3! Software. ORCID ID: 0000-0002-8406-4030

Alaa Nassif

Faculty of Engineering, Al-Wataniya Private University, Hama, Syria
alaa.nassif@wpu.edu.sy, 00963988460098

Dr Nassif is Syrian faculty member who has Ph.D. in dense plasma physics from Al-Baath University, Syria. He is Interested in dense plasma focus simulation (soft X-ray, short lived radioisotopes) and X-ray software. He has an international certificate for the use of Lee model code used in simulation of dense plasma focus from the Asian-African Association for Plasma Training (AAAPT) and UTM University (Malaysia). He participated in the workshop 'Practical skills of university education' in Syria. He published nine papers in Jordan Journal of physics, Science Publishing Group and Al-Baath journal.

Abla Al-Zoubi

Department of Physics, Faculty of science, Al-Baath University, Homs, Syria
aalzoubi@albaath-univ.edu.sy , 00963949542089

Dr Al-Zoubi is a Syrian Assistant Professor. She has a Ph.D. in Optoelectronics from Al-Baath University, Syria. She is interested in the optoelectronic properties of semiconductors, optoelectronic devices (UV detectors and sensors), X-ray software and materials synthesis and nanotechnology. She is a member of the national team for nanotechnology and a sub-committee member in the Syrian Science Olympiad. She attended The 1st Condensed Matter Physics Conference (CMP-1) & Applications in Syria, the First Syrian Conference of Physics (Syria), First Iran-Syria Workshop on Nanomaterial Synthesis & Characterization (Syria). She has published 15 papers in Springer and Elsevier journals and Al-Baath journal.

Nasser Saad Al-Din

Department of Physics, Faculty of science, Al-Baath University, Homs, Syria,
nsaadinaldeen@albaath-univ.edu.sy, 00963933793894

Dr Saad Al-Din is a Syrian professor. He obtained his Ph.D. in solid-state electronics from Aleppo, Syria Perpingnan, France Universities program. He is interested in wide band gap semiconductor devices, solar cells, medical detectors and nanotechnology. He is a member of the national team for nanotechnology. He was a department head, dean, and vice president for Scientific Research & Postgraduate Studies at Al-Baath University. He participated in X-ray course (Kazan, Russia), Medical Physics College 1 and 2 (ICTP, Italy), and the 3rd Saudi Conferences of Environmental on Nanomaterial Synthesis & Characterization (SAK). He has published more than 50 papers with Springer, Elsevier and Al-Baath journal.

References

Afriani, F., Ciswandi, Hermanto, B. and Sudiro, T. (2018). Synthesis of $CuMn_2O_4$ spinel and its magnetic properties characterization. *AIP Conference Proceedings*, **1964**(1), 020016.

Agnew, J.M., Leonard, J.J., Feddes, J. and Feng, Y. (2003). A modified air pycnometer for compost air volume and density determination. *Canadian Bio Systems Engineering*, **45**(n/a), 6.27–6.35.

Barros, B.S., de Melo Costa, A.C.F., Kiminami, R.H.G.A. and da Gama, L. (2004). Preparation and characterization of spinel MCr2O4 (M= Zn, Co, Cu and Ni) by combustion reaction. *Journal of Metastable and Nanocrystalline Materials*, **20**(n/a), 325–32.

Berbenni, V., Milanese, C., Bruni, G., Cofrancesco, P. and Marini, A. (2006). Solid state synthesis of $CaMnO_3$ from $CaCO_3$-$MnCO_3$ mixtures by mechanical energy. *Zeitschrift für Naturforschung B*, **61**(3), 281–6.

Chen, H.Y. and Hsu, D.J. (2014). Characterization of crednerite-Cu1. 1MnO. $9O_2$ films prepared using sol–gel processing. *Applied Surface Science*, **290**(n/a), 161–6.

Das, M.R., Mukherjee, A. and Mitra, P. (2017). Structural, optical and electrical characterization of CBD synthesized CdO thin films: Influence of deposition time. *Materials Science-Poland*, **35**(3), 470–8.

Deraz, N.M. and Abd-Elkader, O.H. (2013). Synthesis and characterization of nano-crystalline bixbyite-hopcalite solids. *Int J Electrochem Sci*, **8**(7), 10112–20.

Deshpande, V.P., Sartale, S.D. and Ubale, A.U. (2016). Synthesis of low resistive transparent nano-crystalline cadmium oxide thin films by chemical route. *Archives of Physics Research*, **7**(2), 1–11.

Durrani, S.K., Hussain, S.Z., Saeed, K., Khan, Y., Arif, M. and Ahmed, N. (2012). Hydrothermal synthesis and characterization of nanosized transition metal chromite spinels. *Turkish Journal of Chemistry*, **36**(1), 111–20.

Enhessari, M., Salehabadi, A., Maarofian, K. and Khanahmadzadeh, S. (2016). Synthesis and physicochemical properties of CuMn. *Int. J. Bio-Inorg. Hybr. Nanomater*, **5**(2), 115–20.

Errandonea, D., Ferrer-Roca, C., Martinez-Garcia, D., Segura, A., Gomis, O., Muñoz, A., Rodriguez-Hernandez, P., Lopez-Solano, J., Iconchel, S. and Sapiña, F. (2010). High-pressure X-ray diffraction AB_2O_4 compounds at high pressures 73 and abinitio study of Ni_2Mo_3N, Pd_2Mo_3N, Pt_2Mo_3N, Co_3Mo_3N, and Fe_3Mo_3N: Two families of ultra-incompressible bimetallic interstitial nitrides. *Physical Review B*, **82**(17), 174105.

George, K. and Sugunan, S. (2008). Nickel substituted copper chromite spinels: Preparation, characterization and catalytic activity in the oxidation reaction of ethylbenzene. *Catalysis Communications*, **9**(13), 2149–53.

Habibi, M.H. and Fakhri, F. (2016). Fabrication and characterization of CuCr2O4 nanocomposite by XRD, FESEM, FTIR, and DRS. Synthesis and reactivity in inorganic, metal-organic, and nano-metal. Chemistry, **46**(6), 847–51.

Shaheen, W.M. and Selim, M.M. (1998). Effect of thermal treatment on physicochemical properties of pure and mixed manganese carbonate and basic copper carbonate. *Thermochimica Acta*, **322**(2), 117–28.

Smart, L.E. and Moore, E.A. (2012). *Solid State Chemistry: An Introduction.* 3rd edition. USA: Taylor and Francis, CRC Press.

Sobhani-Nasab, A., Eghbali-Arani, M., Hosseinpour-Mashkani, S.M., Ahmadi, F., Rahimi-Nasrabadi, M. and Ameri, V. (2020). Eco-friendly preparation and characterization of $CuMn_2O_4$ nanoparticles with the green capping agent and their photocatalytic and photovoltaic applications. *Iranian Journal of Catalysis*, **10**(2), 91–9.

Speakman, S.A. (2014). *Estimating Crystallite Size Using XRD*. MA, USA: MIT Center for Materials Science and Engineering.

Trapp, M., Müller, M.M., Nazarpoor, Z. and Kleebe, H.J. (2017). Full reoxidation of $CuMn_2O_4$ spinel catalyst triggered by epitaxial Mn_3O_4 surface nanocrystals. *Journal of the American Ceramic Society*, **100**(11), 5327–34.

Ubale, A.U., Wadnerkar, S.S., Sononeand, P.N. and Tayade, G.D. (2014). Study of structural optical and electrical properties of CdO thin film. *Archives of Physics Research*, **5**(6), 43–8.

Waskowska, A., Gerward, L., Olsen, J.S., Steenstrup, S. and Talik, E. (2001). $CuMn_2O_4$: Properties and the high-pressure induced Jahn-Teller phase transition. *Journal of Physics: Condensed Matter*, **13**(11), 25–49.

West, A.R. (2014). *Solid State Chemistry and Its Applications*. 2nd edition. USA: John Wiley and Sons.

Zhang, M., Li, W., Wu, X., Zhao, F., Wang, D., Zha, X., Li, S., Liu, H. and Chen, Y. (2020). Low-temperature catalytic oxidation of benzene over nanocrystalline Cu–Mn composite oxides by facile sol–gel synthesis. *New Journal of Chemistry*, **44**(6), 2442–51.

The Scientific Journal of King Faisal University

Basic and Applied Sciences

Nice Bases of QTAG-Modules

Fahad Sikander [1], Tanveer Fatima [2] and Ayazul Hasan [3]

[1] Department of Basic Sciences, College of Science and Theoretical Studies, Saudi Electronic University, Jeddah, Saudi Arabia
[2] Department of Mathematics and Statistics, College of Sciences for Girls, Taibah University, Yanbu, Saudi Arabia
[3] Basic Sciences and Supporting Studies Unit, College of Applied Industrial Technology, Jazan University, Jazan, Saudi Arabia

LINK	RECEIVED	ACCEPTED	PUBLISHED ONLINE	ASSIGNED TO AN ISSUE
https://doi.org/10.37575/b/sci/210031	26/04/2021	14/08/2021	14/08/2021	01/12/2021

NO. OF WORDS	NO. OF PAGES	YEAR	VOLUME	ISSUE
3843	5	2021	22	2

ABSTRACT

A module M over an associative ring R with unity is a QTAG-module if every finitely generated submodule of any homomorphic image of M is a direct sum of universal modules. In this paper, we investigate the class of QTAG-modules having nice basis. It is proved that if H_ω (M) is bounded then M has a bounded nice basis and if H_ω (M) is a direct sum of uniserial modules, then M has a nice basis. We also proved that if M is any QTAG-module, then M⊕D has a nice basis, where D is the h-divisible hull of H_ω (M).

KEYWORDS

QTAG-module, Bounded submodule, Separable submodules, nice submodules

CITATION

Sikander, F., Fatima, T. and Hasan, A. (2021). Nice bases of QTAG-modules. *The Scientific Journal of King Faisal University: Basic and Applied Sciences*, **22**(2), 51–5. DOI: 10.37575/b/sci/210031

1. Introduction

Many concepts for group like purity, projectivity, injectivity, height etc. have been generalized for modules. To obtain results of groups which are not true for modules either conditions have been applied on modules or upon the underlying rings. We imposed the condition on modules that every finitely generated submodule of any homomorphic image of the module is a direct sum of uniserial modules while the rings are associative with unity. After these conditions many elegant results of groups can be proved for $QTAG$-modules which are not true in general. Many results of this paper are the generalization of the papers by Danchev (2007) and Danchev and Keef (2011a).

The study of $QTAG$-modules was initiated by Singh (1979). Mehdi (1984), Mehdi (1985), and Mehdi *et al.* (2005) worked a lot on these modules. They studied different notions and structures of $QTAG$-modules and developed of theory of these modules by introducing several notions, investigated some interesting properties and characterized them. Yet there is much to explore.

In this paper, we shall deal with the modules with a nice basis i.e., the modules which have special representation in terms of certain nice submodules. This class of modules is very large. Our main aim of this paper is to generalize the concept of nice basis of $QTAG$-modules and discuss several results of modules having nice basis. For the detailed literature on nice basis of groups one can go through the following papers: Danchev (2005), Danchev (2007), Danchev and Keef (2011a) and Danchev and Keef (2011b).

2. Preliminaries

All the rings R considered here are associative with unity and right modules M are unital $QTAG$-modules. An element $x \in M$ is uniform, if xR is a non-zero uniform (hence uniserial) module and for any R-module with a unique decomposition series, $d(M)$ denotes its decomposition length. For a uniform element $x \in M$, $e(x) = d(xR)$ and $H_M(x) = sup\left\{d\left(\frac{yR}{xR}\right) \mid y \in M, x \in yR \text{ and } y \text{ uniform}\right\}$ are the exponent and height of x in M, respectively. $H_k(M)$ denotes the submodule of M generated by the elements of height at least k and $H^k(M)$ is the submodule of M generated by the elements of exponents at most k (Khan, 1978). $H_\omega(M)$ denotes the first Ulm-submodule of a module M consisting of all elements of infinite height and $H_{\omega+n}(M) = H_n\big(H_\omega(M)\big)$. M is the h-divisible if $M = M^1 = \bigcap_{k=0}^{\infty} H_k(M)$ and it is h-reduced if it does not contain any h-divisible submodule. In other words, it is free from the elements of infinite height. A submodule N ⊆ M may not be h-divisible in M but if it is contained in some h-divisible submodule K ⊆ M, then it is said to be semi h-divisible and the minimal h-divisible submodule K of M containing N is said to be the h-divisible hull of N.

A $QTAG$-module M is said to be separable, if $M^1 = 0$. A module M is said to be bounded, if there exists an integer n such that $H(x) \leq n$ for every uniform element $x \in M$ (Singh,1979). A submodule N of a $QTAG$-module M is a nice, if for every ordinal σ, there exists an element $x_\sigma \in N_{\sigma+1}/N_\sigma$ which is proper with respect to N_σ (Mehdi *et al.*, 2006). A family of nice submodules $\mathcal{N}$ of submodules of M is called nice system in M if

(i) $0 \in \mathcal{N}$;
(ii) If $\{N_i\}_{i\in j}$ is any subset of $\mathcal{N}$, then $\sum_i N_i \in \mathcal{N}$;
(iii) Given any $N \in \mathcal{N}$ and any countable subset X of M, there exist $K \in \mathcal{N}$ containing $N \cup X$, such that K/N is countably generated.

A h-reduced $QTAG$-module M is called totally projective if it has a nice system. Let M be a QTAG- module. It defines a well ordered sequence of submodules $M = M^0 \supset M^1 \supset M^2 \supset \ldots \supset M^\tau = 0$, for some ordinal τ. Here $M^1 = \bigcup_{k\in\omega} Hk(M)$, $M^{\sigma+1} = (M^\sigma)^1$ and $M^\sigma = \bigcap_{\rho<\sigma} M^\rho$, if σ is a limit ordinal. M^σ is said to be the σ-th Ulm submodule of M.

Several results which hold for TAG-modules also hold good for $QTAG$-modules (Singh, 1979). Notations and terminology are follows from (Fuchs, 1970 and 1973).

Corresponding Author: Fahad Sikander 00966551898691, f.sikander@seu.edu.sa

3. Main Results

The concept of nice basis for the groups was introduced by Danchev (2005) using nice subgroups. Motivated by this, we generalize this concept to nice basis of $QTAG$-modules as follows:

Definition 3.1: A $QTAG$-modules M has a nice basis if it can be expressed as $M = \cup_{k<\omega} M_k$, $M_k \subseteq M_{k+1} \subseteq M$ and each M_k is nice in M and a direct sum of uniserial modules.

Remark 3.2: If each M_k is bounded then M has a bounded nice basis.

Let us start with a useful result:

Propositions 3.3: Let N be a submodule of M such that $H_\omega(N) = H_\omega(M)$. If M has a (bounded) nice basis, then N also has a (bounded) nice basis.

Proof: Let $\{M_k\}_{k<\omega}$ be the (bounded) nice basis of M. Now $M = \bigcup_{k<\omega} M_k$, $M_k \subseteq M_{k+1}$ and every M_k is a (bounded) nice basis of M, which is a direct sum of uniserial modules. Now $N = \bigcup_{k<\omega} (M_k \cap N)$ and all the intersections are (bounded) and the direct sums of uniserial modules. For a limit ordinal σ,

$\cap_{\rho<\sigma}\big((M_k \cap N) + H_\rho(N)\big) \subseteq \cap_{\rho<\sigma}\big(M_k + H_\rho(M)\big) \cap N = (M_k + H_\sigma(M)) \cap N = (M_k + H_\sigma(N) \cap N = H_\sigma(N + (M_k \cap N)$
and the result follows:

Corollary 3.4: A direct summand of a module M with a (bounded) nice basis and a separable complement also has a (bounded) nice basis.

Proof: Let N be a direct summand of M, with a separable complement K. Now $M = K \oplus N$. Since $H_\omega(K) = 0, H_\omega(M) = H_\omega(N)$ and by Proposition 3.3, N has a (bounded) nice basis.

Propositions 3.5: Let N be nice submodule of M such that M/N has a bounded nice basis. Then

(i) If N is bounded, then M has a bounded nice basis;
(ii) If N is a direct sum of uniserial modules, then M has a nice basis.

Proof: We may express $M/N = \bigcup_{k<\omega}(M_k/N)$ where $M_k \subseteq M_{k+1} \subseteq M, M_k/N$ is nice in M/N and it is bounded. Now by (Mehdi, *et al.*, 2005) M_k is nice in M. Since N is bounded M_k must be bounded and (i) follows.

Again M_k/N is bounded by (Singh, 1979), M_k is a direct sum of uniserial modules. Now, $M = \bigcup_{k<\omega} M_k$ and (ii) follows:

Remark 3.6: Since $H_\sigma(M)$ is nice in M for every ordinal σ, if $M/H_\sigma(M)$ has a bounded nice basis and $H_\sigma(M)$ is a direct sum of uniserial modules, then M has a nice basis.

Remark 3.7: If $M/H_\sigma(M)$ has a bounded nice basis and $H_\sigma(M)$ is bounded then M has a bounded nice basis. Here σ is any ordinal number. Also, if M has a bounded nice basis, then $H_\sigma(M)$ and $M/H_\sigma(M)$ have bounded nice bases.

Remark 3.8 If the length of $M\ \alpha < \omega.2$, i.e., $\alpha = \beta + \omega$ for some ordinal β and $M/H_\beta(M)$ has a bounded nice basis, then M has a bounded nice basis.

Proposition 3.9: If $H_\omega(M)$ is a direct sum of uniserial modules, then M has a nice basis. If $H_\omega(M)$ is bounded too then M has a bounded nice basis.

Proof: Since $M/H_\omega(M)$ is separable, it has a bounded nice basis by Remark 3.8. We may express $M/H_\omega(M)$ as $\bigcup_{k<\omega} H^k(M/H_\omega(M))$. Again $H^k(M/H_\omega(M)) = M_k/H_\omega(M)$ for some modules M_k such that $M_k \subseteq M_{k+1} \subseteq M$ and $H_k(M_k) \subseteq H_\omega(M)$. Thus $M = \bigcup_{k<\omega} M_k$ and $H_k(M_k)$ is a direct sum of uniserial modules, M_k is also a direct sum of uniserial modules (Singh, 1979). Since $M_k/H_\omega(M) = H^k(M/H_\omega(M))$ is nice in $M/H_\omega(M)$ and $H_\omega(M)$ is nice in M by (Mehdi, *et al.* 2005) every M_k is nice in M and the result follows.

Proposition 3.10: Let α be an ordinal such that $M/H_\alpha(M)$ is countably generated and $H_\alpha(M)$ has a (bounded) nice basis. Then M has a (bounded) nice basis.

Proof: Let $M/H_\alpha(M) = \bigcup_{k<\omega} H^k(M/H_\alpha(M))$ where $M_k \subseteq M_{k+1} \subseteq M$ and $M_k/H_\alpha(M)$ are finitely generated for every $k \in Z^+$. Now $M = \bigcup_{k<\omega} M_k$ and for every k, $M_k = H_\alpha(M) + T_k$ where T_k are finitely generated and $T_k \subseteq T_{k+1}$. Again

$$H_\alpha(M) = \bigcup_{k<\omega} N_k \quad ,$$

$N_k \subseteq N_{k+1} \subseteq H_\alpha(M)$, such that N_k are nice in $H_\alpha(M)$) and M and N_k are (bounded) direct sums of uniserial modules. Now $M = \bigcup_{k<\omega}(N_n + T_n)$ where $N_n + T_n$ are nice in M, and are (bounded) direct sums of uniserial modules (Singh, 1979) and the result follows.

The following result is an immediate consequence of Proposition 3.10:

Corollary 3.11: If the length of the module M is less than $\omega.2$ and $M/H_\omega(M)$ is countably generated then M has a bounded nice basis.

Proposition 3.12: If M is a module such that $H_\omega(M)$ is countably generated, then M is the union of a countable ascending chain tower of nice direct sums of countably generated modules.

Proof: Since the separable modules have a bounded nice basis $M/H_\omega(M) = \bigcup_{k<\omega}(M_k/H_\omega(M))$ where $M_k/H_\omega(M) \subseteq M_{k+1}/H_\omega(M)$ are nice submodules of $M/H_\omega(M)$ and they are bounded such that $H_k(M_k) \subseteq H_\omega(M)$. Now M_k's are nice in M and they are direct sums of countably generated modules and $M = \bigcup_{k<\omega} M_k$, the result follows.

Following is the immediate consequence of the above propositions:

Corollary 3.13: If M is a $QTAG$-module of length at most $\omega.2$ such that $H_\omega(M)$ is countably generated, then M has a nice basis.

Proposition 3.14: Direct sums of modules with a bounded nice basis have bounded nice basis.

Proof: Let M be a $QTAG$-module such that $M = \oplus_{i\in I} M_i$, where each M_i has a bounded nice basis. Let $M_i = \bigcup_{j<\omega}\{M_{ij}\}$, where $M_{ij} \subseteq M_{ij+1}$, all M_{ij} are bounded by j and M_{ij}'s are nice in M_i. Therefore,

$$M = \oplus_{i\in I}\left(\bigcup_{j<\omega} M_{ij}\right) = \bigcup_{j<\omega}(\oplus M_{ij}) = \bigcup_{j<\omega} P_j$$

where each $P_j = \oplus_{i\in I} M_{ij}$. Now $P_j \subseteq P_{j+1} \subseteq M$, $H^j(P_j) = 0$ and P_j is nice in M.

Now, we will see the behaviour of a $QTAG$-module which contains a submodule with a nice basis under the action of a countable extension of quotients.

Proposition 3.15: Suppose $M = N$ is countably generated, where N is a balanced submodule of a $QTAG$-module M. If N has a (bounded) nice basis, then M has (bounded) nice basis.

Proof: Since we can write $M \cong (N + M)/N$, (Fuchs,1970) the proof follows from Proposition 3.14.

A fully invariant submodule L of M is large in M if $L + B = M$,

for every basic submodule B of M (Sikander *et al.,* 2017). Now, we have the following result:

Corollary 3.16: Let L be any large submodule of a $QTAG$-module M. Then L has a (bounded) nice basis if M has a (bounded) nice basis.

Proof: Since $H_\omega(M) = H_\omega(L)$ (Sikander *et al.,* 2017)., the result follows immediately in view of Proposition 3.3.

We will try to explore the possibility that whether to have a nice basis can be invariantly retrieved under the action of bounded quotients.

Theorem 3.17: Let M be a $QTAG$-module with a submodule N such that $M = N$ is bounded. Then M has a bounded nice basis if and only if N has a bounded nice basis.

Proof: Since $H_m(M) \subseteq N$ for some $m \in Z^+, H_\omega(M) = H_\omega(N)$ and by Proposition 3.1, N has a bounded nice basis. For the converse, suppose N has a bounded nice basis $\{P_n\}_{n<\omega}$. Now $N = \bigcup_{n<\omega} P_n$, $P_n \subseteq P_{n+1}$ and for every $n \geq 1$, P_n is nice in N which is a direct sum of uniserial modules. Therefore, $H_m(M) = \bigcup_{n<\omega}(P_n \cap H_m(M))$, where $P_n \cap H_m(M) \subseteq P_{n+1} \cap H_m(M)$. Since $P_n \cap H_m(M)$ are submodules P_n's of they are bounded and the direct sum of uniserial modules.

On the other hand, for every limit ordinal σ ,

$$\bigcap_{\rho<\sigma}(P_n + H_\rho(M)) = \bigcap_{\rho\leq\rho<\sigma}(P_n + H_\rho(M)) \subseteq \bigcap_{\rho<\sigma}(P_n + H_\rho(M)) = P_n + H_\sigma(N) = P_n + H_\sigma(M)$$

Since P_n are nice in M; all $P_n \cap H_m(M)$ are nice in $H_m(M)$: We infer that $H_m(M)$ has a bounded nice basis, therefore by Proposition 3.9, M has a bounded nice basis as required.

For any $QTAG$-module M, $g(M)$ denotes the smallest cardinal number λ such that M admits a generating set X of uniform elements of cardinality λ i.e., $\#(X) = \lambda$ (Mehran and Singh, 1986). Any $QTAG$-module $M = K \oplus D$, where D is h-divisible and K is h-reduced. M has a nice basis if the h-reduced part K has a nice basis. Here we show that if M is a $QTAG$-module and D is a h-divisible module such that $g(D) \geq g\big(H_\omega(M)\big)$. then $M \oplus D$ must have a nice basis. We define $Bg(M)$ as the cardinality of the minimal generating set of a h-divisible module D such that $M \oplus D$ has a nice basis and we find that $B_g(M) \leq g\big(H_\omega(M)\big)$.

Theorem 3.18: Let M be a $QTAG$-module and D, the h-divisible hull of $H_\omega(M)$. Then $M \oplus D$ has a nice basis.

Proof: Suppose $M \cong M' \oplus D'$, where M' is h-reduced and D' is h-divisible. If D'' is the h-divisible hull for $H_\omega(M')$, then we may put $D = D' \oplus D''$ and assume that M is h-reduced. Suppose $H_\omega(M)$ is finitely generated. Now consider the inclusion map $f_1: H_\omega(M) \to D$ is injective and the identity map $f_2: H_\omega(M) \to H_\omega(M)$. If $H_\omega(M)$ is infinitely generated, then we may define K as the external direct sum $\sum_{x_i \in H_\omega(M)} x_i R$. Now $g(K) = g\big(H_\omega(M)\big) = g(D)$.

Therefore, we may define the embedding $f_1: K \to D$ and $f_2: K \to H_\omega(M)$. In $M \oplus D$, we put $K' = \{(f_2(x), x \mid x \in K\}$ and $D' = \{(0, y) | y \in D\}$.

Now $(K' + D')/K' = (H_\omega(M) \oplus D)/K'$ is a h-divisible submodule of $(M \oplus D)/K'$ so that

$$\frac{M \oplus D}{K'} \cong \frac{(H_\omega(M) \oplus D)}{K'} \oplus \frac{P}{K'},$$

where P is a submodule of $M \oplus D$ containing K' such that

$$\frac{P}{K'} \cong \frac{(M \oplus D)/K'}{(H_\omega(M) \oplus D)/K'} \cong \frac{M \oplus D}{H_\omega(M) \oplus D)} \cong \frac{M}{H_\omega(M)}.$$

If $n < \omega$, let P_n be the submodule of P containing K' such that $(P_n/K') \cong H^n(M/H_\omega(M))$. We may define $Q_n = P_n + H^n(D')$. We have to show that $\{Q_n\}_{n<\omega}$ forms a nice basis for $M \oplus D$. Since $P_n \subseteq P_{n+1}$ and $H^n(D') \subseteq H^{n+1}(D')$, $Q_n = P_n + H^n(D') \subseteq P_{n+1} + H^{n+1}(D') = Q_{n+1}$ and the first condition is satisfied. Now the map $x \to (f_2(x), x)$ extends to an isomorphism and $K \cong K' = Q_0$. If $n > 0$; then $H_n(P_n) \subseteq K'$ and $H_n(D') = 0$ so that $H_n(Q_n) \subseteq K$. Since K' is a direct sum of uniserial modules so is $H_n(Q_n)$ and Q_n.

It remains to show that $\cup\, Q_n = M \oplus D$ and each Q_n is nice in $M \oplus D$. Using the above mentioned isomorphisms, we conclude that

$$\frac{M \oplus D}{K'} \cong \frac{(H_\omega(M) \oplus D)}{K'} \oplus \frac{M}{H_\omega(M)}.$$

The submodule $\frac{Q_n}{K'}$ is mapped onto $\left(\frac{H^n(D') \oplus K)}{K'}\right) \oplus H^n\left(\frac{M}{H_\omega(M)}\right)$. Since $D' = \bigcup_{n<\omega} H^n(D')$, $H_\omega(M) \oplus D = D' + K'$ and $\frac{M}{H_\omega(M)} = \bigcup_{n<\omega} H^n\left(\frac{M}{H_\omega(M)}\right)$, we have $M \oplus D = \bigcup_{n<\omega} Q_n$. These two equations imply that

$$\frac{M \oplus D}{Q_n} \cong \frac{(M \oplus D)/K'}{Q_n/K'} \cong \left(\frac{H_\omega(M) \oplus D}{H^n(D') + K'}\right) \oplus \left(\frac{\mathrm{M}/H_\omega(M)}{H^n(\mathrm{M}/H_\omega(M))}\right) \cong \left(\frac{\mathrm{D}' \oplus K'}{H^n(D') + K'}\right) \oplus H_n\left(\frac{\mathrm{M}}{H_\omega(M)}\right).$$

Now any element of $\frac{\mathrm{D}' \oplus K'}{H^n(D') + K'}$ is represented by an $x \in D'$, which is h-divisible, hence $H(x) = \infty$, so x is proper in this coset. If $x \in H_n\left(\frac{\mathrm{M}}{H_\omega(M)}\right)$ such that $H(x)$ is finite, then such a coset always has a proper element. Therefore, Q_n is nice and $\{Q_n\}_{n<\omega}$ is a nice basis.

Following is the immediate consequence of the above theorem:

Corollary 3.19: Any $QTAG$-module M is a direct summand of a $QTAG$-module with a nice basis.

Proposition 3.20: Let M, D be $QTAG$-modules such that D is h-divisible and $g(D)$ is finite. Then $M \oplus D$ has a nice basis if and only if M has a nice basis.

Proof: If M has a nice basis, then $M \oplus D$ has a nice basis. For the converse, suppose $M \oplus D$ has a nice basis $\{P_n\}_{n<\omega}$. We may express $M = M_0 \oplus D_0$, where M_0 is h-reduced and D_0 is h-divisible. If $g(D_0)$ is infinite, then $M \oplus D \cong M_0 \oplus D_0 \oplus D \cong M_0 \oplus D_0 = M$, and the result follows.

Otherwise, if $g(D_0)$ is finite, then we shall prove that M_0 has a nice basis. Replacing M by M_0 and D by $D_0 \oplus D$ we may assume that M is h-reduced. If $D' = \{0\} \oplus D$, then $D' = H_\omega(M \oplus D)$ and $Q_n = (P_n + D')/D'$ is nice in $(M \oplus D)/D' \cong M$. Since $\bigcup_{n<\omega} P_n = M \oplus D$, we have $\bigcup_{n<\omega} Q_n = (M \oplus D)/D' \cong M$.

Now for each $n < \omega$; there exists an isomorphism $P_n/(P_n \cap D') \to (P_n + D')/D' = Q_n$ .Since $g(D')$ is finite, hence $P_n \cap D'$ must be a direct sum of uniserial modules and $P_n \cap D'$ is finitely generated. Therefore, Q_n is a direct sum of uniserial modules and $\{Q_n\}_{n<\omega}$ is a nice basis for M.

Corollary 3.21: If M is a $QTAG$-module, then $Bg(M)$ is either 0 and M has a nice basis or $B_g(M)$ is an infinite ordinal such that $B_g(M) \leq g(H_\omega(M))$, then M does not have a nice basis.

Proof $B_g(M)$ =0 if and only if M has a nice basis. If M does not have a nice basis then by Proposition 3.8, $B_g(M)$ is not finite. Thus, by Theorem 3.18, $B_g(M) \leq g(H_\omega(M))$.

Proposition 3.22: For a $QTAG$-module M; the following holds:

(i) If K is a separable $QTAG$ -module, then $B_g(M \oplus K) = B_g(M)$.
(ii) If D is a h-divisible module, then then $B_g(M \oplus D)$ is 0, if $g(D) \geq B_g(M)$ or $B_g(M)$ if $g(D) < B_g(M)$.
(iii) If D is h-divisible such that $g(D)$ is finite, then $B_g(M \oplus D) = B_g(M)$.
(iv) For any ordinal σ, $B_g(H_\sigma(M) \leq B_g(M)$.
(v) If $M/H_\omega(M)$ is a direct sum of uniserial modules, then $B_g(M) = B_g(H_\omega(M))$.
(vi) If $H_\omega(M)$ has a nice basis and $M/H_\omega(M)$ is a direct sum of uniserial modules, then $B_g(M) = B_g(H_\omega(M)) = 0$.

Proof: (i) If D is a h-divisible module then by Proposition 3.6, $M \oplus D$ has a nice basis if and only if $M \oplus K \oplus D$ has a nice basis. Therefore $B_g(M \oplus \mathrm{K}) = B_g(M)$.

(ii) If $g(D) \geq B_g(M)$, then $M \oplus \mathrm{D}$ has a nice basis so that $B_g(M \oplus \mathrm{D}) = 0$. Otherwise if $g(D) < B_g(M)$, then for any h -divisible module $D', M \oplus D \oplus D' \cong M \oplus (D \oplus D')$ has a nice basis if and only if $g(D \oplus D') = g(D) + g(D') \geq B_g(M)$ if and only if $g(D') \geq B_g(M)$, if and only if $M \oplus D'$ has a nice basis and the result follows.

(iii) is a direct consequence of (ii), where $B_g(M)$, is 0 or infinite.

(iv) Let $\{P_n\}_{n<\omega}$ be a nice basis for $M \oplus D$, then $\{P_n \cap H_\sigma(M \oplus D)\}_{n<\omega}$ is a nice basis for $H_\sigma(M \oplus D) = H_\sigma(M) \oplus D$.

(v) We have $B_g(H_\omega(M)) \leq B_g(M)$. On the other hand if D is a h -divisible module such that $g(D) = B_g(M)$, then $H_\omega(M) \oplus D = H_\omega(\mathrm{M} \oplus D)$ has a nice basis. Since $\frac{M \oplus D}{H_\omega(M \oplus D)}$ is a direct sum of uniserial modules and $H_\omega(M \oplus D)$ has a nice basis as $(M \oplus D)$ has a nice basis, so that $B_g(M) \leq B_g(H_\omega(M))$ and we are done.

(vi) If $H_\omega(M)$ is a direct sum of uniserial modules, then M and $H_\omega(M))$ both have nice bases and $B_g(M) = 0 = B_g(H_\omega(M))$.

Proposition 3.23: If M and M' are $QTAG$ -modules, then $B_g(M \oplus M') \leq B_g(M) + B_g(M')$.

Proof: Let D and D' be h- divisible modules such that $g(D) = B_g(M), g(D') = B_g(M')$. Then,

$$(M \oplus M') \oplus (D \oplus D') \cong (M \oplus D) \oplus (M' \oplus D').$$

Since $M \oplus D$ and $M' \oplus D'$ have nice basis, their direct sum has a nice basis.

The behavior of bounded nice basis is different from that of nice basis. This can be seen as follows:

Theorem 3.24: Let M be a h-reduced module and D is a h-divisible module. Then M has a bounded nice basis if and only if $M \oplus D$ has a bounded nice basis.

Proof: $\{H^n(D)\}_{n<\omega}$ forms a bounded nice basis for a h-divisible module D. Since direct sums of modules with bounded nice basis, the necessity is done and we may consider that $M \oplus D$ has a bounded nice basis $\{Q_n\}_{n<\omega}$. If $D' = \{0\} \oplus D = H_\omega(M \oplus D)$ and $P_n = (Q_n + D')/D'$, then P_n is nice in $(M \oplus D')/D' \cong M$. Moreover, $P_n = Q_n/(Q_n \cap D')$ must be bounded. Therefore, it is a direct sum of uniserial modules. Since $M \oplus D$ is the union of the ascending chain of modules Q_n. $(M \oplus D')/D' \cong M$ is the union of the of the ascending chain of submodules P_n. Therefore, M has a bounded nice basis.

4. Discussion

We end this article with the following observation:

Suppose M is h-reduced module that does not have a nice basis. If D is a h-divisible module such that $g(D) \geq B_g(M)$, then $M \oplus D$ has a nice basis. On the other hand, if M does not have a bounded nice basis, by Theorem 3.24, $M \oplus D$ does not have a bounded nice basis. This means that there are $QTAG$-modules with a nice basis which do not have bounded nice basis.

Biographies

Fahad Sikander

Department of Basic Sciences, College of Science and Theoretical Studies, Saudi Electronic University, Jeddah, Saudi Arabia, f.sikander@seu.edu.sa, 00966551898691

Dr. Sikander is currently working as an Indian Associate Professor of Mathematics. He received his Ph.D. degree in 2012 from Aligarh Muslim University, Aligarh, India. His area of research are commutative algebra and the generalizations of primary abelian groups. He has published more than 18 research papers in journals of International repute. He delivered invited talk in South Korea at Suwon University. He is serving as a reviewer in Mathematical reviews published by American Mathematical Society, USA.

Fatima Tanveer

Department of Mathematics and Statistics, College of Sciences for Girls, Taibah University, Yanbu, Saudi Arabia, tansari@taibahu.edu.sa, 00966556922945

Dr. Tanveer is an Indian assistant professor in Mathematics at Taibah University. Her areas of research are differential geometry and algebra. She received her doctorate degree from Aligarh Muslim University, Aligarh, India. She published 8 research publications in journals of International repute. She presents her research work in some International Conferences. Earlier, she worked as Lecturer at Department of Mathematics, Jizan University, Jizan, KSA. She is serving as a referee for some journals in Mathematics.

Ayazul Hasan

Department of Mathematics, College of Applied Industrial Technology, Jazan University, Jazan, Saudi Arabia, ayazulh@jazanu.edu.sa, 00966599353722

Dr. Hasan is an Indian associate professor of mathematics. He received his Ph.D. degree in Applied Mathematics in the field of Algebra from Aligarh Muslim University, Aligarh, India, in 2012. He worked as an assistant professor in the Department of Mathematics, Integral University, Lucknow, India, in the 2012-2014 academic years. His research interest is Algebra in general, with an emphasis on rings and modules. He has published more than thirty research papers in refereed international journals.

References

Danchev, P.V. (2005). A nice basis for $S(FG)/G_p$. *Atti Sem. Mat. Fis. Univ.*

Modena e Reggio Emilia, **53**(1), 3–11.

Danchev, P.V. (2007). Nice bases for primary abelian groups. *Ann. Univ. Ferrara, Sec. Math.*, **53**(1), 39–50. DOI: 10.1007/s11565-007-0004-2.

Danchev, P.V. and Keef, P.W. (2011a). The nice basis rank of a primary Abelian group. *Studia Scientiarum Mathematicarum Hungarica*, **48**(2), 247–56. DOI: 10.1556/SSc-Math.48.2011.2.1168.

Danchev, P.V. and Keef, P.W. (2011b). Nice bases and thickness in primary abelian groups. *Rocky Mountain J. Math.* **41**(4), 1127–49, DOI: 10.1216/RMJ-2011-41-4-1127.

Fuchs, L. (1970*). Infinite Abelian Groups, Vol. I.* New York, NY: Academic Press.

Fuchs, L. (1973). *Infinite Abelian Groups, Vol. II.* New York, NY: Academic Press.

Khan, M.Z. (1978). Modules behaving like torsion Abelian groups. *Math. Japonica,* **22**(5), 513–8.

Mehdi, A. and Khan M.Z. (1984). On closed modules. *Kyungpook Math. J.*, **24**(1), 45–50.

Mehdi, A. and Khan M.Z. (1985). On h-neat envelopes and basic submodules. *Tamkang J. Math.*, **16**(2), 71–6.

Mehdi, A., Abbasi, M.Y. and Mehdi, F. (2005), Nice decomposition series and rich modules. *South East Asian J. Math. Math. Sci.*, **4**(1) 1–6.

Mehdi A., Abbasi M.Y. and Mehdi, F. (2006). On $(\omega + n)$ -projective modules. *Ganita Sandesh*, **20**(1) 27–32.

Mehran, H.A. and Singh, S. (1986). On σ -pure submodules of QTAG-modules. *Arch. Math.*, **46**(n/a), 501–10.

Sikander, F., Mehdi, A. and Naji, S.A.R.K. (2017), Different characterizations of large submodules of $QTAG$-modules. *Journal of Mathematics*, **2017**, Article ID 2496246, DOI: 10.1155/2017/2496246.

Singh, S. (1979). Some decomposition theorems in Abelian groups and their generalizations II. *Osaka J. of Math,* **16**(1979), 45–55.

The Scientific Journal of King Faisal University

Basic and Applied Sciences

Lesions in the Hippocampus and Substantia Nigra of Wistar Rats' Brains Induced by Organophosphate Insecticide

Ebtihajah Abd Alrazaq Zaalan, Mahmoud Qassem and Muhammad Muayyad Bilal

Department of Animal Biology, Faculty of Science, University of Aleppo, Aleppo, Syria

LINK	RECEIVED	ACCEPTED	PUBLISHED ONLINE	ASSIGNED TO AN ISSUE
https://doi.org/10.37575/b/sci/210017	23/03/2021	21/08/2021	21/08/2021	01/12/2021
NO. OF WORDS	**NO. OF PAGES**	**YEAR**	**VOLUME**	**ISSUE**
4475	5	2021	22	2

ABSTRACT

As little is known about the neurotoxicity of the histological structure of the brain, this study focuses on the histological side of four- to six-month-old adult Wistar rat brains, which were examined after 0.1 mg\g organophosphate had been administered orally. In this study, the lesions were mainly localized at the hippocampus and substantia nigra (compacta pars) region. Distinct areas of necrotic and apoptotic tissues were detected in the CA1, CA2, and dentate gyrus of the hippocampus and compacta pars of the substantia nigra. Programmed cell death in the dentate gyrus was observed as early as 72 hours after treatment and necrosis of some brain regions. Moreover, Lewy bodies were noticed in the compacta pars of the substantia nigra. The most important symptoms of parkinsonism were observed in the substantia nigra (compacta pars). These were decreased neurons, increased neuronal melanin in the neurons, and increased glial cells. The degeneration of some neurons was reported in the polymorphic and pyramidal layers. The data showed an increase in the density of the axon membrane and several changes to the axis structure, such as the disappearance of the myelin sheath in some areas along the axis.

KEYWORDS

CA1, CA2, cell degeneration, compacta pars, dentate gyrus, Lewy bodies

CITATION

Zaalan, E.A., Qassem, M. and Bilal, M.M. (2021). Lesions in the hippocampus and substantia nigra of Wistar rats' brains induced by organophosphate insecticide. *The Scientific Journal of King Faisal University: Basic and Applied Sciences*, **22**(2), 56–60. DOI: 10.37575/b/sci/210017

1. Introduction

Organophosphorus (OP) compounds are commonly used as insecticides, plasticizers, and fuel additives. These compounds potently inhibit acetylcholinesterase (AChE), which is the enzyme that inactivates acetylcholine in neuronal synapses. Acute exposure to high OP levels can cause a cholinergic crisis in both humans and animals. The acute nervous system toxicity of OP pesticides and its results have been well documented. The inhibition of AChE leads to the accumulation of acetylcholine, which acts as a neurotransmitter in all ganglia in the autonomic nervous system, as well as many synapses in the brain, skeletal neuromuscular junctions, some postganglionic nerve endings of the sympathetic nervous system, and adrenal medulla. Organophosphate affects the long nerves or tracts in the nervous system and causes a symmetrical weakness in the peripheral muscles in the hands and feet, along with sensory impairment (Kamanyire and Karalliedde, 2004). Exposure to pesticides is considered a global health problem. An increased risk of neurodegenerative disorders has been strongly associated with chronic, repeated exposure to organophosphates. Moreover, the chronic neurotoxicity mechanism remains unclear, although it differs from cholinergic affection in acute toxicity. Although chronic exposure usually causes symptoms that are not accompanied by acute cholinergic overstimulation, it is associated with neuropsychiatric conditions, such as anxiety and depression. Furthermore, many reports found a positive correlation between different types of OPs and an increased risk of cognitive deficits and neurodegenerative disorders, such as Parkinson's disease (PD), Alzheimer's disease (AD), and amyotrophic lateral sclerosis (Narayan *et al.,* 2013; Voorhees *et al.,* 2017; Wang *et al.,* 2014). The mechanism behind OP-induced neurodegeneration remains unclear and differs from AChE inhibition, which is involved in acute toxicity. One suggested mechanism for OP-induced neurotoxicity is neuro-inflammation (Banks and Lein, 2012; Diz-Chaves and Garcia-Segura, 2013). This study aims to verify the degenerative effects of long-term exposure to OP on the dopaminergic system in rats and identify the possible contributing mechanisms. PD and AD are the two most common neurodegenerative diseases. PD is clinically depicted by severe motor symptoms, including rigidity, postural instability, a resting tremor, and bradykinesia (Sharma *et al.,* 2013). PD pathology is characterized by progressive degeneration and the loss of dopaminergic (DA) neurons in the substantia nigra (SN) pars compacta. Moreover, the deposition of α-synuclein as insoluble and toxic aggregates are characteristic hallmarks of PD. Regarding AD, patients suffer from an irreversible memory loss, progressive cognitive impairment, language disorder, and impairment in their visuospatial skills due to the degeneration of the hippocampal and cortical neurons and extracellular amyloid plaques. The earliest understanding of the disease pathology of PD and AD focuses on neuronal degeneration and consecutively observed inflammation, which is likely to be activated by the damaged neurons (Blaszczyk, 2018; Maiti et *al.,* 2017). In previous studies, lesions were consistently found in the CAP1 and CAP2 of the hippocampus, amygdala, SN, and neocortex (Nobakht, 2011). Neurodegenerative diseases, including PD and AD, have common features, including the following: protein accumulation, cell death with mitochondrial involvement, oxidative stress, and degeneration of neuromelanin, which is an organic polymer that is produced by the dopamine metabolism (Dugger and Dickson, 2016; Kouli *et al.,* 2020; Martinez et *al.,* 2019). The neurons of the SN contain large amounts of neuromelanin, and the concentration increases with age. However, this was markedly decreased in PD patients. However, PD-like pathologies are characterized by a significant neuronal loss and the emergence of Lewy bodies that are composed of highly phosphorylated a-synuclein, which were observed in the treatment animals after three months (Carbaja *et al.,* 2019; García *et al.,* 2021; Vila, 2019).

2. Materials and Methods

Thirty male Wistar rats were maintained on a 12-hour light/12-hour dark schedule and given unlimited access to rat food and tap water in the Animal Department, Faculty of Science at the University of Aleppo. The animals were divided into two groups. The first group was orally given an aqueous solution of organophosphate (0.1 mg\g body weight)

Corresponding Author: Ebtihajah Abd Alrazaq Zaalan 00963951257098, ba9138527@gmail.com

for four months, and the second group was given water without organophosphate. Their brains were then removed from their skulls and stored for at least three days in the fixative (formaldehyde 4%). Next, each brain was cut using a microtome into a series of sections that were 10 µm–20 µm thick. The serial sections (10 µm–20 µm thick) were then stained using different stains. The first stain was hematoxylin-eosin (H&E), which is distinguished by its good staining cell structures, such as cytoplasm and nuclei. The second was Cresyl violet, which is used for the central nervous system, including the nerve cell contents and Nissl particles. In addition, Colgi and Belcshowsky stains were used for the dendrites of neurons. The stain method was carried out according to the following stages: 1) dissolving paraffin from textile preparations using an electric heater at a temperature of 50° C–52° C; 2) transferring the slides to two baths of xylol for five minutes for each bath; 3) transferring the slides to a series of graduated concentrations of alcohol (100%, 90%, and 70%); and 4) washing them in distilled water to return water to the samples for five minutes per bath. In the H&E staining method, the hematoxylin was used first for five minutes, and then the slides were washed in distilled water and placed in the eosin stain for one minute. Later, the samples were transferred from the colorant to the distilled water and then to a series of gradual concentrations of alcohol (70%, 90%, and 100%) to dehydrate. They were kept in each concentration for one minute, and then they were transferred to two baths of xylol for two minutes each. The tissue preparations were covered in glass screens after an adhesive substance (Canada balsam or DPX) was applied to preserve them. Then, they were placed in a special dryer at a temperature of 37° C until the adhesive dried out.

2.1. Colgi and Beilcshowsky Stain Methods:

If the samples were large, they were divided into small pieces of 4 ml to 5 ml. Once the samples had been washed after the fixer and their tissues had been dried using blotting paper, they were placed in the potassium dichromate 2% solution for two days in the dark. After drying, the samples were transferred to the second solution (silver nitrate 2%) for two days. In this stain method, the double impregnation or Ramon Cajal's staining technique was used. Afterward, the samples were transferred to 1% oxalic acid and washed in 5% sodium thiosulfate. The samples passed an alcohol chain after being dried with blotting paper (70-90-100-Xylol). Later, the sample passed through the paraffin chain, and they were cut into 20 µm–50 µm-thick sections. The slides passed a chain of alcohol xylol (100-90-70-water-70-90-100-xylol). Finally, there was a microscopic examination of the slides.

2.2. Congo Red Stain Method:

In this stain, the sections were deparaffinized, and the water was removed. Then, they were stained in Congo red for 30–60 minutes, rinsed in distilled water, and passed through alkali alcohol for 5–10 seconds. The sections were then washed in distilled water for five minutes, counterstained in hematoxylin for 30 seconds, and washed in distilled water for one minute. Later, the sections were dipped in ammonia water for 30 seconds to turn them blue (the ammonia water was prepared by adding a few drops of ammonium hydroxide to tap water and mixing well). The sections were then rinsed in distilled water for five minutes and dehydrated using 95% alcohol, 100% alcohol, and Xylol.

3. Results

The present histological study of the hippocampus and SN of laboratory rats who were administered organophosphates showed the following results:

3.1. Hippocampus:

Programmed cell death was observed in some small pyramidal cells in the dentate gyrus (DG), and there were many gaps surrounding the neurons.

3.2. Substantia Nigra:

The most important symptoms of parkinsonism were observed in this area, such as reduced neurons, increased neuronal melanin in the neurons, and increased glial cells (Figure 1).

Figure 1: Cresyl violet-stained sections of the rats' hippocampus and SN (one dose of 0.1 mg/g with organophosphate for four successive weeks).

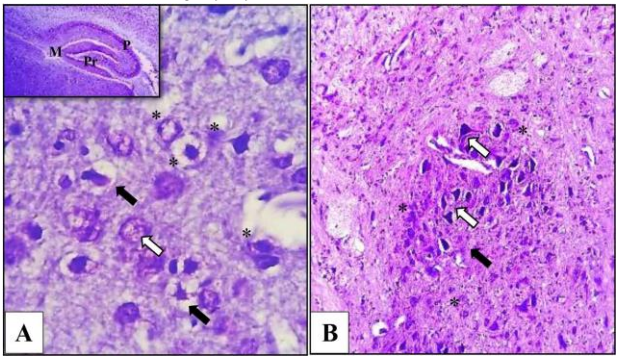

(A): The following three layers of the CA1 region of the hippocampus: the proper molecular layer (M), pyramidal layer (P), and polymorphic layer (Pr). Some small pyramidal cells appeared (arrow), and apoptotic cells appeared in the DG (black arrow). The neurons showed more vacuolation, and the cytoplasm was particularly rich in the Nissl substance of the glial cells (white arrow) x600. **(B):** In SN in PD rats, the major degenerative parkinsonian disorders showed a neuronal loss (black arrow), extra neuronal neuromelanin pigment (white arrow) x400, and gliosis in both sections (*) **(A and B).**

The histological study revealed slight damage to some neurons in the SN with the emergence of gaps around these cells and severe dendritic damage. Moreover, there was a decrease in the Nissl particles within the cytoplasm of the nervous cells and an increase of the amyloid fibers that were stained in Congo red in the space among the neurons. Additionally, as noted, the number of glial cells increased greatly within the sections (Figure 2).

Figure 2: Congo red-stained sections of the SN (a dose of 0.1 mg/day with organophosphate for four successive weeks).

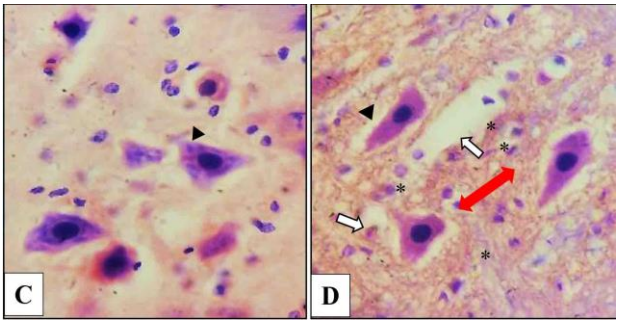

(D): Slight damage to the neuronal cells (black arrow). Microglial cell nuclei were observed in relatively large numbers (*) compared to the control, and necrotic cells were found in healthy ones. Throughout the compacta pars, some cells were also slightly affected. In these cases, the affected cells became vacuolated (white arrow), and the dendrites and cell somites were more severely damaged than the axons. Likewise, the Nissl substance decreased (arrowhead), and there was an increase in the amyloid fibers among the cells (red left-right arrow) compared to the control **(C)** x1000.

Other changes were observed in the compacta pars of the SN, such as

the separation of the components of the cytoplasm, huge gaps around the nuclei of some neurons in this region, and increased glial cells (Figure 3).

Figure 3: The Cresyl violet-stained section of the SN (a dose of 0.1 mg/day with organophosphate for four successive weeks) at the level of the cerebellum (brain stem).

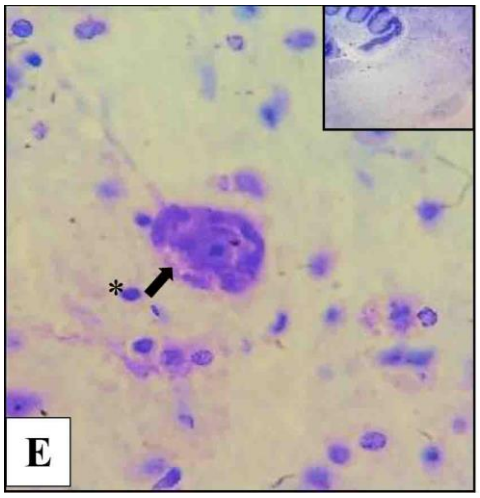

(E): Neuron with segregated cytoplasmic components. Larger vacuolated organelles surround the nucleus (black arrow) x600. The neuron is segregated from its surroundings, and there are increased dark cells, which are probably glia (*).

The Golgi stain in different regions of the hippocampus (CA1, CA2, and CA3) showed a degradation of some neurons in the polymorphic and pyramidal layers after being stained and saturated in silver nitrate (Figure 4).

Figure 4: Colgi cox-stained sections of the rats' hippocampus (a dose of 0.1 mg/day with organophosphate for two successive months).

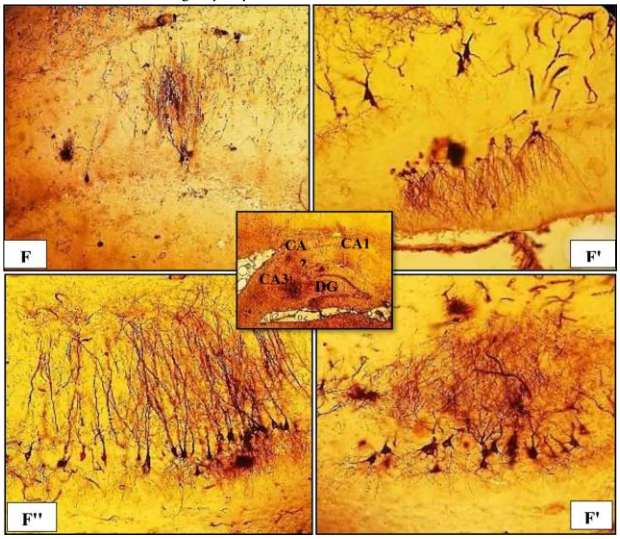

(F) and (F') The CA1 and CA2 regions of the hippocampus proper (molecular layer [M]). **(F")** The CA2 region of the hippocampus proper (polymorphic layer [Pr]). **(F'")** The CA3 region of the hippocampus proper (pyramidal layer [P]) and the cells that were impregnated by silver nitrate in CA1, CA2, and CA3. This was probably degenerated x600.

The Beilschowsky silver nitrate stain was distinguished by the double impregnation in the SN region in the compacta pars. As necrosis emerged in multiple spaces among the neurons with an increased phosphorylation of the proteins in most of the neurons' membranes, these neurons' membranes were saturated with silver nitrate and stained in black dots. Both this and the hematoxylin stain showed visible Lewy bodies in the cytoplasm of neurons as clusters (Figure 5).

Figure 5: Beilschowsky silver nitrate-stained sections of the rats' SN (a dose of 0.1 mg/day with organophosphate for two successive months) at the midbrain level (brain stem) in the compacta pars of the SN.

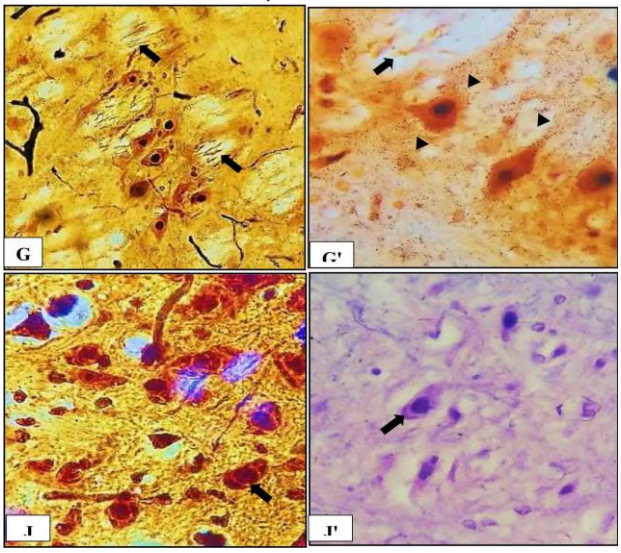

(G) Necrosis in many spaces among the neurons (black arrow) x600. **(G')** The membrane of most neurons stained in silver nitrate concerning the hyperphosphorylation of proteins (arrowhead) x1000. Beilschowsky silver nitrate- and H&E-stained sections of the rats' SNs (a dose of 0.1 mg/day with organophosphate for three successive months). **(J and J')** Lewy bodies (black arrow) in the pigmented cell of the compacta pars x1000 and the increased density of the axon membrane with changes to the structure of the axis, such as the disappearance of the myelin sheath in some areas along the axis. However, Schwann cells were not observed (Figure 6).

Figure 6: Golgi cox- (H and H') and Beilschowsky silver nitrate (I and I')-stained sections of the rats' SN (a dose of 0.1 mg/day with organophosphate for two successive months).

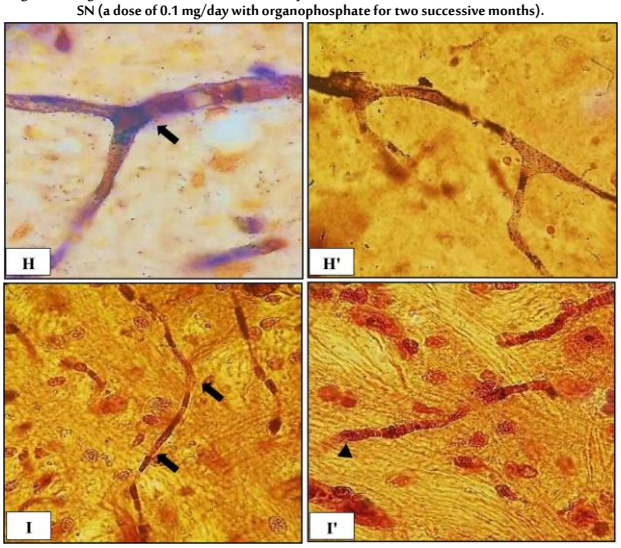

(H) The normal axon with increased membrane density compared to the control **(H')** x1000. **(I)** The axons' structure changed as the myelin sheath disappeared in some areas along the axis (black arrow), while Schwann cells were not observed (arrowhead) compared to the control **(I')** x600.

4. Discussion

Despite the increasing amount of research in this field, the effects of repeated or prolonged organophosphate exposure at low to moderate levels in both humans and animal remains unclear. This

study used lower doses and longer durations of exposure, which caused a barely detectable cholinesterase inhibition, followed by cellular damage in the brain.

Moreover, the study investigated the effects of OP on some regions in the central nervous system that are associated with PD and AD. In brief, the histological effects on the hippocampus and SN of rat brains that were treated with 0.1 mg\g of OP were confirmed.

In conjunction with previous studies, this study found apoptosis, which is programmed cell death, in several small pyramidal cells in the DG of the hippocampus, neuronal loss in the compacta pars of the SN, and dopaminergic degeneration due to chronic treatment with other types of organophosphates (Dorri *et al.,* 2015; Salyha, 2013). Moreover, idiopathic PD was characterized by the progressive loss of dopaminergic neurons in the SN (pars compacta), which leads to dopamine depletion (Dirnberger and Jahanshahi, 2013). This improved after the administration of these compounds, as demonstrated in the current research. Several studies reported a possible correlation between exposure to pesticides and the development of neurodegenerative disorders (Hernández *et al.,* 2016; Sánchez-Santed *et al.,* 2016). Since OPs are the most used pesticides, the previously mentioned studies focused on a link between OPs and the most common neurodegenerative diseases, PD and AD. Interestingly, some types of organophosphates have been proved to induce degeneration in the dopaminergic system (Astiz *et al.,* 2013; Binukumar and Gill, 2011).

Inflammation by insecticides, such as organophosphate, is thought to be the primary pathophysiological reason for neuronal degeneration, which occurs when the neutral amino acid transporter mediates the Na+ dependent entry of organophosphate into dopaminergic neurons. Consequently, organophosphate impairs redox recycling and induces oxidative stress, which leads to neuronal death (Banks and Lein, 2012; Farkhondeh *et al.,* 2020; Pearson and Pate, 2016). The increased permeability of the blood-brain barrier (BBB) and neurovascular dysfunction have been associated with severe conditions of PD. This effect could be linked to the infiltration of inflammation molecules that cause microglia activation and dopaminergic neurons death (Martinez *et al.,* 2019).

Numerous studies have demonstrated that exposure to a variety of OPs at lower and prolonged levels induces major changes in the central nervous system, such as changes to the gene expression, cell signaling pathways, and cellular ultrastructure. Moreover, exposure to various OPs increases the strict inclusion of many glial cells (Voorhees *et al.,* 2017).

It is worth mentioning that microglia are the resident immune cells (macrophages) of the brain, which can be triggered and activated in response to pro-inflammatory triggers or neuronal death. In this case, several reactive oxygen species and pro-inflammatory factors (e.g., tumor necrosis factor α and interleukin-1β) are produced, which contribute to neurotoxicity and degeneration. Similarly, OPs that include malathion may cause an inflammatory response, which could lead to the activation of microglia, as found by several studies (Ahmed et *al.,* 2017).

Since the metabolism of astrocytes is an indissociable link between neuronal health and synaptic functions, it is important to be mindful of how environmental toxicants can impact human health. Furthermore, environmental toxicant exposure can result in glucose dysfunction, including the involvement of the GLUT1 transporter, especially the astrocyte-specific transporter. Within the CNS, there is an overlap between the peripheral and astrocytic mechanisms. The engagement of the CYP detoxification system, which is robustly expressed in astrocytes as part of its role as the primary defense against xenobiotic penetrance into the CNS, suggests that astrocytes are crucial for a system-wide response to toxicants (Jiang *et al.,* 2017; Zhang *et al.,* 2019).

Lewy bodies were visible in the cytoplasm of neurons as clusters, which could be due to the presence of cytoplasmic protein aggregates in dopaminergic neurons. Although certain studies suggested that the progressive rostral spread of the Lewy body pathology reflected the clinical course of PD, other studies indicated that Lewy bodies are not the toxic species that are responsible for cell death. Hence, neuronal death may occur prior to the formation of Lewy bodies in some neurons (Saha *et al.,* 2000)

Additionally, PD patients with a longer disease duration are expected to have a wider regional distribution and greater density of Lewy body pathology combined with nigral cell loss in compacta pars. However, further research suggested that 15% of surviving nigral neurons contain Lewy bodies, and the age-adjusted proportion of Lewy body-bearing neurons is relatively stable throughout the disease duration.

Other studies suggested that the etiology of PD is a genetic basis that interacts with environmental factors.

The current study shows an increase of the amyloid fibers that were stained in Congo red in the spaces between neurons. The deposition of Aβ (mainly Aβ 40 and 42) caused them to form amyloid plaques, which are associated with reactive gliosis (Selkoe, 1994). In these areas, the activated microglia are recruited, and the reactive astrocytes exhibit a morph-functional remodeling, which modifies their interactions with neurons. Despite the reasonably close correlation between the increased phosphorylation and neuron degeneration, this study concludes that exposure to OP compounds degenerates some neurons in the polymorphic and pyramidal layers. This was proven by various staining methods. According to the hypothetical basis of binding silver to disintegrate products of proteins in neurons, this study demonstrates the emergence of necrosis in multiple spaces among the neurons, with an increased phosphorylation of the proteins in most of the neurons' membranes.

Silver-forming complexes with individual amino acids and progressive fragmentation of proteins (proteolysis) in disintegrating neurons leads to expansive sites for silver to form complexes (Anthony et *al.,* 2019).

Biographies

Ebtihajah Abd Alrazaq Zaalan

Department of Animal Biology, College of Science, University of Aleppo, Aleppo, Syria, 00963951257098, ba9138527@gmail.com

Mrs. Zaalan is a Syrian Arab doctoral student who is majoring in biological sciences. She achieved her master's degree in biochemistry at the University of Aleppo in 2016, majoring in the effect of nitrate on nervous tissue. She published several articles on the effects of environmental pollutants on the nervous system's tissues in the journal of the University of Aleppo. Her research interests include the effects of biological pollutants on the tissues of the nervous system and the preventive role of appendectomy-causing neurological diseases.

Mahmoud Radwan Qassem

Department of Animal Biology, Faculty of Science, University of Aleppo, Aleppo, Syria, 00963944799547, kassem-mahmoud@hotmail.com

Prof. Qassem is a Syrian Arab professor. He achieved his Ph.D on the environment and function of vertebrates from the University of Paris, France. He published many university books and more than 50 articles in local and international journals in both Arabic and English. Prof. Qassem participated in local and international conferences. His

primary research interests are the effect of chemical substances and elements on vertebrate tissues and how to protect endangered organisms, such as the Syrian salamander.

Muhammad Muayyad Bilal

Department of Animal Biology, College of Science, University of Aleppo, Aleppo, Syrian Arab Republic, 0096396630732, mmbboss@gmail.com

Prof. Bilal is a Syrian Arab professor. He received a Ph.D in molecular biology and biotechnology (immunology) from the University of Aleppo. He participated in conferences on biological horizons and other topics, such as agricultural and technical engineering. His research interests include the molecular profiling of Leishmaniasis in Aleppo and Leishmania prevention using plant extracts. To pursue his interests, Prof. Bilal published articles on Leishmaniasis prevention in both Arabic and English in the journal of the University of Aleppo.

References

Ahmed, D., Abdel-Rahman, R.H. and Salama, M. (2017). Malathion neurotoxic effects on dopaminergic system in mice: Role of inflammation. *Journal Biomedical Science*, **6**(4), 1–30.

Anthony, J., Intorcia, J., Filon, R., Brittany, H., Geidy, E., Serrano, L.I. and Thomas, B.G. (2019). *A Modification of the Bielschowsky Silver Stain for Alzheimer Neuritic Plaques: Suppression of Artifactual Staining by Pretreatment with Oxidizing Agents*. Arizona, USA: Banner Sun Health Research Institute.

Astiz, M., Diz-Chaves, Y. and Garcia-Segura, L.M. (2013). Sub-chronic exposure to the insecticide dimethoate induces a proinflammatory status and enhances the neuroinflammatory response to bacterial lipopolysaccharide in the hippocampus and striatum of male mice. *Toxicol*, **272**(2), 263–71.

Banks, C.N. and Lein, P.J. (2012). A review of experimental evidence linking neurotoxic organophosphorus compounds and inflammation. *Neurotoxicology,* **33**(3), 575–84.

Binukumar, B.K., Bal, A. and Gill, K.D. (2011). Chronic dichlorvos exposure: Microglial activation, proinflammatory cytokines and damage to nigrostriatal dopaminergic system. *NeuroMolecular Medicine*, **13**(4), 251–65.

Blaszczyk, J.W. (2018). Parkinson's disease and neurodegeneration: GABA-collapse hypothesis. *Frontiers in Neuroscience*, **269**(10), 1–8.

Carbaja, I.C., Laguna, A. and Giménez, J.R. (2019). Brain tyrosinase overexpression implicates age-dependent neuromelanin production in Parkinson's disease pathogenesis. *Nature Communications*, **973**(10), 1–19.

Delle D.A., Klos, K.J. and Fujishiro, H. (2008). Incidental Lewy body disease and preclinical Parkinson disease. *Arch Neurol*, **65**(8),1074–80.

Dennis, W., Dickson, M.D. (2018). Neuropathology of Parkinson disease. *HHS Public Access*, **46**(11), 30–3.

Dirnberger, G. and Jahanshahi, M. (2013). Executive dysfunction in Parkinson's disease. *Journal of Neuropsychology,* **7**(2), 193–224.

Dorri, S.A., Hosseinzadeh, H., Abnous, K., Hasani, F.V. and Robati, R.Y. (2015). Involvement of brain-derived neurotrophic factor (BDNF) on malathion induced depressive-like behavior in subacute exposure and protective effects of crocin. *Iran Journal Basic Medicine,* **18**(10), 958–66.

Dugger, B.N. and Dickson, D.W. (2016). Pathology of neurodegenerative diseases. *Cold Spring Harbor Laboratory Press*, **9**(7), 1–22.

Farkhondeh, T., Mehrpour, O. and Buhrmann, C. (2020). Organophosphorus compounds and MAPK signaling pathways. *International Journal of Molecular Sciences*, **4258**(21), 1–17.

García, A.M., Kun, A. and Calero, M. (2021). The neuromelanin paradox and its dual role in oxidative stress and neurodegeneration. *Antioxidants*, **124**(10), 1–19.

Hernández, A.F., González, A.B., López, F.I. and Lacasaña, M. (2016). Systematic reviews on neurodevelopmental and neurodegenerative disorders linked to pesticide exposure: Methodological features and impact on risk assessment. *Environ Int*, **92-93**(6), 657–79.

Jiang, Q., Zhang, L., Ding, G., Davoodi B.E., Li, Q., Li, L., Sadry, N., Nedergaard, M., Chopp, M. and Zhang, Z. (2017). Impairment of the glymphatic system after diabetes. *Blood Flow Metab*, **37**(4), 1326–37.

Kamanyire, R. and Karalliedde, L. (2004). Organophosphate toxicity and occupational exposure. *Occupational Medicine*, **54**(2), 69–75

Kouli, A., Camacho, M. and Allinson, K. (2020). Neuroinflammation and protein pathology in Parkinson's disease dementia. *Acta Neuropathol Commun*, **211**(8), 1–19.

Maiti, P., Manna, J. and Dunbar, G.L. (2017). Current understanding of the molecular mechanisms in Parkinson's disease: Targets for potential treatments. *Translational Neurodegeneration*, **28**(6), 1–35.

Martinez, L.G., Maccioni, R.B. and Andrade, V. (2019). Neuroinflammation as a common feature of neurodegenerative disorders. *Neuroinflammation in Brain Disorders*, **1008**(10). 1–17.

Narayan, S., Liew, Z., Paul, K., Lee, P.C. and Sinsheimer, J.S. (2013). Household organophosphorus pesticide use and Parkinson's disease. *International Journal of Epidemiology,* **42**(5), 1476–85.

Nury, T., Lizard, G. and Vejux, A. (2020). Lipids nutrients in Parkinson and Alzheimer's diseases: Cell death and cytoprotection. *International Journal of Molecular Sciences*, **2501**(21), 1–19.

Pajares, M., Rojo, A.I. and Manda, G. (2020). Inflammation in Parkinson's disease: Mechanisms and therapeutic implications. *Cells*, **1687**(9), 1–32.

Pearson, J.N. and Pate, M. (2016). The role of oxidative stress in organophosphate and nerve agent toxicity. *HHS Public Access*, **1378**(1), 17–24.

Saha, A.R., Ninkina, N.N., Hanger, D.P., Anderton, B.H. and Davies, A.M. (2000). Induction of neuronal death by alpha-synuclein. *Europe Journal Neuroscience*, **12**(8), 3073–7.

Salyha, Y.T. (2013). Chlorpyrifos leads to oxidative stress-induced death of hippocampal cells in vitro. *Neurophysiol,* **45**(3), 193–9.

Sánchez-Santed, F., Colomina, M.T. and Hernández, E.H. (2016). Organophosphate pesticide exposure and neurodegeneration. *Cortex*, **74**, 417–26.

Selkoe, D.J. (1994). Alzheimer's disease beyond the path to therapeutics. *Neurobiol,* **15**(2), 131–3.

Vila, M.D. (2019). Neuromelanin, aging, and neuronal vulnerability in Parkinson's disease. *Movement Disorders*, **34**(10), 1440–51.

Vital, M.D., Fernagut, P.O. and Canron, M.H. (2009). The nigrostriatal pathway in Creutzfeldt-Jakob disease. *The American Association of Neuropathologists*, **68**(7), 809–15.

Voorhees, J.R., Rohlman, D.S. and Lein, P.J. (2017). Neurotoxicity in preclinical models of occupational exposure to organophosphorus compounds. *Frontiers in Neuroscience,* **10**(590), 1–24.

Wang, A., Cockburn, M. and Ly, T.T. (2014). The association between ambient exposure to organophosphates and Parkinson's disease risk. *Occup Environment Medicine*, **71**(4), 275–81.

Zhang, L., Chopp, M., Jiang, Q. and Zhang, Z. (2019). Role of the glymphatic system in ageing and diabetes mellitus impaired cognitive function. *Stroke Vasc Neurol.,* **4**(2)90–2.

The Scientific Journal of King Faisal University

Basic and Applied Sciences

The Tensor Product of Zero-Divisor Graphs of Variation Monogenic Semigroups

Abolape Deborah Akwu [1] and Bana Al Subaiei [2]

[1] Department of Mathematics, College of Science, Federal University of Agriculture, Makurdi, Nigeria

[2] Department of Mathematics and Statistics, College of Science, King Faisal University, Al Ahsa, Saudi Arabia

LINK	RECEIVED	ACCEPTED	PUBLISHED ONLINE	ASSIGNED TO AN ISSUE
https://doi.org/10.37575/b/sci/210038	31/05/2021	27/08/2021	27/08/2021	01/12/2021

NO. OF WORDS	NO. OF PAGES	YEAR	VOLUME	ISSUE
3381	4	2021	22	2

ABSTRACT

The tensor product of zero-divisor graphs of variation monogenic semigroups $\Gamma(VS^1_{Mn})$ and $\Gamma(VS^2_{Mm})$ is studied. The vertices(x_1^i, x_2^j) and (x_1^k, x_2^f) of the tensor product of this graph are adjacent whenever $gcd(i,k) = 1, i + k > n, gcd(j,f) = 1, j + f > m$. Some properties of tensor product graphs are obtained, such as girth, diameter, chromatic, clique and domination numbers.

KEYWORDS

Variation monogenic semigroup, relatively prime, tensor product, adjacency

CITATION

Akwu, A.D. and Al Subaiei, B. (2021). The tensor product of zero-divisor graphs of variation monogenic semigroups. *The Scientific Journal of King Faisal University: Basic and Applied Sciences*, **22**(2), 61–4. DOI: 10.37575/b/sci/210038

1. Introduction

The zero-divisor graphs on semigroups were widely investigated in many studies; for example, DeMeyer *et al.* (2002), DeMeyer *et al.* (2005), Wright (2007) and Anderson and Badawi (2017).

Das *et al.* (2013) studied zero-divisor graphs of the monogenic semigroup $\Gamma(S_M)$, which is defined as $x^i.x^j = x^{i+j} = 0$ if and only if $i + j > n$. Then, Al Subaiei and Akwu (2020) modified the graph in the work of Das *et al.* (2013) by adding one more condition, $gcd(i,j) = 1$, and named the graph the variation monogenic semigroup $\Gamma(VS_M)$. These two graphs have different properties. For example, when $n = 8$, the graph of Das *et al.* (2013) has $diam(\Gamma(S_{M8})) = 2$, $\mathcal{X}(\Gamma(S_{M8}) = 5$, $\gamma(\Gamma(S_{M8})) = 1$, and $\omega(\Gamma(S_{M8})) = 5$. Meanwhile, the graph of Al Subaiei and Akwu (2020) has $diam(\Gamma(VS_{M8})) = 3$, $\mathcal{X}(\Gamma(VS_{M8}) = 3$, $\gamma(\Gamma(VS_{M8})) = 2$, and $\omega(\Gamma(VS_{M8})) = 3$. Also, when n is prime, the two graphs have different properties. For example, when $n = 7$, the graph of Das *et al.* (2013) has $\mathcal{X}(\Gamma(S_{M7}) = 4, \gamma(\Gamma(S_{M7})) = 1$, and $\omega(\Gamma(S_{M7})) = 4$, while the graph of Al Subaiei and Akwu (2020) has $\mathcal{X}(\Gamma(VS_{M7}) = 3, \gamma(\Gamma(VS_{M7})) = 1$, and $\omega(\Gamma(VS_{M7})) = 3$. These differences led us to further investigate the results of the properties of the variation monogenic semigroup graph, such as the tensor product.

The concept of the tensor product on graphs has been studied well and a sufficient amount of rich material can be found in the literature. Some examples are Harary and Trauth, Jr. (1966), Sampathkumar (1972) and Asmerom (1998). The tensor product of zero-divisor graphs of monogenic semigroups was investigated by Akgunes *et al.* (2014). This work will extend the investigation of the monogenic semigroup graph of Akgunes *et al.* (2014) to the variation monogenic semigroup graph and hence will use the same notation.

A set with an associative binary operation is called a semigroup. The semigroup that is generated by one element is called a monogenic semigroup. A monogenic semigroup with zero is denoted by S_{Mn} where n is the order of the semigroup. The nonzero elements of S_{Mn} are referred to as the vertices of the graph $\Gamma(S_{Mn})$. In Al Subaiei and Akwu's work (2020), the undirected graph of the variation monogenic semigroup with order n denoted by $\Gamma(VS_{Mn})$ was given, and the two vertices x^i and x^j are adjacent if and only if the following conditions are satisfied:

$x^i.x^j = x^{i+j} = 0$ if and only if $i + j > n$ and $gcd(i,j) = 1(*)$ where x^i and $x^j \in V(\Gamma(VS_{Mn}))$ and $1 \le i, j \le n$.

For basic general information about graph theory properties, we refer the reader to Bondy and Murty (1976). In general, for any graph G, $V(G)$ is known as the set of vertices in G. If the two vertices x, y are adjacent, then $xy \in E(G)$. The distance (shortest path) between two vertices is denoted by $d_{\Gamma(G)}$. The *diameter*, denoted by $diam(\Gamma(G))$ is defined as $diam(\Gamma(G)) = max\{d_{\Gamma(G)}(x,y): x, y \in V(\Gamma(G))\}$. The length of the shortest cycle in the graph is known as the *girth*. The *degree* of the vertex x^i, denoted by $deg_{\Gamma(G)}(x^i)$, is the number of vertices that are adjacent to x^i. The maximum degree of $\Gamma(G)$ is denoted by $\Delta(\Gamma(G))$, while the minimum degree of $\Gamma(G)$ is denoted by $\delta(\Gamma(G))$, which means the number of the largest and smallest vertex's degrees, respectively. The subset D of $V(G)$ is a *dominating set* of G if each vertex of $V(G)\backslash D$ is adjacent to at least one vertex of D. The *domination number*, $\gamma(G)$, is the dominating set with minimum cardinality. The *clique number*, $\omega(G)$, is the maximum number of vertices in any clique where the clique is a complete subgraph of graph G. The *chromatic number* of G, $\mathcal{X}$ is the minimum number of colors assigned to the vertices of G such that no two adjacent vertices have the same color. When $\omega(G) = \mathcal{X}(G)$, the graph G is a *perfect graph*, according to Lovasz (1972). For a graph G with order n, a *coprime labeling* of G is a labeling of its vertices with distinct integers $\{1,2,\dots,n\}$ such that the labels on any two adjacent vertices are relatively prime. A *coprime graph* is a graph that has coprime labeling.

Consider the simple graphs G_1 and G_2. It is known that the *tensor product* $G_1 \otimes G_2$ has the vertex set $V(G_1) \times V(G_2)$, where any two vertices, (g_1, g_2) and (h_1, h_2), are adjacent if and only if $g_1h_1 \in E(G_1)$ and $g_2h_2 \in E(G_2)$.

In our work, we will consider the graphs of the variation monogenic semigroup $\Gamma(VS^1_{Mn})$ and $\Gamma(VS^2_{Mm})$ and study the tensor product of these graphs. It is known in the theory of graphs that when any two vertices, (x_1^i, x_2^j) and (x_1^k, x_2^f) are adjacent, it means that $(x_1^i, x_2^j)(x_1^k, x_2^f) \in E(\Gamma(VS^1_{Mn}) \otimes \Gamma(VS^2_{Mm}))$. In this work, two adjacent vertices, (x_1^i, x_2^j) and (x_1^k, x_2^f), will be written as $(x_1^i, x_2^j) - (x_1^k, x_2^f)$. Since the graphs $\Gamma(VS^1_{Mn})$ and $\Gamma(VS^2_{Mm})$ are

Corresponding Author: Bana Al Subaiei banajawid@kfu.edu.sa ,00966500816416

simple, then (x_1^i, x_2^j) is not adjacent to (x_1^k, x_2^f) whenever $i = k$ or $j = f$. Therefore, $(x_1^i, x_2^j) - (x_1^k, x_2^f)$ whenever $x_1^i - x_1^k$ and $x_2^j - x_2^f$. That is:

$$x_1^i x_1^k \in E\left(\Gamma(VS_{Mn}^1)\right) \;\&\; x_2^j x_2^f \in E(\Gamma(VS_{Mm}^2))$$
$$\Updownarrow$$
$$gcd(i,k) = 1, i + k > n, gcd(j,f) = 1, j + f > m$$

2. Results

In this section, we give some tensor product characteristics of the variation monogenic semigroup graphs $\Gamma(VS_{Mn}^1) \otimes \Gamma(VS_{Mm}^2)$. The condition of the greatest common divisor on the graph of the variation monogenic semigroup makes the structure of the proofs in this work depend on the highest prime numbers p_1 and p_2 being less than or equal to n or m, respectively.

The following results give the maximum degree and minimum degree of the tensor product graph $\Gamma(VS_{Mn}^1) \otimes \Gamma(VS_{Mm}^2)$.

2.1. Theorem: Let p_1 and p_2 be the highest prime numbers less or equal to n and m, respectively. Then, the maximum and minimum degrees of $\Gamma(VS_{Mn}^1) \otimes \Gamma(VS_{Mm}^2)$ *are* $\Delta((\Gamma(VS_{Mn}^1) \otimes \Gamma(VS_{Mm}^2))) = (p_1 - 1)(p_2 - 1)$ and $\delta((\Gamma(VS_{Mn}^1) \otimes \Gamma(VS_{Mm}^2))) = 1$ respectively.

Proof. When $p_1 = n$ and $p_2 = m$, then $gcd(p_1, j) = 1$ and $gcd(p_1, k) = 1$ where $1 \le j < n$ and $1 \le k < m$. Hence, the result follows from Akgunes *et al.* (2014). Otherwise, we assume that $p_1 \neq n$, and $p_2 \neq m$, then vertex $(x_1^{p_1}, x_2^{p_2})$ has the maximum degree. Therefore, $(x_1^{p1}, x_2^{p_2}) - (x_1^d, x_2^s)$ when $p_1 + d > n$, $gcd(p_1, d) = 1$, $p_2 + s > m$ and $gcd(p_2, s) = 1$. Hence, $d > n - p_1$ and $s > m - p_2$. Since the graph is a simple graph, $(x_1^{p_1}, x_2^{p_2})$ is not adjacent to itself. Therefore, $deg((x_1^{p_1}, x_2^{p_2})) = |d||s|$, where $|d| = (n - (n - p_1)) - 1 = p_1 - 1$ and $|s| = (m - (m - p_2)) - 1 = p_2 - 1$. Thus, the maximum degree is $(p_1 - 1)(p_2 - 1)$.

Since 1 is relatively prime with any number and $n + 1 > n$ and $m + 1 > m$, the vertex (x_1, x_2) is adjacent only to (x_1^n, x_2^m). So, the minimum degree is 1.

The following two results are on the diameter and girth of the tensor product graph $\Gamma(VS_{Mn}^1) \otimes \Gamma(VS_{Mm}^2)$. The diameter of the tensor product graphs of the monogenic semigroup $\Gamma(S_{Mn}^1) \otimes \Gamma(S_{Mm}^2)$, as shown in Akgunes *et al.* (2014), is 4 when $n \ge m > 3$, and the girth is 3 when $n \ge m > 3$. However, in the case of the tensor product graphs of the variation monogenic semigroup, the diameter is 4 when $n \ge m > 6$, and the girth is 3 when $n, m > 4$ as shown below.

2.2. Theorem: Let $n \ge m$ be positive integers. For any variation monogenic semigroup graphs $\Gamma(VS_{Mn}^1)$ and $\Gamma(VS_{Mm}^2)$ with order n and m, respectively, $diam\left(\Gamma(VS_{Mn}^1) \otimes \Gamma(VS_{Mm}^2)\right) =$

$$\begin{cases} 4, & if\ m > 6 \\ 5, & if\ m \le 6, n > 4\ and\ (n,m) \neq (6,m), where\ gcd(6,m) \neq 1 \\ 7, & if\ (n,m) = (6,2),(6,3),(6,4) \end{cases}$$

Proof. We split the problem into the following cases:

Case 1: If $m > 6$, the diameter can be considered as the distance between (x_1, x_2) and (x_1, x_2^2) whenever n is a positive integer and m is even, which is given below:

$$(x_1, x_2) - (x_1^n, x_2^m) - (x_1^p, x_2^p) - (x_1^n, x_2^{m-1}) - (x_1, x_2^2)$$

where p is a prime number less than n and m in the first and second coordinate, respectively. Also, fr n a positive integer and m odd, the diameter can be viewed as the distance between (x_1, x_2) and (x_1^n, x_2) given as follows:

$$(x_1, x_2) - (x_1^n, x_2^m) - (x_1^p, x_2^p) - (x_1^{n-1}, x_2^m) - (x_1^n, x_2)$$

Hence, the diameter is 4.

Case 2: If $m \le 6, n > 4$ and $(n,m) \neq (6,3),(6,4)$. The diameter of the graph can be viewed as the distance between (x_1, x_2) and (x_1, x_2^m) whenever m is even and is given below:

$$(x_1, x_2) - (x_1^n, x_2^m) - (x_1^p, x_2^p) - (x_1^{p-2}, x_2^m) - (x_1^n, x_2) - (x_1, x_2^m)$$

Also, whenever m is odd, the diameter can be viewed as the distance between (x_1, x_2) and (x_1, x_2^m), given as:

$$(x_1, x_2) - (x_1^n, x_2^m) - (x_1^p, x_2^p) - (x_1^{n-1}, x_2^m) - (x_1^n, x_2) - (x_1, x_2^m)$$

Hence, the diameter is 5.

Case 3: Whenever $(n,m) = (6,2)$, the diameter can be viewed as the distance between (x_1, x_2) and (x_1, x_2^2), given as:

$$(x_1, x_2) - (x_1^6, x_2^2) - (x_1^5, x_2^1) - (x_1^3, x_2^2) - (x_1^4, x_2^1) - (x_1^5, x_2^2) - (x_1^6, x_2^1) - (x_1, x_2^2).$$

Whenever $(n,m) = (6,3)$, the diameter can be viewed as the distance between (x_1, x_2) and (x_1, x_2^3), given as:

$$(x_1, x_2) - (x_1^6, x_2^3) - (x_1^5, x_2^2) - (x_1^2, x_2^3) - (x_1^4, x_2^2) - (x_1^6, x_2^2) - (x_1^6, x_2^1) - (x_1^1, x_2^3).$$

Whenever $(n,m) = (6,4)$, the diameter can be viewed as the distance between (x_1, x_2) and (x_1, x_2^2), given as:

$$(x_1, x_2) - (x_1^6, x_2^4) - (x_1^5, x_2^3) - (x_1^3, x_2^2) - (x_1^4, x_2^3) - (x_1^5, x_2^2) - (x_1^6, x_2^3) - (x_1^1, x_2^2)$$

Hence, the diameter is 7.

2.3. Remark: Whenever $(n,m) = (6,6)$, the diameter is 6, which can be viewed as the distance between (x_1, x_2) *and* (x_1, x_2^2), given as:

$$(x_1, x_2) - (x_1^6, x_2^6) - (x_1^1, x_2^5) - (x_1^6, x_2^4) - (x_1^1, x_2^3) - (x_1^6, x_2^5) - (x_1^6, x_2^2).$$

2.4. Theorem: For any variation monogenic semigroup graphs $\Gamma(VS_{Mn}^1)$ and $\Gamma(VS_{Mm}^2)$, the girth of the graph $\Gamma(VS_{Mn}^1) \otimes \Gamma(VS_{Mm}^2)$ is

$$= \begin{cases} 3, & if\ n,m > 4 \\ 4, & if\ n > 4, and\ 1 < m \le 4 \\ 4, & if\ 1 < n \le 4, and\ m > 4 \\ not\ exists & if\ n \le 4\ and\ m \le 4 \end{cases}$$

Proof. Let p_1 and p_2 be the highest prime numbers less or equal to n and m, respectively. By definition of $\Gamma(VS_{Mn}^1) \otimes \Gamma(VS_{Mm}^2)$, for $n, m > 4$ we have:

$$(x_1^{p_1}, x_2^{p_2}) - (x_1^{p_1-1}, x_2^{p_2-1}) - (x_1^{p_1-2}, x_2^{p_2-2}) - (x_1^{p_1}, x_2^{p_2})$$

Since when $n, m > 4$ we have $gcd(p_i, p_i - 1) = 1$, $p_i + p_i - 1 > n, m$, $gcd(p_i - 1, p_i - 2) = 1$, $p_i - 1 + p_i - 2 > n, m$, $gcd(p_i, p_i - 2) = 1$, and $p_i + p_i - 2 > n, m$. So, $x_i^{p_i} - x_i^{p_i-1}$, $x_i^{p_i-1} - x_i^{p_i-2}$, and $x_i^{p_i} - x_i^{p_i-2}$, where $i = 1$ or 2.

For $n > 4$ and $1 < m \le 4$, we have that, if $m = 4$ or 3:

$$(x_1^{p_1}, x_2^3) - (x_1^{p_1-1}, x_2^2) - (x_1^{p_1-2}, x_2^3) - (x_1^{p_1-1}, x_2^2) - (x_1^{p_1}, x_2^3)$$

while if $m = 2$:

$$(x_1^{p_1}, x_2^2) - (x_1^{p_1-1}, x_2^1) - (x_1^{p_1-2}, x_2^2) - (x_1^{p_1-1}, x_2^1) - (x_1^{p_1}, x_2^2)$$

For $1 < n \le 4$ and $m > 4$, by using a similar argument as above, the result follows (exchange m with n in the above case).

For $n, m \le 4$, it is clear that $x_i^{p-1} x_i^{p-2} \neq 0$ since $2p - 3 \not> n, m$. Therefore, $(x_1^{p_1-1}, x_2^{p_2-1})$ is not adjacent to $(x_1^{p_1-2}, x_2^{p_2-2})$, which implies that there is no cycle connecting $(x_1^{p_1}, x_2^{p_2})$ for $n, m \le 4$.

Hence, the girth does not exist in this case.

For $n = 1$, it is clear from the definition of the tensor product that there is no vertex adjacent to the vertex (x_1, x_2^k). Hence, the result follows.

2.5. Example: Consider the graph $\Gamma(VS_{M5}) \otimes \Gamma(VS_{M10})$. Then, from the above results, $\Delta(\Gamma(VS_{M5}) \otimes \Gamma(VS_{M10})) = 24$, $\delta(\Gamma(VS_{M5}) \otimes \Gamma(VS_{M10})) = 1$, $diam(\Gamma(VS_{M5}) \otimes \Gamma(VS_{M10})) = 4$, and $girth(\Gamma(VS_{M5}) \otimes \Gamma(VS_{M10})) = 3$. While, the graph $\Gamma(VS_{M7}) \otimes \Gamma(VS_{M4})$ has $\Delta(\Gamma(VS_{M7}) \otimes \Gamma(VS_{M4})) = 12$, $\delta(\Gamma(VS_{M7}) \otimes \Gamma(VS_{M4})) = 1$, $diam(\Gamma(VS_{M7}) \otimes \Gamma(VS_{M4})) = 5$, and $girth(\Gamma(VS_{M7}) \otimes \Gamma(VS_{M4})) = 4$.

The following definition apeared in Al Subaiei and Akwu (2020).

2.6. Definition: For a postive integer n, the set $\pi(n) = \{p_1, p_2, \dots, p_k\}$ is the set of consecutive prime numbers less or equal to n such that $p_t + p_{t+1} > n$ and $\pi^*(n) = |\pi(n)|$. Also, for positive integers s_f^* where $\lceil \frac{n}{2} \rceil < s_f^* \leq n$ and the following is satisfied:

1. $s_f^* \notin \pi(n)$
2. $gcd(s_f^*, p_f) = 1$ for all $p_f \in \pi(n)$
3. $gcd(s_f^*, s_l^*) = 1$ for any pair $\lceil \frac{n}{2} \rceil < s_f^*, s_l^* \leq n$

the numbers of s_f^* are denoted by $S^* = |s_f^*|$.

For simplicity, suppose that the graph $\Gamma(VS_{Mn}^1)$ has $\pi^*(n)$ and S_1^*, while the graph $\Gamma(VS_{Mm}^2)$ has $\pi^*(m)$ and S_2^*. It is also known from Al Subaiei and Akwu (2020) that $\mathcal{X}\big(\Gamma(VS_{Mn})\big) = \omega\big(\Gamma(VS_{Mn})\big) = \pi^*(n) + S_1^*$. By using these facts, we establish the following theorems on the chromatic number, clique number and domination number of $\Gamma(VS_{Mn}^1) \otimes \Gamma(VS_{Mm}^2)$.

2.7. Theorem: For any variation monogenic semigroup graphs $\Gamma(VS_{Mn}^1)$ and $\Gamma(VS_{Mm}^2)$, the chromatic number of $\Gamma(VS_{Mn}^1) \otimes \Gamma(VS_{Mm}^2)$ is given as:

$$\mathcal{X}(\Gamma(VS_{Mn}^1) \otimes \Gamma(VS_{Mm}^2)) = \begin{cases} \pi^*(n) + S_1^*, & if\ n \leq m \\ \pi^*(m) + S_2^*, & if\ m < n \end{cases}$$

Proof. Suppose that $n < m$. From the definition of $\pi(n)$ and $\pi(m)$, we know that $(x_1^{p_f}, x_2^{p_l}) - (x_1^{p_t} x^{p_h})$ for any $p_f, p_t \in \pi(n)$ and $p_l, p_h \in \pi(m)$. Also, we know from the definition of the tensor product that $(x_1^{p_f}, x_2^{p_l})$ is neither adjacent to $(x_1^{p_t}, x_2^{p_l})$ nor $(x_1^{p_f}, x^{p_h})$. Since $n < m$, $\pi^*(n) \leq \pi^*(m)$. Then, we can assign all vertices that have the same first coordinator to the same color. For example, all $p_l \in \pi(m)$, $(x_1^{p_f}, x_2^{p_l})$ will be in the same color. Therefore, we need $\pi^*(n)$ distinct colors.

Consider the vertex $(x_1^{p_f}, x_2^{p_l})$ where $p_f \in \pi(n)$ and $p_l \in \pi(m)$. Then, for any prime numbers r, z that satisfy $r \notin \pi(n)$ or $z \notin \pi(m)$, it is clear that the vertices (x_1^r, x_2^j) and (x_1^i, x_2^z) where $1 \leq i \leq n$ and $1 \leq j \leq m$ can be assigned the same color as $(x_1^{p_f}, x_2^{p_l})$. If color C_1 is assigned to vertex $(x_1^{p_f}, x_2^{p_l})$ where $p_f \in \pi(n)$ and $p_l \in \pi(m)$, then it is obvious that $x_1^r x_1^{p_f} \notin E(\Gamma(VS_{Mn}^1))$ and $x_2^z x_2^{p_l} \notin E(\Gamma(VS_{Mn}^2))$. This implies that color C_1 can be assigned to all vertices (x_1^r, x_2^j) and (x_1^i, x_2^z) where $1 \leq i \leq n$ and $1 \leq j \leq m$.

Now, consider the set of vertices $(x_1^{s_{1f}^*}, x_2^{s_{2l}^*})$, $(x_1^{s_{1e}^*}, x_2^{s_{2q}^*})$ such that $s_{1f}^*, s_{1e}^* \notin \pi(n)$, $s_{2l}^*, s_{2q}^* \notin \pi(m)$, $\lceil \frac{n}{2} \rceil < s_{1f}^*, s_{1e}^* \leq n$, and $\lceil \frac{m}{2} \rceil < s_{2l}^*, s_{2q}^* \leq m$. From the definition of s_{1f}^* and s_{2l}^*, we have $(x_1^{s_{1f}^*}, x_2^{s_{2l}^*}) - (x_1^{s_{1e}^*}, x_2^{s_{2q}^*})$ and $(x_1^{p_f}, x_2^{p_l}) - (x_1^{s_{1f}^*}, x_2^{s_{2l}^*})$. Moreover, we know from the definition of the tensor product that $(x_1^{s_{1f}^*}, x_2^{s_{2l}^*})$ is neither adjacent with $(x_1^{s_{1f}^*}, x_2^{s_{2q}^*})$ nor $(x_1^{s_{1e}^*}, x_2^{s_{2l}^*})$. Since $n < m$, $S_1^* \leq S_2^*$. Therefore, S_1^* needs more colors for the vertices $(x_1^{s_{1f}^*}, x_2^{s_{2l}^*})$. The leftover vertices (x_1^g, x_2^h), where $1 < g \leq n$ and $1 < h \leq m$, can be assigned to one of the colors assigned to vertices $(x_1^{s_{1f}^*}, x_2^{s_{2l}^*})$ if $gcd(g, s_{1f}^*) \neq 1$ and $gcd(h, s_{2l}^*) \neq 1$. The vertex (x_1, x_2) can be assigned to any color that has not been assigned to (x_1^n, x_2^m). Therefore, there are $\pi^*(n) + S_1^*$ colors needed to color the graph $\Gamma(VS_{Mn}^1) \otimes \Gamma(VS_{Mm}^2)$. If $m < n$, by using a similar argument, we can show that there are $\pi^*(m) + S_2^*$ colors needed to color the graph $\Gamma(VS_{Mn}^1) \otimes \Gamma(VS_{Mm}^2)$.

2.8. Theorem: For any variation monogenic semigroup graphs $\Gamma(VS_{Mn}^1)$ and $\Gamma(VS_{Mm}^2)$, the clique number of $\Gamma(VS_{Mn}^1) \otimes \Gamma(VS_{Mm}^2)$ is given as:

$$\omega(\Gamma(VS_{Mn}^1) \otimes \Gamma(VS_{Mm}^2)) = \begin{cases} \pi^*(n) + S_1^*, & if\ n \leq m \\ \pi^*(m) + S_2^*, & if\ m < n \end{cases}$$

Proof. Suppose that $n < m$. From the definition of $\pi(n)$ and $\pi(m)$, we know that $(x_1^{p_f}, x_2^{p_l}) - (x_1^{p_t} x^{p_h})$ for any $p_f, p_t \in \pi(n)$ and $p_l, p_h \in \pi(m)$. Also, we know from the definition of the tensor product that $(x_1^{p_f}, x_2^{p_l})$ is neither adjacent to $(x_1^{p_t}, x_2^{p_l})$ nor $(x_1^{p_f}, x^{p_h})$. As $\pi^*(n) \leq \pi^*(m)$ shows, there are $\pi^*(n)$ different vertices that are adjacent to each other. Next, consider the set of vertices $(x_1^{s_{1f}^*}, x_2^{s_{2l}^*}), (x_1^{s_{1e}^*}, x_2^{s_{2q}^*})$ such that $s_{1f}^*, s_{1e}^* \notin \pi(n)$, $s_{2l}^*, s_{2q}^* \notin \pi(m)$, $\lceil \frac{n}{2} \rceil < s_{1f}^*, s_{1e}^* \leq n$, and $\lceil \frac{m}{2} \rceil < s_{2l}^*, s_{2q}^* \leq m$. From the definition of S_1^* and S_2^*, we know that $(x_1^{s_{1f}^*}, x_2^{s_{2l}^*}) - (x_1^{s_{1e}^*}, x_2^{s_{2q}^*})$ and $(x_1^{p_f}, x_2^{p_l}) - (x_1^{s_{1f}^*}, x_2^{s_{2l}^*})$ where $p_f \in \pi(n)$ and $p_l \in \pi(m)$. Since $S_1^* \leq S_2^*$, there are more S_1^* vertices in the clique.

Suppose that p_1 and p_2 are the least prime numbers in $\pi(n)$ and $\pi(m)$, respectively. Consider the vertices (x_1^k, x_2^z), where $1 \leq k < p_1$ and $1 \leq z < p_2$. The vertex (x_1^k, x_2^z) is not adjacent to $(x_1^{p_f}, x_2^{p_l})$ since $k + p_1 < n$ and $k + p_2 < m$. Moreover, (x_1^k, x_2^z) is not adjacent to $(x_1^{s_{1f}^*}, x_2^{s_{2l}^*})$ since $k + s_{1f}^* < n$ and $k + s_{2l}^* < m$. Therefore, the clique number is $\pi^*(n) + S_1^*$ when $m < n$, and by using a similar argument, we can show that $\pi^*(m) + S_2^*$ is the clique number.

Using the knowledge of relatively prime numbers to study the structure of tensor product graphs of the variation monogenic semigroup, as well as observing Theorem 2.7 and Theorem 2.8, since

$$\mathcal{X}(\Gamma(VS_{Mn}^1) \otimes \Gamma(VS_{Mm}^2)) = \omega(\Gamma(VS_{Mn}^1) \otimes \Gamma(VS_{Mm}^2)) = \begin{cases} \pi^*(n) + S_1^*, & if\ n \leq m \\ \pi^*(m) + S_2^*, & if\ m < n \end{cases}$$

we discover that the graph $\Gamma(VS_{Mn}^1) \otimes \Gamma(VS_{Mm}^2)$ preserves the perfectness property, as stated in the next lemma.

2.9. Lemma: The graph $\Gamma(VS_{Mn}^1) \otimes \Gamma(VS_{Mm}^2)$ is a perfect graph.

The tensor product graph of the monogenic semigroup $\Gamma(S_{Mn}^1) \otimes \Gamma(S_{Mm}^2)$ of Akgunes *et al.* (2014) proved that $\mathcal{X}\Big(\Gamma(S_{Mn}^1) \otimes \Gamma(S_{Mm}^2)\Big) = Min\Big(\mathcal{X}\Big(\Gamma(S_M^1)\Big), \mathcal{X}\Big(\Gamma(S_M^2)\Big)\Big)$. This result is also true for the tensor product graph of the variation monogenic semigroup, which can be deduced from Theorem 2.7. So, $\mathcal{X}\Big(\Gamma(VS_{Mn}^1) \otimes \Gamma(VS_{Mm}^2)\Big) = Min(\mathcal{X}(\Gamma(VS_M^1)), \mathcal{X}(\Gamma(VS_M^2)))$.

From Akgunes *et al.* (2014), the domination number of the tensor product of the graph of the monogenic semigroup is 3. However, the domination number of the tensor product of the variation monogenic semigroup graph cannot possibly be 3, as shown below and from Theorem 2.11 in Al Subaiei and Akwu (2020).

2.10. Theorem: For any variation monogenic semigroup graphs $\Gamma(VS_{Mn}^1)$ and $\Gamma(VS_{Mm}^2)$, the domination number of $\Gamma(VS_{Mn}^1) \otimes \Gamma(VS_{Mm}^2)$ is given as:

$$\gamma(\Gamma(VS_{Mn}^1) \otimes \Gamma(VS_{Mm}^2)) = \begin{cases} 2\gamma(\Gamma(VS_{Mn}^1))\gamma(\Gamma(VS_{Mm}^2)), & n\ or\ m\ prime \\ \gamma(\Gamma(VS_{Mn}^1))\gamma(\Gamma(VS_{Mm}^2)), & Otherwise \end{cases}$$

Proof. According to Al Subaiei and Akwu (2020), the domination number of any graph $\Gamma(VS_{Mn})$ is as follows:

- If n is prime, then from $\gamma(\Gamma(VS_{Mn})) = 1$ say x^n.
- If n is not prime and $n - p$ does not contain a prime number t such that $gcd(n, t) \neq 1$, where p is the highest prime number less or equal to n. Then, we need one more vertex, say x^p, such that $\gamma(\Gamma(VS_{Mn})) = 2 = |\{x^n, x^p\}|$.
- If $n - p$ contains a prime number t such that $gcd(n, t) \neq 1$ and $p + t < n$, then we need the additional vertex $x^r, p < r < n$ such that $r + t > n$ and $gcd(r, t) = 1$. Therefore, $\gamma(\Gamma(VS_{Mn})) = 3 = |\{x^n, x^r, x^p\}|$.
- If $n - p$ contains t and q where t is a prime number and $q \equiv 0\ (mod\ t)$ such that $gcd(n, t) \neq 1$, $p + t < n$ and $p + q < n$. Also, for r, where $p < r < n$, $gcd(r, t) = 1$, and $r + t > n$ but $gcd(r, q) \neq 1$. Also, since $gcd(n, t) \neq 1$, we have $gcd(q, n) \neq 1$. Therefore, we need vertex x^s, $p < s < n$ such that $s + q > n$ and $gcd(s, q) = 1$. Then, $\gamma(\Gamma(VS_{Mn})) = 4 = |\{x^n, x^r, x^s, x^p\}|$.

Now, from the above, let $\gamma(\Gamma(VS^1_{Mn})) = k$ and $\gamma(\Gamma(VS^2_{Mm})) = l$. Next, we split the problem into the following two cases:

Case 1: When n and m are both prime or when n or m is prime.

If n is prime and m is not or n and m are both prime, let D represent the domination number and construct $(k + 1) \times l$ Latin square, where $k + 1 = \{x^n, x^{n-1}\}$. Also, if m is prime and n is not, construct $k \times (l + 1)$ Latin square, where $l + 1 = \{x^m, x^{m-1}\}$. Then, the Latin square $(k + 1) \times l$ or $k \times (l + 1)$ gives $2\gamma(\Gamma(VS^1_{Mn}))\gamma(\Gamma(VS^2_{Mm}))$. All vertices of $\Gamma(VS^1_{Mn}) \otimes \Gamma(VS^2_{Mm}) \backslash 2\gamma(\Gamma(VS^1_{Mn}))\gamma(\Gamma(VS^2_{Mm}))$ are adjacent to at least one vertex in $2\gamma(\Gamma(VS^1_{Mn}))\gamma(\Gamma(VS^2_{Mm}))$. Therefore, we have $D = 2\gamma\left(\Gamma(VS^1_{Mn})\right)\gamma\left(\Gamma(VS^2_{Mm})\right)$, which is the desired result.

Case 2: When both n and m are not prime.

Construct Latin square $k \times l$ where k takes care of n number of rows and l takes care of m number of columns. Hence, the Latin square $k \times l$ gives $\gamma\left(\Gamma(VS^1_{Mn})\right)\gamma\left(\Gamma(VS^2_{Mm})\right)$, which is the domination number of $\Gamma(VS^1_{Mn}) \otimes \Gamma(VS^2_{Mm})$ whenever n and m are not prime, since all vertices in $\Gamma(VS^1_{Mn}) \otimes \Gamma(VS^2_{Mm}) \backslash \gamma(\Gamma(VS^1_{Mn}))\gamma(\Gamma(VS^2_{Mm}))$ are adjacent to at least one vertex in $\gamma(\Gamma(VS^1_{Mn}))\gamma(\Gamma(VS^2_{Mm}))$.

2.11. Example: Consider the graph $\Gamma(VS_{M10}) \otimes \Gamma(VS_{M9})$. Then, $\mathcal{X}(\Gamma(VS_{M10}) \otimes \Gamma(VS_{M9})) = 4$, $\gamma(\Gamma(VS_{M10}) \otimes \Gamma(VS_{M9})) = 6$, and $\omega(\Gamma(VS_{M10}) \otimes \Gamma(VS_{M9})) = 4$. While the graph $\Gamma(VS_{M8}) \otimes \Gamma(VS_{M6})$ *has* $\mathcal{X}(\Gamma(VS_{M8}) \otimes \Gamma(VS_{M6})) = 3$, $\gamma(\Gamma(VS_{M8}) \otimes \Gamma(VS_{M6})) = 4$, and $\omega(\Gamma(VS_{M8}) \otimes \Gamma(VS_{M6})) = 3$.

Lastly, we draw our conclusion with the following remark.

2.12. Remark: The tensor product graph $\boldsymbol{\Gamma(VS^1_{Mn}) \otimes \Gamma(VS^2_{Mm})}$ can be viewed as a coprime graph. By Equation $(*)$ and definition of $\boldsymbol{\Gamma(VS^1_{Mn}) \otimes \Gamma(VS^2_{Mm})}$, we have that any pair of vertices in $\boldsymbol{\Gamma(VS^1_{Mn}) \otimes \Gamma(VS^2_{Mm})}$ are adjacent if and only if their labels are relatively prime.

Biographies

Abolape Deborah Akwu

Department of Mathematics, College of Science, Federal University of Agriculture, Makurdi, Nigeria, abolaopeyemi@yahoo.co.uk, 002348055960217

Dr Akwu recieved her PhD and Master's degree from the University of Ibadan, Ibadan, Nigeria in Graph Theory and Abstract Algebra, respectively. She has conducted research on graph theory and algebra-related topics, such as the decomposition of equipartite graphs into edge-disjoint sunlet graphs, outer connected vertex-edge domination number of graphs, decomposition of tensor product graphs into cycle of even length, Neutrosophic groups and Neutrosophic rings. Also, she published articles in journal indexes in Scopus, ISI and MathScinet. ORCID ID: 0000-0002-4665-5040

Bana Al Subaiei

Department of Mathematics and Statistics, College of Science, King Faisal University, Al Ahsa, Saudi Arabia, banajawid@kfu.edu.sa, 00966500816416

Dr Al Subaiei is a Saudi assistant professor in the Mathematics and Statistics Department and has been Vice Dean of Preparatory Year Deanship from 2017 until present. She got her PhD and Master's degrees from the University of Southampton, Southampton, United Kingdom. She has published papers in ISI and Scopus journals. She joined many committees at the department level, college level and university level, such as the main committee of scientific chairs and the committee of development and quality assurance at the College of Science. ORCID ID: 0000-0001-6279-4959

References

Akgunes, N., Das, K. C. and Sinan Cevik, A. (2014). Some properties on the tensor product of graphs obtained by monogenic semigroups. *Applied Mathematics and Computation,* **235**, 352–7.

Al Subaiei, B. and Akwu, A. D. (2020). The zero-divisor graph of variation monogenic semigroups. *Sci. J. King Faisal Univ.,* **21**(2), 189–93. DOI: 10.37575/b/sci/0016

Anderson, D. F. and Badawi, A. (2017). 'The zero-divisor graph of a commutative semigroup: A survey'. *In*: M. Droste, L. Fuchs, B. Goldsmith and L. Strüngmann. (eds.) *Groups, Modules, and Model Theory - Surveys and Recent Developments,* 23–39. Cham: Springer. DOI: 10.1007/978-3-319-51718-6_2

Asmerom, G. A. (1998). Imbeddings of the tensor product of graphs where the second factor is a complete graph. *Discrete Mathematics,* **182**(n/a), 13–9.

Bondy, J. A. and Murty, U. S. (1976). *Graph Theory with Applications*. New York: Elsevier Science Publishing Co., Inc.

Das, K. C., Akgunes, N. and Sinan Cevik, A. (2013). On a graph of monogenic semigroups. *Journal of Inequalities and Applications,* **2013**(1), 1–13.

DeMeyer, F. R. and DeMeyer, L. (2005). The zero-divisor graphs of semigroups. *J. Algebra,* **283**(1), 190–8.

DeMeyer, F. R., McKenzie, T. and Schneider, K. (2002). The zero-divisor graph of a commutative semigroups. *Semigroup Forum,* **65**(2), 206–14.

Harary, F. and Trauth, Jr., C. A. (1966). Connectedness of products of two directed graphs. *SIAM Journal on Applied Mathematics,* **14**(2), 250–4.

Lovasz, L. (1972). Normal hypergraphs and the weak perfect graph conjecture. *Discrete Math,* **2**(3), 253–67.

Sampathkumar, E. (1972). On tensor product graphs. *Journal of the Australian Mathematical Society,* **20**(3), 268–73.

Wright, S. E. (2007). Lengths of paths and cycles in zero-divisor graphs and digraphs of semigroups. *Commun. Algebra*, **35**(6), 1987–91.

المجلة العلمية لجامعة الملك فيصل
The Scientific Journal of King Faisal University
العلوم الأساسية والتطبيقية
Basic and Applied Sciences

فعالية أغشية متركبة نانوية ضد البكتيريا الممرضة المنقولة بالأغذية إيجابية الغرام وسلبية الغرام

خالد سيف الدين [1]، سحر الحريري [1]، عدنان علي نظام [2]، عبيده الحجلي [2]
[1] قسم الكيمياء، كلية العلوم، جامعة دمشق، دمشق، سوريا
[2] قسم علم الحياة النباتية، كلية العلوم، جامعة دمشق، دمشق، سوريا

The Effectiveness of Nanocomposite Films Against Gram-Positive and Gram-Negative Foodborne Pathogenic Bacteria

Khaled Saif-Aldin [1], Sahar Al-Hariri [1], Adnan Ali-Nizam [2] and Obaida Alhajali [2]
[1] Department of Chemistry, Faculty of Science, Damascus University, Damascus, Syria
[2] Department of Plant Biology, Faculty of Science, Damascus University, Damascus, Syria

LINK الرابط	RECEIVED الاستقبال	ACCEPTED القبول	PUBLISHED ONLINE النشر الإلكتروني	ASSIGNED TO AN ISSUE الإحالة لعدد
https://doi.org/10.37575/b/sci/210049	17/08/2021	17/09/2021	12/09/2021	01/12/2021

NO. OF WORDS عدد الكلمات	NO. OF PAGES عدد الصفحات	YEAR سنة العدد	VOLUME رقم المجلد	ISSUE رقم العدد
5577	6	2021	22	2

الملخص

في هذا البحث حُضرت مواد مُتركبة نانوية مكونة من مزيج بوليمر البولي ايثلين منخفض الكثافة الخطي (LLDPE) وجُسيمات أكسيد الزنك النانوي (ZnO-NPs)، وشُكل منها أغشية بخمسة تراكيز وزنية 0.25، 0.5، 1، 2.5، 5% إضافة إلى LLDPE الصرف، بغرض التحقق من دور المواد النانوية في تحسين أداء بعض خصائص بوليمر LLDPE كزيادة العمر الافتراضي للمنتجات الغذائية وحماية المستهلك من البكتيريا المُمرضة في تطبيقات تغليف الغذاء. إذ جرى تقييم الفعالية ضد البكتيريا الممرضة الإشريكية القولونية، والمكورات العنقودية الذهبية، من خلال المعيار"ISO 22196". تؤكد نتائج الاختبار أن الأغشية المتركبة النانوية التي تحتوي على نسب 0.5% فأكثر من أكسيد الزنك النانوي لها فعالية مثبطة لنمو البكتيريا، وتزداد هذه الفعالية بازدياد ZnO-NPs في الطور البوليميري LLDPE، وأن أعلى تأثير مُضاد للبكتيريا كان في الأغشية المتركبة النانوية ذات النسبة 5% وزناً. وتبيّن أن البكتيريا إيجابية الغرام كانت أكثر حساسية لجُسيمات أكسيد الزنك النانوي مقارنة بسلبية الغرام وأنه يُمكن لهذه الأغشية المتركبة النانوية أن توفر طريقة آمنة لحفظ الأغذية دون الحاجة إلى مُعالجة الغذاء.

ABSTRACT

In this research, nanocomposites consisting of a mixture of linear low-density polyethylene polymer (LLDPE) and zinc oxide nanoparticles (ZnO-NPs) were prepared. The films of the composite material were formed with five weight ratios (0.25, 0.5, 1, 2.5, and 5wt%) in addition to pure LLDPE, intended to investigate the role of nanomaterials in improving the performance of some properties of LLDPE polymer such as increasing the shelf life of food products and protecting the consumer from pathogenic germs in food packaging applications. The efficacy was evaluated against pathogenic bacteria, Escherichia coli and Staphylococcus aureus, through the standard "ISO 22196". The test results confirm that the nanocomposite films containing 0.5wt% or more of nano-zinc oxide have bacteriostatic activity. This activity increases with the increase of ZnO-NPs in the LLDPE polymeric phase, and the highest antibacterial effect was in the nanocomposite films of 5wt%. It was found that gram-positive bacteria were more sensitive to ZnO-NPs than gram-negative bacteria and that these nanocomposite films can provide a safe way to preserve food without the need for food processing.

KEYWORDS
الكلمات المفتاحية
Nanocomposite films, zinc oxide nanoparticles, anti-microbial, challenge tests, food packaging
أغشية مُتركبة نانوية، أكسيد الزنك النانوي، الفعالية المضادة للأحياء الدقيقة، اختبار التحدي، تغليف الغذاء

CITATION
الإحالة
Saif-Aldin, K. Al-Hariri, S. Nizam, A.A. and Alhajali, O. (2021). Faeaaliat 'ughshiat mutrkbt nanawiat dida albaktirya almumrdt almanqulat bial'aghdhiat 'iijabiat algharam wasalbiat algharam 'The effectiveness of nanocomposite Films against gram-positive and gram-negative foodborne pathogenic bacteria'. *The Scientific Journal of King Faisal University: Basic and Applied Sciences*, **22**(2), 65–70. DOI: 10.37575/b/sci/210049 [in Arabic]
سيف الدين، خالد والحريري، سحر ونظام، عدنان علي والحجلي، عفيده. (2021). تقييم فعالية أغشية مُتركبة نانوية ضد البكتيريا المُمرضة المنقولة بالأغذية إيجابية الغرام وسلبية الغرام. *المجلة العلمية لجامعة الملك فيصل: العلوم الأساسية والتطبيقية*، **22**(2)، 65-70.

1. المقدمة

تُمثل التعبئة والتغليف دوراً حاسماً في سلسلة الإمداد الغذائي، فعندما لا تُستهلك الأغذية بعد الإنتاج مُباشرة فإنها يجب أن تكون موجودة في حزمة تُلبي العديد من الوظائف، لهذا تتمثل المهمة الرئيسة للتعبئة والتغليف في أن تكون بمثابة حاوية للغذاء تُمكن النقل الفعال في سلسلة التوريد والإمداد بأكملها من الإنتاج حتى الاستهلاك النهائي وذلك من خلال منع أي تغييرات كيميائية أو بيولوجية غير مرغوب فيها، وأن تُشكل العبوة أو الغلاف حاجزاً لحماية الأغذية من التأثيرات البيئية، مثل: الضوء والغبار والرطوبة والأكسجين والتلوث الكيميائي والميكروبيولوجي، ما يحول دون وقوع أي أضرار مادية، إضافة إلى الحماية من التلاعب والسرقة (Hashim, 2011).

تُعّد المواد المُتركبة النانوية فئة جديدة من المواد المُتركبة التي تلقت اهتماماً خاصاً بسبب خصائصها المُحسِنة في النسب المنخفضة جداً مُقارنة بالمواد المالئة التقليدية الأخرى، حيث يمكن لتكنولوجيا النانو المُدخلة حديثاً في صناعة تعبئة وتغليف الغذاء أنْ تُقدِّم حلولاً لتحدِّيات تعبئة وتغليف الغذاء، كنمو الأحياء الدقيقة وقِصَر فترة الصلاحية وبالتالي الحد من فقدان الأغذية. ونتيجة الحاجة لتحسين وظيفة التعبئة والتغليف المتمثلة بالحماية تطورت تقنيات التعبئة والتغليف الجديدة مثل التعبئة والتغليف الفعّال Active Packaging التي تُعرف بأنها نهج مُبتكر لإطالة فترة صلاحية المنتجات الغذائية والحفاظ عليها مع ضمان الجودة والسلامة لها، وتُعد هذه النُظم القائمة على المواد النانوية اللاعضوية جيلاً واعداً من نُظم تعبئة وتغليف المواد الغذائية التي تُحضر من خلال دمج الجُسيمات النانوية اللاعضوية في أغشية البوليمر (Emamifar *et al.*, 2010 : Vilela *et al.*, 2018)

تُعدّ المواد المتركبة النانوية أكثر المجالات نمواً في مجال تكنولوجيا النانو حالياً (Kuorwel *et al.*, 2015). وتحديداً المواد الفعَّالة الملامسة للأغذية والتي تضم جُسيمات نانوية بخصائص مُضادة للأحياء الدقيقة أو كاسحة Scavenging للأكسجين (Hashim, 2011). يُطلق مصطلح المواد المُلامسة للغذاء على المواد والأدوات articles التي تكون على تماس مُباشر مع الغذاء في أثناء إنتاج الغذاء ومعالجته وتخزينه وإعداده وتقديمه (Simoneau *et al.*, 2016). وتؤدي التطورات الجديدة في مجال التقانة النانوية (لاسيما المقدرة على اصطناع أكاسيد معادن نانوية ذات الأيونية العالية بأي شكل أو حجم) إلى تطوير عوامل جديدة مُضادة للبكتيريا. وتكمن ميزة استعمال بعض أكاسيد المعادن النانوية مثل: MgO و CaO و ZnO بأنها تحتوي على عناصر معدنية ضرورية للإنسان، وتبدي فعالية قوية حتى لو أعطيت بكميات قليلة. ومن المتوقع أن

Corresponding Author: Khaled Saif-Aldin 00963934568727, kh.h.saif@gmail.com المؤلف المراسل: خالد سيف الدين

توفر جُسيمات أكسيد الزنك النانوي ZnO-NPs حلولاً لتعبئة وتغليف غذاء آمن ومتاح على نحو أكبر في المستقبل نتيجة لشفافيته الجيدة وثباته الفيزيائي والكيميائي عند درجات الحرارة المرتفعة وكذلك لسعره المنخفض، كما أن إدارة الغذاء والدواء الأمريكية FDA أدرجته مؤخراً واعتُمد كمادة آمنة "GRAS, 21CFR182.8991" (Bisht *et al.*, 2016; Hashim., 2011). وتم اعتمادها كذلك كمادة مالئة مُلامسة للغذاء في البوليميرات من قبل هيئة سلامة الأغذية الأوروبية EFSA في الإصدار رقم 1050 (EFSA, 2016). ونظراً إلى أن التلوث بالأحياء الدقيقة يحدث في الغالب على سطح المُنتج الغذائي، فإن الأساس المنطقي لتطبيق التغليف الفعّال هو منع نمو هذه الأحياء الدقيقة على سطح المُنتج الغذائي من خلال تماس الأغشية المُعالجة مع سطح المادة الغذائية (Orsuwan *et al.*, 2019). ومع ذلك، فإن تسويق المواد المُتركبة المضادة للأحياء الدقيقة يتطلب إثبات فعاليتها التي تحدث عادةً باستعمال طرائق مختبرية يُطلق عليها اختبارات التحدي Challenge Tests وهي إجراءات يتم فيها تحدي المنتج من خلال تعريضه لأنواع مُحددة من البكتيريا والفطريات لتحديد ما إذا كان يتم الحفاظ عليه على نحو مناسب (Russell, 2003). تُصنّف الطرائق التي تُحدد طابع المواد المضادة للأحياء الدقيقة اعتماداً على نتيجة الاختبارات إلى: طرائق كمية Quantitative وطرائق نوعية Qualitative. لا تقدم الطرائق النوعية نتائج قابلة للقياس الكمي إنما يمكن التعبير عن النتائج على أنها "سلبية" أو "إيجابية"، وتُشير الطرائق الكمية إلى مستوى تلوث المواد المدروسة من خلال إحصاء نتائج الاختبار، لذلك تكون هذه الطرائق هي أكثر استعمالاً، ومعظم الطرائق الكمية حساسة Sensitive إلى حد كاف لكنها مُرْهِقة وتستغرق وقتاً طويلاً في مُراقبة الجودة الروتينية واختبارات الفحص (Damian *et al.*, 2014). من طرائق الاختبارات المعيارية الكمية المتاحة لتقييم الفعالية المضادة للأحياء الدقيقة للأسطح أو المواد المُتركبة المُعالجة تبعاً لطبيعتها وشكلها؛ الطريقة "TM 100" الصادرة عن الجمعية الأمريكية لكيميائي النسيج ومُلونيه AATCC، لتقييم مدى فعالية المواد النسيجية المُعالجة المضادة للأحياء الدقيقة (AATCC, 2019). وطريقة اختبار اهتزاز القارورة الديناميكي "ASTM E2149" الصادرة عن الجمعية الأمريكية لاختبار المواد ASTM وهذه الطريقة معنية بتحديد الفعالية المضادة للأحياء الدقيقة لمضادات حيوية ثابتة-غير مُنحلة (زجاج، سيراميك، لدائن، حُبيبات) تحت ظروف التَّماس الديناميكي، إذ تُغمر العينة المُعالجة في كمية وافرة من وسط الاستزراع السائلliquid culture medium (ASTM, 2013). أخيراً طريقة الاختبار اليابانية "JIS Z 2801" التي توفر قياس الفعالية المضادة للبكتيريا على اللدائن والأسطح غير المسامية التي اعتُمدت عام 2007 كطريقة مُعترف بها من قبل المنظمة الدولية للمعايير بترميز "ISO 22196"، وفيها تُستعمل كمية قليلة من وسط الاستزراع السائل لتغطية العينة المُعالجة، ويُستعمل هذا الاختبار على نطاق واسع في الشركات المُصنعة لأنه يتيح الفرصة لسطح المادة المضادة للبكتيريا التَّماس مع وسط الاستزراع السائل للتحقق من فعالية المُنتج قبل تسويقه (Campos *et al.*, 2016; ISO, 2011).

يهدف هذا البحث إلى تحضير وتشكيل أغشية بوليمرات مُتركبة نانوية من جُسيمات أكسيد الزنك النانوي ZnO-NPs كمادة مالئة والبولي ايثلين منخفض الكثافة الخطي LLDPE كطور رابط، وتقييم فعالية هذه الأغشية ضد نوعين من البكتيريا المُمرضة المنقولة بالأغذية هما *الإشريكيّة القولونيّة والمكوّرات العنقوديّة الذهبية* من خلال المعيار القياسي "ISO 22196".

2. المواد وطرائق العمل

2.1. تحضير وتشكيل الأغشية المتركبة النانوية:

حُضرت التراكيز الوزنية للمواد المُتركبة النانوية LLDPE/ZnO-NPs بطريقة مزج الصهارة Melt Blending (Alghdeir *et al.*, 2019). حيث ضُبطت درجة حرارة جهاز الخلاط الحراري ثنائي اللولب عند 130°C وأضُيف 36g من حُبيبات LLDPE الصرف مُباشرة في حجرة الجهاز بالتزامن مع دوران اللولب المزدوج بسرعة 50rpm، وأضُيف بعدها 4g من جسيمات ZnO النانوي التي تم اصطناعها والتحقق من فعاليتها مسبقاً (Saif-Aldin *et al.* 2020). جرى إضافة جسيمات ZnO على نحو تدريجي واستمر المزج مدة 10 دقائق لضمان تجانس وتشتت أفضل للجُسيمات النانوية في الراتنج Resin. وبذلك تم الحصول على عجينة مُركزة master batch من المادة المتركبة تحتوي 10% وزناً من ZnO النانوي. ثم أُخذ أجزاء من العجينة المُركزة ومُزجت مع حبيبات LLDPE بكميات مُناسبة للحصول على النسب المئوية الوزنية الآتية 0.25% و0.5% و 1% و 2.5% و 5% باستعمال الخلاط الحراري ثنائي اللولب نفسه وعند شروط المزج نفسها كما هو موضح في الجدول(1). شُكلت عينات الأغشية الرقيقة Film بطريقة القولبة بالكبس والتسخين عند 140°C تحت ضغط 50 بار باستعمال جهاز المكبس الحراري الهيدروليكي وقالب بلاستيكي مقاوم للحرارة بسماكة 120µm، حُصل على أغشية ذات أبعاد 120µm × 15cm × 15cm من LLDPE الصرف والتراكيز الوزنية الأخرى المطلوبة.

الجدول (1): تحضير التراكيز المئوية الوزنية للبوليميرات المتركبة النانوية LLDPE/ZnO-NPs.

النسبة المئوية الوزنية wt% للمادة المتركبة النانوية	العجينة المركزة wt 10% LLDPE/ZnO-NPs (g)	البولي ايثلين منخفض الكثافة الخطي LLDPE (g)
%0	0	40
%0.25	1	39
%0.5	2	38
%1	4	36
%2.5	10	30
%5	20	20

2.2. تحضير المحاليل وأوساط الاستزراع المُغذية واللَقاح:

2.2.1. الآغار المغذي

وهو وسط تنمية صلب عام (غير انتقائي) استُعمل لتقدير التعداد العام للبكتيريا. حُضر بحل 28g لكل 1000mL ماء مقطر، وعُقم بالاوتوكلاف Autoclave مدة 20 دقيقة في درجة حرارة 121°C عند 1ضغط جوي (يُصب في أطباق بتري بعد انخفاض درجة حرارته إلى نحو 45°C).

2.2.2. المرق المغذي

وهو وسط تنمية سائل غير انتقائي حُضر بحل 6.5g لكل 500mL ماء مقطر، وعُقم بالاوتوكلاف مدة 20 دقيقة في درجة حرارة 121°C عند 1ضغط جوي.

2.2.3. المحلول الملحي

حُضر بحل 4.25 g في 500ml ماء مقطر (من 0.85% إلى 0.9% كلوريد صوديوم وزن/ حجم)، وعُقم بالاوتوكلاف مدة 20 دقيقة عند درجة حرارة 121°C عند 1ضغط جوي.

2.2.4. إعداد اللَقاح Inoculum.

تُعد طريقة تعليق المستعمرة مُباشرة هي الأكثر مُلاءمة لإعداد اللقاح إذ يمكن استعمالها مع معظم الأحياء الدقيقة، وهي الطريقة المُوصى بها في المعيار ISO 22196 (2011)، وكانت خطوات إعداد اللقاح كالتالي: أُخذ كمية من المستعمرات البكتيرية (فتيّة بعمر 24 ساعة) التي على سطح الطبق باستعمال عروة معقّمة وغُمست في أنبوب المحلول الملحي الذي سبق إعداده. ثم مُزج المحلول المُعلق جيداً بجهاز المزج vortex وضُبط نظام التعليق لتحقيق تعكر يعادل 0.5 من معايير McFarland باستعمال مقياس الكثافة الضوئية، نتج عنه تعليق بكتيري يحتوي على نحو 1.5×10^{8}CFU.mL^{-1} ثم أُجريت التخفيفات اللازمة باستعمال المرق المغذي (بعد المزج الجيد في كل مرة) حتى الحصول على التخفيف المطلوب وهو 10×10^{5}CFU.mL^{-1} لكلا النوعين من البكتيريا. تُم استعمال ماصة جديدة لكل خطوة تخفيف، علماً أن المعيار ISO 22196 (2011) يُوجب استعمال نوعين من العزلات البكتيرية المُمرضة هما *الإشريكيّة القولونيّة والمكوّرات العنقوديّة الذهبية* والتي أمكن الحصول عليها من مختبرات قسم علوم الأغذية في كلية الهندسة الزراعية بجامعة دمشق، وأُجري عزلها وتحديد نوعها من مصادر غذائية.

2.3. اختبار فعالية الأغشية المُتركبة النانوية LLDPE/ZnO-NPs:

أُجري الاختبار حسب المعيار ISO 22196 (2011) ومبدأه هو مُقارنة فعالية عينات من أغشية مُعقمة ومُتماثلة بالحجم وحالة السطح، كان أحدها عينة تحكم Control والأخرى ذات أسطح مُعالجة بمادة ZnO-NPs. وفيه وُضع كمية من اللقاح البكتيري على سطح كل عينة، ثم فُرشت بمساعدة غشاء من PET بحيث كان اللقاح كله على تماس مُباشر بسطح العينة في جو رطب، إذ يجب ألا يجف خلال 24 ساعة من الحَضن، ثم جرى تحييد البكتيريا ثم التخفيفات والزرع والحضن انتهاءً بقراءة النتائج. وتم إجراء

خطوات هذا الاختبار كما يلي:

2.3.1. إعداد العينات

تم قطع عينين من الأغشية المتركبة النانوية لكل تركيز وزني إلى أبعاد مُتماثلة 50×50mm إضافة إلى عينين من غشاء بوليمر LLDPE الصرف بالأبعاد نفسها، بحيث أصبح لدينا خمس أغشية متركبة نانوية وغشاء بوليمر LLDPE الصرف لكل نوع بكتيري على حدة.

2.3.2. التعقيم

عُقمت جميع الأغشية المُعالجة وغير المعالجة بمحلول الإيثانول ذو التركيز 70% ثم وُضعت تحت الأشعة فوق البنفسجية مدة 15 دقيقة.

2.3.3. عملية التلقيح Inoculation

وُضعت الأغشية المتركبة النانوية والأغشية الصرفة في أطباق بتري عقيمة (طبق لكل غشاء ولكل نوع بكتيري على حدة)، ثم أُضيفت كمية 0.4ml من اللَقَاح المُعد مُسبقاً على سطح الأغشية المُوزعة في الأطباق. وُضع غشاء البولي ايثلين تيرفثالات PET المُعقم بأبعاد 40×40×0.15mm فوق كل عينة من الأغشية المُعالجة بحيث أصبح اللَقَاح مُحتجز بين الغشائين لضمان توزع اللقاح وتماسه مع سطح الغشاء المُعالج وكذلك منع اللَقَاح من التبخر (يجب الانتباه الى منع تسرب اللَقَاح خارج سطح الغشاء). يوضح الشكل(1) خطوات إجراء عملية التلقيح.

الشكل (1): خطوات عملية التلقيح: (a)إعداد اللقاح البكتيري (b)إضافة اللقاح على سطح الغشاء المُختبر (c)ووضع غشاء PET (d)إغلاق الطبق ثم حضنه

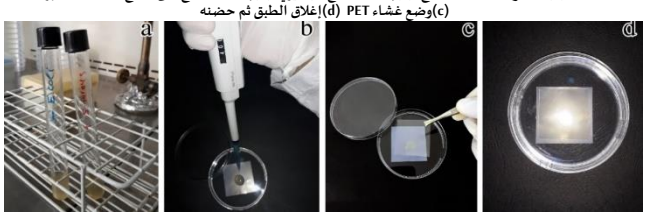

2.3.4. الحَضن

حُضنت جميع أطباق عينات الأغشية المُختبرة (خلال 15 دقيقة من إضافة اللقاح) عند درجة حرارة 37°C ورطوبة نسبية 5±90% مدة 24 ساعة.

2.3.5. تحييد البكتيريا

بعد انتهاء مدة الحضن فُصلت المُستعمرات البكتيرية عن أسطح عينات الأغشية من خلال غسل كل عينة بكمية 10ml من المرق المُغذي كسائل تحييد للبكتيريا، ثم نُقلت البكتيريا المُحيّدة والمُعلقة بالمرق من الأطباق إلى أنابيب مُعقمة.

2.3.6. التخفيفات

أُجريت التخفيفات العشرية، من خلال أخذ 1ml من كل أنبوب واضافتها إلى أنبوب يحتوي 9ml من المحلول الملحي، وكُررت هذه الخطوة (بعد المزج الجيّد في كل مرة) حتى الحصول على التخفيف المناسب (بحيث يُمكن عد المستعمرات في الأطباق لاحقاً) لجميع العينات المُختبرة ولكلا النوعين من البكتيريا. واستعملت ماصة جديدة لكل خطوة تخفيف.

2.3.7. الزرع والحضن

بعد التخفيفات جرى الاستزراع بطريقة صب الطبق pour plate، حيث أُخذ 1ml من كل تخفيف (10^{-3}، 10^{-4}) ووضعت في أطباق بتري جديدة، ثم صب ما يقارب 15ml من الآغار المُغذي في كل طبق وحُرك برفق لتفريق البكتيريا (بثلاثة أطباق كمكررات لكل عينة مُختبرة ولكل نوع بكتيري على حدة)، وتُم استعمال ماصة جديدة لكل خطوة استزراع. تُركت الأطباق بعد ترقيمها مدة 15 دقيقة حتى تصلب الآغار، ثم قُلبت الأطباق ووضعت في الحاضنة عند درجة حرارة 37°C مُدة 24 ساعة. علماً انه تم اختبار العينات بدون إشعاع ضوئي إضافي.

2.3.8. قراءة النتائج

بعد انقضاء زمن الحَضن فُحصت الأطباق وتُم عدّ المستعمرات البكتيرية النامية فيها، وحُسب المتوسط الحسابي لكل تركيز في المكررات الثلاثة لكل منها وقورن مع متوسط عدد مستعمرات أغشية LLDPE الصرف وتم التعبير عنها بالواحدة $CFU.mL^{-1}$، إذ تتضح الفعالية المضادة للأحياء الدقيقة من خلال الحد من المستعمرات البكتيرية. علماً أنه أُجريت تجارب أولية قبل التجربة الأساسية بالخطوات نفسها (بلا مكررات) لتحديد مجال فعالية التراكيز والتخفيفات المناسبة التي تُمكن من إحصاء المستعمرات.

3. النتائج والمناقشة

تم إجراء اختبار فعالية الأغشية المتركبة النانوية LLDPE/ZnO-NPs ضد البكتيريا المُمرضة إيجابية الغرام وسلبية الغرام، وأُحصي التعداد العام للمستعمرات النامية في الأطباق لكلا النوعين من البكتيريا المُختبرة، أظهرت المستعمرات نقط صغيرة بيضاء اللون متشابهة مُتفرقة ضمن وعلى سطح الآغار في كلا الانواع البكتيرية، وأعطت بكتيريا *المكوّرات العنقوديّة الذهبية* لوناً ذهبياً على وسط الآغار المغذي، كما هو واضح في الأشكال (2و3).

الشكل (2): نمو مستعمرات بكتيريا S.aureus : LLDPE-Neat(a) 0.25wt%(b) 0. 5wt%(c) 1wt%(d) 2.5wt%(e) 5wt%(f)

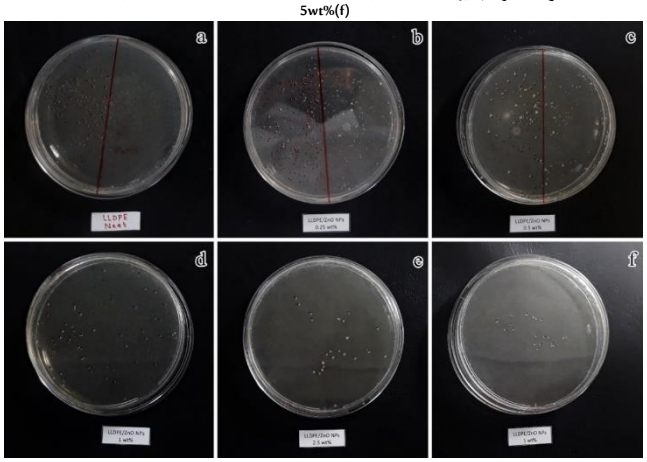

الشكل (3): نمو مستعمرات بكتيريا E.coli : LLDPE-Neat(a) 0.25wt%(b) 0. 5wt%(c) 1wt%(d) 2.5wt%(e) 5wt%(f)

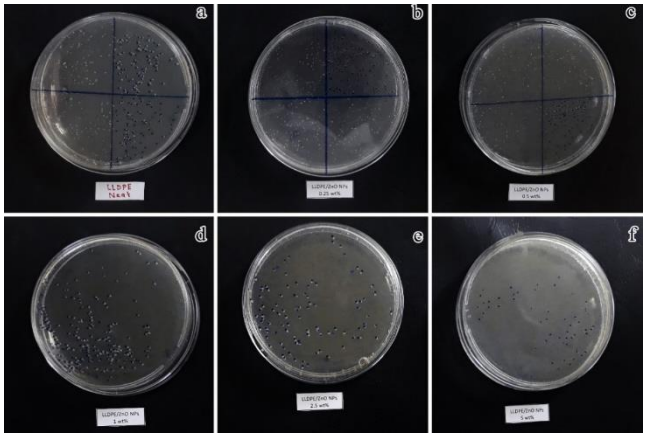

وبينت النتائج أن للأغشية المتركبة النانوية LLDPE/ZnO-NPs فعالية مُضادة لكلا النوعين من البكتيريا وأن هذه الفعالية تزداد بزيادة التركيز الوزني لأكسيد الزنك النانوي في الطور الرابط البوليميري LLDPE. وتبيّن أن البكتيريا إيجابية الغرام كانت أكثر حساسيّة مُقارنة بالبكتيريا سلبية الغرام، وكانت فعالية الأغشية المتركبة LLDPE/ZnO-NPs ذات التركيز الوزني 5% هي الأعلى في كل من بكتيريا *المكوّرات العنقوديّة الذهبية* وبكتيريا *الإشريكيّة القولونيّة*. إذ تُحسب الفعالية المُضادة للأحياء الدقيقة بمقياس تخفيض لوغاريتمي Log Reduction وفقاً للمعادلة (Mania *et al.*, 2020):

$$R = LOG\left(\frac{B}{A}\right)$$

حيث:

- **A:** متوسط عدد الخلايا القابلة للحياة في عينة الاختبار بعد 24 ساعة من الحضانة عند 37°C .
- **B:** متوسط عدد الخلايا القابلة للحياة في عينة التحكم Control بعد 24 ساعة من الحضن عند 37°C .

وذكر Scuri وآخرون (2019) أنه يتم تقييم الفعالية المضادة للأحياء الدقيقة (R) استنادًا إلى التصنيف التالي:
تخفيض لوغاريتمي ≤0.5 ؛ أي لا يوجد فعالية مضادة للأحياء الدقيقة.
تخفيض لوغاريتمي من 0.5 إلى 1؛ أي فعالية مضادة للأحياء الدقيقة طفيفة.
تخفيض لوغاريتمي من ≤1 إلى 2؛ أي فعالية مضادة للأحياء الدقيقة متوسطة.
تخفيض لوغاريتمي من 2 إلى <3؛ أي فعالية مضادة للأحياء الدقيقة جيدة.
تخفيض لوغاريتمي ≥3؛ أي فعالية مضاد للأحياء الدقيقة جيد جداً.

كما يمكن استعمال قيمة الفعالية المضادة للأحياء الدقيقة (R) لوصف وتحديد التخفيضات المئوية من خلال مُقارنة فعالية الأغشية المُعالجة مع أغشية التحكم غير المُعالجة Control بعد زمن التماس، علماً أن طريقة الاختبار لا تُشير إلى الإبلاغ عن تخفيض النسبة المئوية ولكن يتم توفيرها كمعلومات إضافية. إذ يتم ترجمة التخفيض اللوغاريتمي إلى تخفيض كنسبة مئوية والعكس صحيح كما يلي:

- تخفيض لوغاريتمي 1؛ أي أن 1,000, 000 مخفض إلى 100,000 هو تخفيض بنسبة 90%.
- تخفيض لوغاريتمي 2؛ أي أن 1,000, 000 مخفض إلى 10,000 هو تخفيض بنسبة 99%.
- تخفيض لوغاريتمي 3؛ أي أن 1,000, 000 مخفض إلى 1,000 هو تخفيض بنسبة 99.9%.
- تخفيض لوغاريتمي 4؛ أي أن 1,000, 000 مخفض إلى 100 هو تخفيض بنسبة 99.99%.
- تخفيض لوغاريتمي 5؛ أي أن 1,000, 000 مخفض إلى 10 هو تخفيض بنسبة 99.999%.

تسري الأرقام آنفة الذكر فقط عندما يكون التركيز الابتدائي للقاح يعادل $1x10^6$ كما هو الحال في هذا البحث. بالإضافة إلى ذلك، تم تفسير النسبة المئوية لخفض العزلات البكتيريا من حيث الفعالية "المبيدة للبكتيريا" Bactericidal عندما يكون التخفيض >99.9%. والفعالية "المثبطة للبكتيريا" Bacteriostatic عندما يكون التخفيض من 90 إلى 99.9% لكل عينة من الأغشية المتركبة النانوية (Scuri *et al.*, 2019). تؤكد نتائج الاختبار أن الأغشية المتركبة النانوية التي تحتوي على نسب 0.5% فأكثر من أكسيد الزنك النانوي لها فعالية مثبطة لنمو كلا النوعين من البكتيريا وأبدت تأثير مثبطاً *للمكوّرات العنقوديّة الذهبية* يتجاوز 90% مقارنة بأغشية التحكم Control التي لا تحتوي المادة الفعالة ZnO-NPs ، كما هو مبين في الجداول (2 و 3).

الجدول (2): نتائج التعداد العام لبكتيريا الإشريكيّة القولونيّة

اختبار الإشريكيّة القولونيّة							
التركيز الوزني LLDPE/ZnO-NPs		0.0%wt Control	0.25%wt	0.5%wt	1%wt	2.5%wt	5%wt
عدد المستعمرات والتكرار $CFU.mL^{-1}$	1	323×10^{-4}	477×10^{-3}	335×10^{-3}	199×10^{-3}	88×10^{-3}	49×10^{-3}
	2	331×10^{-4}	466×10^{-3}	330×10^{-3}	209×10^{-3}	81×10^{-3}	53×10^{-3}
	3	338×10^{-4}	475×10^{-3}	347×10^{-3}	195×10^{-3}	83×10^{-3}	57×10^{-3}
المتوسط الحسابي X		330.7×10^{-4}	472.7×10^{-3}	337.3×10^{-3}	201×10^{-3}	84×10^{-3}	53×10^{-3}
الانحراف المعياري SD		7.5±	5.9±	8.7±	7.2±	3.6±	4±
الخطأ القياسي SE		4.3	3.4	5	4.2	2.1	2.8
LOG_{10} ($CFU.mL^{-1}$)		6.5	5.7	5.5	5.3	4.9	4.7
R		00	0.8	1	1.2	1.6	1.8

الجدول (3): نتائج التعداد العام لبكتيريا المكوّرات العنقوديّة الذهبية

اختبار الإشريكيّة القولونيّة						
التركيز الوزني LLDPE/ZnO-NPs		0.0%wt Control	0.25%wt	0.5%wt	1%wt	2.5%wt	5%wt
عدد المستعمرات والتكرار $CFU.mL^{-1}$	1	297×10^{-4}	361×10^{-3}	213×10^{-3}	51×10^{-3}	21×10^{-3}	17×10^{-3}
	2	314×10^{-4}	366×10^{-3}	195×10^{-3}	58×10^{-3}	16×10^{-3}	15×10^{-3}
	3	308×10^{-4}	368×10^{-3}	207×10^{-3}	67×10^{-3}	23×10^{-3}	19×10^{-3}
المتوسط الحسابي X		306.3×10^{-4}	365×10^{-3}	205×10^{-3}	58.7×10^{-3}	20×10^{-3}	17×10^{-3}
الانحراف المعياري SD		8.6±	3.6±	9.2±	8±	3.6±	2±
الخطأ القياسي SE		5	2.1	5.3	4.6	2.1	1.4
LOG_{10} ($CFU.mL^{-1}$)		6.49	5.56	5.31	4.77	4.30	4.23
R		0.0	0.9	1.2	1.7	2.2	2.3

وتُبين النتائج أيضاً أن متوسط التعداد العام لبكتيريا *المكوّرات العنقوديّة الذهبية* النامية على وسط الآغار كان أقل من متوسط تعداد بكتيريا *الإشريكيّة القولونيّة*، أي أن البكتيريا إيجابية الغرام أكثر حساسية من البكتيريا سلبية الغرام تجاه الأغشية المُتركبة النانوية LLDPE/ZnO-NPs ويُعزى ذلك إلى الاختلاف في بنية وتركيب الجدار الخلوي للبكتيريا المُختبرة، إذ يمكن ربط العديد من خصائص الخلية بجدارها الخلوي، تمنح هذه الاختلافات في جدار الخلية خصائص مختلفة للخلية لا سيما الاستجابة للإجهادات الخارجية External Stress، بما في ذلك الحرارة والأشعة فوق البنفسجية والمضادات الحيوية(Tiwari, 2017). ففي بكتيريا *المكوّرات العنقوديّة الذهبية* موجبة الجرام يتكون الجدار خلوي من طبقة واحدة فقط من الببتيدوغليكان (Dimapilis *et al.*, 2018; Alhajali *et al*, 2021). في المقابل تمتلك بكتيريا *الإشريكيّة القولونيّة* سالبة الجرام جدار خلوي أقل سمكاً لكنه أكثر تعقيداً إذ يتكون من طبقة من الببْتِيدُوغليكان تغطيها طبقة أخرى تتكون من الفُسفوليبيدات Phospholipids وعَديدُ السَّكاريدِ الدهنية Lipopolysaccharides كغشاء يغطي سطح الخلية، يمكن لهذه الطبقات المكونة لجدار الخلية أن تشكل حاجزاً يمنع اختراق جُسيمات ZnO النانوي ويقاوم تأثيره أو ارتباطه (DaSilva *et al.*, 2019; Wang *et al.*, 2017; Siddique *et al.*, 2013). أيضاً أمكن الحصول على أعلى تأثير مُضاد للبكتيريا في الأغشية المتركبة النانوية ذات النسبة 5% وزناً من ZnO-NPs إذ أظهرت العينات انخفاضاً لوغاريتميًا يعادل 1.8 و 2.3 في عدد خلايا *الإشريكيّة القولونيّة والمكوّرات العنقوديّة الذهبية* والذي يُترجم إلى انخفاض بنسبة 98.4% و 99.4% على التوالي، أي أن لهذه الأغشية فعالية مضادة للبكتيريا جيدة. تتوافق هذه النتائج مع الاختبار الذي أجراه Lee وآخرون حول فعالية المادة LDPE/ZnO-NPs حيث كان التركيز الوزني 5% له فعالية تثبيط *ضد المكوّرات العنقودية الذهبية* بنسبة 99.6% و99.5% *للإشريكية القولونية* (Lee *et al.*, 2018). يتم مقارنة هذه النتائج مع أبحاث أخرى نُلخصها في الجدول (4).

الجدول (4): مُلخص نتائج بعض الأبحاث التي تختبر فعالية بوليمرات مُتركبة نانوية من خلال الاختبار القياسي ISO 22196

المرجع	التركيز الوزني المثبط للبكتيريا ≥90%		التركيز الابتدائي $CFU.mL^{-1}$	طريقة الاختبار المتبعة	نوع المادة النانوية المالئة وحجمها	الطور الرابط
	الإشريكيّة القولونيّة	*المكوّرات العنقوديّة الذهبية*				
البحث الحالي	%1	%0.5	$10x10^5$	ISO 22196 بتعديلات طفيفة	ZnO-NPs 68-46nm	LLDPE
(Lee *et al*/2018)	%1	%0.5	$0.5\text{-}10x10^5$	ISO 22196 بتعديلات طفيفة	ZnO-NPs 10-20nm	LDPE
(Li *et al*/2010)	%1	%0.5	$2\text{-}5x10^6$	ISO 22196 بتعديلات طفيفة	ZnO-NPs 300nm	HDPE
(Bazant *et al*/2018)	%1	%1	$2\text{-}10x10^5$	ISO 22196 بتعديلات طفيفة	Ag-ZnO-NPs 64nm	PP

على الرغم من تقارب النتائج مع هذا البحث إلا أنه يوجد بعض الفروق في نسبة الفعالية، وتُعزى هذه الفروق إلى عدة عوامل تتأثر بها فعالية الأغشية المتركبة النانوية المضادة للبكتيريا، كحجم الجسيمات النانوية المستعملة وشكلها المورفولوجي، إذ يُعود الأداء المرتفع لفعالية الجُسيمات النانوية إلى النسبة العالية من مساحة سطحها إلى حجمها وهو السبب الرئيس لفعالية الجُسيمات النانوية اللاعضوية المضادة للأحياء الدقيقة (Hashim, 2011). وكذلك اختلاف العزلات البكتيرية المُختبرة من ناحية المُقاومة عن الأبحاث السابقة، إضافة إلى التعديلات المُتبعة في إجراء الاختبار القياسي ISO-22196 ، ففي بحث أجراه Wiegand وآخرون (2018) حول العوامل الفيزيُولُوجِيّة Physiological التي تؤثر في نتيجة اختبار مُضادات الأحياء الدقيقة وفقاً للمعيار ISO-22196 من خلال إجراء اختبار روبن الكُلي (Round Robin Test) لمُقارنة وتقييم فعالية المواد المُضادة للأحياء الدقيقة، أشار البحث إلى ضرورة السرد الدقيق لجميع التعديلات في اختبار المعيار القياسي ISO-22196 وذلك لتمكين تقييم النتائج التي يتم الحصول عليها، إضافة إلى ذلك حدد البحث أربعة عوامل حاسمة تؤثر في نتائج الاختبار على

سلسلة من التجارب وهي: زمن الحضن والتركيز الابتدائي للبكتيريا والحالة الفيزيُولُوجيّة للبكتيريا (مرحلة النمو ثابتة أو أسية) وتركيز المغذيات. وأوصى البحث على وجوب الاتفاق على تعريفات موحدة لمصطلحات الفعالية المضادة للبكتيريا بما فيها التأثير المُثبط للبكتيريا Bacteriostatic والتأثير المُبيد للبكتيريا Bactericidal وذلك لتبسيط تنظيم ومُقارنة النتائج.

وفيما يتعلق بآلية فعالية الأغشية المتركبة النانوية المضادة للبكتيريا LLDPE/ZnO-NPs فإن إحدى الآليات هي تحرير جُسيمات أكسيد الزنك النانوية لأيونات Zn^{2+} التي يمكن أن تخترق غشاء الخلية وتلحق الضرر بمحتويات الخلية البكتيرية (Mania *et al*, 2020).أيضاً هناك آلية أخرى مُحتملة إذ اقترح Sirelkhatim وآخرون (2015) آلية تفاعل تفصيلية تشرح هذه الظاهرة على النحو التالي: تتكون بنية النطاق الإلكتروني لأكسيد الزنك النانوي كمادة شبه موصلة، من نطاق التوصيل CB ونطاق التكافؤ VB. وعند تشعيع أكسيد الزنك النانوي بالطاقة الضوئية مثل الأشعة فوق البنفسجية أو الضوء المرئي فإنه يَمتص فوراً الإشعاع الناتج مع فوتونات طاقة أكبر أو تساوي من 3.3eV، وبالتالي يتم تحفيز الإلكترونات لتنتقل من نطاق التكافؤ VB إلى نطاق التوصيل CB. نتيجة لذلك تتشكل ثقوب موجبة الشحنة positive holes (h^+) في نطاق التكافؤ VB، بينما تنشأ إلكترونات حرة داخل نطاق التوصيل CB. يعمل هذا الثقب الإيجابي (h^+) وهو مؤكسد مُباشر وضروري لإنشاء جذور الهيدروكسيل التفاعلية $^{\bullet}OH$ كمؤكسدات رئيسة في نظام التحفيز الضوئي. وتعمل الإلكترونات الموجودة في نطاق التوصيل CB على إرجاع الأكسجين reduce oxygen، الذي يمتصه المحفز الضوئي مُنتجاً فوق الأكسيد $\bullet O_2^-$ ليتفاعل مع H^+ مولداً جذور $HO_2^{\bullet}$. يتداخل $HO_2^{\bullet}$ مع الإلكترونات e^- التي تولد أنيونات بيروكسيد الهيدروجين التي تتفاعل مع H^+ لإنتاج جزيئات بيروكسيد الهيدروجين H_2O_2 (Khezrianjoo *et al*, 2019; Arakha *et al*, 2015; Sirelkhatim *et al*, 2015). يُمكن لبيروكسيد الهيدروجين H_2O_2 اختراق غشاء الخلية وقتل البكتيريا، علماً أن بعض الأبحاث ذكرت أن لجسيمات أكسيد الزنك النانوي ZnO-NPs سمية انتقائية للخلايا بدائية النواة على الخلايا حقيقية النواة (Kadiyala *et al*, 2018).

4. الاستنتاجات والتوصيات

حضرت مواد متركبة نانوية مكونة من مزيج LLDPE وجُسيمات ZnO النانوي وتم تقييم فعاليتها ضد كل من بكتيريا *المكوّرات العنقوديّة الذهبية* و بكتيريا *الإشريكيّة القولونيّة* من خلال المعيار ISO 22196 ، أظهرت النتائج أن للأغشية المتركبة النانوية فعالية مثبطة لكلا النوعين من البكتيريا المختبرة وتزداد هذه الفعالية بازدياد التركيز الوزني للمادة المالئة ZnO-NPs في الطور البوليمري LLDPE وتؤكد هذه النتائج أن البكتيريا إيجابية الغرام أكثر عرضة للتثبيط مُقارنة بالبكتيريا سلبية الغرام، ويعود هذا الاختلاف في الفعالية إلى البنية والتركيب الكيميائي لجدار الخلايا في كلا النوعين من البكتيريا. وبالتالي من المحتمل جداً أن يقلل مسار العمل هذا على نحو فعال من الحمل البكتيري المرتبط بسطح الغذاء ويزيد من العمر الافتراضي للمنتجات الغذائية المُعبأة في الأغشية المتركبة النانوية LLDPE/ZnO-NPs. نوصي بتحضير وتشكيل المادة المتركبة النانوية LLDPE/ZnO-NPs بنسب مئوية وزنية 1% وتقييم فعاليتها في تغليف أغذية حقيقية، كما نوصي باستعمال المعيار ISO 22196 في اختبار وتقييم فعالية المواد المُتركبة النانوية غير المسامية عموماً، وكذلك اختبار وتقييم فعالية الأغشية المُتركبة النانوية LLDPE/ZnO-NPs في بكتيريا السلمونيلّة Salmonella والعَطيفَة Campylobacter والليستَريّة Listeria باعتبارها أهم الأنواع البكتيرية المُمرضة المنقولة بالأغذية حسب تقرير السلامة الغذائية لمنظمة الصحة العالمية WHO لعام 2019.

نبذة عن المؤلفين

خالد حمود سيف الدين

قسم الكيمياء، كلية العلوم، جامعة دمشق، دمشق، سوريا، kh.h.saif@gmail.com، 00963934568727

أ. السيف الدين، سوري، أستاذ، ماجستير في الكيمياء (جامعة دمشق)، دبلوم دراسات عليا في التأهيل التربوي ومشرف على الجوانب التطبيقية في قسم الكيمياء بكلية العلوم على مواد الكيمياء العضوية والغروبات والجزيئات الضخمة. عضو في الجمعية الكيميائية السورية ووحدة المبادرة السورية للتقانة النانوية، مشارك في عدة دورات تدريبية وطنية منها "تقنيات تصنيع وتوصيف الأفلام الرقيقة" ودورة "السلامة الكيميائية وإدارة النفايات الكيميائية" في هيئة الطاقة الذرية السورية، ودورة "طرائق تحليل الغذاء" في الجمعية الكيميائية السورية، حاصل على شهادة تقدير في معرض الباسل للإبداع والاختراع، نشر عدة أبحاث علمية في مجلات محكمة، مجلة الكيمياء الأردنية ومجلة جامعة البعث للعلوم الأساسية.

رقم الأوركيد: 0000-0001-5924-2694

سحر نزال الحريري

قسم الكيمياء، كلية العلوم، جامعة دمشق، دمشق، سوريا، saharalhariri0@gmail.com، 00963993750464

د. الحريري، سورية، دكتور مساعد، دكتوراه في الكيمياء العضوية اختصاص علم المواد وكيمياء البوليمرات (معهد البولي تكنيك الوطني في غرونوبل-فرنسا). مُحاضرة في جامعة دمشق لطلاب السنة الثالثة والرابعة من الكيمياء التطبيقية وإشراف على طلاب الدراسات العليا. مدير البحوث في بوليمر لطلاب الدراسات العليا (دبلوم). المدير المشارك للبحوث في المنتجات الطبيعية لطلاب الدراسات العليا (دبلوم). مشاركة في مؤتمرات علمية وطنية، ونشر اكثر من 20 ورقة علمية في مجلات محكمة.

رقم الأوركيد: 0000-0002-1242-2310

عدنان أحمد علي نظام

قسم علم الحياة النباتية، كلية العلوم، جامعة دمشق، دمشق، سوريا، adnizam60@yahoo.com، 00963955525210

أ.د. العلي نظام، سوري، أستاذ دكتور، دكتوراه ميكروبيولوجيا المياه (جامعة باكو -أذربيجان)، محاضر في كلية العلوم ورئيس قسم علم الحياة النباتية سابقاً، وعضو هيئة تحرير مجلة جامعة دمشق للعلوم الأساسية، عضو في مركز القياس والتقويم بوزارة التعليم العالي والبحث العلمي السورية، أشرف على 20 طالب ماجستير و7 طلاب دكتوراه، نشر 70 ورقة علمية في مجلات محكمة، مؤلف ومشارك في تأليف 9 كتب في جامعة دمشق، مشاركة في مؤتمرات علمية دولية ووطنية، مدرس في المعهد العلي للترجمة والترجمة الفورية، حاصل على عدة جوائز إبداعية.

رقم الأوركيد: 0000-0002-4866-8363

عبيده نزيه الحجلي

قسم علم الحياة النباتية، كلية العلوم، جامعة دمشق، دمشق، الجمهورية العربية السورية، obaida.alhajali20@gmail.com، 00963955101317

أ. الحجلي، سوري، أستاذ، ماجستير علم حياة نباتية (جامعة دمشق)، مشرف على الجوانب التطبيقية في قسم علم الحياة النباتية بكلية العلوم-جامعة دمشق بالمواد التالية "ميكروبيولوجيا المياه، ميكروبيولوجيا الصناعية، بيولوجيا الأحياء الدقيقة". مشارك في عدة دورات تدريبية وطنية منها "التحوير الوراثي في النبات" التي أقامتها هيئة الطاقة الذرية السورية، مُحاضر في الدورات التدريبية "تطبيقات التقانات الحيوية في البيولوجيا" و"طرائق تشخيص بعض العوامل المرضة باستعمال التقانات التقليدية والجزيئية" التي أقيمت في جامعة دمشق. نشر عدة أبحاث علمية في مجلات محكمة في: مجلة جامعة دمشق للعلوم الأساسية، مجلة جامعة طرطوس للبحوث والدراسات العلمية.

رقم الأوركيد: 0000-0001-8576-180X

شكر وتقدير

يتقدم المؤلفون بخالص الشكر والعرفان للدكتورة آسيا خطاب والدكتور مالك الغدير على ما قدموه من مساعدة في إنجاز هذا البحث.

المراجع

AATCC. (2019). *Assessment of Antimicrobial Finishes on Textile Materials*. North Carolina: Technical Manual Method American Association of Textile Chemists and Colorists.

Alghdeir, M., Mayya, K. and Dib, M. (2019). Characterization of nano-silica/low-density polyethylene nanocomposite materials. *Journal of Nanomaterials*, **2019**(7),1–8. DOI: 10.1155/2019/4184351

Alhajali, O. and Adnan, A. (2021). Phytochemical Screening and Antibacterial Activity of Pistacia Atlantica and Pinus canariensis Extracts. *Journal of the Turkish Chemical Society Section A: Chemistry*, **8**(2), 403–18. DOI: 10.18596/jotcsa.836074

Arakha, M., Saleem, M., Mallick, B.C. and Jha, S. (2015). The effects of interfacial potential on antimicrobial propensity of ZnO nanoparticles. *Scientific Reports*, **5**(1), 1–10. DOI: 10.1038/srep09578

ASTM. (2013). *Standard Test Method for Determining the Antimicrobial Activity of Antimicrobial Agents under Dynamic Contact Conditions*. West Conshohocken, PA: American Society for Testing and Materials.

Bazant, P., Sedlacek, T., Kuritka, I., Podlipny, D. and Holcapkova, P. (2018). Synthesis and effect of hierarchically structured Ag-ZnO hybrid on the surface antibacterial activity of a propylene-based elastomer blends. *Materials*, **11**(3), 363. DOI: 10.3390/ma11030363

Bisht, G. and Rayamajhi, S. (2016). ZnO nanoparticles: a promising anticancer agent. *Nanobiomedicine*, **3**(n/a), 3–9. DOI: 10.5772/63437

Campos, M.D., Zucchi, P.C., Phung, A., Leonard, S.N. and Hirsch, E.B. (2016). The activity of antimicrobial surfaces varies by testing protocol utilized. *PLoS ONE*, **11**(8), 1–11. DOI: 10.1371/journal.pone.0160728

Da Silva, B.L., Abuçafy, M.P., Manaia, E.B., Junior, J.A.O., Chiari-Andréo, B.G., Pietro, R.C.R. and Chiavacci, L.A. (2019). Relationship between structure and antimicrobial activity of zinc oxide nanoparticles: An overview. *International journal of nanomedicine*, **14**(n/a), 9395–409. DOI: 10.2147/IJN.S216204

Damian, L. and Patachia, S. (2014). Method for testing the antimicrobial character of the materials and their fitting to the scope. Bulletin of the Transilvania University of Brasov. *Engineering Sciences. Series I*, **7**(2), 37.

Dimapilis, E.A.S., Hsu, C.S., Mendoza, R.M.O. and Lu, M.C. (2018). Zinc oxide nanoparticles for water disinfection. *Sustainable Environment Research*, **28**(2), 47–56. DOI: 10.1016/j.serj.2017.10.001

EFSA Panel on Food Contact Materials, Enzymes, Flavourings and Processing Aids (CEF). (2016). Safety assessment of the substance zinc oxide, nanoparticles, for use in food contact materials. *EFSA Journal*, **14**(3),1–8. DOI: 10.2903/j.efsa.2016.4408

Emamifar, A., Kadivar, M., Shahedi, M. and Soleimanian-Zad, S. (2010). Preparation and evaluation of nanocomposite LDPE films containing Ag and ZnO for food-packaging applications. *Advanced Materials Research*, **129-131**(n/a) 1228–32. DOI: 10.4028/www.scientific.net/AMR.129-131.1228

Hashim, A.A. (2011). *Advances in Nanocomposite Technology*. Rijeka, Croatia: BoD–Books on Demand.

ISO 22196. (2011). *Plastics-Measurement of Antibacterial Activity on Plastic Surfaces*. 2nd Edition. London: International Organization for Standardization.

Kadiyala, U., Turali-Emre, E.S., Bahng, J.H., Kotov, N.A. and VanEpps, J.S. (2018). Unexpected insights into antibacterial activity of zinc oxide nanoparticles against methicillin resistant Staphylococcus aureus (MRSA). *Nanoscale*, **10**(10), 4927–39. DOI: 10.1039/C7NR08499D

Khezrianjoo, S., Lee, J., Kim, K.H. and Kumar, V. (2019). Eco-toxicological and kinetic evaluation of TiO_2 and ZnO nanophotocatalysts in degradation of organic dye. *Catalysts*, **9**(10), 1–20. DOI:10.3390/catal9100871

Kuorwel, K.K., Cran, M.J., Orbell, J.D., Buddhadasa, S. and Bigger, S.W. (2015). Review of mechanical properties, migration, and potential applications in active food packaging systems containing nanoclays and nanosilver. *Comprehensive Reviews in Food Science and Food Safety*, **14**(4), 411–30. DOI: 10.1111/1541-4337.12139

Lee, W. and Ko, S. (2018). A Study on the functionality and stability of LDPE-Nano ZnO composite film. *Korean Journal of Packaging Science and Technology*, **24**(1), 27–34. DOI: 10.20909/kopast.2018.24.1.27

Li, S.C. and Li, Y.N. (2010). Mechanical and antibacterial properties of modified nano-ZnO/high-density polyethylene composite films with a low doped content of nano-ZnO. *Journal of Applied Polymer Science*, **116**(5), 2965–9. DOI: 10.1002/app.31802

Mania, S., Cieślik, M., Konzorski, M., Święcikowski, P., Nelson, A., Banach, A. and Tylingo, R. (2020). The synergistic microbiological effects of industrial produced packaging polyethylene films incorporated with zinc nanoparticles. *Polymers*, **12**(5), 1198. DOI: 10.3390/polym12051198

Orsuwan, A., Kwon, S., Bumbudsanpharoke, N. and Ko, S. (2019). Novel LDPE-riboflavin composite film with dual function of broad-spectrum light barrier and antimicrobial activity. *Food Control*, **100**(n/a), 176–82. DOI: 10.1016/j.foodcont.2019.01.012

Rosende, M., Miró, M., Salinas, A., Palerm, A., Laso, E., Frau, J., Puig, J., Matas, J. M. and Doménech-Sánchez, A. (2020). Cost-Effectiveness analysis of chlorine-based and alternative disinfection systems for pool waters. *Journal of Environmental Engineering*, **146**(1), 1–10. DOI: 10.1061/(ASCE)EE.1943-7870.0001610

Russell, A. D. (2003). Challenge testing: Principles and practice. *International Journal of Cosmetic Science*, **25**(3), 147–53. DOI: 10.1046/j.1467-2494.2003.00179.x

Saif-Aldin, K., Al-Hariri, S. and Ali-Nizam, A. (2020). Effectiveness of ZnO nano particles against the foodborne microbial pathogens E.coli and S. aureus. *Jordan Journal of Chemistry (JJC)*, **15**(2), 87–94. DOI: 10.47014/15.2.4

Scuri, S., Petrelli, F., Grappasonni, I., Idemudia, L., Marchetti, F. and Di Nicola, C. (2019). Evaluation of the antimicrobial activity of novel composite plastics containing two silver (I) additives, acyl pyrazolonate and acyl pyrazolone. *Acta Bio Medica: Atenei Parmensis*, **90**(3), 370–7 DOI: 10.23750/abm.v90i3.8561

Siddique, S., Hussain, Z., Shahid, S. and Yasmin, F. (2013). Preparation, characterization and antibacterial activity of ZnO nanoparticles on broad spectrum of microorganisms. *Acta chimica Slovenica,* **60**(3), 660–5.

Simoneau, C., Raffael, B., Garbin, S., Hoekstra, E., Mieth, A., Lopes, J.A. and Reina, V. (2016). *Non-Harmonised Food Contact Materials in the EU*. European Union: Regulatory and market situation. JRC Science for Policy Report. DOI: 10.2788/234276

Sirelkhatim, A., Mahmud, S., Seeni, A., Kaus, N. H.M., Ann, L.C., Bakhori, S. K.M., Hasan, H. and Mohamad, D. (2015). Review on zinc oxide nanoparticles: antibacterial activity and toxicity mechanism. *Nano-Micro letters*, **7**(3), 219–42. DOI: 10.1007/s40820-015-0040-x

Tiwari, A. (2017). Handbook of antimicrobial coatings. Manoa, USA: Elsevier.

Vilela, C., Kurek, M., Hayouka, Z., Röcker, B., Yildirim, S., Antunes, M.D.C. and Freire, C.S. (2018). A concise guide to active agents for active food packaging. *Trends in Food Science and Technology*, **80**(n/a), 212–22. DOI: 10.1016/j.tifs.2018.08.006

Wang, L., Hu, C. and Shao, L. (2017). The antimicrobial activity of nanoparticles: present situation and prospects for the future. *International journal of nanomedicine*, **12**(n/a). 1227–1249. DOI: 10.2147/IJN.S121956

Wiegand, C., Völpel, A., Ewald, A., Remesch, M., Kuever, J., Bauer, J., Griesheim, S., Hauser, C., Thielmann, J., Tonndorf-Martini, S., Sigusch, B.W., Weisser, J., Wyrwa, R., Elsner, P., Hipler, U., Roth, M., Dewald, C., Ludecke-Beyer, C. and Bossert, J. (2018). Critical physiological factors influencing the outcome of antimicrobial testing according to ISO 22196/JIS Z 2801. *PLoS ONE*, **13**(3), 1–15. DOI: 10.1371/journal.pone.0194339

The Scientific Journal of King Faisal University

Basic and Applied Sciences

Human Bocavirus in Children with Respiratory Tract Infection: Molecular and Serological Detection

Arwa Mujahid Al-Shuwaikh

Department of Microbiology, College of Medicine, Al-Nahrain University, Baghdad, Iraq

LINK	RECEIVED	ACCEPTED	PUBLISHED ONLINE	ASSIGNED TO AN ISSUE
https://doi.org/10.37575/b/med/210054	01/09/2021	16/10/2021	16/10/2021	01/12/2021

NO. OF WORDS	NO. OF PAGES	YEAR	VOLUME	ISSUE
4985	5	2021	22	2

ABSTRACT

Human bocavirus (HBoV) is a parvovirus identified mostly in children under the age of two who have a respiratory illness. The goal of this study was to use molecular and serological techniques to investigate the prevalence of HBoV as well as the clinical characteristics of Iraqi children with respiratory tract infections (RTIs). The study included 91 children ranging in age from 1–36 months. Nasopharyngeal/throat swab samples were collected, processed and tested for HBoV DNA detection by Polymerase Chain Reaction. In addition, Enzyme Linked Immunosorbent Assay (ELISA) was used to detect HBoV infection indirectly by measuring HBoV-IgM antibodies in serum. HBoV was found in 9.9% and 16.5% of samples, respectively, using the PCR and ELISA techniques. The ELISA test demonstrated a sensitivity, specificity, and positive predictive value of 90.2%, 77.8% and 97.4%, respectively, when compared to PCR. HBoV infection was associated with clinical symptoms such as vomiting and asthma ($P<0.05$). The PCR technique was effective in detecting persistent HBoV infections in hospitalised children; however, combining it with an ELISA test improved the accuracy of diagnosing acute HBoV infections (rather than bystander/passenger RTIs) by assessing specific IgM antibodies in serum.

KEYWORDS

Chest infection, HBoV, ELISA, PCR, under-five children, Iraq

CITATION

Al-Shuwaikh, A.M. (2021). Human bocavirus in children with respiratory tract infection: Molecular and serological detection. *The Scientific Journal of King Faisal University: Basic and Applied Sciences*, **22**(2), 71–5. DOI:10.37575/b/med/210054

1. Introduction

Respiratory infections are the most common causes of death worldwide. Using sensitive viral detection methods, new viruses that could play a role in respiratory infection are being found at an increasing rate (Martin *et al.*, 2010). In 2005, Tobias Allander and his colleagues in Sweden detected an unknown virus belonging to Parvoviridae in children with respiratory tract diseases. The name "Human Bocavirus (HBoV)" was given to the virus (Zaghloul, 2011). HBoV is a single-stranded DNA virus that belongs to Parvoviridae (Parvovirinae subfamily) and Bocavirusgenus. It is tiny, icosahedral, and non-enveloped. It is categorised into four main species, HBoV1 through 4 (Bhat and Almajhdi, 2021).

The size of HBoV genome is around 5.3 kb and has three open reading frames (ORFs) that encode NS1 and NP1 non-structural and VP1 and VP2 structural proteins (Watanabe *et al.*, 2018). HBoV1 was originally discovered in children who had respiratory infections, but HBoV-2 to HBoV-4 are mostly detected in feces and only rarely in the respiratory tract (Kantola *et al.*, 2011; Broccoloa *et al.*, 2015; Watanabe *et al.*, 2018). However, because HBoV is frequently associated with other agents and Koch's modified postulates are inapplicable, there is debate about HBoV's true role as a respiratory and gastrointestinal pathogen (Chuang *et al.*, 2011, Watanabe *et al.*, 2018; Bhat and Almajhdi, 2021).

The virus has been found in children with RTIs around the world, showing that it is prevalent (Sloots *et al.*, 2006; Chuang *et al.*, 2011). The total prevalence of HBoV is reported to be 6.3%, with an average ranging from 1.0% to 56.8% worldwide (Guido *et al.*, 2016). Pneumonia, bronchitis, and bronchiolitis are the most prevalent HBoV symptoms (Lau *et al.*, 2007). There have been numerous life-threatening reported cases of respiratory HBoV1 infections (Ziemele *et al.*, 2019).

Traditional PCR, real-time PCR, ELISA, recombinant capsid proteins (VP2) or virus-like particle (VLP) based immunoassay are currently used to detect HBoV.In addition, Sequence-Independent, Single-Primer Amplification (SISPA) techniques in combination with Next Generation Sequencing (NGS) will be applied in future for rapid and simultaneous detection of pathogen sequences (Hao*et al.*, 2015; Guido*et al.*, 2016). Until now, there have been no cell lines and animal models available for Bocavirus isolation, therefore, the mechanisms of latency, persistence, and reinfection are currently unknown (Bhat and Almajhdi, 2021).

HBoV has been detected in nasal, blood, saliva, feces, urine and environmental samples (i.e. river water and sewage), which has raised worries about its existence in transfusion therapy (Zaghloul, 2011; Guido *et al.*, 2016; Mohammad *et al.*, 2019). The goal of this study was to see if there were any associations between HBoV detection at the molecular and serological levels in Iraqi children with respiratory infections and clinical characteristics.

2. Material and Methods

2.1. Specimen Collection:

Samples were collected from 91 children under the age of five with respiratory infections who were admitted to paediatric hospitals (Al-Imammain Al-Kadhimain Teaching Hospital, Al Kadhimiya Pediatric Hospital, and Central Teaching Hospital of Pediatrics)in Baghdad, Iraq, from January to April 2017. This study was authorised by the Institute Review Board at Al-Nahrain College of Medicine, and the children's parents or guardians gave their informed consent. An attending physician examined all the patients. Three-millilitre universal transport media with nasopharyngeal/throat swabs (Cat.#: 80346C & 80503CS, Copan Diagnostic, Italy) were used. The samples were kept at -80°C. Furthermore, leftover blood from the chemistry laboratory was collected and serum was separated at 3000 rpm for 20 min and stored at -20°C until it was used.

Corresponding Author: Arwa Mujahid Al-Shuwaikh 009647903396565, arwa_alshwaikh_2004@yahoo.com

2.2. DNA Extraction:

Following the manufacturer's instructions, DNA samples were extracted using DNA/RNA prep kits from Sacace Biotec. The concentration and purity of DNA were measured using BioDrop. The extract was kept at -20°C until it was used.

2.3. Polymerase Chain Reaction (PCR):

The lyophilised primers 188F (5′-GAGCTCTGTAAGTACTATTAC-3′) and 542R (5′-CTCTGTGTTGACTGAATACAG-3′) (Kaplan *et al.*, 2006) that target the non-structural protein-1 gene (NP-1, which is more conserved than the VP1/2 gene, yielding a 354 bp amplicon) were generated per the manufacturer's directions (Alpha DNA, Canada). The PCR reaction mixture included the following: 12.5 µl of GoTaq (R) Green Master Mix (Promega, USA), 2 µl of each forward and reverse primer, 3 µl of DNA extract, and nuclease-free water (Promega, USA), bringing the total volume to 25 µl. In PCR Thermal Cycler (Eppendorf, Germany), the following program was utilised: initial denaturation at 95°C for 5 min, then 35 cycles of denaturation, annealing and extension at 94°C for 1 min, 59°C for 1 min, and 72°C for 2 min, respectively, followed by a final extension at 72°C for 10 min. To confirm amplification, agarose electrophoresis on gel (1%) (Promega, USA) with ethidium bromide (0.5 mg/ml) (Promega, USA) in 1xTBE buffer (Promega, USA) using a 100-bp DNA marker (Promega, USA) was done. The PCR products consisted of one band of 354 bp. To monitor assay performance, positive (HBoV-positive samples) and negative (nuclease-free water) controls were included in all runs (Figure 1).

2.4. DNA Sequencing:

For confirmation, one HBoV amplicon was chosen for Sanger sequencing. The sequencing done by Macrogen Inc. The observed DNA sequences were then compared to the retrieved HBoV DNA sequences (GenBank acc. MF314144.1) on the NCBI. The local isolate sequences were deposited at GenBank under the acc.MH591416 (HBoV-1/Baghdad-82/Iraq/2018).

2.5. Serology:

Ninety-one serum samples were analysed, according to the manufacturer's directions, for HBoV IgM antibodies using ELISA (Glory Science Co., Ltd, China). Antibodies specific to Bocavirus-IgM were coated on the Sandwich-ELISA microtiter plate. To prepare the sample, serum was diluted 5-fold with 40µl of sample diluents from the kit and 10µl of the serum samples to sample wells and, thereafter, incubated for 30 min at 37°C. After that, the wells were washed five times and a Horseradish Peroxidase (HRP), labelled anti-Bocavirus-IgM, was added to each well (except the blank well) and incubated for 30 min at 37°C to bind them to the HBoV IgM. Free components were washed five times. All wells had chromogen A and B added to them, and they were incubated in the dark for 15 min at 37°C. After the addition of the stop solution, the optical density (OD) of each well was determined at a wavelength of 450 nm and interpreted as positive or negative when compared to the cut-off value.

2.6. Statistical Analysis:

Based on PCR as the gold standard method, the validity and predictability of ELISA (sensitivity, specificity, positive predictive value (PPV) and negative predictive values (NPV)) were evaluated by Chi-Square (χ^2). Also, χ^2tests were used to determine the association between the presence of HBoV infection, clinical data and demographic data. Statistical significance was defined as a *P* value of < 0.05.

3. Result

3.1. Frequency of HBoV:

This cross-sectional study included 91 children. Their mean age (6.87 ± 6.38 SD) ranged from 1–36 months, with 38 (41.8%) females and 53 (58.2%) males. A combination of HBoV-DNA detection by PCR and/or HBoV-IgM detection by ELISA resulted in a total HBoV detection in 17 (18.7%) of 91 patients (Table 1). Only nine of 91 patients (9.9%) tested positive for HBoV-DNA, and only two of them were not identified by ELISA. However, 15 of 91 patients (16.5%) tested positive for anti HBoV IgM and seven of them were confirmed by PCR. Based on PCR, the sensitivity, specificity, PPV and NPV were calculated to compare PCR and ELISA. According to the findings of this study, the sensitivity of ELISA was 90.2% and the specificity was 77.8%, with a likelihood ratio of 19.49 (Table 2).

3.2. Demographic Data and Clinical Characteristics:

The age distribution revealed that 88.9% of HBoV-DNA-positive samples and 86.7% of HBoV-IgM-positive samples came from children aged 1 to 12 months (*P*=0.007) and (*P*=0.075), respectively. Fever, cough, dyspnea, cyanosis, vomiting, pneumonia, bronchiolitis, asthma, weight loss, pertussis and wheezing are common clinical symptoms in this age group (Table 1).

There was no statistical significance between HBoV DNA and/or IgM status and the sex or mean age (*P*>0.05). Furthermore, although not statistically significant, HBoV infections were found in 15.8% of children with pneumonia and 22.2% of children with bronchiolitis. Clinical symptoms of HBoV infection such as fever, cough, dyspnea, cyanosis and weight loss were not significant (*P*>0.05). However, clinical symptoms such as vomiting (*P*=0.028) and asthma (*P*=0.002) were statistically significant (*P*<0.05) (Table 3).

Table (1): Study population and HBoV infection in comparison with age groups.

Characteristics		Age Group 1–12 m No. (%)	13–24 m No. (%)	25–36 m No. (%)	*P*-value
Demographics					
Age in months (mean 6.87 ± 6.38 SD)		82 (90.1)	8 (8.8)	1 (1.1)	0.000*
Sex	Female (n=38, 41.8%)	1 (2.6)	3 (7.9)	34 (89.5)	
	Male (n=53,58.2%)	0 (0.0)	5 (9.4)	48 (90.6)	0.483
Clinical Signs and Symptoms					
Fever (n=77)		70 (90.9)	6 (7.8)	1 (1.3)	0.675
Cough (n=72)		64 (88.9)	7 (9.7)	1 (1.4)	0.719
Dyspnea (n=44)		42 (95.5)	2 (4.5)	0 (0.0)	0.228
Cyanosis (n=5)		5 (100)	0 (0.0)	0 (0.0)	0.748
Vomiting (n=12)		9 (75)	2 (16.7)	1 (8.3)	0.019*
Pneumonia (n=38)		35 (92.1)	3 (7.9)	0 (0.0)	0.668
Bronchiolitis (n=9)		9 (100)	0 (0.0)	0 (0.0)	0.578
Asthma (n=6)		5 (83.3)	1 (17.6)	0 (0.0)	0.757
Weight loss (n=13)		12 (92.3)	1 (7.7)	0 (0.0)	0.907
Pertussis (n=5)		5 (100)	0 (0.0)	0 (0.0)	0.748
Wheezing (n=17)		16 (94.1)	1 (5.9)	0 (0.0)	0.791
Viral Infection					
HBoV-DNA (n=9, 9.9%)	+ve	8 (88.9)	0 (0.0)	1 (11.1)	0.007*
	-ve	74 (90.2)	8 (9.8)	0 (0.0)	
HBoV-IgM-Ab (n=15, 16.5%)	+ve	13 (86.7)	1 (6.7)	1 (6.7)	0.075
	-ve	69 (90.8)	7 (9.2)	0 (0.0)	
HBoV DNA&/or IgM (n=17, 18.7%)	+ve	15 (88.2)	1 (5.9)	1 (5.9)	0.102
	-ve	67 (90.5)	7 (9.5)	0 (0.0)	

Table (2): ELISA sensitivity and specificity confirmed by PCR.

Category		PCR (n =91) HBoV-DNA +veNo. (%)	HBoV-DNA -ve No. (%)	Total No. (%)
ELISA (n =91)	HBoV-IgM +ve	7 (77.8)	8(9.8)	15(16.5)
	HBoV-IgM -ve	2 (22.2)	74(90.2)	76(83.5)
	Total No. (%)	9 (9.9)	82 (90.1)	91 (100)
Statistics		P<0.001		
Sensitivity		90.2 %		
Specificity		77.8 %		
PPV		97.4 %		
NPV		47.7 %		
Likelihood Ratio (LR)		19.499		

Table (3): Demographics, clinical signs and symptoms with regard to HBoV status.

Characteristics		HBoV DNA &/or IgM		*P*-value
		+ve No. (%)	-ve No. (%)	
Demographics				
Age (mean ± SD) months		17 (18.68) (6.64±9.35)	74 (81.32) (6.91±5.56)	0.875
Sex	Female (n=38)	8 (21.1)	30 (78.9)	0.623
	Male (n=53)	9 (17)	44 (83)	
Clinical signs and symptoms				
Fever (n=77)		14 (18.2)	63 (81.8)	0.774
Cough (n=72)		15 (20.8)	57 (79.2)	0.305
Dyspnea (n=44)		8 (18.2)	36 (81.8)	0.906
Cyanosis (n=5)		0 (0.0)	5 (100)	0.270
Vomiting (n=12)		5 (41.7)	7 (58.3)	0.028*
Pneumonia (n=38)		6 (15.8)	32 (84.2)	0.549
Bronchiolitis (n=9)		2 (22.2)	7 (77.8)	0.774
Asthma (n=6)		4 (66.7)	2 (33.3)	0.002*
Weight loss (n=13)		3 (23.1)	10 (76.9)	0.661
Pertussis (n=5)		1 (20.0)	4 (80)	0.938
Wheezing (n=17)		1 (5.9)	16 (94.1)	0.133

Figure 1: HBoV amplicon electrophoresis. Lane 1 represents a DNA marker, lane 2 represents a positive control and lane 3 represents a negative control. Negative samples in lanes 4, 5, 8, 10, 12 and 13, and positive samples in lanes 6, 7, 9 and 11.

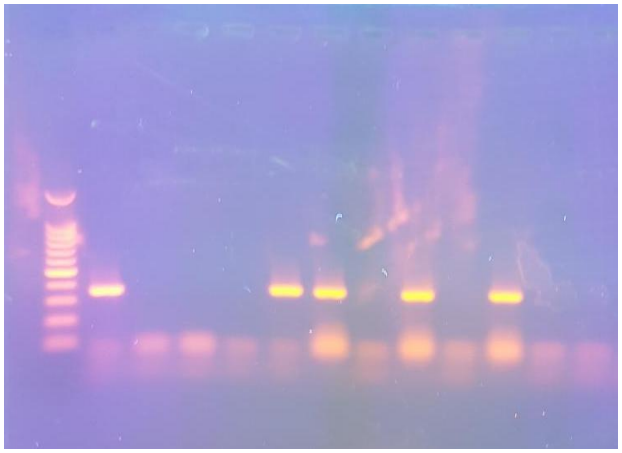

3.3. HBoV1 DNA Sequencing:

HBoV genomic sequences were highlighted in (Table 4). The amplified sequence was extended from 2340 to 2693 of the NCBI reference DNA sequence (GenBank acc. no. MF314144.1). The grey regions refer to forward and reverse primers. The alignment of the sequenced sample showed the absence of any mutation in the analysed specimen when compared to the referring HBoV sequences (Figure 2). Local isolate sequences were deposited at GenBank (acc. MH591416).

The NP1 amino acid sequence that was included within the 354 bp amplicon is:

[MSSGNMKDKHRSYKRKGSPERGERKRHWQTTHHRSRSRS
PIRHSGERGSGSYHQEHPISHLSSCTASKTSDQVMKTRESTSG
KKDNRTNPYTVFSQHR]

Table (4): The PCR amplicon within the HBoV genomic locus.

Amplicon	Referring locus sequences (5′–3′)*	Length
HBoV	GAGCTCTGTAAGTACTATTACTTTCTTTAACACTTGGCACGCACAGCCACGTGACGAAGATG AGCTCAGGGAATATGAAAGACAAGCATCGCTCCTACAAAAGAAAAGGGAGTCCAGAAAGA GGGGAGAGGAAGAGACACTGGCAGACAACTCATCACAGGAGCAGGAGCCGCAGCCCGAT CCGACACAGTGGGGAGAGAGGCTCGGGCTCATATCATCAGGAACACCCAATCAGCCACCT ATCGTCTTGCACTGCTTCGAAGACCTCAGACCAAGTGATGAAGACGAGGGAGAGTACATCGGGG AAAAAAGACAATAGAACAAATCCATACACTGTATTCAGTCAACACAGAG	354 bp

*The reverse primer was placed in a reverse complement mode.

Figure 2. DNA sequences alignment of the observed local viral sequences with its corresponding reference sequences of the 354 bp amplicon within the HBoV-DNA sequences. The symbol "ref" refers to the NCBI referring sequence.

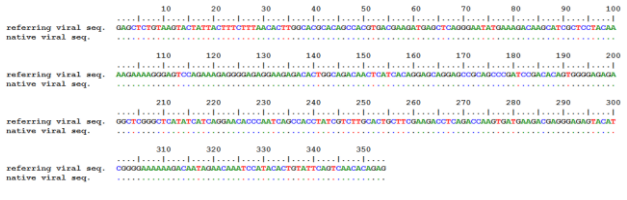

4. Discussion

In this study, only nine cases (9.9%) of children with respiratory illnesses tested positive for HBoV-DNA infection (Table 1). This result was predicted by considering the prevalence of HBoV in respiratory samples. The prevalence of HBoV infection varies from 2.7–19%, with the majority occurring in children under the age of two (Lindner and Modrow, 2008; Ziemele *et al.*, 2019). In addition, HBoV DNA was 56.8%, 19%, 18.3%, 7.6%, 5%; 2.3% and 1.9%, in Egypt, Finland, Jordan, Iran, Taiwan, Turkey and Kuwait, respectively (Kaplan *et al.*, 2006; Allander *et al.*, 2007; Chuang *et al.*, 2011; Guido *et al.*, 2016), depending on the study design, laboratory technology, patient age and symptoms (upper or lower RTI) (Kantola *et al.*, 2008; Chuang *et al.*, 2011; Gu et *al.*, 2017). However, the low prevalence in our findings may be due to the small samples size used, which was limited to one region of Iraq and one winter season. Although HBoV infections have been found primarily in winter (January and February) (Guido *et al.*, 2016; Mohammad *et al.*, 2019), a rise in infections has been observed in the spring and summer (Lindner and Modrow, 2008; Calvo *et al.*, 2010).

When molecular and serological techniques were compared (Table 2), eight (9.8%) patients had HBoV-IgM-positive but PCR-negative results. This discrepancy could be due to blood being taken after viral nucleic acid was eliminated from the respiratory tract, or due to hospitalised patients requiring more time before testing (Al-Shuwaikh *et al.*, 2018). Furthermore, depending on assay sensitivity, the samples could have low HBoV loads (Allander *et al.*, 2007). Serology antigens are based on HBoV (Broccoloa *et al.*, 2015), and several studies have shown that despite there being no cross reactivity between the two human parvovirus's antibodies (i.e. HBoV and Parvovirus B19 antibodies) (Endo *et al.*, 2007; Kantola *et al.*, 2008; Malecki *et al.*, 2011), HBoV2–4 co-circulation may influence HBoV serological tests (Kantola *et al.*, 2011; Hao*et al.*, 2015; Ziemele *et al.*, 2019). The unavailability of monospecific HBoV antibodies is one of the key obstacles in understanding the epidemiology of HBoV (Hustedt *et al.*, 2012). Serology, on the other hand, is critical because viremia can only be detected during active infection (Broccoloa *et al.*, 2015). Lindner *et al.* (2008) stated that their ELISA had high sensitivity and specificity with a PPV of 97% in wheezing children. In agreement with our findings, Zaghloul (2011) mentioned that PCR and ELISA were used to detect the presence of HBoV and both tests were extremely sensitive and specific. According to one study, serologic analysis or serum PCR are required for an accurate HBoV diagnosis, whereas PCR of nasopharyngeal aspirates alone is insufficient (Söderlund-Venermo *et al.*, 2009).

HBoV infections in the airways are systemic and cause humoral immune responses (Allander *et al.*, 2007; Kantola *et al.*, 2008; Ziemele *et al.*, 2019). Humans are infected with HBoV2–4 less frequently than HBoV1 and have weaker B-cell responses (Kantola *et al.*, 2011). IgG seropositivity increased with age (Endo *et al.*, 2007; Malecki *et al.*, 2011), reaching up to 95% in adults (Moesker *et al.*, 2015). As a result, discrepancies in results may also be related to variances in the age groups studied in different studies (Hao *et al.*, 2015). Our findings show that two children had HBoV-positive PCR results but no HBoV-IgM Ab (Table 2), this could be explained by the fact that a low viral load does not always indicate acute primary infection, which is consistent with previous findings (Söderlund-Venermo *et al.*, 2009). Furthermore, HBoV is a common virus that can cause persistent infections (without viremia) in the respiratory tract mucosa (Broccoloa *et al.*, 2015). HBoV is also commonly transmitted among children in day care or within families, which makes it easy for airways to be contaminated (Kantola *et al.*, 2008). As a result, interpreting PCR results in a clinical setting can be as difficult as interpreting serological testing.

According to the findings of this study, there is no statistically significant corelation between HBoV DNA and/or IgM status and the sex or mean age of the patient, which is similar to the findings of Mohammad *et al.* (2019) (Table 3). The majority of the children aged (1–12m) had HBoV-DNA-positive (88.9%, *P*=0.007) and HBoV-IgM-positive results (86.7%, *P*=0.075), but there was no clear link between HBoV infection and clinical symptoms except for those of vomiting (*P*=0.019) (Table 1) and asthma (*P*=0.002) (Table 3). The fact that many viruses exhibit clinical symptoms that are similar (Calvo *et al.*, 2010; Malecki *et al.*, 2011; Ziemele *et al.*, 2019) makes it unclear whether the symptoms were caused by the other viruses**.** Our findings revealed that four out of six (66.7%) asthmatic children were infected with HBoV (a significant corelation) (Table 3). However, viral infections in airways are present in a wide range of asthma patients during exacerbations (Costa *et al.*, 2014), with rhinovirus (RhV), respiratory syncytial virus (RSV) and HBoV being the most commonly found (Mandelcwajg *et al.*, 2010). Also, a significant relation was found between HBoV infection and vomiting. This may be due to respiratory viruses in infants frequently being associated with gastrointestinal manifestations. In addition, according to one study, up to 18% of hospitalised children with pneumonia tested HBoV positive (Kaplan *et al.*, 2006). HBoV has been shown in other studies to infect the lower respiratory tract, including the bronchioles (Söderlund-Venermo *et al.*, 2009; Calvo *et al.*, 2015; Guido *et al.*, 2016; Mohammad *et al.*, 2019). According to several studies, 6.6% and 40% of hospitalised HBoV- infected patients, require an intensive care unit stay and oxygen therapy, respectively (Arnold *et al.*, 2006; Chow *et al.*, 2008; Chow *et al.*, 2009).

Our results showed that one out five(20%)of patients had HBoV co-infection with Pertussis (Table 3). Patients with HBoV have a significant rate (83%) of co-infection (Bhat and Almajhdi, 2021). Infants and young children have immature immune systems (Ali *et al.*, 2019), therefore, infections with more than six pathogens in a single patient requires hospitalisation. HBoV tends to be associated with other respiratory viruses and bacteria, e.g. RSV, human RhV, adenovirus, metapneumovirus and *Streptococcus* spp (Lindner and Modrow, 2008, Malecki *et al.*, 2011; Mohammad *et al,* 2019). However, Moesker*et al.* (2015) found that in children, a single HBoV infection could induce severe acute respiratory infection (SARI) even in the absence of other viral and bacterial infections. In addition, a high viral load (>10^4 copies/ml) has been linked to more severe clinical symptoms and extended hospitalisation times (Broccoloa *et al.*, 2015; Guido *et al.*, 2016). However, this study cannot exclude other viral and bacterial co-infections. Importantly, the samples had previously been tested for RSV-RNA, which was found in 44% of the cases (data not shown). Rasheed *et al.* (2019) reported that 71% of children (<5 years) with lower RTI had such a viral infection, whether solitary or mixed, and two out of six HBoV-positive children had co-infection (HBoV and RhV).

Mutation and recombination events cause genetic variations in HBoVs (Broccoloa *et al.*, 2015). Based on the NP1 gene, sequenced HBoV local isolates(HBOV/Baghdad/82/2017) (GenBank acc. MH591416) have been identified with high sequence homology with the reference isolate (HBoV/ACRI_0111/USA/2016) (GenBank acc. MF314144.1) in Table 4 and Figure 2, indicating that HBoV is distributed worldwide. The non-structural genes were present, conserved regions of the viral genome. Further studies on the genes encoding the capsid proteins are needed since they showed the most variation, especially at its 3`end (Lindner and Modrow, 2008; Mohammad *et al.*, 2019).

5. Conclusion

This study has demonstrated the prevalence of HBoV in hospitalised children with RTIs in Baghdad, Iraq. The occurrence of HBoV was not statistically associated with clinical manifestations such as fever, cough, dyspnea, cyanosis, weight loss, pneumonia and bronchiolitis. However, a significant association was found in HBoV infection with vomiting and asthma. The PCR technique was more sensitive and specific than ELISA for the diagnosis of HBoV. ELISA, however, was a reliable serologic technique for detecting acute HBoV infections by measuring IgM antibodies in serum.

Biography

Arwa Mujahid Al-Shuwaikh

Department of Microbiology, College of Medicine, Al-Nahrain University, Baghdad, Iraq. 009647903396565, arwa_alshwaikh_2004@yahoo.com

Dr. Al-Shuwaikh is an Iraqi assistant professor at the College of Medicine, Al-Nahrain University in Baghdad, Iraq. She earned her PhD in Medical Microbiology in 2013. She has experience in both undergraduate and postgraduate teaching and training. She is the head of the Continuing Education Unit at the College of Medicine. She has participated in many national and international seminars, workshops, and conferences. She has several publications in the field of medical microbiology with a minor specialty in virology. ORCID: 0000-0002-2468-9629.

Acknowledgements

For their assistance in collecting samples, we thank the workers at Al-Imammain Al-Kadhimain Teaching Hospital, Al Kadhimiya Pediatric Hospital, and Central Teaching Hospital of Pediatrics. Prof. Dr. Ahmed Abdel-Moneim of Beni Suef University also deserves special thanks for providing the positive control. A fellowship from L'Oreal-UNESCO for Women in Science Levant and Egypt 2017 sponsored this research.

References

Ali, S.H., Al-Shuwaikh, A.M.A. and Arif, H.A. (2019). An investigation of risk factors associated with respiratory syncytial virus infection in a sample of infants and young children from Baghdad. *Journal of Biotechnology Research Center*, **13**(1), 29–34.

Allander, T., Jartti, T., Gupta, S., Niesters, H.G.M., Lehtinen, P., Osterback, R., Vuorinen, T., Waris, M., Bjerkner, A., Tiveljung-Lindell, A., van den Hoogen, B.G., Hyypia, T. and Ruuskanen, O. (2007). Human bocavirus and acute wheezing in children. *Clinical Infectious Diseases*, **44**(7), 904–10. DOI: 10.1086/512196

Allander, T., Tammi, M.T., Eriksson, M., Bjerkner, A., Tiveljung-Lindell, A. and Andersson, B. (2005). Cloning of a human parvovirus by molecular screening of respiratory tract samples. *Proceedings of the National Academy of Sciences USA*, **102**(36), 12891–6. DOI: 10.1073/pnas.0504666102

Al-Shuwaikh, A.M.A, Ali, S.H. and Arif, H.S. (2018). Detection of respiratory syncytial virus in infants and young children with chest infection: A comparison of reverse transcription-PCR technique to chromatographic immunoassay and enzyme linked immunosorbent assay. *Iraqi Journal of Medical Sciences*, **16**(3), 319–26. DOI: 10.22578/IJMS.16.3.11

Arnold, J.C., Singh, K.K., Spector, S.A. and Sawyer M.H. (2006). Human bocavirus: Prevalence and clinical spectrum at a children's hospital. *Clinical Infectious Diseases*, **43**(3), 283–8.DOI: 10.1086/505399

Bhat R. and Almajhdi, F.N. (2021). Induction of immune responses and immune evasion by human bocavirus. *International Archives of Allergy and Immunology*, **182**(8),728–35. DOI: 10.1159/000514688

Broccoloa, F., Falconeb, V., Espositoc S. and Toniolod, A. (2015). Human bocaviruses: Possible etiologic role in respiratory infection. *Journal of Clinical Virology*, **72**(n/a), 75–81. DOI: 10.1016/j.jcv.2015.09.008

Calvo, C., García-García, M.L., Pozo, F., Paula, G., Molinero, M., Calderon, A., González-Esguevillas, M. and Casas, I. (2015). Respiratory syncytial virus coinfections with rhinovirus and human bocavirus in hospitalized children. *Medicine*, **94**(42), e1788.DOI:10.1097/MD.0000000000001788

Calvo, C., Pozo, F., García-García, M.L., Sanchez, M., Lopez-Valero, M., Pérez-Breña, P. and Casas, I. (2010). Detection of new respiratory viruses in hospitalized infants with bronchiolitis: A three-year prospective study. *Acta Paediatrica*, **99**(n/a), 883–7. DOI: 10.1111/j.1651-2227.2010.01714.x

Chow, B.D. and Esper, F.P. (2009). The human bocaviruses: a review and discussion of their role in infection. *Clinics in Laboratory Medicine*, **29**(4), 695–713.DOI:10.1016/j.cll.2009.07.010

Chuang, C.Y., Kao, C.L., Huang, L.M., Lu, C.Y., Shao, P.L., Lee, P.I. and Chang, L.Y. (2011).Human bocavirus as an important cause of respiratory tract infection in Taiwanese children. *Journal of Microbiology, Immunology and Infection*, **44**(5), 323–7.

Costa, L.D., Costa, P.S. and Camargos, P.A. (2014). Exacerbation of asthma and airway infection: Is the virus the villain? *Jornal de Pediatria*, **90**(6), 542–55.DOI:10.1016/j.jped.2014.07.001

Endo, R., Ishiguro, N., Kikuta, H., Teramoto, S., Shirkoohi, R., Ma, X., Ebihara, T., Ishiko, H. and Ariga, T. (2007). Seroepidemiology of human bocavirus in Hokkaido prefecture, Japan. *Journal of Clinical Microbiology*, **45**(10), 3218–23. DOI:10.1128/JCM.02140-06

Gu, K, Van Caeseele, P, Dust, K. and Ho. J. (2017). Atypical pneumonia due to human bocavirus in an immunocompromised patient. *Canadian Medical Association Journal*, **189**(19), E697–9. DOI: 10.1503/cmaj.161134

Guido, M., Tumolo, M.R., Verri, T., Romano, A., Serio, F., De Giorgi, M., De Donno, A., Bagordo, F. and Zizza, A. (2016). Human bocavirus: Current knowledge and future challenges. *World Journal of Gastroenterology*, **22**(39), 8684–97.DOI: 10.3748/wjg.v22.i39.8684

Hao, Y., Gao, J., Zhang, X., Liu, N., Li, J., Zheng L. and Duan, Z. (2015). Seroepidemiology of human bocaviruses 1 and 2 in China. *PLoS ONE*, **10**(4), e0122751. DOI: 10.1371/journal.pone.0122751

Hustedt, J.W., Christie, C., Hustedt, M.M., Esposito, D. and Vazquez, M. (2012). Seroepidemiology of human bocavirus infection in Jamaica. *PLoS ONE*, **7**(5), e38206. DOI:10.1371/journal.pone.0038206

Kantola, K., Hedman, L., Allander, T., Jartti, T., Lehtinen, P., Ruuskanen, O., Hedman, K. and Soderlund-Venermo, M. (2008). Serodiagnosis of human bocavirus infection. *Clinical Infectious Diseases*, **46**(4), 540–6.DOI:10.1086/526532

Kantola, K., Hedman, L., Arthur, J., Alibeto, A., Delwart, E., Jartti, T., Ruuskanen, O., Hedman, K. and Soderlund-Venermo, M. (2011). Seroepidemiology of human bocaviruses 1–4. *The Journal of Infectious Diseases*, **204**(1), 1403–12.DOI:10.1093/infdis/jir525

Kantola, K., Hedman, L. and Tanner, L. (2015). B-cell responses to human bocaviruses 1–4: New insights from a childhood follow-up study. *PLoS ONE*, **12**(2), e0172078. DOI: 10.1371/journal.pone.0139096

Kaplan, N.M., Dove, W., Abu-Zeid, A.F., Shamoon, H.E., Abd-Eldayem, S.A. and Hart, C.A. (2006). Human bocavirus infection among children, Jordan. *Emerging Infectious Diseases*, **12**(9), 1418–20.

Lau, S.K., Yip, C.C., Que, T.L., Lee, R.A., Au-Yeung, R.K., Zhou, B., So, L.Y., Lau, Y.L., Chan, K.H., Woo, P.C. and Yuen, K.Y. (2007). Clinical and molecular epidemiology of human bocavirus in respiratory and fecal samples from children in Hong Kong. *The Journal of Infectious Diseases*,**196**(7), 986–93. DOI: 10.1086/521310

Lindner, J. and Modrow, S. (2008). Human bocavirus: A novel parvovirus to infecthumans. *Intervirology*, **51**(2),116–22. DOI:10.1159/000137411

Malecki, M., Schildgen, V. and Schildgen, O. (2011). Human bocavirus: Still more questions than answers. *Future Virology*, **6**(9), 1107–14.DOI:10.2217/fvl.11.78

Mandelcwajg, A., Moulin, F., Menager, C., Rozenberg, F., Lebon, P. and Gendre, D. (2010). Underestimation of influenza viral infection in childhood asthma exacerbations. *The Journal of Pediatrics*, **157**(3), 505–6. DOI: 10.1016/j.jpeds.2010.04.067

Martin, E.T., Fairchok, M.P., Kuypers, J., Magaret, A., Zerr, D.M., Wald, A. and Englund, J.A. (2010). Frequent and prolonged shedding of bocavirus in young children attending daycare. *The Journal of Infectious Diseases*, **201**(1), 1625–32. DOI: 10.1086/652405

Moesker, F.M., van Kampen, J.J.A., van der Eijk, A.A., van Rossum, A.M.C., de Hoog, M., Schutten, M., Smits, S.L., Bodewes, R., Osterhausk, A.D.M.E. and Fraaij, P.L.A. (2015). Human bocavirus infection as a cause of severe acute respiratory tract infection in children. *Clinical Microbiology and Infection*, **21**(10), 964.e1–964.e8. DOI: 10.1016/j.cmi.2015.06.014

Mohammad, M., Yavarian, J., Karbasizade, V., Moghim, S., Esfahani B.N. and Hosseni, N.S. (2019). Phylogenetic analysis of human bocavirus in children with acute respiratory infections in Iran. *Acta Microbiologica et Immunologica Hungarica*, **66**(4), 485–97. DOI: 10.1556/030.66.2019.017

Rasheed, Z.S., Al-Shuwaikh, A.M.A. and Issa, K.R. (2019). Multiplex RT-PCR based detection of human bocavirus and other respiratory viruses in infants and young children with lower respiratory tract infection. *Iraqi Journal of Medical Sciences*, **17**(1), 74–82. DOI: 10.22578/IJMS.17.1.11

Sloots, T.P., McErlean, P., Speicher, D.J., Arden, K.E., Nissen, M.D.and Mackay, I.M. (2006). Evidence of human coronavirus HKU1 and human bocavirus in Australian children. *Journal of Clinical Virology*, **35**(1), 99–102. DOI: 10.1016/j.jcv.2005.09.008

Söderlund-Venermo, M., Lahtinen, A., Jartti, T., Hedman, L., Kemppainen, K., Lehtinen, P., Allander, T., Ruuskanen, O. and Hedman, K. (2009). Clinical assessment and improved diagnosis of bocavirus-induced wheezing in children, Finland. *Emerging Infectious Diseases*, **15**(9),1423–30. DOI: 10.3201/eid1509.090204

Watanabe, A.S.A., Luchs, A. and Leal, E. (2018). Complete genome sequences of six human bocavirus strains from patients with acute gastroenteritis in the north region of Brazil. *Viruses*, **6**(17), e00235–18. DOI: 10.1128/genomeA.00235-18

Zaghloul, M.Z. (2011). Human bocavirus (HBoV) in children with respiratory tract infection by enzyme linked immunosorbent assay (ELISA) and qualitative polymerase chain reaction (PCR). *Virology Journal*, **8**(n/a), 239. DOI: 10.1186/1743-422X-8-239

Ziemele, I., Xu, M., Vilmane, A., Rasa-Dzelzkalçja, S., Hedman, K., Söderlund-Venermo, M., Gardovska, D., Nora-Krûkle, Z. and Murovska, M. (2019). Serodiagnosis of human bocavirus 1 infection among hospitalised children with lower respiratpry tract infection in Latvia. *Proceedings of the Latvian Academy of Sciences, Section B*,**73**(4), 288–95. DOI:10.2478/prolas-2019-0046

The Scientific Journal of King Faisal University

Basic and Applied Sciences

Simulation of Surface Plasmon Resonance (SPR) of Silver with Titanium Oxide as a Bi-Layer Biosensor

Farah Jawad Kadhum [1], Shaymaa Hasssn Kafi [1], Asrar Abdulmunem Saeed [1], Ali Abid Dawood Al-Zuky [1] and Anwar Hassn Al-Saleh [2]

[1] Physics Department, College of Science, Mustansiriyah University, Baghdad, Iraq

[2] Department of Computer Science, College of Science, Mustansiriyah University, Baghdad - Iraq

LINK	RECEIVED	ACCEPTED	PUBLISHED ONLINE	ASSIGNED TO AN ISSUE
https://doi.org/10.37575/b/sci/210046	17/08/2021	04/11/2021	04/11/2021	01/12/2021

NO. OF WORDS	NO. OF PAGES	YEAR	VOLUME	ISSUE
4768	5	2021	22	2

ABSTRACT

Surface plasmon resonance (SPR) is a highly sensitive method for monitoring changes in the optical characteristics that are near the sensor surface. It can be stimulated by an evanescent field that comes from the total internal reflection of the backside of the sensor surface in the Otto setup. In this setup, SPR can be used to build a simulation model at different thicknesses of titanium oxide (TiO2) (dTiO2 = 50 nm) and silver (Ag) (dAg = 10–80 nm) layers, which are deposited on the semicircular glass prism D-ZLAF50 by using water as a sensing medium. The surface plasmon resonance angle (θSPR) properties were calculated; SPR was not observed in the ultraviolet region (300 nm) or in the infrared region at 800 nm, but appeared strongly in the visible region at 600 and 700 nm and in the infrared region (900 and 1000 nm). The best sensitivity (S = 140) can be observed in the visible region, where the values of SPR dip length (Ld) and full-width half maximum (FWHM) are very good at silver layer thicknesses 40–60 nm; therefore, the proposed sensor can be used in the visible and infrared regions at the wavelengths 600, 700, 900, and 1000 nm.

KEYWORDS

biosensor, liquid sensor, sensitivity, surface plasmons, surface plasmon resonance, theoretical model

CITATION

Kadhum, F.J., Kafi, S.H., Al-Zuky, A.A., Saeed, A.A. and Al-Saleh, A.H. (2021). Simulation of surface plasmon resonance (SPR) of silver with titanium oxide as a bi-layer biosensor. *The Scientific Journal of King Faisal University: Basic and Applied Sciences*, **22**(2), 76–80. DOI: 10.37575/b/sci/210046

1. Introduction

Surface plasmon resonance (SPR) is considered an optical phenomenon that is caused by free electron oscillation at the interface between a metallic surface and an insulating layer, where the incident electromagnetic wave's wavelengths coincide with the wavelengths of the surface electrons under p-polarization light (Reather, 1980). When the incident light has a transverse magnetic (TM) polarization (p-polarization) at a given angle on the film metal, the momentum of the incident light equals that of the plasmon, and then resonance occurs; this is known as surface plasmon resonance . Here, the SPR angle is considered the precise angle at which the resonance occurs and the reflected light is damped (Liedberg *et al.*, 1983). Due to their appealing qualities of estimating and exacting the sensing and providing a fast response, real-time detection, and effective label-free lighting control capabilities, SPR sensors have been extensively explored (Nguyen *et al.*, 2015).

Surface plasmon resonance has typically been used to test bio-sensitivity on noble metallic surfaces such as gold and silver. These minerals (or metals) show a few benefits over other types of minerals, as SPR bands are visible and near-infrared frequencies, their surface chemistry is well-defined and easy to manipulate, and films can be made by using several deposition processes (Homola *et al.*, 1999). The most well-known application of SPR is in bio-sensitivity, where biomolecule attachment causes a minor change in the refractive index of the insulated medium near the interface that can be detected by a change in the reflection of the metal surface (Hoa *et al.*, 2007). The resonance angle changes according to the concentration of the target analysis when biomolecules cling to a metal surface (Liedberg *et al.*, 1983). SPR biosensors have been widely used in various analytical research domains due to their advantages, such as their sensitivity, quantitative response, and quick and label-free detection (Shankaran *et al.*, 2007). SPRs dissipate their electromagnetic waves through the metallic layer interaction. Electromagnetic wave loss can be due to the free electron scattering in the plasmonic layer and optical absorption throughout the electronic inter-band transitions. The sensitivity of SPR measurement varies significantly according to the type of the dielectric (liquid or gas) and the type of configuration (prism, optical fibre, and diffraction grating) (Yang *et al.*, 2018).

Several researchers have studied the SPR sensor system and worked on designing SPR systems that are used as sensors to detect any change in the optical properties of the media under the study.

One of the most important of these studies is Fontana's (2006) Mathcad software that was used to determine the optimum thickness of the deposited layers (Au, Ag, Al, and Cu films) on BK7 glass as the coupling prism material for the maximum SPR sensitivity based on the incident light's wavelength. Another important study by Wu *et al.* (2010) confirmed that the SPR biosensor based on the graphene deposition on gold was more sensitive than the classic SPR thin gold biosensor. The greater absorption of biomolecules onto graphene accounts for its higher sensitivity. In addition, Deng *et al.* (2010) simulated and designed a prism-based SPR sensor by using an Otto configuration, in which a thin layer of gold and another layer (dielectric SiO_2) were deposited on a prism with the use of a 650 nm laser to obtain plasmonic resonance of the layered system. A photodetector monitors the reflected beam as a function of the angle of incidence. The benefits of better SPR detection over traditional detection include a sharper resonance peak and narrower half-width, in addition to better sensitivity, contrast, and detection efficiency. In contrast, Maharana *et al.* (2013) improved the electric field at the sensing layer interface by using graphene as a dielectric overlayer on SPR-active metal Ag.

In comparing what is known as Au and Ag arrangement, we find that their sensor performs better. Rouf and Haque (2018) designed a bimetallic SPR sensor from a pair of silver-gold, in addition to the use of an air gap layer and a thin coating of an indium phosphide. Moreover, they studied different reflectivity curves and performance parameters, and their biosensor was able to detect 1/1000 of the RIU variation medium for the sensing. Lin and Chen (2019) developed an Au-Ag-TiO_2 graphene-based SPR biosensor, demonstrating the

Corresponding Author: Farah Jawad Kadhum 009647704535571, farahjawadalnuaimi@uomustansiriyah.edu.iq

existence of biosensors with a higher sensitivity; meanwhile, the resolution was higher than traditional biosensors. Here, the result shows the effects of the target reflectivity at the resonance angle and prism on the design of an Au-Ag-TiO_2 graphene-based SPR biosensor, in which the biosensor with the BK7 prism has the least refractive index (RI) among the three prisms, and it also has the least FWHM when obtaining S = 100°/RIU. Therefore, it is thought that the proposed genetic algorithm-based design method can be used to improve the performance of an SPR biosensor with any multi-layer structure (Haque *et al.,* 2019). A high-sensitivity SPR sensor on a two-core photonic crystal fibre can detect a low RI. Moreover, a numerical analysis of a two-core, and very sensitive plasmonic refractive index sensor was proposed for low refractive index detection. Akafzade *et al.* (2021) demonstrated a new SPR sensor made from a multi-layer Ag/Si_3N_4/Au nanostructure, which performed admirably at measuring the relative glucose concentrations in glucose/water mixtures. According to computer simulations, the electric field on the surface of this multi-layer sensor is up to 50% greater than on a gold film sensor.

The system that consists of a semicircular D-ZLAF50 glass prism is deposited on two layers, where the first is titanium oxide (TiO_2) with a thickness of 50 nm, and the second is silver (Ag), a thin film with variable thickness from 10 nm to 80 nm. The sensing medium is water, and the complex refractive indices of the materials approved in the study were obtained from the database available on the website refractiveindex.info (Polyanskiy, 2008–2020).

The current work aims to find plasmonic resonance in a wide range of wavelengths and to determine its location in the proposed sensor model's spectral bands by creating a simulation program. The reflectivity of the electromagnetic waves in the range 300 nm to 1000 nm was calculated by adopting Fresnel equations and using a proposed plasmonic resonance transfer matrix.

2. Material and Methods

Surface plasmon resonance occurs when a momentum transfer happens between the evanescent wave that passes through a thin metal layer and a surface plasmon excitation with the same momentum. These waves will be generated if the incident light comes from the side of the plasmonic material, such as glass, and has a higher refractive index, such that at a specific angle, the optical absorption of incidence light will increase. When this angle equals the SPR angle of the specific material and wavelength, the plasmonic dip height will reach the maximum (i.e. the minimum reflectivity). The reflectivity of the plasmonic film can be normal at all angles except for short-range SPR angles (θ_{SPR}), where the absorption reaches the maximum point. The maximum absorption will occur when the incident light's wave vector coincides with the surface plasmons' wave vector (Bhowmik *et al.*, 2016).

A multi-layer structure's reflectance and transmittance can be measured by using the transfer matrix method. In contrast, the traditional transfer matrix implies coherent light propagation, but results in narrow oscillations in a system's observed reflectance and transmittance spectra. These oscillations are not visible in practice due to interference-destroying effects. As a result, interference-destroying effects should be included to provide a practical explanation of the optical properties of multi-layer systems.

All past attempts to alter the transfer matrix to accommodate an incoherent intervention and partial coherence failed. The square of an amplitude of the electric field or Fresnel coefficients are used in the proposed methods to analyse the incoherent event. In partial coherence, the macroscopic surface or the interface roughness simulation is achieved by multiplying the Fresnel coefficients with the correction factors (Bhowmik *et al.*, 2016).

Fresnel's Equations are used to calculate the reflectivity of the material's multiple layers that are deposited on a given surface, where the electric and magnetic field amplitudes on the first boundary (E_a & H_a) and the N-layer model are connected to those on the last boundary (E_N & H_N) through the total characteristic matrix (Ouyang *et al.,* 2016):

$$\begin{bmatrix} E_a \\ H_a \end{bmatrix} = \left[\prod_{i=1}^{N} M_i\right] \begin{bmatrix} E_N \\ H_N \end{bmatrix} = \begin{bmatrix} m_{11} & m_{12} \\ m_{21} & m_{22} \end{bmatrix} \begin{bmatrix} E_N \\ H_N \end{bmatrix} \quad (1)$$

M_i: is an actual transfer matrix of the i-th layer (i = 1 to N), arranged in sequential order between a prism and a sensing layer, and it is calculated through the following (Shalabney and Abdulhalim, 2010):

$$M_i = \begin{bmatrix} cos\delta_i & \frac{isin\delta_i}{\gamma_i} \\ i\gamma_i sin\delta_i & cos\delta_i \end{bmatrix} \quad (2)$$

In this case, the optical phase addition caused by a single field passage over the layer, δ_i, is given by the following (Bhowmik *et al.,* 2016):

$$\delta_i = \left(\frac{2\pi}{\lambda}\right) n_i d_i cos\theta_i \quad (3)$$

Where λ: is the wavelength of incident light in a vacuum, n_i: is a refractive index, d_i is a thickness, and θ_i: is the incidence angle of the i-th layer. For p-polarization, the parameter for each layer γ_i is the following (Shalabney and Abdulhalim, 2010):

$$\gamma_i = \frac{n_i\sqrt{\varepsilon_0\mu_0}}{cos\theta_i} \quad (4)$$

Where ε_0: the vacuum permittivity, and μ_0: the permeability.

When we test several layers in thin films, it appears that the CTM method's strength is better estimated. The electric and magnetic fields within the i-th layer with both interfaces were related to an interference matrix M_i at that layer in Eq. (1). The total interference matrix of the entire multi-layer structure was obtained by using M because the electrical and magnetic fields' transverse components appear at any interface that is free of a net charge and current. The reflection and transmission indices (r and t) through the films may be calculated as follows (Shalabney and Abdulhalim, 2010):

$$r = \frac{\gamma_N m_{11} + \gamma_0\gamma_N m_{12} - m_{21} - \gamma_0 m_{22}}{\gamma_N m_{11} + \gamma_0\gamma_N m_{12} + m_{21} + \gamma_0 m_{22}} \quad (5)$$

$$t = \frac{2\gamma_0\left(\frac{n_N}{n_0}\right)}{\gamma_N m_{11} + \gamma_0\gamma_N m_{12} + m_{21} + \gamma_0 m_{22}} \quad (6)$$

From Eq. (5), the multi-layer stack's reflectance $R = |r|^2$ can be determined to get an incident light energy pattern redistribution. As a result, reflected field power as a function of incident angle was converted into SPR waves. Eq. (6) may be also used to measure the transmission across a multi-layer stack $T = |t|^2$.

Figure 1 shows a schematic design of the proposed SPR sensor. All metals have complex dielectric constants, and the metals with a larger negative real fraction and smaller positive imaginary fraction have good plasmonic effects. When electronic excitation occurs, the light will be absorbed. Silver is chemically stable and interacts very poorly with the atmosphere and other chemicals. It is optically transparent in the range of UV to IR 250–900 nm, and it has a relatively large refractive index, as well as thermal stability, hardness, chemical inertness, a low cost, and good chemical stability (Santos *et al.*, 2013). A good and stable plasmon sense system can be constructed by

depositing a thin layer of the silver on a prism (Gupta and Sharma, 2005). The response of this sensing system to the gases and liquids can be increased by depositing an additional layer of TiO_2 because the dielectric layer of titanium oxide provides many exceptional properties. At the interface between the superoxide layer and the sensor medium, the TiO_2 also increases the local electron field strength. Any change in the refractive index of the sensing medium or an increase in the electronic field strength causes an increase in the shift of the SPR wavelength, which therefore results in an improved sensitivity (Díaz-Herrera *et al.*, 2010).

Figure 1: Schematic diagram of the proposed SPR sensor (glass prism half-sphere).

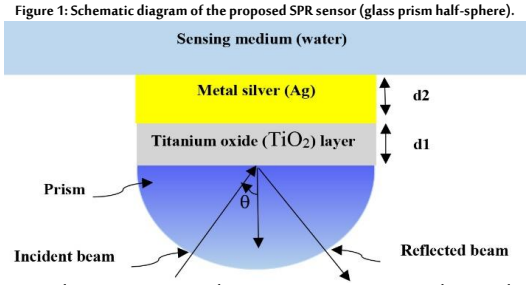

In the simulation steps, an electromagnetic wave with wavelengths ranging from 300 nm to 1000 nm was adopted to find the spectrum regions where the SPR phenomenon occurs. In this study, an Otto configuration with a D-ZLAF50 glass half sphere prism was used. A layer of TiO_2 with a constant thickness of 50 nm was deposited on the prism, and then another layer of Ag with a different thickness (10–80 nm) was deposited, with water used as a medium for biological or chemical sensitivity. The SPR dip must be deep enough, sharp, and in high contrast for the sensor in order to be effective and good. A very wide SPR dip indicates the possibility of a wider range of an incident SPR angle, and thus it makes the sensitivity of the sensor worse. In summary, these parameters were changed during the simulation:

- Electromagnetic waves: wavelengths ranging from 300 nm to 1000 nm with step changes 100 nm from ultraviolet wavelength to near-infrared wavelength.
- The amount of change in the refractive index of the external sensing medium in contact with the sensor:($\Delta n = 0, 0.02, 0.05, and\ 0.1$).
- Dielectric (TiO_2) layer thickness constant d_{TiO2} = 50 nm.
- Silver layer thickness: (10-80) nm with step changes 10 nm.

An important note is that as the incident wavelengths change, the refractive indices of the system materials ((prism D-ZLAF50) glass, dielectric (TiO2), silver, and water) will change. The simulation program was performed by developing Yamamoto's algorithms in 'Surface Plasmon Resonance (SPR) Theory' (Yamamoto, 2002).

3. Results and Discussion

The optimum film thickness of the metal-based SPR sensor has the SPR reflectivity curve produced by a sensor structure that shows the maximum possible loss in the reflectivity. It also produces the narrowest possible FWHM of the SPR dip, with the length of the SPR dip close to one. Figure 2 shows the reflectivity curves for the TiO_2 50 nm thickness layer, and Ag of thickness varying from 10 nm to 80 nm with steps 10 nm. It is identified by the angle of the surface plasmon resonance (θSPR). The angle of the incidence at which the minimum reflection occurs corresponds to the maximum energy loss due to the excitation of the surface plasmon. The characteristics of the reflectivity curves and the occurrence of SPRs can be summarized as follows:

- By using a silver thickness of 10 nm and 20 nm, there are no instances of SPR that can be used in the sensing process. For 30 nm thickness, the SPR states began to appear at the wavelengths of 600 nm, the state of SPR improved at the wavelength of 700 nm, the state of SPR completely disappeared at the wavelength of 800 nm, but it appeared strongly at the wavelengths 900 nm and 1000 nm.
- SPRs become very strong by using silver with a thickness between 40 nm and 50 nm, they weaken slightly at 60 nm thickness, and they are even weaker at 70–80 nm silver thickness for all used wavelengths.
- The SPR angle shifted slightly towards the higher values with an increase in the refractive index of the sensing medium Δn; this agrees with Deng and Liu (2010).

Figure 2: Shows the relation between the reflectance in the incident angle of the different thickness Ag layer and different wavelengths.

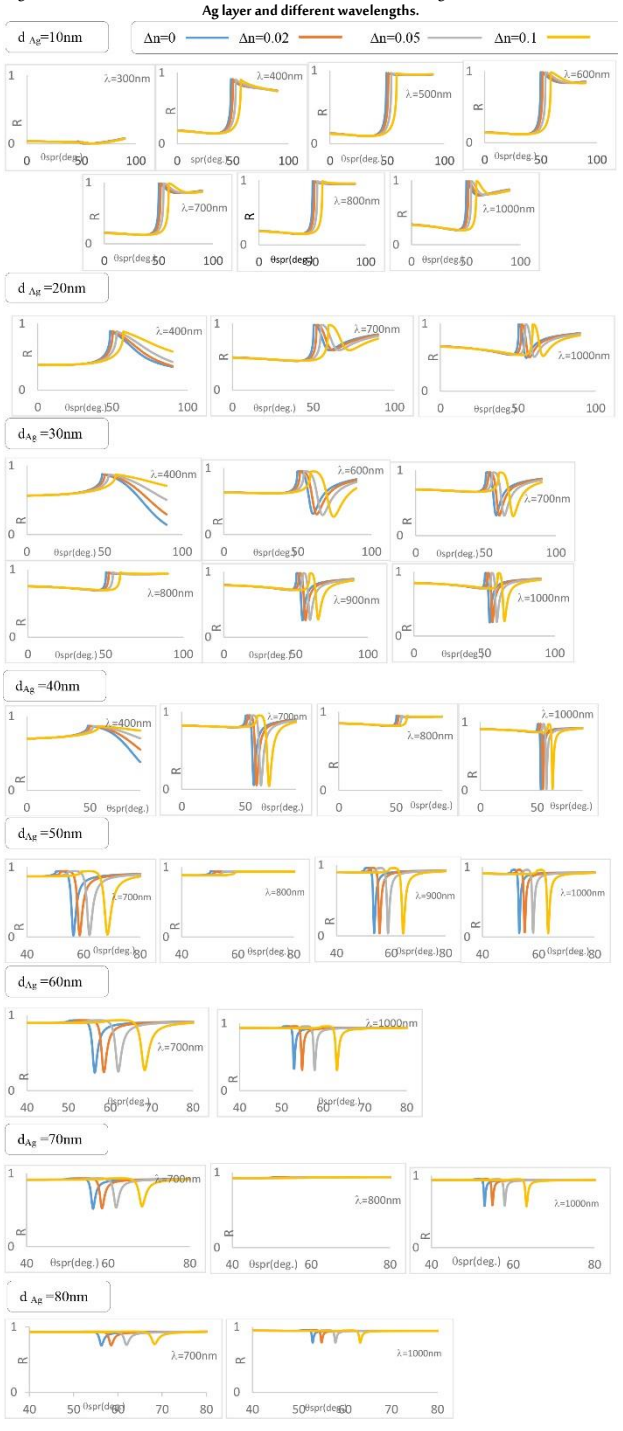

The computed SPR dip properties – FWHM and the height (L_d) and the best SPR sensor that gives a sharper FWHM and longer L_d and that approaches one – also compute the sensor sensitivity by using the following (Seo *et al.*, 2017):

$$S = \frac{\Delta\theta spr}{\Delta n_{dio}} \qquad (8)$$

Figure 3 illustrates the computed FWHM and the length (L_d) of the

SPR dip with the change in the outer medium refractive index.

It is noted that the FWHM for the SPR dip is gradually decreasing in all cases with an increased silver thickness, but the best cases were those using the wavelengths 1000 nm and 900 nm. It was also observed that the SPR dip length (L_d) increased till it reached its peak at the silver thickness between 40 nm and 60 nm, and then it gradually decreased when the silver thickness increased. This information helped determine the best silver thickness for use in the sensor. This happens when the FWHM is rather small and the SPR dip length (L_d) is large, and it helps achieve the sensing purpose of the sensor. This was achieved within a silver thickness range of 40 nm to 60 nm. The value ranges in this silver thickness (d_{Ag}) were as follows: the L_d were $\cong$ 0.8–0.9 for the wavelengths 600, 700, 900, and 1000 nm, and the best values for the L_d were for the SPR dip length at the wavelengths of 900 and 1000 nm and Δn=0.1. As for the FHWM values when using Δn=0.1 with the 600 nm wavelength within 15.2–3.5 degrees in a changing of d_{Ag}, the FWHM values improved, and the SPR dip became narrower when using the 700 nm wavelength, with its value becoming 9.7–1.8 degrees with different d_{Ag}. Then, the FWHM began to decrease further, which means that the SPR dip became narrower when using the wavelength 1000 nm, and its FWHM value became 4–0.5 degrees with different d_{Ag}.

Figure 3: Shows the Full-Width Half Maximum (FWHM) and length dip Ld with the change refractive index of layer thin films for different thickness Ag and wavelengths.

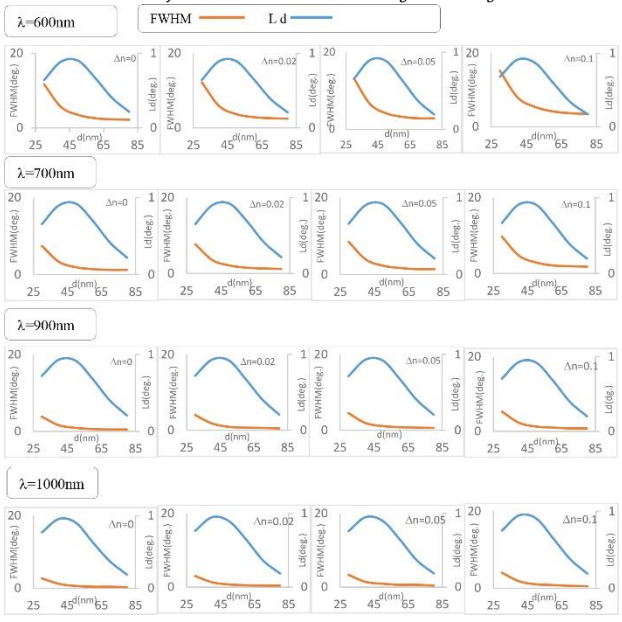

The relationship between sensitivity related to the changing thickness of the Ag layer and the refractive indices of sensing medium $\Delta n = (0.02, 0.05, and\ 0.1)$ is shown in Figure 4, where the relationship between sensitivity and change in the silver thicknesses was stable for all thickness ranges. However, the sensitivity was highest at 600 nm, followed by 700 nm, 900 nm, and 1000 nm. It can also be noted that the sensitivity increases with the increase of the change in the refractive index of the sensing medium Δn. The best sensitivity values (S) were when using the wavelength λ = 600 nm, where its values ranged between S = 102 and 140 for thicknesses from d_{Ag} = (30–80) nm and Δn = 0.1, which agrees with research by Rouf and Haque (2018).

Figure 4: Illustrates the sensitivity related to thicknesses of Ag layers at a different wavelength with the refractive index Δn.

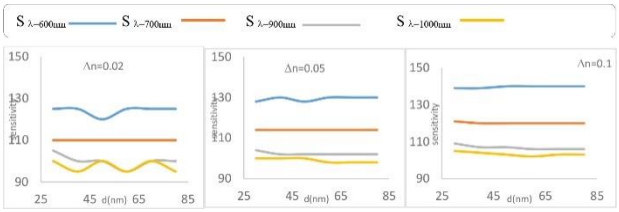

The proposed system can be adopted as an effective biological sensor within the visible-infrared spectrum region at a wavelength of 600, 700, 900, and 1000 nm.

4. Conclusions

Form the results of this study, the following points are concluded:

- When applying the simulation algorithm to the proposed sensor in this study, it is observed that the SPR phenomenon cannot appear in the ultraviolet region, but it appears weakly in the visible region, starting at a wavelength of 600 nm, and then it is improved further at a wavelength of 700 nm. While in the infrared region, SPR disappears completely at a wavelength of 800 nm and appears strongly at the wavelengths 900 nm and 1000 nm.
- In the visible region of the spectrum, the best working stability of the sensor is obtained at a wavelength of 600 nm. Where the sensitivity is obtained with values of S = 102–140, the SPR dip length is within the limits of $L_d \cong$ (0.8–0.9) and FWHM = 15.2–3.5 degrees, for thickness, and d = 30–80 nm, for sensing the change of the refractive index of the Aqueous medium ranges between Δn = 0.01–0.1.
- In the infrared region, the values of SPR dip length (L_d) and full-width half maximum (FWHM) are very good at the silver layer thicknesses 40–60 nm. The best values for the L_d were $\cong$ (0.8–0.9) for the SPR dip length at the wavelengths 900 and 1000 nm and Δn = 0.1. After that, the FWHM begins to decrease further, which means that the SPR dip becomes narrower when using the wavelength 1000 nm, and its FWHM value becomes 4–0.5 degrees with different d_{Ag}.

The proposed system can be used as an effective biosensor within the visible and infrared spectral regions of wavelengths 600, 700, 900 and 1000 nm at a silver layer thickness of 40 to 60 nm.

Acknowledgements

The authors would like to thank Department of Physics/ College of Science/ Mustansiriyah University (www.uomustansiriyah.edu.iq) Baghdad-Iraq for its support in the present work.

Biographies

Farah Jawad Kadhum

Department of Physics, College of Science, Al-Mustansiriyah University, Baghdad, Iraq, farahjawadalnuaimi@uomustansiriyah.edu.iq, 009647704535571

Mrs Kadhum is an Iraqi assistant Professor. She has a master's degree in physics from the Department of Applied Sciences, Al-Technology University, Iraq. Her field of interest is material physics and she has published more than 30 articles in global, regional, and local scientific journals. Some papers are in Scopus and Clarivate indices in the fields of material physics, polymer and laser dyes, spectroscopy, and molecular physics. She has participated in several local and regional seminars, workshops, and conferences. ORCID: 0000-0002-7188-8823

Shaymaa Hassan Kafi

Department of Physics, College of Science, Al-Mustansiriyah University, Baghdad, Iraq, shaymaa.h.kafy@uomustansiriyah.edu.iq, 00964779957787

Mrs Kafi is an Iraqi assistant lecturer at the Department of Physics, College of Science, Al-Mustansiriyah University. She obtained her master's degree in physics from the College of Science, Al-

Mustansiriyah University, Iraq. Her specialization is optics. She has published more than 10 articles in global, regional, and local scientific magazines; some are in Scopus and Clarivate indices in the field of optics physics. She has participated in several local and regional seminars, workshops, and conferences. She has received many certificates of appreciation for her active participation in training workshops. ORCID: 0000-0003-0737-6580

Asrar Abdulmunem Saeed

Department of Physics, College of Science, Al-Mustansiriyah University, Baghdad, Iraq, dr.asrar@uomustansiriyah.edu.iq, 009647707782082

Dr Saeed is an Iraqi assistant professor at the Department of Physics, College of Science, Al-Mustansiriyah University. She has a PhD degree in physics from the Department of Physics, College of Science, Baghdad University. She specializes in material physics. She supervises several postgraduate master's and doctoral students. She has published more than 30 articles in global, regional, and local scientific magazines; some are in Scopus and Clarivate indices in the fields of material physics, polymer and laser dyes, spectroscopy, and molecular physics. ORCID: 0000-0003-4677-7598

Ali Abid Dawood Al-Zuky

Department of Physics, College of Science, Al-Mustansiriyah University, Baghdad, Iraq, prof.alialzuky@uomustansiriyah.edu.iq, 009647706040619

Dr Al-Zuky is an Iraqi professor at the Department of Physics, College of Science, Al-Mustansiriyah University. He has a PhD degree in physics from the Department of Physics, College of Science, University of Baghdad, Iraq. He specializes in digital image processing and artificial intelligence. He has supervised more than 50 postgraduate students in the fields of physics, computers, computer engineering, and medical physics. He has published more than 150 scientific papers in scientific magazines and conferences. He has received many certificates of appreciation for his active participation in training workshops. ORCID: 0000-0002-3087-3908

Anwar Hassan Al-Saleh

Department of Computer Science, College of Science, Al-Mustansiriyah University, Baghdad, Iraq, anwar.h.m@uomustansiriyah.edu.iq, 009647707782082

Mrs Al-Saleh is an Iraqi assistant Professor at the Department of Computer Science, College of Science, Al-Mustansiriyah University. She obtained a master's degree in computer science from the College of Science, Al-Mustansiriyah University, Iraq. She specializes in image processing and has published more than 20 articles in global, regional, and local scientific magazines; some are in Scopus and Clarivate indices in the field of image processing. She has participated in several local and regional seminars, workshops, and conferences. ORCID: 0000-0001-9833-7119

References

Akafzade, H., Hozhabri, N. and Sharma, S.C. (2021). Highly sensitive plasmonic sensor fabricated with multi-layer Ag/Si3N4/Au nanostructure for the detection of glucose in glucose/water solutions. *Sensors and Actuators A: Physical*, **317**(n/a), 112430.

Bhowmik, B., Manjuladevi, V., Gupta, R. and Bhattacharyya, P. (2016). Highly selective low-temperature acetone sensor based on hierarchical 3-D TiO 2 nanoflowers. *IEEE Sensors Journal*, **16**(10), 3488–95.

Deng, Y. and Liu, G. (2010). Surface plasmons resonance detection based on the attenuated total reflection geometry. *Procedia Engineering. Elsevier*, **7**(n/a), 432–5.

Díaz-Herrera, N., González-Cano, A., Viegas, D.C. andand Santos, J.L. (2010). Refractive index sensing of aqueous media based on plasmonic resonance in tapered optical fibres operating in the 1.5 μm region. *Sensors and Actuators B: Chemical*, **146**(1), 195–8.

Fontana, E. (2006). Thickness optimization of metal films for the development of surface-plasmon-based sensors for nonabsorbing media. *Applied Optics. Optical Society of America*, **45**(29), 7632–42.

Gupta, B.D. and Sharma, A.K. (2005). Sensitivity evaluation of a multi-layered surface plasmon resonance-based fiber optic sensor: A theoretical study', *Sensors and Actuators B: Chemical*, **107**(1), 40–6.

Haque, E., Mahmuda, S., Hossain, M.A., Hai, N.H., Namihira, Y. and Ahmed, F. (2019). Highly sensitive dual-core PCF based plasmonic refractive index sensor for low refractive index detection. *IEEE Photonics Journal*, **11**(5), 1–9.

Hoa, X.D., Kirk, A.G. and Tabrizian, M. (2007). Towards integrated and sensitive surface plasmon resonance biosensors: A review of recent progress. *Biosensors and bioelectronics. Elsevier*, **23**(2), 151–60.

Homola, J., Yee, S.S. and Gauglitz, G. (1999). Surface plasmon resonance sensors. *Sensors and Actuators B: Chemical*, **54**(1–2), 3–15.

Liedberg, B., Nylander, C. and Lunström, I. (1983) Surface plasmon resonance for gas detection and biosensing. *Sensors and Actuators*, **4**(n/a), 299–304.

Lin, C. and Chen, S. (2019). Design of high-performance Au-Ag-dielectric-graphene based surface plasmon resonance biosensors using genetic algorithm. *Journal of Applied Physics*, **125**(11), 113101.

Maharana, P.K. and Jha, R. (2013/12/17-18). Enhancing performance of SPR sensor through electric field intensity enhancement using graphene. In: *Workshop on Recent Advances in Photonics (WRAP)*, IEEE, pp. 1–2, New Delhi, India.

Nguyen, H.H., Park, J., Kang, S. and Kim, M. (2015). Surface plasmon resonance: A versatile technique for biosensor applications. *Sensors, Multidisciplinary Digital Publishing Institute*, **15**(5), 10481–510.

Ouyang, Q., Zeng, S., Jiang, L., Hong, L., Xu, G., Xuan-Quyen, D., Qian, J., He, S., Qu, J., Coquet, P. and Ken-Tye Y. (2016). Sensitivity enhancement of transition metal dichalcogenides/silicon nanostructure-based surface plasmon resonance biosensor. *Nature Publishing Group*, **6**(1), 1–13.

Polyanskiy, M. (2008-2020). *Refractive Index*. Available at: https://refractiveindex.info (accessed on 10/08/2021).

Reather H., (1980). *Excitation of Plasmons and Interband Transitions by Electrons*. Springer: Berlin, Germany.

Rouf, H.K. and Haque, T. (2018). Performance Enhancement of Ag-Au Bimetallic Surface Plasmon Resonance Biosensor using InP. *Progress in Electromagnetics Research*, **76**(n/a), 31–42.

Santos, D.F., Guerreiro, A. and Baptista, J.M. (2013). Numerical investigation of a refractive index SPR D-type optical fiber sensor using COMSOL multiphysics. *Photonic Sensors. Springer*, **3**(1), 61–6.

Seo, M., Lee, J. and Lee, M. (2017). Grating-coupled surface plasmon resonance on bulk stainless steel. *Optics Express, Optical Society of America*, **25**(22), 26939–49.

Shalabney, A. and Abdulhalim, I. (2010). Electromagnetic fields distribution in multi-layer thin film structures and the origin of sensitivity enhancement in surface plasmon resonance sensors. *Sensors and Actuators A: Physical*, **159**(1), 24–32.

Shankaran, D.R., Gobi, K.V. and Miura, N. (2007). Recent advancements in surface plasmon resonance immunosensors for detection of small molecules of biomedical, food and enviro nmental interest. *Sensors and Actuators B: Chemical*, **121**(1), 158–77.

Wu, L., Chu, H.S., Koh, W.S. and Li, E.P. (2010). Highly sensitive graphene biosensors based on surface plasmon resonance. *Optics express Optical Society of America*, **18**(14), 14395–400.

Yamamoto's, M. (2002). Surface Plasmon Resonance (SPR) Theory. *Review of Polarography*, **48**(3), 209–37

Yang, L., Wang, J., Li-zhi, Y. and Zheng-Da, H. (2018). Characteristics of multiple Fano resonances in waveguide-coupled surface plasmon resonance sensors based on waveguide theory. *Scientific Reports*, **8**(1), 1–10.

The Scientific Journal of King Faisal University

Basic and Applied Sciences

A Novel Design of Continuous Culture for In Vitro Formation of Gallstones by *Salmonella Typhi*

Sahira I.H. Al-Sanjary and Amera M.M. Al-Rawi

Department of Biology, College of Science, University of Mosul, Mosul, Iraq

LINK	RECEIVED	ACCEPTED	PUBLISHED ONLINE	ASSIGNED TO AN ISSUE
https://doi.org/10.37575/b/sci/210055	26/09/2021	26/11/2021	26/11/2021	01/12/2021

NO. OF WORDS	NO. OF PAGES	YEAR	VOLUME	ISSUE
4431	5	2021	22	2

ABSTRACT

The current research focused on detecting the role of *Salmonella typhi* (*S. typhi*) in the formation of gallbladder stones in the laboratory following isolation and diagnosis of *S. typhi* from bile samples of patients suffering from gallstone. Locally and for the first time, a novel continuous culture was designed, and Brilliant Green Bile Broth (BGBB) was used by adding 60% cholesterol and 20% Calcium Carbonate ($CaCO_3$) to form the gallstone nucleation. The continuous culture was inoculated with 1% *S. typhi* then incubated in optimal conditions for 20 days. After 14 days of incubation, results revealed the formation of spherical aggregations with various sizes in the test flask compared to the control flask. Moreover, an increase in the size of the stone formed was observed after 20 days of incubation. The morphology of cholesterol and Calcium Carbonate crystals were studied using light, fluorescent and scanning electron microscopes, and the functional groups were diagnosed using the Fourier transform infrared spectrometry (FTIR) technique.

KEYWORDS

Biliary microbiota, model Bile, polysaccharide production

CITATION

Al-Sanjary, S.I.H. and Al-Rawi, A.M.M. (2021). A novel design of continuous culture for in vitro formation of gallstones by *Salmonella typhi*. *The Scientific Journal of King Faisal University: Basic and Applied Sciences*, **22**(2), 81–5. DOI: 10.37575/b/sci/210055

1. Introduction

Salmonella enterica subspecies *enterica* serovar *typhi* is described as part of the intestinal family; *S. typhi* is characterised by rod-shaped, flagellated, aerobic, Gram-negative bacilli. This bacterium invades the mucus surface of the intestine, causing an infection that spreads to infect the liver, pancreas, and bone marrow, and their ability to survive in bile and intestine with the presence of bile salts causes a chronic infection without any symptoms. Epidemic studies on *S. typhi* showed that most chronic infections are accompanied by gallstones (Di Ciaula *et al.*, 2019; Di Domenico *et al.*, 2017).

Gallstones are considered one of the primary digestive system diseases affecting humans (Kadhim, 2020; Al- Amedy *et al.*, 2020). The bile is a homogenous yellow-greenish liquid that is sterile under normal circumstances and consists of bile acids, salts, lecithin, and cholesterol (Rudling *et al.*, 2019). The supersaturation of the bile is regarded as the first step of gallstone formation compared to the bile acids, salts, and lecithin. The cholesterol determines the physical state of the bile and other factors that decrease the solubility of the cholesterol in the bile, and the presence of Mg^{++} and Ca^{++} are the critical factors in the formation of the nucleation of the cholesterol stone (Murphy *et al.*, 2020). Moreover, the increase of bile concentration, the slow discharge of the bile, the change in the bile contraction, the excessive secretion of the mucin or infection of bile ducts with some bacteria or diseases like sickle-cell disease increases the red blood corpuscles breaking and results in vast amounts of bilirubin (Grigor'eva and Romanova, 2020).

Bacteria play an essential role in the formation of the gallstone, and this motivated the researchers to study the role of bacteria and their relationship with gallstone formation (Di Ciaula *et al.*, 2018). Various types of bacteria were isolated from the patients suffering from gallstone using different microbiological and molecular techniques, including *E. coli*, *Salmonella spp*, *Enterococcus spp*, *Klebsiella spp*, *Enterobacter spp*, *Citrobacter spp*, *Staphylococcus spp*, *Pseudomonas spp*, and *Acinetobacter spp*. (Grigor'ova and Romanova, 2020; Hazrah *et al.*, 2004). Researchers pointed to the role of microbes that produce urease enzyme in terms of gallstone crystals precipitation, and they confirmed that urease production changes pH values, which in turn causes the precipitation of calcium crystals (Belzer *et al.*, 2006). Wang and his colleagues (2020) demonstrated intestinal microbes in gallstone formation, although the epidemic and the mechanism of the gallstone formation are not yet understood.

Until now, there has been no local study on the critical role of *S. typhi* in forming gallstones because all the previous – local or international – studies have focused on the bacterium's ability to precipitate the crystals. The current study aimed at investigating the role played by *S. typhi* in the stages of gallstone formation using a new continuous culture system designed for *in vitro* conditions with a suitable medium as a model for bile.

2. Materials and Methods

2.1. Isolation and Identification of *S. Typhi*:

Bile samples were obtained from patients subjected to gallbladder cholecystectomy at Alzahrawi Teaching Hospital and Alzahrawi Private Hospital in Mosul City. A sterilised syringe was used to take 2–5 ml of bile and was immediately inoculated on MacConkey agar, SS agar and XLD agar. The plates were incubated at 37ºC for 24 hours. Several diagnostic biochemical tests were conducted, as mentioned in (Willey *et al.*, 2017). These tests included indole production, methyl red test, Voges–Proskauer, citrate utilisation test, urease enzymes production, cytochrome oxidase, catalase, and TSI test.

VITEK2 compact system was employed using the diagnostic kit of Enterobacteriaceae to confirm the diagnosis, and the work method followed according to the instructions of the manufacturing company, Bio Merieux, for diagnosis (Renaud *et al.*, 2005).

2.2. Slime Production Test:

The pure isolates were inoculated on Congo red agar and incubated at 37ºC for 24 hours. Positive isolates were investigated by the appearance of black colonies, while the negative isolates appeared

Corresponding Author: Sahira Idrees H. Al-Sanjary 009647715531518, asahera34@gmail.com

in reddish pink (Freeman *et al.,* 1989).

2.3. *In Vitro* Formation of Cholesterol Gallstones:

2.3.1. Design of the continuous culture system

This system was designed to be used in preparing a continuous culture for *S.typhi* and using Brilliant Green Bile Broth (BGBB) as a model for the bile. The system consists of the continuous culture flask with its accessories as follows:

A glass flask with a side glass arm, an air pump to provide oxygen, a collecting tank with a volume of (250 cm^3) with a tap to control the addition of (25 cm^3 / hour) of the sterilised bile to get a dilution average of (0.05 / hour). Steel holders with clamp bottles were used to collect the excess solution from the culture flask, which was changed every 24 hours; a water bath with a thermometer was used to keep the temperature at 37ºC. All the accessories of the system were sterilised by autoclaving at (121 ºC) for 15 minutes.

2.3.2. Preparing the Culture

After confirming the diagnosis of *S.typhi* and testing its ability for slime production, a culture was prepared by inoculating the bacteria in a Brain Heart Infusion (BHI) medium and incubating at 37ºC for 18 hours.

2.3.3. A Model for Continuous Culture of Gallstone Nucleation *In Vitro*

A BGBB medium was prepared as a model of the bile; it contained 2% ox bile as a suitable nutritious media for *S.typhi*. Cholesterol was gradually added to the culture, and saturation was reached at a concentration of 60%. Calcium carbonate ($CaCo_3$) was added at a concentration of 20% with continuous stirring to form the nucleation of the stone. Then the pH was set to 7.2 using a pH-meter and sterilised with the autoclave at 121ºC for 15 minutes.

A 500 cm^3 sample of artificial bile was placed in the continuous culture flask and inoculated with 1% (5 cm^3) of *S.typhi* culture growing on BHI (18 hours old), which equals (5×10^5 CFU / cm^3). The flask was incubated under optimum temperature and pH. Excess liquid was discharged from the culture through a lateral discharge tube with the continuous addition of the artificial bile as drops (an average of 25 cm^3 / hour). A second sample was prepared that contained the same components but without *S.typhi* as a control sample.

After seven days of inoculating the continuous culture, a new *S.typhi* culture was added (18 hours old) and a size of 5 cm^3 growing on BHI to ensure the continuity of the metabolic activity with continuous incubation under optimum temperature and pH. Continuous culture persisted for 20 days from the beginning of inoculation.

2.4. Detection of the Crystals Forming the Stones with the Presence of *S.typhi*:

2.4.1. Examination under the Light Microscope

A light microscope was used to detect the stones' formation and observe *S.typhi* in the precipitate. From day one to day 10 of continuous culture, a precipitate drop was sampled daily and placed on a clean glass slide. Safranin stain was added, and a cover slide was fixed on top. It was examined using (100 X) magnification power (Sharma *et al*., 2020) and then photographed using the digital camera of the microscope (CH3 ORF 200, Olympus optical Co., Ltd., Japan).

2.4.2. Examination under the Fluorescent Microscope

A fluorescent microscope was used to detect *S.typhi* and its ability to produce polysaccharides and to detect crystals forming the stones by following the steps:

- Acridine orange dye was prepared by dissolving 0.1 gram of the dye in 100 ml of distilled water.
- Thin smears of the precipitate formed every day from the first day of continuous culture to 10 days were prepared and left to dry at room temperature. Smears were fixed using ether mixed with methanol in a ratio of (1:1) for ten minutes and then washed with distilled water.
- The slides were immersed in ethanol 50% and 70% for two minutes and stained with acridine orange for five minutes.
- The slides were washed with distilled water for one minute, then rinsed in phosphate buffer solution for 1-2 minutes, then dried, examined by the fluorescent microscope, and photographed (MacCarthy and Senne, 1980).

2.4.3. Examination under the Scanning Electron Microscope

The Scanning Electron Microscope (SEM) Inspect S50/FE/ Company- Netherland, at the College of Sciences, Kufa University was used. First, the specimen was prepared (the stone formed after 20 days of continuous culture), the stone was crushed and left to dry at room temperature for 15 minutes. Then carbon adhesive tape was fixed on the specimen holder surface (Aluminum stubs), and then the specimen was placed on the stubs. Then, the specimen was coated with gold using Sputter Coater (Quorum- 15 ORES- England) for 10 minutes, then the specimen on the stubs was moved to its place inside the microscope chamber, examined and photographed with the electron microscope camera that is connected to the computer of the microscope (Echlin, 2009).

2.4.4. Measurement with the Fourier Transform Infrared Spectroscope

The FTIR (Alpha-Bruker-Germany) at the College of Sciences, Kufa University, was used. The stones were crushed into fine powder; 2 mg of the powdered stone sample was used to make potassium bromide (KBr) discs. Then the specimen was analysed and measured using the Fourier transform infrared spectrometer (FTIR) at a frequency of 500-4000 cm^{-1} and a resolution of 4 cm^{-1} (Ha and Park, 2018).

3. Results

3.1. Isolation and Identification

Each isolate was initially identified using the Gram stain, and the culture characteristics of *S. typhi* on the selective media included MacConkey, SS, and XLD agar after they were incubated aerobically at 37ºC for 24 hours. The colonies of *S. typhi* appeared pale on MacConkey agar and paled with a black centre on SS agar. While they appeared pink with black centres on XLD agar. Moreover, the biochemical tests showed their ability to produce the catalase and positive methyl red test, and the VITEK2 compact system 99% match was given. Isolates of *S. typhi* showed a positive result in producing the polysaccharides as black colonies appeared on Congo red medium.

3.1.1. Results of *In Vitro* Nucleation of Gallstones Using the Continuous Culture System

Following the addition of cholesterol to BGBB, cholesterol crystals were dissolved at concentrations less than (6 mg / 10 cm^3). The gradual increase of cholesterol concentration resulted in the precipitation of crystals at the bottom of the continuous culture flask until it reached the concentration of 60%. In order to provide optimum conditions for gallstone formation, calcium carbonate was added to the flask. The gallstone was formed *in vitro*. Two models were prepared; the first represents the experiment flask, and the second is the control flask that contains the same components but without *S. typhi*.

The crystallisation process started seven days after inoculating the continuous culture with a new culture of the same bacteria, revealing the evident effect of the supersaturation of cholesterol

crystals. After 14 days of incubation at optimum conditions, tiny spherical aggregations with various sizes were observed in the flask compared to the control flask without *S. typhi* in which only a white precipitate was noticed. After 20 days of incubation, a continual increase was observed in the sizes of the stones in the experiment flask. Figure (1).

Figure 1: Formation of stones in the experiment flask compared to the control flask.

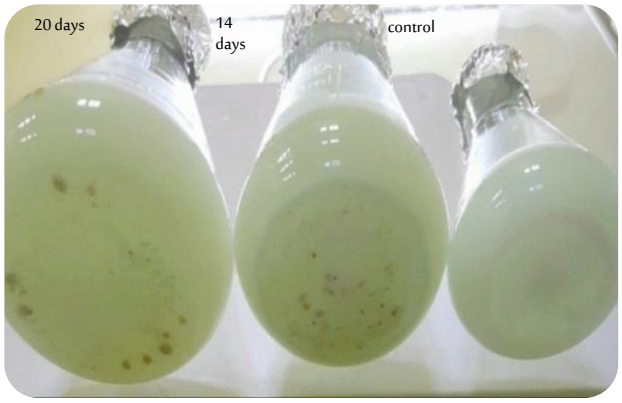

The precipitate was examined using the light microscope to investigate the shapes of the crystals from the fifth-day sample. Results showed the individual cholesterol crystals with their typical plate-like shape with *S .typhi* that were clear by microscope. The eighth-day sample showed that the cholesterol crystals plates are assembled, while the tenth-day sample showed the cholesterol crystals as compacted agglomerations, as shown in Figure 2.

Figure 2: Shapes of the cholesterol crystals of the eighth-day sample by the light microscope.

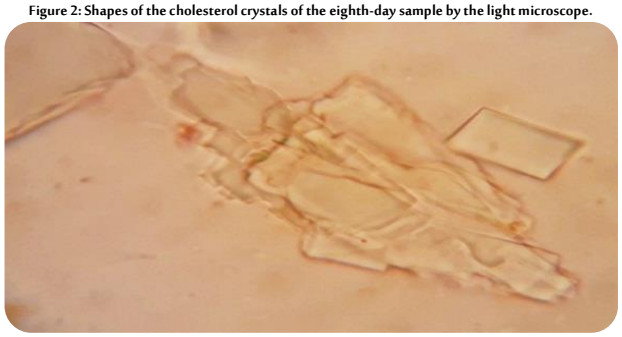

Using the fluorescent microscope appearance of *S. typhi* with the stone-forming crystals surrounded by a viscous material (polysaccharide) was evident in the seventh-day sample Figure 3.

Figure 3: *S. typhi* with crystals surrounded by polysaccharides using the fluorescent microscope.

The scanning electron microscope images of the cholesterol stones formed *in vitro* showed that they appeared as regular plate-like or as lamellar-like crystals or as irregular aggregations with different sizes and three-dimensional crystals using various magnification powers. While calcium carbonate crystals appeared as cubic three-dimensional shapes and spherical, as shown in Figure 4.

Figure 4: Cholesterol and calcium carbonate crystals under the scanning electron microscope.

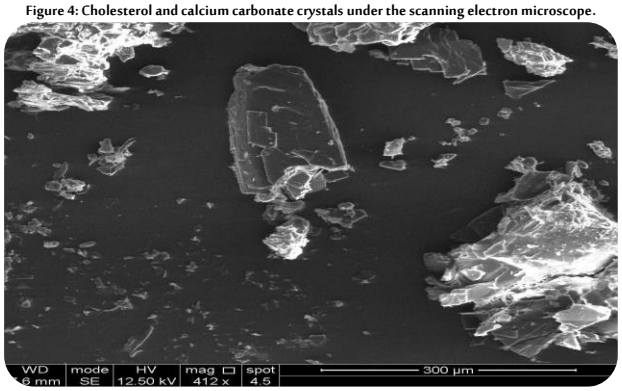

The results of FTIR various peaks for cholesterol and $CaCO_3$ revealed the absorption peak at 3382 cm^{-1} and 2935 cm^{-1} due to CH asymmetric stretching of CH_2 and CH_3, respectively. The peak at 1162 cm^{-1} and 1048 cm^{-1} is due to the functional groups C-C of the cholesterol. The absorption peak at 1457 cm^{-1} shows the presence of the C–O group in the calcium carbonate, and an absorption peak appeared at 1379 cm^{-1} due to CH bending of CH_3 of the cholesterol figure 5.

Figure 5: Infrared spectrum of cholesterol stones formed *in vitro*.

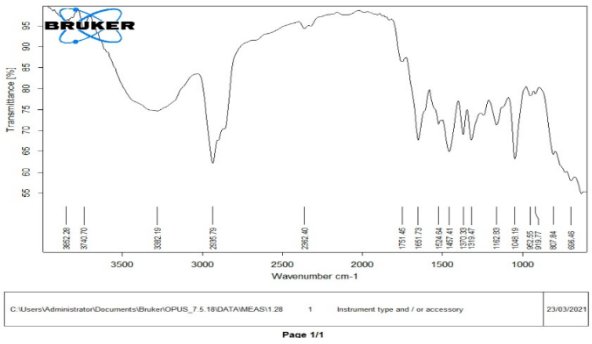

4. Discussion

The results of *S. typhi* identification were identical to the diagnostic tests of *S. typhi*, as mentioned by Willey *et al.*, 2017. The *S. typhi* showed the inability of producing the urease enzyme that hydrolyses urea into ammonia and carbon dioxide, the resulting ammonia raises the pH of the medium, making it alkaline, and therefore the colour changed from yellow to pink. In addition, the isolate showed the ability to produce polysaccharides. When the diagnosis of *S. typhi* was confirmed by using the VITEK2 compact technique, it showed a 99% matching, so this technique is considered quick and accurate in diagnosing bacteria.

In this study, the BGBB medium was used due to its suitability as an alternative medium, providing appropriate conditions for the growth of *S. typhi*, which are similar to the conditions of the bile in the human body. Additionally, the medium contains ox bile, which is chemically similar to the bile of the human. Therefore, the continuous culture provides similar conditions as in the human body; the chemical composition and the components necessary for the growth of *S.typhi*. The pH value and temperature were fixed, the surplus was removed from the continuous culture, and it was provided with the artificial model of the bile, which supports *S. typhi* to achieve stable growth for several generations.

Bile is one of the biological materials that prevent the growth of bacteria; despite this, bacteria were isolated from the bile and the gallstones. Previous studies confirm the role of the bacteria in precipitating the stone crystals. However, no previous study shows the S. typhi role in forming the gallstone and increasing its

solidification.

This study is regarded as the first to highlight the role of *S.typhi* through designing a continuous culture, which provides the optimal conditions for growth and preparing an artificial model of bile to manifest the ability of *S. typhi* to form the cholesterol stones *in vitro*.

S.typhi can colonise the gallbladder, causing chronic infection, primarily due to the existence of gallstones without symptoms and its ability to form the biofilm on the gallstone and the surfaces covered with cholesterol in the laboratory. In a study by Crawford et *al.* (2010), 5% of *S. typhi* was isolated from the gallbladder containing stones, diagnosed using Multiplex PCR. Van Den Berg and his colleagues (2000) pointed out the role of calcium ions and high cholesterol concentration in forming the gallstone when they incubated a human gallstone isolated in a culture saturated with cholesterol and containing a specific calcium concentration. After incubation, they noticed an increase in stone diameter due to the precipitation of the cholesterol crystals and calcium ions on the stones.

Sharma *et al.* (2013) indicated that calcium carbonate plays a vital role in forming the nucleation of crystals. When calcium carbonate is not present, no precipitation occurs, and crystallisation nucleation is not formed. Castro-Torres *et al.* (2015) demonstrated that the presence of the cholesterols crystals alone is not sufficient to form the nucleation of gallstone crystallisation. Several factors play an essential role in forming the nucleation of gallstone, such as calcium ions Ca^{+2} and magnesium ions Mg^{+2} when the cholesterol concentration is high.

In this study, the results of the light microscope elucidate the cholesterol crystal shapes as a single regular plate or as assembled plates with the presence of *S. typhi* attached to the crystal surfaces. With the continuous incubation in suitable conditions, the culture was in progress. By the seventh day, a new culture was added with an 18-hour culture to enhance the metabolic activity of the bacteria. It was observed that a viscous matter was formed that encompasses the crystals and *S. typhi,* and crystallised materials covered a viscous material.

By using the scanning electron microscope, the results follow what has been reported by Sharma *et al.* (2020), that the cholesterol crystals and calcium carbonate can be observed clearly with the bacteria attached to the surfaces of the crystals due to its virulence factors, which help them to attach to the precipitated hard surfaces.

After the tenth day of incubation, the crystallised materials began to change gradually into small spherical masses. On the fourteenth day, an increase in the size of crystallised material was observed, and this agrees with the conclusions of Costa *et al.* (2018) that the slime provides high viscosity and consequently helps in the cohesion and attachment of crystals. Wang *et al.* (2018) demonstrated that the slime is a polymer that forms cross-linkage that aid in precipitating the crystals. They emphasised that slime production is more important than β-glucuronidase, which plays a vital role in forming the gallstone. The polysaccharide acts as additional power that increases the cohesion and adhesion of the crystals; this is a distinguishing characteristic of *S.typhi*.

Sharma *et al.* (2020) concluded that the presence of polysaccharide producing bacteria has a greater effect on forming the crystal agglomerations in a shorter time than the models inoculated with urease or β – glucuronidase producers.

Moreover, FTIR results of stones showed that they consist of cholesterol and calcium carbonate, which agree with what has been reported by Sharma *et al.* (2020), who observed the emergence of absorption peaks at 3387 cm^{-1} and 2939 cm^{-1} that were due to CH asymmetric stretching of CH_2 and CH_3 respectively. In addition, the emergence of absorption peaks at 1162 cm^{-1} and 1052 cm^{-1} belong to the C–C group, which is considered one of the functional groups of cholesterol, and the absorption peak at 1458 cm^{-1} represents the functional group C–O of calcium carbonate. Results are also consistent with Ha and Park (2018); absorption peaks at 3395 cm^{-1} and 2930 cm^{-1} belonging to the functional groups of cholesterol during the analysis of the cholesterol stones isolated from humans.

Kleiner *et al.* (2002) confirmed the presence of calcium carbonate by the emergence of an absorption peak at 1463 cm^{-1}, which indicates the presence of the functional group C–O of calcium carbonate in addition to the presence of absorption peaks at 3398 cm^{-1}, 2933 cm^{-1} and 1056 cm^{-1} that belong to the various functional groups of cholesterol.

S. typhi can form cholesterol stones under continuous culture using an *in vitro* artificial model of the bile. The ability of *S. typhi* to produce slime as a polysaccharide provides a sufficient viscosity for the adhesion of the bacteria to the crystal surfaces, the crystals with each other, and the agglomeration and the quick growth of the crystals to become mature stone. Also, *S. typhi* possesses virulence factors that enhance the agglomeration, and also there are certain factors related to the bile components and its chemical structure, altogether leading to the formation of the gallstone.

Biographies

Sahira Idrees H. Al-Sanjary

Department of Biology, College of Science, University of Mosul, Mosul, Iraq, 009647715531518, asahera34@gmail.com

Mrs Al-Sanjary, Iraqi, is a lecturer at the College of Science, University of Mosul, Iraq. She is currently a PhD applicant in the field of microbiology at the College of Science in Iraq. She obtained her MSc degree from Mosul University. She is a member of the bacterial bank in the Biology Department, Mosul University; she has one patent in microbial ecology, she has more than 12 articles and has participated in three scientific conferences. Her research interest is Microbiology and Molecular Biology.

Amera Mahmood M. Al-Rawi

Department of Biology, College of Science, University of Mosul, Mosul, Iraq, 009647740855469, amesbio5@uomosul.edu.iq

Dr Al-Rawi is an Iraqi Professor, editor-in-chief of Al-Rafidain Journal of Science and supervisor of the bacterial bank in the Biology Department. She has seven patents in different fields of microbiology and five pieces of research under evaluation to obtain patent certification. She is a supervisor of 45 MSc and PhD students and has published more than 125 articles and participated in more than 70 scientific conferences. Her research interest is Microbiology. ORCID: 0000-0001-8924-8149.

References

Al-Amedy, O.S., Saido, G.A. and Hussein, M.R. (2020). Assessment of the women's knowledge regarding cholelithiasis diseases in Duhok city. *Mosul Journal of Nursing*, **8**(1), 42–59. DOI: 10.33899/mjn.2020.164623.

Belzer, C., Kusters, J.G., Kuipers, E.J. and Vanvleit, A.H.M. (2006). Urease induced calcium precipitation by Helicobacter species may initiate gallstone formation. *Gut*, **55**(11), 1678–9. DOI: 10.1136/gut.2006.098319

Castro- Torres, I.G., Cardenas- Vazquez, R., Velazquez- Gonzalez, C., Ventura- Martinez, R., Delao-Arciniega, M., Naranjo- Rodriguez, E.B. and Martinez- Vazquez, M. (2015). Future therapeutic targets for the treatment and prevention of cholesterol gallstones. *Eur. J. pharmacol,* **765**(n/a), 366–74. DOI: 10.1016/j.ejphar.2015.08.045

Costa, O.Y.A., Raaijmakers, J.M. and kuramae, E.E. (2018). Microbial extracellular polymeric substances: Ecological function and impact on soil aggregation-review. *Frontiers in Microbiology*,

9(n/a), 1635. DOI: 10.3389/fmicb.2018.01636

Crawford, R.W., Rosales- Reyes, R., Ramirez- Aguilar, M.L.,Chapa- Azuela, O., Alpuche- Aranda, C. and Gunn, J.S. (2010). Gallstone play a significant role in *salmonella spp*. Gallbladder colonisation and carriage. *Proc Natl Acad Sci USA*, **107**(9), 4353–8. DOI: 10.1073/pnas.1000862107

Di Ciaula, A., Wang, D.Q. and Portincasa, P. (2018). Update on the pathogenesis of cholesterol gallstone disease. *Curr. Opin. Gastroenterol,* **34**(2), 71–80. DOI: 10.1097/MOG.0000000000000423

Di Ciaula, A., Garruti, G., Frühbeck, G., De Angelis, M., De Bari, O., Wang, D., Lammert. F. and Portincasa, P. (2019). The role of diet in the pathogenesis of cholesterol gallstones. *Curr Med Chem.*, **26**(19), 3620–38. DOI: 10.2174/0929867324666170530080636.

Di Domenico, E.G., Cavallo, I., Pontone, M., Toma, L. and Ensoli, F. (2017). Biofilm producing *Salmonella typhi*: Chronic colonisation and development of gallbladder cancer. *Int. J. Mol. Sci*, **18**(9), 1887. DOI: 10.3390/ijms18091887

Echlin, P. (2009). *Handbook of Sample Preparation for Scanning Electron Microscopy and X-Ray Microanalysis*. London: Springer Science Business Media.

Freeman, D.J., Falkiner, F.R. and Keane, C.T. (1989). New method for detecting slime production by coagulase negative Staphylococci. *J Clin Pathol.*, **42**(8), 872–4. DOI: 10.1136/jcp.42.8.872

Grigor'eva, I.N. and Romanova, T.I. (2020). Gallstone disease and microbiome. *Microorganisms,* **8**(6), 835. DOI: 10.3390/microorganisms8060835

Ha, BJ and Park, S. (2018). Classification of gallstones using Fourier-Transform Infrared spectroscopy and photography. *Bio Materials Research*, **22**(1), 2–8. DOI:10.1186/s40824-018-0128-8

Hazrah, P., Oahn, K. T.H., Tewari, M., Pandey, A.K., Kumar, K., Mohapatra, T. M. and Shukla, H.S. (2004). The frequency of live bacteria in gallstones. *HPB*, **6**(1), 28–32. DOI: 10.1080/13651820310025192

Kadhim, H.M. (2020). Review of pathogenicity and virulence determinants in *Salmonella*. *Eurasian Journal of Biosciences*, **14**(1), 377–81. DOI:10.36380/scil.2019.wvj21

Kleiner. O., Ramesh, J., Huleihel, M., Cohen, B., Kantarovich, K., Levi, C., Polyak, B., Marks, R.S., Mordechai, J., Cohen, Z. and Ordechai, S. (2002). A comparative study of gallstones from children and adults using FTIR spectroscopy and fluorescence microscopy. *BMC Gastroenterology*, **2**(1), 3. DOI:10.1186/1471-230X-2-3

MacCarthy, L.R. and Senne, J.E. (1980). Evaluation of Acridine orange for Detection of Microorganisms in Culture. *J. Clin. Microbiol*, **11**(3), 281–5. DOI: 10.1128/JCM.11.3.281-285.1980

Murphy, M.C., Gibney, B., Gillespie, C., Hynes, J. and Bolster, F. (2020). Gallstones top to toe: What the radiologist needs to know? *Insights into Imaging*, **11**(1), 13. DOI: 10.1186/s13244-019-0825-4.

Renaud, F.N., Bergeron, E., Tigaud, S., Fuhrmann, C., Gravagna, B., Freney, J. (2005). Evaluation of the new Vitek 2 GN card for the identification of gram-negative bacilli frequently encountered in clinical laboratories. *Eur. J. Clin. Microbiol. Infect. Dis,* **24**(10), 671–6.
DOI: 10.1007/s10096-005-0026-6.

Rudling, M., Laskar, A., and Straniero, S. (2019). Gallbladder bile super saturated with cholesterol in gallstone patient preferentially develops from shortage of bile acids. *J. Lipid. Res*, **60**(3), 498–505. DOI: 10.1194/jlr.S091199

Sharma, R., Sachan, S.G. and Sharma, S.R. (2020). *In vitro* analysis of gallstone formation in the presence of bacteria. *Indian journal of Gastroenterology*, **39**(5), 473–80. DOI: 10.1007/s12664-020-01055-6.

Sharma, R., Sachan, S.G. and Sharma. S.R. (2013). Urease and slime producing bacterial activity results in gallstone precipitation and solidification. *Arch. Clin Infect Dis*, **8**(4), 1–6. DOI: 10.5812/archcid.17090

Van Den Berg, A.A., Van Buul, J.D., Ostrow, J.D. and Groen, A.K. (2000). Measurement of cholesterol gallstone growth *in vitro*. *J. Lipid. Res.*, **41**(2), 189–94. DOI: 10.1016/S0022-2275(20)32051-4

Wang, Q., Hao, C., Yao, W., Zhu, D., Lu, H., Li, L., Ma, B., Sun, B., Xue, D. and Zhang, W. (2020). Intestinal flora imbalance affects bile acid metabolism and is associated with gallstone formation. *BMC Gastrenteriology,* **20**(59), 2–13. DOI: 10.1186/s12876-020-01195-1

Wang, Y., Qi, M., Qin, C. and Hong, J. (2018). Role of the biliary microbiome in gallstone disease. Expert Rev. *Gastroenterol Hepatol*, **12**(12), 1193–205. DOI: 10.1080/17474124.2018.1533812.

Willey, J.M., Sherwood, L.M. and Woolverton, C.J. (2017). *Prescott's Microbiology*. 10th edition. USA: McGraw-Hill Education, Inc.

The Scientific Journal of King Faisal University

Basic and Applied Sciences

Global Convergence of Nonlinear Conjugate Gradient Coefficients with Inexact Line Search

Awad Abdelrahman [1], Osman O. O. Yousif [1], Mogtaba Mhammed [2] and Murtada K. Elbashir [3]

[1] Department of Mathematics, Faculty of Mathematical and Computer Sciences, University of Gezira, Wad Madani, Sudan
[2] Department of Mathematics, College of Science, Majmaah University, Zulfi, Saudi Arabia
[3] Department of Information Systems, College of Computer and Information Sciences, Jouf University, Sakaka, Saudi Arabia

LINK	RECEIVED	ACCEPTED	PUBLISHED ONLINE	ASSIGNED TO AN ISSUE
https://doi.org/10.37575/b/sci/210058	26/09/2021	26/11/2021	26/11/2021	01/12/2021

NO. OF WORDS	NO. OF PAGES	YEAR	VOLUME	ISSUE
3796	6	2021	22	2

ABSTRACT

Nonlinear conjugate gradient (CG) methods are significant for solving large-scale, unconstrained optimization problems, providing vital knowledge to determine the minimum point or optimize the objective functions. Many studies of modifications for nonlinear CG methods have been carried out to improve the performance of numerical computation and to establish global convergence properties. One of these studies is the modified CG method, which has been proposed by Rivaie *et al.* (2015). In this paper, we modify their work in such a way that one can obtain efficient numerical performance and global convergence properties. Due to the widespread use of the strong Wolfe line search in practice, our proposed modified method implemented its use. At the same time, to show the performance of the modified method in practice, a numerical experiment is performed.

KEYWORDS

Unconstrained optimization; conjugate gradient method; sufficient descent property; global convergence

CITATION

Abdelrahman, A., Yousif, O.O.O., Mhammed, M. and Elbashir, M.K. (2021). Global convergence of nonlinear conjugate gradient coefficients with inexact line search. *The Scientific Journal of King Faisal University: Basic and Applied Sciences*, **22**(2), 86–91. DOI: 10.37575/b/sci/210058

1. Introduction

Due to their global convergence and low memory requirements, conjugate gradient methods are widely used for solving unconstrained optimization problems. The unconstrained optimization problems can be formulated as follows:

$$\min_{x\in R^n} f(x), \tag{1.1}$$

where $f: R^n \to R$ is nonlinear, continuously differentiable, and its gradient is denoted by $g(x)$, which should be available, when applied to solve the Problem (1.1), starting from an initial point $x_0 \in R^n$, and follows the iteration formula:

$$x_{k+1} = x_k + \alpha_k d_k \ , \quad k = 0,1,2 \ldots, \tag{1.2}$$

where $\alpha_k > 0$ is a step-size. The step-size is determined by a line search, and d_k is the search direction defined by:

$$d_k = \begin{cases} -g_k & \text{if } k = 0, \\ -g_k + \beta_k d_{k-1} & \text{if } k \geq 1, \end{cases} \tag{1.3}$$

where $g_k = \nabla f(x_k)$ is the gradient vector of the function f at x_k and g_k^T is the transpose of g_k. The value β_k is a scalar known as the CG coefficient. The well-known classical CG methods formulas for β_k are:

$$\beta_k^{HS} = \frac{g_k^T(g_k - g_{k-1})}{(g_k - g_{k-1})^T d_{k-1}}, \tag{1.4}$$

$$\beta_k^{FR} = \frac{g_k g_k}{g_{k-1}^T g_{k-1}}, \tag{1.5}$$

$$\beta_k^{PRP} = \frac{g_k^T(g_k - g_{k-1})}{g_{k-1}^T g_{k-1}}, \tag{1.6}$$

$$\beta_k^{CD} = -\frac{g_k^T g_k}{d_{k-1}^T g_{k-1}}, \tag{1.7}$$

$$\beta_k^{LS} = -\frac{g_k^T(g_k - g_{k-1})}{d_{k-1}^T g_{k-1}}, \tag{1.8}$$

$$\beta_k^{DY} = \frac{g_k^T g_k}{(g_k - g_{k-1})^T d_{k-1}}. \tag{1.9}$$

To analyze the convergence, the CG methods are implemented under exact and inexact line searches. If the line search is exact, the step length α_k is obtained in the direction d_k by the rule:

$$f(x_k + \alpha_k d_k) = \min_{\alpha \geq 0} f(x_k + \alpha d_k). \tag{1.10}$$

In the inexact line search, α_k can be obtained using the strong Wolfe line search, in which the following conditions satisfy:

$$f(x_k + \alpha_k d_k) \leq f(x_k) + \delta \alpha_k g_k^T d_k, \tag{1.11}$$

$$|g(x_k + \alpha_k d_k)^T d_k| \leq -\sigma g_k^T d_k, \tag{1.12}$$

where $0 < \delta < \sigma < 1$.

To prove the global convergence of CG methods, the following sufficient descent condition is always required:

:

$$g_k^T d_k \leq -c\|g_k\|^2 , \ \text{for } k \geq 0 \text{, where } c > 0 \tag{1.13}$$

The performance and behavior of different conjugate gradient methods for general non-quadratic functions with an inexact line search correspond to different choices for the important coefficient β_k. The global convergence properties of CG methods are essential properties for studying the coefficient β_k and obtaining good numerical performance. The CG methods were categorized by Andrei (2011) into three different methods: the classical CG method, the scaled CG method, and the hybrid and parameterized CG method. Al-Baali (1985), Touati-Ahmed and Storey (1990), and Gilbert and Nocedal (1992) used the inexact line search with a strong Wolfe condition in order to analyze the global convergence properties of FR(1.5) is known as Fletcher and Reeves (1964) and PRP(1.6) is known as Polak–Ribiere–Polyak (1969) methods. Al-Baali (1985) proved the global convergence of the FR method if the strong Wolfe line search is used and the parameter σ is restricted in $(0, \frac{1}{2})$. In addition, Guanghui *et al.* (1995) extended Al-Baali's (1985) result with the case that $\sigma = \frac{1}{2}$. The PRP and HS(1.4) is known as Hestenes and Steifel (1952) methods have excellent performance in practical computation, due to the inclusion of an approximate restart feature when jamming occurs, but their convergence properties are not perfect (Jiang *et al.*, 2018). Nevertheless, both perform better than FR in practical computations. The study of the PRP method has an efficient approach and has made significant improvements. Gilbert and Nocedal (1992) proceeded with classificatory analysis and concluded that the PRP method is

Corresponding Author: Awad Abdelrahman Abdalla Mohammed 00249962255448, awad.abdalla26@yahoo.com

globally convergent if β_k^{PRP} is constrained to be non-negative and α_k is determined by a line search step satisfying the sufficient descent condition $g_k^T d_k \leq -c\,\|g_k\|^2$.

Many studies have been carried out to establish global convergence and obtain competitive numerical results by proposing new methods or modifying existing methods.

Rivaie *et al.* (2012) have proposed a new coefficient denoted by β_k^{RMIL}, as follows:

$$\beta_k^{RMIL} = \frac{g_k^T(g_k - g_{k-1})}{\|d_{k-1}\|^2},$$

which is globally convergent and has good performance when it is applied under exact line search. Dai (2016) made a simple modification to Rivaie *et al.* (2012), and, on this basis, Yousif (2020) established the sufficient descent conditions and global convergence using the strong Wolfe line search. Additionally, Rivaie *et al.* (2015) proposed a new class of nonlinear conjugate gradient coefficients with exact and inexact line searches and named this the RMIL+ method. The coefficient β_{k+1} in RMIL+ method is defined as follows:

$$\beta_{k+1}^{RMIL+} = \frac{g_{k+1}^T(g_{k+1} - g_k - d_k)}{\|d_k\|^2}, \quad (1.14)$$

In this paper, in order to obtain better numerical performance than the methods in Rivaie *et al.* (2012), Rivaie *et al.* (2015), and Yousif (2020), we performed a modification on the method in Rivaie *et al.* (2015). In Section 2, we present a modified CG method and algorithm. The descent property and the global convergence under the strong Wolfe line search are described in Section 3. In Section 4, we present preliminary numerical results and discussion. Lastly, in Section 5, we present a conclusion.

2. Simple Modification of the RMIL+ Method

In this section, we modify the CG method in Rivaie *et al.* (2015), known as the RMIL+ method, to obtain better results. We refer to the modified method by MRMIL+, and its coefficient is defined as follows:

$$\beta_{k+1}^{MRMIL+} = \max\{0, \beta_{k+1}^{RMIL+}\}. \quad (2.1)$$

Clearly, from (2.1), the suggested coefficient satisfies the following two inequalities:

$$\beta_{k+1}^{MRMIL+} \leq \frac{\|g_k\|^2}{\|d_k\|^2}, \text{ if } \frac{g_{k+1}^T g_k + g_{k+1}^T d_k}{\|d_k\|^2} \geq 0. \quad (2.2)$$

$$\beta_{k+1}^{MRMIL+} \leq m\frac{\|g_k\|^2}{\|d_k\|^2}, \text{ if } \frac{g_{k+1}^T g_k + g_{k+1}^T d_k}{\|d_k\|^2} < 0, \text{ where } m > 1. \quad (2.3)$$

To distinguish between RMIL+ in Rivaie *et al.* (2015), and RMIL+ in Yousif (2020), we use MRMIL instead of RMIL+ as used in Rivaie *et al.* (2015).

By defining a new coefficient in (2.1), we can define the following new algorithm:

Algorithm 1

- **Step 1**: Initialization given x_0 , set $k = 0$.
- **Step 2**: Compute β_{k+1} based on (2.1).
- **Step 3**: Compute d_{k+1} based on (1.3). If $g_k = 0$, then stop.
- **Step 4**: Compute α_k based on a strong Wolfe line search (1.11), (1.12).
- **Step 5**: Updating new point based on (1.2).
- **Step 6**: Convergent test and terminal criteria.

If $f(x_{k+1}) \leq f(x_k)$ and $\|g_k\| \leq \epsilon$, then stop.

Otherwise go to Step 1 with $k = k + 1$.

3. Convergence Analysis

In this section, using the strong Wolfe line search, we will show the convergence properties of MRMIL +; essentially, the convergence properties of Algorithm 1. Since global convergence involves satisfying the sufficient descent condition, we first prove sufficient descent. The following basic assumption on the objective function f is always needed in the analysis of CG methods' global convergence properties, and Lemma 1 is needed to show the sufficient descent condition and global convergence properties of the MRMIL + method.

Assumption 1

(i) F(x) is bounded below on the level set on R^n and is continuously differentiable in a neighborhood N of the level set $\Gamma = \{x \in R^n | f(x) \leq f(x_0)\}$ at the initial point x_0, there exists a constant $B > 0$ such that:

$$\|x - y\| \leq B, \quad \forall x, y \in N \quad (3.1)$$

(ii) The gradient $g(x) = \nabla f(x)$ is Lipschitz continuous in N, so a constant $L > 0$ exists, such that:

$$\|g(x) - g(y)\| \leq L\|x - y\| \text{ for anyx, y } \epsilon \text{ N.} \quad (3.2)$$

By using the Assumption 1, there exists a constant $\lambda \geq 0$ such that:

$$\|g(x)\| \leq \lambda \quad \forall x \in \Gamma. \quad (3.3)$$

For example, if a function satisfying Assumption 1 is the Rosenbrock function (Andrei, 2008), which is defined as:

$$f(x) = 100(x_2 - x_1^2)^2 + (1 - x_1)^2, \; x \in \mathbb{R}^2,$$

with

$$\nabla f(x) = \begin{pmatrix} -400x_1(x_2 - x_1^2) + 2(1 - x_1) \\ 200(x_2 - x_1^2) \end{pmatrix}.$$

So, for the initial point $x_0 = [-1 \quad 1]$, we get

$$\nabla f(x_0) = \begin{pmatrix} 4 \\ 0 \end{pmatrix}, \text{ and } \|\nabla f(x_0)\| = \sqrt{(4)^2 + (0)^2} = \sqrt{16} = 4.$$

Lemma 1: Let the sequences $\{g_k\}$ and $\{d_k\}$ be generated by Algorithm 1. Then for $\sigma < \frac{1}{2}$ and $k \geq 0$, we have:

$$\frac{\|g_k\|}{\|d_k\|} \leq \frac{2}{4 - 3\tau}, \quad (3.4)$$

$$\frac{\|g_k\|}{\|d_k\|} \leq \frac{m}{m - \tau}, \quad (3.5)$$

where $\tau \in (\frac{2}{3}, 1)$, and $m > 1$.

Proof: The proof is by induction. For $k = 0$, it is obvious that $\frac{\|g_0\|}{\|d_0\|} = 1 \leq \frac{2}{4-3\tau}, \frac{\|g_0\|}{\|d_0\|} = 1 \leq \frac{m}{m-\tau}$. Next, assume that (3.4) and (3.5) are both true for $k \geq 1$. Then by rewriting equation (1.3) for $k + 1$ and then by using the dot product, we get:

$$d_{k+1}.d_{k+1} = (-g_{k+1} + \beta_{k+1}d_k).(-g_{k+1} + \beta_{k+1}d_k),$$

which leads to:

$$\|d_{k+1}\|^2 = \|g_{k+1}\|^2 - 2\beta_{k+1}g_{k+1}^T d_k + (\beta_{k+1}\|d_k\|)^2. \quad (3.6)$$

Again rewriting (1.3) as:

$$d_{k+1} + g_{k+1} = \beta_{k+1}d_k, \quad (3.7)$$

and then from the definition of the dot product, we obtain:

$$\|d_{k+1}\|^2 + \|g_{k+1}\|^2 + 2g_{k+1}^T d_{k+1} = (\beta_{k+1}\|d_k\|)^2. \quad (3.8)$$

Substituting (3.8) in (3.6), led to:

$$\|d_{k+1}\|^2 + \|g_{k+1}\|^2 + 2g_{k+1}^T d_{k+1} = \|d_{k+1}\|^2 - \|g_{k+1}\|^2 + 2\beta_{k+1}g_{k+1}^T d_k,$$

$$2\|g_{k+1}\|^2 + 2g_{k+1}^T d_{k+1} = 2\beta_{k+1}g_{k+1}^T d_k,$$

$$\|g_{k+1}\|^2 + g_{k+1}^T d_{k+1} = \beta_{k+1}g_{k+1}^T d_k,$$

$$\|g_{k+1}\|^2 = -g_{k+1}^T d_{k+1} + \beta_{k+1}g_{k+1}^T d_k. \quad (3.9)$$

Taking the absolute value of both sides of (3.9) and (1.12), we have:

$$\|g_{k+1}\|^2 = \left|-g_{k+1}^T d_{k+1} + \beta_{k+1} g_{k+1}^T d_k\right| \le \left|g_{k+1}^T d_{k+1}\right| + \sigma\left|\beta_{k+1}\right|\left|g_k^T d_k\right|. \quad (3.10)$$

Applying the Cauchy-Schwartz inequality, and using (2.2), we get:

$$\|g_{k+1}\|^2 \le \|g_{k+1}\|\|d_{k+1}\| + \sigma\frac{\|g_{k+1}\|^2}{\|d_k\|^2}\|g_k\|\|d_k\|,$$

$$\|g_{k+1}\|^2 \le \|g_{k+1}\|\|d_{k+1}\| + \sigma\|g_{k+1}\|^2\frac{\|g_k\|}{\|d_k\|}.$$

Applying induction hypothesis of Lemma1, we obtain:

$$\|g_{k+1}\|^2 \le \|g_{k+1}\|\|d_{k+1}\| + \frac{2\sigma}{4-3\tau}\|g_{k+1}\|^2.$$

By letting $\gamma = \frac{2\sigma}{4-3\tau}$, then:

$$\|g_{k+1}\|^2 - \gamma\|g_{k+1}\|^2 \le \|g_{k+1}\|\|d_{k+1}\|,$$

$$\|g_{k+1}\|^2(1-\gamma) \le \|g_{k+1}\|\|d_{k+1}\|,$$

$$\frac{\|g_{k+1}\|}{\|d_{k+1}\|} \le \frac{1}{1-\gamma} \le \frac{2}{4-3\tau}. \quad (3.11)$$

From (3.10), and applying the Cauchy–Schwartz inequality, and from (2.3), we get:

$$\|g_{k+1}\|^2 \le \|g_{k+1}\|\|d_{k+1}\| + \sigma m\frac{\|g_{k+1}\|^2}{\|d_k\|^2}\|g_k\|\|d_k\|,$$

$$\|g_{k+1}\|^2 \le \|g_{k+1}\|\|d_{k+1}\| + \sigma m\|g_{k+1}\|^2\frac{\|g_k\|}{\|d_k\|}.$$

Applying induction hypothesis, we obtain:

$$\|g_{k+1}\|^2 \le \|g_{k+1}\|\|d_{k+1}\| + \frac{\sigma m}{m-\tau}\|g_{k+1}\|^2.$$

By letting $\vartheta = \frac{\sigma m}{m-\tau}$, then:

$$\|g_{k+1}\|^2 - \vartheta\|g_{k+1}\|^2 \le \|g_{k+1}\|\|d_{k+1}\|,$$

$$\|g_{k+1}\|^2(1-\vartheta) \le \|g_{k+1}\|\|d_{k+1}\|,$$

$$\frac{\|g_{k+1}\|}{\|d_{k+1}\|} \le \frac{1}{1-\vartheta} \le \frac{m}{m-\tau}. \quad (3.12)$$

Therefore, from (3.11) and (3.12), Lemma 1 holds for $k+1$. The proof is completed.

3.1. Sufficient Descent Condition:

Theorem 1. Suppose Assumption 1 is true, then Algorithm 1 satisfies the sufficient descent property (1.13) with:

$$c = 1 - \frac{2\sigma}{4-3\tau} \quad \text{and} \quad c = 1 - \frac{\sigma m}{m-\tau}.$$

Proof: From (1.4) and (2.2), then:

$$g_{k+1}^T d_{k+1} = -\|g_{k+1}\|^2 + \beta_{k+1} g_{k+1}^T d_k \le -\|g_{k+1}\|^2 + \frac{\|g_{k+1}\|^2}{\|d_k\|^2} g_{k+1}^T d_k. \quad (3.14)$$

from (1.12) and the Cauchy–Schwartz, we get:

$$g_{k+1}^T d_{k+1} \le -\|g_{k+1}\|^2 + \frac{\|g_{k+1}\|^2}{\|d_k\|^2} g_{k+1}^T d_k \le -\|g_{k+1}\|^2 + \sigma\frac{\|g_{k+1}\|^2}{\|d_k\|^2}\|g_k\|\|d_k\| = -\|g_{k+1}\|^2 + \sigma\|g_{k+1}\|^2\frac{\|g_k\|}{\|d_k\|}.$$

From (3.4) in Lemma1, we obtain:

$$g_{k+1}^T d_{k+1} \le -\|g_{k+1}\|^2 + \frac{2\sigma}{4-3\tau}\|g_{k+1}\|^2 = -\|g_{k+1}\|^2\left(1 - \frac{2\sigma}{4-3\tau}\right) \quad (3.15)$$

In addition, from (3.14), (2.3), (1.12), and Cauchy–Schwartz inequality, we get:

$$g_{k+1}^T d_{k+1} \le -\|g_{k+1}\|^2 + \frac{\|g_{k+1}\|^2}{\|d_k\|^2} g_{k+1}^T d_k \le -\|g_{k+1}\|^2 + \sigma m\frac{\|g_{k+1}\|^2}{\|d_k\|^2}\|g_k\|\|d_k\| = -\|g_{k+1}\|^2 + \sigma m\|g_{k+1}\|^2\frac{\|g_k\|}{\|d_k\|}.$$

From (3.5) in Lemma1, we obtain:

$$g_{k+1}^T d_{k+1} \le -\|g_{k+1}\|^2 + \frac{\sigma m}{m-\tau}\|g_{k+1}\|^2 = -\|g_{k+1}\|^2\left(1 - \frac{\sigma m}{m-\tau}\right). \quad (3.16)$$

Therefore, from (3.15), (3.16), we can deduce that (1.13) holds for $k \ge 0$. The proof is completed.

3.2 Global Convergence:

Lemma 2. Suppose Assumption 1 holds true. Consider any CG method of from (1.3), where d_{k+1} is a descent search direction and α_k satisfies the strong Wolfe line search. The following condition, known as the Zoutendijk condition, holds:

$$\sum_{k=1}^{\infty}\frac{\|g_k\|^4}{\|d_k\|^2} < \infty.$$

For the proof of this Lemma 2. Please refer to Zoutendijk (1970).

Theorem 2. Suppose that Assumption 1 holds true. Then Algorithm 1 is convergent, as follows:

$$\lim_{k\to\infty}\|g_k\| = 0 \quad \text{or} \quad \sum_{k=1}^{\infty}\frac{\|g_k\|^4}{\|d_k\|^2} < \infty.$$

Proof: We use a contradiction; that is, if Theorem 2 is not true, then there exists a constant $\epsilon > 0$, such that:

$$\|g_k\| \ge \epsilon. \quad (3.17)$$

We can rewrite (1.3) as:

$$d_{k+1} = -g_{k+1} + \beta_{k+1} d_k \quad (3.18)$$

and multiply both sides of (3.18) by d_{k+1}, thus obtaining:

$$\|d_{k+1}\|^2 = -g_{k+1}^T d_{k+1} + \beta_{k+1} d_{k+1}^T d_k. \quad (3.19)$$

Case 1, using (2.2), and divide both sides of (3.19) by $\|g_{k+1}\|^4$, we obtain:

$$\frac{\|d_{k+1}\|^2}{\|g_{k+1}\|^4} \le -\frac{g_{k+1}^T d_{k+1}}{\|g_{k+1}\|^4} + \frac{\|g_{k+1}\|^2}{\|d_k\|^2}\frac{d_{k+1}^T d_k}{\|g_{k+1}\|^4},$$

applying the Cauchy–Schwartz, we get:

$$\frac{\|d_{k+1}\|^2}{\|g_{k+1}\|^4} \le -\frac{g_{k+1}^T d_{k+1}}{\|g_{k+1}\|^4} + \frac{1}{\|d_k\|}\frac{\|d_{k+1}\|}{\|g_{k+1}\|^2},$$

$$\le -\frac{1}{2}\left(\frac{g_{k+1}}{\|g_{k+1}\|^2} + \frac{d_{k+1}}{\|g_{k+1}\|^2}\right)^2\frac{1}{2}\frac{\|g_{k+1}\|^2}{\|g_{k+1}\|^4} - \frac{1}{2}\frac{\|d_{k+1}\|^2}{\|g_{k+1}\|^4} + \frac{1}{\|d_k\|}\frac{\|d_{k+1}\|}{\|g_{k+1}\|^2},$$

$$\le -\frac{1}{2}\frac{1}{\|g_{k+1}\|^2} - \frac{1}{2}\frac{\|d_{k+1}\|^2}{\|g_{k+1}\|^4} + \frac{1}{\|d_k\|}\frac{\|d_{k+1}\|}{\|g_{k+1}\|^2},$$

$$\le -\frac{1}{2}\frac{\|d_{k+1}\|^2}{\|g_{k+1}\|^4} + \frac{1}{\|d_k\|}\frac{\|d_{k+1}\|}{\|g_{k+1}\|^2},$$

$$\frac{3}{2}\frac{\|d_{k+1}\|^2}{\|g_{k+1}\|^4} \le \frac{1}{\|d_k\|}\frac{\|d_{k+1}\|}{\|g_{k+1}\|^2},$$

From (3.4) in Lemma 1, we get:

$$\frac{\|d_{k+1}\|}{\|g_{k+1}\|^2} \le \frac{2}{3}\frac{1}{\|d_k\|} \le \frac{2}{3}\frac{\mu}{\|g_k\|}, \text{ where } \mu = \frac{2}{4-3\tau}.$$

Squaring both sides of the above inequality, we obtain:

$$\frac{\|d_{k+1}\|^2}{\|g_{k+1}\|^4} \le \frac{4}{9}\frac{\mu^2}{\|g_k\|^2},$$

$$\frac{\|d_{k+1}\|^2}{\|g_{k+1}\|^4} \le \frac{4}{9}\frac{\mu^2}{\|g_k\|^2} \le \frac{4\mu^2}{9}\sum_{i=0}^{k}\frac{1}{\|g_k\|^2} \le \frac{4\mu^2}{9}\frac{k}{\epsilon^2},$$

$$\frac{\|g_{k+1}\|^4}{\|d_{k+1}\|^2} \ge \frac{9\epsilon^2}{4\mu^2 k}. \quad (3.20)$$

Therefore, from (3.20) and (3.17), it follows that:

$$\sum_{k=0}^{\infty}\frac{\|g_{k+1}\|^4}{\|d_{k+1}\|^2} = \infty.$$

This contradicts the Zoutendijk condition in Lemma 2. Therefore, the proof is completed.

Case 2, using (2.3) and dividing both sides of (3.19) by $\|g_{k+1}\|^4$, we obtain:

$$\frac{\|d_{k+1}\|^2}{\|g_{k+1}\|^4} \le -\frac{g_{k+1}^T d_{k+1}}{\|g_{k+1}\|^4} + m\frac{\|g_{k+1}\|^2}{\|d_k\|^2}\frac{d_{k+1}^T d_k}{\|g_{k+1}\|^4},$$

applying the Cauchy–Schwartz inequality, we get:

$$\frac{\|d_{k+1}\|^2}{\|g_{k+1}\|^4} \le -\frac{g_{k+1}^T d_{k+1}}{\|g_{k+1}\|^4} + \frac{m}{\|d_k\|}\frac{\|d_{k+1}\|}{\|g_{k+1}\|^2},$$

$$\le -\frac{1}{2}\left(\frac{g_{k+1}}{\|g_{k+1}\|^2} + \frac{d_{k+1}}{\|g_{k+1}\|^2}\right)^2 - \frac{1}{2}\frac{\|g_{k+1}\|^2}{\|g_{k+1}\|^4} - \frac{1}{2}\frac{\|d_{k+1}\|^2}{\|g_{k+1}\|^4} + \frac{m}{\|d_k\|}\frac{\|d_{k+1}\|}{\|g_{k+1}\|^2},$$

$$\le -\frac{1}{2}\frac{1}{\|g_{k+1}\|^2} - \frac{1}{2}\frac{\|d_{k+1}\|^2}{\|g_{k+1}\|^4} + \frac{m}{\|d_k\|}\frac{\|d_{k+1}\|}{\|g_{k+1}\|^2},$$

$$\le -\frac{1}{2}\frac{\|d_{k+1}\|^2}{\|g_{k+1}\|^4} + \frac{m}{\|d_k\|}\frac{\|d_{k+1}\|}{\|g_{k+1}\|^2},$$

$$\frac{3}{2}\frac{\|d_{k+1}\|^2}{\|g_{k+1}\|^4} \leq \frac{m}{\|d_k\|}\frac{\|d_{k+1}\|}{\|g_{k+1}\|^2},$$

From (3.5) in Lemma 1, we get:

$$\frac{\|d_{k+1}\|}{\|g_{k+1}\|^2} \leq \frac{2}{3}\frac{m}{\|d_k\|} \leq \frac{2}{3}\frac{m\rho}{\|g_k\|}, \text{ where } \rho = \frac{m}{m-\tau},$$

Squaring both sides of the above inequality, we obtain:

$$\frac{\|d_{k+1}\|^2}{\|g_{k+1}\|^4} \leq \frac{4}{9}\frac{m^2\rho^2}{\|g_k\|^2},$$
$$\frac{\|d_{k+1}\|^2}{\|g_{k+1}\|^4} \leq \frac{4}{9}\frac{m^2\rho^2}{\|g_k\|^2} \leq \frac{4m^2\rho^2}{9}\sum_{i=0}^{k}\frac{1}{\|g_k\|^2} \leq \frac{4m^2\rho^2}{9}\frac{k}{\epsilon^2},$$
$$\frac{\|g_{k+1}\|^4}{\|d_{k+1}\|^2} \geq \frac{9\epsilon^2}{4m^2\rho^2 k}. \qquad (3.21)$$

Therefore, from (3.21) and (3.17), it follows that:

$$\sum_{k=0}^{\infty}\frac{\|g_{k+1}\|^4}{\|d_{k+1}\|^2} = \infty.$$

This contradicts the Zoutendijk condition in Lemma 2. Therefore, the proof is completed.

4. Numerical Results and Discussion

In this section, to show the efficiency of the proposed method in practice, we compare it with the RMIL, MRMIL, and RMIL+ methods. Most of the test problems used are from Andrei (2008). The condition $\|g_k\| \leq \epsilon$ where $\epsilon = 10^{-6}$ is used as a stopping criterion. All methods are run on a PC ACER (Intel® Core™ i3-3217u CPU @ 1.8 GHZ, with 4.00 GB RAM, Windows 10 Home Premium). The comparison is based on the number of iterations and CPU time. The strong Wolfe line search is used as the inexact line search. The performance results are shown in Figures 1 and 2, respectively, using the performance profile introduced by Dolan and More (2002). In Table 1, Dim is for the dimension of the test functions.

In the Dolan and More performance, we use the performance profile to introduce the notion of a means to evaluate and compare the performance of the set solvers S on a test set p. Assuming n_s solvers and n_p problems exist, for each problem p and solver s, they defined $t_{p,s}$ as computing time (the number of iterations or CPU time or others) required to solve problem p by solver S. They compared the performance on problem p by solver S with the best performance by any solver in this problem by using the performance ratio:

$$r_{p,s} = \frac{t_{p,s}}{\min\{t_{p,s} : s \in S\}}.$$

Suppose that a parameter $r_M \geq r_{p,s}$ for all p and S is chosen, and $r_{p,s} = r_M$ if and only if solver S does not solve problem p. The performance solver S of the given problems must be robust, but we would like to obtain all evaluation performance of the solver; thus, it was defined:

$$P(t)_s = \frac{1}{n_p}\text{size}\{p \in P : r_{p,s} \leq t\}.$$

The $P(t)_s$ was probability for solver $s \in S$ that a performance ratio $r_{p,s}$ was within a factor $t \in R$ of efficient ratio. Then, function P_s was the cumulative distribution function for the performance ratio. The performance profile $P: R \to [0,1]$ as a solver as non-decreasing, piecewise, and continuous from the right. The value $P(1)_s$ is the probability that the solver will perform better than the rest of the solvers. In all, a solver with high values of $P(t)_s$ or at the top right of the figures is preferable or represents a robust solver.

Table 1: A list of test problems

No.	Problems	Dim	Initial points
1	Booth	2	(5, 5) (8, 8)
2	Three-hump camel	2	(-1, 2) (-1, 1)
3	Six-hump camel	2	(-1, 2) (5, 5)
4	Trecanni	2	(-5, -5) (10, 10)
5	Zettl	2	(-1, 2) (7, 7)
6	Leon	2	(0, 0) (-1, -1)
7	Extended. Maratos	4	(5,5,5,5) (10,10,10,10)
8	Arwhead	4	(-1,-1,-1,-1) (10,10,10,10)
9	Freudenstein & Roth	4	(-1, -1, -1, -1) (5, 5, 5, 5)
10	Generalized Quadratic	10	(2, 2, ..., 2) (10, 10, ..., 10)
11	Fletcher	10	(0, 0, ..., 0) (10, 10, ..., 10)
12	Generalized Tridiagonal 1	10	(2, 2, ..., 2) (-3, -3, ..., -3)
13	Hager	10	(1, 1, ..., 1) (-5, -5, ..., -5)
14	Ex. White & Holst	500	(-1.2, -1.2, ..., -1.2) (3, 3, ..., 3)
		1000	(2, 2, ..., 2) (-5, -5, ..., -5)
15	Extended Rosenbrock	1000	(3, 3, ..., 3) (10, 10, ..., 10)
		10000	(-1, -1, ..., -1) (-2, -2, ..., -2)
16	Extended Himmelblau	1000	(-1, -1, ..., -1) (20, 20, ..., 20)
		10000	(-1, -1, ..., -1) (20, 20, ..., 20)
17	Shallow	1000	(-5, -5, ..., -5) (5, 5, ..., 5)
18	Extended Beale	1000	(-1, -1, ..., -1) (2, 2,...,2)
		10000	(-1, -1, ..., -1) (0.2, 0.2, ..., 0.2)
19	Extended DENSCHNB	10 100	(-2, -2, ..., -2) (-10, -10, ..., -10) (1, 1, ..., 1) (-20, -20, ..., -20)
20	Extended Penalty	10 100	(5, 5, ..., 5) (-10, -10, ..., -10) (5, 5, ..., 5) (-10, -10, ..., -10)
21	Matyas	2	(10,10)
22	Colville	4	(-3,-3,-3,-3) (10,10,10,10)
23	Dixon and Price	100	(-2,...,-2) (10,...,10)
24	Sum squares	4 100	(-2,...,-2) (-2,...,-2)
25	Extended Wood	4	(10,...,10) (-1,...,-1)
26	Strait	4 100 1000	(-1,...,-1) (5,...,5) (5,...,5)
27	ARWHEAD	10	(-2,...,-2)
28	Generalized Rosenbrock	10	(-5,...,-5)
29	Quartic	100	(-4,...,-4)
30	DIXON3DQ	10 100	(-10,...,-10) (-7,...,-7)
31	NONSCOMP	10	(2,...,2)
32	POWER	100	(-5,...,-5)
33	Quadratic QF1 Extended	100	(3,...,3)
34	Quadratic Penalty QP2	10 1000	(10,...,10) (-3,...,-3)
35	Quadratic Penalty QP1	1000	(-3,...,-3)

Figure 1: Performance profile based on the number of iterations

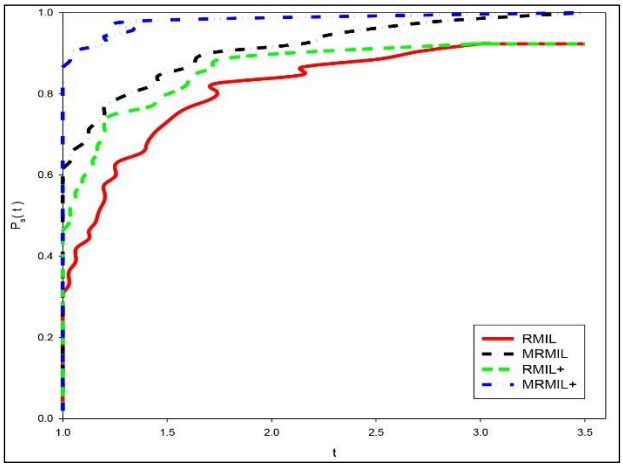

Figure 2: Performance profile based on the CPU time

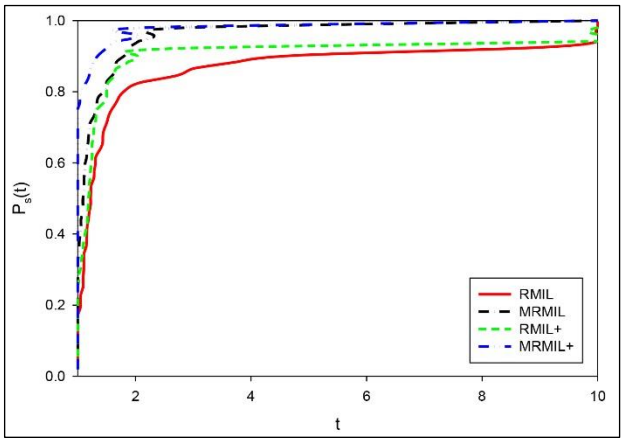

Clearly from Figs. 1 and 2, the MRMIL+ curve lies above the RMIL, MRMIL, and RMIL+ curves. Therefore, the MRMIL+ method performs much better than the other three methods. Moreover, MRMIL and MRMIL+ methods solve all problems, whereas RMIL+ and RMIL solve about 83% of the problems. Therefore, since MRMIL+ has the top curve and it solves all problems, we can conclude that it is the best method.

5. Conclusion

In this paper, based on Rivaie *et al.* (2015), we have presented a modified version of the RMIL+ conjugate gradient method. The proof of the sufficient descent property and of the global convergence of our modified method when it is applied under the strong Wolfe line search has been established. Moreover, to show its efficiency in practical computation, we have compared it with the RMIL, MRMIL, and RMIL+ methods. The result of this comparison is that our modified method performs much better than the others.

Biographies

Awad Abdelrahman

Department of Mathematics, Faculty of Mathematical and Computer Sciences, University of Gezira, Wad Madani, Sudan, awad.abdalla26@yahoo.com, 00249962255448

Dr. Abdelrahman (Sudanese) is an assistant Professor at the University of Gezira. He has received his Ph.D. degree in mathematical sciences from the University of Malaysia Terengganu, Malaysia in 2017. Also, he is now a head of the documentation committee and a member of the courses development committee. He is interested in optimization and computational mathematics. He supervised undergraduate and M.Sc. students. He has participated in conferences in Malaysia and Sudan and served as a co-chair of the ICCCEEE18 conference, held in Khartoum in 2018. ORCID: 0000-0001-5467-5124.

Osman Omer Osman Yousif

Department of Mathematics, Faculty of Mathematical and Computer Sciences, University of Gezira, Wad Madani, Sudan, osman_om@hotmail.com, 00249119733535

Dr. Yousif (Sudanese) is an assistant professor at the University of Gezira, Sudan since 2017 after the approval of his Ph.D. degree from University of Malaysia Terengganu, Malaysia. Also, he is now the head of Mathematics Department. His research interests lie at the intersection of computational mathematics and optimization methods. He has supervised many graduation projects in these areas. Besides, he has participated in four conferences as a presenter in Malaysia and published four papers in ISI- and Scopus-indexed journals.

Mogtaba Mohammed

Department of Mathematics, College of Science, Majmaah University, Zulfi, Saudi Arabia, mogtaba.m@mu.edu.sa, 00966543244128

Dr Mohammed (Sudanese) is an associate professor. He has received a Ph.D. and a post doctorate scholarship in mathematical sciences from the University of Pretoria, South Africa. He is interested in mathematical modelling and computational mathematics. He has supervised several M.Sc. students and B.Sc. students. In addition, he has many papers published in ISI- and Scopus-indexed journals. He has been invited to give talks in several international conferences.

Murtada K. Elbashir

Department of information system, College of Computer and Information Sciences, Jouf University, Sakaka, Saudi Arabia, mkelfaki@ju.edu.sa, 00966557186485

Dr. Elbashir (Sudanese) is an associate professor. His Ph.D. degree is in computer science and technology from Central South University, Changsha, China. His current research interest includes machine learning and bioinformatics. He has more than 20 papers published in ISI- and Scopus-indexed journals. He has participated in different conferences in Sudan, China and South Africa. Also, he has been invited to give talks in several international conferences. He has supervised several M.Sc. and Ph.D. students.

References

Al-Baali, M. (1985). Descent property and global convergence of the Fletcher-Reeves method with inexact line search. *IMA Journal of Numerical Analysis*, **5**(1), 121–4.

Andrei, N. (2008). An unconstrained optimization test functions collection. *Adv. Model. Optim*, **10**(1), 147–61.

Andrei, N. (2011). Open problems in nonlinear conjugate gradient algorithms for unconstrained optimization. *Bulletin of the Malaysian Mathematical Sciences Society*, **34**(2), 19–330.

Dai, Y.H. and Yuan, Y. (1999). A nonlinear conjugate gradient method with a strong global convergence property. *SIAM Journal on Optimization*, **10**(1), 177–82.

Dai, Z. (2016). Comments on a new class of nonlinear conjugate gradient coefficients with global convergence properties. *Applied Mathematics and Computation*, **276**(n/a), 297–300.

Dolan, E.D. and Moré, J.J. (2002). Benchmarking optimization software with performance profiles. *Mathematical Programming*, **91**(2), 201–13.

Gilbert, J.C. and Nocedal, J. (1992). Global convergence properties of conjugate gradient methods for optimization. *SIAM Journal on Optimization*, **2**(1), 21–42.

Guanghui, L., Jiye, H. and Hongxia, Y. (1995). Global convergence of the Fletcher-Reeves algorithm with inexact linesearch. *Applied Mathematics-A Journal of Chinese Universities*, **10**(1), 75–82.

Fletcher, R. (1987). *Practical Method of Optimization, Unconstrained Optimization*. New York: John Wiley and Sons.

Fletcher, R. and Reeves, C.M. (1964). Function minimization by conjugate gradients. *The computer journal*, **7**(2), 149–54.

Hestenes, M.R. and Stiefel, E. (1952). Methods of conjugate gradients for solving linear systems. *J. Res. Nat. Bur. Standards*, **49**(6), 409–35.

Jiang, X. and Jian, J. (2019). Improved Fletcher–Reeves and Dai–Yuan conjugate gradient methods with the strong Wolfe line search. *Journal of Computational and Applied Mathematics*, **348**(n/a), 525–34.

Liu, Y. and Storey, C. (1991). Efficient generalized conjugate gradient algorithms, part 1: Theory. *Journal of Optimization Theory and Applications*, **69**(1), 129–37.

Rivaie, M., Mamat, M. and Abashar, A. (2015). A new class of nonlinear conjugate gradient coefficients with exact and inexact line searches. *Applied Mathematics and Computation*, **268**(n/a), 1152–63.

Rivaie, M., Mamat, M., June, L. W. and Mohd, I. (2012). A new class of nonlinear conjugate gradient coefficients with global convergence properties. *Applied Mathematics and Computation*, **218**(22), 11323–32.

Polak, E. and Ribiere, G. (1969). Note on the convergence of conjugate direction methods. *Mathematical Modeling and Numerical Analysis*, **3**(1), 35–43.

Powell, M.J. (1984). Nonconvex minimization calculations and the conjugate gradient method. In: M.J Powell (ed.) *Numerical Analysis*. Berlin, Germany: Springer.

Touati-Ahmed, D. and Storey, C. (1990). Efficient hybrid conjugate gradient techniques. *Journal of Optimization Theory and Applications*, **64**(2), 379–97.

Yousif, O.O.O. (2020). The convergence properties of RMIL+ conjugate gradient method under the strong Wolfe line search. *Applied Mathematics and Computation*, **367**(1), 124777.

Zoutendijk, G. (1970). Nonlinear programming, computational methods. In: J. Abadie (ed.) *Integer and Nnonlinear Programming*. Amsterdam, Switzerland: North-Holland.

The Scientific Journal of King Faisal University

Basic and Applied Sciences

Thermal Behavior Assessment of Natural Stone Buildings in the Semi-Arid Climate

Racha Djedouani [1], Lazhar Gherzouli [2] and Hakan Elçi [3]

[1] Civil Engineering and Hydraulics Laboratory, 8 Mai 1945 University, Guelma, Algeria
[2] Applied Civil Engineering Laboratory, Larbi Tebessi University, Tébessa, Algeria
[3] Geotechnical Department, Torbali vocational school, Dokuz Eylül University, İzmir, Turkey

LINK	RECEIVED	ACCEPTED	PUBLISHED ONLINE	ASSIGNED TO AN ISSUE
https://doi.org/10.37575/b/eng/210043	12/08/2021	26/11/2021	26/11/2021	01/12/2021
NO. OF WORDS	**NO. OF PAGES**	**YEAR**	**VOLUME**	**ISSUE**
5978	8	2021	22	2

ABSTRACT

This paper aims to assess the effects of harsh climatic conditions' interactions with natural stone on thermal inertia properties and the thermal performance of ancient residential buildings. As the type of stone differs, its thermo-physical components differ; therefore, its interactions with environmental factors vary. For this purpose, an experimental measurement was conducted on many buildings with different orientations in a semi-arid climate and validated by a simulation performed by the "EnergyPlus 9.3" software. Results showed that the important outdoor temperature gap between day and night influences the natural stone thermos-physical properties used in construction. The stone components affected by the thermal shock effect weathering are eroded over time, then saturated with water, and affect the thermal conductivity coefficient of stone; however, this directly changes the indoor thermal comfort and performance of buildings. Additionally, the high indoor relative humidity percentage and the absence of natural ventilation have an important influence on the ambient temperature values recorded. This paper discusses the experimental measurement results compared to the simulation results.

KEYWORDS

Thermal performance, building envelope, thermal inertia, limestone, Tébessa, Algeria

CITATION

Djedouani, R., Gherzouli, L. and Elçi, H. (2021). Thermal behavior assessment of natural stone buildings in the semi-arid climate. *The Scientific Journal of King Faisal University: Basic and Applied Sciences*, **22**(2), 92–9. DOI: 10.37575/b/eng/210043

1. Introduction

Currently, global warming is hardly disputed by the international scientific community since significant effects can already be observed on a global scale. Indeed, it is noticed that there is a rise in the average temperature of the atmosphere and the oceans, massive melting of snow and ice, and rising sea levels. According to the latest forecasts from the Intergovernmental Panel on Climate Change (IPCC), the Earth could experience global warming from 1.8 C° to 4 C° by 2100 if no action to reduce greenhouse gases (GhG) is taken (Kaemmerlen, 2009). Otherwise, with globally excessive energy consumption, the demand for energy saving strategies increases (El-Darwish and Gomaa, 2017).

Algeria, like other countries, aims to reduce energy consumption in several sectors, with the buildings sector as the largest overall energy consumption consumer, accounting for more than 60% (Djedouani *et al.,* 2020). Since ancient buildings' renewal rate is low, this objective can only be achieved through a massive effort of thermal improvement to reduce heating and cooling energy consumption. Therefore, it becomes necessary to optimize the energy performance of ancient buildings, especially those built with local materials and traditional techniques before the first thermal regulations in 1974 and when no performance criteria matched current standards (Rabouille, 2014).

In other words, buildings should have a high energy performance to decrease their energy consumption. Nevertheless, this issue is complex and multidimensional as it spans building envelope performance, indoor environmental conditions, and user demands (Košir, 2016). One might argue that the main goal of a building is to provide an environment acceptable to building users (Hensen, 1991). The building skin is the physical barrier between the external environment and the internal conditioned space. The building envelope consists of doors and windows, a roof, walls, and insulating materials to prevent heat transfer from the interior to the exterior in the winter and vice versa in the summer. (El-Darwish and Gomaa, 2017). Since the building envelope separates the external environment from the internal space, it is one of the key factors affecting the buildings' energy consumption (Hailu, 2021). Thus, improving the energy performance of the building envelope improves the energy performance of the whole building.

For ancient buildings, which are the subject of our study, the major passive method used to control the indoor environment and store energy was to construct thick walls built on heavy construction materials to induce their thermal inertia parameter. Systems with the highest thermal inertia are considered the lowest energy systems (Orosa and Oliveira, 2012). This parameter contributes to creating favorable indoor thermal comfort conditions without using cooling and heating energy. The building walls store the thermal energy during the daytime then release it during the night, especially in climates with high diurnal temperature fluctuations (Verbeke and Audenaert, 2018).

In most cases, thermal inertia is defined as how quickly a building reacts to external disturbances. A building's response to the solicitation depends largely on the thermal properties of the construction materials. Buildings will react differently depending on their ability to store and transport heat. Therefore, there is a coupling problem between thermal conductivity (λ), heat capacity (C), and density (ρ), which introduces the two concepts of thermal diffusivity and thermal effusivity.

$$\text{Thermal diffusivity} = \lambda / \rho C \ [m^2/s] \quad (1)$$

$$\text{Thermal effusivity} = \sqrt{(\lambda \rho C)} \ [J/m^2.K.s.1/2] \quad (2)$$

Thus, thermal inertia depends on environmental interactions with the building construction materials, which relate to several parameters such as their thermos-physical properties, disposition within the building envelope, the architectural characteristics of the building, and the climatic conditions (Chahwane, 2012). All these properties affect thermal performance. Therefore, controlling the thermo-physical characteristics of the construction materials of the building envelope assists in reducing energy consumption (Aste *et al.,* 2009).

In this respect, many studies have proved the thermal inertia parameter effectiveness in the field of building energy storage and interior thermal comfort. However, it is clear in northeastern Algeria, specifically in the Tébessa province, which is influenced by a semi-

Corresponding Author: Racha Djedouani 002136575497805, djedouani.racha@univ-guelma.dz

arid climate, that ancient buildings consume more energy than modern buildings, which were built with new and lightweight construction materials. This refers to some inconsistencies. Hence, this paper will discuss climatic factors' impact on thermal inertia and, thus, on the energy performance of these ancient buildings. This process requires studying buildings' thermal performance to understand the effect of each parameter and find the best thermal improvements regarding building orientation.

Many authors have conducted quantitative studies on the behavior of ancient buildings and confirmed that reducing the energy demand and regulating indoor thermal comfort is influenced by several parameters such as construction materials (Rais *et al.,* 2021). In addition, a study by Evola *et al.* (2017) compared, using experimental measurements and dynamic simulations, the thermal behavior of modern and traditional envelopes and showed that ancient buildings are often characterized by high thermal inertia due to the thickness of the walls. Indeed, the relative impact of this phenomenon is influenced by several factors, including climate, especially in arid and semi-arid climatic contexts, where the recorded temperature degrees considerably vary.

If harsh climatic conditions affect the thermal performance of construction materials, then Boumezbeur *et al.* (2015) proved that harsh environmental factors affect the natural stone used in construction in Tébessa, consequently changing and decreasing their mineralogical contents and properties and decaying their texture. As the type of stone differs, its thermo-physical components differ; therefore, its interaction with environmental factors varies. On this account, the objective of the current research is to define the impact of harsh climatic conditions of cold semi-arid contexts on the thermal properties of stones used in ancient building construction and its effect on a building's thermal inertia. This work contributes by improving thermal performance response to energy challenges while ensuring the thermal comfort of a building's users.

1. Case Study

1.1. The Climatic Context:

This study focuses on residential buildings built in the colonial district of Hammamet city in the Tébessa province of northeastern Algeria. This region is influenced by a semi-arid cold climate Bsk, according to the Köppen-Geiger climate classification based on annual and monthly mean temperature and precipitation values (Szabó-Takács *et al.,* 2019). Figure 1(a) shows that the annual mean winter temperatures recorded by the meteorological station of Tébessa over 30 years do not exceed 18 C°, supporting Kottek *et al.* (2006). They explained that this climate is determined by the annual mean temperature, which should be less than 18°C, while the accumulated annual precipitation is more than a 5 mm dryness threshold; this last part depends on the annual precipitation cycle and the annual mean temperature. It is calculated by:

$$\text{Dryness threshold} = \begin{cases} 2\{\text{annual mean temperature}\} \text{ if at least 2/3 of the annual precipitation occurs in winter.} \\ 2\{\text{annual mean temperature}\} + 28 \text{ if at least 2/3 of the annual precipitation occurs in summer.} \\ 2\{\text{annual mean temperature}\} + 14 \text{ otherwise.} \end{cases}$$

Indeed, this semi-arid climate is characterized by different temperatures between day and night. The data climate from Tébessa's meteorological station for 30 years, illustrated in Figure 1(b), shows that January is the coldest month, with a mean temperature of 6 C°. The minimum average temperature is around 3 C °, and the maximum average temperature is around 11 C°. Additionally, the lowest temperature recorded during this month is -3 C°, while the average number of frosty days is 19 days a year (Figure 1[c]).

Fig. 1. Data climate of Hammamet, Tébessa; The annual mean temperature in Hammamet, Tébessa (a); Temperature range in Hammamet, Tébessa (b); Number of frosty days in Hammamet, Tébessa (c).

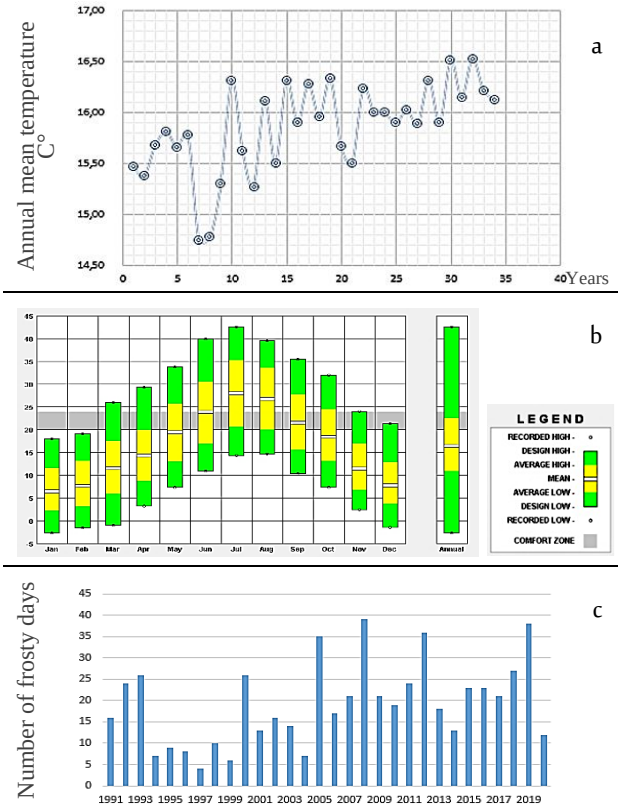

The region's precipitation is low at 342.5 mm, with March representing the wettest month with an average of 44.8 mm of precipitation. July is the hottest and driest month, with an average temperature of 27C° and average precipitation of 11.3 mm, as shown in Table 1.

Table 1. Average monthly precipitation in Hammamet, Tébessa.

	Jan	Feb	Mar	Apr	May	Jun	Jul	Aug	Sep	Oct	Nov	Dec	Annual
Average Precipitation mm (in)	27.1 (1.07)	30.3 (1.2)	44.8 (1.8)	30.6 (1.2)	36.5 (1.4)	31.2 (1.2)	11.3 (0.4)	25.1 (1)	29.4 (1.2)	23.6 (0.9)	29 (1.1)	23.6 (0.9)	342.5 (13.5)

1.2. Energy Consumption:

Recent research has proved that buildings' energy consumption is affected by climate. A study by Guedamsi *et al.* (2016) shows three climatic zones in Algeria according to heating energy consumption costs. In Tébessa, the cost of thermal energy requirements for heating is in the second zone due to their harsh winter conditions. According to the Algerian Industrial Energy Company, which specializes in the distribution of electricity and natural gas, the case study shows high energy consumption, while the heating energy consumption in the district study accounts for 11,037.6 m^3 per year of each residential building compared to the 1012 m^3average yearly gas consumption of a residential building. However, it is important to emphasize some contradictions in this case considering the characteristics of natural stone buildings to reduce energy consumption.

1.3. Case Study Description:

All the residential buildings in the studied colonial district are built of natural stone extracted from the Gaagaa quarry in Hammamet, Tébessa, during Algeria's colonial period (before the first thermal regulations in 1974). To cover all possible cases, the four residential buildings on the ground floor, denoted by Building 1, Building 2, Building 3, and Building 4 with different orientations, were chosen as

studied buildings in this research, as shown in Figure 2.

All buildings contain three rooms, a kitchen, and a bathroom at a height of 3.20 m. They are covered with a sloped tile roof using wood supports, while the roof punch height is 1 m distance from the false ceiling to the ridge board. The openings are made of 0.03 m thick wood, and the door measurements are 2.20 m×0.9 m. The window measurements in Building 1 and Building 2 are 1.20 m×1.20 m, and the window measurements of Building 3 and Building 4 are 1.50 m×1.20 m. Figure 2 shows the buildings' details and the room where the experimental measurements were performed.

Fig. 2. Details of buildings studied (Room studied, Facade of building, Location, and Orientation); Building 1 (a); Building 2 (b); Building 3 (c); Building 4 (d) (Source the author, 2021).

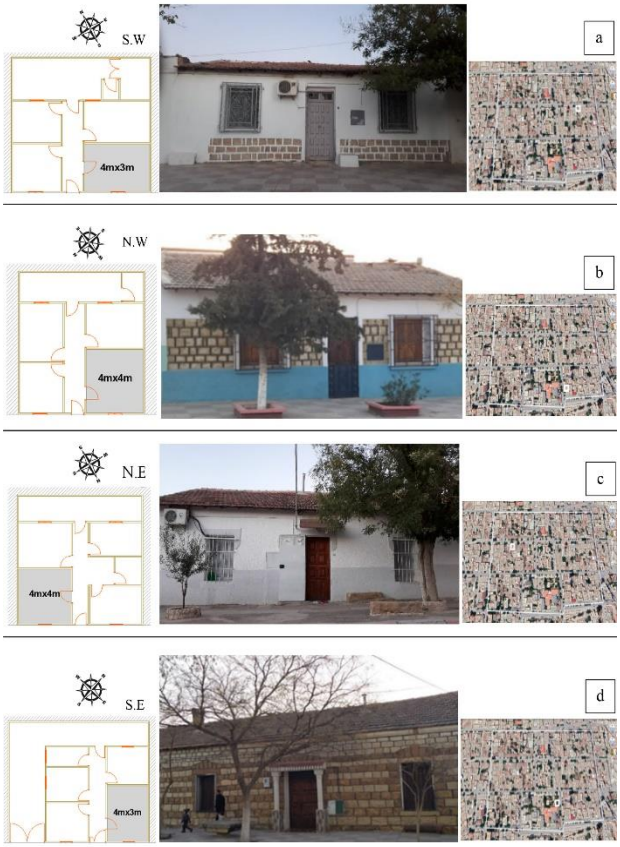

This study is conducted on the facade of each building to study the stone wall thermal behavior in this climatic context. The details of the interior and exterior construction materials and their thermos-physical properties are illustrated in Table 2.

Table 2. Thermos-physical properties of the facade materials.

Materials	Layer thickness [m]	Conductivity [w/m.k]	Specific heat [kj/kg.k]	Density [kg/m3]
Plaster coating	0.02	0.57	1008	1150
Cement mortar	0.03	0.80	850	1900
Naturel stone	0.30	1.40	1000	2475
Cement mortar	0.03	0.80	850	1900
Plaster coating	0.02	0.57	1008	1150

3. Materials and Methods

Three studies were carried out to understand and evaluate the thermal behavior of the natural stone buildings, starting from the measurement in situ to the chemical analyses to determine the stone type samples, then the validation and the verification of results with the energy simulation.

3.1. Determination of Stone Type:

Two methods can be used to classify natural stone. First, the classification of natural stone types according to geological origin, which are igneous rocks, sedimentary rocks, and metamorphic rocks. The second is based on an implementation basis, such as strength characteristics, hardness, porosity, color, and durability (Tumac and Shaterpour-Mamaghani, 2018). In general, igneous rocks, sedimentary rocks, and metamorphic rocks are classified according to their genesis, structure, texture, and mineral composition.

The visual inspection of the studied samples shows that they are classified as sedimentary rocks. Since sedimentary rocks can be of detrital, chemical, or biochemical origin, a chemical analysis is considered the best method to determine the stone type by revealing its chemical components. For this purpose, many laboratory studies were carried out to analyze the stone samples.

To determine the mineralogical and petrographic properties of the Gaagaa stone, sampling was completed to represent the general quarry, and five thin sections were prepared. According to TS EN 12407 (2019), mineral percentages were determined by making a petrographic analysis of the thin sections at 10X magnification of crossed nicol, using an Olympus BX41 polarizing microscope. The chemical properties of the stone belonging to the Gaagaa quarry and its main oxides (%) were determined in the Acme laboratory (in Canada), using the Inductively Coupled Plasma Emission Spectrometer (ICP-ES) method. Additionally, X-ray diffraction techniques were used to determine the mineralogical composition of the Gaagaa stone.

Fig. 3. Stone samples extracted from Gaagaa Quarry (a); Gaagaa limestone (A, B, C) Dendritic texture (C, D), Thin section view (F) (b); X-ray diffraction of Gaagaa limestone (c).

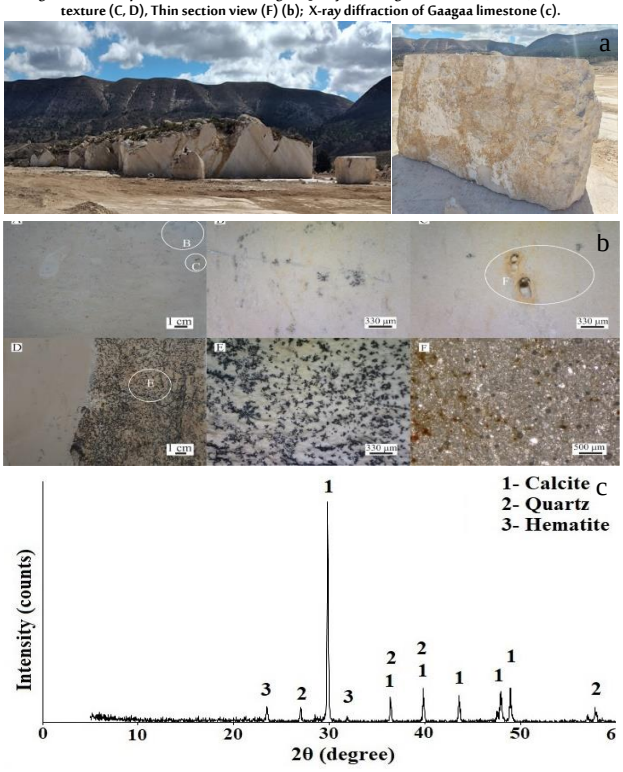

The stone from the Gaagaa quarry (Figure 3[a]) has the appearance of a carbonate rock with a pinkish light-yellow color, sometimes with brown and black spots (Figure 3[b] A, B, and C). Closed discontinuities are rarely observed in the stone (Figure 3[b] D). When these discontinuity planes are opened, a black dendritic texture predominates along the discontinuity surface (Figure 3[b] E). In the petrographic analysis of the stone, the main mineral component is calcite (90%), accompanied by a small amount of quartz (5%). Brown spots observed on the surface of limestone at the macro scale are recognized as iron oxide in the petrographic analysis. Bioclasts observed in the stone are lamellibranch remains and spicule fossils of echinoids, ostracods, rudists, and gastropods. The stone from the Gaagaa quarry is a fine-grained biomicritic-biosparitic limestone with varying pore sizes and

geometry.

Chemical compositions of the Gaagaa stone are given in Table 3. The stone contains two main oxides: calcium oxide (CaO; 52.58%) and silicon dioxide (SiO2; 4.51%). The ignition loss value of the Gaagaa stone is 41.7%. The main crystalline compounds found were calcite, quartz, and hematite by the X-ray technique (Figure 3. [c]).

Table 3. Percentages of major element oxides in the Gaagaa limestone.

SiO_2	Al_2O_3	Fe_2O_3	MgO	CaO	Na_2O	K_2O	TiO_2	P_2O_5	MnO	Cr_2O_3	Ba	Ni	Sr	Zr	Y	Nb	Sc	*LOI	Sum
%											ppm							%	
4,51	0,34	0,14	0,37	52,58	0,14	0,03	0,02	0,07	0,02	0,004	8	<20	1104	7	5	<5	<1	41,7	99,97

The Gaagaa limestone is a highly porous, low-density limestone. Compressive strength, bending strength, and abrasion resistance are sufficient for general construction purposes, but its high porosity leaves it highly vulnerable to environmental effects (Djedouani *et al.,* 2021). The material properties of the Gaagaa limestone are given in Table 4.

Table 4. Material properties of the Gaagaa limestone.

Property	Standard	Mean ± Standard deviation
Apparent density - kg/m3	TS EN 1936	2475 ± 41
Open porosity - %	TS EN 1936	5,948 ± 0,873
Real density - kg/m3	TS EN 1936	2670 ± 4
Total porosity - %	TS EN 1936	7,302 ± 0,23
Water absorption -%	TS EN 13755	2,349 ± 0,383
Uniaxial compressive strength -MPa	TS EN 1926	132.76 ± 17,25
Flexural strength - MPa	TS EN 12372	9,59 ± 1,82
Böhme abrasion -mm3	TS EN 14157	24226 ± 1796
Sound speed - m/s	TS EN 14579	3782 ± 136
Hardness (mohs)	TS TS 6809	2.5-3

The age of the limestone is Turonian. Many researchers stated that the Turonian limestone, which is widely distributed in the region, was also used in the construction of historical buildings in Tébessa and that this stone is very sensitive to weathering due to environmental effects (Boumezbeur *et al.,* 2015; Nasri *et al.,* 2018).

3.1.1. The Measurements in Situ

This investigation was carried out during the winter to evaluate the thermal behavior of natural stone buildings at this time. The coldest measurement days were determined by the representative week and day method, "design week and day." It was calculated with the meteorological data of Hammamet, Tébessa, especially its temperature values. It determined the average daily temperature of the coldest month (January) over 30 years to obtain the average outdoor temperature for each day in the month, then the lowest value of the average temperature was matched to the coldest day (Khadraoui *et al.,* 2018). Table 5 shows that the third week in January (in blue) is the coldest week of the year in Hammamet, Tébessa province.

Table 5. Design week and design day.

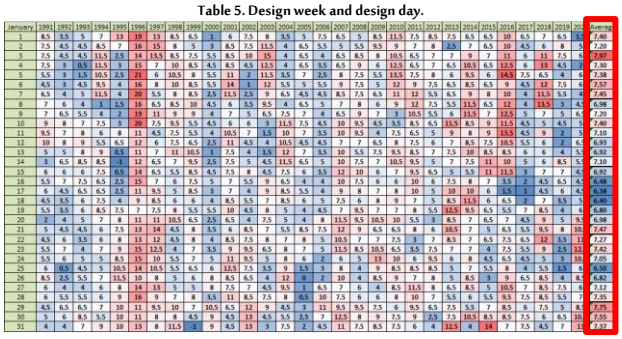

3.1.2. Presentation and Protocol for Taking Measurements

The measurements were taken twice every hour for three days in January (the 16th,17th, and 18th), 2021. The windows were opened every morning for one hour to simulate the residents' behavior from 9:00 h to 10:00 h, while all doors were closed throughout the measurement period. The measurements were taken in the living room in natural conditions and without any heating system while the dwelling was uninhabited to ensure that protocol was carried out in passive control systems.

3.1.3. Measurement Instruments

To conduct measurements, three types of instruments, illustrated in Figure 4, were used in this investigation. An infrared thermometer was pointed at the middle of the studied wall to measure the internal and external surface temperature. In addition, the hygrothermometer measured the air's moisture content to determine its relative indoor and outdoor humidity and ambient temperature. The thermal anemometer was used for measuring the indoor and outdoor wind speed and installed in the middle of the studied room 1.5 m above the floor.

Fig. 4. Measurement instruments; Infrared thermometer (a), Hygro-thermometer (b), Thermal anemometer (c).

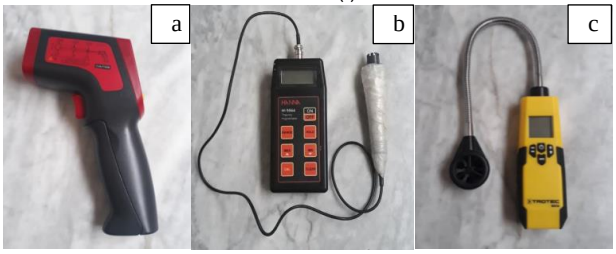

3.2. The Energy Simulation:

A thermal dynamic simulation with the "EnergyPlus 9.3" software was used to validate the experimental results of the thermal behavior of the natural stone buildings. A climate file based on the Tébessa meteorological station was generated by the "Meteonorme 7" software in "epw" format and used in this simulation. The simulation was conducted according to experimental measurement protocol, where each space represents a thermal zone. Additionally, no outside obstructions were introduced because the opposite buildings did not cast shadows on the facade of the studied buildings.

4. Results and Discussion

The three main thermal comfort parameters of temperature, relative humidity, and wind speed were measured to study the thermal performance of the natural stone buildings.

4.1. Results of the Measurements in Situ:

Figure 5 illustrates the measurements in situ obtained for all buildings studied. It was revealed that the different building orientations did not affect the results obtained where all the graphs of the external surface temperature are slightly different. As the building orientation changes, the heat gain of walls changes, depending on how long it is exposed to the sun during the day. Thermal inertia consists of the accumulation of heat in the envelope for restitution inside by radiation. The complexity of this phenomenon lies in the fact that the heat flow through the envelope successively increases material temperatures (Chuayb, 2015), which affects their thermo-physical properties, but not the thermal inertia of the envelope.

It was observed that the outdoor temperature increases during the day and then significantly decreases at night in a short period (less than12 hours). The maximum value of 11.6 C° was recorded at 10:00 h on the first day. On the second and third day, the highest recorded temperatures were 13.3 C° and 17.7 C° at 16:00 h. The lowest temperature was recorded on the first day (5.7 C°) at 00h. The values of 4.2 C° and 6.1 C° were record on the second and third days at 16:00 h.

The temperature difference between day and night reached 5.7 C°, 9.1 C°, and 11.6 C° each day, respectively. This important gap significantly influences the limestone used in construction because the heating and cooling of this stone type affect its components. As a result, it deteriorates and erodes; this is called the thermal shock effect weathering (Yavuz *et al.,* 2006).

The indoor relative humidity rises at night to 73.1% in Building 1, 66.7% in Building 2, 70.3% in Building 3, and 63.5% in Building 4. It decreases during the day to 38.2% in Building 1, 36.2% in Building 2, 39.2% in

Building 3, and 44.3% in Building 4. There was a coherence between the indoor and outdoor relative humidity, which reached a maximum value of 84% at night and a minimum value of 24% during the day.

Fig. 5. Results of the measurements in situ of the buildings.

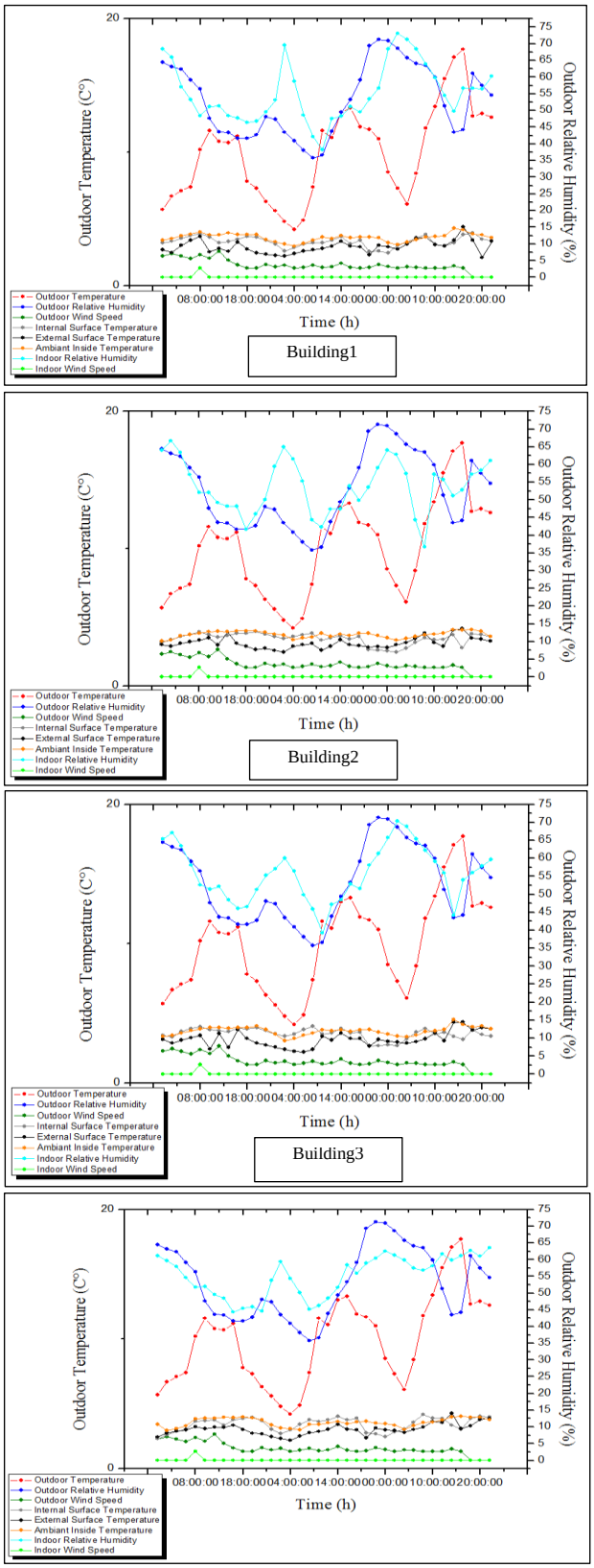

These high indoor relative humidity values were due to the water saturation of the limestone used in construction. The components affected by the thermal shock effect weathering are eroded over time, then filled with water coming from the sub-basement of the building (Nguyen *et al.,* 2020).

On the other hand, it was revealed that the ambient inside temperature values were low compared to the outdoor temperature values over the three days in the four buildings. The values recorded in Building 1 ranged from 14.7 C° to 9.3 C°, 13.4 C° to 10.1 C° in Building 2, 15.1 C° to 9.3 C° in Building 3, and 13.1 C ° to 8.9 C ° in Building 4. It was noticed that these values are lower than the standards recognized in the thermal comfort of residential buildings. The highest outdoor temperature recorded in the last two days was at 16h, while the highest ambient inside temperature recorded was at 14h, 18h, 20h, and 20h in Building 1, Building 2, Building 3, and Building 4, respectively, with a maximum difference of four hours between the two peaks. This low thermal phase shift reduces the thermal inertia of buildings (Yam *et al.,* 2003).

The external and internal surface temperature curves in the four cases are almost the same as the ambient inside temperature. It was noticed that there was a considerable coherence between them. The values of the external surface temperature recorded in Building 1 range from 15.1 C° to 5.9 C°, 13.6 C° to 7 C° in Building 2, 14.5 C° to 6.2 C° in Building 3, and 14.1 C ° to 6 C° in Building 4. The values of the internal surface temperature recorded in Building 1 range from 13.3 C° to 7.3 C°, 12.8 C° to 7 C° in Building 2, 13.3 C° to 7.8 C° in Building 3, and 13.7 C° to 6.4 C° in Building 4. A difference of two degrees was recorded between the external and internal surface temperatures in the day, while the highest difference of six degrees was recorded at night.

The convergence of these temperature results is due to the influence of the thermal shock effect weathering on the thermos-physical properties of the limestone, where this allows the voids caused by this phenomenon to be filled with water, and make the stone more conductive, knowing that the stone saturated with water has a higher thermal conductivity ecoefficiency than the dry stone. Consequently, the stone's thermal inertia decreases, as shown in this case study. Additionally, these buildings' thermal inertia is almost lower than natural stone buildings' usual thermal inertia.

However, it was revealed that the outdoor wind speed was rather high, ranging between 7.1 m/s and 2.7 m/s. The indoor wind speed of the four buildings studied is void over the three days, even when the windows were open in the morning, except the first day where the outdoor wind speed was estimated at 6.8 m/s at 8h, and the indoor wind speed was 2.7 m/s. The most important element noticed was a lack of good natural ventilation in the buildings during the day, except when the outdoor wind speed exceeded 6 m/s. The very high indoor relative humidity percentage and the absence of natural ventilation had a significant influence on the ambient inside temperature values (Sanchez *et al.,* 2016).

4.2. Results of the Energy Simulation:

The energy simulation results in Figure 6 of the outdoor temperature, the outdoor relative humidity, and the outdoor wind speed showed a strong agreement between the simulation and experimental results.

Fig. 6. Results of the energy simulation of the buildings.

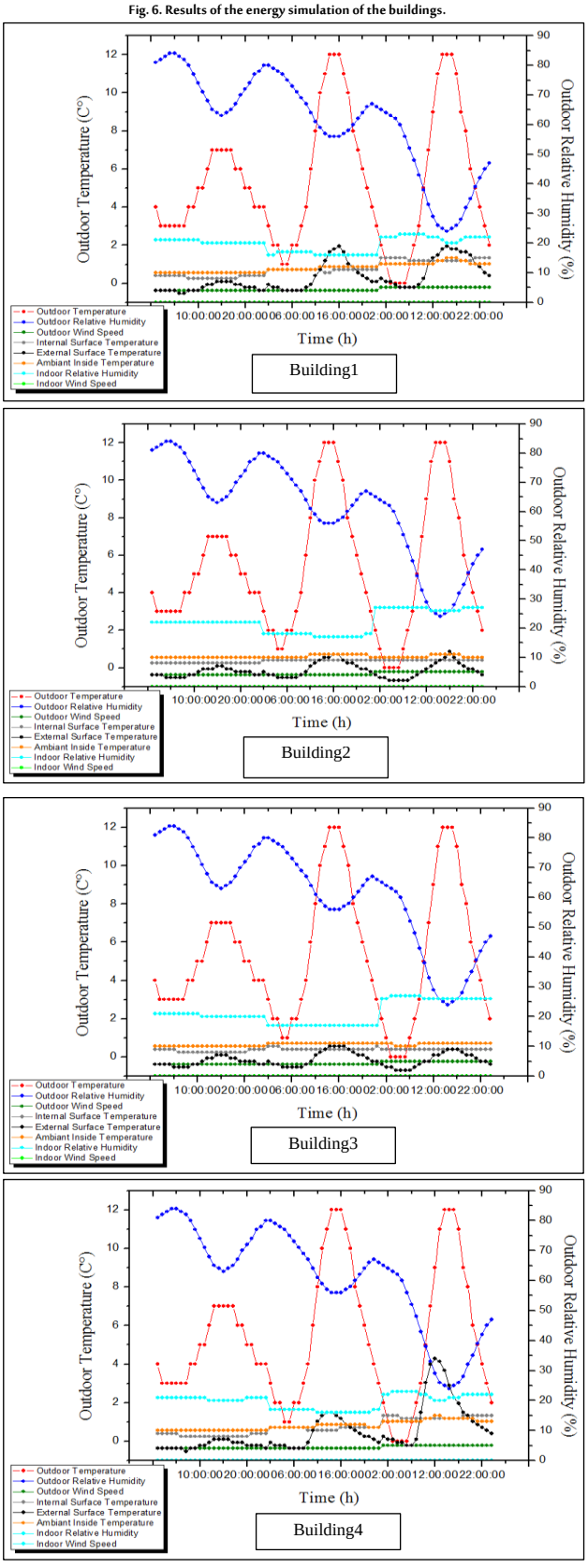

The simulation outside temperature result differences, the outside relative humidity results, the outside wind speed results, and the experimental results are consequences of the gap between the measurements in situ values and the climatic file values (Khadraoui *et al.,* 2018), which has a direct influence on the external surface temperature and the internal surface temperature on the ambient inside temperature. In addition, it affects the indoor relative humidity and the indoor wind speed simulation results.

It is important to notice a certain coherence between the measured and simulated curves of temperature and wind speed parameters in the four buildings. The simulated indoor relative humidity curve is almost constant and does not exceed 27% in the four cases studied. This significant difference between the simulation and experimental indoor relative humidity results shows that the energy simulation does not consider the current degradation state of the natural stone used in these buildings, where the thermos-physical properties of the limestone used in the energy simulation are related to the normal state of the limestone. Thus, the thermos-physical properties' value changes due to climatic factors have an important influence on the simulation results. However, the simulated indoor relative humidity curves show the results of the relative humidity in the buildings built in natural stone in the normal state, without exposure to harsh environmental factors over time.

5. Conclusion

This paper analyzed the significant impact of harsh climatic factor interactions with the thermos-physical properties of natural stone used in construction on the thermal inertia of ancient residential buildings over time. The research results showed that building orientation does not affect the thermal behavior of the natural stone walls. Limestone showed weak resistance in the semi-arid climate under the important temperature gap between day and night. Its components were affected by the thermal shock effect weathering and saturated with water arising from the sub-basement of the building, causing an increase in the thermal conductivity coefficient; therefore, the thermal inertia and the thermal efficiency of the natural stonewall are reduced.

On the other hand, the results show a low thermal phase shift reducing the thermal inertia of buildings, the very high indoor relative humidity values recorded, and how the absence of natural ventilation affects the indoor thermal comfort, explaining the buildings' thermal performance decreasing. The wicked agreement between the experimental and simulation results is the consequence of the gap between the measurements in situ values and the climatic file values, and the difference between the currents thermos-physical properties of stone affected by the climatic context and the normal state of the thermos-physical properties.

6. Suggestions and Recommendations

More research is needed to study climate effects on natural stone durability used in construction and define suitable stone types in the harshest climates. All ancient natural stone buildings need a thermal correction to improve their thermal performance.

Biographies

Racha Djedouani

Civil Engineering and Hydraulics Laboratory, 8 Mai 1945 University, Guelma, Algeria, djedouani.racha@univ-guelma.dz, 002136575497805

Mrs. Djedouani is an Algerian doctoral student at the University of 8 Mai 1945 in Guelma, Algeria. She is affiliated with the Civil Engineering and Hydraulics laboratory. In 2016, she earned her master's degree from Larbi Tebessi University in Tébessa, Algeria. She has participated in several national and international conferences in Germany, Turkey, Tunisia, and Algeria. Her work is published in several conference proceedings. She is interested in research related to building materials, energetic performance, green building, and sustainable architecture. ORCID: 0000-0002-8616-5759.

Lazhar Gherzouli

Department of Architecture, Faculty of Sciences and Technology, Larbi Tebessi University, Tébessa, Algeria, lazhar.gherzouli@univ-tebessa.dz, 00213663028951

Dr. Gherzouli is an Algerian senior lecturer and researcher. In 2007, he graduated from Mohamed Khider University in Biskra, Algeria. He is the head of a research team in the Applied Civil Engineering laboratory at Larbi Tebessi University in Tébessa, Algeria. He is the supervisor of several Ph.D. students and the teacher of several class in the urban planning and architecture field. He is interested in research related to sustainable architecture. He has published many ISI/Scopus-indexed articles in highly peer-reviewed journals. ORCID: 0000-0001-6097-2205.

Hakan Elçi

Geotechnical Department, College of Engineering, Dokuz Eylül University, İzmir, Turkey, hakan.elci@deu.edu.tr, 00905356474538

Dr. Elçi is a Turkish associate professor. He is a graduate of Dokuz Eylül Üniversity in Izmir, Turkey. He is the director of the Natural Stone Building laboratory of Torbali vocational school, Dokuz Eylül Üniversity in Izmir, Turkey. He is the author of seven ISI/Scopus-indexed articles with the largest global publishers (Elsevier, Springer). His work is cited 239 times in different countries. He is interested in research related to geology, natural stone, building materials, environmental impact, rocks, and concrete. ORCID: 0000-0003-2945-2548.

Acknowledgements

This study was supported by the Ministry of Higher Education and Scientific Research of Algeria.

References

Aste, N., Angelotti, A. and Buzzetti, M. (2009). The influence of the external walls thermal inertia on the energy performance of well insulated buildings. *Energy and Buildings*, **41**(11), 1181–7. DOI: 10.1016/j.enbuild.2009.06.005

Boumezbeur, A., Hmaidia, H. and Belhocine, B. (2015). Limestone weathering and deterioration in the Tébessa Roman Wall NE Algeria. *Engineering Geology for Society and Territory*, **8**(n/a) 169–74. DOI: 10.1007/978-3-319-09408-3_27

Chahwane, L. (2011). *Valorisation de L'inertie Thermique Pour la Performance Energétique des Bâtiments* 'Valuation of Thermal Inertia for the Energy Performance of Buildings'. PhD Thesis, University of Grenoble, Grenoble, France. [in French]

Chuayb, M.H.M.A. (2015). *Application de Quelques Notions de la Conception Bioclimatique Pour L'amélioration de la Température Interne d'un Habitat* 'Application of some Notions of Bioclimatic Design for Improving the Internal Temperature of a Habitat'. PhD Thesis, University of Saida, Saida, Algeria. [in French]

Djedouani, R., Elçi, H., Hacımustafaoğlu, R. and Gherzouli, L. (2021). Tébessa (Algeria) limestone for restoration work to Roman historical building in Tébessa. In: *The Sixth International Stone Congress*, Marble Izmir Fair, Izmir, Turkey. 25-28/08/2021.

Djedouani, R., Gherzouli, L. and Elçi, H. (2020). The effect of the thermal inertia on the thermal behavior of building stone wall in semi-arid climate. In: *The Third International Congress on Architecture and Design,* Hilton Istanbul Zeytinburnu, Istanbul, Turkey. 18-19/04/2020.

El-Darwish, I. and Gomaa, M. (2017). Retrofitting strategy for building envelopes to achieve energy efficiency. *Alexandria Engineering Journal*, **56**(4), 579–89. DOI: 10.1016/j.aej.2017.05.011

Evola, G., Marletta, L., Natarajan, S. and Patanè, E.M. (2017). Thermal inertia of heavyweight traditional buildings: Experimental measurements and simulated scenarios. *Energy Procedia*, **133**(n/a), 42–52. DOI : 10.1016/j.egypro.2017.09.369

Ghedamsi, R., Settou, N., Gouareh, A., Khamouli, A., Saifi, N., Recioui, B. and Dokkar, B. (2016). Modeling and forecasting energy consumption for residential buildings in Algeria using bottom-up approach. *Energy and Buildings*, **121**(n/a), 309–17. DOI: 10.1016/j.enbuild.2015.12.030

Hailu, G. (2021). Energy systems in buildings. *Energy Services Fundamentals and Financing*, **1**(n/a), 181–209. DOI: 10.1016/B978-0-12-820592-1.00008-7

Hensen, J. L. M. (1991). *On the Thermal Interaction of Building Structure and Heating and Ventilating System*. PhD Thesis, University of Technology Eindhoven, Eindhoven, Netherlands.

Kaemmerlen, A. (2009). *Transfert de Chaleur à Travers les Isolants Thermiques du Batiment* 'Heat Transfer through Building Thermal Insulators'. PhD Thesis, University of Henri Poincaré-Nancy 1, Nancy, France. [in French]

Khadraoui, M.A. and Sriti, L. (2018). The impact of facade materials on the thermal comfort and energy efficiency of offices buildings. *Journal of Building Materials and Structures*, **5**(1), 55–64. DOI: 10.5281/zenodo.1285954

Košir, M. (2016). Adaptive building envelope: an integral approach to indoor environment control in buildings. In: P. Ponce, A.M. Gutiérrez, L.M. Ibarra (eds.) *Automation and Control Trends*. Rijeka, Croatia. DOI: 10.5772/64951

Kottek, M., Grieser, J., Beck, C., Rudolf, B. and Rubel, F. (2006). World map of the Köppen-Geiger climate classification updated. *Meteorologische Zeitschrift,* **15**(3), 259–63. DOI: 10.1127/0941-2948/2006/0130

Nasri, F., Boumezbeur, A., and Benavente, D. (2019). Influence of the petrophysical and durability properties of carbonate rocks on the deterioration of historic constructions in Tébessa (northeastern Algeria). *Bulletin of Engineering Geology and the Environment*, **78**(6), 3969–81. DOI: 10.1007/s10064-018-1410-7

Nguyen, S.H., Do, T.T. and Ambre, J. (2020). Study on INTOC waterproofing technology for basement of high-rise buildings. In: *The fifth International Conference on Green Technology and Sustainable Development (GTSD),* University of Danang, Da Nang, Vietnam, 27-28/11/ 2020.

Orosa, J.A. and Oliveira, A.C. (2012). A field study on building inertia and its effects on indoor thermal environment. *Renewable Energy*, **37**(1), 89–96. DOI: 10.1016/j.renene.2011.06.009.

Rabouille, M. (2014). *Recherche de la Performance en Simulation Thermique Dynamique: Application à la Réhabilitation des Bâtiments* 'Performance Research in Dynamic Thermal Simulation: Application to the Rehabilitation of Buildings'. PhD Thesis, University of Grenoble, Grenoble, France. [in French]

Rais, M., Boumerzoug, A. and Baranyai, B. (2021). Energy performance diagnosis for the residential building façade in Algeria. *Pollack Periodica*, **16**(2), 136–42. DOI: 10.1556/606.2020.00204.

Sanchez, E., Rolando, A., Sant, R. and Ayuso, L. (2016). Influence of natural ventilation due to buoyancy and heat transfer in the energy efficiency of a double skin facade building. *Energy for sustainable development*, **33**(10), 139–48. DOI: 10.1016/j.esd.2016.02.002.

Szabó-Takács, B., Farda, A., Skalák, P. and Meitner, J. (2019). Influence of Bias correction methods on simulated Köppen– Geiger climate zones in Europe. *Climate*, **7**(2), 18. DOI: 10.3390/cli7020018.

TS EN 12372 (2013). *Natural Stone Test Methods. Determination of Flexural Strength under Concentrated Load*. Ankara. Turkey: Turkish Standardization Institute.

TS EN 12407 (2019). *Natural Stone Test Methods - Petrographic Examination*. Ankara. Turkey: Turkish Standardization Institute.

TS EN 13755 (2014). *Natural Stone Test Methods Determination of Water Absorption at Atmospheric Pressure*. Ankara. Turkey: Turkish Standardization Institute.

TS EN 14157 (2017). *Natural Stone Test Methods Determination of the Abrasion Resistance.* Ankara. Turkey: Turkish Standardization Institute.

TS EN 14579 (2006). *Natural Stone Test Methods Determination of Sound Speed Propagation.* Ankara. Turkey: Turkish Standardization Institute.

TS EN 1926 (2007). *Natural Stone Test Methods Determination of Uniaxial Compressive Strength.* Ankara. Turkey: Turkish Standardization Institute.

TS EN 1936 (2010). *Natural Stone Test Methods Determination of Real Density and Apparent Density and of Total and Open Porosity.* Ankara. Turkey: Turkish Standardization Institute.

Tumac, D. and Shaterpour-Mamaghani, A. (2018). Estimating the sawability of large diameter circular saws based on classification of natural stone types according to the geological origin. *International Journal of Rock Mechanics and Mining Sciences*, **101**(n/a), 18–32. DOI: 10.1016/j.ijrmms.2017.11.014.

Verbeke, S. and Audenaert, A. (2018). Thermal inertia in buildings: A review of impacts across climate and building use. *Renewable and Sustainable Energy Reviews*, **82**(3), 2300–18. DOI: 10.1016/j.rser.2017.08.08.

Yam, J., Li, Y. and Zheng, Z. (2003). Nonlinear coupling between thermal mass and natural ventilation in buildings. *International Journal of Heat and Mass Transfer*, **46**(7), 1251–64. DOI: 10.1016/S0017-9310(02)00379-4.

Yavuz, H., Altindag, R., Sarac, S., Ugur, I. and Sengun, N. (2006). Estimating the index properties of deteriorated carbonate rocks due to freeze–thaw and thermal shock weathering. *International Journal of Rock Mechanics and Mining Sciences*, **43**(5), 767–75. DOI: 10.1016/j.ijrmms.2005.12.004.

المجلة العلمية لجامعة الملك فيصل
The Scientific Journal of King Faisal University
العلوم الأساسية والتطبيقية
Basic and Applied Sciences

مقارنة تأثير مستخلصي الثوم والزنجبيل مع عقار Glibenclamide في بعض المعايير الكيميائية عند الفئران المستحدث فيها داء السكري

خلود مصطفى شيخ يوسف [1]، هيام كامل فاضل [1]، مفيد ياسين [2]
[1] قسم علم الحياة الحيوانية، كلية العلوم، جامعة تشرين، اللاذقية، سوريا
[2] قسم الكيمياء التحليلية والغذائية، كلية الصيدلة، جامعة تشرين، اللاذقية، سوريا

Comparison of Garlic and Ginger Extract with Glibenclamide on Some Biochemical Standards in Diabetic Mice

Kholoud Mustafa Sheikh Yousef [1], Hiam Kamel Fadel [1] and Mofeed Yaseen [2]
[1] Department of Zoology, Faculty of Science, Tishreen University, Lattaki, Syria
[2] Department of Analytical Chemistry, Faculty of Pharmacy, Tishreen University, Syria

LINK الرابط	RECEIVED الاستقبال	ACCEPTED القبول	PUBLISHED ONLINE النشر الإلكتروني	ASSIGNED TO AN ISSUE الإحالة لعدد
https://doi.org/10.37575/b/sci/210045	17/08/2021	26/11/2021	26/11/2021	01/12/2021

NO. OF WORDS عدد الكلمات	NO. OF PAGES عدد الصفحات	YEAR سنة العدد	VOLUME رقم المجلد	ISSUE رقم العدد
4918	6	2021	22	2

الملخص

تهدف هذه الدراسة إلى المقارنة بين تأثير مستخلصي الثوم والزنجبيل معاً مع عقار Glibenclamide بمستويات كل من الغلوكوز، الكوليسترول الكلي والغليسيريدات الثلاثية في مصل دم الفئران البيضاء المستحدث فيها داء السكري. أُجري البحث على أربعين فأراً من ذكور الفئران سلالة Balb/c، وزّعت على أربع مجموعات (10 فئران لكل مجموعة). أظهرت النتائج حدوث ارتفاع معنوي(p<0.05) في تركيز الغلوكوز والكوليسترول والغليسيريدات الثلاثية في مصل الدم لمجموعة الفئران المحقونة بالألوكسان مقارنة مع الشاهدة الفيزيولوجية، كما أظهرت النتائج حدوث انخفاض معنوي (p<0.05) في تركيز الغلوكوز والكوليسترول والغليسيريدات الثلاثية في مصل الدم لمجموعه الفئران المعالجة بالثوم والزنجبيل مقارنة مع المجموعة الشاهدة. فقد بينت نتائج الدراسة التأثير المهم لمستخلصي الثوم والزنجبيل في خفض مستوى غلوكوز الدم والكوليسترول والغليسيريدات الثلاثية) بشكل مكافئ لعقار Glibenclamide المعروف كخافض سكر فموي.

ABSTRACT

This study aimed to determine the effect of ethanolic extract of garlic (*Allium sativum* s.) and ginger on the levels of glucose, cholesterol, and triglycerides in the blood serum of adult white mice with induced diabetes. This study included 40 male mice of Balb/c, which were divided into four experimental groups (ten mice per group). The results showed a significant increase (p<0.05) in the concentration of glucose, cholesterol and triglycerides in the blood serum of the group of mice injected with alloxan compared with the physiological control. The results also showed a significant decrease (p<0.05) in the concentration of glucose, cholesterol and triglycerides in the blood serum of the group of mice treated with garlic and ginger extract compared to control glucose. Results showed that ethanolic extract of garlic (*Allium sativum* s.) and ginger has an important effect on lowering the level of biochemical to normal values equivalent to glibenclamide.

KEYWORDS
الكلمات المفتاحية
Alcoholic extract, alloxan, glucose, balb/c total cholesterol, triglycerides
مستخلص كحولي، الألوكسان، الغلوكوز، الكوليسترول الكلي، الغليسيريدات الثلاثية، Balb/c

CITATION
الإحالة
Yousef, K.M.S., Fadel, H.K. and Mofeed Yaseen, M. (2021). Muqaranat tathir mustakhlisi althawm walzanjabil mae eaqar Glibenclamide fi baed almaeayir alkimyahiawiat eind alfiran almustahdath fiha da' alsukari 'Comparison of garlic and ginger extract with glibenclamide on some biochemical standards in diabetic mice'. *The Scientific Journal of King Faisal University: Basic and Applied Sciences*, **22**(2), 100–5. DOI: 10.37575/b/sci/210045 [in Arabic]
يوسف، خلود مصطفى شيخ وفاضل، هيام كامل وياسين، مفيد. (2021). مقارنة تأثير مستخلصي الثوم والزنجبيل مع عقار Glibenclamide في بعض المعايير الكيميائية عند الفئران المستحدث فيها داء السكري. *المجلة العلمية لجامعة الملك فيصل: العلوم الأساسية والتطبيقية*، **22**(2)، 100-105.

1. مقدمة

أسهمت الصناعات الدوائية في إنقاذ البشرية من الآفات المرضية، إلا أنّها باتت هاجساً يؤرق الناس لما لها من آثار جانبية سلبية، لذا بدأ الاهتمام في السنوات الأخيرة بالطب الشعبي، والاستفادة من الأدوية المصنّعة من مصادر طبيعية. ومن الأمراض التي انتشرت بشكل كبير حسب المصادر العالمية مرض السكري من النمط الثاني (Zimmet *et al.*, 2001)، لذلك أجريت ومازالت تجرى الأبحاث في مناطق مختلفة من العالم بهدف إيجاد علاج شافٍ لذلك الداء، بعد أن وجدوا عدم نجاح عمليات زراعة البنكرياس السليم في أجسام مرضى السكري إضافةً إلى التكاليف الباهظة.

اتجهت الأبحاث إلى تجريب النباتات والأعشاب الطبية لتجنب الآثار السلبية للأدوية الكيميائية المستخدمة لخفض غلوكوز الدم (Lachin and Reza, 2012) فالعقار يؤدي استخدامه على المدى البعيد إلى احتشاء العضلة القلبية بسبب أثره القوي على المستقبلات القلبية Steven *et al.*, (2007).

يعدّ الثوم من أهم النباتات الطّبيّة حيث أنّه يحتوي على كثير من المواد الفعّالة ذات الخصائص الغذائية والطبية المهمة، لذلك توّجه العديد من الباحثين لدراسة تأثيراته العلاجية في حالات مرضية متعددة، وهو يستخدم بشكل مسحوق أو حبوب أو زيت على نطاق واسع لعلاج ارتفاع ضغط الدم والدهون (Elkhayam *et al.*, 2003).

إنّ الباحث Kazem (2014) فقد درس أثر مرض السكري في خصوبة إناث الفئران البالغة -المستحدث فيها داء السكري بالألوكسان 150 ملغ/كغ من وزن الجسم-وعند استخدام مستخلص الثوم بجرعة 5 ملغ /كغ ولمدة 28 يوم ظهر تحسن واضح في مستوى الأنسولين وانخفاض مستوى الغلوكوز في الدم وبالتالي أدى إلى رفع خصوبة الإناث. كما أكد الباحث Recinella *et al.* (2021) أنّ مستخلص الثوم يلعب دور وقائي لقلب الفأر من خلال عمله كمضاد للالتهابات ومضاد للأكسدة.

كما أمكن التعرف على العديد من المواد الفعّالة الموجودة في مستخلص الثوم مثل Allin و هو من مشتقات الحمض الأميني Cystein الذي يتحول إلى Allicinالعامل الأساس كمضاد حيوي (Cavilloto *et al.*, 1944).

كما بّين الباحث Batiha *et al.* (2020) أنّ للثوم العديد من الخصائص البيولوجية بما فيها مضادات للسرطانات ومضادات للأكسدة ومضادة لتصلب الشرايين وارتفاع ضغط الدم لكون الثوم غني بالمكونات النباتية الحاوية على الكبريت مثل Allicin Allin.

بينت دراسة Liu *et al.* (2005) أنّ المكونين الأساسيان من مكونات الثوم هما S-Allyl Cysteine Sulfoxide و Diallyl Trisulfide وهما مركبان كبريتيان لهما دور

Corresponding Author: Kholoud Mustafa Sheikh Yousef 00963988274735, kholodsh39@gmail.com المؤلف المراسل: خلود مصطفى شيخ يوسف

في زيادة فعالية الأنسولين المفرز من خلايا بيتا في البنكرياس عند الفئران الشاهدة والفئران المستحدث عندها داء السكري.

وقد أكدّ الباحثان Islam and Chomi (2008) الدور نفسه لهذين المكونين في رفع مستوى الأنسولين عند معالجة الحيوانات بمستخلص الثوم.

ولمستخلص الزنجبيل دور هام في انخفاض مستوى الدهون أثناء معاملة الجرذان بالمستخلص المائي للزنجبيل بعد 2-4 أسابيع من الحقن (El-Sayed *et al.*, 2010).

وأثبت الباحث Tzeng *et al.* (2013) فعالية المستخلص الإيتانولي للزنجبيل التي تشبه فعّالية الأنسولين في خفض سكر الدم لمرضى السكري، إضافة إلى الدور الواضح في خفض الضرر الكلوي عند الفئران المستحدث فيها داء السكري بالستربتوزوتوسين مقارنة مع عقار الميتفورمين، إذ كشفت الفحوصات النسيجية تحسن واضح في التغييرات المرضية في كبيبات الكلية بعد العلاج بهذا المستخلص.

كما أنّ العلاج الطويل الأمد بالزنجبيل لم يؤثر على مستويات غلوكوز الدم فقط، بل خفّض الكوليسترول والغليسيريدات الثلاثية وزاد من نسبة هرمون الأنسولين وفقدان الوزن في الحيوانات المصابة بالسكري من النمط الأول (Abdulrazaq *et al.*, 2011; Akhani *et al.*, 2004)

وبيّن الباحث (El Sayed et al., 2010) الدور المهم للمستخلص المائي للزنجبيل بجرعة 200-400ملغ/كغ من وزن الجسم في خفض كوليسترول وأن تأثيره أكثر فعالية من عقار أتورفاستاتين (عقار مخفّض للكوليسترول) بجرعات 200-400ملغ/كغ.

إنّ الزنجبيل يمتلك الكثير من المركبات الكيميائية النباتية ذات الخصائص الطبية كمركب الجنجرول Gingerol الذي يزيد من النشاط الإفرازي لخلايا بيتا (ß) في البنكرياس (Akhani *et al.*, 2004)، إضافة إلى مركب Gingerol هناك الفلافونيدات Flavonoids مثل kaempferol, Quercetin, and Curcumin (Tzeng *et al.*, 2012).

تتكون جذور الزنجبيل من zingiberene ، β-bisabolene، α-farnesene، shogaol، β-sesquiphellandrene و α-curcumene (Hiba *et al.*, 2012).

ومن خلال ما تقدّم، تبين أمامنا لجوء الكثيرين إلى الخوض في تجارب عدّة لإيجاد دواء فعّال لداء السكر كونه يهدد ملايين الناس من مختلف الفئات العمرية بعيداً عن التأثيرات الجانبية السلبية للأدوية الكيميائية المصنّعة.

2. أهداف وأهمية البحث

نهدف من البحث إلى المقارنة بين تأثير المستخلص الكحولي للثوم والزنجبيل معاً مع عقار Glibenclamide في المعايير الكيميائية الحيوية (الغلوكوز، الكوليسترول الكلي والغليسيريدات الثلاثية) في مصل دم الفئران المستحدث فيها داء السكري وإثبات أهميتها وأثرها الفعّال.

نظراً للأهمية الطبية لنباتي الثوم والزنجبيل، تمّ دراسة تأثير المستخلص الكحولي لهذين النباتين وأثرها في خفض سكر الدم لدى مرضى السكري، وإمكانية الإقلال ما أمكن من استخدام الأدوية الكيميائية وتجنّب الآثار الجانبية السلبية لها، ومقارنة هذه الفعالية مع عقار مخفّض لغلوكوز الدم.

3. طرائق البحث ومواده

3.1. تحضير المستخلص الكحولي للثوم والزنجبيل:

تمّ تحضير المستخلص الكحولي للثوم عن طريق نقع 320 غ من مسحوق الثوم في 640 مل إيتانول (95%) لمدة ثلاثة أيام، ثم جفف المذيب بالمبخّر الدوار بدرجة حرارة 40 ولمدة ساعة ونصف للحصول على مستخلص جاف (Tzenge *et al.*, 2013)، كما تمّ تحضير مستخلص الزنجبيل بنفس الطريقة السابقة.

3.2. تحضير تراكيز المستخلص النباتي:

- يُذاب (اغ) من المادة المجففة في (10مل) من المحلول الفيزيولوجي (0,9%)
- حُضّر منها جرعات مقدارها (500) ملغ / كغ من وزن الفأر.

3.3. حيوانات التجربة (Experimental Animals):

استُخدمت ذكور الفئران البيضاء من سلالة Balb-c، التي أُحضرت من مركز البحوث العلمية في برزة (دمشق) بعمر تراوح بين (4-5) أسابيع و وزن بين (25-30) غرام أقلمت الفئران في المخبر.

3.3.1. استحداث مرض السكري تجريبياً Induction & Experimental Diabetes

تمّ استحداث مرض السكري في ذكور الفئران من خلال حقنها تحت الجلد Subcutaneous بمادة الألوكسان بجرعة واحدة (200) ملغ/كغ من وزن الجسم (Kako*et al.*, 1995).

تمّ تجويع حيوانات التجربة لمدة (12) ساعة ثم سمح لها بعد الحقن بتناول الغذاء ومحلول الغلوكوز 5% لمنع الهبوط الحاد في تركيز السكر في الدم (Chahlia, 2009)، أمّا الحيوانات الشاهدة فقد حقنت بـ (0.05) مل من المحلول الفيزيولوجي الملحي فقط، ثم أعطيت الماء والغذاء بشكل طبيعي. بعد ذلك تمّ التّأكد من حدوث مرض السكري من خلال قياس نسبة السكر في الدم بجهاز تحليل السكر في الحيوانات المعدّة للدراسة والمعاملة بالألوكسان بعد ثلاثة أيام من عملية الحقن.

3.3.2. معاملة الحيوانات

قُسّمت ذكور الفئران إلى أربع مجموعات، كل مجموعه ضمت 10 فئران كما يلي:

- الشاهدة الفيزيولوجية، حُقنت كلّ منها بالمحلول الفيزيولوجي الملحي تركيزه (0.9) % يومياً لمدة عشرة أيام.
- الشاهدة السكرية (المجموعة التي تمّ استحداث داء السكري فيها فقط).
- المجموعة المعالجة الأولى المستحدث فيها داء السكري والمحقونة بمستخلصي الثوم والزنجبيل معاً بجرعة مقدارها 500 ملغ/كغ من وزن الجسم ولمدة عشرة أيام.
- المجموعة المعالجة الثانية المستحدث فيها داء السكري والمجرعة بالعقار الدوائي (Glibenclamide) بجرعة مقدارها 5 ملغ/كغ من وزن الجسم ولمدة عشرة أيام.

3.3.3. الحصول على الدم

تمّ جمع الدم من الفئران التّجريبّية من طعنة القلب بوساطة محاقن الأنسولين وذلك بعد تخديرها بالكلوروفورم كما تمّ الحصول على مصل الدم بوضع الأنابيب في مثفلة بسرعة 3500 دورة /بالدقيقة ولمدة 10 دقائق. استُخدم المصل الناتج لقياس مستويات الغلوكوز والكولسترول الكلّي والغليسيريدات الثلاثية.

4. التحليل الإحصائي

خضعت نتائج التّجارب للتّحليل الإحصائي باستخدام البرنامج SPSS Statistics 17.0 (Statistical Package for Social Sciences)، واستُخرجت المتوسطات الحسابية، وأُجري اختبار ستودنت للعيّنات المستقلة (Independent Samples Test) كما تمّ اختبار ستودنت للعينات المرتبطة (Paired Samples Statistics)، إضافةً إلى استخراج القيمة الاحتمالية p لكلّ اختبار ومقارنتها مع مستوى المعنوية 0.05 حيث نقبل بوجود فرق معنوي عندما تكون القيمة الاحتمالية أصغر من مستوى المعنوية.

5. النتائج

5.1. متوسط السكر في مصل دم الفئران بعد المعالجة بمستخلصي الثوم والزنجبيل:

تم قياس متوسط سكر الدم للفئران التجريبية بعد المعالجة بمستخلصي الثوم والزنجبيل ومقارنتهما مع المجموعة التي تم استحداث داء السكري فيها وأيضاً تمّت مقارنتهما مع المجموعة الأخرى التي تمّت معالجتها بعقار Glibenclamide، حيث تمّ استخدام اختبار ستودنت للعينات المستقلة paired sample t-test للمقارنة كما يوضح الجدول الآتي.

الجدول (1): التغيرات بسكر دم الفئران المعالجة بمستخلصي الثوم والزنجبيل معاً بالمقارنة مع المستحدث فيها داء السكري والمجموعة المعالجة بعقار Glibenclamide

groups	Mean	p-value	t-test
الشاهدة الفيزيولوجية	141.00±21.72	0**	6.17
المستحدث فيها داء السكر	395.14± 114.79		
المستحدث فيها داء السكر	395.14± 114.79	0.012*	-2.90
المعالجة بمستخلص الثوم والزنجبيل	253.88±71.54		
المعالجة بمستخلص الثوم والزنجبيل	253.88±71.54	0.102n.s	1.78
المعالجة بعقار glibenclamide	193.80± 25.43		

*p<0.05 n.s p=non-significant (p>0.05)
** p<0.01

بيّنت نتائج التحليل الإحصائي أنّه توجد فروق معنوية ذات دلالة إحصائية في متوسط سكر الدم للفئران بعد المعالجة بمستخلصي الثوم والزنجبيل بالمقارنة مع المجموعة التي تمّ استحداث داء السكر فيها، وأنّ المعالجة بمستخلصي الثوم والزنجبيل خفّض من نسبة سكر الدم في دم الفئران بنسبة 35.75%، بينما عند مقارنة المجموعة المعالجة بمستخلصي الثوم والزنجبيل مع عقار Glibenclamide وُجد أنّه لا توجد فروق معنوية ذات دلالة إحصائية في متوسط سكر الدم بين المجموعتين، وأظهرت قيمة t test أنّ متوسط السكر بعد المعالجة بمستخلص الثوم والزنجبيل أعلى من متوسط السكر بعد المعالجة بعقار Glibenclamide بنسبة 31% .

5.2. متوسط تركيز الكوليسترول في الفئران بعد المعالجة بمستخلصي الثوم والزنجبيل معاً:

تمّ قياس متوسط الكوليسترول الكلي للفئران التجريبية بعد المعالجة بمستخلصي الثوم والزنجبيل ومقارنتهما مع المجموعة التي تمّ استحداث داء السكري فيها ومع المجموعة التي تمّت معالجتها بعقار Glibenclamide، حيث تمّ استخدام اختبار ستودنت للعينات المستقلة Paired Sample T-Test للمقارنة كما يوضح الجدول الآتي.

الجدول (2): التغيرات بالكوليسترول الكلي للفئران المعالجة بمستخلصي الثوم والزنجبيل معاً بالمقارنة مع المستحدث فيها داء السكري والمجموعة المعالجة بعقار Glibenclamide

groups	Mean	p-value	t-test
الشاهدة الفيزيولوجية	164.63±32.74	0.001**	4.50
المستحدث فيها داء السكر	313.41±87.05		
المستحدث فيها داء السكر	313.41±87.05	0.010*	-3.03
المعالجة بمستخلص الثوم والزنجبيل	215.50±26.49		
المعالجة بمستخلص الثوم والزنجبيل	215.50±26.49	0.932n.s	-0.09
المعالجة بعقار Glibenclamide	218±75.88		

*p<0.05 n.s p=non-significant(p>0.05)
** p<0.01

أظهرت نتائج التحليل الإحصائي وجود فروق معنوية (قيمة p-value>0.05) ذات دلالة إحصائية في متوسط الكوليسترول بعد المعالجة بمستخلصي الثوم والزنجبيل بالمقارنة مع المجموعة التي تم استحداث السكر أي أن المعالجة بمستخلصي الثوم والزنجبيل خفّض من نسبة الكوليسترول في دم الفئران بنسبة 31.18%، بينما لا توجد فروق معنوية ذات دلالة إحصائية في متوسط الكوليسترول بعد المعالجة بمستخلص الثوم والزنجبيل بالمقارنة مع عقار Glibenclamide ومن قيمة t-test أظهر أنّ المعالجة بمستخلصي الثوم والزنجبيل خفّضت متوسط الكوليسترول بنسبة تفوق المعالجة بعقار Glibenclamide بمقدار1.15%.

5.3. متوسط تركيز الغليسيريدات الثلاثية في الفئران بعد المعالجة بمستخلصي الثوم والزنجبيل معاً:

تمّ قياس متوسط تركيز الغليسيريدات الثلاثية للفئران التجريبية بعد المعالجة بالمستخلص الكحولي للثوم والزنجبيل معاً ومقارنتها مع المجموعة التي تمّ استحداث داء السكري فيها ومع المجموعة الأخرى التي تم معالجتها بعقار glibenclamide ، حيث تمّ استخدام اختبار ستودنت للعينات المستقلة Paired Sample T-Test للمقارنة كما يوضح الجدول الآتي.

الجدول(3) التغيرات بالغليسريدات الثلاثية للفئران المعالجة بمستخلصي الثوم والزنجبيل معاً بالمقارنة مع المستحدث فيها داء السكري والمجموعة المعالجة بعقار Glibenclamide

groups	Mean	p-value	t-test
الشاهدة الفيزيولوجية	215.50±45.26	0.001**	4.36
المستحدث فيها داء السكر	504.29±181.75		
المستحدث فيها داء السكر	504.29±181.75	0**	-4.89
المعالجة بمستخلص الثوم والزنجبيل	188.50±23.42		
المعالجة بمستخلص الثوم والزنجبيل	188.50±23.42	0**	1.78
المعالجة بعقار glibenclamide	294.00±23.77		

** p<0.01

أظهرت نتائج التحليل الإحصائي أنه توجد فروق معنوية ذات دلالة إحصائية(قيمة p-value<0.05) في متوسط الغليسيريدات بعد المعالجة بمستخلصي الثوم والزنجبيل معاً بالمقارنة مع المجموعة التي تمّ استحداث داء السكر فيها ، وأنّ هناك انخفاض معنوي في متوسط الغليسيريدات بعد المعالجة بمستخلص الثوم والزنجبيل أي أن المعالجة بمستخلص الثوم والزنجبيل خفّض من نسبة الغليسيريدات في دم الفئران بنسبة 62.62% ويوضح ذلك الشكل(3-32)، بينما توجد فروق معنوية ذات دلالة إحصائية في متوسط الغليسيريدات بعد المعالجة بمستخلصي الثوم والزنجبيل معاً بالمقارنة مع عينة عقار Glibenclamide حيث بيّنت قيمة t test أنّ المعالجة بمستخلصي الثوم والزنجبيل خفّضت متوسط الغليسريدات الثلاثية بنسبة تفوق المعالجة بعقار Glibenclamide بمقدار 35.88%.

6. المناقشة

6.1. تركيز غلوكوز الدم عند الفئران التجريبية:

أدى حقن الألوكسان بجرعة 200 ملغ / كغ من وزن الفأر إلى ارتفاع معنوي في تركيز غلوكوز الدم إذ بلغ مستواه (395±114.79) ملغ/دل بعد أن كان (141±21.72) ملغ/دل في الشاهدة الفيزيولوجية تتوافق هذه النتائج مع ما توصل إليه عدد من الباحثين (Badawi *et al.*, 2013; Al-Hilfy, 2012; Fadel *et al.*, 2015).

يعود سبب تأثيره إلى إحداث تغيرات في نسيج البنكرياس وتأثيره الانتقائي بشكل خاص لخلايا بيتا البنكرياسية، وبالتالي الاستنزاف السريع لهذه الخلايا في جزر لانغرهانس (Szkudelski, 2001; Lenzen, 1988) إذ أنه يتفاعل مع مجموعة السلفودريل (SH) الموجودة في بنية أنزيم Glucokinase الموجود في أغشية خلايا بيتا إذ يؤدي تثبيط الأنزيم السابق إلى استمرار إفراز الأنسولين والمساهمة في تخريب خلايا بيتا (Vijayanand *et al.*, 2011; Mbaka *et al.*, 2010).

تبيّن من نتائج الدراسة فعالية الجرعة (500ملغ/كغ) من المستخلص الكحولي للثوم والزنجبيل في خفض غلوكوز الدم عند معاملة المجموعات التجريبية به فقد بلغ مستوى غلوكوز الدم (253) ملغ/دل بعد أن كان (395) ملغ/دل في المجموعة المستحدث فيها داء السكر.

يعود سبب تأثير المستخلص الكحولي للثوم والزنجبيل، في خفض غلوكوز الدم إلى أنّ المستخلص يعدّ كاسح للجذور الحرة ويزيد من الأنزيمات المضادة للأكسدة Glutathionperoxidas- Glutathione Catalase-Superoxide dismutase، إضافة إلى احتوائه على كميات كبيرة من الفلافونيدات خاصة مركب Genistein- Resveratrol (Montserrat *et al.*, 2008; Shahriar, 2012) التي تؤدي إلى إصلاح وترميم خلايا بيتا وبالتالي زيادة إفرازها للأنسولين. أو يعود السبب إلى دور المركبات Allixin، S-Allyl Cysteine Sulfoxide، Diallyltrisulfide الهامة الموجودة بمستخلص الثوم في رفع إنتاج الأنسولين بالمجموعات التي تم تغذيتها بهذا المستخلص (Sakura, 2005; Liu *et al.*, 2005; Augusti *et al.*, 1996) ومركب gingerol الموجود بمستخلص الزنجبيل الذي يعتبر المادة الأكثر فعالية لزيادة حساسية خلايا بيتا المفرزة للأنسولين (Akhani *et al.*, 2004).

وعند مقارنة تأثير هذا المستخلص مع فعالية عقار Glibenclamide تبين أنه يساهم في إنقاص تركيز السكر في الدم بشكل مكافئ للعقار الدوائي حسب الجدول (1)، يعود السبب إلى أن الثوم والزنجبيل يعملان على خفض غلوكوز الدم عن طريق زيادة تكوين الغليكوجين من الغلوكوز الزائد في

الجسم بآلية تشبه آلية عقار Glibenclamide عن طريق تثبيط أنزيم غلوكوز-6 فوسفاتاز (Gupat *et al.*, 2005) وقد توافق ذلك مع نتائج الباحثين (Eidi *et al.*, 2006; Kazem, 2014).

إنّ للعقار الدوائي سلبيات تتمثل في أنّ استخدامه على المدى الطويل يؤدي إلى حالات اختناق واحتشاء العضلة القلبية والسكتات بسبب ألفته القوية على المستقبلات القلبية S4R2A فضلاً عن ألفته الانتقائية لخلايا بيتا SRR1 (Steven *et al.*, 2007). كما أن الثوم والزنجبيل بفضل المركبات الكيميائية الهامه في مكوناته أهما Allixin، S-Allyl Cysteine Sulfoxide، Diallyl Trisulfide (Sakurai, 2005; liu *et al.*, 2005) ومركب الـ Gingerol الموجود بمستخلص الزنجبيل (Akhani *et al.*, 2004) يؤدي إلى زيادة تحسس خلايا بيتا لمستوى سكر الدم وارتفاع إنتاج الأنسولين كرد فعل على ارتفاع نسبة السكر في الدم (يكون هذا الارتفاع لدقائق محدودة فالعمر النصفي للأنسولين 5 دقائق) حتى تعود بالنهاية مستويات السكر والأنسولين إلى قيمها الطبيعية وبالتالي يحمي مستخلص الزنجبيل والثوم من المضاعفات الجانبية لمرض السكري (Ezeasuka *et al.*, 2015).

6.2. تركيز الكوليسترول الكلي عند الفئران التجريبية:

نتج عن استحداث داء السكر بالألوكسان في المجموعات التجريبية ارتفاع معنوي ($P<0.05$) في تركيز الكوليسترول الكلي، فقد وصل مستواه في المجموعات التجريبية إلى نحو(313.41±87.05)ملغ/دل بعد أن كان مستواه في الحيوانات الشاهدة الفيزيولوجية (164±33)ملغ/دل هذه النتائج تتوافق مع ما توصل إليه الباحثون (Eidi *et al.*, 2006; Sheweita *et al.*, 2001)

ولعلّ الزيادة الكبيرة في تركيز الكوليسترول في مصل الدم تعود إلى اضطرابات نتيجة تأثير مرض السكري على عمليات الاستقلاب، وتأثيره على هرمون الأنسولين الذي يؤدي غيابه إلى نشاط أنزيم Cholesterol Acyl-Transferase الذي يعمل هو بدوره على زيادة امتصاص الكوليسترول قبل الأمعاء، وبالتالي ارتفاع مستويات الكوليسترول في مصل الدم (Hori *et al.*, 2014)، كما تُستعمل الدهون بدلا من الغلوكوز في عملية الأكسدة وينتج عنها زيادة في تركيز الحموض الدهنية الحرةFree Fatty acid ، التي تتحول في الكبد إلى دهون مفسفره Phospolipids و إلى Acety – COA وهذا يُسهم في تشكل الكوليسترول وارتفاع مستواه (Al-Zorri, 2009).

أن المعالجة بمستخلصي الثوم والزنجبيل خفّضت من نسبة الكوليسترول في دم الفئران بنسبة 31.18% بالمقارنة مع المجموعة التي تم استحداث داء السكري فيها، كما أظهرت النتائج أنّ المعالجة بمستخلصي الثوم والزنجبيل خفّضت متوسط الكوليسترول بنسبة تفوق المعالجة بعقار Glibenclamide بمقدار1.15%.

لعلّ الدور الهام والفعّال للثوم والزنجبيل وفعاليتهما الكبيرة في خفض مستوى الكوليسترول في مصل الدم يكمن في تنشيط النظام الدفاعي الإنزيمي المضاد للأكسدة داخل الجسم بالإضافة إلى احتوائه على مواد طبيعية مضادة للأكسدة مثل فيتامين C، والسيلينيوم التي تحمي LDL من عملية الأكسدة، إضافةً إلى احتواء هذا المستخلص على مركبات قد تعمل على تثبيط أنزيم Hydroxymethylglutaryl المسؤول عن بناء الكوليسترول (Hasan*et al.*, 2006).

كما أنّ انخفاض الكوليسترول الكلي في مصل الدم يتزامن مع انخفاض مستوى الغلوكوز وذلك بسبب هرمون الأنسولين الذي يثبّط الأنزيم المسؤول عن امتصاص الكوليسترول الكلي في الأمعاء Cholesterol Acyl-Transferase (Rajagopal and Sasikala, 2008).

أي أن المستخلص يعمل بطريقة غير مباشرة في خفض نسبة الكوليسترول الكلي بمصل الدم عن طريق خفض نسبة الغلوكوز بزيادة هرمون الأنسولين وبطريقة أخرى مباشرة بتثبيط الأنزيم المسؤول عن بناء الكوليسترول، أما عقارGlibenclamide فإنه يعمل بآلية وحيدة لخفض الكوليسترول وهي زيادة حساسية خلايا بيتا لإفراز الأنسولين.

6.3. تركيز الغليسيريدات الثلاثية عند الفئران التجريبية:

إنّ استحداث داء السكر في ذكور الفئران البيض بوساطة الألوكسان في الدراسة الحالية أدى إلى حدوث ارتفاع معنوي ($p>0.05$) في مستوى تركيز الغليسيريدات الثلاثية كما في الجدول(3)، إذ كان تركيز الغليسيريدات في الشاهدة الفيزيولوجية(45±215) ملغ/دل وأصبح بعد الحقن بالألوكسان (181.75±504.29) ملغ/دل، تزامن ارتفاع تراكيز الغليسيريدات الثلاثية في مصل دم الفئران المستحدث فيها مرض السكري ، عند ارتفاع قيم الغلوكوز، وهذا يعود إلى غياب هرمون الأنسولين الذي كان له دور في زيادة نشاط أنزيم ليباز Hormone Sensitive Lipase (HSL) المسؤول عن تجزئة الغليسيريدات الثلاثية إلى أحماض دهنية وغليسرول التي يتم امتصاصها من قبل الخلايا الدهنية (Nelson and Cox, 2005; Yassin and Nwafy, 2007). وفي حال غياب أو نقص تركيز هرمون الأنسولين تتراكم الأحماض الدهنية والغليسرول في مصل الدم وتعد حينها كمصدر بديل للطاقة Pushparaj *et al.*, 2000).

وعلى هذا فإنّ نتائج التحليل الإحصائي في الدراسة الحالية هذه تُظهر أنّ حقن المستخلص الكحولي للثوم والزنجبيل يؤدي إلى انخفاض معنوي($p>0.05$) في مستوى تركيز الغليسيريدات الثلاثية في الفئران المعالجة مقارنةً مع المجموعة المستحدث فيها داء السكري وهذا ما يتفق مع ما توصل إليه الباحث Elkhayam *et al.* (2003) بينما خفّض المستخلص متوسط الغليسريدات الثلاثية بنسبة تفوق المعالجة بعقار glibenclamide بمقدار35.88% كما يظهر الجدول رقم (3).

قد يعود سبب خفض مستخلص الثوم والزنجبيل للغليسيريدات الثلاثية في مصل دم الفئران السكرية، لاحتواء هذه المستخلصات على الفلافونيدات، التي تؤدي إلى تنشيط أنزيم Lipoprotein Lipase (LPL) الذي يعمل بدوره على تجزئة الغليسيريدات الثلاثية إلى حموض دهنية يتم امتصاصها من قبل الخلايا الدهنية وبالتالي انخفاض تركيزه في مصل الدم (Nasstrom, 2004).

كما أنّ انخفاض مستوى غلوكوز الدم في الفئران المعالجة بمستخلصي الثوم والزنجبيل يقترن بانخفاض مستوى تركيز الغليسيريدات الثلاثية، يعود ذلك إلى وجود هرمون الأنسولين الذي ينشط أنزيم Lipoprotein Lipase (LPL) والذي يزيل بدوره الغليسيريدات والأحماض الدهنية المتراكمة في مصل الدم لتحويلها إلى دهون خزينة داخل الخلايا الدهنية (Nelson and Cox, 2005).

أي أنّ لمستخلصي الثوم والزنجبيل دور مهم في خفض الأنواع المختلفة من الدهون وخفض بيروكسيداز الدهون ورفع مستوى الغلوتاتيون وبالتالي يرفع من مستوى مضادات الأكسدة الطبيعية داخل الجسم.

وبالتالي يعود سبب خفض المستخلص للغليسيريدات بنسبة تفوق العقار لأنه يعمل في خفض نسبة الغليسريدات الثلاثية بمصل الدم عن طريق خفض نسبة الغلوكوز وبالتالي زيادة هرمون الأنسولين من جهة وتنشيط أنزيم Lipoprotein Lipase (LPL) المسؤول عن تجزئة الغليسريدات الثلاثية من جهة أخرى، أما عقار Glibenclamide يعمل بآلية وحيدة لخفض الغليسيريدات الثلاثية وهي زيادة حساسية خلايا بيتا لإفراز الأنسولين فقط.

7. الاستنتاجات والتوصيات

نستنتج من هذه الدراسة الدور المهم لمستخلصي الثوم والزنجبيل في خفض مستويات سكر الدم والكوليسترول الكلي والغليسيريدات الثلاثية بشكل مكافئ لعقار Glibenclamide، لذا نوصي بالاستفادة من المواد الفعّالة لمستخلصي الثوم والزنجبيل في صنع عقاقير دوائية تضاهي دور العقاقير الكيميائية ذات التأثرات الجانبية السليبة.

7(2), 62–6.

Batiha, J., Beshbishy, A., Wasef, L. and Elewa, Y. (2020). Chemical constituents and pharmacological activities of garlic (*allium sativum* l.), *Nutrients,* **12**(n/a), 2–21

Chahlia, N. (2009). Effect of *capparis decidua* on hypolipidemic activity in rats. *J Med Plant Res*, **3**(6), 481–4.

Eidi, A., Eidi, M. and Esmaeili, E. (2006). Antidiabetic effect of garlic (*Allium sativum* L.) in normal and streptozotocin-induced diabetic rats. *Phytomedicine Iran*, **13**(n/a), 624–9.

Elkayam, A., Mirelman, D. and Peleg, E. (2003). The effects of allicin on weight in fructose-induced hyperinsulinemic, hyperlipidemic, hypertensive rats. *Am. J. Hypertension*, **16**(n/a), 1053–65.

El-Sayed, M.A., Yassin, A.Z., El-Shenawy, M.A. and Bassant, M.M. (2010). Anti hypercholesterolaemic effect of ginger rhizome (*Zingiber officinale*) in rats. *Inflammo pharmacol.* **19**(n/a), 309–25.

Ezeasuka, F.J., Ezejindu, D.N., Akudike, C.J. and Ndukwe, G.U. (2015). Hepatoprotective effects of ginger (*zingiber officinale*) on mercury-induced hepatotoxicity in adult female wistar rats. *Advances in Life Science and Technology*, 39(n/a), 7–12

Fadel, H., Darwes, M. and Sheikh Yousef, Kh. (2015). Effect of an aqueous extract of oleander plant according to white created albino mouse which has got diabetes. *Tishreen University Journal for Scientific Research - Biological Sciences*, **37**(5), 220–35.

Gupta, R.K., Kesari, A.N., Watal, G., Murthy, P.S., Chandra, R., Maithal, K. and Tandon V. (2005). Hypoglycemic and antidiabetic effect of aqueous extract of leaves of *Annona squamosa* l. in experimental animal. *Current Science*, **88**(8), 1244–54.

Hiba, A.H., Ayad, M.R., Raauf, B.M. and Bassam, A.H. (2012). Chemical composition and antimicrobial activity of the crude extracts isolated from *zingiber officinale* by different solvents. *PharmaceutIca Analytica Acta*, **3**(9), 1–5.

Hasan, f., Rahim, M. and Mohammed, K. (2006). Effect of some plant extracts on blood sugar level in normal and experimentally diabetic male rats. *Karkok University Journal*, **1**(1), 13–23.

Hori, M., Satoh, M., Furukawa, K., Sakamoto, Y., Hakamata, H., Komohara, Y., Takeya, M., Sasaki, Y., Miyazaki, A. and Horiuchi, S. (2014). *Acyl-Coenzyme A: Cholesterol Acyltransferase-2 (ACAT-2) Is Responsible for Elevated Inteiated Fenugreek or Licorice in Alloxn-Induced Diabetic Rats*. Cairo, Egypt: Energy Authority.

Islam, M.S. and Choim, H. (2008). Comparative effects of dietary ginger (*Zingiber officinale*) and garlic (*Allium sativum*) investigated in a type 2 diabetes model of rats. *J Med Food*, **11**(11), 152–9

Kako, M., Miura, T., Usami, M., Katom A. and Kodowaki, S. (1995). Hypoglycemic effect of the rhizomes of Ophiopoganis tuber in normal and diabetic mice. *Biol Parm Bull,* **18**(5), 785–7.

Kazem, E.M. (2014). Effect of insulin on conception of females of mouse and treatment of deficiency by aged garlic extract. *Karbala University Scientific Journal*, **12**(3), 56–9.

Lachin, T. and Reza, H. (2012). Anti-Diabetic Effect of Cherries in Alloxan Induced Diabetic Rats. *Patents on Endocrine, Metabolic & Immune Drug Discovery Iran*, **6**(n/a), 67–72.

Lenzen, S. and Panten, U. (1988). Alloxan history and mechanism of action. *Spriger Journal*, **31**(6), 337–42.

Liu, C.T., Hse, H., Lii, C.K., Chen, P.S. and Sheen, L.Y. (2005). Effects of garlic oil and diallyltrisulfide on glycemic control in diabetic rats. *Eur J Pharmacol*, **516**(n/a), 165–73.

Mbaka, G.O., Adeyemi, O.O. and Adesina, S.A. (2010). Anti- diabetic activity of the seed extract of sphenocentrumjollyanum and morphological changes on pancreatic beta cells in alloxan- induced diabetic rabbits. *Journal of Med. Sci.*, **1**(11), 550–6.

Montserrat, p., Anna, C., Isabel, B., Genma, M., Lius, A. and Anna, A. (2008). Bioactivity of favonoids on insulin secreting cells. *Comperhensiv Reviews in Food Science and Food Safety,* **17**(6), 299–308.

Nasstrom, B. (2004). Lipoprotein lipase in hemodialysis patients and healthy controls. *Umeå University Med. Dissertations*, **921**(n/a), 1–65.

Nelson, D.L. and Cox, M.M. (2005). *Lehminger Principles of Biochemistry'*. 4th edition. USA: Worth Publishers.

Pushparaj, P., Tan, CH. and Tan, B.K. (2000). Effects of *Averrho ebilimli* leaf extract on blood glucose and lipids in streptozotocin diabetic rats. *Journal Ethnopharmacol*, **72**(n/a), 69–76.

Rajagopal, K. and Sasikala, *K. (2008).* Antihyperglycemic and antihyperlipidemic effects of *Nymphae astellata* in alloxan induced diabetic rats. *Singapore Med. J*, **49**(n/a), 137–41.

Recinella, A., Chiavaroli, L., Masciulli, F., Fraschetti, C. and Filippi, A. (2021). Protective effects induced by a hydroalcoholic *Allium sativum* extract in isolated mouse heart. *Nutrients,* **13**(n/a), 2–21.

نبذة عن المؤلفين

خلود شيخ يوسف

قسم علم الحياة الحيوانية، كلية العلوم، جامعة تشرين، اللاذقية، سوريا، kholodsh39@gmail.com، 00963988274735

السيدة شيخ يوسف ،طالبة دكتوراه (جامعة تشرين)،سورية، ماجستير في قسم علم الحياة الحيوانية ،قامت بالمشاركة بمهمة تبادل ثقافي مع جمهورية مصر العربية ، نشرت العديد من المقالات العلمية المحلية في كل من مجلتي جامعتي تشرين وحماه وأيضاً مقالة في المجلة العربية للعلوم والأبحاث بغزة ومعظم أبحاثها تتعلق بتأثير المستخلصات النباتية على داء السكري عند الفئران البيضاء ،مدرّسة لمادة الفيزيولوجيا والغدد الصم في مخابر كلية العلوم وكلية الصيدلة بجامعة تشرين ،شاركت في عدد من المؤتمرات العلمية في جامعة تشرين ، ومدرّسة في مديرية التربية التابعة لمحافظة اللاذقية.

هيام فاضل

قسم علم الحياة الحيوانية، كلية العلوم، جامعة تشرين، اللاذقية، سوريا، hiamf77@gmail.com، 00963933654954

أ.د. فاضل دكتوراه (كرسنا دار)، سورية، أستاذ ،مشرف رئيس ،رئيسة قسم علم الحياة الحيوانية للعام 2009-2010-2011، عضوة في وضع المعايير الأكاديمية الوطنية لتطوير التعليم العالي في سورية(NARS) دمشق، لها 13 مقالات ومؤلفات وأبحاث علمية محكمة في كرسنا وريفا ومشتهر ومصر وجامعة طشقند ومجلة جامعة تشرين كما شاركت كعضو في عدد من لجان التحكيم لدراسات دكتوراه وماجستير في كل من جامعتي تشرين و حلب و أشرفت على خمس رسائل ماجستير ودكتوراه بقسم علم الحياة الحيوانية بعدد من الندوات والمؤامرات العلمية (الاتحاد السوفييتي، المؤتمر الفيزيولوجي بمدينة ريفا).

مفيد ياسين

قسم الكيمياء التحليلية والغذائية، كلية الصيدلة، جامعة تشرين، اللاذقية، سوريا، moufid_yassin68@gmail.com، 00963933987774

أ.د. ياسين دكتوراه (رومانيا)، سوري، أستاذ مشارك، عميد كلية الصيدلة، مدير المعهد الطبي للعام 2020، له العديد من المؤلفات والأبحاث العلمية في مجلات عالمية ومحلية، معظم أبحاثه تتعلق بكيمياء الأغذية وبشكل رئيسي بأغذية الأطفال المصنعة. قام بإجراء عشرات الأبحاث عن مدى مطابقة الأصناف المحلية لمعايير الجودة العالمية ونشر العديد من الأبحاث التي كان لها كبير الأثر في المساعدة على التوعية بأضرار المواد المصنعة والمعلبة على الصحة العامة، قام بمهمة بحثية علمية في مدينة "مسوري" الهندية ونشر نتائج البحث في مجلات دولية محكمة وباللغة الإنكليزية.

المراجع

Abdulrazaq, N.B., Cho, M.M., Win, N.N., Zaman, R. and Rahman, M.T. (2011). Beneficial effects of ginger (*Zingiber Officinale*) on carbohydrate metabolism in streptozotocin-induced diabetic Rats. *British Journal of Nutrition*, **108**(7), 1194–201.

Akhani, S.P., Vishwakarma, S.L. and Goyal, R.K. (2004). Antidiabetic activity of *zingiber officinale* in streptozotocin induced type 1 diabetic rats. *Journal of Pharmacy and Pharmacology*, **56**(1), 101–5.

Augusti, K.T. and Sheela, C.G. (1996). Antiperoxideeffect of S-allyl cysteine sulfoxide, an insulin secretagogue, in diabetic rats. *Experientia*, **52**(n/a), 115–12.

AL-Hilfy, J. (2012). Effect of green tea aqueous extract on body weight, glucose level, and kidney functions in diabetic male albino rats. *Journal of Al-Nahrain University, Science*. **15**(3), 161–6.

Al-Zorri, S.CH. (2009). *Some Physiological and Histological Effect of Alcoholic Extract Tribul usterrestris in Diabetic Female Rabbits*. Master´s Dissertation, University of Baghdad, Baghdad, Iraq.

Badwi, S., Ahmed, S. and AL-Ani, N. (2013). Effect of ethanolic olive leaf and its callus ethanol extracts in alloxan- induced diabetic mice Blood glucose and lipid profiles, *Journal of Biotechnology Research Center*,

Steven, E., Nissen, M.D. and Kathy Wolski, M.P.H. (2007). Effect of rosiglitazone on the risk of ryocardial infarction and death from cardiovascular causes. *The New England Journal of Medicin*, **356**(n/a), 2457–71

Szkudelski, T. (2001). The mechanism of alloxan and streptozotocin action in B cell of the rat pancreas. *Physiol Res*, **50**(n/a), 537–46.

Shahriar, Kh. and Robin, J.M. (2012). Chromon and flavonoi alkaloids: Occurence and bioactivity. *Molecules Journal MDPi*, **17**(1), 191–206.

Sheweita, S.A., El-Gabar, M.A. and Bastawy, M. (2001). Carbon tetrachloride-induced changes in the activity of phase II drug-metabolizing enzyme in the liver of male rats. *Role of Antioxidants Toxicology*, **165**(n/a), 217–24.

Tzeng, F., LIOUS, SH., CHANG, J. and LIU, M. (2013). The ethanol extract of *Zingiber zerumbet* attenuates streptozotocin-induced diabetic nephropathy in rats thing. *Evid Based Complement Alternat Med*, **2013**(340645), 1–5. DOI: 10.1155/2013/340645

Vijayanand, S. and Wrsely, E.G. (2011). Evaluation of antidiabetic activity of meliaazadirach on alloxan induced diabetic rats. *Inter J. of Current Pharm*, **3**(4), 37–40.

Yassin, M.M. and Mwafy, S.N. (2007). Protective potential of *Glimepirideandnerium oleander* extract on lipid profile, body growth rate, and renal function in streptozotocin-induced diabetic rats. *Turk J Biol*, **31**(2), 95–102.

Zimmet, P., Alberti, K.G. and Shaw, J. (2001). Global and societal implications of the diabetes epidemic. *Nature,* **414**(6865), 782–7.

The Scientific Journal of King Faisal University

Basic and Applied Sciences

Asymmetric Encryption Method Proposed for Arabic Letters Using Artificial Neural Networks

Mohammad Taha Kafarnawi

Department of Control and Automation Engineering ,College of Electrical and Electronic Engineering , Aleppo University, Aleppo, Syria

LINK	RECEIVED	ACCEPTED	PUBLISHED ONLINE	ASSIGNED TO AN ISSUE
https://doi.org/10.37575/b/eng/210044	16/08/2021	26/11/2021	26/11/2021	01/12/2021
NO. OF WORDS	**NO. OF PAGES**	**YEAR**	**VOLUME**	**ISSUE**
6048	7	2021	22	2

ABSTRACT

Asymmetric encryption algorithms suffer the problem of high execution time. This paper presents a proposed methodology to perform encryption and decryption of messages written in Arabic, using artificial intelligence represented by artificial neural networks based on the RSA algorithm. The method is based on dividing the message into partial messages. The arrays of weights and biases in the neural network layers are considered the encryption or decryption key, according to their function. All steps of the proposed method and how it works were shown and used in the MATLAB environment to design a system for encrypting and decrypting messages written in Arabic. The results proved the effectiveness of the proposed methodology and its superiority over the RSA algorithm in terms of execution time for both encryption and decryption. The encryption time in the proposed algorithm is close to the time of decryption, unlike what it was in the RSA algorithm, where the encryption time was relatively much greater than the decryption time. The proposed method was tested on four text files of 50KB, 100KB, 150KB, and 200KB, over two hundred iterations. The average improvement in execution time was 1,330ms and 4,497.5ms for encoding and decoding, respectively.

KEYWORDS

Data protection, decryption, execution time, security, RSA algorithm, performance

CITATION

Kafarnawi, M.T. (2021). Asymmetric encryption method proposed for Arabic letters using artificial neural networks. *The Scientific Journal of King Faisal University: Basic and Applied Sciences*, **22**(2), 106–12. DOI: 10.37575/b/eng/210044

1. Introduction

Cryptography is one of the most important techniques used to protect data against illegal access and tampering. Many algorithms are used to perform encryption. Encryption algorithms are classified into two types: symmetric encryption algorithms, such as the AES encryption algorithm, and asymmetric encryption algorithms, such as the RSA algorithm. RSA is considered one of the most important asymmetric encryption algorithms, developed by the three scientists Ron Rivest, Adi Shamir and Leonard Adleman, and is named by their initials. The RSA algorithm consists of three main stages: the stage of key generation, the stage of encryption, and the stage of decryption. The public key (PU) is generated to be used in encrypting the message before sending it and the private key (PR) is used to decrypt the message at the receiver, according to the next steps (Intila *et al.*, 2019; Moghaddam *et al.*, 2013; Amalarethinam and Leena, 2016). The Advanced Encryption Standard (AES), also known by its original name Rijndael, is a specification for the encryption of digital data established by the U.S. National Institute of Standards and Technology (NIST) in 2001. The AES is a subset of the Rijndael block cipher developed by two Belgian cryptographers, Vincent Rijmen and Joan Daemen, who submitted a proposal to the NIST during the AES selection process. In the United States, the AES was announced by the NIST on November 26, 2001. The AES uses the same key in both encryption and decryption (Lu *et al.*, 2021). The basic difference between the two types is the key used in encryption and decryption. In symmetric encryption, the same key is used for both encryption and decryption, while asymmetric encryption algorithms use two different keys. One of them is a public key for data encryption and the other is a private key for decryption. Private and public keys are different from each other, but they are related to each other. The public key is available to all users, while the private key is hidden, secure, and only owned by its owner. One of the disadvantages of asymmetric encryption is that it takes much longer than symmetric encryption (Taleb and Obaid, 2020). Each type of encryption has advantages and disadvantages. Symmetric encryption algorithms are much faster because they require low computational cost and they are simpler, but their main weakness is that hackers may discover the key because of only using one key for both data encryption and decryption, so the key must remain secure (Taleb and Obaid, 2020). Asymmetric encryption solves the problem of publishing key by using public keys for encryption and private keys for decryption, but this type of encryption is very slow compared to asymmetric encryption because it requires much more computational resources due to the length of the keys. The bottom line is that symmetric encryption is faster than asymmetric encryption, but it is less secure. Asymmetric encryption is more confidential and provides a higher degree of data protection. Moreover, asymmetric encryption provides the features of verification, authentication, and non-repudiation. However, it suffers from relative slowness compared to symmetric encryption. A Slovak study in late 2019 presented an attempt to employ convolutional neural networks in symmetric encryption to perform the standard AES encryption algorithm. The study concluded with one recommendation and the result, which is the possibility of using convolutional neural networks in the field of encryption in addition to the other fields, but only to encrypt files of small sizes (Forgá and Okay, 2019).

In 2020, a group of researchers in Singapore used a Graphics Processing Unit (GPU) to accelerate the work of convolutional neural networks in order to employ them in the symmetric encryption process. The model provides cloud computing to protect user data. Deep Learning as a Service (DLaaS) technology is employed. Two image databases were able to encrypt with different times and with two different performances (Al Badawi *et al.*, 2020). The researchers proposed an encryption model based on integrating a chaotic diagram with multi-layered perceptron neural networks to encode grayscale images by segmentation of message to encrypt and then collect the sub-messages (Kengnou *et al.*,

Corresponding Author: Mohammad Taha Kafarnawi 00963947478706, mtktaha@gmail.com

2014). Some studies use neural networks in the process of some functions of the RSA algorithm as functions of key generation (Haghipour and Sokouti, 2009). The assistant professors, Navita and Barchi, presented a research paper for a theoretical study of the possibility of using neural networks in the field of encryption using neural networks trained by the back propagation algorithm. They did not apply it but indicated the possibility of applying it in the Matlab environment (Agarwal *et al.*, 2013). An encoding and decryption model based on the chaotic scheme and the artificial neural network with an encryption and decryption algorithm to raise the level of confidentiality was also presented, but this study considered neural networks as a supportive part rather than an essential part in the encryption and decryption process (Al-Abaidy, 2020). Another study tried to employ neural networks to perform the encryption task, but it was weak, and the use of neural networks was limited to the generation of encryption keys and the field of generating the keys; it did not present a clear method of using neural networks to perform encryption and decryption in their total form (Al Azawee, *et al.*, 2015). Chaotic technology was also used to improve neural networks to perform encryption and decryption and proposed what is called chaotic neural networks (CNN), but it was of great complexity and included three stages: the stage of generation of the chaotic key and education, the stage of generation of the chaotic chain, and the encryption process. However, this method needs a new training process every time to generate the weights required for the encryption stage (Bevi *et al.*, 2018). Therefore, this research aims to propose a method to perform asymmetric encryption using artificial neural networks for the entire process in order to speed up the encryption process, to improve asymmetric encryption, and to encrypt data in less time and at higher speed. The importance of research in the field of protection against tampering or viewing of data applies to all the stages: transferring through computer networks and storing, securing, protecting to a high degree, achieving the characteristics of authentication and verification, and to get the feature of non-deny in a relatively short time. The artificial neural networks are employed in the field of asymmetric encryption and data protection. The method proposed by this research to employ the artificial neural network to achieve asymmetric encryption of Arabic characters is meant to protect data written in the Arabic language and can be used in the field of e-government to protect data from tampering, forgery, or access in a short time, encoding a larger amount of data in less time. This research is characterized by proposing a method to make the Artificial Neural Network (ANN) completely perform the encryption and decryption functions.

2. Materials and Working Methods

This research was achieved in four steps:

- Suggesting a general method to perform asymmetric coding using Artificial Neural Networks (ANN) and defining the stages of design.
- Explanation of the mechanism of performing asymmetric encryption of Arabic letters using the proposed neural networks and determining the public key that is called the encryption key.
- Explanation of the mechanism of performing asymmetric decryption of Arabic letters using the proposed neural networks and determining the private key that is called the decryption key.
- Practical application using the Matlab environment, getting conclusions, comparing with the RSA algorithm, and analyzing the results.

2.1. The Proposed Method to Achieve Asymmetric Encoding of Arabic Characters:

Figure 1 shows the scheme of the proposed method for performing asymmetric encryption and decoding Arabic letters, which works as follows:

- **The Coding Section**: As shown in Figure 1-a, it consists of several stages:
  - **The Input**: This is the text of the message written in Arabic M. The computer representation of Arabic characters according to the Unicode code starts with the number 1,536 and ends with the number 1,791, and the field of representation of the Arabic characters is [06FF-0600] in the hexadecimal counter-system (2021, Unicode organization).
  - **The Segmentation Stage**: The message M is distributed to partial messages mi. Each message consists of two Arabic letters, which means the length of the partial message is 32 bits because the Unicode code represents each letter in two bytes.
  - **Encryption Stage**: The partial messages are distributed by artificial neural networks designed to perform encryption (the design of ANN will be explained in section 2.2), where the input of each network is a partial message, inputs = mi. The public encryption key Puk is the weights and biases of each layer in a neural network and is presented by the following matrix:

    $$Puk = [W_h\ b_h\ W_o\ b_o] \quad (1)$$

    Where:

    W_h: weights matrix in Hidden Layer

    b_h: biases matrix in Hidden Layer

    W_o: weights matrix in Output Layer

    b_o: biases matrix in Output Layer

    Determining the encryption key is done by specifying W_h, b_h, W_o, and b_o, which will be clarified in section 2.2. The output of this stage is partial codes, outputs = ci, each code corresponding to the partial message of the input of the neural network.
  - **Collection Stage**: At this stage, the sub-ciphers are compiled to get the output of the coding stage, which represents the total code of the message C.

- **The decoding section**: As shown in Figure 1-b, it consists of several stages:
  - **Input**: It is code message *C*, resulting from the encryption stage.
  - The segmentation stage: the code message C is distributed to the sub-codes *Ci*; each code consists of two characters, meaning the length of the partial code is 32 bits because the Unicode code represents each character with two bytes.
  - **Decryption Stage**: The partial codes are distributed by artificial neural networks designed for decryption. (The design of ANN will be explained in section 3.2). The input of each network is a partial code, outputs = c_i, and the private decryption key $\Pr k$ is the weights and offsets of each layer in the neural network and is presented by the following matrix:

    $$\Pr k = [W_{hd}\ b_{hd}\ W_{od}\ b_{od}] \quad (2)$$

    Where:

    W_{hd}: weights array in hidden layer in ANN for decryption.

    b_{hd}: biases array in hidden layer in ANN for decryption.

    W_{od}: weights array in output layer in ANN for decryption.

    b_{od}: biases array in output layer in ANN for decryption.

    Determining the decryption key is achieved by specifying W_{hd}, b_{hd}, W_{od}, and b_{od}, which will be clarified in section 3.2. The output of this stage is partial messages. Outputs = m, with each code corresponding to the partial message of the output of the neural network.
  - **Collection Stage**: At this stage, the partial messages mi are collected to get the output of the decoding stage, which represents the total message M.

Figure 1: The proposed method for performing asymmetric encoding of Arabic characters

A – Encryption section

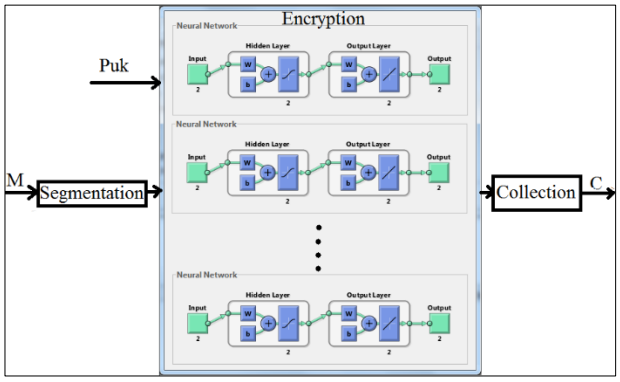

B - Decryption section

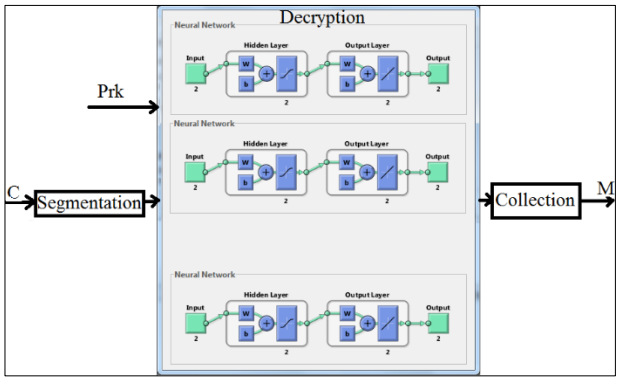

2.2. Design of Neural Networks to Perform Encryption and Generate the Public Encryption Key:

The process of designing the ANN to perform encryption was based on the RSA algorithm, and the following is a summary of RSA steps (Shambhavi and Sharma, 2018):

- Randomly generate two large prime numbers, p and q.
- Calculate the shared part between the public and private key, according to the equation:

$$n = p.q \quad (3)$$

- Calculate the factor $\emptyset$ according to the equation:

$$\emptyset(n) = (p-1)(q-1) \quad (4)$$

- Choose an integer at random, e, through the equation:

$$1 < e < \emptyset(n) \quad (5)$$

Where gcd is the greatest common divisor:

$$\gcd(e, \emptyset(n)) = 1 \quad (6)$$

- Using the extended Euclid algorithm, calculate the integer number d:

$$d = e^{-1} \pmod{\emptyset(n)} \quad (7)$$

Where mod is the remainder operation.

- The public key $Pu = (e, n)$ is used to encrypt the text via the equation:

$$C = M^e \pmod{n} \quad (8)$$

- The private key $PR = (d, n)$ is used for decryption using the equation:

$$M = C^d \pmod{n} \quad (9)$$

Where e is the Encryption Exponent, d is the Decryption Exponent, while n is called the modulus.

The process of encryption and the generation of the encryption key using ANN was carried out in three stages:

- Forming a database for a single ANN: the number of Arabic characters represented by the computer according to the Unicode code is 16 x 16 = 256, so the number of possibilities needed to form the database is 256^2 = 6,5536, because one partial message (m_i) consists of two characters. All the possibilities of the partial message (m_i) are taken and encoded by using the RSA algorithm using equation (8) after generating the cipher key using equations (3) to (7). All the codes (c_i) corresponding to all the possibilities of the partial message (m_i) are found. Pairs of the database from the input of a neural network and its corresponding desired output $\{m_{i,\ ci}\}$ are formed. The formed database is divided into three groups: the training set, the test set, and the validation set, where each set has 65,536 desired input and output pairs. This is to ensure that the network is trained, tested, and verified on all possibilities of receiving the partial message.
- Training the ANN and finding the encryption key *Puk*: a two-layer ANN is proposed; a hidden layer and an output layer, each layer containing two neurons because the input and output are composed of two Arabic letters. The network was trained according to the Levenberg-Marquardt algorithm with the following relationship (Du and Stephanus, 2018):

$$\omega_{K+1} = \omega_K - \left[J^T J + \mu I\right]^{-1} J^T \mathrm{e} \quad (10)$$

Where ω_{K+1} : the new weight (adjusted) and ω_K : the old weight (before modification).

J : Jacobian matrix, which is the value of the first derivative of the network errors related to weights and biases in backpropagation.

μ : Learning rate speeds up or slows down the network training process.

I : Identification matrix.

e : The error or difference between the current network output and the desired output.

Figure 2 shows the training, validation, and test curves of the two-part cryptographic ANN. The performance curve shows the extent of training and learning of the network, where it is found that the value of the mean squared error $MSE = 3.69e-5$. The training, validation, and test curves are identical, as shown in Figure 2, and match the fit and performance curves for all training, validation, and testing data. The reason for this is that the training, validation, and test sets match. The training is repeated until MSE equals zero or is stopped at maximum epochs equal to 1,000. The fit curves gave a fit ratio of R = 100% = 1 for all training, validation, testing, and all data. As a result, the weights and offsets (W_h) , (b_h), (W_o), and (b_o) are found, which constitute the general encryption key given by the relation (1), which is required to perform the encryption process using the ANN according to the following equation:

$$c_i = f_1\,(W_o\, f_2\,(W_h\, m_i + b_h) + b_o) \quad (11)$$

Where f_1 is the function of the activation of the output layer neurons and is a linear function given by the relation:

$$y = x \quad (12)$$

and where f_2 is the function of activation of the hidden layer neurons and is the tansig function that is given by the relation:

$$y = \tan sig(x) = \frac{2}{1+e^{-2x}} - 1 \quad (13)$$

Figure 2: Curves for an artificial coding neural network
A - Performance curves

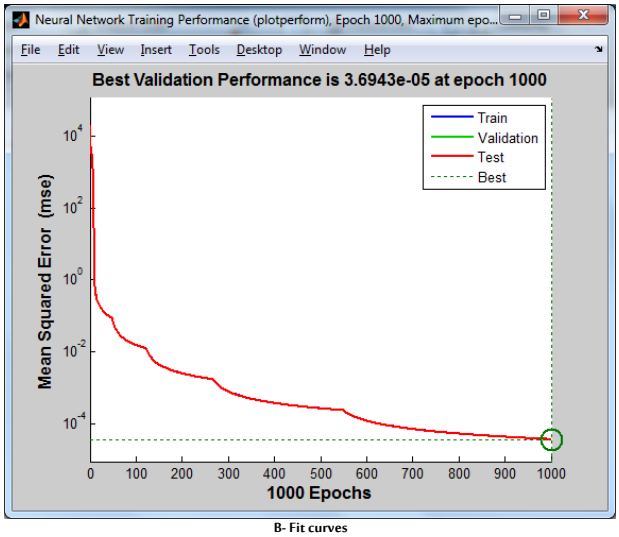

B- Fit curves

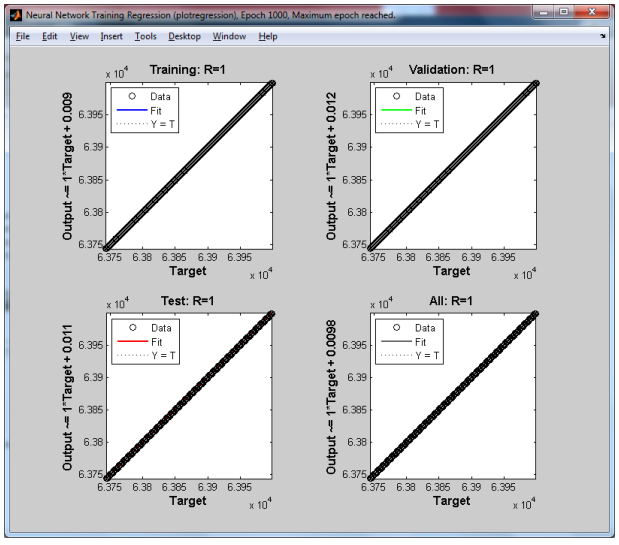

- Determining the number of ANN needed to encode the total Arabic message M: This is done by determining the degree of division for the length of M, estimated by the number of bits, and the length of the partial message mi, estimated in bits, which is 32 bits. The partial message is made up of two Arabic letters, each character with a length of 16 bits according to the computer representation in Unicode. If the degree of division is 128 bits, the number of neural networks is 128 / 32 = 4. In addition, if the degree of division is higher, for example 256, the number of neural networks is 8. This step is important for making the encryption process faster, especially when using multi-core computers with a parallel structure. Therefore, it is more efficient than the process of designing a single neural network to encrypt the entire degree of division in terms of speed, in addition to the almost impossibility of building an ANN with relatively high degrees of division. If we want to design a single ANN to encrypt the message with a degree of division of 128 bits at once, the number of Arabic characters will be 8 in one partial message. Thus, the number of possibilities is e + 19256^8=1.8447. This needs supercomputers in terms of memory size and execution speed to conduct the training process and determine the encryption key.

2.3. Design of Neural Networks to Perform Decryption and Generate the Decryption Private Key:

The process of decrypting and generating the decryption key Prk is carried out using ANN, according to three stages:

- **Configuring a Database for Decryption Artificial Neural Network**: The same database formed to train the neural network is used to perform encoding but with opposite pairs, so the input is (c_i) and the desired output is (m_i), that is, the database is pairs to train the neural network for decoding {c_i m_i}. This database is divided into three groups: the training set, the test set, and the validation set, where each set has 65,536 desired input-output pairs. This is to ensure that the decryption network is trained, tested, and verified on all the possibilities of the partial code.
- **Training the Artificial Neural Network to Decode and Generate the PRK Decryption Key**: A two-layer ANN is proposed, having a hidden layer and an output layer, each layer containing two neurons because the input and output are composed of two characters. The network has been trained according to the Levenberg-Marquardt algorithm that is presented by the relation (10). Figure 3 shows the training, validation, and testing curves of the decoding ANN, consisting of two parts. The performance curve, which shows how well the network is trained and learned, is where we find that the value of the mean squared error MSE = 3.84e-5, as shown in the figure. The fit and performance curves are the same for all training, validation, and test data due to the matching sets for the training, validation, and test data. The fit curves gave a fit ratio R = 100% = 1 for training data, validation data, testing data, and total data. As a result, the weights and biases of the decoding network W_{hd}, b_{hd}, W_{od}, and b_{od} are found, and they constitute the decoding key given by the relation (2), which is required to perform the decoding process using the ANN, according to the following equation:

$$m_i = f_1\left(W_{od}\, f_2\left(W_{hd}\, c_i + b_{hd}\right) + b_{od}\right) \qquad (14)$$

Where:

f_1 is the function of the activation of the output layer neurons, and it is a linear function given by the relationship (12)

f_2 is the function of activation of the hidden layer neurons, and it is the tansig function that is given by the relation (13)

Figure 3: Curves of an artificial neural network for decoding
A - Performance curves

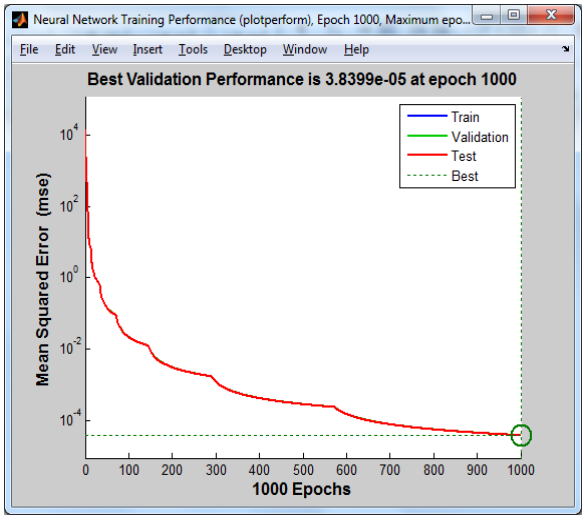

B - Fit curves

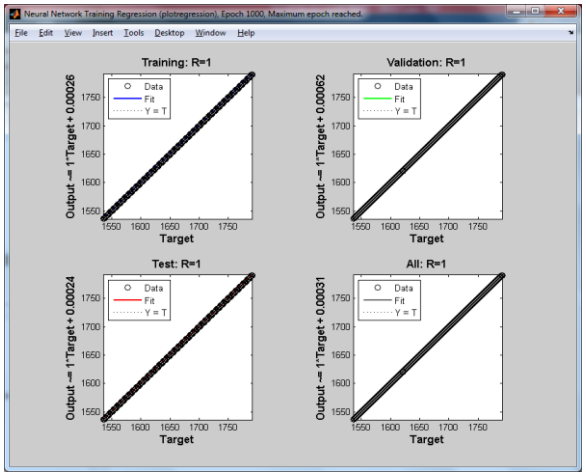

- Determining the number of ANN needed to decrypt the total cipher

C: This is done in the same way that was used in the encryption process, and the number of neural networks needed for decoding is identical to the number of neural networks needed to perform the encryption.

3. Results and Discussion

The proposed methodology for encoding and decoding using ANN has been applied and programmed in the MatLab environment using the Graphical User Interface (GUI) technology as shown in Figure 4A, where the Arabic text message is entered by downloading a text file with an extension (.txt) through the software button "M" in the encryption section, then performing the encryption using neural networks and the general encryption key by programming the equation (11) in the steps shown in section 2.1 after obtaining the encryption key as explained in section 2.2.

Figure 4B shows the encoding output of the message written in Arabic that appears by pressing the "C" software button. It is clear from the figure that the encoding output is Chinese characters, which are represented by the computer according to the Unicode code within a specified minimum limit estimated in hexadecimal and decimal: (F900)16 = (63,744)10, and the maximum limit estimated in hexadecimal and decimal: (F9FF)16 = (63,999)10. This explains the desired output range in the fitting curves for the coding neural network shown in Figure 2B. It should be noted that the two programmed functions shown in Table (1) were used to obtain the digital encoding of the computer representation of Arabic characters according to the Unicode code when starting the encryption procedure and upon completion of the decryption process to move between characters and numeric representation according to the Unicode code. As for the decryption process, it was done by the programming equation (14) in the steps shown in section 2.1 of the decryption section. This is after obtaining the decryption key as shown in section 2.3. Figure 3C shows the results of the decryption, which is the entered Arabic message. This output appears by pressing the "M" button in the decryption section shown in Figure 4A, where the range of Arabic letters is limited by the two limits: minimum (0600)16 = (1,536)10 and maximum (ff06)16 = (1,791)10. This is confirmed by the fit curves shown in Figure 3B for training the artificial neural decoding network.

Table (1): Programming functions used to switch between Arabic characters and Unicode

programming form	programming function
M_values = unicode2native(M, ISO-8859-1')	Converts the letter M to Unicode
C = native2unicode(C_values)	Converts the Unicode of the message encoding output C_values to C

Figure 4: The proposed method for performing asymmetric encoding of Arabic characters using artificial intelligence.
A - Practical application of the proposed method with GUI technology

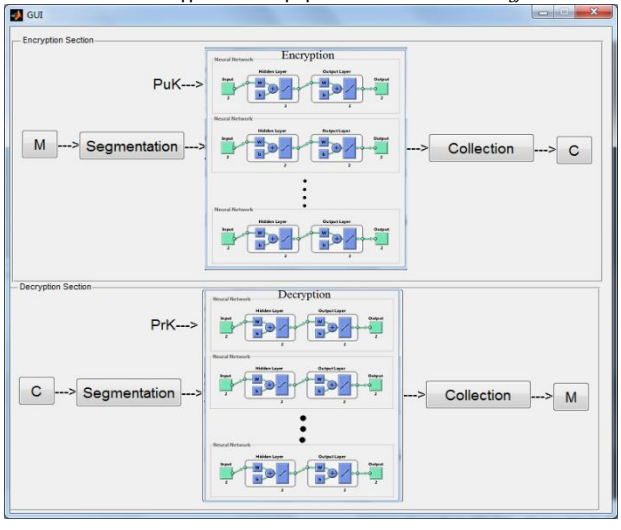

B - Encryption result C

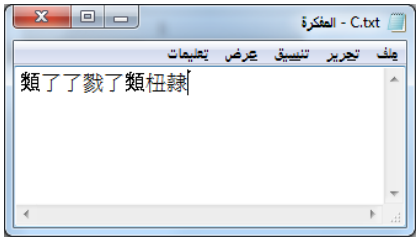

C - Decryption result M

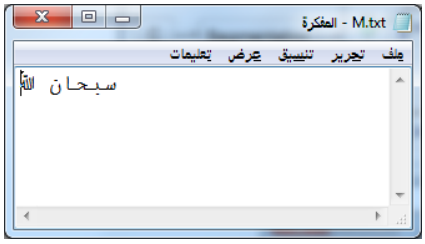

The results were obtained by testing the proposed encryption mechanism by encrypting and decrypting four sizes of Arabic messages, calculating the average execution time for two hundred iterations, and comparing those times with the execution times of the RSA algorithm to encrypt and decrypt the same message sizes with the same average number of iterations. The message sizes encrypted were 50KB, 100KB, 150KB, and 200KB. Figure 5 shows the encryption and decryption times that were obtained, where the proposed methodology for performing encryption and decryption using ANN proved superior to the RSA algorithm in terms of execution time for both encryption and decryption. This can be explained by the fact that the arithmetic operations needed by the proposed methodology to perform encryption are less complex than those required for the RSA algorithm, since the RSA algorithm contains an exponentiation with a relatively large number. Thus, the number of multiplication operations is many. In addition, the remainder of the division requires repeated subtraction operations, the number of which increases with the increase in the value of the number resulting from the exponent operation, and this is not needed for the proposed methodology to perform the encryption. The proposed method requires only a specific number of multiplications and additions because the structure of the neural network is simple and consists of only two neurons, distributed in two layers. This is evident in the decoding time of both the proposed methodology and the RSA algorithm (Figure 5B), because the resulting number of encryptions is greater than the number to be encrypted. As is clear from the computer representation of the Arabic characters to be encrypted and the computer representation of the Chinese characters resulting from the encryption process that is required to be decrypted to return to the Arabic characters, the private key in the RSA algorithm is greater than the public key. This leads to an increase in the RSA decryption time, making it longer than the RSA encryption time. This is due to the increase in the repeated subtraction operations with an increase in the value of the decryption key and the value of the number when decrypting compared to when encrypting. In the proposed methodology, the number of computer operations does not change, which makes the decoding time not very different from the encoding time. Table (2) shows the improvement resulting from the proposed methodology, which is the difference in time required to perform both encryption and decryption for both the RSA algorithm and the proposed methodology when encrypting four files of different sizes (50KB, 100KB, 150KB, and 200KB). The average improvement in time for the four files is 1,330ms and 4,497.5ms for encryption and decryption, respectively. A comparison was made between the proposed methodology and two reference studies that employ neural networks in the field of encryption using the RSA algorithm. The comparison was made in terms of execution time by calculating the average encryption and decoding time for one byte

by depending on the execution time of the largest file to discover the feasibility of the proposed methodology. The comparison showed the effectiveness of the proposed method and its superiority over the two proposed methods in the reference studies (Yousif *et al.*, 2017; Chakraborty *et al.*, 2018), as shown in Table (3). The reason for the superiority of the proposed methodology is due to two main factors. The first is the presence of a partial degree of 32 bits, which leads to a simple ANN structure consisting of only two neurons per layer. The second factor is that the proposed mechanism relies completely on the ANN for the encryption and decryption processes and there are no auxiliary algorithms, as their presence leads to additional execution times.

Figure 5: Comparison of the execution time of the proposed methodology for performing asymmetric encryption of Arabic characters using artificial intelligence with the RSA algorithm.

A - Encryption time

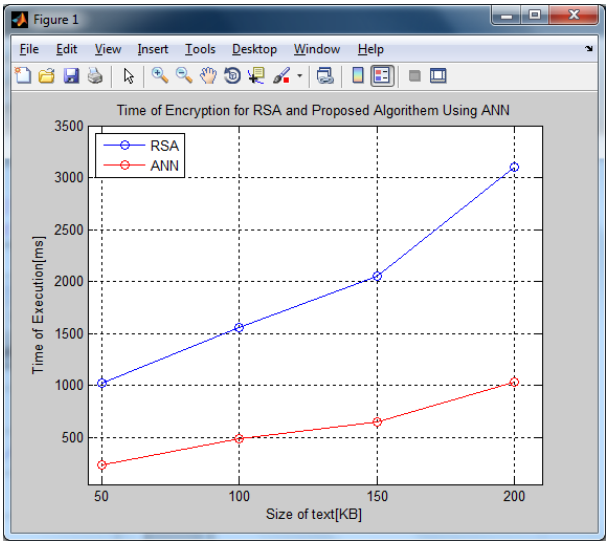

B - Decryption time

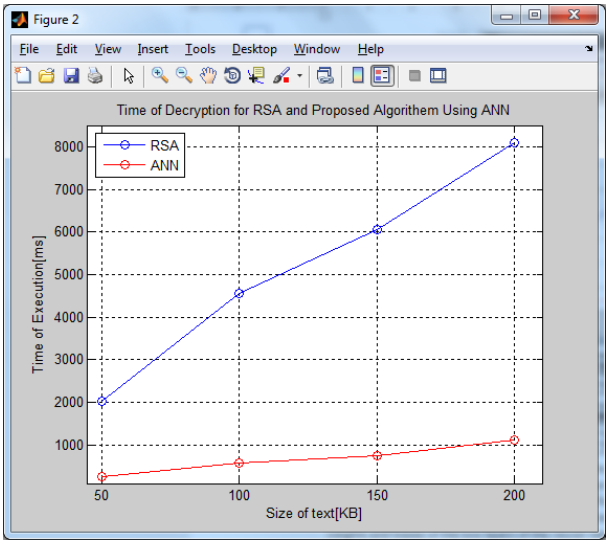

Table (2): The amount of improvement in execution time of the proposed methodology compared to the RSA algorithm

File size	50KB	100KB	150KB	200KB
Encryption time [ms]	780	1,070	1,400	2,070
Decryption time [ms]	1,760	3,970	5,290	6,970

Table (3): Comparison between the algorithm proposed in this research and two algorithms proposed in two reference studies

The method	Average encryption time of one byte	Average decryption time of one byte
Proposed method	5ns	5.37ns
(Yousif *et al.*, 2017)	84ns	270ns
(Chakraborty *et al.*, 2018)	253ns	253ns

The protection of data by encrypting according to the proposed mechanism based on ANN gives complete effectiveness and the ability to encrypt and decrypt, so neural networks can be used to perform asymmetric encryption and decryption to protect data from tampering, illegal access and securely allows for digital signatures, verification, authentication, and non-denial. The method used is highly effective against hacking because it depends on a key consisting of four unknowns in the form of matrixes, which are the matrixes of weights and biases of the two layers of the neural network. The process of network training needs to define the code, which can only be obtained by knowing the key of the original RSA algorithm. Thus, the degree of protection of the proposed mechanism depends on the degree of the original algorithm. It is equal when trying to break it by breaking the original algorithm and superior when trying to hack it by means of probability, because the number of unknowns in the key of the proposed method is greater than in the RSA algorithm. The degree of confidentiality of the proposed method can be increased by using dynamic keys and changing the weights through periodic network training, which increases the confidentiality and degree of protection used and the improbability of breaking it. The code resulting from the proposed mechanism is not necessarily Arabic letters, which increases the number of possibilities in front of the hacker, and the experimentation process does not work for penetration. With the presence of the order factor, a hacker may use experimental letters that give a correct arrangement in terms of language but are not necessarily the correct word, and this method needs scrutiny, which forces the hacker to analyze every possibility. Hackers are faced with an infinite number of possibilities, 'and they soon realize that the code is impossible to break. The encryption and decryption process used in the RSA algorithm depends on two equations with fixed functions; the method is clear to the hacker and the strength of the algorithm lies in the encryption key only. The proposed methodology uses two activation functions, and different activation functions can be used, not only the tansig and linear functions. This increases the confidentiality of encryption by adding a factor of insularity to the method and by the presence of more than one possibility to perform encryption and decryption by changing the activation functions according to their number and order of use in each layer. The process of generating keys in the RSA algorithm is dependent on a fixed methodology, and the strength of this methodology is a factor of randomness in choosing the cryptographic parameters represented by the two large primes, q and p. In the proposed methodology, the method of generating the keys is not fixed because an algorithm other than RSA can be used as the original algorithm to obtain training pairs. The proposed method depends on the original algorithm only for the encryption key to obtain the training pairs. After obtaining the code, it does not need the private key, which means that it needs only one key. Therefore, symmetrical algorithms, such as the AES algorithm, can also be used to design the encryption and decryption keys for the proposed method, which contributes to the reduction in the design time needed for encryption and decryption with neural networks. The proposed methodology is not affected by the original algorithm used (whether RSA or others) to design it in terms of encryption and decryption time, but it — the original algorithm — affects the values of weights and biases, and therefore the values of the encryption and decryption keys.

4. Conclusion

In this research, a methodology was proposed to encrypt and decrypt messages, written in Arabic, by using artificial intelligence represented by artificial neural networks, to determine how this network was designed to perform asymmetric encryption, and to discover how to obtain the private and public keys of the proposed mechanism. This mechanism proved highly effective and superior to the RSA algorithm in terms of execution time, both in encryption and decryption. In

addition, a software system was designed to perform encryption and decryption in the MatLab programming environment. It proved effective and gave an accuracy of 100% in retrieving 10,000 encrypted messages of different sizes. The average improvement in encryption and decryption time was 1,330ms and 4,497.5ms, respectively, for text message sizes of 50KB, 100KB, 150KB, and 200KB.

Biography

Mohammad Taha Kafarnawi

Computer and Automatic Control Engineering Department, University of Aleppo, Aleppo, Syria, mtktaha@gmail.com, 00963947478706

Dr Kafarnawi is a University of Aleppo graduate. He is a recipient of Al-Basel Award for Academic Excellence, ranked first. He obtained his PhD in Computer and Automatic Control Engineering, Tishreen University. He is a Member of the teaching staff at the University of Aleppo since 2010. He Published research papers in Aleppo University research, Tishreen University research, and the French journal Energy Procedia. He has a patent in field of artificial intelligence and control. He also teaches at Tishreen University, Ittihad University and Cordoba Private University.

References

Al-Abaidy, S.A. (2020). Artificial neural network based image encryption technique. *Int. J. Services Operations and Informatics*, **10**(3), 181–9.

Agarwal, N. and Agarwal, P. (2013). Use of artificial neural network in the field of security. *MIT International Journal of Computer Science & Information Technology*, **3**(1), 42–44.

Al Azawee, H., Husien, S. and Mohd Yunus, M.A. (2015). Encryption function on artificial neural network. *Springer, Neural Comput & Applic*. **2015**(3), a/b. DOI 10.1007/s00521-015-2028-3

Al Badawi, A., Chao, J., Lin, J. Mun, C.F., Jie Sim, J., Meng Tan, B.H., Nan, X.M., Aung, K.M. and Chandrasekhar, V. (2020). Towards the AlexNet moment for homomorphic encryption: HCNN, the first homomorphic CNN on encrypted data with GPUs. *IEEE Transactions on Emerging Topics in Computing*, **9**(n/a), 1330–43. DOI: 10.1109/TETC.2020.3014636.

Bevi, A.R., Tumu, S. and Prasad, N.V. (2018). Design and investigation of a chaotic neural network architecture for cryptographic applications. *Computers and Electrical Engineering/Elsevier*. **72**(2018) 179–90.

Chakraborty, M., Jana, B., Mandal, T. and Kule, M. (2018). A Performance Analysis of RSA Scheme using artificial neural network. In: *2018 9th International Conference On Computing, Communication and Networking Technologies (ICCCNT)*, Bengaluru, India, 10-12/07/2018.

Du, Y. and Stephanus, A. (2018). Levenberg-Marquardt neural network algorithm for degree of arteriovenous fistula stenosis classification using a dual optical photoplethysmography sensor. *Sensors (Basel)*, **18**(7), 1–18. DOI: 10.3390/s18072322.

Faraz, F.M., Maen, T.A. and Omidreza, K. (2013). A hybrid encryption algorithm based on RSA small-e and efficient-RSA for cloud computing environments. *Journal of Advances in Computer Network*, **1**(3), 238–41.

Forgá, R. and Okay, M. (2019). Contribution to symmetric cryptography by convolutional neural networks. *Slovak Academy of Sciences*, **2**(16), n/a.

George Amalarethinam, D.I. and Leena, H.M. (2017). Enhanced RSA algorithm with varying key sizes for data security in cloud. *IEEE,* **9**(17), 172–5.

Haghipour, S. and Sokouti, B. (2009). Approaches in RSA cryptosystem using artificial neural network. *Oriental Journal of Computer Science & Technology*, **2**(1), 11–17

Intila, C., Gerardo B. and Medina R. (2019). A study of public key 'e' in RSA algorithm. In: *International Conference on Information Technology and Digital Applications (ICITDA 2018),* Manila, Philippines, 08-09/11/2018. *IOP Conference Series: Materials Science and Engineering*, **482**(012016), 1–9. DOI:10.1088/1757-899X/482/1/012016

Kengnou Telem, A.N., Segning, C., Kenne, G. and Fotsin, H.B (2014). A simple and robust gray Image encryption scheme using chaotic logistic map and artificial neural network. *Hindawi Publishing Corporation*, **2014**(n/a), 1–13.

Lu, Z.M. and Mohamed, H. (2021). A complex encryption system design implemented by AES. *Journal of Information Security*, **12**(2), 177–87. DOI:10.4236/jis.2021.122009

Omar, G.A. and Shawkat, K.G. (2018). A survey on cryptography algorithms. *International Journal of Scientific and Research Publications (IJSRP)*, **8**(7), 495–516.

Shambhavi, D. and Sonal, S. (2018). Enhanced RSA algorithm for data security in cloud. *IRE Journals*, **1**(9), 2456–8880.

Taleb Obaid, A.S. (2020). Study a public key in RSA algorithm. *EJERS, European Journal of Engineering Research and Science*, **5**(4), 395–8.

Unicode Organization. Available at: https://home.unicode.org/ (accessed on 3/3/2021)

Yousif, E.Y. and ANabi, M.A.B. (2017). Performance enhancement of RSA algorithm using artificial neural networks. *International Journal of Computer Science and Mobile Computing*, **6**(9), 21–7.

The Scientific Journal of King Faisal University

Basic and Applied Sciences

Impact of Solvents, Magnesium Oxide and Aluminium Oxide Nanoparticles on the Photophysical Properties of Acridine Orange Dye

Fairooz Faeq Kareem, Mahasin F. Hadi Al-Kadhemy and Asrar Abdulmunem Saeed

Department of Physics, College of Science, Mustansiriyah University, Baghdad, Iraq

LINK	RECEIVED	ACCEPTED	PUBLISHED ONLINE	ASSIGNED TO AN ISSUE
https://doi.org/10.37575/b/sci/210047	18/08/2021	26/11/2021	26/11/2021	01/12/2021

NO. OF WORDS	NO. OF PAGES	YEAR	VOLUME	ISSUE
5495	7	2021	22	2

ABSTRACT

Absorption and fluorescence spectroscopy techniques were applied to investigate the photophysical characteristics of acridine orange (AO) dye in solvents that included distilled water, dimethyl sulfoxide (DMSO), acetone and ethanol in various concentrations (1×10-4—1×10-6) M. All of the samples were served at room temperature. The relationships between various parameters describing the strength of optical transitions in atoms and molecules were reviewed. This study expresses various viewpoints by describing how concentration and solvent affect the dye's absorption and fluorescence spectra. The absorption spectra of AO exhibit a band at (490 nm), except for DMSO, which shifts more towards red by 5 nm. The fluorescence spectra show a blue shift in AO aqueous solution around 6 nm until (0.5×10-4) M, followed by a red shift at around 7 nm at (1×10-6) M. There is a blue shift in (1×10-5) M for DMSO at around 4 nm, then a 10 nm red shift in higher concentrations as well as a 9 nm red shift in acetone and 6 nm in ethanol. Adding magnesium oxide nanoparticles (MgO NPs) quenched AO in both absorption and fluorescence spectra, whereas maximum fluorescence and intensity increased when aluminium oxide nanoparticles (Al2O3 NPs) were added to the solution.

KEYWORDS

Laser dye, absorption spectrum, fluorescence spectrum, MgO NPs, Al2O3 NPs

CITATION

Kareem, F. F., M. F. H. Al-Kadhemy, and A. A. Saeed. (2021). Impact of solvents, magnesium oxide and aluminium oxide nanoparticles on the photophysical properties of acridine orange dye. *The Scientific Journal of King Faisal University: Basic and Applied Sciences*, **22**(2), 113–9. DOI: 10.37575/b/sci/210047

1. Introduction

Acridine is a cationic dye that shares a common aromatic structure with multiple acridine dyes (Sharma *et al.* 2003). Acridine has various applications in fluorescence microscopy, endomicroscopy, intraoperative, fluorescence guidance, photodynamic therapy, sonodynamic therapy and radio dynamic therapy (Byvaltsev *et al.* 2019).

Acridine derivatives form an important class of heterocycles containing nitrogen due to their broad range of pharmaceutical properties. In the nineteenth century, acridine derivatives were used industrially as pigments and dyes. More critical to the pharmaceutical industry, acridines are used as dyes, fluorescent materials for visualisation of biomolecules and in laser technologies. The properties of acridines are attributed to their semi-planar heterocyclic structure, which appreciably interacts with different biomolecular targets. Acridine/acridone derivatives are found in natural plants and various marine organisms (Kowalewska *et al.* 2017).

The $S_0 \longrightarrow S_1$ and $S_0 \longrightarrow S_2$ bands in acridine orange (AO) are red shifted in polar solvents compared to non-polar solvents, indicating that the transitions are $\pi \rightarrow \pi^*$ in nature. The ground state has a higher charge character than the excited state. In contrast, the $S_0 \longrightarrow S_3$ bands are blue-shifted in polar compared to non-polar solvents (Sikiru *et al.* 2016).

Nanomaterials, particularly metal and metal oxide nanoparticles, are a special class of materials with unique physical and chemical properties that have a wide range of applications. Magnesium oxide nanoparticles (MgO NPs) have been used in electronics, catalysis, additives, ceramics, photochemical products, paints and medicine (Musarat *et al.* 2020). Engineered aluminium oxide nanoparticles (Al_2O_3 NPs) have commercial potential in catalysis, polymer modification and heat transfer fluids (Sunandan *et al.* 2013). Kumar *et al.* (2018) investigated the use of MgO as the adsorbent for methylene blue (MB) removal. It is also possible to extract spectral information from the adsorbed compounds using nanoporous aluminium oxide, as demonstrated by Hotta *et al.* (2010).

Absorption and fluorescence spectra reveal significant changes due to aggregations, which can be useful as the parameters change when the concentration of AO decreases. This study aims to characterise AO's absorption and fluorescence properties as a function of its concentration by calculating the quantum yield, extinction coefficient, Stokes shift, radiative lifetime and fluorescence lifetime. As AO is used in medical applications and MgO and Al_2O_3 are used in industrial applications at low cost, metal oxide nanoparticles were added to the AO water solution and studied as a new work.

2. Experimental Work

2.1 Materials:

AO ($C_{17}H_{19}N_3.1/2ZnCl_2.HCl$, molecular weight 369.94 g/mol) from Qualikems Fine Chem Pvt. Ltd. was dissolved in distilled water, dimethyl sulfoxide (DMSO), acetone and ethanol. Distilled water (H_2O) with (10.2) polarity and DMSO (C_2H_6OS) with (7.2) polarity (Lide, 2010) were procured from Greyhound Chromatography and Allied Chemicals. Acetone (CH_3COCH_3) with (5.1) polarity (Lide, 2010) was acquired from HI Media Laboratories Pvt. Ltd, and ethanol (C_2H_5OH) with (4.0) polarity (Lide, 2010) was procured from Finchley, London. The solvents were supplied with 99% purity in terms of mass percentage.

Magnesium oxide (MgO with an average diameter of 40 nm and 99.9% purity) was obtained from Intelligent Materials Pvt. Ltd. Alumina oxide (Al_2O_3 with an average diameter of 20—30 nm and 99.9% purity) was obtained from China.

2.2 Preparation of Samples:

AO dye solution with a primary concentration of (1×10^{-2}) M was prepared by dissolving appropriate amounts of dye (weighted by a Mattler balance of 0.1 mg sensitivity) in the solvents. The amount of dye, m (in g), was calculated using equation (1) (Al-Kadhemy *et al.* 2020):

Corresponding Author: Fairooz Faeq Kareem 009647703467140, cenderlla78@yahoo.com

$$m = \frac{M_W V C}{1000} \quad (1)$$

where M_w is the molecular weight of dye (g/mole), V is the volume of the solvent (ml) and C is the dye concentration (M), which was then diluted to get concentrations in the range of (1×10^{-2}) M to (1×10^{-6}) M as shown in equation (2) (Krolenko *et al.* 2006; Saeed *et al.* 2020).

$$C_1 V_1 = C_2 V_2 \quad (2)$$

where C_1 is high concentration, V_1 is the volume before dilution, C_2 is low concentration and V_2 is the total volume after dilution. It was noted that the prepared solutions had good homogeneity.

Nano (MgO and Al_2O_3) was added to the dye solution in 0.002 g and 0.004 g amounts. The mixture for both nanomaterials was added to the dye solution to investigate the best number of nanoparticles to enhance the photophysical properties of the organic dye. All of the samples were prepared using a hot plate magnetic stirrer until the (MgO and Al_2O_3) nanoparticles were diffused homogeneously through the AO distilled water solution. All of the samples were kept in a dark place to avoid any possibility of photo-bleaching or the dye fading. The samples were used immediately after preparation.

Spectrophotometric measurements were taken with a UV-Visible spectrophotometer (T70/T80) and (SHIMADZU RF-5301pc) for absorption and fluorescence spectra for all samples, respectively. All of the figures were created with Origin Pro 2019b.

3. Theory and Calculations

The intensity of light absorption at wavelength λ by an absorbing medium is characterised by absorbance A (λ) or transmittance T (λ), defined as (Valeur 2012):

$$A(\lambda) = log\frac{I_o}{I} = -\log(\lambda) \quad (3)$$

where I_o and I are the light intensities of the beams entering and leaving the absorbing medium, respectively. In many cases, the absorbance of a sample follows the Beer–Lambert Law (Valeur 2012).

$$A(\lambda) = \log\frac{I_o}{I} = \varepsilon(\lambda) l C \quad (4)$$

where $\varepsilon(\lambda)$ is the molar absorption coefficient that represents a molecule's ability to absorb light in a given solvent (commonly expressed in L mol^{-1} cm^{-1}), C is the concentration (in M) of the absorbing species and L is the absorption path length (thickness of the absorbing medium in cm). According to classical theory, molecular absorption of light can be described by considering the molecule as an oscillating dipole, which allows us to introduce a quantity called the oscillator strength (*f*), which is directly related to the integral of the absorption band as follows (Dihingia *et al.* 2019):

$$f = 2303\ \frac{mC_o^2}{N_a\ \pi e^2\ n} \int \varepsilon(\bar{\nu}) d\bar{\nu} \quad (5)$$

where m and e are the mass and charge of an electron, respectively, Co is the speed of light, n is the index of refraction and $\overline{\nu}$ is the wavenumber (in cm^{-1}). Oscillator strength, *f*, is a ratio that compares the strength of the transition with that of a bound electron behaving as a 3D harmonic oscillator. For strong molecular transitions, *f* values are close to 1 (sometimes they even slightly exceed this value). For weak transitions, *f* values can be several orders of magnitude lower than 1 and as low as 10^{-8}. For $n \longrightarrow \pi^*$ transitions, the values of ε are in the order of a few hundred or less and those of *f* are no greater than $\sim10^{-3}$. For $\pi \longrightarrow \pi^*$ transitions, the values of ε and *f* are, in principle, much higher (except in symmetry-forbidden transitions); *f* is close to 1 for some compounds, which corresponds to values of ε that are of the order of 10^5. *f* is a dimensionless quantity (Birks 1973).

Fluorescence quantum yield (Φ_F) is the ratio of the number of emitted photons (over the entire duration of decay) to the number of absorbed photons (Valeur 2012).

$$\Phi_F = \frac{\text{number of photons emitted}}{\text{number of photons absorbed}} = \frac{\int Area\ under\ the\ fluoresence\ spectrum}{\int Area\ under\ the\ absorption\ spectrum} \quad (6)$$

where the number of photons emitted and absorbed are in the integrated area under the fluorescence and absorption spectrum, respectively.

Radiative lifetime (τ_{FM}) has been related to the extinction coefficient using a variety of formulas. Bowen and Woks' method is the easiest to utilise (Valeur 2012):

$$\frac{1}{\tau_{FM}} = 2.88 \times 10^{-9} n^2 \bar{\nu}^2 \int \varepsilon(\bar{\nu}) d\bar{\nu} \quad (7)$$

where ($\int \varepsilon\ (\bar{\nu})\ d\bar{\nu}$) is the area under the curve of the molecular extinction coefficient plotted against the wavenumber, $\bar{\nu}$ is the wavenumber of the maximum in the absorption band and n is the refractive index of the solvent.

Then, fluorescence lifetime (τ_F) is obtained using the following equation (Valeur 2012):

$$\tau_F = \phi_F \tau_{FM} \quad (8)$$

Stokes shift ($\Delta\bar{\nu}$) is the term used to describe the difference in the wavelength at which a molecule emits light and is relative to the wavelength at which the molecule was excited (Al-Kadhemy and Nasser 2018).

$$\Delta\bar{\nu} = \bar{\nu}_{abs.} - \bar{\nu}_{flu.} \quad (9)$$

This important parameter can provide information about excited states. For instance, when the dipole moment of a fluorescent molecule is higher in an excited state than in a ground state, the Stokes shift increases with solvent polarity (Takashi *et al.* 2010).

The full width at half maximum (FWHM) is calculated by knowing the half intensity of absorption or fluorescence spectra that determines the half-width of spectra by slipping towards the x-axis, which represents the wavelength in nanometres (Lewkowics 2006). The FWHM is the function of the possibility of tunability in the active medium laser.

4. Results and Discussion

The absorption spectra of AO laser dye in different solvents (distilled water, DMSO, acetone and ethanol) at various concentrations (1×10^{-4}, 0.5×10^{-4}, 1×10^{-5}, 0.5×10^{-5} and 1×10^{-6}) M is illustrated in Figure (1). The maximum excitation and emission (λ_{max}) for standard AO (in aqueous solution) is (494 nm) and (525 nm), respectively (Krolenko *et al.* 2006).

Figure (1a) shows AO dissolved in distilled water. It is a noticeably wide spectrum with the maximum absorption wavelength constant at all concentrations at 490 nm and around 470 nm at the shoulder. This is consistent with Krolenko *et al.* (2006). The intensity of absorption increases as the concentration increases. A further increase in concentration leads to a decrease in the absorption band at 490 nm, and the shoulder increases at 470 nm, which can be assigned to the dimer and monomer (Falcone *et al.* 2002; Markarian and Gohar 2015).

This can be observed in Figure (1b) where AO is dissolved in DMSO, which is less polar than distilled water. The same behaviour is noticed for maximum absorption wavelength, which is unchangeable with increasing concentrations, but a red shift occurs and becomes 495 nm compared to the water solvent. Absorption intensity increases with increasing concentration, which is in agreement with Markarian and Gohar (2015). In both of the solvents mentioned above, the FWHM decreases with increasing concentration, and the spectra become narrower. The physical and chemical characteristics of DMSO are unique, and it has a higher polarity than both ethanol and acetone. It has a high dielectric constant, making charge separation simple, and it is soluble in a wide range of ionic, polar and polarisable molecules.

DMSO is also a good solvent for olefin polymerisation because its hydrogen atoms are resistant to being removed in free-radical processes. DMSO solvates cations, in general, due to the increased electron density of the oxygen atom and the steric availability of oxygen. The basicity of DMSO is somewhat higher than that of water because of the increased electron density near the oxygen atom. DMSO's capacity to compete successfully for hydrogen donor molecules is a key element in its influence on various reaction speeds. As the reactivity of bases in DMSO increases, a variety of base-catalysed elimination and cleavage processes can be carried out at room temperature or temperatures much lower than normal.

Acetone (Figure (1c)) and ethanol (Figure (1d)) have lower polarity than water; therefore, the maximum absorption wavelength does not change with increased concentrations of AO and remains at 490 nm with the smaller shoulder at 470 nm. Absorbance increases regularly with increasing concentration due to an increase in the number of excited AO molecules from a ground state to the first excited state, which aligns with Al Hussainey *et al.* (2018). For both solvents, the FWHM of absorption spectra (increase in acetone and decrease in ethanol) increases the concentrations. Table (1) displays all of the results that are discussed above.

Comparing the absorbance results for all of the previous solvents shows that the maximum wavelength of absorption spectrum remains constant, except for DMSO, which shifts more towards red by 5 nm. Absorbance increases with the increasing polarity of the solvent and has the highest absorbance for water with higher polarity.

Figure (1): Absorption spectra of AO in a) distilled water; b) DMSO; c) acetone; d) ethanol in various concentrations

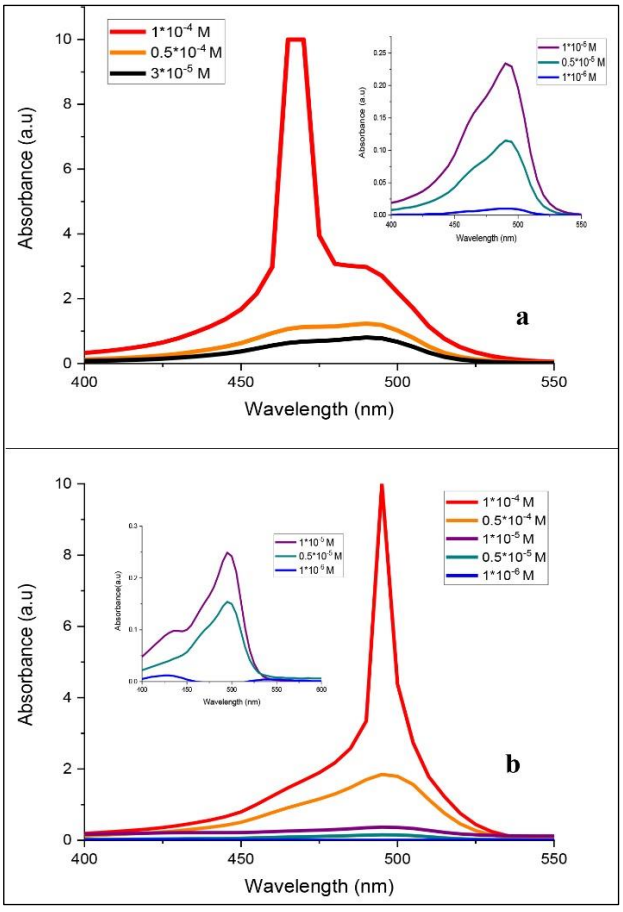

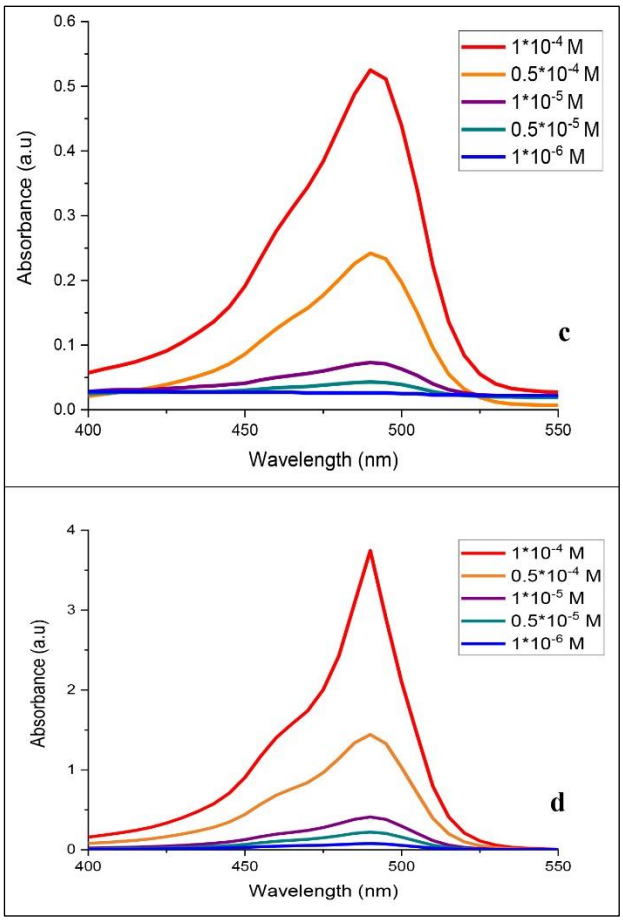

Table (1): Absorption parameters for AO in different solvents with different concentrations

Solvents	C (M)	λ_{absmax} (nm)	$I_{abs\ max}$	FWHM (nm)
Distilled water	1×10^{-4}	490	2.98	12.68
	0.5×10^{-4}	490	1.23	58.81
	1×10^{-5}	490	0.23	52.93
	0.5×10^{-5}	490	0.11	51.53
	1×10^{-6}	490	0.01	56.66
	3×10^{-5}	490	0.80	56.67
DMSO	1×10^{-4}	495	2.88	8.20
	0.5×10^{-4}	495	1.84	44.57
	1×10^{-5}	495	0.24	53.93
	0.5×10^{-5}	495	0.15	55.58
	1×10^{-6}	490	0.07	155.84
Acetone	1×10^{-4}	490	0.52	53.55
	0.5×10^{-4}	490	0.24	57.50
	1×10^{-5}	490	0.07	210
	0.5×10^{-5}	490	0.04	170
	1×10^{-6}	490	0.04	35
Ethanol	1×10^{-4}	490	3.75	29.30
	0.5×10^{-4}	490	1.44	42.64
	1×10^{-5}	490	0.41	43.99
	0.5×10^{-5}	490	0.23	44.95
	1×10^{-6}	490	0.08	51.67

As a result of fast internal conversion from higher initial excited states to the lowest vibrational energy level of an excited state, the emission spectrum is independent of excitation energy (wavelength). The vibrational energy level spacing in the ground and excited states of many common dyes is similar, leading to a fluorescence spectrum that strongly matches the absorption spectrum. This is because the most optimal transitions of absorption and fluorescence are the same. Figure (2) shows the fluorescence spectra of AO laser dye in different solvents (distilled water, DMSO, acetone and ethanol) at various concentrations (1×10^{-4}, 0.5×10^{-4}, 1×10^{-5}, 0.5×10^{-5}, 1×10^{-6}) M. The detailed vibrational structure is usually lost, and the fluorescence spectrum behaves as a broad band.

Figure (2a), which is related to the fluorescence spectra of AO dissolved in distilled water, shows the effects of increasing the fluorescence intensity with increasing concentration until aggregation occurs at (1×10^{-4}) M. The maximum fluorescence

wavelength decreases when the concentration increases from 1×10^{-6} M to 0.5×10^{-4} M (blue shift about 7 nm), then the red shift is obtained (about 6 nm) for 1×10^{-4}M.

Figure (2b), where AO is dissolved in DMSO, shows the effects of decreasing the maximum fluorescence wavelength while increasing the concentration; a blue shift occurs around 4 nm for 1×10^{-5}M, then a red shift is shown for the higher concentration of 10 nm. The fluorescence intensity increases with increased concentration, except for 1×10^{-4} M, where it decreased due to dye aggregation.

For AO dissolved in acetone (Figure (2c)), a red shift can be noted (towards a long wavelength) at around 9 nm as fluorescence intensity increases when the concentration is increased.

The maximum wavelength of fluorescence spectra of AO dissolved in ethanol, as shown in Figure (2d), directly increases with concentration and obtains a 6 nm red shift. Fluorescence intensity increased until 1×10^{-4} M, then decreased as a result of the formation of dye aggregation. Inner filter effects and aggregation can reduce the fluorescence intensity when fluorescent dye concentrations are high. As seen from the fluorescence results of increasing acridine concentration, photons generated at wavelengths corresponding to the intersection between the absorption and emission spectra may be reabsorbed (auto-absorption by solution), as shown in research by Al-Kadhemy and Nasser (2018) (Albani 2007). For all solvents, the FWHM of fluorescence spectra decreased when concentration increased, as shown in Table (2).

Figure (2): Fluorescence spectra of AO in a) distilled water; b) DMSO; c) acetone; d) ethanol in various concentrations

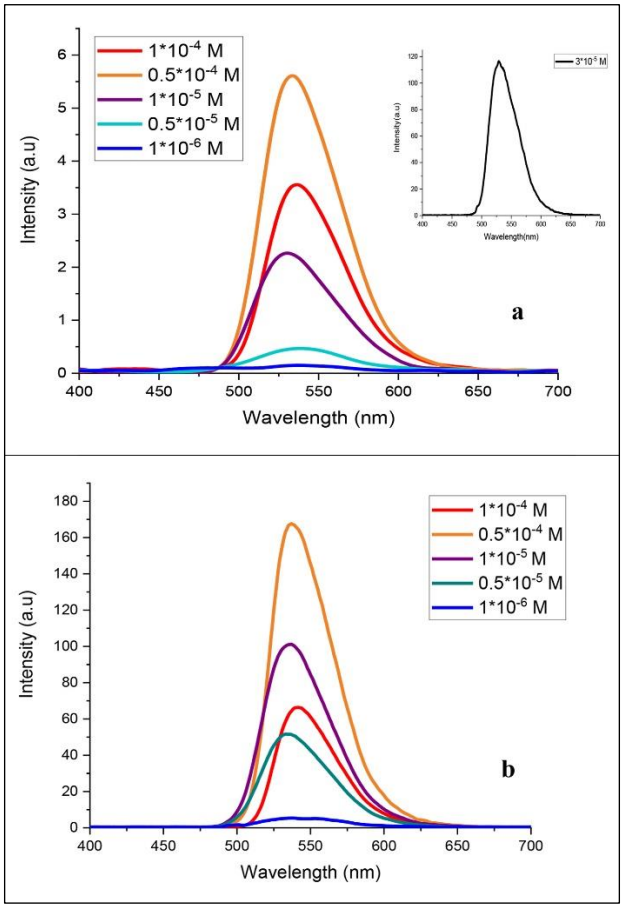

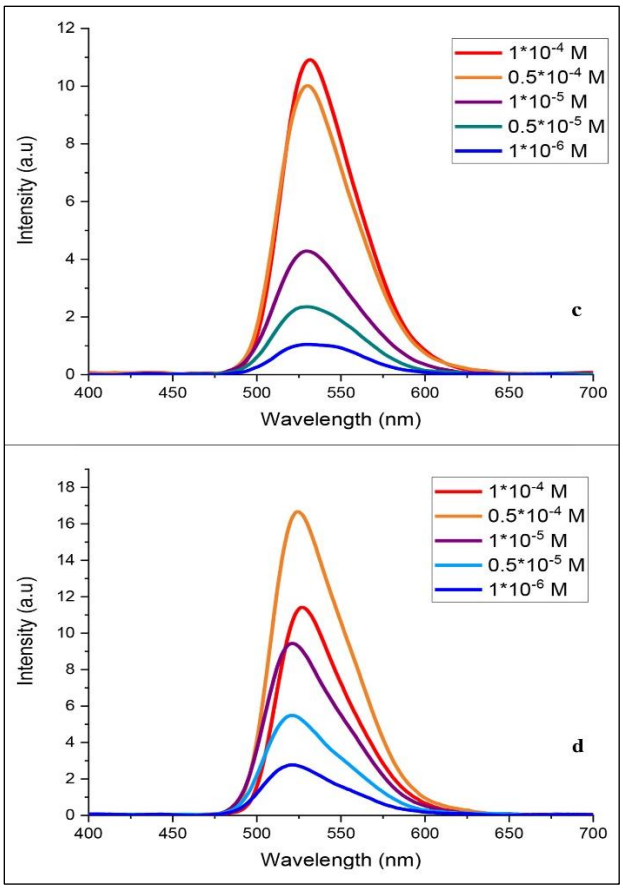

Table (2): Fluorescence parameters for AO in different solvents with different concentrations

Solvents	C (M)	$\lambda_{fluo.max}$ (nm)	$I_{fluo.\ max.}$	FWHM (nm)
Distilled water	1×10^{-4}	536	3.85	55.58
	0.5×10^{-4}	533	5.60	56.74
	1×10^{-5}	530	2.33	60.84
	0.5×10^{-5}	539	0.47	67.98
	1×10^{-6}	537	0.18	86.27
	3×10^{-5}	529	117.19	22.66
DMSO	1×10^{-4}	540	0.40	16.17
	0.5×10^{-4}	536	1.00	20.22
	1×10^{-5}	530	0.59	15.33
	0.5×10^{-5}	535	0.30	24.08
	1×10^{-6}	534	0.32	19.74
Acetone	1×10^{-4}	530	1.01	21
	0.5×10^{-4}	529	0.93	50.39
	1×10^{-5}	527	0.41	18.09
	0.5×10^{-5}	521	0.22	14.18
	1×10^{-6}	521	0.12	5
Ethanol	1×10^{-4}	527	11.4	48.01
	0.5×10^{-4}	524	16.6	52.27
	1×10^{-5}	521	9.4	53.08
	0.5×10^{-5}	520	5.5	53.4
	1×10^{-6}	521	2.7	54.6

The oscillator strength (f) counts how much of the total oscillating potential is used for a specific transition. It was calculated from equation (5), with all of the f results less than 1, so the type of transition is $\pi \longrightarrow \pi^*$, as shown in Table (3).

As the energy required for fluorescence emission transitions (see Figs. (2, 3)) often becomes less than that associated with absorption, the emitted photons tend to have less energy and are shifted to higher wavelengths as a result. Stokes shift is a phenomenon that affects almost all dyes in a solution. The quick decay of excited electrons to the lowest vibrational energy level of the first excited state is the fundamental cause of Stokes shift. Fluorescence emission is also influenced by transitions to higher vibrational energy levels of the ground state, resulting in additional excitation energy loss caused by thermal equilibration of extra vibrational energy.

AO is a cationic dye that is protonated at a pH lower than 10, even in aqueous-only solutions. An important property of acridine is that its spectrum does not agree with Beer–Lambert law (as shown in DMSO

and distilled water) due to molecular aggregation as a result of strong dipole–dipole interaction in aggregate units. It should be noted that the aggregates, particularly dimers compared to monomers, show different photophysical and spectroscopic properties. In general, the photophysical and spectroscopic properties of dye molecules depend upon the aggregation type. There are numerous spectroscopic studies regarding self-association and protonation of acridine in aqueous solutions. This result is in agreement with Falcone *et al.* (2006) and Robinson *et al.* (1972).

To illustrate the overlap between absorption and fluorescence spectra, the best concentration of acridine dissolved in distilled water was (3×10^{-5}) M, as shown in Figure (3a). The maximum absorption wavelength (λ_{abs}) was 490 nm, and the fluorescence wavelength (λ_{fluo}) was 529 nm. Figure (3b) displays the best concentration of AO dissolved in DMSO at (1×10^{-5}) M, which obeys Beer–Lambert law. The maximum absorption wavelength (λ_{abs}) was 490 nm, and the fluorescence wavelength (λ_{fluo}) was 521 nm.

The best concentration of AO dissolved in acetone was (1×10^{-5}) M, which obeys Beer–Lambert law. The maximum absorption wavelength (λ_{abs}) was 495 nm, and the fluorescence wavelength (λ_{fluo}) was 530 nm, as shown in Figure (3c). Figure (3d) displays the best concentration of AO dissolved in ethanol at (1×10^{-5}) M, which obeys Beer–Lambert law. The maximum absorption wavelength (λ_{abs}) was 490 nm, and the fluorescence wavelength (λ_{fluo}) was 521 nm.

Figure (3) demonstrates that Stokes shift increases when the concentrations in all acridine dye solutions are increased (except the acridine water solution), as seen in Table (3). Additionally, the fluorescence spectrum is typically a mirror image of the absorption spectrum resulting from the ground to the first excited state transition. Furthermore, all peaks are symmetric.

The magnitude of Stokes shift is influenced by the dye and its solvation environment. It is measured from equation (9), with greater Stokes shifts appearing in more polar solvents. As seen in Figure (3) and the data in Table (3), Stokes shift is highest in water (more polar) and lowest in ethanol (less polar). Stokes shift is necessary for fluorescence imaging measurements to have such great sensitivity, and because of the red emission shift, precise bandwidth optical filters can effectively stop excitation light from reaching the detector, allowing the relatively faint fluorescence signal (with a small number of released photons) to be detected against a low-noise background.

Figure (3): Absorption and fluorescence spectra of AO in a) distilled water; b) DMSO; c) acetone; d) ethanol at the best concentration

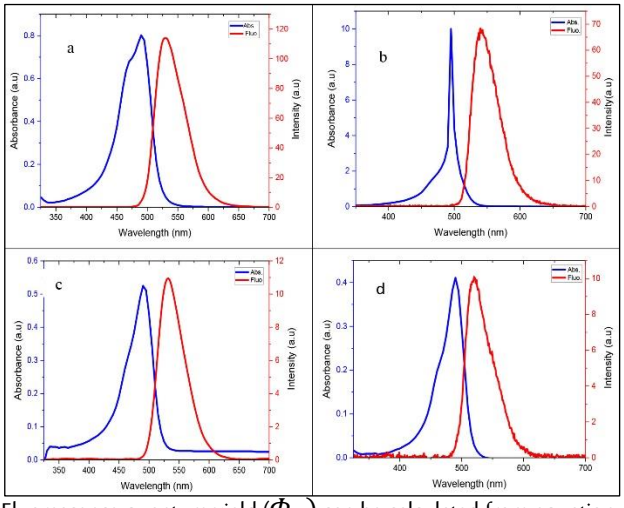

Fluorescence quantum yield (Φ_F) can be calculated from equation (6) for all solvents, as shown in Table (3). The best value is (0.97) in distilled water at a concentration of (0.5×10^{-4}) M. Their values did not exceed 1 and varied with changing concentrations and solvents for the AO dye. For the absorption spectra of all samples, the radiative lifetime (τ_{FM}) is calculated from equation (7). Generally, the maximum value is (55.5) ns for a concentration of (1×10^{-4}) M in DMSO. Their values differ according to concentrations and solvents. From these two parameters and as stated by equation (8), the fluorescence lifetime (τ_F) is planned, as seen in Table (3). The best value is in acetone, especially at the concentration of (0.5×10^{-4}) M, resulting in (13.5) ns.

Table (3): Photophysical parameters for AO in different solvents with different concentrations

Solvents	C (M)	Stokes shift (nm)	f	Φ_F	τ_{FM} (ns)	τ_F (ns)
Distilled water	1×10^{-4}	46	0.37	0.45	3.7	1.6
	0.5×10^{-4}	43	0.24	0.97	6.1	5.9
	1×10^{-5}	40	0.20	0.43	7.4	3.1
	0.5×10^{-5}	49	0.19	0.86	7.7	6.6
	1×10^{-6}	47	0.09	0.42	5.41	2.2
	3×10^{-5}	39	0.25	0.54	5.94	3.2
DMSO	1×10^{-4}	45	0.02	0.03	55.5	1.6
	0.5×10^{-4}	41	0.03	0.28	33.5	9.3
	1×10^{-5}	35	0.11	0.18	9.6	1.7
	0.5×10^{-5}	40	0.05	0.14	19.9	2.7
	1×10^{-6}	44	0.14	0.005	7.7	0.03
Acetone	1×10^{-4}	40	0.08	0.38	17.1	6.4
	0.5×10^{-4}	39	0.09	0.89	15.2	13.5
	1×10^{-5}	37	0.24	0.51	5.9	3.00
	0.5×10^{-5}	31	0.56	0.26	2.5	0.65
	1×10^{-6}	31	0.56	0.35	1.3	0.45
Ethanol	1×10^{-4}	37	0.17	0.08	7.9	0.6
	0.5×10^{-4}	34	0.19	0.23	7.2	1.6
	1×10^{-5}	31	0.30	0.44	4.6	2.02
	0.5×10^{-5}	30	0.34	0.45	4.0	1.8
	1×10^{-6}	31	0.84	0.49	1.6	0.7

The best concentration of AO dissolved in distilled water that obeys Beer–Lambert law is (3×10^{-5}) M mixed with (MgO and Al_2O_3) nanoparticles. To study the effect of these NPs on acridine dye solution, Figure (4) displays the absorption spectra of AO with different amounts of (MgO and Al_2O_3) nanoparticles. The maximum absorption wavelength (λ_{abs}) for AO in an aqueous solution is 490 nm with 0.80 maximum intensity. When MgO NPs are added to AO, the intensity decreases to 0.58, which may be related to MgO's ability to adsorb AO. The intensity of adding Al_2O_3 NPs to AO is 0.94, which raises the spectrum. The intensity of mixed (MgO and Al_2O_3) nanoparticles is 0.65, which also decreases the absorption spectrum. The maximum absorption wavelength (λ_{abs}) is 490 nm in all samples of NPs/AO aqueous dye solution.

Fig. (4): Absorption spectra of AO with (0.004 and 0.002) g of (MgO and Al_2O_3) nanoparticles

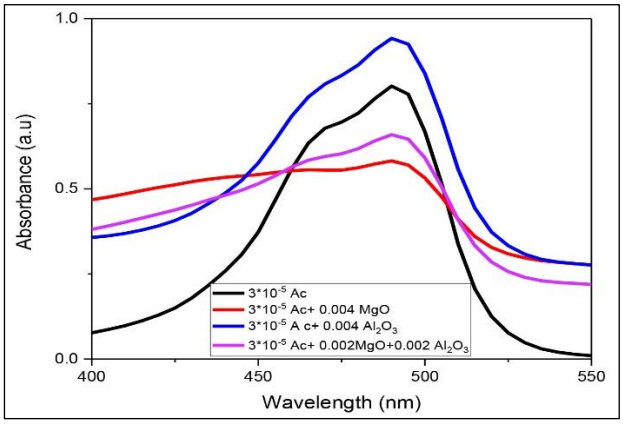

Figure (5) displays the fluorescence spectra of AO with different amounts of (MgO and Al_2O_3) nanoparticles. The maximum wavelength for AO in an aqueous solution is 529 nm with 117.19 maximum intensity. Maximum fluorescence wavelength and intensity both decreased when MgO NPs were added to AO. There was a noticeable increase in maximum fluorescence wavelength and intensity when Al_2O_3 NPs were added. Finally, adding the (MgO and Al_2O_3) mixture to the AO dye solution resulted in an increase in the maximum fluorescence wavelength and decreased intensity, as seen

in Table (4).

Fig. (5): Fluorescence spectra of AO with (0.004 and 0.002) g of (MgO and Al_2O_3) nanoparticles

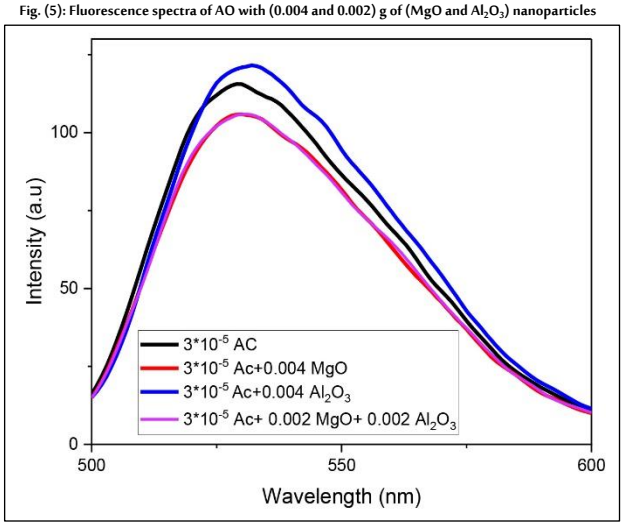

Table (4) shows that adding MgO decreased the absorption and fluorescence spectra intensity as well as the maximum wavelength.

Table (4) also displays an increase in both the maximum wavelength and intensity for absorption and fluorescence spectra. The result demonstrates that MgO NPs quench AO in both absorption and fluorescence spectra, and increase the maximum fluorescence and intensity when adding Al_2O_3 NPs to the solution. It is clear that the absorption spectra increased with the increased particle size of NPs. Al is a metal; therefore, it may generate electrons and transform into a cation. Al_2O_3 NPs may also absorb water, making them useful as a drying agent. Due to its great stability, it is also considered an oxidising agent.

Stokes shift in AO aqueous solution is best at a concentration of 39 (see Table 3). When MgO is added to the AO aqueous solution, Stokes shift decreases to 37. Adding Al_2O_3 enhances the Stokes shift, and it becomes 41 in both the Al_2O_3 AO aqueous solution and a mix of MgO and Al_2O_3 AO aqueous solution. This result leads to a rise in fluorescent molecules in an excited state.

Table (4): Spectral information for (MgO and Al_2O_3) – AO aqueous dye solution

AO in distilled water (3×10^{-5}) M	Amount of MgO NPs (g)	Amount of Al_2O_3 NPs (g)	λabs max (nm)	Labs	λfluo max (nm)	Ifluo	Stokes shift (nm)
	0.004	0	490	0.58	527	105.97	37
	0	0.004	490	0.73	531	123.67	41
	0.002	0.002	490	0.65	531	106.87	41

5. Conclusions

In this work, the effects of solvent and concentration were studied in the absorption and fluorescence spectra of AO. Analysis of four different organic solvents found:

- The intensity and wavelength of the peak of the absorption spectra of acridine dye depend on the type of solvent used.
- There is a red shift of around 5 nm in the maximum wavelength for DMSO, while it remained constant in the other solvents under study.
- The fluorescence spectra of acridine dye solutions shift towards the long wavelength (red shift) with increased concentration.
- The observed results of the fluorescence intensity of AO change significantly due to dye aggregation and strong intermolecular Van der Waals-like attractive forces between the molecules.
- Oscillator strength is less than 1, so the transition is $\pi \rightarrow \pi^*$.
- Stokes shift is highest in water (more polar) and lowest in ethanol (less polar).
- The best value of fluorescence quantum yield in distilled water is around 0.97.
- The fluorescence lifetime was calculated and found that the best value is 13.5 ns in acetone.
- The addition of MgO NPs led to an AO quench in both absorption and fluorescence spectra and an increase in the maximum fluorescence and intensity when Al_2O_3 NPs were added to the solution.

Biographies

Fairooz Faeq Kareem

Department of Physics, College of Science, Mustansiriyah University, Baghdad, Iraq, cenderlla78@yahoo.com, 009647703467140

Mrs Kareem is an Iraqi PhD student in the Department of Physics, College of Science, Mustansiriyah University. She obtained her MSc in Material Physics-Polymers at Mansoura University, Egypt in 2015. She participated in the Sixth International Scientific Conference on Optical Spectrums at the National Research Centre in Cairo in 2015. She participated in a course to develop the capabilities and skills of education staff in Baghdad. She also participated in a workshop to change the physics curriculum textbook at the intermediate stage.

Mahasin F. Hadi Al-Kadhemy

Department of Physics, College of Science, Mustansiriyah University, Baghdad, Iraq, dr.mahasin@uomustansiriyah.edu.iq, 009647705303964

Dr Al- Kadhemy is an Iraqi professor at Mustansiriyah University. She specialises in Material Physics. She has supervised several postgraduate students and published more than 80 articles in global, regional and local journals, some of which are Scopus and Clarivate indexed in the fields of Material Physics, Ceramic Materials, Polymer and Laser dyes, Spectroscopy and Molecular Physics. She has participated in several local and regional seminars, workshops and conferences.

Asrar Abdulmunem Saeed

Department of Physics, College of Science, Mustansiriyah University, Baghdad, Iraq, dr.asrar@uomustansiriyah.edu.iq, 009647901827609

Dr Saeed is an Iraqi assistant professor. She specialises in Material Physics and has supervised several postgraduate master's and doctoral students and published more than 30 articles in global, regional and local journals, some of which are included in Scopus and Clarivate indexes in the fields of Material Physics, Polymer and Laser dyes, Spectroscopy and Molecular Physics. She has participated in several local and regional seminars, workshops and conferences.

ORCID: 0000-00034677-7598

References

Al Hussainey, A.M., Mahmoud, R.K. and Ashrafi, T.M. (2018). Study the optical and spectral properties of the acridine dye as an effective medium in dye lasers. *Journal of University of Babylon for Pure and Applied Sciences*, **26**(10), 167–75.

Albani, J.R. (2007). *Principles and Applications of Fluorescence Spectroscopy*. The UK: Blackwell Publishing Company. DOI: 10.1002/9780470692059.

Al-Kadhemy, M.F. and Nasser, A.A. (2018). Investigation fluorescence energy transfer between two laser dyes: Coumarin 102 and Rhodamine B dissolved in chloroform solvent. *Journal of College of Education*, **1**(3), 141–58.

AL-Kadhemy, M.F., Abbas, K.N. and Abdalmuhadi, W.B. (2020). Physical properties of Rh6G laser dye combined in polyvinyl alcohol films as heat sensor. *IOP Conference Series: Materials Science and Engineering* **928**(7), 072126. DOI: 10.1088/1757-899X/928/7/072126.

Birks, J.B. (1973). Photophysics of Aromatic Molecules. *Wiley Interscience*, **74**(12), 1294–5. DOI: 10.1002/bbpc.19700741223.

Byvaltsev, V.A., Bardonova, L.A. and Onaka, N.R. (2019). Acridine orange: A review of novel applications for surgical cancer imaging and therapy. *Frontiers in Oncology* **9**(925), 1–8. DOI: 10.3389/fonc.2019.00925.

Dihingia, S., Bora, D., Singha, R. and Saikia, P. (2019). Comparative study of oscillator strengths in dye and metal doped silica glasses. *Journal of Physics: Conference Series,* **1330(**1), 1–6. DOI: 10.1088/1742-6596/1330/1/012019.

Falcone, R.D., Correa, N.M. Biasutti, M.A. and Silber, J.J. (2002). Acid-base and aggregation processes of acridine orange base in n-

Heptane/AOT/water reverse micelles. *Langmuir*, **18**(6), 2039–47. DOI: 10.1021/la011411b.

Falcone, R.D., Correa, N.M., Biasutti, M.A. and Silber, J.J. (2006). The use of acridine orange base (AOB) as molecular probe to characterize nonaqueous AOT reverse micelles. *Journal of Colloid and Interface Science*, **296**(1), 356–64. DOI: 10.1016/j.jcis.2005.08.049.

Hotta, K., Yamaguchi, A. and Teramae, N. (2010). Properties of a metal clad waveguide sensor based on a nano porous-metal-oxide/metal multilayer film. *Analytical Chemistry*, **82**(14), 6066–73. DOI: 10.1021/ac100654b.

Kowalewska, M.G., Cholewiński, G. and Dzierzbicka, K. (2017). Recent developments in the synthesis and biological activity of acridine/acridone analogues. *The Royal Society of Chemistry,* **7**(26), 15776–804. DOI: 10.1039/c7ra01026e.

Krolenko, S.A., Adamyan, S.Ya., Belyaeva, T.N. and Mozhenok, T.P. (2006). Acridine orange accumulation in acid organelles of normal and vacuolated frog skeletal muscle fibres. *Cell Biology International*, **30**(11), 933–9. DOI: 10.1016/j.cellbi.2006.06.017.

Kumar, V., Ayushi, J., Shweta, W. and Surinder, K.M. (2018). Synthesis of biosurfactant-coated magnesium oxide nanoparticles for methylene blue removal and selective Pb^{+2} sensing. *IET Nanobiotechnology*, **12**(3), 241–53. DOI: 10.1049/iet-nbt.2017.0118.

Lewkowics, J. (2006). *Principles of Fluorescence Spectroscopy*. 3rd edition. Switzerland: Springer Nature.

Lide, D.R. (2010). *CRC Handbook of Chemistry and Physics*. London: Taylor and Francis Group LLC.

Markarian, S.A. and Gohar, A.S. (2015). The effect of dimethylsulfoxide on absorption and fluorescence spectra of aqueous solutions of acridine orange base. *Spectrochimica Acta - Part A: Molecular and Biomolecular Spectroscopy,* **151**(n/a), 662–6. DOI: 10.1016/j.saa.2015.06.126.

Musarat, A., AlMusayeiba, N.M., Alarfaj,N.A., El-Tohamy,M.F. and Oraby, H.F. (2020). Biogenic green synthesis of MgO nanoparticles using *Saussurea costus* biomasses for a comprehensive detection of their antimicrobial, cytotoxicity against MCF-7 breast cancer and Photocatalysis Potentials. *PLoS ONE,* **15**(8), 1–23. DOI: 10.1371/journal.pone.0237567.

Robinson, B.H., Loffler, A. and Schwarz, G. (1972). Thermodynamic behaviour of acridine orange in solution. *Journal of the Chemical Society*, **69**(1), 56–69.

Saeed, A.A., Kadhum, F.J., Abbas, K.N., Al-Kadhemy, M.F. and Neamah, Z.J. (2020). Effects of anthracene doping ratio and UV irradiation time on photo-fries rearrangement of polycarbonate. *Baghdad Science Journal*, **17**(2), 652–62. DOI: 10.21123/bsj.2020.17.2(SI).0652.

Sharma, V.K., Sahare., P.D., Rastogi, R.C., Ghoshal, S.K. and Mohan, D. (2003). Excited state characteristics of acridine dyes: Acriflavine and acridine orange. *pectrochimica Acta - Part A: Molecular and Biomolecular Spectroscopy*, **59**(8), 1799–804. DOI: 10.1016/S1386-1425(02)00440-7.

Sikiru A.A., Nelson, O.O., Bamgbose, J.T. and Abideen I.A. (2016). Solvent enhancement of electronic intensity in acridine and 9-aminoacridine. *Journal of Saudi Chemical Society* **20**(1), S286–92. DOI: 10.1016/j.jscs.2012.11.002.

Sunandan, P., Swayamprava, D., Prathna, T.C., Shruti, T., Radhika. M., Ashok, M.R., Chandrasekaran, N. and Amitava, M. (2013). Cytotoxicity of aluminium oxide nanoparticles towards fresh water algal isolate at low exposure concentrations. *Aquatic Toxicology* 132–133(n/a), 34–45. DOI: 10.1016/j.aquatox.2013.01.018.

Takashi, K., Fujii, K. and Sakoda, K. (2010). Ultrafast energy transfer in a multichromophoric layered silicate. *Physics and Materials Chemistry*, **114**(2), 983–9. DOI: 10.1021/jp910341f.

Valeur, B. (2012). *Molecular Fluorescence Principles and Application*. 2nd edition. Weinheim: Wiley-VCH Verlag GmbH.

The Scientific Journal of King Faisal University

Basic and Applied Sciences

Treatment of Turbine Blades via Cr_2O_3-Ni5%Al System Using Plasma Thermal Spraying

Esraa H. Mouhson [1], Sufian H. Humeedi [2], Salih Y. Darweesh [3] and Adnan R. Ahmed [4]

[1] Salah-Alddin Education, Ministry of Education, Tikrit, Iraq
[2] Physics Department, College of Science, Tikrit University, Tikrit, Iraq
[3] Physics Department, College of Education TuzKhurmatu, Tikrit University, Tikrit, Iraq
[4] Physics Department, College of Education for Pure Sciences, Tikrit University, Tikrit, Iraq

LINK	RECEIVED	ACCEPTED	PUBLISHED ONLINE	ASSIGNED TO AN ISSUE
https://doi.org/10.37575/b/sci/210036	01/08/2021	30/11/2021	30/11/2021	01/12/2021

NO. OF WORDS	NO. OF PAGES	YEAR	VOLUME	ISSUE
4782	5	2021	22	2

ABSTRACT

A plasma thermal spraying method was used for the purpose of coating the pre-prepared surfaces of turbine blades. Chromium oxide (Cr2O3) was used as a matrix reinforced with a metal material of Ni-5%Al at rates of 10, 20, 30, 40 and 50. The cermet powders were stirred for one hour then used to coat bases of steel (316L). A spray distance of 8cm was applied, and the binding material of Ni-22%Cr-10%Al-1%Y was sprayed with a thickness of 100µm. Then, the reinforced matrix was sprayed with a thickness of 300–350µm and the final thickness of the samples prepared was 400–450µm. The samples produced were sintered at 900°C for an hour and a half and underwent a hardness test, which gave the best hardness of the samples after sintering at a reinforcement rate of 50% by 612Hv. The lowest porosity value for the above rate was obtained at 3.88%. The results of the adhesive strength gave a value of 31.5 MPa after sintering and at the same 50% reinforcement. The results of the scanning electron microscope (SEM) showed that there was weakness and cracking in the coating layers at the low reinforcement ratios. However, the mechanical and physical properties improved with the increase in reinforcement ratios to reach the highest value of 50%.

KEYWORDS

Adhesion force, ceramites, scanning electron microscope, Vickers hardness

CITATION

Mouhson, E. H., Humeedi, S. H., Darweesh, S. Y. and Ahmed, A. R. (2021). Treatment of turbine blades via cr_2o_3-Ni5%al system using plasma thermal spraying. *The Scientific Journal of King Faisal University: Basic and Applied Sciences*, **22**(2), 120–4. DOI: 10.37575/b/sci/210036

1. Introduction

Thermal spraying techniques have occupied an advanced position in coating processes. They allow the use of a wide range of materials, starting from materials with low melting points to those with high melting points. These techniques require high accuracy and control of the parameters and conditions of coating, such as material feeding rate, air thrust and distance between the spray gun and the base in order to obtain coatings with good adhesive strength, as well as high synthetic and mechanical properties (Darweesh *et al.*, 2019). Thermal spraying techniques represent the most important methods used industrially in the surface oxidation of industrial supplies, especially in coating large pieces efficiently with high deposition rates. Some composites can be used for coating mixed with other materials or separately (Berndt *et al.*, 2003; Kucuk *et al.*, 2000). In surface engineering technology, coating is generally applied to create physical and mechanical properties for important classification and technical characteristics, such as acceptable performance service, cost reduction over time, the resistance of the specified surface to wear, reusing the corrosive part of the surface and the treatment of mechanical corrosion, such as pitting and thermal barrier (Sarikaya, 2005). The selection of cermet composite materials consisting of ceramic oxides with high melting temperatures, such as Al_2O_3, TiO_2, or ZrO_2, with additives from metal materials is called cermet. Cermet materials have physical properties that are common in ceramic and metal materials. They have high thermal and mechanical properties in various technological applications. In recent years, researchers have made a great effort to use these composites on a large scale in many electrical and thermal applications, which creates excellent barrier properties in thermal barrier coating, especially in jet engines, marine engines and gas turbines (Gibson, 2016). Composite materials are usually influenced by the properties of the materials involved in its synthesis that include the matrix and reinforcing phase. The matrix is usually represented by the continuous phase in composite material. It works to hold together elements and materials of reinforcement and bind the parts together to form a coherent synthetic system that can produce excellent mechanical properties, including increased toughness and light weight. Therefore, attention is paid to the production of composite materials as a substitute for traditional engineering materials, such as metals, alloys or polymers. Reinforcement materials strengthen the matrix. They may be ceramic, metal or polymeric materials in the form of powders, fibres or flakes (Ahmed *et al.*, 2020). Accordingly, different coating techniques are used. These techniques may include plasma spraying, wire arc spraying and high velocity oxy-fuel spraying. The coating is applied using these techniques to protect external surfaces from erosion and cracking. In this regard, titanium oxide is one of the most important ceramic materials that helps to protect surfaces because of its high protection features in terms of resistance to corrosion and wear (Abdulla *et al.*, 2020). Chromium oxide has a very high hardness level, in addition to its multiple applications in the field of ceramic materials due to its high strength, hardness and friction. Its melting point is also very high, and it works extremely well with many metals, such as iron, nickel and aluminium, as a protective layer against the effects of various loads (Hakan *et al.* 2008). The current research aims to identify a technique to treat the turbine blades used in electrical power plants where the surfaces develop corrosion and cracks due to being exposed to a high degree of evaporation. This study examines the synthetic and mechanical properties of the system used for coating those turbine blades.

2. Experimental Details

2.1. Raw Materials:

The binder was the powder Ni-22%Cr-10%Al-1%Y with a thickness

Corresponding Author: Salih Y. Darweesh 009647703978848, salih.younis@tu.edu.iq

of 100μm manufactured by Amdry 962, with a granular size of +53–106μm). The reinforcement material was Ni5%Al, manufactured by Metco 480NS, with a granular size of +45–90μm. The matrix was chromium oxide (Cr_2O_3) of thickness with reinforcement reaching 300–350μm manufactured by WISDOM with a granular size of +11–45μm.

2.2. Preparation Method:

The cermet composite was prepared by taking Cr_2O_3 as a matrix and nickel-aluminium (Ni5%Al) with different reinforcement ratios (10, 20, 30, 40 and 50%). The powders were then well stirred using an electric mixer for two hours. A first thermal treatment of the cermet composite powders was then performed before the coating process at 100°C for 30 minutes using a German electric furnace containing a thermostat. The coating bases were made of STAL Steel 316L type. Next, they were cut and grinded to the appropriate dimensions required to be placed in the sampling holder and washed with alcohol to remove any lubricants. A sandblast device produced by Amin Tech was used to increase the samples' surface roughness. The grain used for roughing was sand with five bar pressure and diameters ranging from 0.7mm to 1.6mm. After roughing was completed, the bases were prepared for the spraying process. The coating was applied to the bases using the thermal spray process by plasma with the METCO 3MB device of American origin. This technique was used to coat all the samples prepared. The spray gun generated an electric arc producing plasma. The arc moved between the water-cooled copper anode electrode and the cathode electrode made of tungsten, continuously injecting the arc with the initial gas mixture, which usually consists of argon or nitrogen and secondary gas (5–20%) of the initial gas that consists of helium or hydrogen. The gas mixture was ionised and plasma was formed. Secondary gases were used to increase the ionisation energy of the arc gas mixture and raise the plasma thermal content to produce higher temperatures at a lower energy level. Plasma is a conductive gas and sometimes referred to as the 'fourth state of matter'. Despite the high temperatures of plasma that can reach 10000°C or 30000°C, little heat is transmitted to the work piece, so it remains relatively cold. Spray parameters were selected through a series of tests to ensure layers of coating with good adhesive strength and specific thickness to qualify for the study of the physical properties of coating. Thermal treatment of samples resulting from plasma thermal spraying was also applied at 900°C for two hours. The spray parameters are shown in Table 1.

Table 1: The Parameters of Plasma Spraying

Parameter	NiCrAlY	TiO_2+Ni5Al
Gun Type	3MB METCO	**3MB METCO**
Argon flow rate (SCFH)	**80**	80
Hydrogen gas flow rate (SCFH)	**15**	15
Current (A)	**450**	500
Voltage (V)	**50**	55
Argon powder carrier gas	**30**	30
Powder feed rate (Lbs./Hr.)	**10**	25
Spray distance	**12**	8

3. Examinations and Tests

3.1. Hardness Test:

Vickers hardness was measured for the coated samples after grinding and polishing before and after the thermal treatments. The indentation used was a pyramidal diamond indenter with an angle of 136° between the opposite sides that applied a load of 100gm for 10 seconds. It was automatically lifted after the illumination of the light indicator at the end of the specified time. The dimensions of the impression in the two axes and in two perpendicular directions were calculated by considering five readings and calculating their arithmetic mean to find the value of hardness from the digital screen installed on the device directly. The following formula represents Vickers hardness (Shahdad *et al.*, 2007):

$$Hv = 1.854 \frac{P}{{d_{av}}^2} \quad \text{..... (1)}$$

where (H_V): Vickers hardness, (P): the load applied (gm) and d_{av}: the mean of the indenter diameter. The hardness was measured in several different areas of the sample, and the hardness of the edges and centre were calculated to obtain an approximate value of the hardness rate.

3.2. Porosity Test:

The presence of pores in thermal spray coating is one of the most important features of the coating. These pores affect the properties of the coating; therefore, it is necessary to know their ratio in the coating. The porosity test was performed by using samples of the coating layer after removing it from the matrix when performing the test. Archimedes' principle (immersion method) was adopted in the calculation of porosity ratio in accordance with standard specification no. ASTM-C 830 (Mohammed *et al.*, 2018), which includes the following steps:

- Drying samples of the composite material for 30 minutes using an electric furnace (Heraeus) at 75°C, then weighing the samples using a sensitive balance (±0.001mgm). This weight is called W_1.
- Immersing the samples in a container filled with distilled water for 24 hours, then weighing the samples saturated with water, heating them to 100°C, leaving them to cool then weighing them again. This weight is called W_2.
- Weighing the samples immersed and suspended in distilled water. This weight is called W_3.
- Calculating the ratio of open pores (P_o %) using the following equation (Mohammed *et al.*, 2018):

$$P_o\,\% = [(W_2 - W_1) / (W_2 - W_3)] \times 100 \quad \text{.....(2)}$$

3.3. Adhesion Test:

An adhesion test of the coating layer was performed using a tensile device with a maximum load of 1.5 Ton, in accordance with the standard technical specification (ASTM - (C 633)) [10]. The following steps were followed when performing the test:

- Preparing the samples of the matrix without coating in a number equal to the unsprayed samples with the same standard dimensions.
- Performing chemical cleaning using alcohol for both unsprayed and sprayed samples in order to remove the effects of pollutants that obstruct the process of adhesing the two pieces together.
- Using the adhesive (epoxy) to fix the two samples together (unsprayed and sprayed), putting a regular thin layer of adhesive on the coating surface to cover the area, then pressing the two pieces together for approximately two hours. After that, putting them in a drying furnace for 24 hours at 50°C. Prior to the tensile experiment, regular adhesion is necessary, and the tensile force applied when performing the test should be completely vertical on the coating surface.
- Applying tensile load to each test sample at a tensile rate (1mm/min) until the sample failed as the highest load applied is recorded.
- Calculating the adhesion or cohesion strength of the coating on the composite material using the following equation (Swain *et al.*, 2020):

$$\text{Adhesion Force} = \frac{F}{A} \quad \text{.....(3)}$$

3.4. Scanning Electron Microscope Test:

The scanning electron microscope consists of an electron generator that produces the electrons required to run the microscope, two convex lenses and an object lens as in an optical microscope are used to obtain a clear and detailed map (the only difference is that these lenses are not glass but made from a magnetic material capable of changing the path of electrons and controlling them). All this is carried out in a vacuum chamber to avoid the effect of air particles on the electrons. There is also a sample chamber, where the sample is placed to be examined so it is isolated from vibrations,

because the microscope is very sensitive to motion. For this reason, it is usually placed on the ground floor of the laboratory. It has a sensor that reveals how electrons and samples interact and another sensor that records the movement of secondary electrons emitted from the sample surface. There are also X-ray sensors that allow researchers to obtain information about the composition of samples of elements called EDS, giving the microscope a 3D image of the sample with the smallest details. Handling this device is relatively easy, and the data and surface topography can be collected in no more than five minutes (Reimer, 2013).

4. Results and Discussion

4.1. The Effect of Reinforcement Ratio on the Micro Hardness:

Figure 1 shows the effect of the metal reinforcement ratio on the micro-hardness of the metal-based system before and after the thermal sintering process. It can be observed that at the low reinforcement ratios, hardness was low due to high porosity at these ratios. In the case of high reinforcement ratios, hardness will be high where porosity is as low as possible. Prior to the thermal treatment, the hardness of the steel base (316L) was calculated and found to be 233Hv. When applying plasma thermal spraying, the values of hardness were calculated and found to increase with the rise in oxide reinforcement ratios, reaching the highest value of 498Hv at the ratio of 50% NiAl. When performing the thermal treatment at 900°C for two hours, the values of hardness increased, reaching the highest value of 612Hv at the same ratio as above. It improved the hardness due to the low ratio of pores and the effect of nickel that has high hardness, thus improving the properties of the coating layer as a result of the sintering process and spreading that increased the strength of mechanical binding between the cermet coating layer and the base metal. In addition, the binder layer had a significant effect on the improvement of the mechanical properties of the system (Kumar *et al.*, 2020; Riyadi *et al.*, 2020). The relationship between porosity and hardness is a clear inverse relationship, as increasing the percentage of porosity will negatively affect the prepared models and the hardness value will decrease. This depends largely on the homogeneity and binding strength of the surface because the increase in porosity on the surface acts in the form of gaps, which in turn are considered superficial defects that reduce the binding between the ceramitic components.

Figure 1: The Effect of the Reinforcement Ratio on Micro-Hardness Before and After Sintering

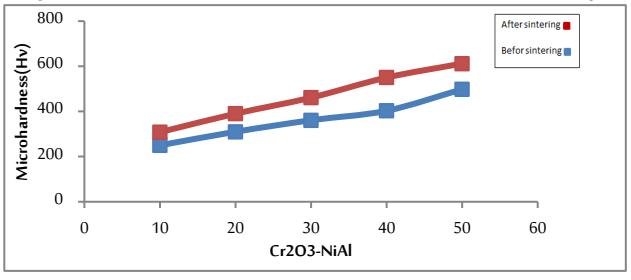

4.2. The Effect of Reinforcement Ratio on Porosity:

Porosity is one of the distinctive features determining the strength and weakness of the cermet layer through the ratios of open pores within the coating. It was tested in this study and the results are shown in Figure 2, which represents porosity before and after the thermal treatment (sintering). It was found that the use of low reinforcement ratios produces high porous values for the coating layer that gradually decrease with the increase of the metal part (NiAl) until it reaches 50% NiAl, the ratio that gave the lowest porous ratio, which is 5.2% before thermal treatment. The reason for high porosity may be the inability of molten droplets to fully flatten and connect with other droplets due to the high cooling rate experienced by the droplets during their spread that results from heat withdrawal to the base. Therefore, the droplets will suffer from thermal contraction after solidification (Ahmed *et al.*, 2020; Darweesh, 2014). When performing the thermal treatment of the cermet coating layers, it was observed that the porous ratio was lower than before the thermal treatment, reaching the lowest ratio at 50% NiAl, which is 3.88%. This means that sintering leads to the adequate rate of atoms spread to form new binding areas between layers through the movement of atoms between them in an attempt to close pores (Dahham *et al.*, 2020).

Figure 2: Changes in Porosity Ratios with Reinforcement Before and After Sintering

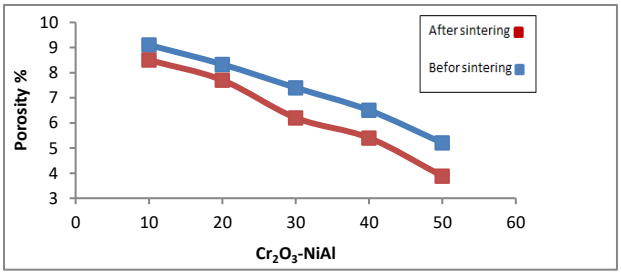

4.3. The Reinforcement Ratio Raises the Adhesion Strength:

Adhesion strength refers to the binding strength between the base surface and the cermet coating layer. The results of testing these samples show a value of 24 MPa adhesion strength before the thermal treatment and 31.5 MPa after the thermal treatment of the samples for two hours at 900°C. Figure 3 shows that adhesion strength is low when the ratio of the binder is low and this strength gradually increases as the ratio of the binder increases, until reaching the highest value of adhesion strength at the ratio 50% NiAl. This decrease is caused by the binder creating areas of correlation between the atoms of the coating material and itself at the expense of the adhesion strength between the coating layer and the base. When applying the thermal treatment of samples at 900°C for two hours, the value of the adhesion strength increased because the temperature reduced the porosity of the coating layer, increasing both hardness and adhesive strength accordingly (Sabard *et al.*, 2020; Abd Razzaq, 2019).

Figure 3: The Relationship of the Adhesion Strength with the Ratio of the Additive Before and After Sintering

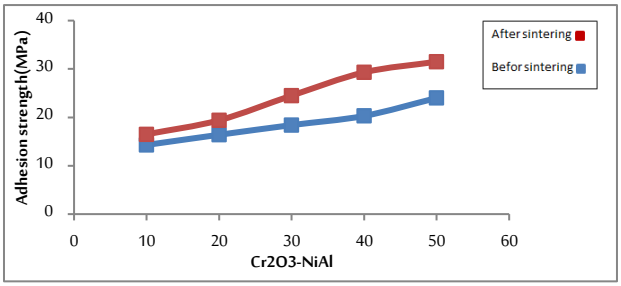

4.4. Compositional Properties with Changing Ratios of Reinforcement by SEM:

Changes in adding the metal powder (Ni-5Al%) as a reinforcement material to (Cr_2O_3) were studied by using an SEM. Images were taken at different depths (μm) to identify the most important characteristics and features of the surface after the thermal sintering of samples prepared by plasma thermal spraying. Figure 4.a shows an SEM image of Cr_2O_3, which shows that the powder used is a homogeneous spherical shape and has no significant impurities. Figure 4.b shows an SEM image of the powder of the binder (Ni5%Al), which is a mixture of nickel (95%) and aluminium (5%).

In this regard, both nickel and aluminium are highly homogeneous and there is a distribution and spread between them. This shows that the powder used is spherical, indicating the purity and homogeneity of the two powders. Therefore, the homogeneity with the reinforcement material is greater when performing the process of thermal spraying by plasma, because the impurities work on placing interfaces, which also increases porosity ratios within the surface and weakens the samples. The results on the surface of the samples are very clear, as the sintering process has a significant effect on the recrystallization and fusion of the atoms that make up each surface, which helps to improve the mechanical properties of the samples.

Figure 4: SEM Image (a) Cr_2O_3, (b) Ni5%Al

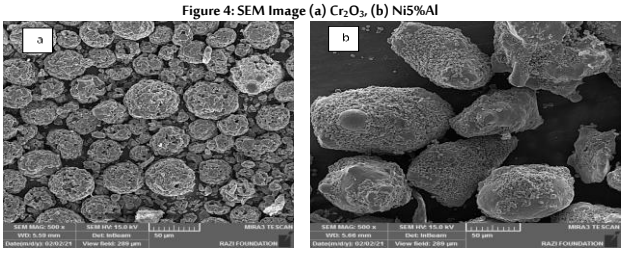

Figure 5 presents an SEM image of sprayed samples after sintering at 900 °C for two hours. Figure 5.a represents an image of coating by reinforcement of 10% NiAl. The bonding material is completely distributed within the matrix, but this layer suffers from weakness in the coating as the surface shows heterogeneity due to the low ratio of bonding material (Ni-Al). The bonding material increases the binding of oxide to the surface at a high temperature, which means that the bonding material is sufficient to form molten areas on the base and then generate areas of chemical interactions that increase the strength of adhesion (Darweesh *et al.*, 2019). Figure 5.b shows an image of coating at the reinforcement ratio of 20% NiAl. There appear to be cracks on the coating surface due to the low ratio of bonding material, which leads to the lack of homogeneity. However, Figure 5.c shows the coating layer reinforced by 30%NiAl. The increase in reinforcement ratios leads to an improvement in the coating layer and approximate disappearance of cracks. Figure 5-d shows a reinforcement by 40% NiAl, and there is a homogeneous distribution of composites to the surface of chromium oxide. In addition, the SEM image demonstrates a great homogeneity of the surface. This change in surface improvement is caused by the formation of correlation areas between the cermet coating layers following the processes of sintering and the spread of atoms as they attempt to close pores when performing thermal treatment, due to the increase in bonding material (NiAl). Figure 5.e presents the SEM image of reinforcement material (50% NiAl). It shows a clearly defined distribution of both the matrix (TiO_2) and reinforcement material (Ni-5% Al), demonstrating the semi-complete disappearance of cracks and pores within the cermet surface (50% Cr_2O_3-50%NiAl). This means that the surface becomes homogeneous and consistent with the bonding material (dark areas). Additionally, there is a spread and alloying correlation between the components of the stirred cermet composites. This means that the adhesion strength is low when the ratio of the bonding material is low, and this strength increases gradually as the ratio of the bonding material increases until reaching the highest value of adhesion strength at the ratio of 50% of the bonding material (Darweesh *et al.*, 2019). When observing Figure 5, we can see that there are significant differences between each concentration, which indicates that the addition of the metal part has changed the structure of the prepared models and improved both physical and mechanical properties.

Figure 5: SEM and EDS Image of the Cermet Composite (Cr2O3-%Ni-5%Al) Where: (a) 10% NiAl, (b) 20% NiAl, (c) 30% NiAl, (d) 40% NiAl, (e) 50% NiAl

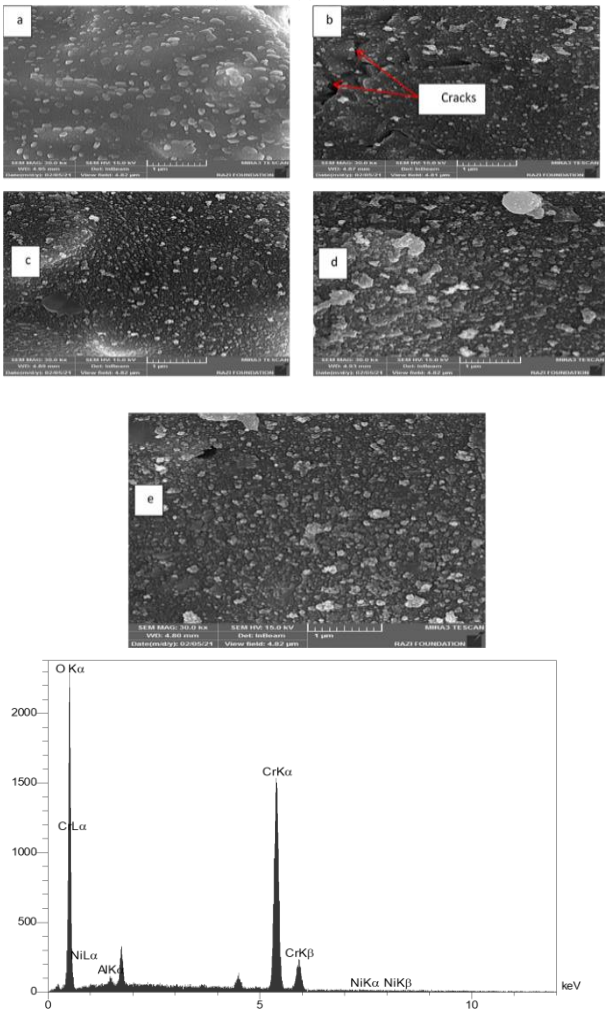

5. Conclusions

The current research shows that the plasma thermal spraying technique produces a cermet composite layer of Cr_2O_3 based matrix reinforced by particles of nickel-aluminium powder (Ni5%Al) as a binder with good adhesion on the alloy base of St.St. 316L. After the coating process and sintering at 900°C for two hours, increasing the ratio of the reinforced binder (Ni5%Al) in the composite material layer to 50% reduces porosity and increases hardness. Therefore, the coating layer has excellent properties. Adhesion strength between the base surface and the composite material layer also improves with an increase in the ratio of reinforcement material to 50%. The SEM results also reveal a clear homogeneity and cohesion between the cermet composites as evidence of the binding strength of materials used, including Cr_2O_3 and the binder of nickel-aluminium. The strength of homogeneity and the absence of defects, especially at 50% of Ni-5%Al is evidence of improved compositional structure of the prepared samples.

Biographies

Esraa H. Mouhson

Salah-Alddin Education, Ministry of Education, Tikrit, Iraq, maldoury93@gmail.com, 009647705669067

Mrs. Mouhson is an Iraqi teacher. She obtained a master's degree in Physics in 2018 from the Physics Department, College of Education for Pure Sciences, Tikrit University, Iraq. Her main field of interest is Physics of Materials. She has completed many research and scientific activities through participating in Tikrit University conferences and publishing research with the same specialty. She participated in the 2018 Crete University Conference, as well as many Physics Department's activities, such as courses and seminars.

Sufian H. Humeedi

Physics Department, College of Science, Tikrit University, Tikrit, Iraq, sufianhh@yahoo.com, 009647702797851

Mr. Hamidi has been an Iraqi teacher since 2011. He obtained a master's degree in 2004 from the Physics Department, College of Education for Pure Sciences, Tikrit University, Iraq and attended several local and international seminars in the field of physics. He has had a number of research studies published locally and globally. He has also had many articles dealing with physics in general and physics of materials in particular published in various journals.

Salih Y. Darweesh

Physics Department, College of Education Tuzkormato, Tikrit University, Tikrit, Iraq, salih.younis@tu.edu.iq, 009647703978848

Dr Darweesh is Iraqi. He obtained a doctorate in physics from the Physics Department, College of Education for Pure Sciences, Tikrit University, Iraq in 2018. Also, the researcher has published many papers within scopes containers as well as at the local level, has participated in many conferences in Iraq and other countries and is currently the head of the physics department at the College of Education, Tuzkormato, Tikrit University, Iraq. The researcher has had many articles published in the field of material physics and in magazines within Scopes, as well as supervising postgraduate students.

Adnan R. Ahmed

Physics Department, College of Education for pure Sciences, Tikrit University, Tikrit, Iraq, amazon9797@yahoo.com, 009647701217821

Dr Ahmed, PhD (Tikrit University), is an Iraqi. He has participated in several international and local conferences. He is currently supervising several postgraduate students working on physics related subjects at the University of Tikrit, in addition to those who were awarded their degrees.

References

Abd Razzaq, A. (2019). The effect of laser and thermal treatment on the hardness and adhesion force on the cermet coating by thermal spray technique. *Iraqi Journal of Physics (IJP)*, **17**(42), 85–95. DOI: 10.30723/ijp.v17i42.416

Abdulla, A. N., Jassim, I. K. and Darweesh, S. Y. (2020). The effects of nano titanium oxide addition on the structural and mechanical properties of an Ni-Al_2O_3 system using the powder method. *Scientific Journal of King Faisal University: Basic and Applied Sciences*, **21**(2), 207–11. DOI: 10.37575/b/sci/2377.

Ahmed, H. H., Ahmed, A. R., Darweesh, S. Y., Khodair, Z. T. and Al-Jubbori, M. A. (2020). Processing of turbine blades using cermet composite materials. *Journal of Failure Analysis and Prevention*, **20**(6), 2111–8. DOI: 10.1007/s11668-020-01027-0

Berndt, M. L. and Berndt, C. C. (2003). Thermal spray coatings. *Corrosion: Fundamentals, Testing, and Protection*, **13**(n/a), 803–13.

Dahham, A. T., Humeedi, S. H., Darweesh, S. Y. and Khodair, Z. T. (2020). The effect of adding nickel content to turbine blades coating using thermal flame spraying. *Scientific Journal of King Faisal University, Basic and Applied Sciences*, **21**(2), 29–34. DOI: 10.37575/b/sci/2413

Darweesh, S. Y. (2014). *Study of Physical Properties of Cermet Coating Layers (Al_2O_3+ ZrO_2+ Ni-Al) Prepared by Flame Thermal Spray Technology*. Master's Dissertation, University of Tikrit, Tikrit, Iraq.

Darweesh, S. Y., Ali, A. M., Khodair, Z. T. and Majeed, Z. N. (2019). The effect of some physical and mechanical properties of cermet coating on petroleum pipes prepared by thermal spray method. *Journal of Failure Analysis and Prevention*, **19**(6), 1726–38. DOI: 10.1007/s11668-019-00772-1

Darweesh, S. Y., Jassim, I. K., and Mahmood, A. S. (2019). Characterization of cermet composite coating Al2O3-Ni system. *Journal of Physics: Conference Series*, **1294**(2), 022011.

Gibson, R. F. (2016). *Principles of Composite Material Mechanics*. Boca Raton: Florida CRC press.

Hakan, C., Celik, E. and Kusoglu, M.I. (2008). Tribological behaviour of Cr_2O_3 coatings as bearing materials. *Journal of Materials Processing Technology*, **196**(1–3), 259–65.

Kucuk, A., Lima, R. S. and Berndt, C. C. (2000). Composite coatings of Si_3 N 4-soda lime silica produced by the thermal spray process. *Journal of Materials Engineering and Performance*, **9**(6), 603–8. DOI: 10.1361/105994900770345449

Kumar, D., Shree, G. and Dwivedi, V. K. (2020). Wear and hardness evaluation of electrodeposited Ni-SiC nanocomposite coated copper. *International Journal of Microstructure and Materials Properties*, **15**(2), 87–106. DOI: 10.1504/IJMMP.2020.106921

Mohammed, S. F. and Darweesh, S. Y. (2018). Effect of thermal treatment on some physical and mechanical properties of cermet coating by flame spraying technology. *Journal of University of Babylon for Pure and Applied Sciences*, **26**(7), 269–80.

Reimer, L. (2013). *Transmission Electron Microscopy: Physics of Image Formation and Microanalysis* (Vol. 36). USA: Springer.

Riyadi, T. W. B. (2020). Structure and properties of Ni**–** Al**–** Ti systems formed by combustion synthesis. *Materials Science Forum*, **991**(n/a), 44–50. DOI: 10.4028/www.scientific.net/MSF.991.44

Sabard, A., McNutt, P., Begg, H. and Hussain, T. (2020). Cold spray deposition of solution heat treated, artificially aged and naturally aged Al 7075 powder. *Surface and Coatings Technology*, **385**(n/a), 125367. DOI: 10.1016/j.surfcoat.2020.125367.

Sarikaya, O. (2005). Effect of some parameters on microstructure and hardness of alumina coatings prepared by the air plasma spraying process. *Surface and Coatings Technology*, **190**(2–3), 388–93. DOI: 10.1016/j.surfcoat.2004.02.007.

Shahdad, S. A., McCabe, J. F., Bull, S., Rusby, S. and Wassell, R. W. (2007). Hardness measured with traditional Vickers and Martens hardness methods. *Dental Materials*, **23**(9), 1079–85. DOI: 10.1016/j.dental.2006.10.001.

Swain, B., Mallick, P., Bhuyan, S. K., Mohapatra, S. S., Mishra, S. C. and Behera, A. (2020). Mechanical properties of NiTi plasma spray coating. *Journal of Thermal Spray Technology*, **29**(5), 741–55, DOI: 10.1007/s11666-020-01017-6.

The Scientific Journal of King Faisal University

Basic and Applied Sciences

The Effect of Sweet Lupine Seed Hulls on the Probiotic Viability of Strained Yogurt

Fahad Al-Asmari

Department of Food and Nutrition Sciences, College of Agricultural and Food Sciences, King Faisal University, Al Ahsa, Saudi Arabia

LINK	RECEIVED	ACCEPTED	PUBLISHED ONLINE	ASSIGNED TO AN ISSUE
https://doi.org/10.37575/b/agr/210061	08/09/2021	30/11/2021	30/11/2021	01/12/2021

NO. OF WORDS	NO. OF PAGES	YEAR	VOLUME	ISSUE
4639	5	2021	22	2

ABSTRACT

Recent advances in gut microbial flora research have shown the health benefits of probiotic bacterial strains on the small and large intestines. These strains, particularly Bifidobacterium, offer health advantages, including obesity, atopic diseases, inflammatory bowel diseases, and intestinal cancers in the human body. However, food components, additives, and processing-related factors can have an impact on probiotic survival. As a result, adding appropriate supplements to increase the viability of probiotics may be necessary for some food products. This study investigated the influence of sweet lupine (*Lupineus albus* L.) seed hulls (SLSH) on the probiotic viability of strained yogurt. Traditional strained yogurt prepared using Bifidobacterium bifidum and the two starter culture strains Streptococcus thermophiles, and Lactobacillus bulgaricus. The strained yogurt was supplemented with different concentrations of SLSH (1, 2, and 3%). Over 7 to 14 days of cold storage, the total bacterial cells were enumerated. The result showed B. bifidum strains increasing more than double with a slight decrease in the starter culture strains. The overall acceptance of strained yogurt supplemented with 1% SLSH was convenient, compared to 2% and 3% of SLSH.

KEYWORDS

Probiotics, viability, lupine, B. bifidum, strained yogurt

CITATION

Al-Asmari, F. (2021). The effect of sweet lupine seed hulls on the probiotic viability of strained yogurt. *The Scientific Journal of King Faisal University: Basic and Applied Sciences*, **22**(2), 125–9. DOI: 10.37575/b/agr/210061

1. Introduction

Over the last few decades, the consumption of probiotics has increased due to their therapeutic and beneficial health impacts on the host when consumed adequately. The effect of probiotics, including intestinal microflora improvement, minimizing cholesterol level in the blood, increasing immune response, and strengthening the body's natural defense mechanisms, has been reported (Chen *et al.*, 2019; Fernandez and Marette, 2017; Jackson and Jewell, 2019; Lau and Chye, 2018; Mani-López *et al.*, 2014). The bacterial strains belonging to Bifidobacteria and Lactobacilli, the most important probiotic microorganisms allied with the human digestive tract, have been introduced in current food products such as yogurt, ice cream, and cheese (Bayar *et al.*, 2018; Moineau-Jean *et al.*, 2019; Mollakhalili *et al.*, 2017).

The most commonly used probiotics are *Lactobacillus acidophilus* NCFB 1748, *Lactobacillus casei* Shirota, *Lactobacillus johnsonii* LA1, and *Bifidobacterium bifidum*. These organisms have shown significant health effects when consumed (Founden *et al.*, 2000). There is a minimum amount of live bacterial cells consumed to observe the beneficial effect of probiotics. The suggested number of daily intake is between 108 and 109 CFU/g (Knorr, 1998). Likewise, regular yogurt contains about 108 to 1011 CFU/g of bacterial cells (Vanderhoof and Young, 1998).

The quantity of bacterial cells in commercial products is often not as much concern as the probiotic instability during the storage period (Sodini *et al*, 2002). Several studies have examined improving the viability of probiotics, but rarely are studies carried out to explore the effect of sweet lupine seed hulls on probiotic viability. A study conducted by Martinez-Villaluenga *et al.* (2006) found that a significant growth level of *Bifidobacterium* spp. was observed when a lupine kernel fiber diet was ingested and compared with the control. Another study carried out by Smith *et al.* (2006) showed that the Raffinose family of oligosaccharides extracted from lupine seeds acted as prebiotics in fermented milk probiotics.

Sweet lupine (*Lupineus albus* L.), known as white lupine, is an annual legume cultivated across the continents, particularly in the Mediterranean basin and South America. It is rich source of protein (34% - 44%), non-starch polysaccharides (30–40%), crude fiber (15% - 18%) and oil (5–15%). Also, it has been used in folk medicine to treat skin and diabetes diseases (Santiago Quiles *et al.*, 2010). Additionally, when compared to many other legumes, lupine has a lower level of antinutritional factors such as lectins and protease inhibitors that reduce protein digestibility (Carvajal-Larenas *et al.*, 2016). The current food applications are utilizing lupine flour and proteins in bakery, and lupine hulls in meat products as a fat replacer and a dietary fiber source (Gulewicz *et al.*, 2008; Visvanathan *et al.*, 2020).

Several studies have identified various phytochemicals in the lupine hulls; antioxidant isoflavone genistein, apigenin derivatives with antioxidant properties (Ranilla *et al.*, 2009), vitamin E isomers α-, β-, γ- and δ-tocopherol (Torres, Frias, and Vidal-Valverde, 2005), anti-tumor phytosterols (Bhardwaj *et al.*, 2004), anti-inflammatory phytosterol β-sitosterol (Loizou *et al.*, 2010) in the lupine hulls. Therefore, the study aimed to evaluate the effect of sweet lupine seed hulls (SLSH) on probiotic viability in strained yogurt products.

2. Materials and Methods

2.1. Preparation of Sweet Lupine Seed Hulls (SLSH):

The collection of the sweet lupine seeds was from local shops in Cairo, Egypt. The seeds were washed and soaked at 5°C for about 5 hours, then blanched at 90°C for one hour in boiling water and, cooled using tap water. The seeds then peeled, and the hulls dried at 43°C for 30 hours. The hulls were ground into a fine powder using a kitchen grinder.

2.2. Bacterial Strains:

Commercial freeze-dried yogurt starter cultures strains of *Streptococcus thermophilus* TH-4, *Lactobacillus bulgaricus* YCX31 (freeze-dried DVS-type), and a single probiotic strain, *Bifidobacterium bifidum* UABb-10, were obtained from Chr. Hansen, Denmark.

Corresponding Author: Fahad Al-Asmari 00966533551663, falasmari@kfu.edu.sa

2.3. Preparation of Lupine Hulls Strained Yogurt:

Strained yogurt was prepared using a traditional method of eliminating excess whey from low-free milk yogurt described by Yamani and Abu-Jaber (1994). Three samples of fresh milk—each containing 2 L—were supplemented with different concentrations of SLSH as (1%, 2%, and 3%) represented as (T_1, T_2, and T_3), respectively. All mixtures were heated to 90°C for 10 min and homogenized to mix all ingredients thoroughly. The heated mixtures were cooled to 42°C, while 3% of starter culture and 1% of *B. bifidum* were inoculated. Upon attaining pH 4.6, the mixture was cooled to 7°C to stop the fermentation process. The formed yogurt was placed in cloth bags and left to drain by gravity at 5 – 10°C overnight and then stored in the refrigerator. Physicochemical, microbiological, and organoleptic properties were analyzed and assessed after storage days one, seven, and 14 (Fig. 1).

Fig.1: Steps of producing traditional strained yogurt supplemented with SLSH.

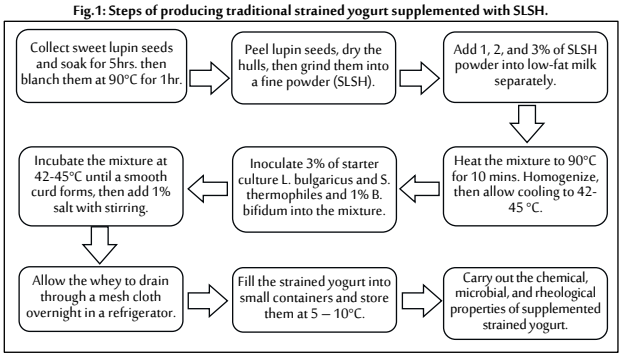

2.4. Physicochemical Analysis:

Physicochemical analyses of SLSH including pH, and acidity, were carried out according to official analysis methods (AOAC, 2010). Acetic and lactic acid content was measured by HPLC according to Akalin *et al.* (2002). For extraction of acids, 4 g of strained yogurt sample was diluted to 25 mL with 0.1N H_2SO_4, homogenized, and centrifuged at 5000x for 10 min. The aliquots 2 mL of supernatant were filtered through Whatman 0.20 µm and analyzed through HPLC as described by Bevilacqua and Califano (1989).

2.5. Organoleptic Assessment:

Appearances, consistency, flavor, and overall acceptance parameters of strained yogurt, supplemented with different concentrations of SLSH, were evaluated by ten panelists.

2.6. Enumeration of Microbial Cells:

For the enumeration, appropriate dilution of each sample was plated, in triplicates, using Petri dishes. Strains *L. bulgaricus* and *S. thermophilus* were enumerated on MRS and the *S. thermophilus* agars, respectively. The *B. bifidum* was enumerated, using a double-layered technique, on Lithium chloride-sodium propionate agar as described by Lapierre, Undeland, and Cox, (1992). Incubation of the plates was at 37°C for 48 hours.

5.7. Statistical Analysis:

All data are presented as mean ±SD for three replicates for each sample. The comparisons were performed using the one-way analysis of variance of the SPSS software. The differences among the means at $P< 0.05$ were compared, using Duncan's multiple analysis methods.

3. Results and Discussion

3.1. Physicochemical Analysis:

The physicochemical characteristic of strained yogurt supplemented with different concentrations of SLSH, were illustrated in Table 1. There were no significant differences in pH values between the control and the supplemented samples (T_1, T_2, and T_3) over the same storage conditions. During the first seven days of storage the strained yogurt stored at 5°C to 10°C, showed the pH value dropped from 4.63 to 3.33 in (T_1), from 4.68 to 3.41 in (T_2), and from 4.84 to 3.48 in (T_3), compared to the control that dropped from 4.58 to 3.41. In contrast, as pH values were dropped during the first 7 days, a slight increase was noted on the 14th day of storage. This result agrees with the previous study conducted by Jakubowska and Karamucki (2020) on natural yogurt. He observed a slight increase in the pH value after 21 days of storage from 4.13 to 4.16. The result obtained by Eissa *et al.* (2010) differed from the above result, showing a steady decrease in the pH value with prolonged storage time of natural yogurt. This figure may attribute to the high water-binding capacity of lupine insoluble fiber (Turnbull *et al.*, 2005), which can dilute the produced acidity.

An assessment was made of the acidity levels of the strained yogurt supplemented with different concentrations of SLSH. In the (T_1) sample, the acidity increased from 1.35 to 2.13, from 1.31 to 2.06 in T_2, and from 1.30 to 1.89 in (T_3.) The acidity of the control sample increased from 1.28 to 1.62 under the same conditions. The result showed no significant differences between the control sample and the supplemented samples. The increase of acidity observed after 14 days of storage could be due to the phase change of calcium phosphate from the soluble phase to the colloidal one, which resulted from the liberation of hydrogen ions (Hattem *et al.*, 2011). This result is consistent with the report published by Alqahtani *et al.* (2021), who produced strained yogurt with sweet lupine husk with no significant differences in pH values and acidity between the control and the supplemented samples. In general, the acidity of yogurt is affected by the activity of its microflora, which is diverse in its activities of acidifying, proteolytic and lipolytic processes (Jakubowska and Karamucki, 2020)

Also, the lactic acid amount produced in strained yogurt was increased from 4.49 mg/kg in control to 5.96 mg/kg in T_2 during 14 days of storage. Although the capacity of the hull's fiber in diluting the form acidity, the amount of lactic acid formed in T_2 was significant. Although lactic acid production in a fermented dairy product is an essential indication for starter culture viability, in this case, most of the lactose that provides a carbon source for the microorganisms was removed by eliminating excess whey during the strained yogurt processing. In addition, the acetic acid value was increased in all supplemented samples compared to the control sample over the storage period.

Table 1: The physicochemical characteristics of strained yogurt supplemented with different concentrations of sweet lupine seed hulls (SLSH)
Each value represents mean (n =3) ±SD

Chemical properties	Day	Control	T_1 SLSH (1%)	T_2 SLSH (2%)	T_3 SLSH (3%)
pH	1	4.58 ±0.02	4.63 ±0.02	4.68 ±0.02	4.84 ±0.02
	7	3.41±0.02	3.33±0.02	3.41±0.02	3.48±0.02
	14	3.78±0.02	3.75±0.02	3.68±0.02	3.81±0.02
Acidity %	1	1.28 ±0.16	1.35 ±0.01	1.31 ±0.02	1.30 ±0.01
	7	1.62 ±0.02	2.13 ±0.05	2.06 ±0.05	1.89 ±0.01
	14	2.23±0.02	2.05±0.08	2.18±0.01	1.934±0.01
Acetic Acid (mg/kg)	1	0.39 ±0.005	0.55±0.01	0.61±0.01	0.41±0.02
	7	0.60±0.01	1.30±0.01	1.25±0.01	0.90±0.01
	14	0.80±0.01	1.21±0.01	1.22±0.01	1.121±0.02
Lactic Acid (g/kg)	1	3.44±0.01	4.55±0.01	4.96±0.01	4.98±0.02
	7	4.03±0.06	5.40±0.005	5.40±0.01	5.20±0.01
	14	4.49±0.01	5.95±0.01	5.96±0.15	5.93±0.05

3.2. Bacterial Enumeration:

The bacterial enumerations of *S. thermophilus*, *L. bulgaricus*, and *B. bifidum* was illustrated in Table 2. The microbial cell counts of *S. thermophilus* fluctuated during the storage period regardless of the concentration of SLSH. The initial counts of (T_1), (T_2), and (T_3) were 7.5,

7.4, and 7.2 Log_{10} CFU/g respectively, then increased to 8.0, 8.0, and 8.2 Log_{10} CFU/g respectively on day 7, then reduced again to 7.0, 6.9 and 6.5 Log_{10} CFU/g respectively on day 14. Meanwhile, the control sample showed a steady decrease in microbial cell counts during the storage period. Similarly, *L. bulgaricus's* initial count declined from 8.7, 8.4, and 8.1 Log_{10} CFU/g in (T_1), (T_2), and (T_3) samples to 7.9, 7.5, and 7.3 Log_{10} CFU/g, respectively after 14 days. Meanwhile, the count of the control sample also declined from 8.5 to 7.8 Log_{10} CFU/g along the storage timeline.

Table 2 shows the variation in the microbial cell count of strained yogurt supplanted with SLSH. The maximum decrease in microbial cell counts was observed at 14 days of storage after 3% of SLSH was added. The microbial cell counts of *L. bulgaricus* decreased more slowly than *S. thermophilus* counts under the same conditions. Therefore, *Lactobacillus* bacteria showed more tolerance towards the storage temperatures (*i.e.*, 4 – 5°C) than *Streptococcus* bacteria. An explanation is the one-way antagonistic effects of *L. bulgaricus* against other starter cultures, particularly at higher temperatures (> 5 °C). At temperatures ranging from 5 to 10°C, the *L. bulgaricus* strains grow faster and produce lactic acid and hydrogen peroxide. These substances are the most important viability-reducing factors during cold storage (Mortazavian and Sohrabvandi, 2006; Shah *et al.*, 1995). In general, the increase in storage temperature increased the metabolic activities of bacterial cells, increasing cell death (Mortazavian *et al.*, 2006).

Sady *et al.* (2007) reported that the concentration of *S. thermophilus* and *L. bulgaricus* in natural yogurt was increased slightly during the first three days, then decreased to the lowest level after 14 days storage. Also, the reduction in *S. thermophilus* was higher than *L. bulgaricus*, as *S. thermophilus* is less tolerant to high acidity, while *L. bulgaricus* strains can survive in an environment with a pH below 4.0 (Jakubowska and Karamucki, 2020). Generally, the yogurt whey containing large numbers of *S. thermophilus*, and *L. bulgaricus*, was lost during the production of the strained yogurt. Thus, the bacterial count that remained in strained yogurt is usually similar to those in regular yogurt.

The viability of *B. bifidum* was assessed in the strained yogurt, supplemented with different concentrations of SLSH. The microbial cell counts of *B. bifidum* obtained from the (T1) sample increased significantly compared to the control. The microbial cell counts were increased more than double from 0.2 Log_{10} CFU/g in the control sample to 0.6 Log_{10} CFU/g in (T_1) after 14 days of storage. Whereas microbial cell counts of (T_2) and (T_3) almost remained the same during the storage period. The improvement of microbial cell counts *B. bifidum* may attribute to the carbohydrate levels in SLSH or its alkaloids (Al-hamdani *et al.*, 2015).

The result agrees with previous studies on oat mash, showing an increase in viability and survival of probiotics (Akalın *et al.*, 2012; Champagne *et al.*, 2011). A study carried out by Phuapaiboon *et al.* (2013) revealed that the probiotic viability of natural yogurt supplemented with pineapple improved during storage. Elsanhoty and Ramadan (2018) carried out a study that found the probiotic viability of yogurt supplemented with barley β-glucan improved over the storage period. Also, a recent study conducted by El-Sattar *et al.* (2020), who used guava seeds powder in natural yogurt, found an increase in *B. bifidum* and *L. acidophilus* viability during storage compared to control samples. Therefore, adding a small amount of SLSH (*i.e.*, 1%) to fermented dairy products may improve the probiotic viability during the storage period and, further study on the action mechanism of SLSH may be needed.

Table 2: Bacterial count of strained yogurt samples supplemented by different concentrations of sweet lupine seed hulls (SLSH) over the storage period.

Bacteria strain	Day	Control	T1 (1% SLSH)	T2 (2% SLSH)	T3 (3% SLSH)
S. thermophilus (Log_{10} CFU/g)	1	8.3	7.5	7.4	7.2
	7	8.0	8.0	8.0	8.2
	14	7.1	7.0	6.9	6.5
L.bulgaricus (Log_{10} CFU/g)	1	8.5	8.7	8.4	8.1
	7	8.3	8.3	8.1	7.7
	14	7.8	7.9	7.5	7.3
B. bifidum (Log_{10} CFU/g)	1	1.3	2.7	2.3	2.1
	7	1.6	2.0	0.6	0.4
	14	0.2	0.6	0.3	0.2

3.3. Organoleptic Assessment of Strained Yogurt Supplemented with SLSH:

An organoleptic assessment of strained yogurt supplemented with different concentrations of SLSH is illustrated in Table 3. In general, the results did not show a statistically significant effect of using 1% and 2% SLSH on stained yogurt.

Appearance scores slightly decreased with the increase of SLSH concentration during the storage period. The score of the control sample ranged from 8.33 to 7.33 during storage. The score of the (T_3) sample decreased during storage from 6.17 on day 1 to 5.50 on day 14. Thus, a lower concentration of SLSH (*i.e.*, T_1 and T_2) showed a better score. Also, an increase of SLSH concentration was led to a slight increase in the consistency in (T_1) and (T_2) samples. By contrast, the consistency of the strained yogurt showed a decrease in the (T_3) sample compared to the control sample. So, a suitable amount of SLSH in strained yogurt would increase its consistency because of its capacity to act as a stabilizer. The SLSH as polysaccharides can hold water and bond between the particles (Hussein *et al.*, 2011). In turn, adding more SLSH may cause grittiness in texture.

Furthermore, the flavor score of strained yogurt slightly decreased from 7.83 in the control sample to 7.17 in the (T_1) sample over 14 days of storage. However, the flavor scores declined after higher concentrates of SLSH were added under the same conditions. This reduction is probably because of the adverse effects of curd fiber presented in SLSH which reflect the strained yogurt's flavor (Fernández-Garía *et al.*, 1998; Alqahtani *et al.*, 2021).

Overall, the sensory evaluation of strained yogurt supplemented with SLSH varied depending on the concentration of SLSH. In general, the effect of 1% SLSH was convenient in terms of appearance, consistency, and flavor over the storage period. However, a higher concentration of SLSH led to lower acceptance in the same previous parameters.

Table 3: Organoleptic assessment of strained yogurt supplemented with different concentrations of sweet lupine seed hulls (SLSH)

Parameters	Day	Control	T_1 (1% SLSH)	T_2 (2% SLSH)	T_3 (3% SLSH)
Appearance	1	8.33 ±0.52	7.50±0.55	7.33±0.52	6.17±0.75
	7	7.50±0.55	7.17±0.75	6.50±0.55	6.33±0.52
	14	7.33±0.52	6.33±0.52	6.33±0.52	5.50±0.55
Consistency	1	8.67±0.52	8.67±0.52	8.50±0.55	7.50±0.55
	7	8.00±0.63	8.67±0.52	8.17±0.75	7.17±0.75
	14	8.00±0.63	8.17±0.41	8.17±0.75	7.00±0.63
Flavor	1	7.50±0.84	7.43±0.75	7.50±0.55	6.33±0.82
	7	7.33±0.82	7.33±0.52	6.50±0.55	6.50±0.55
	14	7.83±0.41	7.17±0.75	6.50±0.55	6.00±0.63
Overall acceptance	1	8.17±0.41	7.17±0.41	6.67±0.52	6.67±0.82
	7	8.17±0.41	7.17±0.75	6.17±0.75	6.33±0.82
	14	7.33±0.52	6.83±0.75	6.33±0.52	5.83±0.75

Each value represents mean (n=6) ±SD

4. Conclusion

This study presented the effect of sweet lupine seed hulls (SLSH) on the probiotic viability of strained yogurt. Total acidity, acetic acid, and lactic acid production in strained yogurt increased across all concentrations of SLSH. Over the 14-day storage period, the *S. thermophilus* count decreased with an increasing amount of SLSH, as opposed to a slight increase in the *L. bulgaricus* count from 7.8 Log_{10} CFU/g in the control sample to 7.9 Log_{10} CFU/g in the (T_1) sample. This decreased again over the remaining concentrations under the

same conditions. The *B. bifidum* strain's count more than doubled after 14 days of storage, from 0.2 Log10 CFU/g in the control sample to 0.6 Log10 CFU/g in the (T_1) sample. While the rest of the SLSH concentration showed no improvement in B. bifidum viability. The sensory evaluation of strained yogurt supplemented with SLSH including, appearance, consistency, and flavor, were consistent with 1% SLSH. A higher concentration of SLSH may cause poor appearance and flavor.

Biography

Fahad Al-Asmari

Department of Food and Nutrition Sciences, College of Agricultural and Food Sciences, King Faisal University, Al Ahsa, Saudi Arabia, 00966533551663, falasmari@kfu.edu.sa

Dr. Al-Asmari is a Saudi assistant professor in the Department of Food and Nutrition Sciences at King Faisal University. He obtained his PhD. from the University of Queensland, Australia. He has published some research papers in international journals ranked by Clarivate Analytics and Scopus. He is also a member of many professional societies, including the Saudi Society for Food and Nutrition (SSFN), the Australian Institute of Food Science and Technology (AIFST), and the Australian Society for Microbiology (ASM). He is interested in topics that relate to natural antimicrobial, novel packaging systems, photodynamic treatment, and food safety. ORCID: 0000-0003-4253-2796

References

Akalin, A., Gönç, S. and Akbaş, Y. (2002). Variation in organic acids content during ripening of pickled white cheese. *Journal of Dairy Science,* **85**(7), 1670–6.

Akalın, A., Unal, G., Dinkci, N. and Hayaloglu, A. (2012). Microstructural, textural, and sensory characteristics of probiotic yogurts fortified with sodium calcium caseinate or whey protein concentrate. *Journal of Dairy Science,* **95**(7), 3617–28.

Al-hamdani, H.M.S., Al-Anbary, E.H. and Rafat, M.A. (2015). Effect of lupine (*Lupineus albifrons*) flour on microbial and sensory properties of local yoghurt. *Advance Life Science Technology,* **34**(2), 196–201.

Alqahtani, N., Barbabosa-, A. and Alnemr, T. (2021). Influence of sweet lupinee husk's addition on fat-free stirred yogurt properties. *International Journal of Dairy Science,* **16**(1), 41–7.

Association of Official Agricultural Chemists and Horwitz, W. (1975). *Official Methods of Analysis*. Washington, DC, United State: AOAC.

Bayar, E., Sh, D., Ishii, S., Miyazaki, K. and Yoshida, T. (2018). Antibacterial activity of Bifidobacteria isolated from infant faeces. *Proceedings of the Mongolian Academy of Sciences*, **58**(3), 44–52.

Bevilacqua, A. and Califano, A. (1989). Determination of organic acids in dairy products by high performance liquid chromatography. *Journal of Food Science,* **54**(4), 1076.

Bhardwaj, H.L., Hamama, A.A. and van Santen, E. (2004). White lupine performance and nutritional value as affected by planting date and row spacing. *Agronomy Journal,* **96**(2), 580–3.

Carvajal-Larenas, F., Linnemann, A., Nout, M., Koziol, M. and Van Boekel, M. (2016). *Lupineus mutabilis*: composition, uses, toxicology, and debittering. *Critical Reviews in Food Science and Nutrition,* **56**(9), 1454–87.

Champagne, C.P., Ross, R.P., Saarela, M., Hansen, K.F. and Charalampopoulos, D. (2011). Recommendations for the viability assessment of probiotics as concentrated cultures and in food matrices. *International Journal of Food Microbiology,* **149**(3), 185–93.

Chen, M., Ye, X., Shen, D. and Ma, C. (2019). Modulatory effects of gut microbiota on constipation: The commercial beverage yakult shapes stool consistency. *Journal of Neurogastroenterology and Motility,* **25**(3), 475.

Eissa, E., Ahmed, I., Yagoub, A. and Babiker, E. (2010). Physicochemical, microbiological and sensory characteristics of yoghurt produced from goat milk. *Livestock Research for Rural Development,* **22**(8), 247–53.

Elsanhoty, R.M. and Ramadan, M.F. (2018). Changes in the physicochemical and microbiological properties of probiotic-fermented low-fat yoghurt enriched with barley β-glucan during cold storage. *Journal for Dairy Production and Processing Improvement,* **68**(4), 295–309.

El-Sattar, A., Ramadan, M.F. and El-Wahed, A. (2020). Production of probiotic low-fat yoghurt supplemented with guava seeds powder. *Journal of Food and Dairy Sciences,* **11**(4), 91–6.

Fernández-Garía, E., McGregor, J.U. and Traylor, S. (1998). The addition of oat fiber and natural alternative sweeteners in the manufacture of plain yogurt. *Journal of Dairy Science,* **81**(3), 655–63.

Fernandez, M.A. and Marette, A. (2017). Potential health benefits of combining yogurt and fruits based on their probiotic and prebiotic properties. *Advances in nutrition,* **8**(1), 155–64.

Founden, R., Mogensen, G., Tanaka, R. and Salimen, S. (2000). Culture containing dairy products-effect on intestinal microfelora, human nutrition and health-current knowledge and future perspectines. *Bull. International Dairy Federation,* **35**(n/a), 21–37.

Gulewicz, P., Martínez-Villaluenga, C., Frias, J., Ciesiołka, D., Gulewicz, K. and Vidal-Valverde, C. (2008). Effect of germination on the protein fraction composition of different lupine seeds. *Food Chemistry,* **107**(2), 830–44.

Hattem, H., A., Manal, S., Hanna and Ahmadi, E. (2011). A study on the effect of thermal treatment on composition and some properties of camel milk. *Slovak Journal of Animal Science,* **44**(3), 97–102.

Hussein, M., Hassan, F.A., Daym, H.A., Salama, A., Enab, A. and Abd El-Galil, A.A. (2011). Utilization of some plant polysaccharides for improving yoghurt consistency. *Annals of Agricultural Sciences,* **56**(2), 97–103.

Jackson, M.I. and Jewell, D.E. (2019). Balance of saccharolysis and proteolysis underpins improvements in stool quality induced by adding a fiber bundle containing bound polyphenols to either hydrolyzed meat or grain-rich foods. *Gut Microbes,* **10**(3), 298–320.

Jakubowska, M. and Karamucki, T. (2020). The effect of storage time and temperature on the quality of natural yoghurt. *Acta Scientiarum Polonorum Zootechnica,* **18**(4), 29–38.

Knorr, D. (1998). Technology aspects related to microorganisms in functional foods. *Trends in Food Science and Technology,* **9**(8-9), 295–306.

Lapierre, L., Undeland, P. and Cox, L. (1992). Lithium chloride-sodium propionate agar for the enumeration of bifidobacteria in fermented dairy products. *Journal of Dairy Science,* **75**(5), 1192–6.

Lau, L.Y.J. and Chye, F.Y. (2018). Antagonistic effects of *Lactobacillus plantarum* 0612 on the adhesion of selected foodborne enteropathogens in various colonic environments. *Food Control,* **91**(n/a), 237–47.

Loizou, S., Lekakis, I., Chrousos, G.P. and Moutsatsou, P. (2010). β-Sitosterol exhibits anti-inflammatory activity in human aortic endothelial cells. *Molecular Nutrition and Food Research,* **54**(4), 551–8.

Mani-López, E., Palou, E. and López-Malo, A. (2014). Probiotic viability and storage stability of yogurts and fermented milks prepared with several mixtures of lactic acid bacteria. *Journal of Dairy Science,* **97**(5), 2578–90.

Martinez-Villaluenga, C., Frias, J., Gómez, R. and Vidal-Valverde, C. (2006). Influence of addition of raffinose family oligosaccharides on probiotic survival in fermented milk during refrigerated storage. *International Dairy Journal,* **16**(7), 768–74.

Moineau-Jean, A., Champagne, C.P., Roy, D., Raymond, Y. and LaPointe, G. (2019). Effect of Greek-style yoghurt manufacturing processes on starter and probiotic bacteria populations during storage. *International Dairy Journal,* **93**(n/a), 35–44.

Mollakhalili, M., Mortazavian, A.M., Sohrabvandi, S., Cruz, A. and Mohammadi, R. (2017). Probiotic supplements and food products: Comparison for different targets. *Applied Food Biotechnology,* **4**(3), 123–32

Mortazavian, A., Ehsani, M., Mousavi, S., Reinheimer, J.A., Emamdjomeh, Z., Sohrabvandi, S. and Rezaei, K. (2006). Preliminary investigation of the combined effect of heat treatment and incubation temperature on the viability of the probiotic microorganisms in freshly made yogurt. *International Journal of Dairy Technology,* **59**(1), 8–11.

Mortazavian, A. and Sohrabvandi, S. (2006). *Probiotics and Food Probiotic Products; Based on Dairy Probiotic Products*. Tehran: Eta Publication.

Phuapaiboon, P., Leenanon, B. and Levin, R.E. (2013). Effect of *Lactococcus lactis* immobilized within pineapple and yam bean segments and Jerusalem artichoke powder on its viability and quality of yogurt. *Food and Bioprocess Technology,* **6**(10), 2751–62.

Ranilla, L.G., Genovese, M.I. and Lajolo, F.M. (2009). Isoflavones and antioxidant capacity of Peruvian and Brazilian lupine cultivars. *Journal of Food Composition and Analysis,* **22**(5), 397–404.

Sady, M., Domagala, J., Grega, T. and Kalicka, D. (2007). Effect of storage time

on the microflora of yoghurt with amaranth seeds and oat grains. *Food Science Technology Quality,* **14**(6), n/a.

Santiago Quiles, M.R., Oquendo-Jiménez, I., Herreño-Saénz, D. and Antoun, M.D. (2010). Genotoxicity of alkaloid-rich extract from Lupineus termis seeds. *Pharmaceutical Crops*, **1**(1), 18–23.

Shah, N.P., Lankaputhra, W.E., Britz, M.L. and Kyle, W.S. (1995). Survival of Lactobacillus acidophilus and Bifidobacterium bifidum in commercial yoghurt during refrigerated storage. *International Dairy Journal,* **5**(5), 515–21.

Smith, S.C., Choy, R., Johnson, S.K., Hall, R.S., Wildeboer-Veloo, A.C. and Welling, G.W. (2006). Lupine kernel fiber consumption modifies fecal microbiota in healthy men as determined by rRNA gene fluorescent in situ hybridization. *European Journal of Nutrition,* **45**(6), 335–41.

Sodini, I., Lucas, A., Oliveira, M., Remeuf, F. and Corrieu, G. (2002). Effect of milk base and starter culture on acidification, texture, and probiotic cell counts in fermented milk processing. *Journal of Dairy Science,* **85**(10), 2479–88.

Torres, A., Frias, J. and Vidal-Valverde, C. (2005). Changes in chemical composition of lupine seeds (*Lupineus angustifolius*) after selective α-galactoside extraction. *Journal of the Science of Food and Agriculture,* **85**(14), 2468–74.

Turnbull, C.M., Baxter, A.L. and Johnson, S.K. (2005). Water-binding capacity and viscosity of Australian sweet lupine kernel fibre under in vitro conditions simulating the human upper gastrointestinal tract. *International Journal of Food Sciences and Nutrition,* **56**(2), 87–94.

Vanderhoof, J.A. and Young, R.J. (1998). Use of probiotics in childhood gastrointestinal disorders. *Journal of Pediatric Gastroenterology and Nutrition,* **27**(3), 323–32.

Yamani, M.I. and Abu-Jaber, M.M. (1994). Yeast flora of labaneh produced by in-bag straining of cow milk set yogurt. *Journal of Dairy Science,* **77**(12), 3558–64.

The Scientific Journal of King Faisal University

Basic and Applied Sciences

Deep Capsule Network for Facial Emotion Recognition

Tegani Salem [1] **and Telli Abdelmoutia** [2]

[1] LESIA Laboratory, Department of Electrical Engineering, Faculty of Science and Technology, Biskra University, Biskra, Algeria
[2] Department of Computer Science, Faculty of Exact Sciences and Natural and Life Sciences, Biskra University, Biskra, Algeria

LINK	RECEIVED	ACCEPTED	PUBLISHED ONLINE	ASSIGNED TO AN ISSUE
https://doi.org/10.37575/b/cmp/210063	08/09/2021	30/11/2021	30/11/2021	01/12/2021

NO. OF WORDS	NO. OF PAGES	YEAR	VOLUME	ISSUE
5799	6	2021	22	2

ABSTRACT

Although the classification of images has become one of the most important challenges, neural networks have had the most success with this task; this has shifted the focus towards architecture-based engineering rather than feature engineering. However, the enormous success of the convolutional neural network (CNN) is still far from comparable to the human brain's performance. In this context, a new and promising algorithm called a capsule net that is based on dynamic routing and activity vectors between capsules appeared as an efficient technique to exceed the limitations of the artificial neural network (ANN), which is considered to be one of the most important existing classifiers. This paper presents a new method-based capsule network with light-gradient-boosting-machine (LightGBM) classifiers for facial emotion recognition. To achieve our aim, there were two steps to our technique. Initially, the capsule networks were merely employed for feature extraction. Then, using the outputs computed from the capsule networks, a LightGBM classifier was utilised to detect seven fundamental facial expressions. Experiments were carried out to evaluate the suggested facial-expression-recognition system's performance. The efficacy of our proposed method, which achieved an accuracy rate of 91%, was proven by its testing the results on the CK+ dataset.

KEYWORDS

Image classifications, LightGBM, machine learning, computer vision, CNN, deep learning

CITATION

Salem, T. and Abdelmoutia, T. (2021). Deep capsule network for facial emotion recognition. *The Scientific Journal of King Faisal University: Basic and Applied Sciences*, **22**(2), 130–5. DOI: 10.37575/b/cmp/210063

1. Introduction

Some tasks that are considered simple for the human brain, such as facial recognition, detection and segmentation, present a challenging problem for computer vision systems. These vision systems are created using predictive classification modelling, and they made progress in terms of the development of robust systems over the last decade with regard to use of this natural type of human communication (Black and Yacoob, 1995; Essa and Pentland, 1997; Terzopoulos and Waters, 1990; Yacoob and Davis, 1996). Nowadays, tasks relating to computer vision require efficiency at solving common problems like facial recognition, detecting objects, translating languages, age estimation and object segmentation. Even classical artificial intelligence and all of its complicated functions and instructions cannot solve these complex problems, which has led to the creation of new models of deep learning (Mellouk and Handouzi, 2020), such as CNNs.

However, CNNs experience considerable difficulties when trying to recognise small datasets, different poses and deformed objects, even though they require a lot of data for training. As a result of these challenges, a new architecture has been invented within the field of deep learning called capsule networks. They have met expectation levels as they have outperformed CNNs in relation to solving the problems mentioned above and giving highly accurate results in various fields (Hong *et al.*, 2021; Tiwari and Jain, 2021).

In this study, the system of inputting images into our model has been implemented, which is a new method based on deep learning for the detection of facial expressions to predict seven main facial expressions: fear, anger, surprise, happiness, sadness, contempt and disgust.

2. Related Works

In recent years, novel recognition frameworks (Kim *et al.*, 2015; Liu *et al.*, 2014; Ranzato *et al.*, 2011) that have depended on the use of a CNN have produced impressive performances in terms of facial-expression-recognition systems; they have also been utilised for object recognition and feature extraction. A CNN with many convolutions and pooling layers can extract multi-level and higher features from the local area or the full face, and they perform well in relation to facial-emotion-picture-feature classification. Furthermore, a range of convolutional neural-network architectures (Ko, 2018) has been modelled in several studies to identify emotions after the successful introduction of CNNs for various computer vision tasks. A CNN can extract features automatically, capturing all potential complicated non-linear relationships between them. They have also been demonstrated to have promising capabilities for emotion categorisation, as shown in certain studies (Mehendale, 2020; Minaee *et al.*, 2021; Valdenegro-Toro *et al.*, 2019).

Some techniques (Minaee *et al.*, 2021; Valdenegro-Toro *et al.*, 2019; Zeng *et al.*, 2018) concentrate on creating new classifiers and feature extractors for emotion classification (Kim *et al.*, 2013). Substituting the softmax layer with a classifier at the last step in the model of deep learning allows for finer tweaking of the lower-level features. However, because a CNN's underlying data representation ignores crucial spatial hierarchies between complex and simple objects, it cannot accomplish rotational invariance. Nonetheless, when it comes to facial emotion identification, a facial picture can be rotated or translated. The presence of a part is noted by the max-pooling layer in a CNN but not the spatial relationship between the parts themselves. As a result, there is no pose connection between lower-level features that make up a higher-level feature. On the other hand, this connection is critical when developing solid high-level features that help categorisation; the goal is to present a network that can simulate an image's hierarchical connections.

With regard to the extraction of features after studying works by Patrick *et al.* (2019), Tereikovska *et al.* (2019) and Zhang and Xiao, (2020), an architecture based on the capsule network is suggested,

Corresponding Author: Tegani Salem 00213663544420, salem.tegani@univ-biskra.dz

which is a collection of neurons' outputs that reflect several features of the same thing. A capsule network has several layers, each of which includes numerous capsules that were first presented by Sabour *et al.* (2017). In the last step of the facial-emotion-recognition (FER) system, the LightGBM classifier is applied to avoid all of the problems associated with CNNs, leading to a robust model for this system.

3. Description and Backgrounds

3.1. Facial Emotion Recognition:

Humans need to convey their intentions and emotional state so that they can interact with their environment, and facial emotions are a natural way and the universal language that humans use for this purpose. Darwin's work was responsible for the first examination of emotion-based signals as expressed by human faces (Darwin and Prodger, 1998). Several studies have been conducted concerning FER because of its utility in many fields and other systems based on human–computer interactions, such as robotics and gaming, marketing, criminal interrogations, biometric technology and surveillance systems. In the last century, Friesen and Ekman (1976), Ekman (1993), Matsumoto (1992) completed research in relation to the FER phenomenon. The majority of the systems they employed attempted to recognise six prototypic emotion categories: happiness/disgust, anger/surprise and sadness/fear. Contempt was added later on in 1986 to the set of basic facial expressions.

There are two main categories for FER systems based on their feature representations (Corneanu *et al.*, 2016): dynamic sequences and static images (spatial information used to represent features). Starting with these two methods, multimodal systems have used many audio approaches as well as electrocardiograms (ECGs) and electroencephalographs (EEGs) to assist with the recognition of emotion. Leading on from this, nonverbal communication involves facial expressions. Factors such as tone of voice and the context of the words in the argument may distract the investigator and divert their attention away from observing the subject's facially expressed emotion. However, the technology involved in automatic facial emotion recognition systems is not impacted by contextual interference. Medical treatment systems, psychiatric care, driver-fatigue detectors, and computer-animation technology have made gains from the implementation of automatic FER methods. The seven basic emotions categories are attempted to be identified by the technology involved in facial emotion recognition systems.

FER is based on three techniques (Corneanu *et al.*, 2016; Sun *et al.*, 2017): extracting the appearance of features, deriving geometric features and utilising hybrid techniques. The geometric features of the face are obtained from elements of the face itself (the nose, the eyes, the eyebrows, the mouth, etc.) and face shapes. Meanwhile, appearance-based features are retrieved using the face's texture, wrinkles and any furrows that are caused by facial emotions. Deep learning using CNNs' architecture has become more popular throughout recent years because of its efficiency in extracting the features from image-based data, but it performs less well when the characteristics of the face are deformed. On the other hand, capsule networks can extract data from deformed images, and their intensive computation tasks can run on the graphics processing unit (GPU), which offers reliable results in a short amount of time.

3.2. Capsule Networks' Architecture:

This architecture created by Hinton *et al.* (2011) originated to replace CNNs' architecture. A capsule is a network of neutrons that accepts vectors as an input and an output, which is different from CNNs as they only accept scalar values. The capsule property of being equivariant gives it the ability to learn the deformations and the features of an image besides the viewing conditions. Then, each single capsule network contains a group of neurons in which their output represents a different feature for a similar characteristic. As a result, this advantage allows the system to recognise the entire face starting by recognising its elements. For example, when the CNN detects a face, it detects it even if it has an incorrect eye position. Therefore, equivariance makes sure that the features of the face are present and located in their natural position in the detected image. As a result, the efficiency of this property made it desirable for capsule networks.

There are three main methods for capsule implementations in the literature: capsules based on dynamic routing where each capsule can call active capsules from the levels below (Sabour *et al.*, 2017). Second, the capsule of transforming auto-encoders, which backpropagates the difference between target outputs and the actual ones, is used to learn the weights of the connections (Hinton *et al.*, 2011). Third, rather than utilising vector outputs, Hinton suggested that the input and output of a capsule should be represented as matrices. The dynamic routing was also replaced with an approach called expectation maximization (EM) to decrease the size of the transformation matrices among capsules (Hinton *et al.*, 2018). Capsules differentiate from classical CNNs that have been modified from scalar into vector features in capsules, and they use the dynamic routing method based on the same mechanism in place of the max-pooling layer. The use of max pooling was discontinued because it does not consider spatial relations and only retains prominent information, which makes the trained model incapable of recognising spatial positions between facial features. If the facial elements in an image are not organised in a natural order, CNNs still define them as faces; meanwhile, capsules work differently by using vectors to recognise faces out of order based on the spatial information that is already stored in the vector. This is the main disparity between the two methods.

Capsule networks and and a LightGBM have been applied in relation to facial emotion image classification during this specific project. Mapping a matrix of pixel values to an emotion classification involves levels of abstraction that make it applicable for studying deep architectures. More importantly, the learned intermediate representations of face types, given that the forehead, eyes and lips are part of the overall picture, are more qualitatively interpretable. The model efficiently masters this particular classification task once these features are learned in supervised training. Furthermore, this deep engineering outperforms results from more shallow networks.

3.3. Light Gradient Boosting Machine:

In 2017 Ke *et al.* (2017) introduced a new learning algorithm – the LightGBM. This approach is based on the platform of a gradient-boosting decision tree (Friedman, 2001). LightGBM is very accurate and displayed a fast level of training efficiency with regard to lots of applications as opposed to traditional gradient-boosting decision trees, which are considered time-consuming and have computational complexities. In addition, the LightGBM method has been used successfully for regression (Singh *et al.*, 2020) and classification (Yang and Shi, 2019). Its success gave the green light for new techniques to be used, including exclusive features bundling and one-sided gradient analysis.

A leaf-wise leaf development methodology with depth limitation has been used. Information about the positioning of the level may at the same moment divide the leaves of the same stratum, making multithreading optimisation simple and allowing complexity to be controlled. That will lessen the quantity of errors and will raise the

degree of precision. Regarding the depth limitation of the leaf-wise, it can guarantee a high-productivity level as it is equipped to forestall the over-fitting simultaneously. The pace of the cache hit was streamlined, and the multithreading was upgraded. Meanwhile, LightGBM is a decision-making method that is built on a histogram-based decision tree and employs histogram subtraction. This method has added the standards of a decision to the features of the category to dodge extra computational and memory overheads. It is made through the transformation of features into a one-hot characteristic with multi-dimensions.

4. Experiments and Models

In this section, the outlines of the specific model, experiments and training steps are presented. The model of our approach to be learned was developed with the following function:

$$F: (X_j) \rightarrow \{P_i \mid 0 < i < 7\}$$

The input of the function is any given image (X_j), and it outputs the probability of belonging to each class (P_i). The main challenge faced here was using a small dataset. The equation is divided into two functions within the architecture because of the dual utilisations: a) identifying the features of the image and b) using those features for the classification. An important aspect of our approach is achieved through a deep neural network, and a probability prediction is realised using a LightGBM classifier, which is explained in subsections 4.2 and 4.3.

4.1. Pre-processing:

First, the presence of noise has an impact on the accuracy of FER. As a result, the pre-processing step within FER systems is extremely important and demands careful filter selection. In our work, the picture may have noise or blurring artifacts at first, which might degrade recognition accuracy. To increase the image's overall quality, the image-appearance filters were applied, specifically the median filter (MF) and the histogram-equalization (HE) technique on the original CK+ database to optimise the model's solidity in relation to noise. The median filter's function computes the median of the entirety of the pixels' values under the kernel window, and this result is used to replace the central pixel. This is highly effective for reducing random noise. The result is shown in Figure 1. Moreover, the HE technique was used to improve the picture's contrast and normalise its illumination effects to remove any abnormalities in the its lighting and background noise.

Figure 1: The Result of the First Step

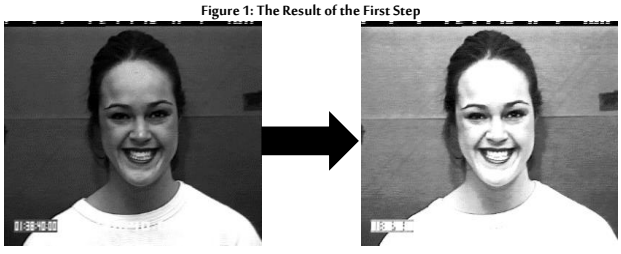

Second, the employment of a face detector is a critical stage in the recognition process, since the face is the only important aspect of the picture, and all facial landmarks associated with emotions are only found on this part of the body. Because of the head's changing poses or movements, detection is often incorrect or too difficult, meaning the majority of face-detection techniques are based on the face alone. For Viola and Jones (2001), this technique was a well-known and extensively used classic face-detection method that was freely accessible in various modes of implementation; moreover, it is highly capable of detecting faces that are facing forward. Indeed, it is more reliable than other detection algorithms, such as the deep dense face detector (DDFD) method, and it also consumes fewer resources and takes less time. Raw pictures may be cropped to retrieve the facial region using the identified face-bounding box. This approach can minimise the amount of time spent on computational calculations, and it is able to highlight the actual facial area.

Finally, all cropped images were standardized to a uniform size of 48x48 pixels. This step is necessary to shorten the processing time, as shown in Figure 2.

Figure 2: The Result of Pre-Processing Step

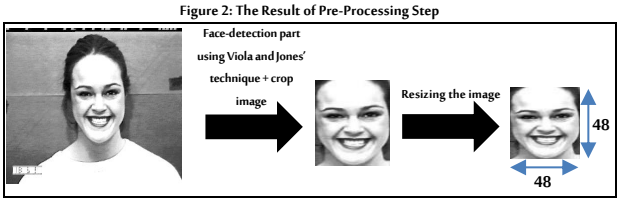

4.2. Neural Network Architecture:

Neural networks are the de-facto standard for most image-processing tasks. Especially when it comes to feature extraction, recent advancements in CNNs and their spatial invariance have shown significant improvements in terms of accuracy and scalability. Nevertheless, the key drawback of such an approach is the need for a large dataset and long training times. To train a large neural network to an acceptable level of accuracy, thousands of images are needed, yet this was not the case during our research; a dataset of around 1,000 images was used. This makes learning which features to extract a significantly difficult problem. For this reason, in this research, the use of convolutional layers was limited. Instead, the capsule layers recently published by Sabour *et al.* (2017) were introduced.

Capsule networks try to deal with a theoretical problem introduced by convolutional networks. One main element that affects the success of convolutional networks is their max-pooling layers. This pooling operation is the reason for the loss of valuable spatial information between layers in convolutional networks. This drawback is addressed using a dynamic routing algorithm, which selects information and sends it to upper layers but only to capsules that really match those features. Capsule networks have displayed on-par performances with convolutional networks but with a smaller number of training parameters. This fact makes capsule networks a good option to train networks with small datasets; hence, in this study, the applicability of capsule networks combined with a classical approach was explored.

An overall summary of the layers used in the image-feature-identification network is shown in Table 1. Those layers can be categorised into three main components in the model, namely the convolutional module, the capsule module and the feature-explanation module.

Table 1: Composition of layers in neural network.

Layer	Units	Parameters
Convolutional	256 x (40x40) kernels	62464
Primary Capsule	32 8-dim capsules	5308672
Explain Capsule	7 16-dim capsules	7340032
Fully Connected 1	100 neurons	11300
Fully Connected 2	7 neurons	707

- **Convolutional module**: this module was used to expand the features of the image. In a deep convolutional network, convolutional layers initially learn very low-level image features like colour densities and edges. Here, the same was done using a convolutional layer.
- **Capsule module**: this is where the core functionality of the model lies. It has two layers; the layer of the primary capsule has 32 capsules, and each capsule has eight 9x9 kernels with a stride of two. There each capsule generates a 16x16x8 tensor, which is fed into the expansion layer that has seven capsules. Here, seven capsules were selected, which corresponds to the number of emotions in our classification.

The output of the capsules was expected to be an expansive feature regarding how the attributes show up on the image effect for each class.

In order to optimise those predicted features, it was decided that a fully connected network would be utilised, which is known as a feature-explanation module. It has two layers with 100 and seven neurons, respectively. This whole deep neural network was trained as one separate network to perform the emotion classification task. Our deep capsule network architecture (Figure 3) has three main components: the convolutional layer, the capsule module, and the fully connected feature-expansion component. The representation of extracted features from the first fully connected layer was fed into the LightGBM classifier for further classification.

Figure 3: Overall Architecture of our Model

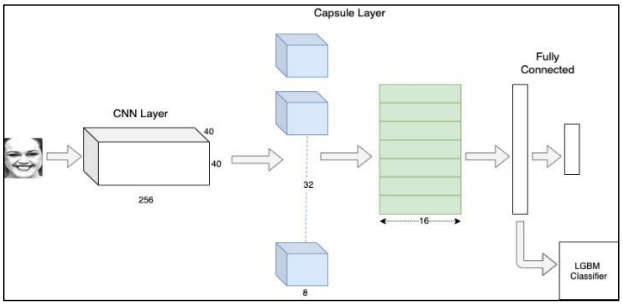

4.3. Classical Classifier:

The accuracy achieved when using the deep neural networks in isolation could be improved by employing an ensemble model; an ensemble would be created using a classical classifier. The utilisation of classical approaches combined with a methodology like SVM is standard. Nevertheless, a classical classifier that was combined with the features extracted from a deep neural network was used here. During this research, several classifiers were tested but we finally settled on an LGBM classifier with 70 estimators. LGBM classifiers use Light GBM algorithm, which in turn utilise algorithms relating to tree-based learning. The novelty of the LightGBM is that it grows trees vertically, while other algorithms do it horizontally. Since, it grows tree leaf-wise, it will then grow the leaf with the greatest delta loss, which reduces the occurrence of even greater losses compared to level-wise algorithms.

4.4. Optimisation and Learning:

The learning within this model is a two-part process. First, it needs to optimise and train the deep neural networks and then train the classical classifier with selected features that have selected dimensions. When training the neural network, it was done as an end-to-end process. The final target of the network is not feature engineering but doing a final prediction for detected emotion. It must optimize a cost function established with the intention in order to learn optimal settings. The categorical cross-entropy function is used to measure prediction accuracy:

$$L(X_i, \theta) = -\sum_{i}^{C} t_i \log F(X_i)$$

Where

X_i: input image

θ : parameters of the model

C: number of classes

t_i: the expected prediction

The output is one-hot encoded; hence, t_i is non-zero for only one class. The above equation tries to maximise the probability of that expected class. Moreover, since the probability of other classes is ignored, it has to use softmax activation in the last layer of the model. This makes sure the sum of all the probabilities equals one. After the deep learning model is trained to a sufficient level, an accuracy rate of about 91% using this model alone is achieved. Nevertheless, with an ensemble model, the improvement in accuracy could be enhanced. Before the final classification layer is completed, the feature representation for the image from the dense layer as an input to the LightGBM classifier is used. LightGBM is a classifier that is trained with an input vector of 100 dimensions that are compared with the class labels.

4.5. Training and Dataset:

Our models are trained on a machine with Windows 10 Professional, an Intel Xeon processor and a NVidia K80 GPU with a 24GB memory. As shown in Figure 4, the model was trained for 100 epochs; during this time, training accuracy grew from 20% to 97%. Also, as observed after 80 epochs, the model started to overfit, meaning it was suitable to use for the evaluations.

Figure 4: Loss and Training Accuracy of our Model

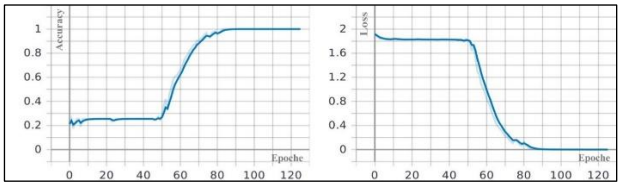

At the same time, the CK+ (Lucey *et al.*, 2010) dataset was also used to train our dataset, which contains images belonging to the seven categories of emotions.[1] Altogether, there 984 images. The dataset with a 0.7 ratio to the validation and training set was split. Owing to the database's dimensions, the validation set for testing was used as well. Different classes of dataset did not have the same number of images. Specifically, the image distribution was 135 image showing anger, 207 images of happiness, 249 images denoting surprise, 75 images showcasing fear, 84 images displaying sadness, 177 images highlighting disgust and 57 images showing contempt.

5. Results and Discussion

In this research paper, our main model consists of a capsule-based feature extractor and a LightGBM classifier. The primary model obtained a 91% accuracy rate during the test with the CK+ dataset, as shown in Table 2.

Table 2: Accuracies Achieved for Test Set with Different Models

Model	Accuracy
CN- based model	0.814
SVM classifier	0.746
Capsule-based model	0.854
Capsule feature extractor + LightGBM classifier	0.910

Apart from this main model, a few other experiments were conducted in order to compare our approach with others, including a classical CNN-based image classifier and an SVM classifier. In addition, before integrating the LGBM classifier, only the capsule-based model was used as a benchmark for the expected results. Table 3 depicts the results achieved through these different approaches.

Table 3: Matrix Confusion of our Approach

Emotions	Angry	Contempt	Disgust	Happy	Fear	Surprise	Sad
Angry	0.9062	0.0000	0.0000	0.0000	0.0000	0.0000	0.0938
Contempt	0.0000	0.7391	0.0000	0.0000	0.1304	0.0000	0.1304
Disgust	0.0000	0.0000	1.0000	0.0000	0.0000	0.0000	0.0000
Happy	0.0000	0.0182	0.0000	0.9455	0.0364	0.0000	0.0000
Fear	0.1200	0.0400	0.0000	0.0000	0.8400	0.0000	0.0000
Surprise	0.0000	0.0137	0.0000	0.0000	0.0548	0.8904	0.0411
Sad	0.0870	0.0000	0.0000	0.0000	0.0000	0.0000	0.9130
Accuracy	0.9061 = 90.61 %						

1https://sites.pitt.edu/~emotion/ck-spread.htm (with permission from copy right holder (©Jeffrey Cohn))

When the results of Table 3 are examined, a few important facts about the model can be noticed. Compared to other models, our proposed architecture has achieved very high levels of accuracy. This high accuracy rate can be attributed to two separate modules: the capsule feature extractor and the LightGBM classifier. Other baseline methods were conducted in order to get an understanding of this contribution.

Usually, deep learning methods are very good at image classification and feature extraction, especially CNNs. Nevertheless, in our case, the convolutional layer-based method was only able to achieve 81.4% accuracy. However, the model capsule layer-based was able to achieve 85.4% accuracy. This observation can be attributed to the size of the dataset that was used; our training dataset only had around 600 images as capsule networks have a superior ability to converge using only a very small number of samples. That is because there is no data loss as in convolutional neural layers. Since CNN uses max-pooling, which literally selects and keeps the most significant number in a matrix, which contrasts with the dynamic routing mechanism used in capsule layers, there could be high chance of data loss in convolutional layer-based models.

In our research, a capsule network was only used for the purpose of feature extraction rather than classification. In order to make sure that this is the optimal method for extracting features, a SVM classifier was used and its results were compared its with those from the capsule-based model. The SVM-based model was only able to achieve 74.6% accuracy. This is because it does not have the advanced capability of capsule networks or convolutional networks to extract important features. Instead, SVM tries to use all of the features that are fed into the classifier model.

As a final step in our experiment, our capsule model was integrated with an LightGBM classifier and was able to achieve around a 6% improvement in accuracy. This means it can be hypothesised that capsule networks are better feature extractors and the LGBM classifier can conduct better classifications when the dataset is small. The accuracies achieved with the final capsule model are not similar throughout all the six classes in the database. Below, Figure 5 represents our obtained results of the proposed approach.

Figure 5: Loss and Accuracy of our Model Validation

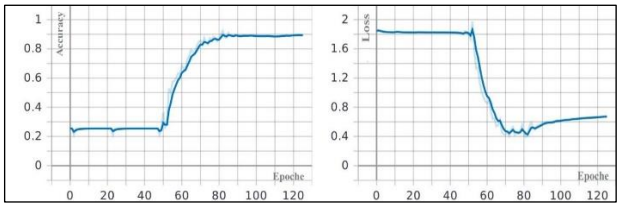

Only the emotion class of disgust achieved 100% accuracy. This could be because significant visual cues are available in this category of pictures. Figure.6 highlights some samples from the disgust emotion category.

Figure 6: Our CK+ Dataset with Samples from Disgust Category.

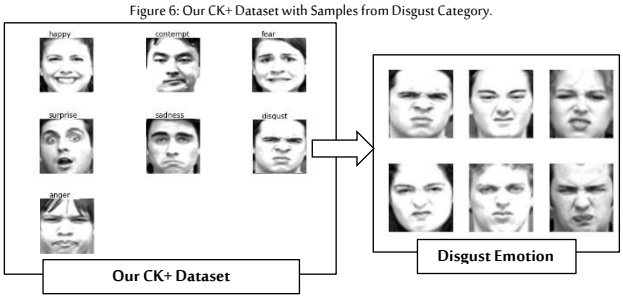

In all the samples of the disgust category in Figure 6, there is a main common visual cue around the eyes. Among these faces, the eyes are shown as a continuous black shape; this feature might be the cause of there being such a high level of precision. In any of the other classes, such noteworthy features were not observed.

6. Conclusions

A novel technique for face emotion identification is provided in this research. The suggested system can extract feature points and recognise facial displays of emotion from pictures. However, the extraction of exact facial features may be a difficult process at times, and it generally necessitates a large number of calculations. Using capsule nets for the extraction of characterisations was proposed in our study, followed by the employment of LightGBM for the classification process. The average identification performance for facial expressions might be as high as 91% accurate. In comparison with some current methods, this outcome is highly promising.

There are some ideas and many different experiments, tests adaptations that have been left open for future research. Upcoming work will concern itself with applying this model to other datasets (i.e. big datasets, multi-operation datasets and sequence videos). In addition, different methods using three-dimensional models will be tested and will integrate a new category of emotions.

Biographies

Tegani Salem

Department of Electrical Engineering, Faculty of Science and Technology, Biskra University, Biskra, Algeria, salem.tegani@univ-biskra.dz , 00213663544420

Mr. Tegani is an Algerian PhD student in electrical engineering. He obtained a master's degree in computer science (Decision-making and Multimedia) from Biskra University in Algeria in 2016. He is also a member of the Expert Systems, Imaging and their Applications in Engineering (LESIA) Research Laboratory at Biskra University and the PRFU project (Big Data Classification Using Machine Learning Approaches. Code: C00L07UN070120220004). He is currently working on a doctoral LMD thesis – *Recognizing Facial Emotions Using Deep Learning and Multiple-observations Datasets* – and specialises in remote monitoring.

Telli Abdelmoutia

Department of Computer Science, Faculty of Exact Sciences and Natural and Life Sciences, Biskra University, Biskra, Algeria, a.telli@univ-biskra.dz, 00213541340479

Dr. Telli is an Algerian Lecturer. He received his PhD from Biskra University in Algeria in 2018 with a cotutelle from Artois University in Lille (France). Additionally, he received his habilitation of science from Biskra University in 2021. His current research interests include the representation of knowledge, big data, machine learning, the management of uncertainties and conflicts in priority knowledge bases. Furthermore, he is the Head of the PRFU project. ORCID: 0000-0002-2907-9782.

References

Black, M.J. and Yacoob, Y. (1995). Tracking and recognizing rigid and non-rigid facial motions using local parametric models of image motion. In: *Proceedings of IEEE International Conference on Computer Vision*, Cambridge, MA, USA, 20-23/06/1995. DOI: 10.1109/ICCV.1995.466915.

Corneanu, C.A., Simón, M.O., Cohn, J.F. and Guerrero, S.E. (2016). Survey on rgb, 3d, thermal, and multimodal approaches for facial expression recognition: History, trends, and affect-related applications. *IEEE Transactions on Pattern Analysis and Machine Intelligence,* **38**(8), 1548–68. DOI: 10.1109/TPAMI.2016.2515606.

Darwin, C. and Prodger, P. (1998). *The Expression of the Emotions in Man*

and Animals. Oxford: Oxford University Press.

Ekman, P. (1993). Facial expression and emotion. *American psychologist,* **48**(4), 384–92. DOI : 10.1037/0003-066X.48.4.384.

Essa, I.A. and Pentland, A.P. (1997). Coding, analysis, interpretation, and recognition of facial expressions. *IEEE Transactions on Pattern Analysis and Machine Intelligence,* **19**(7), 757–63. DOI: 10.1109/34.598232.

Friedman, J.H. (2001). 1999 Reitz Lecture. *The Annals of Statistics,* **29**(5), 1189–232.

Friesen, W.V. and Ekman, P. (1976). *Pictures of Facial Affect*. Palo Alto, CA, USA: Consulting Psychologists Press.

Hinton, G.E., Krizhevsky, A. and Wang, S.D. (2011). Transforming auto-encoders. In: *International Conference on Artificial Neural Networks*, Espoo, Finland, 14–17/06/2011.

Hinton, G.E., Sabour, S. and Frosst, N. (2018). Matrix capsules with EM routing. In: *6th International Conference on Learning Representations*, Vancouver Convention Center, Vancouver, BC, Canada, 30–03/04–05/2018.

Hong, C., Chen, L., Liang, Y. and Zeng, Z. (2021). Stacked capsule graph autoencoders for geometry-aware 3D head pose estimation. *Computer Vision and Image Understanding*, **208**(n/a), 103224.

Ke, G., Meng, Q., Finley, T., Wang, T., Chen, W., Ma, W. and Liu, T.-Y. (2017). Lightgbm: A highly efficient gradient boosting decision tree. *Advances in Neural Information Processing Systems*, **30**(n/a), 3146–54.

Kim, B.-K., Lee, H., Roh, J. and Lee, S.-Y. (2015). Hierarchical committee of deep cnns with exponentially-weighted decision fusion for static facial expression recognition. In: *Proceedings of the 2015 ACM on International Conference on Multimodal Interaction*, Seattle, Washington, USA, 09–13/11/2015.

Kim, S., Kavuri, S. and Lee, M. (2013). Deep network with support vector machines. In: *International Conference on Neural Information Processing*, (pp. 458–65), Springer, Berlin, Heidelberg, 3–7/11/2013. DOI: 10.1007/978-3-642-42054-2_57.

Ko, B.C. (2018). A brief review of facial emotion recognition based on visual information. *Sensors,* **18**(2), 401. DOI : 10.3390/s18020401.

Liu, M., Shan, S., Wang, R. and Chen, X. (2014). Learning expressionlets on spatio-temporal manifold for dynamic facial expression recognition. In: *Proceedings of the IEEE conference on Computer Vision and Pattern Recognition*, Columbus, OH, USA, 23–28/06/2014.

Lucey, P., Cohn, J.F., Kanade, T., Saragih, J., Ambadar, Z. and Matthews, I. (2010). The extended cohn-kanade dataset (ck+): A complete dataset for action unit and emotion-specified expression. In: *2010 IEEE Computer Society Conference on Computer Vision and Pattern Recognition-Workshops*, San Francisco, CA, USA, 13–18/06/2010.

Matsumoto, D. (1992). More evidence for the universality of a contempt expression. *Motivation and Emotion,* **16**(4), 363–8.

Mehendale, N. (2020). Facial emotion recognition using convolutional neural networks (FERC). *SN Applied Sciences,* **2**(3), 1–8.

Mellouk, W. and Handouzi, W. (2020). Facial emotion recognition using deep learning: Review and insights. *Procedia Computer Science,* **175**(n/a), 689–94.

Minaee, S., Minaei, M. and Abdolrashidi, A. (2021). Deep-emotion: Facial expression recognition using attentional convolutional network. *Sensors,* **21**(9), 3046. DOI: 10.3390/s21093046

Patrick, M.K., Adekoya, A.F., Mighty, A.A. and Edward, B.Y. (2019). Capsule networks – a survey. *Journal of King Saud University, Computer and Information Sciences*, **x**(x), x-x. DOI: 10.1016/j.jksuci.2019.09.014

Ranzato, M.A., Susskind, J., Mnih, V. and Hinton, G. (2011). On deep generative models with applications to recognition. In *CVPR* 2011, **n/a**(n/a), 2857–64.

Sabour, S., Frosst, N. and Hinton, G.E. (2017). Dynamic routing between capsules. In: *Proceedings of the 31st International Conference on Advances in Neural Information Processing Systems*, Long Beach, California, USA, 04/12/2017.

Singh, S.P., Singh, P. and Mishra, A. (2020). Predicting potential applicants for any private college using lightGBM. In: *2020 International Conference on Innovative Trends in Information Technology (ICITIIT),* Kottayam, India, 13–14/02/2020.

Sun, W., Zhao, H. and Jin, Z. (2017). An efficient unconstrained facial expression recognition algorithm based on stack binarized auto-encoders and binarized neural networks. *Neurocomputing,* **267**(n/a), 385–95.

Tereikovska, L., Tereikovskyi, I., Mussiraliyeva, S., Akhmed, G., Beketova, A. and Sambetbayeva, A. (2019). Recognition of emotions by facial geometry using a capsule neural network. *International Journal of Civil Engineering and Technology,* **10**(3), 1424–34.

Terzopoulos, D. and Waters, K. (1990). Analysis of facial images using physical and anatomical models. In: *Proceedings Third International Conference on Computer Vision*, Osaka, Japan, 4–7/12/1990.

Tiwari, S. and Jain, A. (2021). Convolutional capsule network for COVID-19 detection using radiography images. *International Journal of Imaging Systems and Technology,* **31**(2), 525–39.

Valdenegro-Toro, M., Arriaga, O. and Plöger, P. (2019). Real-time convolutional neural networks for emotion and gender classification. In: *Proceedings of ESANN 2019 Conference, European Symposium on Artificial Neural Networks*, Bruges, Belgium, 24–26/04/2019.

Viola, P. and Jones, M. (2001). Rapid object detection using a boosted cascade of simple features. In: *Proceedings of the 2001 IEEE Computer Society Conference on Computer Vision and Pattern Recognition*. CVPR 2001, Kauai, HI, USA, 8–14/12/2001.

Yacoob, Y. and Davis, L.S. (1996). Recognizing human facial expressions from long image sequences using optical flow. *IEEE Transactions on Pattern Analysis and Machine Intelligence,* **18**(6), 636–42.

Yang, C. and Shi, Z. (2019). Research in breast cancer imaging diagnosis based on regularized lightGBM. In: *International Conference on Cyberspace Data and Intelligence, and Cyber-Living, Syndrome, and Health*, Beijing, China, 16–18/12/2019

Zeng, N., Zhang, H., Song, B., Liu, W., Li, Y. and Dobaie, A.M. (2018). Facial expression recognition via learning deep sparse autoencoders. *Neurocomputing,* **273**(c), 643–49.

Zhang, J. and Xiao, N. (2020). Capsule network-based facial expression recognition method for a humanoid robot. *Recent Trends in Intelligent Computing, Communication and Devices*, **1006**(n/a), 113–21.

إرشادات التسليم (المجلة العلمية لجامعة الملك فيصل)

Submission Guidelines (The Scientific Journal of King Faisal University)

1. General Information

- The Journal publishes in English and Arabic.
- There are no submission or publication fees.
- It takes up to 100 days from submission to publication.
- Manuscripts must be submitted to the appropriate managing editor:
  - The Managing Editor of Basic and Applied Sciences: secretary-b@kfu.edu.sa. The associate editor will check if the author has followed the Submission Instructions. If not, the manuscript will be sent back to the author. If the instructions are followed, the associate editor will create an account and send the author the username and password to log in using our online submission system (ScholarOne): https://mc04.manuscriptcentral.com/sjkfub.
  - The Managing Editor of Humanities and Management Sciences (educational manuscripts only): sjkfu-assed@kfu.edu.sa. The associate editor will check if the author has followed the Submission Instructions. If not, the manuscript will be returned to the author. If followed, the associate editor will create an account and send the author the username and password to log in using our online submission system (ScholarOne): https://mc04.manuscriptcentral.com/sjkfuh.
  - The Managing Editor of Humanities and Management Sciences (non-educational manuscripts): sjkfu-hm@kfu.edu.sa. The associate editor will check if the author has followed the Submission Instructions. If not, the manuscript will be returned to the author. If followed, the associate editor will create an account and send the author the username and password to log in using our online submission system (ScholarOne): https://mc04.manuscriptcentral.com/sjkfuh.

2. Pre-Submission Guidelines

- **Content**: Authors must ensure a clearly articulated academic contribution to the field, clarity of abstracts, quality of and conformity to the stated aims and scope of the Journal and readability of their manuscripts.
- **Manuscript Word Limit**: Manuscripts must not exceed 8,000 words, considering all inclusions (e.g. references, tables, figures).
- **Abstract Word Limit**: Abstracts must not exceed 200 words.
- **Title Word Limit**: Manuscript titles must not exceed 15 words.
- **Keyword Limit**: Keywords must not exceed six words and must not be used in the manuscript title.
- **Number of Tables and Figures**: Tables, figures, abbreviations and footnotes must be kept to a minimum. Tables and figures must not exceed six, each.
- **Reference Limit**: There must be no more than 40 references unless the manuscript is a review article or equivalent.
- **Quotations**: A quotation must not exceed 50 words. Longer quotations required due to the nature of the academic field must be justified in the cover letter.
- **Appendixes**: Appendixes are not allowed. If readers would like to access appendixes, they can reach out to corresponding authors.
- **Linguistic Quality**: Manuscripts must be written at an acceptable language level.
- **Plagiarism**: The Journal maintains a strict plagiarism policy.
- **Reviewers**: Authors must suggest five reviewers, who are specialised in the field of the manuscript, are not affiliated with authors' institutions, are at least associate professors and have not worked on joint projects with authors. Reviewers' names, phone numbers, email addresses, academic field, academic rank and institutions must be provided.
- **Documents Required**: Title page (with author details) and main document (without author details):
  - **Title Page**: It must consist of the following: the manuscript title, author details, minor and major field of the topic, 80-word bio and acknowledgements (optional). Below are explanations of how the author details and bio are written.
  - **Main Manuscript**: It must be submitted in MSWord format. It must consist of the following: manuscript title, abstract, keywords, main body and references.
- **Author Details**: Author details must be included in the following order: full name, department, college, university, city and country (or the equivalent). In the absence of an employer, one may write 'Independent Researcher'. Ranks (e.g. Dr and Prof.) must not be included. A star '*' should be placed next to the corresponding author's name. Below is an example:

  Abdulrahman Essa Al Lily*
  Department of Curriculum and Teaching Methods, College of Education, King Faisal University, Al Ahsa, Saudi Arabia
- **Bio**: The bio must be in the following format: the author's name, under which is written the author's department, college, university, city, country (or equivalent), the author's contact number and email address, under which is written an 80-word description of the author. Author's names and affiliations are not part of the 80-word count. If the author has an ORCID number or personal website, this can be included at the end of the description. Below is an example:

  Abdulrahman Essa Al Lily
  Department of Curriculum and Teaching Methods, College of Education, King Faisal University, Al Ahsa, Saudi Arabia, 00966000000000, scijkfu@kfu.edu.sa
  Prof. Al Lily is an Oxford graduate, Saudi professor, a former national-centre director, editor-in-chief (Scopes) and bestselling author (Amazon). He has coined 4 theories (e.g. 'Multiple Stupidities', "Retroactivism' and 'On-the-Go Sourcing') and 3 notions ('Crowd-Authoring', 'Crowd-Reflecting' and 'Door-Knocking'). His work is translated into 7 languages (including Spanish, Filipino, Indonesian, Chinese and Italian). His interviews is in 5 languages (including, French, Spanish and German). He has published 24 ISI/Scopus-indexed articles with the globally largest publishers (Elsevier, Springer, Taylor & Francis, Wiley, SAGE, Cogent, Palgrave, Nature Research & Oxford). His work is cited by 35 countries (Including Hungary, Serbia, Russia, Peru, Korea, Colombia, Switzerland, Netherlands, Sweden, Finland and Latvia) in 6 languages (including Turkish and Lithuanian). He has worked as a consultant for such institutions as Wikipedia and the University of Hanover. He worked during the summer in New Zealand and Italy. He has participated in conferences in Singapore, Greece, Spain, US, Japan & Bulgaria.
  ORCID: 0000-0002-5116-422X.
  Website: https://abdulallily.wordpress.com/

3. Post-Reviewing Guidelines

- **Page Settings**: Page size is A4. Margins are 2.5 cm, each side. Any standard font is acceptable.
- **Headings**: There must be no more than three levels of headings. The first level of headings must be numbered: 1., 2., 3., etc. The second level of headings must be numbered: 1.1., 1.2., 1.3., etc. The third level of headings must be numbered: 1.1.1., 1.1.2., 1.1.3, etc. The headings for abstracts, bios and references must not be numbered.
- **Tables and Figures**: Captions must be above tables and figures. In the body, 'see above' or 'see below' must not be used. Instead, use 'see Table 1' or 'see Figure 1'.
- **Measuring Units**: In the case of using local measuring units in the manuscript, the equivalent of international units must be included. Scientific rather than provincial terms must be used. Currencies must be in U.S. dollars.
- **Footnotes**: Footnotes must be kept to a minimum. They must be referred to in the text in uppercase numbers. Footnotes must appear at the bottom of the page on which they are introduced.
- **References**: Authors must follow the APA style of referencing. References must be arranged alphabetically. The reference list must not be numbered. Non-English references must be "romanised" into English.
- **Digital Object Identifier (DOI)**: If a reference has a DOI, it must be included.

Proofreading Certificates: Once accepted, manuscripts must be sent by authors to an accredited proofreading company. A proofreading certificate must be submitted to the Journal. A suggested company is: proofreadmyessay.co.uk

1. معلومات عامة

- **أخلاقيات البحث**: لا تقبل المجلة استلام أي ورقة أو تحكيم يتضمن أي نوع من أنواع التحامل أو العدوانية أو التطرف أو التشدد الأيديولوجي (سواء كان ذلك موجها لشخص، أو مدرسة فكرية، أو طائفة، أو جنس، أو أيديولوجية بعينها). كما لا تقبل استلام الأبحاث أو تقييمات المحكمين التي تحمل أفكاراً تناهض الأمن الفكري والمجتمعي، أو تُعزز الإرهاب والأفكار المتطرفة، أو تحضّ عليها تصريحاً أو تلميحاً.
- **أوقات العمل**: تقوم المجلة بمهمة استلام الأوراق العلمية على مدار العام، وفي حالة وجود توقف سيتم وضع رد تلقائي على البريد الإلكتروني.
- **رسوم النشر**: المجلة لا تتقاضى أي أجر أو رسوم مالية مقابل عملية النشر العلمي وإجراءاته (النشر مجانًا لجميع الباحثين).
- **لغة النشر**: تقبل المجلة أبحاثاً مكتوبة باللغة العربية أو اللغة الإنجليزية.
- **مدة النشر**: بعد انضمام المجلة إلى المعرف الرقمي العالمي الموحد (DOI) أصبح بإمكان أي بحث جديد مرسل للمجلة أن ينشر على الموقع الإلكتروني للمجلة برقم المعرف الرقمي (DOI) في غضون فترة لا تزيد عن 100 يوم عمل منذ تسليمه للمجلة وأعطائه رقم قيد.
- **آلية تسليم الورقة**: يجب تسليم الورقة للمحرر المناسب، وفقاً للآتي:
  - تسلم أوراق العلوم الأساسية والتطبيقية إلى سعادة محرر فرع العلوم الأساسية والتطبيقية: secretary-b@kfu.edu.sa. سيقوم المحرر بتدقيق الورقة للتأكد من اتباعها لـ "تعليمات النشر". في حال عدم اتباع التعليمات، فستعاد الورقة للمؤلف. في حال اتباع التعليمات، فسيقوم المحرر بإنشاء حساب للمؤلف وتزويده باسم المستخدم وكلمة السر لتسليم ورقته من خلال نظام التسليم الإلكتروني (ScholarOne): https://mc04.manuscriptcentral.com/sjkfub.
  - تسلم أوراق العلوم الإنسانية والإدارية (الأبحاث التربوية فقط) إلى سعادة محرر فرع العلوم الإنسانية والإدارية للقضايا التربوية: sjkfu-assed@kfu.edu.sa. سيقوم المحرر بتدقيق الورقة للتأكد من اتباعها لـ "تعليمات النشر". في حال عدم اتباع التعليمات، فستعاد الورقة للمؤلف. في حال اتباع التعليمات، فسيقوم المحرر بإنشاء حساب للمؤلف وتزويده باسم المستخدم وكلمة السر لتسليم ورقته من خلال نظام التسليم الإلكتروني (ScholarOne): https://mc04.manuscriptcentral.com/sjkfuh.
  - تسلم أوراق العلوم الإنسانية والإدارية (الأبحاث غير التربوية) إلى سعادة محرر فرع العلوم الإنسانية والإدارية للقضايا غير التربوية: sjkfu-hm@kfu.edu.sa. سيقوم المحرر بتدقيق الورقة للتأكد من اتباعها لـ "تعليمات النشر". في حال عدم اتباع التعليمات، فستعاد الورقة للمؤلف. في حال اتباع التعليمات، فسيقوم المحرر بإنشاء حساب للمؤلف وتزويده باسم المستخدم وكلمة السر لتسليم ورقته من خلال نظام التسليم الإلكتروني (ScholarOne): https://mc04.manuscriptcentral.com/sjkfuh.
- **الرسائل العلمية**: تقبل المجلة الأوراق المستلة من الرسائل العلمية، على أن يتم النص على ذلك.
- **الحقوق الفكرية**: جميع حقوق الطبع والنشر محفوظة للمجلة، ولا يسمح بإعادة طبع أو نشر أي جزء من المجلة أو نسخه بأي شكل وبأي وسيلة كانت إلكترونية أو آلية بما في ذلك التصوير والتسجيل والإدخال في أي نظام حفظ معلومات أو استعادتها دون الحصول على موافقة كتابية من رئيس هيئة التحرير.
- **آراء المؤلفين**: الآراء المضمنة في الأوراق المنشورة تعبر عن وجهات نظر كتابها ولا تعبر بالضرورة عن وجهة نظر المجلة.
- **فلسفة الأوراق العلمية**: لا تستقبل المجلة الأوراق العلمية التي لا تراعي المحاور الآتية ولا تحقق مدى عاليا في كل محور:
  - مدى احتمالية اقتباس الورقة من قبل بحوث أخرى في كلاريفيت وسكوبس خلال عامين قادمين؛ حيث إن هذا يعد أحد المتطلبات المهمة لتصنيف المجلة في قاعدة بيانات سكوبس.
  - مدى فائدة الورقة للقارئ الدولي ومدى اتساع جمهور الورقة خارج نطاق المكان والزمان واللغة. يُعرف القارئ الدولي هنا بأنه "شخصية اعتبارية محايدة (سواء شخص، مجموعة، جهة، مؤسسة أو مُنظمة) لا تشترك مع المؤلف في الحدود الزمانية والمكانية واللغوية التي كُتبت بها الورقة".
- **ضرورة اتباع الإرشادات**: وفقاً لسياسة المجلة، فإنه يتوجب على أصحاب السعادة الباحثين ضبط ورقتهم وفقاً لملف "إرشادات التسليم"، واتباعها حرفياً وبدقة متناهية وعالية جداً، حيث إن عدم الالتزام بها بأي وجه من الأوجه سيمثل عائقاً لنشر الورقة. نؤكد الضرورة القصوى للاتباع الحرفي والدقيق لهذه الإرشادات. إن المجلة تسعى جاهدة أن تكون مصنفة في عدد من قواعد البيانات المتميزة عالمياً مما يتطلب دقة عالية في ضبط الورقة، وعليه وجب توخي الحذر التام في كيفية ضبط الورقة وفقاً للمطلوب، حيث إن آلية صياغة المراجع، على سبيل المثال، هي العنصر الأهم لقواعد البيانات العالمية. في حالة قيام المؤلف بإرسال الورقة إلى المجلة، وتبين لهيئة التحرير وجود بعض الإرشادات لم يتم اتباعها، فإنه سيتم إرجاع الورقة للمؤلف، وسيتم إخباره بعدم اتباعه للإرشادات، بدون تحديد أي من الإرشادات لم يتم اتباعها، وذلك لأن الوقت للأسف لا يتسع للمجلة لأن تزود كل مؤلف بتغذية فردية عن أي من الإرشادات لم يتم مراعاتها، كما أنه بناء على سياسة المجلة فإن السادة الباحثين هم المعنيون بالدرجة الأولى من التأكد من اتباع كافة الإرشادات. ولذلك ننصح سعادة المؤلف الرئيس، بعد الانتهاء من ضبط الورقة، بأن يقوم بإرسال الورقة للمؤلفين الآخرين (وأيضاً لزميل من غير المؤلفين) للتأكد من أن جميع الإرشادات قد اتبعت. كما ننصح أصحاب السعادة المؤلفين أن يقوموا أيضاً بالاستعانة بطرق واستراتيجيات أخرى يرون أنها قد تساعدهم في التأكد من اتباع كافة الإرشادات؛ فعلى سبيل المثال، القيام بطباعة ملف "إرشادات التسليم"، ثم وضع علامة "صح" بجانب كل فقرة من الإرشادات للتأكد من تغطية جميع الإرشادات. تؤكد المجلة لأصحاب السعادة المؤلفين أنها من خلال خطتها الاستراتيجية الحالية تسعى لأن تكون منار التميز في العالم العربي (بجميع ما يتطلبه التميز من عمل شاق ودقة)، وهذا قد يزيد العبء على المجلة والمؤلف والمحكمين وجميع "أصحاب الشأن" على حد سواء. سيمنح المؤلف فرصتين كحد أعلى لاتباع التعليمات، وفي حالة عدم قيامه بذلك، فإن هيئة التحرير ستقون بطي قيد البحث، حتى وإن أوصى المحكمون بقبول البحث. اتباع التعليمات تحمل نفس الماهية التي تحملها القيمة العلمية للورقة.
- **متعارضات**: في حالة تضارب توصيات المحكمين مع إرشادات النشر، فيتم استبعاد توصيات المحكمين وتعتمد إرشادات النشر، مع ضرورة إعلام المحرر بهذا التضارب.

2. شروط لا يتم استلام الورقة دونها

- **المستندات المطلوبة**: يجب تسليم ملفين على صيغة الوورد (DOC)، وهما كالتالي:
  - الملف الأول تحت مسمى "بيانات الباحث" (Title Page): يجب ترتيب هذا الملف كالتالي:
    - عنوان الورقة بالعربي (غير مطلوب إذا كانت الورقة باللغة الإنجليزية).
    - بيانات المؤلف بالعربي (على أن يتضمن اسم المؤلف، اسم القسم، اسم الكلية، اسم الجامعة، اسم المدينة، واسم الدولة، البريد الإلكتروني، رقم الواتساب). في حالة عدم وجود قسم أو كلية أو جامعة، يكتب ما يعادلها. في حالة عدم الانتساب لجامعة، يكتب "باحث مستقل" (غير مطلوب إذا كانت الورقة باللغة الإنجليزية).
    - عنوان الورقة بالإنجليزي.
    - بيانات المؤلف بالإنجليزي (على أن يتضمن اسم المؤلف، اسم القسم، اسم الكلية، اسم الجامعة، اسم المدينة، واسم الدولة، البريد الإلكتروني، رقم الواتساب). في حالة عدم الانتساب لجامعة، يكتب "Independent Researcher".
    - تحديد تخصص الورقة: 1) التخصص العام، 2) التخصص الدقيق ، 3) التخصص الأدق من الدقيق.
    - نبذة من 80 كلمة عن كل مؤلف. أدناه توضيح عن كيفية كتابة النبذ (إذا كانت الورقة بالعربي فتكتب النبذة بالعربي، وإذا كانت الورقة بالإنجليزي، فتكتب النبذة بالإنجليزي).
    - شكر وتقدير (اختياري).

- الملف الثاني تحت عنوان "ملف البحث" (Main Document): تتبع المجلة سياسة التحكيم المزدوج مجهول الهوية، وعليه يجب على المؤلف عدم تضمين ما يكشف هويته في "ملف البحث"، حيث ان "ملف البحث" سيرسل كما هو للمحكمين. يجب ترتيب الملف كالتالي:
  - عنوان الورقة بالعربي (غير مطلوب إذا كانت الورقة باللغة الإنجليزية).
  - ملخص الورقة بالعربي (غير مطلوب إذا كانت الورقة باللغة الإنجليزية).
  - الكلمات المفتاحية بالعربي (غير مطلوب إذا كانت الورقة باللغة الإنجليزية).
  - عنوان الورقة بالإنجليزي.
  - ملخص البحث بالإنجليزي.
  - الكلمات المفتاحية بالإنجليزي.
  - مضمون البحث.
  - المراجع.

- **"نبذة عن المؤلف"**: يجب تزويد نبذة عن كل مشارك في البحث. تتضمن النبذة الاسم، ثم أدناه اسم القسم، الكلية، الجامعة، المدينة، الدولة (أو ما يوازيه)، رقم الواتساب مع فتح الخط الدولي، البريد الإلكتروني، ثم أدناه نبذة عن الباحث (من 80 كلمة لكل باحث، علماً أن اسم الباحث و مكان العمل لا يحسب من هذه الـ 80 كلمة). إذا كان لدى الباحث رقم أوركيد و/أو صفحة شخصية، فيدرج في نهاية النبذة. يجب أن تتضمن النبذة جنسية المؤلف، وأعلى درجة علمية حصل عليها (مثلاً، ماجستير، دكتوراه) واسم الجامعة التي حصل منها على هذه الدرجة. يمكن للمؤلف الكتابة في النبذة عن نشاطه البحثي واهتماماته البحثية ومدى التأثير الوطني والعالمي الذي حققه ومدى قدرته على التواصل خارج نطاق مكان عمله وشيء من نشاطه في المؤتمرات والدورات التدريبية. النبذة هي وسيلة مهمة يستطيع الباحث من خلالها التعريف بنفسه وتسويق ذاته؛ فينبغي أن تحظى باهتمام عال من قبل المؤلف. ترتب النبذ وفقاً لترتيب المؤلفين. أدناه مثال على ذلك:

  عبدالرحمن عيسى الليلي
  قسم المناهج وطرق التدريس، كلية التربية، جامعة الملك فيصل، الأحساء، المملكة العربية السعودية، 00966000000000، scijkfu@kfu.edu.sa

  أ.د. الليلي دكتوراه (أكسفورد)، سعودي، أستاذ دكتور، مدير مركز وطني، رئيس هيئة تحرير (سكوبس)، أعماله في 7 لغات (منها، إسباني، فلبيني، إندونيسي، صيني، إيطالي)، مقابلاته في 5 لغات (منها، فرنسي، إسباني، ألماني)، مؤسس 4 نظريات (منها، "Multiple Stupidities" و"Retroactivism" و"On-the-Go Sourcing") و 3 منهجيات ("Crowd-Authoring" و"Crowd-Reflecting" و"Door-Knocking")، أكثر مبيعاً (أمازون)، نشر مع أكبر دور نشر (Nature Research, Cogent, Palgrave, Elsevier, Springer, Taylor & Francis, Wiley, Sage, Oxford)، نشر 24 ورقة في ISI و/أو سكوبس، أبحاثه مقتبسة من قبل 35 دولة (منها المجر، صربيا، روسيا، بيرو، كوريا، كولومبيا، سويسرا، هولندا، السويد، فنلندا، لاتفيا) في 6 لغات (منها، التركية و الليتوانية)، عمل خلال الصيف في نيوزلندا وايطاليا. شارك بأوراق في مؤتمرات سنغافورة، اليونان، اليابان، بلغاريا وغيرها. عمل مستشاراً لمؤسسات منها الويكيبيديا و جامعة هانوفر.
  رقم الأوركيد (ORCID): 0000-0002-5116-422x
  الموقع الشخصي: https://abdulrahmanallily.wordpress.com

- **عدد كلمات الورقة**: ألا يتجاوز عدد كلمات الورقة 8000 كلمة في أي حال من الأحوال (شاملة كل شيء، بما في ذلك المراجع والجداول والأشكال والملخص وبيانات المؤلفين والهوامش والرومنة وكل شيء).
- **الملخص**: ألا يزيد الملخص عن 200 كلمة. لا يسمح بإدراج مراجع أو اقتباسات في الملخص.
- **عدد كلمات العنوان**: ألا يزيد عنوان الورقة عن 15 كلمة.
- **عدد الكلمات المفتاحية**: أن تحتوي الورقة على ست كلمات مفتاحية باللغة العربية وترجمتها بالإنجليزية، ويجب ألا يكون قد سبق ذكرها في العنوان، كما يجب ألا تزيد كل كلمة مفتاحية عن كلمتين.
- **عدد الجداول والرسومات**: ينبغي تقليص عدد الجداول والرسومات والاختصارات والحواشي السفلية، قدر المستطاع. يجب ألا تتضمن الورقة أكثر من (6) جداول و (6) صور/أشكال. علماً أن عدم وجود أشكال بالورقة لا يعني أن عدد الجداول يمكن أن يزيد عن (6)، وعدم وجود جداول بالورقة لا يعني أن عدد الأشكال يمكن أن يزيد عن (6). يجب ألا يزيد عدد السطور عن 20 وعدد الأعمدة عن 7 في كل جدول من الجداول.
- **الجودة اللغوية**: يجب أن يكون البحث مكتوبًا بمستوى لغوي صحيح مقبول. كما يجب على المؤلف الضغط على أيقونة "المراجعة اللغوية" في ملف الوورد للتأكد من عدم وجود أخطاء لغوية.
- **عدد المراجع**: يجب ألا يزيد عدد المراجع عن 40 مرجعًا (إلا في حالة كون الورقة "مراجعة أدبية").
- **الاقتباس**: يجب أن تكون نسبة الاقتباس غير المشروع 0%.
  - يسري ذلك على نوعي الاقتباس: الاقتباس الذاتي و الاقتباس من الآخرين. ويقصد بالاقتباس الذاتي أن ينقل الباحث من عمل آخر له قام بنشره من قبل دون أن يشير إلى النقل.
  - يستثنى من الاقتباس غير المشروع تلك العبارات والجمل المتداولة التي لا تُمثل انتهاكا لحقوق الآخرين، ولا تطعن في الأصالة العلمية؛ مثل عبارة:
    والجدول يُوضح معاملات متغيرات الدراسة التي وضعت في قائمة الاستقصاء التي اعتمد عليها الباحث في تجميع البيانات الأولية.
  - في حالة الاقتباس الحرفي ولجعل الاقتباس مشروعاً، فيجب ألا يزيد عن 30 كلمة، وتوضع في علامة تنصيص، ويذكر اسم المرجع ورقم الصفحة. مثال على ذلك:
    ويجدر الإشارة إلى أنه "يعد التعليم عن بعد في زمن الكورونا مختلفاً بشكل أساسي وجوهري عن "التعليم عن بعد" التقليدي من عدة أوجه، أولها كونه مفاجئا وغير مخطط له مسبقاً" (العلي، 2020: 15).
  - غير مسموح بالاقتباس الحرفي إلا في حالة الضرورة القصوى والمبررة؛ حيث مفترض من المؤلف أن يعيد صياغة أي اقتباس بأسلوبه الشخصي.
  - في حالة كون أن طبيعة التخصص تتطلب اقتباسات مطولة، فيجب تبرير ذلك في الخطاب الموجه للمجلة أثناء التسليم.
- **العبارات غير الأكاديمية**: يجب أن تكون اللغة المكتوب بها الورقة لغة علمية أكاديمية مباشرة تبتعد عن الإسهاب الذي لا علاقة له بالورقة من الناحية العلمية، وأيضا تبتعد عن تكرار الجمل والمعاني المعلومة بالضرورة؛ ومن الأمثلة على ذلك ما يرد في مقدمة البحث وخاتمته لدى بعض الباحثين: (فإن أكن أصبت فمن الله وحده وله المنة على ذلك، وإن تكن الثانية فمن نفسي ومن الشيطان، والله الهادي إلى سواء السبيل..)، (أحمد الله أن أعانني ويسر لي إتمام هذا البحث بعدما لاقيت فيه من عناء وجهد طيلة شهور متتابعة، فإن أصبت فإمساك بمعروف، وإن تكن الأخرى فتسريح بإحسان..)، (حفظه الله ورعاه وسدد على طريق الخير خطاه..)، (رحمه الله وطيب ثراه..)، ونحو ذلك، ويستثنى من ذلك ما يتعلق بالأنبياء والمرسلين: (صلى الله عليه وسلم)، (عليه السلام).
- **المرفقات/الملاحق**: ألا تتضمن الورقة مرفقات، وفي حال ضرورة المرفقات فإنها توضع في المتن، أو يتم وضع رابط للمرفقات على الإنترنت (يتم تزويد الملحقات فقط في حالة طلب المحكمين لها).

3. إجراءات يطلب من المؤلف عملها فقط بعد صدور قرار المحكمين

- **مقاس الصفحة**: يكون مقاس الصفحة A4، على عمود واحد، الهوامش 2.5 سم من جميع الجهات، ويكون نوع الخط من الخطوط الدارج استخدامها، ويكون حجم الخط مقبولا.
- **جودة اللغة**: يجب التأكد من الخلو التام من وجود أي ملاحظات لغوية.
- **العناوين**:
  - لا يزيد عدد مستويات العناوين عن ثلاثة. أي يسمح فقط بعناوين أساسية، وفرعية وفرعية فرعية فقط. أي كون هناك عناوين فرعية فرعية فرعية غير مسموح لتجاوزها ثلاثة مستويات. الأساسية والفرعية. يجب ترقيمها كالتالي: 1.، 2.، 3.، وتحت 1. يكون 1.1.، 1.2.، 1.3.، وتحت 1.1. يكون 1.1.1.، 1.1.2.، 1.1.3.، وهكذا. يجب ألا يتم ترقيم عنوان الملخص، والنبذة عن المؤلف والمراجع.

- المجلة لا تستقبل عناوين الأبحاث التي تدور حول فرد بعينه أو قصيدة بعينها أو كتاب بعينه؛ مثل: "المفارقة الشعرية في شعر أبي الحسن القيرواني"، "حجيّة المنجز الكلامي في مقدّمة دلائل الإعجاز لعبد القاهر الجرجاني"، "هرمية المصطلح البلاغي والنقدي عند الجاحظ"، "النسق البنيوي في قصيدة أبي ذؤيب الهذلي في رثاء أولاده الخمسة".
- نظراً لكون المجلة العلمية لجامعة الملك فيصل مجلة متعددة التخصصات تندرج ضمن المنصات العالمية للبحث العلمي فإن هذا يتطلب من الباحثين كتابة عنوان الورقة وملخصها باللغة العلمية المباشرة بصياغة سهلة بعيدة عن التعقيد مما ييسر لكل قارئ في مختلف التخصصات فهم مضمون الورقة وعنوانها وملخصها.
- لا تنشر المجلة الأوراق التي تتحدد بذكر مدينة أو محافظة بعينها في العنوان البحثي (يمكن الاكتفاء بذكر اسم الدولة فقط إذا لزم الأمر)، وذلك لأن تخصيص اسم مدينة بعينها يحدد من نسبة الاستشهادات للورقة بعد نشرها، لأنه غالباً ما تكون هذه المدينة غير معلومة أو غير ذات اهتمام من القراء، وهذا يتعارض مع سياسة المجلة في استقطاب الأوراق ذات العمومية والانتشار الواسع. وإذا أراد الباحث أن يخصص محافظة أو مدينة ما، فيمكنه الإشارة لذلك في ملخص الورقة وحدودها المكانية وليس في العنوان.

- **التواريخ والأرقام**: يجب أن تكون جميع تواريخ الورقة بالميلادي وبأرقام إنجليزية (سواء في المتن أو المراجع).
- **الجداول**: يتم كتابة رقم وعنوان الشكل أو الجدول أعلاه. في المتن، يتم الإشارة إلى الجدول أو الشكل دائماً برقمه سواءً قبل أو بعد وضعه، وترقم الجداول تسلسليا حسب تسلسل ذكرها في المتن.
- **العملات**: يجب كتابة القيمة بالدولار بين قوسين، بعد أي قيمة مذكورة بالريال السعودي أو أي عملة أخرى.
- **الاختصارات**: عند استخدام رموز لاختصار مصطلح، فيجب أن يذكر نص المصطلح كاملا في أول مرة يرد فيها في نص البحث. علما أن المسموح به ثلاث اختصارات على الأكثر.
- **المقاييس الرياضية**: يجب استخدام الاختصارات المقننة دوليا بدلا من كتابة الكلمة كاملة مثل سم، ملم، كلم و% (لكل من سنتمتر، مليمتر، كيلومتر والنسبة المئوية، على الترتيب). يفضل استخدام المقاييس المترية وفي حالة استخدام وحدات أخرى يكتب المعادل المتري لها بين أقواس مربعة. في حالة ذكر وحدات قياس أو أسماء درجة إقليميا للكائنات الحية في المتن يذكر عقبها مباشرة المقابل لها بالوحدات القياسية أو الاسم اللاتيني للكائن. يجب أن تكون جميع العملات بالدولار الأمريكي.
- **الحواشي**: يفضل تقليص الحواشي، ولكن في حالة الحاجة لها، فيشار إلى الحاشية في المتن بأرقام بين قوسين مرتفعة عن السطر، ترقم الحواشي داخل المتن وتكتب حواشي كل صفحة أسفلها مفصولة عن المتن بخط ولا تجمع في نهاية المتن. يعاد ترقيم الحواشي ابتداءً من الرقم 1 مع بداية كل صفحة جديدة.
- **الهوامش السفلية**: تأخذ المراجع المدرجة في الحواشي السفلية ترقيماً متسلسلاً لكل صفحة بحيث يوضع رقم الحاشية بين قوسين علويين ()، وتكون جميع العناصر الببليوجرافية لكل مرجع مرتبة وفقا للترتيب المذكور في قائمة المراجع، سواء ذكرت البيانات كاملة أو مختصرة، كما يجب التأكد من أن جميع المراجع الواردة في المتن والحواشي مذكورة في قائمة المراجع، كما يجب ألا تكون هنالك مراجع بالقائمة لم يشر إليها في المتن.
- **روابط المراجع**:
  - **للمراجع العربية**: في حالة الرغبة في إدراج رابط لمرجع عربي، فيكتب بعد المرجع "متوفر بموقع:" ثم يدرج الرابط، وبعد الرابط يفتح قوس ويكتب "تاريخ الاسترجاع:" ثم يدرج التاريخ على هذه الصيغة "2020/07/27"، ثم يغلق القوس.
  - **للمراجع الإنجليزية**: في حالة الرغبة في إدراج رابط لمرجع إنجليزي، فيكتب بعد المرجع "Available at:" ثم يدرج الرابط، وبعد الرابط يفتح قوس ويكتب "accessed on" ثم يدرج التاريخ على هذه الصيغة "2020/07/27"، ثم يغلق القوس.
- **ترتيب قائمة المراجع**: يجب ترتيب المراجع هجائياً. ويجب عدم ترقيم قائمة المراجع.
- **مرجعان لمؤلف في سنة واحدة**: في حالة وجود مرجعين لمؤلف واحد في سنة واحدة، فللتمييز بينهما يكتب حرف بجانب التاريخ كالآتي: (2020أ)، (2020ب)، وبالإنجليزي (2020a)، (2020b)
- **DOI للمرجع**: عند استعمال مراجع لها رقم DOI، يجب ذكر هذا الرقم.
- **المراجع داخل المتن**: بخصوص آلية كتابة المراجع داخل المتن:
  - إذا كان المرجع في بداية الجملة، يكتب اسم عائلة الباحث/الباحثين يليها تاريخ النشر بين قوسين. مثال: "ذكر الصالح والأحمد (2020) بأن..."
  - إذا كان المرجع في نهاية الجملة، فيكتب بين قوسين اسم عائلة الباحث/الباحثين، ثم فاصلة، ثم تاريخ النشر. مثال: "وهذا هو أساس المشكلة (الصالح والأحمد، 2020)."
  - في حالة كون المرجع لأكثر من باحثين فيكتب اسم عائلة الباحث الأول متبوعا بكلمة "وآخرون". مثال: "ذكر المحمد وآخرون (2020) بأن..." أو "وهذا ما يسمى بالتعليم المدمج (العلي وآخرون، 2020)."
  - يجب تدوين رقم الصفحة المقتبس منها داخل المتن. أدناه أمثلة على كيفية عمل هذا التدوين:
    - "وهذه من القضايا الأساسية التي ستساهم في تطور التعليم العالي" (المحمد، 2020: 15).
    - ذكر المحمد (2020: 15) أن هذه "من القضايا الأساسية التي ستساهم في تطور التعليم العالي".
    - ذكر المحمد (2020) أن هذه "من القضايا الأساسية التي ستساهم في تطور التعليم العالي" (ص. 15).
- **المراجع في قائمة المراجع**: لا يتم استخدام كلمة "وآخرون" (. et al) في قائمة المراجع.
- **صفحات الويكيبيديا**: لا يسمح باقتباس صفحات الويكيبيديا.
- **تعريف الرومنة**: يجب رومنة/ترجمة قائمة المراجع العربية. يقصد بالرومنة النقل الصوتي للحروف إلى الإنجليزية، أي تحويل منطوق الحروف العربية إلى حروف إنجليزية. تتم الرومنة عن طريق مترجم قوقل (http://translate.google.com)، حيث إن في كتابة أي جملة في مترجم قوقل (مثلاً: " إنجازات جامعة الملك فيصل منذ تأسيسها")، فستكون رومنة هذه الجملة متوفرة بأسفل النص " iinjazat jamieat almalik faysal mundh tasisiha"، وترجمتها متوفرة على الجنب (Achievements of King Faisal University since its foundation). رومنة المراجع العربية لا يعني حذف المراجع العربية. فالمراجع العربية والمرومنة تبقى سوياً. توضع أولاً المراجع العربية، يليها المراجع المرومنة والإنجليزية. تدمج المراجع المرومنة والإنجليزية سوياً وترتب هجائياً.
- **تعديلات هيئة التحرير على عنوان الورقة**: يحقّ لهيئة التحرير إعادة صياغة عنوان الورقة في المرحلة الأخيرة للنشر (قبل الإحالة لعدد)، وذلك وفقاً لمقتضيات التوجه التطويري العام للمجلة حالياً، والذي يتطلب الاقتصار على نشر العناوين: "الموجزة، والبسيطة، والواضحة، والعامة التي لا تشتمل على صف دراسي بعينه أو جامعة أو محافظة أو مدينة بعينها في العنوان" وبالتالي سيتم استبعاد أية كلمة غير ضرورية من العنوان لأن هذه المصطلحات تحدّ من نسبة انتشار البحث، وشموليته، وتقلل من نسبة اقتباسه واستشهاداته من قبل الباحثين.
- **شهادة مراجعة لغوية**: في حالة قبول الورقة للنشر، فإنه سيطلب من المؤلف إرسال ورقته لشركة معتمدة لمراجعة الورقة من قبل متحدثي اللغة الإنجليزية كلغة أم، وموافاة المجلة بشهادة إثبات مراجعة لغوية من قبل الشركة. إذا كانت الورقة باللغة العربية، فإن المراجعة تكون لعنوان الورقة والملخص باللغة الإنجليزية. وإذا كانت الورقة باللغة الإنجليزية، فإن المراجعة تكون على الورقة كاملة. تكون هذه المراجعة اللغوية كمرحلة أخيرة قبل نشر الورقة وبعد إدخال كامل ملاحظات المحكمين والمحررين وهيئة التحرير. أدناه إحدى هذه الشركات والتي تقوم بالمراجعة اللغوية خلال 24 ساعة:
https://proofreadmyessay.co.uk

4. آلية كتابة الدوريات والمجلات في المراجع (يطلب عملها فقط في حالة قبول الورقة للنشر)

4.1. كتابة الدوريات والمجلات العربية في قائمة المراجع

يبدأ كل مرجع باسم العائلة للمؤلف الأول، ثم فاصلة، ثم الاسم الأول واسم الأب للمؤلف الأول، ثم فاصلة، ثم اسم العائلة للمؤلف الثاني، ثم فاصلة، ثم الاسم الأول واسم الأب للمؤلف الثاني، ثم حرف العطف "و" ثم اسم العائلة للمؤلف الثالث، ثم فاصلة، ثم الاسم الأول واسم الأب للمؤلف الثالث، ثم نقطة، ثم فتح قوس، ثم التاريخ، ثم إغلاق القوس، ثم نقطة، ثم عنوان البحث، ثم نقطة، ثم اسم المجلة يكون مكتوبا بشكل مائل، ثم فاصلة، ثم رقم المجلد مكتوبا بشكل عريض، ثم فتح قوس، ثم

يكتب رقم العدد، ثم يغلق القوس، علماً أنه لا يوجد مسافة بين رقم المجلد ورقم العدد، ثم فاصلة، ثم رقم أول صفحة للبحث، ثم علامة "-" ثم رقم آخر صفحة للبحث. (مع مراعاة أن حرف العطف "و" يوضع دائما قبل المؤلف الأخير أيًّا كان عدد المؤلفين). أدناه مثال على ذلك:

الأحمد، محمد عبدالرحمن، العلي، إسماعيل صلاح والصالح، أحمد محمد. (2020). إنجازات جامعة الملك فيصل منذ تأسيسها. *المجلة العلمية لجامعة الملك فيصل: فرع العلوم الإنسانية والإدارية*، **13**(2)، 213-223.

في حالة عدم وجود تاريخ، فتكتب العبارة التالية "د.ت." في مكان التاريخ، سواء في المتن أو المرجع. على سبيل المثال:

الأحمد، محمد عبدالرحمن، العلي، إسماعيل صلاح والصالح، أحمد محمد. (د.ت.). إنجازات جامعة الملك فيصل منذ تأسيسها. *المجلة العلمية لجامعة الملك فيصل: فرع العلوم الإنسانية والإدارية*، **13**(2)، 213-223.

في حالة عدم وجود رقم مجلد، فتكتب العبارة التالية "بدون رقم مجلد" في مكان رقم المجلد. على سبيل المثال:

الأحمد، محمد عبدالرحمن، العلي، إسماعيل صلاح والصالح، أحمد محمد. (2020). إنجازات جامعة الملك فيصل منذ تأسيسها. *المجلة العلمية لجامعة الملك فيصل: فرع العلوم الإنسانية والإدارية*، **بدون رقم مجلد** (2)، 213-223.

في حالة عدم وجود رقم عدد، فتكتب العبارة التالية "بدون رقم عدد" في مكان رقم العدد. على سبيل المثال:

الأحمد، محمد عبدالرحمن، العلي، إسماعيل صلاح والصالح، أحمد محمد. (2020). إنجازات جامعة الملك فيصل منذ تأسيسها. *المجلة العلمية لجامعة الملك فيصل: فرع العلوم الإنسانية والإدارية*، **13**(بدون رقم عدد)، 213-223.

في حالة عدم وجود أرقام صفحات، فتكتب العبارة التالية "بدون أرقام صفحات" في مكان أرقام الصفحات، أو رقم مسلسل البحث في مجلات الأونلاين. على سبيل المثال:

الأحمد، محمد عبدالرحمن، العلي، إسماعيل صلاح والصالح، أحمد محمد. (2020). إنجازات جامعة الملك فيصل منذ تأسيسها. *المجلة العلمية لجامعة الملك فيصل: فرع العلوم الإنسانية والإدارية*، **13**(2)، بدون أرقام صفحات.

4.2. كتابة الدوريات والمجلات الإنجليزية في قائمة المراجع

يبدأ كل مرجع باسم العائلة للمؤلف الأول، ثم فاصلة، ثم الحرف الأول من الاسم الأول للمؤلف الأول، ثم نقطة، ثم الحرف الأول لاسم الأب للمؤلف الأول، ثم نقطة، ثم فاصلة، ثم اسم العائلة للمؤلف الثاني، ثم فاصلة، ثم الحرف الأول من الاسم الأول للمؤلف الثاني، ثم نقطة، ثم الحرف الأول لاسم الأب للمؤلف الثاني، ثم نقطة، ثم حرف العطف "and" (وليس "&") ثم اسم العائلة للمؤلف الثالث، ثم فاصلة، ثم الحرف الأول من الاسم الأول للمؤلف الثالث، ثم نقطة، ثم الحرف الأول لاسم الأب للمؤلف الثالث، ثم نقطة، ثم فتح قوس، ثم التاريخ بالميلادي، ثم إغلاق القوس، ثم نقطة، ثم عنوان البحث بحروف صغيرة (صمول small)، ثم فتح علامة تنصيص واحدة، ثم عنوان البحث بحروف صغيرة (صمول small؛ يستثنى من ذلك الكلمة الأولى وأسماء الأشخاص وأسماء الأماكن وأسماء الجنسيات واللغات والأسابيع والشهور فيبقى الحرف الأول منها بحروف كبيرة، كابتل capital)، ثم إغلاق علامة التنصيص، ثم نقطة، ثم اسم المجلة مترجما (أو مرومن) يكون مكتوبا بشكل مائل والحرف الأول من كل كلمة يكون كبيرا (كابتل capital؛ يستثنى من ذلك أدوات التنكير والتعريف مثل "a" و "an" و "the" وحروف الجر مثل "to" و "of" و "in" وأدوات الربط "and" و "but" و "or" فيبقى الحرف الأول منها بحروف صغيرة، إلا إذا كانوا في بداية اسم المجلة فيكون الحرف الأول منها بحروف كبيرة)، ثم فاصلة، ثم رقم المجلد مكتوبا بشكل عريض، ثم فتح قوس، ثم يكتب رقم العدد، ثم يغلق القوس، علماً أنه لا يوجد مسافة بين رقم المجلد ورقم العدد، ثم رقم أول صفحة للبحث، ثم علامة "-" ثم رقم آخر صفحة للبحث، ثم نقطة، ثم تكتب "[in Arabic]" أدناه مثال على رومنة المرجع العربي:

Al Ahmed, M.A., Al Ali, I.S. and Al Salah, A.M. (2020). Iinjazat jamieat almalik faysal mundh tasisiha 'Achievements of King Faisal University since its foundations'. *The Scientific Journal of King Faisal University: Humanities and Management Sciences*, **13**(2), 213-223. [in Arabic]

في حالة كون المرجع بلغة غير العربية وغير الإنجليزية، وهذه اللغة تستخدم حروف غير إنجليزية، فتتم رومنة العنوان بالطريقة نفسها التي تتم بها رومنة العناوين العربية. ولكن، في حالة كون الدورية بلغة غير العربية وغير الإنجليزية، ولكن هذه اللغة تستخدم الحروف الإنجليزية نفسها، فلا حاجة لرومنة عنوان البحث، ويكتفى بإبقاء العنوان في لغته الأصل ووضع الترجمة في علامة تنصيص. فعلى سبيل المثال، في حالة كون الدورية باللغة

Al Ahmed, K.A., Al Muhammed, S.F. and Al Saleh, A.F. (2020). The history of agriculture in Al Ahsa. *The Scientific Journal of King Faisal University: Humanities and Management Sciences*, **13**(2), 213-222.

في حالة عدم وجود تاريخ، فيكتب "n/a". على سبيل المثال:

Al Ahmed, K.A., Al Muhammed, S.F. and Al Saleh, A.F. (n/a). The history of agriculture in Al Ahsa. *The Scientific Journal of King Faisal University: Humanities and Management Sciences*, **13**(2), 213-222.

في حالة عدم وجود رقم مجلد، فيكتب "n/a". على سبيل المثال:

Al Ahmed, K.A., Al Muhammed, S.F. and Al Saleh, A.F. (2020). The history of agriculture in Al Ahsa. *The Scientific Journal of King Faisal University: Humanities and Management Sciences*, **n/a**(2), 213-222.

في حالة عدم وجود رقم عدد، فيكتب "n/a". على سبيل المثال:

Al Ahmed, K.A., Al Muhammed, S.F. and Al Saleh, A.F. (2020). The history of agriculture in Al Ahsa. *The Scientific Journal of King Faisal University: Humanities and Management Sciences*, **13**(n/a), 213-222.

في حالة عدم وجود أرقام صفحات، فيكتب "n/a". على سبيل المثال:

Al Ahmed, K.A., Al Muhammed, S.F. and Al Saleh, A.F. (2020). The history of agriculture in Al Ahsa. *The Scientific Journal of King Faisal University: Humanities and Management Sciences*, **13**(2), n/a.

4.3. رومنة/ترجمة الدوريات والمجلات غير الإنجليزية في قائمة المراجع

يبدأ كل مرجع باسم العائلة للمؤلف الأول، ثم فاصلة، ثم الحرف الأول من الاسم الأول للمؤلف الأول، ثم نقطة، ثم الحرف الأول لاسم الأب للمؤلف الأول، ثم نقطة، ثم فاصلة، ثم اسم العائلة للمؤلف الثاني، ثم فاصلة، ثم الحرف الأول من الاسم الأول للمؤلف الثاني، ثم نقطة، ثم الحرف الأول لاسم الأب للمؤلف الثاني، ثم نقطة، ثم حرف العطف "and" (وليس "&") ثم اسم العائلة للمؤلف الثالث، ثم فاصلة، ثم الحرف الأول من الاسم الأول للمؤلف الثالث، ثم نقطة، ثم الحرف الأول لاسم الأب للمؤلف الثالث، ثم نقطة، ثم فتح قوس، ثم التاريخ بالميلادي، ثم إغلاق القوس، ثم نقطة، ثم عنوان البحث (مرومن) بحروف صغيرة (صمول small)، ثم فتح علامة تنصيص واحدة، ثم عنوان البحث مترجما بحروف صغيرة (صمول small؛ يستثنى من ذلك الكلمة الأولى وأسماء الأشخاص وأسماء الأماكن وأسماء الجنسيات واللغات والأسابيع والشهور فيبقى الحرف الأول منها بحروف كبيرة، كابتل capital)، ثم إغلاق علامة التنصيص، ثم نقطة، ثم اسم المجلة مترجما (أو مرومن) يكون مكتوبا بشكل مائل والحرف الأول من كل كلمة يكون كبيرا (كابتل capital؛ يستثنى من ذلك أدوات التنكير والتعريف مثل "a" و "an" و "the" وحروف الجر مثل "to" و "of" و "in" وأدوات الربط "and" و "but" و "or" فيبقى الحرف الأول منها بحروف صغيرة، إلا إذا كانوا في بداية اسم المجلة فيكون الحرف الأول منها بحروف كبيرة)، ثم فاصلة، ثم رقم المجلد مكتوبا بشكل عريض، ثم فتح قوس، ثم يكتب رقم العدد، ثم يغلق القوس، علماً أنه لا يوجد مسافة بين رقم المجلد ورقم العدد، ثم فاصلة، ثم رقم أول صفحة للبحث، ثم علامة "-" ثم رقم آخر صفحة للبحث. أدناه مثال على ذلك:

الألمانية، فيبدأ المرجع باسم العائلة للمؤلف الأول، ثم فاصلة، ثم الحرف الأول من الاسم الأول للمؤلف الأول، ثم نقطة، ثم الحرف الأول لاسم الأب للمؤلف الأول، ثم نقطة، ثم فاصلة، ثم اسم العائلة للمؤلف الثاني، ثم فاصلة، ثم الحرف الأول من الاسم الأول للمؤلف الثاني، ثم نقطة، ثم الحرف الأول لاسم الأب للمؤلف الثاني، ثم نقطة، ثم حرف العطف "and" (وليس "&") ثم اسم العائلة للمؤلف الثالث، ثم فاصلة، ثم الحرف الأول من الاسم الأول للمؤلف الثالث، ثم نقطة، ثم الحرف الأول لاسم الأب للمؤلف الثالث، ثم نقطة، ثم فتح قوس، ثم التاريخ بالميلادي، ثم إغلاق القوس، ثم نقطة، ثم عنوان البحث باللغة الألمانية (صمول small)، ثم فتح علامة تنصيص واحدة، ثم عنوان البحث مترجما بحروف صغيرة (صمول small؛ يستثنى من ذلك الكلمة الأولى وأسماء الأشخاص وأسماء الأماكن وأسماء الجنسيات واللغات والأسابيع والشهور فيبقى الحرف الأول منها بحروف كبيرة، كابتل capital)، ثم إغلاق علامة التنصيص، ثم نقطة، ثم اسم المجلة مترجما يكون مكتوبا بشكل مائل والحرف الأول من كل كلمة يكون كبيرا (كابتل capital؛ يستثنى من ذلك أدوات التنكير والتعريف مثل "a" و "an" و "the" وحروف الجر مثل "to" و "of" و "in" وأدوات الربط "and" و "but" و "or" فيبقى الحرف الأول منها بحروف صغيرة، إلا إذا كانوا في بداية اسم المجلة فيكون الحرف الأول منها بحروف كبيرة)، ثم فاصلة، ثم فتح قوس، ثم يكتب رقم العدد، ثم يغلق القوس، علماً أنه لا يوجد مسافة بين رقم المجلد ورقم العدد، ثم رقم أول صفحة للبحث، ثم علامة "-" ثم رقم آخر صفحة للبحث، ثم نقطة، ثم تكتب "[in German]" أدناه مثال على ذلك:

Al Ahmed, M.A., Al Ali, I.S. and Al Salah, A.M. (2020). Erfolge der King Faisal University seit ihrer gründung 'Achievements of King Faisal University since its foundations'. *The Scientific Journal of King Faisal University: Humanities and Management Sciences*, **13**(2), 213-223. [in German]

5. آلية كتابة المؤتمرات والندوات والملتقيات في المراجع (يطلب عملها فقط في حالة قبول الورقة للنشر)

5.1. كتابة المؤتمرات والندوات والملتقيات العربية في قائمة المراجع

يبدأ كل مرجع باسم العائلة للمؤلف الأول، ثم فاصلة، ثم الاسم الأول واسم الأب للمؤلف الأول، ثم فاصلة، ثم اسم العائلة للمؤلف الثاني، ثم فاصلة، ثم الاسم الأول واسم الأب للمؤلف الثاني، ثم حرف العطف "و" ثم اسم العائلة للمؤلف الثالث، ثم فاصلة، ثم الاسم الأول واسم الأب للمؤلف الثالث، ثم نقطة، ثم فتح قوس، ثم التاريخ، ثم إغلاق القوس، ثم نقطة، ثم عنوان البحث، ثم نقطة، ثم يكتب "في:" ثم يكتب اسم المؤتمر بشكل مائل، ثم فاصلة، ثم اسم مكان انعقاد المؤتمر، ثم فاصلة، ثم اسم مدينة المؤتمر، ثم فاصلة، ثم اسم دولة المؤتمر، ثم فاصلة، ثم تاريخ انعقاد المؤتمر، ثم نقطة. (مع مراعاة أن حرف العطف "و" يوضع دائما قبل المؤلف الأخير أيًّا كان عدد المؤلفين). أدناه مثال على ذلك:

الأحمد، محمد عبدالرحمن، العلي، إسماعيل صلاح والصالح، أحمد محمد. (2020). الموهبة في التعليم العالي. في: *الملتقى الوطني الأولى لمنسقي الموهوبين، جامعة الملك فيصل*، الأحساء، المملكة العربية السعودية، 2020/03/05-03.

5.2. كتابة المؤتمرات والندوات والملتقيات الإنجليزية في قائمة المراجع

يبدأ كل مرجع باسم العائلة للمؤلف الأول، ثم فاصلة، ثم الحرف الأول من الاسم الأول للمؤلف الأول، ثم نقطة، ثم الحرف الأول لاسم الأب للمؤلف الأول، ثم نقطة، ثم فاصلة، ثم اسم العائلة للمؤلف الثاني، ثم فاصلة، ثم الحرف الأول من الاسم الأول للمؤلف الثاني، ثم نقطة، ثم الحرف الأول لاسم الأب للمؤلف الثاني، ثم نقطة، ثم حرف العطف "and" (وليس "&") ثم اسم العائلة للمؤلف الثالث، ثم فاصلة، ثم الحرف الأول من الاسم الأول للمؤلف الثالث، ثم نقطة، ثم الحرف الأول لاسم الأب للمؤلف الثالث، ثم نقطة. ثم فتح قوس، ثم التاريخ بالميلادي، ثم إغلاق القوس، ثم نقطة، ثم عنوان البحث بحروف صغيرة (صمول small)، ثم فتح علامة تنصيص واحدة، ثم عنوان البحث مترجما بحروف صغيرة (صمول small؛ يستثنى من ذلك الكلمة الأولى وأسماء الأشخاص وأسماء الأماكن وأسماء الجنسيات واللغات والأسابيع والشهور فيبقى الحرف الأول منها بحروف كبيرة، كابتل capital)، ثم إغلاق علامة التنصيص، ثم نقطة، ثم اسم المجلة مترجما يكون مكتوبا بشكل مائل والحرف الأول من كل كلمة يكون كبيرا (كابتل capital؛ يستثنى من ذلك أدوات التنكير والتعريف مثل "a" و "an" و "the" وحروف الجر مثل "to" و "of" و "in" وأدوات الربط "and" و "but" و "or" فيبقى الحرف الأول منها بحروف صغيرة، إلا إذا كانوا في بداية اسم المجلة فيكون الحرف الأول منها بحروف كبيرة)، ثم فاصلة، ثم اسم مكان المؤتمر، ثم فاصلة، ثم اسم مدينة المؤتمر، ثم فاصلة، ثم اسم دولة المؤتمر، ثم فاصلة، ثم تاريخ انعقاد المؤتمر، ثم نقطة. أدناه مثال على ذلك:

Al Ahmed, K.A., Al Muhammed, S.F. and Al Saleh, A.F. (2020). Giftedness and creativity. In: *The First National Symposium for the Coordinators of the Gifted*, King Faisal University, Al Ahsa, Saudi Arabia, 03-05/03/2020.

5.3. رومنة/ترجمة المؤتمرات والندوات والملتقيات غير الإنجليزية في قائمة المراجع

يبدأ كل مرجع باسم العائلة للمؤلف الأول، ثم فاصلة، ثم الحرف الأول من الاسم الأول للمؤلف الأول، ثم نقطة، ثم الحرف الأول لاسم الأب للمؤلف الأول، ثم نقطة، ثم فاصلة، ثم اسم العائلة للمؤلف الثاني، ثم فاصلة، ثم الحرف الأول من الاسم الأول للمؤلف الثاني، ثم نقطة، ثم الحرف الأول لاسم الأب للمؤلف الثاني، ثم نقطة، ثم حرف العطف "and" ثم اسم العائلة للمؤلف الثالث، ثم فاصلة، ثم الحرف الأول من الاسم الأول للمؤلف الثالث، ثم نقطة، ثم الحرف الأول لاسم الأب للمؤلف الثالث، ثم نقطة. ثم فتح قوس، ثم التاريخ بالميلادي، ثم إغلاق القوس، ثم نقطة، ثم عنوان البحث (مرومن) بحروف صغيرة (صمول small)، ثم فتح علامة تنصيص واحدة، ثم عنوان البحث مترجما بحروف صغيرة (صمول small؛ يستثنى من ذلك الكلمة الأولى وأسماء الأشخاص وأسماء الأماكن وأسماء الجنسيات واللغات والأسابيع والشهور فيبقى الحرف الأول منها بحروف كبيرة، كابتل capital)، ثم إغلاق علامة التنصيص، ثم نقطة، ثم يكتب "In:"، ثم يكتب اسم المؤتمر مترجما (أو مرومن) يكون مكتوبا بشكل مائل والحرف الأول من كل كلمة يكون كبيرا (كابتل capital؛ يستثنى من ذلك أدوات التنكير والتعريف مثل "a" و "an" و "the" وحروف الجر مثل "to" و "of" و "in" وأدوات الربط "and" و "but" و "or" فيبقى الحرف الأول منها بحروف صغيرة، إلا إذا كانوا في بداية اسم المجلة فيكون الحرف الأول منها بحروف كبيرة)، ثم فاصلة، ثم اسم مكان المؤتمر مترجما (أو مرومن)، ثم فاصلة، ثم يكتب اسم مدينة المؤتمر بالإنجليزي، ثم فاصلة، ثم اسم دولة المؤتمر بالإنجليزي، ثم فاصلة، ثم تاريخ انعقاد المؤتمر، ثم نقطة، ثم يكتب "[in Arabic]" أدناه مثال على رومنة المرجع العربي:

Al Ahmed, K.A., Al Muhammed, S.F. and Al Saleh, A.F. (2020). Al'iibdae fi altaelim aleali 'Creativity in higher education'. In: *The First National Symposium for the Coordinators of the Gifted*, King Faisal University, Al Ahsa, Saudi Arabia, 03-05/03/2020. [in Arabic]

في حالة كون المرجع بلغة غير العربية وغير الإنجليزية، وهذه اللغة تستخدم حروف غير إنجليزية، فتتم رومنة العنوان بالطريقة نفسها التي تتم بها رومنة العناوين العربية. أما في حالة كون المرجع بلغة غير العربية وغير الإنجليزية، ولكن هذه اللغة تستخدم الحروف الإنجليزية، فلا حاجة لرومنة عنوان البحث، ويكتفى بإبقاء العنوان في لغته الأصل ووضع الترجمة في علامة تنصيص. فعلى سبيل المثال، في حالة كون المرجع باللغة الفرنسية، فيبدأ المرجع باسم العائلة للمؤلف الأول، ثم فاصلة، ثم الحرف الأول من الاسم الأول للمؤلف الأول، ثم نقطة، ثم الحرف الأول لاسم الأب للمؤلف الأول، ثم نقطة، ثم فاصلة، ثم اسم العائلة للمؤلف الثاني، ثم فاصلة، ثم الحرف الأول من الاسم الأول للمؤلف الثاني، ثم نقطة، ثم الحرف الأول لاسم الأب للمؤلف الثاني، ثم نقطة، ثم حرف العطف "and" ثم اسم العائلة للمؤلف الثالث، ثم فاصلة، ثم الحرف الأول من الاسم الأول للمؤلف الثالث، ثم نقطة، ثم الحرف الأول لاسم الأب للمؤلف

الثالث، ثم نقطة. ثم فتح قوس، ثم التاريخ بالميلادي، ثم إغلاق القوس، ثم نقطة، ثم عنوان البحث باللغة الفرنسية (صمول small)، ثم فتح علامة تنصيص واحدة، ثم عنوان البحث مترجما بحروف صغيرة (صمول small؛ يستثنى من ذلك الكلمة الأولى وأسماء الأشخاص وأسماء الأماكن وأسماء الجنسيات واللغات والأسابيع والشهور فيبقى الحرف الأول منها بحروف كبيرة، كابتل capital)، ثم إغلاق علامة التنصيص، ثم نقطة، ثم يكتب "In:"، ثم يكتب اسم المؤتمر مترجما يكون مكتوبا بشكل مائل والحرف الأول من كل كلمة يكون كبيرا (كابتل capital؛ يستثنى من ذلك أدوات التنكير والتعريف مثل "a" و "an" و "the" وحروف الجر مثل "to" و "of" و "in" وأدوات الربط "and" و "but" و "or" فيبقى الحرف الأول منها بحروف صغيرة، إلا إذا كانوا في بداية اسم المجلة فيكون الحرف الأول منها بحروف كبيرة)، ثم فاصلة، ثم اسم مكان المؤتمر مترجما، ثم فاصلة، ثم يكتب اسم مدينة المؤتمر بالإنجليزي، ثم فاصلة، ثم اسم دولة المؤتمر بالإنجليزي، ثم فاصلة، ثم تاريخ انعقاد المؤتمر، ثم نقطة، ثم يكتب "[in French]". أدناه مثال على رومنة المرجع الفرنسي:

Al Ahmed, K.A., Al Muhammed, S.F. and Al Saleh, A.F. (2020). Créativité dans l'enseignement supérieur 'Creativity in higher education'. In: *The First National Symposium for the Coordinators of the Gifted*, King Faisal University, Al Ahsa, Saudi Arabia, 03-05/03/2020. [in French]

6. آلية كتابة الكتب في قائمة المراجع (يطلب عملها فقط في حالة قبول الورقة للنشر)

ملاحظات:

- إذا كانت طبعة الكتاب هي الطبعة الأولى، فلا يكتب أي شيء بخصوص رقم الطبعة.
- تصاغ مراجع التقارير والدراسات الصادرة عن وزارات ومؤسسات حكومية وغير حكومية بالطريقة نفسها التي تصاغ بها الكتب.

6.1. كتابة الكتب العربية في قائمة المراجع

يبدأ كل مرجع باسم العائلة للمؤلف الأول، ثم فاصلة، ثم الاسم الأول واسم الأب للمؤلف الأول، ثم فاصلة، ثم اسم العائلة للمؤلف الثاني، ثم فاصلة، ثم الاسم الأول واسم الأب للمؤلف الثاني، ثم حرف العطف "و" ثم اسم العائلة للمؤلف الثالث، ثم فاصلة، ثم الاسم الأول واسم الأب للمؤلف الثالث، ثم نقطة، ثم فتح قوس، ثم التاريخ، ثم إغلاق القوس، ثم نقطة، ثم عنوان الكتاب بخط مائل، ثم نقطة، ثم اسم مدينة الناشر، ثم فاصلة، ثم اسم دولة الناشر، ثم نقطتين رأسيتين، ثم اسم الناشر. (مع مراعاة أن حرف العطف "و" يوضع دائما قبل المؤلف الأخير أيًا كان عدد المؤلفين). أدناه مثال على ذلك:

الأحمد، محمد عبدالرحمن، العلي، إسماعيل صلاح والصالح، أحمد محمد. (2020). *إنجازات جامعة الملك فيصل منذ تأسيسها*. السعودية: مكتبة جرير.

في حالة وجود رقم طبعة، فيكتب التالي:

الأحمد، محمد عبدالرحمن، العلي، إسماعيل صلاح والصالح، أحمد محمد. (2020). *إنجازات جامعة الملك فيصل منذ تأسيسها*. الطبعة الثانية. الرياض، السعودية: مكتبة جرير.

في حالة كون الكتاب مترجمًا، فيكتب بعد اسم المؤلف: "ترجمة: اسم العائلة، الاسم الأول اسم الأب". أدناه مثال على ذلك:

وايت، جولي. ترجمة: الأحمد، محمد عبدالرحمن، العلي، إسماعيل صلاح والصالح، أحمد محمد. (2020). *إنجازات جامعة الملك فيصل منذ تأسيسها*. الطبعة الثانية. الرياض، السعودية: مكتبة جرير.

في حالة كون الكتاب محققاً، فيكتب بعد اسم المؤلف: "تحقيق: اسم العائلة، الاسم الأول اسم الأب". أدناه مثال على ذلك:

الخالد، محمد. تحقيق: الأحمد، محمد عبدالرحمن. (2020). *إنجازات جامعة الملك فيصل منذ تأسيسها*. الطبعة الثانية. الرياض، السعودية: مكتبة جرير.

6.2. كتابة الكتب الإنجليزية في قائمة المراجع

يبدأ كل مرجع باسم العائلة للمؤلف الأول، ثم فاصلة، ثم الحرف الأول من الاسم الأول للمؤلف الأول، ثم نقطة، ثم الحرف الأول لاسم الأب للمؤلف الأول، ثم نقطة، ثم فاصلة، ثم اسم العائلة للمؤلف الثاني، ثم فاصلة، ثم الحرف الأول من الاسم الأول للمؤلف الثاني، ثم نقطة، ثم الحرف الأول لاسم الأب للمؤلف الثاني، ثم نقطة، ثم حرف العطف "and" (وليس "&") ثم اسم العائلة للمؤلف الثالث، ثم فاصلة، ثم الحرف الأول من الاسم الأول للمؤلف الثالث، ثم نقطة، ثم الحرف الأول لاسم الأب للمؤلف الثالث، ثم نقطة، ثم فتح قوس، ثم التاريخ بالميلادي، ثم إغلاق القوس، ثم نقطة، ثم عنوان الكتاب بحروف مائلة والحرف الأول من كل كلمة يكون كبيرا (كابتل capital؛ يستثنى من ذلك أدوات التنكير والتعريف مثل "a" و "an" و "the" وحروف الجر مثل "to" و "of" و "in" وأدوات الربط "and" و "but" و "or" فيبقى الحرف الأول منها بحروف صغيرة، إلا إذا كانوا في بداية اسم المجلة فيكون الحرف الأول منها بحروف كبيرة)، ثم نقطة، ثم اسم مدينة الناشر، ثم فاصلة، ثم اسم دولة الناشر، ثم نقطتين رأسيتين، ثم اسم الناشر، ثم نقطة. أدناه مثال على ذلك:

Al Ahmed, K.A., Al Muhammed, S.F. and Al Saleh, A.F. (2020). *The History of Agriculture in Al Ahsa*. Saudi Arabia: Jarir Bookstore.

في حالة وجود رقم طبعة، فيكتب التالي:

Al Ahmed, K.A., Al Muhammed, S.F. and Al Saleh, A.F. (2020). *The History of Agriculture in Al Ahsa*. 2nd edition. Riyadh, Saudi Arabia: Jarir Bookstore.

6.3. رومنة/ترجمة الكتب غير الإنجليزية في قائمة المراجع

ملاحظة: عند رومنة/ترجمة مراجع الكتب العربية فإنه لا يكتب اسم المحقق.

يبدأ كل مرجع باسم العائلة للمؤلف الأول، ثم فاصلة، ثم الحرف الأول من الاسم الأول للمؤلف الأول، ثم نقطة، ثم الحرف الأول لاسم الأب للمؤلف الأول، ثم نقطة، ثم فاصلة، ثم اسم العائلة للمؤلف الثاني، ثم فاصلة، ثم الحرف الأول من الاسم الأول للمؤلف الثاني، ثم نقطة، ثم الحرف الأول لاسم الأب للمؤلف الثاني، ثم نقطة، ثم حرف العطف "and" (وليس "&") ثم اسم العائلة للمؤلف الثالث، ثم فاصلة، ثم الحرف الأول من الاسم الأول للمؤلف الثالث، ثم نقطة، ثم الحرف الأول لاسم الأب للمؤلف الثالث، ثم نقطة، ثم فتح قوس، ثم التاريخ بالميلادي، ثم إغلاق القوس، ثم نقطة، ثم عنوان الكتاب (مرومن) بحروف مائلة والحرف الأول من كل كلمة يكون كبيرا (كابتل capital)، ثم فتح علامة تنصيص واحدة، ثم عنوان الكتاب مترجما والحرف الأول من كل كلمة يكون كبيرا (كابتل capital؛ يستثنى من ذلك أدوات التنكير والتعريف مثل "a" و "an" و "the" وحروف الجر مثل "to" و "of" و "in" وأدوات الربط "and" و "but" و "or" فيبقى الحرف الأول منها بحروف صغيرة، إلا إذا كانوا في بداية اسم المجلة فيكون الحرف الأول منها بحروف كبيرة) والكلمة غير مائلة، ثم إغلاق علامة التنصيص، ثم نقطة، ثم اسم مدينة الناشر مترجمة، ثم فاصلة، ثم اسم دولة الناشر مترجمة، ثم نقطتين رأسيتين، ثم اسم الناشر مترجما (أو مرومن)، ثم نقطة، ثم تكتب "[in Arabic]" أدناه مثال على رومنة المرجع العربي:

Al Ahmed, M.A., Al Ali, I.S. and Al Salah, A.M. (2020). *Iinjazat Jamieat Almalik Faysal Mundh Tasisiha* 'Achievements of King Faisal University since its Foundations'. Riyadh, Saudi Arabia: Jarir Bookstore. [in Arabic]

في حالة كون الكتاب بلغة غير العربية وغير الإنجليزية، ولكن هذه اللغة تستخدم حروف غير إنجليزية، فتتم رومنة العنوان بالطريقة نفسها التي تتم بها رومنة العناوين العربية. ولكن، في حالة كون الكتاب بلغة غير العربية وغير الإنجليزية، ولكن هذه اللغة تستخدم الحروف الإنجليزية

نفسها، فلا حاجة لرومنة عنوان الكتاب، ويكتفى بإبقاء العنوان في لغته الأصل ووضع الترجمة في علامة تنصيص. فعلى سبيل المثال، في حالة كون الكتاب باللغة الألمانية، فيبدأ المرجع باسم العائلة للمؤلف الأول، ثم فاصلة، ثم الحرف الأول من الاسم الأول للمؤلف الأول، ثم نقطة، ثم الحرف الأول لاسم الأب للمؤلف الأول، ثم نقطة، ثم فاصلة، ثم اسم العائلة للمؤلف الثاني، ثم فاصلة، ثم الحرف الأول من الاسم الأول للمؤلف الثاني، ثم نقطة، ثم الحرف الأول لاسم الأب للمؤلف الثاني، ثم نقطة، ثم حرف العطف "and" (وليس "&") ثم اسم العائلة للمؤلف الثالث، ثم فاصلة، ثم الحرف الأول من الاسم الأول للمؤلف الثالث، ثم نقطة، ثم الحرف الأول لاسم الأب للمؤلف الثالث، ثم نقطة، ثم فتح قوس، ثم التاريخ بالميلادي، ثم إغلاق القوس، ثم نقطة، ثم عنوان الكتاب باللغة الألمانية بحروف مائلة والحرف الأول من كل كلمة يكون كبيرا (كابتل capital)، ثم فتح علامة تنصيص واحدة، ثم عنوان الكتاب مترجما والحرف الأول من كل كلمة يكون كبيرا (كابتل capital؛ يستثنى من ذلك أدوات التنكير والتعريف مثل "a" و "an" و "the" وحروف الجر مثل "to" و "of" و "in" وأدوات الربط "and" و "but" و "or" فيبقى الحرف الأول منها بحروف صغيرة، إلا إذا كانوا في بداية اسم المجلة فيكون الحرف الأول منها بحروف كبيرة) والكلمة غير مائلة، ثم إغلاق علامة التنصيص، ثم نقطة، ثم اسم مدينة الناشر مترجمة للإنجليزي، ثم فاصلة، ثم اسم دولة الناشر مترجمة للإنجليزي، ثم نقطتين رأسيتين، ثم اسم الناشر مترجما للإنجليزي، ثم نقطة، ثم تكتب "[in German]" أدناه مثال على رومنة المرجع الألماني:

Al Ahmed, M.A., Al Ali, I.S. and Al Salah, A.M. (2020). *Erfolge der King Faisal University seit ihrer Gründung'* Achievements of King Faisal University since its Foundations'. Riyadh, Saudi Arabia: Jarir Bookstore. [in German]

7. آلية كتابة فصل من كتاب في قائمة المراجع (يطلب عملها فقط في حالة قبول الورقة للنشر)

7.1. كتابة فصل في كتاب عربي في قائمة المراجع

يبدأ كل مرجع باسم العائلة للمؤلف الأول، ثم فاصلة، ثم الاسم الأول واسم الأب للمؤلف الأول، ثم فاصلة، ثم اسم العائلة للمؤلف الثاني، ثم فاصلة، ثم الاسم الأول واسم الأب للمؤلف الثاني، ثم حرف العطف "و" ثم اسم العائلة للمؤلف الثالث، ثم فاصلة، ثم الاسم الأول واسم الأب للمؤلف الثالث، ثم نقطة، ثم فتح قوس، ثم التاريخ، ثم إغلاق القوس، ثم نقطة، ثم عنوان الفصل، ثم نقطة، ثم يكتب "في:" ثم يكتب الاسم الأول، ثم اسم الأب، ثم اسم العائلة للمؤلف الأول، ثم فاصلة، ثم يكتب الاسم الأول، ثم اسم الأب، ثم اسم العائلة للمؤلف الثاني، ثم حرف العطف "و"، ثم يكتب الاسم الأول، ثم اسم الأب، ثم اسم العائلة للمؤلف الثالث، ثم يفتح قوس ويكتب "محررون" (أو محرر إذا كان مفردا)، ثم يغلق القوس، ثم اسم الكتاب بخط مائل، ثم نقطة، ثم اسم مدينة الناشر، ثم فاصلة، ثم اسم دولة الناشر، ثم نقطتين رأسيتين، ثم اسم الناشر. (مع مراعاة أن حرف العطف "و" يوضع دائما قبل المؤلف الأخير أيًّا كان عدد المؤلفين). أدناه مثال على ذلك:

الأحمد، محمد عبدالرحمن، العلي، إسماعيل صلاح والصالح، أحمد محمد. (2020). الموهبة في التعليم العالي. في: محمد الصالح، إبراهيم العبدالرحمن وصلاح الخالد (محررون) *الإبداع في العالم العربي*. الرياض، السعودية: مكتبة العبيكان.

7.2. كتابة فصل في كتاب إنجليزي في قائمة المراجع

يبدأ كل مرجع باسم العائلة للمؤلف الأول، ثم فاصلة، ثم الحرف الأول من الاسم الأول للمؤلف الأول، ثم نقطة، ثم الحرف الأول لاسم الأب للمؤلف الأول، ثم نقطة، ثم فاصلة، ثم اسم العائلة للمؤلف الثاني، ثم فاصلة، ثم الحرف الأول من الاسم الأول للمؤلف الثاني، ثم نقطة، ثم الحرف الأول لاسم الأب للمؤلف الثاني، ثم نقطة، ثم حرف العطف "and" (وليس "&") ثم اسم العائلة للمؤلف الثالث، ثم فاصلة، ثم الحرف الأول من الاسم الأول للمؤلف الثالث، ثم نقطة، ثم الحرف الأول لاسم الأب للمؤلف الثالث، ثم نقطة، ثم فتح قوس، ثم التاريخ بالميلادي، ثم إغلاق القوس، ثم نقطة، ثم عنوان الفصل بحروف صغيرة (صمول small؛ يستثنى من ذلك الكلمة الأولى وأسماء الأشخاص وأسماء الأماكن وأسماء الجنسيات واللغات والأسابيع والشهور فيبقى الحرف الأول منها بحروف كبيرة، كابتل capital)، ثم نقطة، ثم يكتب "In:"، ثم يكتب الحرف الأول من الاسم الأول للمؤلف الأول، ثم نقطة، ثم الحرف الأول لاسم الأب للمؤلف الأول، ثم نقطة، ثم اسم العائلة كاملاً للمؤلف الأول، ، ثم فاصلة، ثم يكتب الحرف الأول من الاسم الأول للمؤلف الثاني، ثم نقطة، ثم الحرف الأول لاسم الأب للمؤلف الثاني، ثم حرف العطف "and" (وليس "&")، ثم يكتب الحرف الأول من الاسم الأول للمؤلف الثالث، ثم نقطة، ثم الحرف الأول لاسم الأب للمؤلف الثالث، ثم نقطة، ثم اسم العائلة كاملاً للمؤلف الثالث، ثم يفتح قوس ويكتب "eds." (أو "ed." إذا كان مفردا)، ثم يغلق القوس، ثم اسم الكتاب بخط مائل والحرف الأول من كل كلمة يكون كبيرا (كابتل capital؛ يستثنى من ذلك أدوات التنكير والتعريف مثل "a" و "an" و "the" وحروف الجر مثل "to" و "of" و "in" وأدوات الربط "and" و "but" و "or" فيبقى الحرف الأول منها بحروف صغيرة، إلا إذا كانوا في بداية اسم المجلة فيكون الحرف الأول منها بحروف كبيرة)، ثم نقطة، ثم اسم مدينة الناشر، ثم فاصلة، ثم اسم دولة الناشر، ثم نقطتين رأسيتين، ثم اسم الناشر. أدناه مثال على ذلك:

Al Ahmed, K.A., Al Muhammed, S.F. and Al Saleh, A.F. (2020). Giftedness and creativity. In: A.E. Al Ibrahim, A.L. Al Salim and R.E. Al Rashid (eds.) *Creativity in the Arab World*. Riyadh, Saudi Arabia: Obeikan Bookstore.

7.3. رومنة/ترجمة فصل في كتاب غير إنجليزي في قائمة المراجع

يبدأ كل مرجع باسم العائلة للمؤلف الأول، ثم فاصلة، ثم الحرف الأول من الاسم الأول للمؤلف الأول، ثم نقطة، ثم الحرف الأول لاسم الأب للمؤلف الأول، ثم نقطة، ثم فاصلة، ثم اسم العائلة للمؤلف الثاني، ثم فاصلة، ثم الحرف الأول من الاسم الأول للمؤلف الثاني، ثم نقطة، ثم الحرف الأول لاسم الأب للمؤلف الثاني، ثم نقطة، ثم حرف العطف "and" (وليس "&") ثم اسم العائلة للمؤلف الثالث، ثم فاصلة، ثم الحرف الأول من الاسم الأول للمؤلف الثالث، ثم نقطة، ثم الحرف الأول لاسم الأب للمؤلف الثالث، ثم نقطة، ثم فتح قوس، ثم التاريخ بالميلادي، ثم إغلاق القوس، ثم نقطة، ثم عنوان الفصل (مرومن) بحروف صغيرة (صمول small)، ثم فتح علامة تنصيص واحدة، ثم عنوان الفصل مترجما بحروف صغيرة (صمول small؛ يستثنى من ذلك الكلمة الأولى وأسماء الأشخاص وأسماء الأماكن وأسماء الجنسيات واللغات والأسابيع والشهور فيبقى الحرف الأول منها بحروف كبيرة، كابتل capital)، ثم إغلاق علامة التنصيص، ثم نقطة، ثم يكتب "In:"، ثم يكتب الحرف الأول من الاسم الأول للمؤلف الأول، ثم نقطة، ثم الحرف الأول لاسم الأب للمؤلف الأول، ثم نقطة، ثم اسم العائلة كاملاً للمؤلف الأول، ، ثم فاصلة، ثم يكتب الحرف الأول من الاسم الأول للمؤلف الثاني، ثم نقطة، ثم الحرف الأول لاسم الأب للمؤلف الثاني، ثم نقطة، ثم اسم العائلة كاملاً للمؤلف الثاني، ثم حرف العطف "and" (وليس "&")، ثم يكتب الحرف الأول من الاسم الأول للمؤلف الثالث، ثم نقطة، ثم الحرف الأول لاسم الأب للمؤلف الثالث، ثم نقطة، ثم اسم العائلة كاملاً للمؤلف الثالث، ثم يفتح قوس ويكتب "eds." (أو "ed." إذا كان مفردا)، ثم يغلق القوس، ثم اسم الكتاب (مرومن) بخط مائل والحرف الأول من كل كلمة يكون كبيرا (كابتل capital)، ثم فتح علامة تنصيص واحدة، ثم عنوان الكتاب مترجما والحرف الأول من كل كلمة يكون كبيرا (كابتل capital؛ يستثنى من ذلك أدوات التنكير والتعريف مثل "a" و "an" و "the" وحروف الجر مثل "to" و "of" و "in" وأدوات الربط "and" و "but" و "or" فيبقى الحرف الأول منها بحروف صغيرة، إلا إذا كانوا في بداية اسم المجلة فيكون الحرف الأول منها بحروف كبيرة)، ثم نقطة، ثم اسم مدينة الناشر مترجمة، ثم فاصلة، ثم اسم دولة الناشر مترجما، ثم نقطتين رأسيتين، ثم اسم الناشر مترجما (أو مرومن)، ثم نقطة، ثم تكتب "[in Arabic]" أدناه مثال على رومنة المرجع العربي:

Al Ahmed, K.A., Al Muhammed, S.F. and Al Saleh, A.F. (2020). Al'iibdae fi altaelim aleali 'Creativity in higher education'. In: M. Al Saleh, I. Al

Abdulrahman and S. Al Khalid (eds.) *Al'iibdae Fi Alealam Alearabii'* Creativity in the Arab World'. Riyadh, Saudi Arabia: Obeikan Bookstore. [in Arabic]

في حالة كون الفصل بلغة غير العربية وغير الإنجليزية، ولكن هذه اللغة تستخدم حروف غير إنجليزية، فتتم رومنة العنوان بالطريقة نفسها التي تتم بها رومنة العناوين العربية. ولكن، في حالة كون الفصل بلغة غير العربية وغير الإنجليزية، ولكن هذه اللغة تستخدم الحروف الإنجليزية نفسها، فلا حاجة لرومنة عنوان الفصل والكتاب، ويكتفى بإبقاء العنوان في لغته الأصل ووضع الترجمة في علامة تنصيص. فعلى سبيل المثال، في حالة كون الفصل باللغة الألمانية، فيبدأ المرجع باسم العائلة للمؤلف الأول، ثم فاصلة، ثم الحرف الأول من الاسم الأول للمؤلف الأول، ثم نقطة، ثم الحرف الأول لاسم الأب للمؤلف الأول، ثم نقطة، ثم فاصلة، ثم اسم العائلة للمؤلف الثاني، ثم فاصلة، ثم الحرف الأول من الاسم الأول للمؤلف الثاني، ثم نقطة، ثم الحرف الأول لاسم الأب للمؤلف الثاني، ثم نقطة، ثم حرف العطف "and" (وليس "&") ثم اسم العائلة للمؤلف الثالث، ثم فاصلة، ثم الحرف الأول من الاسم الأول للمؤلف الثالث، ثم نقطة، ثم الحرف الأول لاسم الأب للمؤلف الثالث، ثم نقطة، ثم فتح قوس، ثم التاريخ بالميلادي، ثم إغلاق القوس، ثم نقطة، ثم فتح علامة تنصيص واحدة، ثم عنوان الفصل مترجما للإنجليزية بحروف صغيرة (صمول small؛ يستثنى من ذلك الكلمة الأولى وأسماء الأشخاص وأسماء الأماكن وأسماء الجنسيات واللغات والأسابيع والشهور فيبقى الحرف الأول منها بحروف كبيرة، كابتل capital)، ثم إغلاق علامة التنصيص، ثم نقطة، ثم يكتب "In:"، ثم يكتب الحرف الأول من الاسم الأول للمؤلف الأول، ثم نقطة، ثم الحرف الأول لاسم الأب للمؤلف الأول، ثم نقطة، ثم اسم العائلة كاملاً للمؤلف الأول، ، ثم فاصلة، ثم يكتب الحرف الأول من الاسم الأول للمؤلف الثاني، ثم نقطة، ثم الحرف الأول لاسم الأب للمؤلف الثاني، ثم نقطة، ثم اسم العائلة كاملاً للمؤلف الثاني، ثم حرف العطف "and" (وليس "&")، ثم يكتب الحرف الأول من الاسم الأول للمؤلف الثالث، ثم نقطة، ثم الحرف الأول لاسم الأب للمؤلف الثالث، ثم نقطة، ثم اسم العائلة كاملاً للمؤلف الثالث، ثم يفتح قوس ويكتب "eds." (أو "ed." إذا كان مفردا)، ثم يغلق القوس، ثم اسم الكتاب باللغة الألمانية بخط مائل والحرف الأول من كل كلمة يكون كبيرا (كابتل capital)، ثم فتح علامة تنصيص واحدة، ثم عنوان الكتاب مترجما للإنجليزية والحرف الأول من كل كلمة يكون كبيرا (كابتل capital؛ يستثنى من ذلك أدوات التنكير والتعريف مثل "a" و "an" و "the" وحروف الجر مثل "to" و "of" و "in" وأدوات الربط "and" و "but" و "or" فيبقى الحرف الأول منها بحروف صغيرة، إلا إذا كانوا في بداية اسم المجلة فيكون الحرف الأول منها بحروف كبيرة)، ثم فتح قوس، ثم اسم مدينة الناشر مترجمة للإنجليزية، ثم فاصلة، ثم اسم دولة الناشر مترجما للإنجليزية، ثم نقطتين رأسيتين، ثم اسم الناشر مترجما للإنجليزية، ثم نقطة، ثم تكتب "[in German]" أدناه مثال على رومنة المرجع الألماني:

Al Ahmed, K.A., Al Muhammed, S.F. and Al Saleh, A.F. (2020). Kreativität in der hochschulbildung 'Creativity in higher education'. In: M. Al Saleh, I. Al Abdulrahman and S. Al Khalid (eds.) *Kreativität in der Arabischen Welt* 'Creativity in the Arab World'. Riyadh, Saudi Arabia: Obeikan Bookstore. [in German]

8. آلية كتابة رسائل الماجستير والدكتوراه في قائمة المراجع (يطلب عملها فقط في حالة قبول الورقة للنشر)

8.1. كتابة رسائل الماجستير والدكتوراه العربية في قائمة المراجع

يبدأ كل مرجع باسم العائلة للمؤلف، ثم فاصلة، ثم الاسم الأول واسم الأب للمؤلف، ثم نقطة، ثم فتح قوس، ثم التاريخ، ثم إغلاق القوس، ثم نقطة، ثم عنوان الرسالة بخط مائل، ثم نقطة، ثم يكتب "رسالة ماجستير" أو "رسالة دكتوراه"، ثم فاصلة، ثم اسم الجامعة، ثم فاصلة، ثم اسم المدينة، ثم فاصلة، ثم اسم الدولة، ثم نقطة. أدناه مثال على ذلك:

الأحمد، محمد عبدالرحمن. (2020). *تأملات في الإبداع*. رسالة دكتوراه، جامعة الملك فيصل، الأحساء، السعودية.

8.2. كتابة رسائل الماجستير والدكتوراه الإنجليزية في قائمة المراجع

يبدأ كل مرجع باسم العائلة للمؤلف، ثم فاصلة، ثم الحرف الأول من الاسم الأول للمؤلف، ثم نقطة، ثم الحرف الأول لاسم الأب للمؤلف، ثم نقطة، ثم فتح قوس، ثم التاريخ بالميلادي، ثم إغلاق القوس، ثم نقطة، ثم عنوان الرسالة بحروف مائلة والحرف الأول من كل كلمة يكون كبيرا (كابتل capital؛ يستثنى من ذلك أدوات التنكير والتعريف مثل "a" و "an" و "the" وحروف الجر مثل "to" و "of" و "in" وأدوات الربط "and" و "but" و "or" فيبقى الحرف الأول منها بحروف صغيرة، إلا إذا كانوا في بداية اسم المجلة فيكون الحرف الأول منها بحروف كبيرة)، ثم نقطة، ثم يكتب " Master's Dissertation" إذا كانت رسالة ماجستير أو "PhD Thesis" إذا كانت رسالة دكتوراه، ثم فاصلة، ثم اسم الجامعة، ثم فاصلة، ثم اسم المدينة، ثم فاصلة، ثم اسم الدولة، ثم نقطة. أدناه مثال على ذلك:

Al Ahmed, K.A. (2020). *The History of Agriculture in Al Ahsa*. PhD Thesis, King Faisal University, Al Ahsa, Saudi Arabia.

8.3. رومنة/ترجمة رسائل الماجستير والدكتوراه غير الإنجليزية في قائمة المراجع

يبدأ كل مرجع باسم العائلة للمؤلف الأول، ثم فاصلة، ثم الحرف الأول من الاسم الأول للمؤلف الأول، ثم نقطة، ثم الحرف الأول لاسم الأب للمؤلف الأول، ثم نقطة، ثم فتح قوس، ثم التاريخ بالميلادي، ثم إغلاق القوس، ثم نقطة، ثم عنوان الرسالة (مرومن) بحروف مائلة والحرف الأول من كل كلمة يكون كبيرا (كابتل capital)، ثم فتح علامة تنصيص واحدة، ثم عنوان الرسالة مترجما والحرف الأول من كل كلمة يكون كبيرا (كابتل capital؛ يستثنى من ذلك أدوات التنكير والتعريف مثل "a" و "an" و "the" وحروف الجر مثل "to" و "of" و "in" وأدوات الربط "and" و "but" و "or" فيبقى الحرف الأول منها بحروف صغيرة، إلا إذا كانوا في بداية اسم المجلة فيكون الحرف الأول منها بحروف كبيرة) والكلمة غير مائلة، ثم إغلاق علامة التنصيص، ثم نقطة، ثم يكتب "Master's Dissertation" إذا كانت رسالة ماجستير أو "PhD Thesis" إذا كانت رسالة دكتوراه، ثم فاصلة، ثم اسم الجامعة، ثم فاصلة، ثم اسم المدينة، ثم فاصلة، ثم اسم الدولة، ثم نقطة، ثم تكتب "[in Arabic]" أدناه مثال على رومنة المرجع العربي:

Al Ahmed, M.A. (2020). *Tamalat Fi Al'iibdae* 'Reflections on Creativity'. PhD Thesis, King Faisal University, Al Ahsa, Saudi Arabia. [in Arabic]

في حالة كون الرسالة بلغة غير العربية وغير الإنجليزية، ولكن هذه اللغة تستخدم حروف غير إنجليزية، فتتم رومنة العنوان بالطريقة نفسها التي تتم بها رومنة العناوين العربية. ولكن، في حالة كون الرسالة بلغة غير العربية وغير الإنجليزية، ولكن هذه اللغة تستخدم الحروف الإنجليزية نفسها، فلا حاجة لرومنة عنوان الرسالة، ويكتفى بإبقاء العنوان في لغته الأصل ووضع الترجمة في علامة تنصيص. فعلى سبيل المثال، في حالة كون الرسالة باللغة الألمانية، فيبدأ المرجع باسم العائلة للمؤلف الأول، ثم فاصلة، ثم الحرف الأول من الاسم الأول للمؤلف الأول، ثم نقطة، ثم الحرف الأول لاسم الأب للمؤلف الأول، ثم نقطة، ثم فتح قوس، ثم التاريخ بالميلادي، ثم إغلاق القوس، ثم نقطة، ثم عنوان الرسالة باللغة الألمانية بحروف مائلة والحرف الأول من كل كلمة يكون كبيرا (كابتل capital)، ثم فتح علامة تنصيص واحدة، ثم عنوان الرسالة مترجما والحرف الأول من كل كلمة يكون كبيرا (كابتل capital؛ يستثنى من ذلك أدوات التنكير والتعريف مثل "a" و "an" و "the" وحروف الجر مثل "to" و "of" و "in" وأدوات الربط "and" و "but" و "or" فيبقى الحرف الأول منها بحروف صغيرة، إلا إذا كانوا في بداية اسم المجلة فيكون الحرف الأول منها بحروف كبيرة) والكلمة غير مائلة، ثم إغلاق علامة التنصيص، ثم نقطة، ثم يكتب "Master's Dissertation" إذا كانت رسالة ماجستير أو "PhD Thesis" إذا كانت رسالة دكتوراه، ثم فاصلة، ثم اسم الجامعة بالإنجليزي، ثم فاصلة، ثم اسم المدينة بالإنجليزي، ثم فاصلة، ثم اسم الدولة بالإنجليزي، ثم نقطة،

ثم تكتب "[in German]" أدناه مثال على ذلك:

Al Ahmed, M.A. (2020). *Überlegungen zur Kreativität* 'Reflections on Creativity'. PhD Thesis, King Faisal University, Al Ahsa, Saudi Arabia. [in German]

9. آلية كتابة موقع إلكتروني في قائمة المراجع (يطلب عملها فقط في حالة قبول الورقة للنشر)

ملاحظة: المراجع المأخوذة من شبكة المعلومات يلزم فيها كتابة العنوان التفصيلي الذي يفتح الصفحة الخاصة بالمرجع مباشرة وليست الصفحة العامة للموقع. يجب ألا يزيد عدد حروف الرابط عن 120 حرف.

9.1. كتابة موقع إلكتروني عربي في قائمة المراجع

يبدأ كل مرجع باسم العائلة للمؤلف الأول، ثم فاصلة، ثم الاسم الأول واسم الأب للمؤلف الأول، ثم فاصلة، ثم اسم العائلة للمؤلف الثاني، ثم فاصلة، ثم الاسم الأول واسم الأب للمؤلف الثاني، ثم حرف العطف "و" ثم اسم العائلة للمؤلف الثالث، ثم فاصلة، ثم الاسم الأول واسم الأب للمؤلف الثالث، ثم نقطة، ثم فتح قوس، ثم التاريخ، ثم إغلاق القوس، ثم نقطة، ثم العنوان بخط مائل، ثم نقطة، ثم يكتب "متوفر بموقع:" ثم يدرج الرابط، وبعد الرابط يفتح قوس ويكتب "تاريخ الاسترجاع:" ثم يدرج التاريخ على هذه الصيغة "2020/07/27"، ثم يغلق القوس. (مع مراعاة أن حرف العطف "و" يوضع دائما قبل المؤلف الأخير أيًا كان عدد المؤلفين). أدناه مثال على ذلك:

الأحمد، محمد عبدالرحمن، العلي، إسماعيل صلاح والصالح، أحمد محمد. (2020). *إنجازات جامعة الملك فيصل منذ تأسيسها*. متوفر بموقع: https://www.kfu.edu.sa/ar/Departments/Sjournal/Pages/home.aspx (تاريخ الاسترجاع: 2020/07/27)

9.2. كتابة موقع إلكتروني إنجليزي في قائمة المراجع

يبدأ كل مرجع باسم العائلة للمؤلف الأول، ثم فاصلة، ثم الحرف الأول من الاسم الأول للمؤلف الأول، ثم نقطة، ثم الحرف الأول لاسم الأب للمؤلف الأول، ثم نقطة، ثم فاصلة، ثم اسم العائلة للمؤلف الثاني، ثم فاصلة، ثم الحرف الأول من الاسم الأول للمؤلف الثاني، ثم نقطة، ثم الحرف الأول لاسم الأب للمؤلف الثاني، ثم نقطة، ثم حرف العطف "and" (وليس "&") ثم اسم العائلة للمؤلف الثالث، ثم فاصلة، ثم الحرف الأول من الاسم الأول للمؤلف الثالث، ثم نقطة، ثم الحرف الأول لاسم الأب للمؤلف الثالث، ثم نقطة، ثم فتح قوس، ثم التاريخ بالميلادي، ثم إغلاق القوس، ثم نقطة، ثم العنوان بحروف مائلة والحرف الأول من كل كلمة يكون كبيرا (كابتل capital؛ يستثنى من ذلك أدوات التنكير والتعريف مثل "a" و "an" و "the" وحروف الجر مثل "to" و "of" و "in" وأدوات الربط "and" و "but" و "or" فيبقى الحرف الأول منها بحروف صغيرة، إلا إذا كانوا في بداية اسم المجلة فيكون الحرف الأول منها بحروف كبيرة) والكلمة غير مائلة، ثم إغلاق علامة التنصيص، ثم نقطة، ثم يكتب "Available at:" ثم يدرج الرابط، وبعد الرابط يفتح قوس ويكتب "accessed on" ثم يدرج التاريخ على هذه الصيغة "2020/07/27"، ثم يغلق القوس. أدناه مثال على ذلك:

Al Ahmed, K.A., Al Muhammed, S.F. and Al Saleh, A.F. (2020). *The History of Agriculture in Al Ahsa*. Available at: https://www.kfu.edu.sa/ar/Departments/Sjournal/Pages/home.aspx (accessed on 10/12/2020)

9.3. رومنة/ترجمة موقع إلكتروني غير إنجليزي في قائمة المراجع

يبدأ كل مرجع باسم العائلة للمؤلف الأول، ثم فاصلة، ثم الحرف الأول من الاسم الأول للمؤلف الأول، ثم نقطة، ثم الحرف الأول لاسم الأب للمؤلف الأول، ثم نقطة، ثم فاصلة، ثم اسم العائلة للمؤلف الثاني، ثم فاصلة، ثم الحرف الأول من الاسم الأول للمؤلف الثاني، ثم نقطة، ثم الحرف الأول لاسم الأب للمؤلف الثاني، ثم نقطة، ثم حرف العطف "and" (وليس "&") ثم اسم العائلة للمؤلف الثالث، ثم فاصلة، ثم الحرف الأول من الاسم الأول للمؤلف الثالث، ثم نقطة، ثم الحرف الأول لاسم الأب للمؤلف الثالث، ثم نقطة، ثم فتح قوس، ثم التاريخ بالميلادي، ثم إغلاق القوس، ثم نقطة، ثم العنوان (مرومن) بحروف مائلة والحرف الأول من كل كلمة يكون كبيرا (كابتل capital)، ثم فتح علامة تنصيص واحدة، ثم العنوان مترجما والحرف الأول من كل كلمة يكون كبيرا (كابتل capital؛ يستثنى من ذلك أدوات التنكير والتعريف مثل "a" و "an" و "the" وحروف الجر مثل "to" و "of" و "in" وأدوات الربط "and" و "but" و "or" فيبقى الحرف الأول منها بحروف صغيرة، إلا إذا كانوا في بداية اسم المجلة فيكون الحرف الأول منها بحروف كبيرة) والكلمة غير مائلة، ثم إغلاق علامة التنصيص، ثم نقطة، ثم يكتب "Available at:" ثم يدرج الرابط، وبعد الرابط يفتح قوس ويكتب "accessed on" ثم يدرج التاريخ على هذه الصيغة "2020/07/27"، ثم يغلق القوس، ثم تكتب "[in Arabic]". أدناه مثال على رومنة المرجع العربي:

Al Ahmed, M.A., Al Ali, I.S. and Al Salah, A.M. (2020). *Iinjazat Jamieat Almalik Faysal Mundh Tasisiha* 'Achievements of King Faisal University since its Foundations'. Available at: https://www.kfu.edu.sa/ar/Departments/Sjournal/Pages/home.aspx (accessed on 10/12/2020) [in Arabic]

في حالة كون الموقع بلغة غير العربية وغير الإنجليزية، ولكن هذه اللغة تستخدم حروف غير إنجليزية، فتتم رومنة العنوان بالطريقة نفسها التي تتم بها رومنة العناوين العربية. ولكن، في حالة كون الموقع بلغة غير العربية وغير الإنجليزية، ولكن هذه اللغة تستخدم الحروف الإنجليزية نفسها، فلا حاجة لرومنة عنوان الموقع، ويكتفى بإبقاء العنوان في لغته الأصل ووضع الترجمة في علامة تنصيص. فعلى سبيل المثال، في حالة كون الموقع باللغة الألمانية، فيبدأ المرجع باسم العائلة للمؤلف الأول، ثم فاصلة، ثم الحرف الأول من الاسم الأول للمؤلف الأول، ثم نقطة، ثم الحرف الأول لاسم الأب للمؤلف الأول، ثم نقطة، ثم فاصلة، ثم اسم العائلة للمؤلف الثاني، ثم فاصلة، ثم الحرف الأول من الاسم الأول للمؤلف الثاني، ثم نقطة، ثم الحرف الأول لاسم الأب للمؤلف الثاني، ثم نقطة، ثم حرف العطف "and" (وليس "&") ثم اسم العائلة للمؤلف الثالث، ثم فاصلة، ثم الحرف الأول من الاسم الأول للمؤلف الثالث، ثم نقطة، ثم الحرف الأول لاسم الأب للمؤلف الثالث، ثم نقطة، ثم فتح قوس، ثم التاريخ بالميلادي، ثم إغلاق القوس، ثم نقطة، ثم العنوان باللغة الألمانية بحروف مائلة والحرف الأول من كل كلمة يكون كبيرا (كابتل capital)، ثم فتح علامة تنصيص واحدة، ثم العنوان مترجما للإنجليزية والحرف الأول من كل كلمة يكون كبيرا (كابتل capital؛ يستثنى من ذلك أدوات التنكير والتعريف مثل "a" و "an" و "the" وحروف الجر مثل "to" و "of" و "in" وأدوات الربط "and" و "but" و "or" فيبقى الحرف الأول منها بحروف صغيرة، إلا إذا كانوا في بداية اسم المجلة فيكون الحرف الأول منها بحروف كبيرة) والكلمة غير مائلة، ثم إغلاق علامة التنصيص، ثم نقطة، ثم يكتب "Available at:" ثم يدرج الرابط، وبعد الرابط يفتح قوس ويكتب "accessed on" ثم يدرج التاريخ على هذه الصيغة "2020/07/27"، ثم يغلق القوس، ثم تكتب "[in German]". أدناه مثال على ذلك:

Al Ahmed, M.A., Al Ali, I.S. and Al Salah, A.M. (2020). *Erfolge der King Faisal University seit ihrer Gründung* 'Achievements of King Faisal University since its Foundations'. Available at: https://www.kfu.edu.sa/ar/Departments/Sjournal/Pages/home.aspx (accessed on 10/12/2020) [in German]

Generalized Groups	الزمر المعممة
An IoT Based Model for a Trucking Transport System Using Predictive Analytics	An IoT Based Model for a Trucking Transport System Using Predictive Analytics
Study of the Electric Quadrupole Transitions in 50-51Mn Isotopes by Using F742pn and F7cdpn Interactions	F7cdpn و F742pn باستعمال تفاعلات Mnدراسة الانتقالات رباعية القطب الكهربائي في نظائر 50-51
Determining Optimal Conditions of Diacetyl Production Produced by Lactococcus Lactis Bacteria	Lactococcus Lactis تعيين بعض الظروف المثلى لإنتاج ثنائي الأستيل من قبل بكتيريا
Land Use/Land Cover Change Detection in the Baer and Al-Bassit Region, Latakia, Syria, 1972–2018	كشف تغير استعمالات الأراضي/الغطاء الأرضي في منطقة البابر والبسيط، اللاذقية، سورية خلال الفترة 1972-2018
Investigation of Phytochemical and Evaluation of Antioxidant and Antibacterial Activities from Abies Extract	متوفر فقط باللغة الإنجليزية
Effect of Citrus Limon Essential Oil on Lipid Profile and Obesity in Wistar Rats	تأثير الزيت الأساسي لليمون على الدهون والسمنة في فئران ويستار
Vegetation Monitoring in the Saudi Marsh Environment Using Geospatial Technologies	رصد الغطاء النباتي في بيئة السبخات السعودية باستخدام التقنيات الجيومكانية
Synthesis and Characterisation of Structural and Electrical Properties of CuMn2O4 Spinel Compound	متوفر فقط باللغة الإنجليزية
Nice Bases of QTAG-Modules	متوفر فقط باللغة الإنجليزية
Lesions in the Hippocampus and Substantia Nigra of Wistar Rats' Brains Induced by Organophosphate Insecticide	متوفر فقط باللغة الإنجليزية
The Tensor Product of Zero-Divisor Graphs of Variation Monogenic Semigroups	متوفر فقط باللغة الإنجليزية
The Effectiveness of Nanocomposite Films Against Gram-Positive and Gram-Negative Foodborne Pathogenic Bacteria	فعالية أغشية مُتركبة نانوية ضد البكتيريا المُمرضة المنقولة بالأغذية إيجابية الغرام وسلبية الغرام
Human Bocavirus in Children with Respiratory Tract Infection: Molecular and Serological Detection	متوفر فقط باللغة الإنجليزية
Simulation of Surface Plasmon Resonance (SPR) of Silver with Titanium Oxide as a Bi-Layer Biosensor	متوفر فقط باللغة الإنجليزية
A Novel Design of Continuous Culture for In Vitro Formation of Gallstones by Salmonella Typhi	متوفر فقط باللغة الإنجليزية
Global Convergence of Nonlinear Conjugate Gradient Coefficients with Inexact Line Search	متوفر فقط باللغة الإنجليزية
Thermal Behavior Assessment of Natural Stone Buildings in the Semi-Arid Climate	متوفر فقط باللغة الإنجليزية
Comparison of Garlic and Ginger Extract with Glibenclamide on Some Biochemical Standards in Diabetic Mice	مقارنة تأثير مستخلصي الثوم والزنجبيل مع عقار Glibenclamide في بعض المعايير الكيمياحيوية عند الفئران المستحدث فيها داء السكري
Asymmetric Encryption Method Proposed for Arabic Letters Using Artificial Neural Networks	متوفر فقط باللغة الإنجليزية
Impact of Solvents, Magnesium Oxide and Aluminium Oxide Nanoparticles on the Photophysical Properties of Acridine Orange Dye	متوفر فقط باللغة الإنجليزية
Treatment of Turbine Blades via Cr2O3-Ni5%Al System Using Plasma Thermal Spraying	متوفر فقط باللغة الإنجليزية
The Effect of Sweet Lupine Seed Hulls on the Probiotic Viability of Strained Yogurt	متوفر فقط باللغة الإنجليزية
Deep Capsule Network for Facial Emotion Recognition	متوفر فقط باللغة الإنجليزية